The Road to Discovery: Detector Alignment, Electron Identification, Particle Misidentification, WW Physics, and the Discovery of the Higgs Boson

John Alison

a dissertation

in

Physics and Astronomy

Presented to the Faculties of the University of Pennsylvania
in Partial Fulfillment of the Requirements for the Degree of Doctor of Philosophy
2012

I. Joseph Kroll, Professor, Physics
Supervisor of Dissertation

A. T. Charlie Johnson, Professor, Physics
Graduate Group Chairperson

Dissertation Committee
Bhuvnesh Jain, Professor, Physics
I. Joseph Kroll, Professor, Physics
Elliot Lipeles, Assistant Professor, Physics
Burt Ovrut, Professor, Physics
H.H. Williams, Professor, Physics

The Road to Discovery: Detector Alignment, Electron Identification, Particle Misidentification, WW Physics, and the Discovery of the Higgs Boson

To the Penn Army.

To Brig, Elliot, Evelyn and Joe.

To my family and friends.

To Steph.

ABSTRACT

The Road to Discovery: Detector Alignment, Electron Identification, Particle Misidentification, WW Physics, and the Discovery of the Higgs Boson

John Alison

I. Joseph Kroll

The Standard Model of particle physics has been tested by many experiments and describes all observed phenomena up to the highest particle interaction energies. The existence of a scalar particle, the Higgs boson, is central to the theory. The Higgs boson was the only fundamental particle that had not been observed prior to the turn-on of the Large Hadron Collider (LHC). This thesis describes a progression of research that builds to a search for the Higgs boson using the ATLAS detector at the LHC. The search uses the signature of the Higgs boson decaying to a pair of W bosons (WW). Both W bosons are required to decay leptonically into a charged lepton and a neutrino. This signature suffers from many sources of background; the most important are continuum electroweak WW production and the production of single W bosons accompanied by a jet misidentified as a lepton (W+jet background). To understand and quantify these backgrounds, a measurement of the WW cross section has been performed, and analysis techniques have been developed to model the W+jet background. This thesis presents the measurement of the WW cross section using 1.02 fb^{-1} of $\sqrt{s} = 7$ TeV collision data and documents the method for modeling the W+jet background. Understanding the detector is a crucial first step in these analyses. This thesis describes two commissioning activities: detector alignment and prompt electron identification. Detector alignment is needed to accurately reconstruct the trajectory of charged particles in the ATLAS Inner Detector (ID). This thesis documents the alignment of the Transition Radiation

Tracker, a key component of the ID. Charged leptons (electrons and muons) are signatures of many of the most interesting physics processes at hadron colliders, and the efficient and reliable identification of charged leptons is critical to the physics program at ATLAS. This thesis describes work on electron identification used both for real-time selection of interesting events and for physics analysis. Finally, the search for the Higgs boson in the $H \to WW^{(*)} \to l\nu l\nu$ channel is presented using 4.7 fb^{-1} of $\sqrt{s} = 7$ TeV collision data and 5.8 fb^{-1} of $\sqrt{s} = 8$ TeV collision data.

Contents

Abstract v

Contents vi

1 Introduction and Theoretical Background 1

1.1 Standard Model and the Higgs . . . 1

1.2 Standard Model Predictions . . . 5

1.3 The Higgs Boson at the LHC . . . 9

1.4 Conclusion . . . 9

2 The Large Hadron Collider 11

2.1 Overview . . . 11

2.2 The 2010-2012 LHC Data-Sets . . . 12

3 The ATLAS Experiment 15

3.1 Overview . . . 15

3.2 The Inner Detector . . . 17

3.3 The Calorimeter System . . . 19

3.4 The Muon Spectrometer . . . 20

3.5 Conclusion . . . 21

4 Reconstruction and Commissioning 23

4.1 Particle Reconstruction . . . 23

4.2 Trigger . . . 30

4.3 Pile-Up . . . 31

4.4 Commissioning . . . 32

4.5 Conclusion . . . 33

5 Detector Alignment 34

5.1 Introduction to Detector Alignment . . . 34
5.2 Track-Based Alignment . . . 39
5.2.1 Mathematical Formalism . . . 41
5.2.2 Matrix Inversion . . . 43
5.2.3 Weak Modes . . . 45
5.3 Alignment Validation . . . 50
5.4 ATLAS Inner Detector Alignment . . . 51

6 TRT Alignment 61

6.1 TRT Construction . . . 61
6.2 TRT Alignment Levels . . . 65
6.3 L1 Barrel Alignment . . . 69
6.4 L1 End-cap Alignment . . . 71
6.5 L2 Barrel Alignment . . . 74
6.5.1 L2 Barrel Alignment Using TRT Stand-Alone Tracks . . . 74
6.5.2 L2 Barrel Alignment Using Combined ID Tracks . . . 79
6.5.3 Difference in L2 Alignment Constants . . . 80
6.5.4 Barrel A/C Side Differences: "The ϕ Structure" . . . 83
6.6 L2 End-cap Alignment . . . 87
6.6.1 L2 End-cap Alignment with Cosmic-Ray Data . . . 87
6.6.2 L2 End-cap Alignment with Collision Data . . . 88
6.7 Evidence for End-cap Wheel Distortions . . . 91
6.8 Wire-level End-cap Alignment . . . 93
6.9 Wire-level Barrel Alignment . . . 97
6.10 End-cap Alignment along Z . . . 99
6.11 Conclusion . . . 102

7 Electron Identification 105

7.1 Electron Reconstruction. . . . 105
7.2 Discriminating Variables for Electron Identification. . . . 110
7.3 Electron Operating Points . . . 119
7.3.1 The isEM Menu . . . 119

7.3.2 Data-Driven isEM Optimization . . . 121
7.3.3 The isEM++ menu . . . 125
7.3.4 Coping with High Luminosity Running Conditions in the 2012 Data Taking. 128
7.3.5 The Future of Electron Identification . . . 130
7.4 Conclusion . . . 132

8 WW Physics 134
8.1 Introduction and Motivation . . . 134
8.2 Signature and Event Selection . . . 139
8.3 Background Estimation . . . 145
8.3.1 Drell-Yan Background . . . 146
8.3.2 Top Background . . . 148
8.3.3 W+jet Background . . . 149
8.3.4 Di-boson Background . . . 150
8.4 Separating SM WW from $H \to WW^{(*)}$ . . . 151
8.5 Conclusion . . . 155

9 The Fake Factor Method 156
9.1 Introduction . . . 156
9.2 Fake Factor Method . . . 160
9.2.1 Motivation of Fake Factor Method . . . 163
9.3 Application of the Fake Factor Method to Di-Lepton Events . . . 168
9.3.1 Denominator Definitions . . . 169
9.3.2 Fake Factor Measurement . . . 173
9.3.3 Fake Factor Systematics . . . 181
9.3.3.1 Sample Dependence . . . 182
9.3.3.2 Lepton Contamination in the Di-Jet Control Sample . . . 187
9.3.3.3 Pile-Up Uncertainty . . . 188
9.3.3.4 Summary of Fake Factor Systematics. . . . 188
9.3.4 Background Prediction . . . 189
9.3.4.1 Non-Trigger-able W+jet Control Region . . . 193
9.3.4.2 Jet Counting . . . 194
9.3.5 Data-Driven Validation of the Background Modeling . . . 198
9.4 Extension of the Fake Factor Method for Multiple Sources of Background . . . 202
9.4.1 Bias From Multiple Sources of Background . . . 203

9.4.2 Extending the Fake Factors Method to Account for Multiple Sources of Background . . . 205
9.4.3 Bias in Extended Method . . . 209
9.4.4 Application to Electron Heavy-Flavor Fakes . . . 211
9.5 Conclusion . . . 218

10 WW Cross Section Measurement **219**
10.1 Analysis Overview . . . 219
10.2 Data Set and MC Samples . . . 220
10.3 Event Selection . . . 221
10.4 Background Estimation . . . 226
10.4.1 Z/γ^* Background . . . 226
10.4.2 Top Background . . . 228
10.4.3 W+jet Background . . . 229
10.4.4 Di-boson Background . . . 232
10.5 WW acceptance . . . 232
10.6 Results . . . 234
10.7 Conclusion . . . 235

11 Search for $H \to WW^{(*)}$ **236**
11.1 Analysis Overview . . . 236
11.2 Data Sets and MC Samples . . . 238
11.3 Event Selection . . . 240
11.3.1 0-Jet Analysis . . . 243
11.3.2 1-Jet Analysis . . . 247
11.3.3 2-Jet Analysis . . . 251
11.4 Background Estimation . . . 252
11.4.1 Standard Model WW Background . . . 253
11.4.2 Top Background . . . 255
11.4.3 Z/γ^* Background . . . 256
11.4.4 W+jet Background . . . 257
11.4.5 Di-boson Background . . . 260
11.5 Systematics . . . 260
11.6 Statistical Model . . . 263
11.7 Results . . . 264

11.7.1 Results of the 2011 Analysis . . . 264
11.7.2 Results of the 2012 Analysis . . . 266
11.7.3 Combined Results . . . 267
11.8 Conclusion . . . 269

12 Combined Higgs Results **272**
12.1 Overview of other Higgs searches at ATLAS . . . 272
12.1.1 $H \to ZZ^{(*)} \to llll$ . . . 272
12.1.2 $H \to \gamma\gamma$ . . . 275
12.1.3 $H \to WW^{(*)}$ . . . 279
12.2 Higgs Combination . . . 283
12.3 Results . . . 285
12.4 Conclusions . . . 287

A Alignment Toy **290**
A.1 Alignment Procedures. . . . 292
A.1.1 Performance of Alignment. . . . 292
A.2 Study vs nHits. . . . 294
A.3 Study vs resolution. . . . 295
A.4 Study vs phi Spread. . . . 296
A.5 χ^2 minimization. . . . 296

B Fake Factor Derivations **298**
B.1 Calculation of Corrected Fake Factors in the General Case. . . . 298
B.2 Extending the Fake Factor Method to Include Electron Background from W+light-flavor, W+heavy-flavor, and Wγ . . . 300

C Appendix with List of Tables **304**

List of Tables **304**

D Appendix with List of Figures **311**

List of Figures **311**

Bibliography **338**

Preface

In a specialized field such high energy physics it is difficult to present ones work in a way that is useful for other members of the field without being at a level of detail inappropriate for the generally informed, interested reader. Striking this balance of detail is hard, and I have not attempted to do so in this thesis. What I have tried to do is make all parts of the thesis appropriate to someone. By this I mean I have written each section with a particular audience in mind, but that different sections are written for different audiences. The categories of target audience considered are the following:

General Scientist: This is the interested non-physicist. They are familiar with basic techniques of science (histograms, quantitative analysis, etc.) but do not necessarily practice them. They have a general familiarity with physics but not particle physics. This audience is interested in the general ideas and basic concepts of the methods used, not the details.

HEP Graduate Student: This group is familiar with HEP at an introductory graduate student level. They understand basic jargon and are able, and willing, to find more details from the references. They are interested in gaining a better understanding of techniques they have heard about.

HEP Scientist: This is the experienced HEP scientist. They are active in collider physics research but are not acquainted with details of the particular subject. This would be the level of detail appropriate for an approval talk. (If you know what an approval talk is, you count as a HEP Scientist)

Reference: These sections are aimed at HEP scientists familiar with the particular subject and are interested in the details. The audience I have in mind here are HEP experimentalists wanting to repeat the measurement/procedure or physicists that have used similar techniques and want to compare details.

The breakdown of the target audiences of the different sections in the thesis are as follows:

Chapter	Target Audience
1. Introduction	General Scientist
2. LHC	General Scientist
3. Atlas	General Scientist
4. Reconstruction and Commissioning	HEP Graduate Student
5. Alignment	HEP Graduate Student
6. TRT Alignment	Reference
7. Electron Identification	Reference
8. WW Physics	General Scientist
9. Fake Factor Method	Reference
10. WW Cross Section Measurement	HEP Scientist
11. Hww Search	HEP Scientist
12. Combined Higgs Results	General Scientist

There are many good introductions to particle physics. The sections intended for a general audience are not meant to replace these, but rather to motivate the work that follows in a coherent way, omitting much of the detail. I hope the sections aimed at "HEP Graduate Students" provide a unique perspective to these topics from someone that has recently learned the details, and that the "HEP Scientist" sections can serve as a guide to what needs to be done to explain an analysis to ones colleagues, and convince them that it is correct. The reference sections represent most of the original work presented in this thesis. I have attempted to present an overview of these sections, at a more general level, in other places in the text. The general reader should feel free to skip these sections, just as the interested physicist should feel free to skip *to* these sections. My hope is that this modular approach will allow the thesis to be valuable inside the HEP community, while still presenting the research in a meaningful way to those outside the field.

Chapter 1

Introduction and Theoretical Background

The Standard Model of particle physics has been tested by many experiments and has been shown to accurately describe particle interactions at the highest energies produced in the laboratory. The existence of a scalar particle, known as the Higgs boson, is central to the theory. The Higgs boson ("Higgs") breaks electro-weak symmetry and provides mass to the elementary particles. Prior to the turn-on of the LHC, the Higgs was the only fundamental particle in the Standard Model that had not been observed.

The remainder of the chapter is organized as follows: Section 1.1 gives a basic introduction to the Standard Model of particle physics and the role of the Higgs. Section 1.2 describes several tests of the Standard Model and implications for the Higgs. Section 1.3 describes Higgs production at the LHC.

1.1 Standard Model and the Higgs

The Standard Model (SM) [1, 2, 3, 4] is a description of nature in terms of fundamental particles and their interactions. It has been developed over a number of decades, and its development has been guided both by theoretical predictions and experimental discoveries. The SM encompasses three of the four fundamental forces of nature: electromagnetism, the strong interaction and the weak interaction. Apart from gravity, the interactions described by the SM are responsible for all aspects of daily life. Electromagnetism describes the interaction of electrons with nuclei and is thus responsible for all of chemistry and biology. The strong force describes the interactions within the nucleus. The weak force provides a description of radioactivity and nuclear fusion, which powers the stars.

The SM describes nature using a mathematical formalism known as quantum field theory [5]. The fundamental particles are represented by the states of quantized fields. Quarks and leptons

constitute matter and are associated with fields of half integer spin, referred to as "fermion" fields. The dynamics of this system, *i.e.*, the motion and interactions of excitations in the fields, is governed by a mathematical quantity referred to as the Lagrangian.

The SM is a particular type of quantum field theory known as a gauge theory. The Lagrangian of the SM is invariant under space-time dependent continuous internal transformations of the group $SU(3) \times SU(2) \times U(1)$. This invariance is referred to as gauge invariance and is critical for ensuring that the theory is renormalizable. Renormalizability is a necessary form of consistency; theories which are not renormalizable lack predictive power. Additional quantum fields are required to ensure gauge invariance. These fields are have spin one and are referred to as "gauge fields". The excitations of the gauge fields correspond to particles referred to as "gauge bosons". In the standard model twelve gauge fields are included in the Lagrangian, eight for the generators of $SU(3)$, three for the generators of $SU(2)$, and one for the $U(1)$ generator.

In principle, what has been described above is enough to define a theory of particles and their interactions. In fact, the $SU(3)$ gauge symmetry coupled to the quarks correctly describes the strong interaction, with the eight $SU(3)$ gauge fields associated to the different colored states of the gluon. Gluons have been observed experimentally [6, 7] and interact with quarks as predicted in the SM.

A problem arises when considering the part of the SM that describes the electromagnetic and weak interactions, governed by the $SU(2) \times U(1)$ symmetry. To preserve gauge invariance, the gauge fields must be added without mass terms. This implies that the gauge bosons should appear as mass-less particles, as is the case for gluons. However, to properly describe the weak force, the gauge bosons associated to it are required to have a large mass, seemingly in contradiction with the prediction.

The masses of the quarks and leptons pose another problem. The weak interaction violates parity, coupling differently to left and right-handed quark and lepton helicity states. To account for this in the SM, the left and right-handed fermions are treated as different fields with different couplings. A fermion mass term in the Lagrangian would couple these different fields and thus break gauge invariance. A gauge invariant left-handed weak interaction implies that the fermion fields should not have mass terms and that the quarks and leptons which appear in nature should be mass-less particles. This, again, is in direct conflict with observation.

From a theoretical point of view, both of the these problems can be overcome by what is referred to as "spontaneous symmetry breaking" [8, 9, 10, 11, 12, 13]. The idea is that additional quantum fields are added to the theory that couple to the electro-weak $SU(2) \times U(1)$ gauge fields. These fields have zero spin and are referred to as "scalar" fields. The scalar fields are included in a way that respects the $SU(2) \times U(1)$ symmetry and preserves the gauge invariance of the Lagrangian. The

trick is that the scalar fields are added with a special form of interaction such that zero values of the fields do not correspond to the lowest energy state. While the actual interaction in the Lagrangian preserves the $SU(2) \times U(1)$ symmetry, the ground state of the field will necessarily break it. As a result, the Lagrangian preserves gauge invariance, despite the fact that the particular state that describes nature does not exhibit $SU(2) \times U(1)$ symmetry. In this sense the symmetry is said to be "spontaneously broken".

The upshot of the spontaneous symmetry breaking is that in nature the scalar fields will take on a non-zero value, referred to as the "vacuum expectation value", or vev. The vev will couple to the fermion and gauge fields in a way that is equivalent to having mass terms, but nevertheless preserves gauge invariance. As a result, the fermions and weak gauge bosons can appear in nature as massive particles, consistent with observation. The masses of the gauge bosons are set by the vev and by the couplings associated to the gauge symmetry and are thus constrained by the theory. The fermion masses, on the other-hand, depend on arbitrary coupling parameters that must be input to the theory. Through spontaneous symmetry breaking, massive fermions and weak bosons can be accommodated in a gauge invariant way.

The SM as sketched above provides a theory for describing massive fermions interacting via the electromagnetic, the strong, and the parity-violating weak force. The predictions of the SM have been tested over many years, by many different experiments, and have been shown to accurately describe all of the observed data. Focusing on the electro-weak sector, examples of the impressive agreement of SM predictions with observed data are shown in Figures 1.1 and 1.2. Figure 1.1 shows the hadronic cross-section in e^+e^- collisions as a function of the center-of-mass energy [14]. The black curve shows the cross section of electron-positron collisions to fermions prediction by the SM; the points give the measurements from various different experiments. The falling cross-section at low center-of-mass energy and the peak due to Z boson production are accurately described by the SM. The figure also shows the agreement of the observed LEP-II data with the SM prediction for $e^+e^- \to WW$. This process is sensitive to the ZWW coupling, which is a direct consequence of the gauge structure of the theory. Figure 1.2 shows a summary of various SM cross section predictions and their measurements in $\sqrt{s} = 7$ TeV pp collisions at the LHC [15]. An impressive agreement is found over many orders of magnitude.

Another consequence of the spontaneous symmetry breaking is the prediction of a massive scalar particle. The interactions that generate the vev give mass to one of the additional scalar fields. This field should appear in nature as a neutral massive spin-zero boson, referred to as the "Higgs" boson. The mass of the Higgs boson depends on an arbitrary parameter associated to the symmetry breaking and is thus an input to the theory. The interactions of the Higgs boson with the fermions

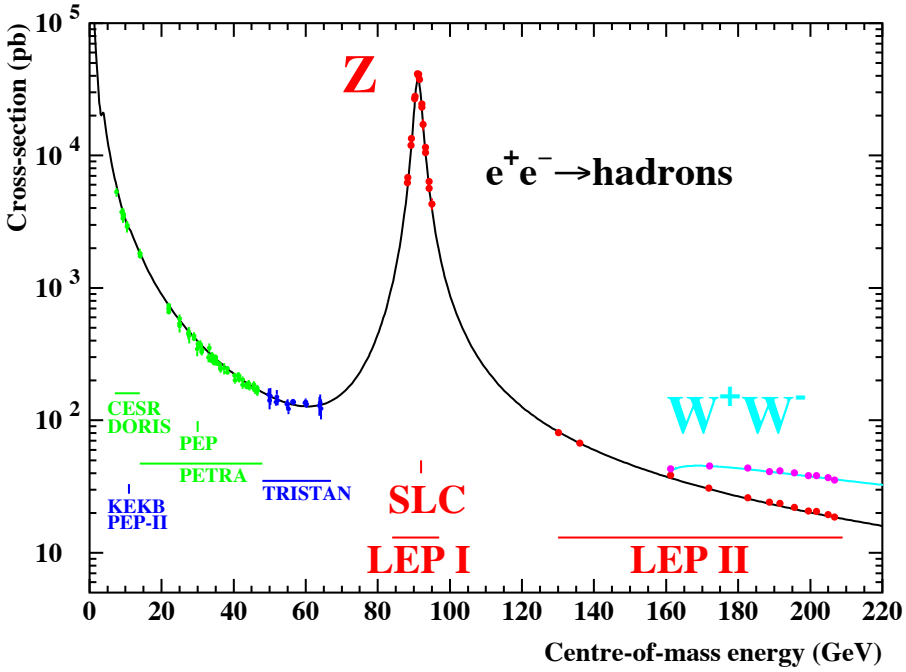

Figure 1.1: The hadronic cross-section in electron-positron collisions as a function of center-of-mass energy. The solid line is the prediction of the SM, and the points are the experimental measurements. Also indicated are the energy ranges of various e^+e^- accelerators. The cross-sections have been corrected for the effects of photon radiation.

and gauge bosons are, however, fixed by the theory. The couplings to gauge bosons are fixed by the gauge couplings, and the couplings to fermions are fixed by the fermion masses; the Higgs boson couples to fermions proportionally to their mass. As of the beginning of the LHC running, the Higgs boson had not been observed experimentally.

As mentioned above, the mass of the Higgs boson is not predicted by the SM. There are no rigorous bounds on the Higgs mass from theory alone [16]. The Higgs must be massive to generate the spontaneous symmetry breaking, and if it is assumed that perturbation theory is valid, the mass of the Higgs should be below about a TeV. The next section will describe constraints on the Higgs mass from measurements of the other electro-weak parameters.

The Higgs boson is a necessary ingredient in the SM for ensuring gauge invariance. Masses for the fermions and gauge bosons are allowed at the price of an additional scalar particle, the Higgs boson. A search for the Higgs bosons at the LHC is the subject of this thesis. The following section describes constraints and experimental limits on the Higgs boson mass prior to 2011.

The SM presented above is the minimal version that spontaneously breaks the electro-weak symmetry. More complex arrangements of scalar fields can be added to the theory. In general,

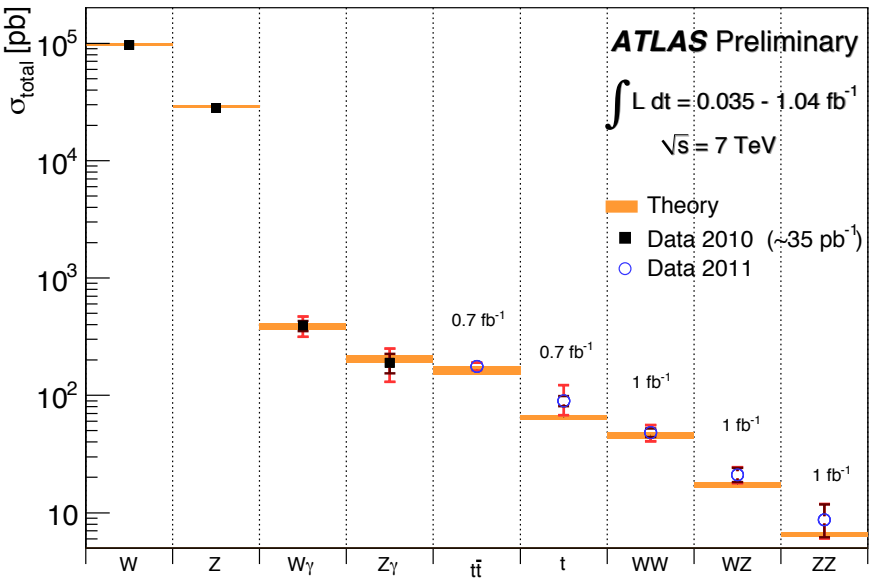

Figure 1.2: Summary of several Standard Model total production cross section measurements compared to the corresponding theoretical expectations. The dark error bar represents the statistical uncertainly. The red error bar represents the full uncertainty, including systematics and luminosity uncertainties. The W and Z vector-boson inclusive cross sections were measured with 35 pb^{-1} of integrated luminosity. All other measurements were performed using the 2011 data-set. The top quark pair production cross-section is based on a statistical combination of measurements in the single-lepton, di-lepton and all-hadronic channels using up to 0.7$fb^{-1}$of data. The single-top measurement uses 0.7$fb^{-1}$of data. The WW and WZ and ZZ measurements were made using 1.02fb^{-1}.

these lead to additional physical particles, but serve the purpose of gauge invariant mass generation. These more complicated extensions are not considered in this thesis. The reader is directed to References [16, 17, 18] for more information.

1.2 Standard Model Predictions

The SM had been established in its current form by 1972. It has predicted many phenomena that were later observed experimentally. The existence of a weak neutral interactions is one consequence of SM. At the time, no such interactions, referred to as "neutral currents", were known. In 1973, the Gargamelle bubble chamber [19] observed weak neutral currents in neutrino scattering.

Another consequence of the SM is the existence of the massive gauge bosons associated to the weak force. The SM gives an unified description of the electromagnetic and weak interactions. As a result, the weak and electromagnetic couplings are related to the masses of the weak gauge

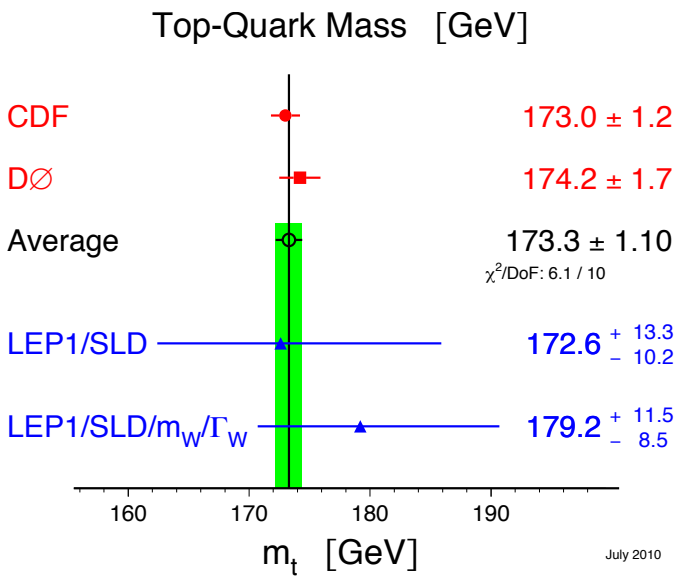

Figure 1.3: Results on the mass of the top quark. The direct measurements of m_t from Run-II of the Tevatron (top) are compared with the indirect SM predictions (bottom)

bosons. Based on the measurements of the electromagnetic coupling, the muon lifetime, and neutral currents, the masses of the W and Z bosons are predicted by the SM. In 1983, the W and Z bosons were discovered by the UA1 and UA2 experiments [20, 21] [22, 23] with masses consistent with the theoretical expectation, another triumph of the SM.

In the 1990s, the LEP [24] and SLC [25] e^+e^- colliders began measuring Z boson parameters with high precision. These measurements were all found to be consistent with SM predictions. Assuming the validity of the SM, these accurate measurements can be used to estimate parameters not directly observable in e^+e^- collisions. Unobserved particles can effect measured quantities through quantum loop corrections. The SM predicts the form of these corrections, so measured quantities can be used to infer properties of the particles participating in the loops.

An example of this type of analysis for the top-quark mass is shown in Figure 1.3. The value of the top mass enters into loop corrections in $e^+e^- \rightarrow b\bar{b}$ events and in the W mass and width. The bottom two points in the figure show the predicted values of the top-quark mass from using measurements of the e^+e^- data (LEP1/SLD) and including direct measurements of the W mass and width (LEP1/SLD/m_W/Γ_W). These predictions are self consistent and agree with direct measurements of the top-quark mass by the CDF and D0 experiments [26, 27, 28], shown in the top of the figure. Before the discovery of the top-quark in 1994, the electro-weak measurements allowed the top-quark mass to be predicted, again showing the power of the SM.

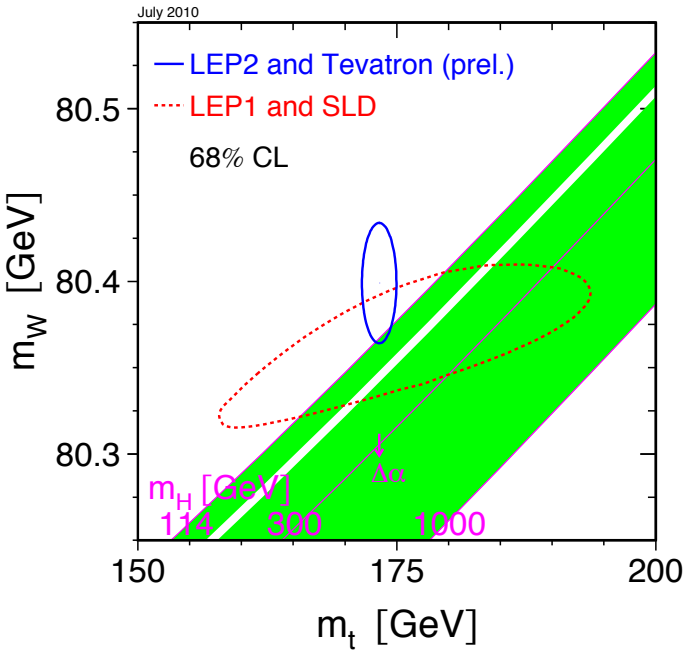

Figure 1.4: The comparison of the indirect constraints on m_W and m_t based on LEP-I/SLD data (dashed contour) and the direct measurements from the LEP-II/Tevatron experiments (solid contour). In both cases the 68% CL contours are given. The shaded band shows the SM relationship for the masses as a function of the Higgs mass. The regions excluded by direct searches, < 114 GeV and 158 GeV $-$ 175 GeV, or disfavored by theory, > 1 TeV, are not shown. The arrow labeled $\Delta\alpha$ shows the variation of this relation with one of the SM parameters. This variation gives an additional uncertainty to the SM band shown in the figure.

Figure 1.4 shows direct and indirect measurements of the top-quark and W masses and their predicted relation. The SM with the LEP/SLC data give the indirect prediction of m_t and m_W shown by the dashed red curve. The direct measurements of the top mass, from the Tevatron, and the W mass, from LEP-II and the Tevatron, are shown in blue. The observed consistency is a critical test of the SM.

Given the consistency seen thus far, this analysis can be repeated, using the top and W masses as inputs, to predict the mass of the Higgs boson. The Higgs boson also contributes to measured quantities through loop corrections. The measured W and top-quark masses are particularly sensitive to the size of the Higgs mass. The shaded band in Figure 1.4, shows the dependence of the Higgs mass on m_W and m_t. The SM can predict the value of Higgs mass, using other measured quantities, even though the Higgs boson has not been observed,

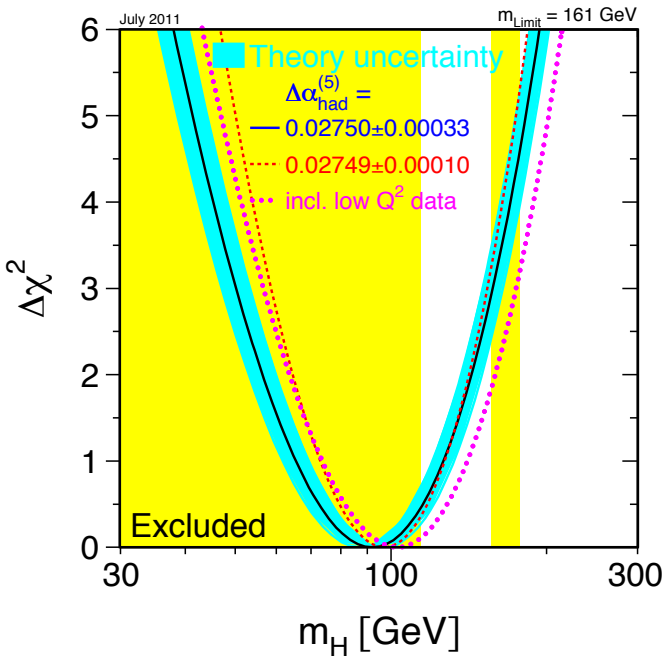

Figure 1.5: Standard Model prediction of the Higgs mass. The line is the result of the fit using data at the Z pole, and the direct determinations of m_t,m_W, Γ_w. The band represents an estimate of the theoretical error due to missing higher order corrections. The vertical band shows the 95% CL exclusion limit on m_h from the direct searches at LEP-II (up to 114 GeV) and the Tevatron (158 to 175 GeV). The dashed curve shows the result of using a different values of $\Delta\alpha^{(5)}_{\rm had}$. The dotted curve corresponds to a fit including lower energy data.

The blue band in Figure 1.5 shows the SM prediction of the Higgs boson mass using all relevant data, as of July 1011 [29]. The minimum value shows the SM best fit, which gives a prediction slightly below 100 GeV. The width of the curve gives the uncertainty associated to the prediction. The yellow areas show the values of Higgs mass excluded by direct searches. As of 2011, the relevant exclusions were from LEP-II [30] and the Tevatron [31, 32, 33]. LEP-II has excluded Higgs boson masses below 114 GeV, and the Tevatron has excluded Higgs boson masses in the range 158-175 GeV. Considering these exclusions, the SM predicts a Higgs boson with mass below ∼160 GeV at the 95% confidence level and below ∼200 GeV at the 99% confidence level [14]. As further discussed in Chapter 8, the SM prediction of the Higgs boson mass guides the analyses presented in this thesis.

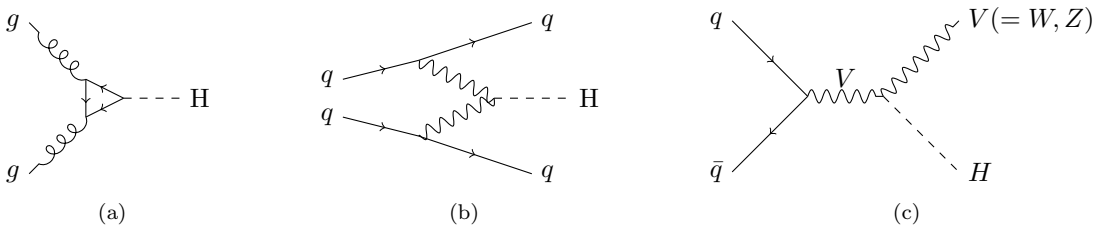

(a) (b) (c)

Figure 1.6: Leading order Feynman diagrams for Higgs production at the LHC. (a) The gluon fusion diagram proceeds via top-quark loop. (b) The vector-boson fusion diagram results in a final state with the Higgs and two jets. (c) The associated production diagram results in a final state with the Higgs and a W or Z boson. The relative size of the cross-sections of the different processes is shown in Figure 1.7.

1.3 The Higgs Boson at the LHC

A primary motivation for the construction of the LHC was to discover or exclude the Higgs boson, or simply "Higgs". One of the main reasons the Higgs has remained elusive is that it couples weakly to ordinary matter. As mentioned above, the Higgs couples to fermions proportionally to their mass. The particles collided in e^+e^- and hadron machines either have relatively small mass, *e.g.,* electrons and first-generation quarks, or do not directly couple to the Higgs, *e.g.,* gluons. As a result, Higgs production is a rare process. However, the large data sets of high energy collisions produced by the LHC will provide sensitivity to Higgs production throughout the relevant mass range.

The important Higgs production diagrams at the LHC are shown in Figure 1.6. The cross sections of these various processes are shown in Figure 1.7, as a function of Higgs mass [34, 35]. The "gluon fusion" process, shown in Figure 1.6a, is the dominant Higgs production mechanism. Gluon fusion is shown, in blue, at the top in Figure 1.7. It has a production cross section of ∼20 pb for m_h= 120 GeV in $\sqrt{s}$ = 7 TeV collisions. Higgs production is orders of magnitude smaller than many electro-weak processes, as can be seen by comparison with Figure 1.2. Searching for this small Higgs signal under the pile of other electro-weak processes is one of the biggest challenges of the Higgs searches presented in this thesis.

1.4 Conclusion

This concludes the basic introduction to the SM and the Higgs boson. The SM provides a theoretically consistent, and experimentally verified, framework for describing the strong and electro-weak forces. The theory predicts the existence of an additional particle, the Higgs boson, which was unobserved before the turn on of the LHC. The work documented in this thesis builds to a search

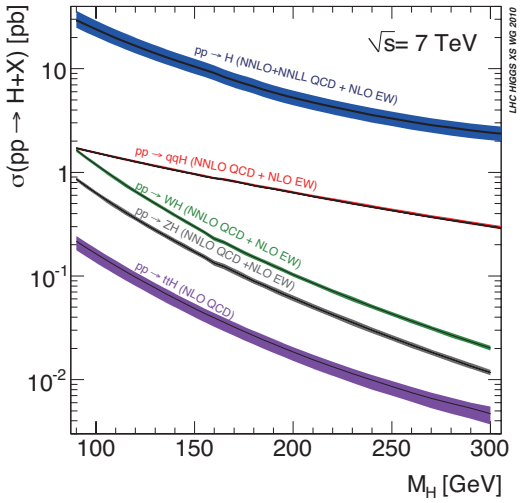

Figure 1.7: Standard Model Higgs boson cross sections for the various production mechanisms shown in Figure 1.6. The process in Figure 1.6a is shown in blue, Figure 1.6b in red, and the processes corresponding to Figure 1.6c are shown in green and black. The lowest band is an additional Higgs production mode not discussed in this thesis.

for, and a discovery of, the Higgs boson. Chapters 2 to 7 describe the experimental inputs and what it takes to be able to use them effectively. Chapter 8 motivates the particular Higgs search strategy employed in this thesis. Chapters 9 and 10 sharpen the analysis tools needed for the search. And finally, Chapters 11 and 12 give the search results and present the discovery of the Higgs boson.

Chapter 2

The Large Hadron Collider

This chapter provides a brief introduction to the Large Hadron Collider (LHC). More information about the design, construction and operation of the LHC can be found in References [36, 37, 38].

The remainder of the chapter is organized as follows: Section 2.1 provides an overview of the LHC and its injection chain. Section 2.2 describes the data sets provided by the LHC for the work in this thesis.

2.1 Overview

The LHC is a super-conducting accelerator and collider installed in a 27 km long circular tunnel that is buried 100 m underground. The LHC is located at the European Organization for Nuclear Research (CERN). It sits across the border of France and Switzerland, near the city of Geneva. A diagram of the LHC is shown in Figure 2.1. The tunnel was originally constructed between 1984 and 1989 for the CERN LEP machine [24]. The LHC collides protons at four locations along the ring of the machine, corresponding to the location of the four LHC experiments: ALICE [39], ATLAS [40], CMS [41], and LHCb [42]. Inside the LHC, beams of protons travel in opposite directions in separate beam pipes. They are guided around the accelerator ring by a strong magnetic field, achieved with super-conducting magnets. The LHC is designed to produce collisions with a center of mass energy of $\sqrt{s} = 14$ TeV.

The LHC is only the final stage is a series of machines used to accelerate the protons to increasingly higher energies. Protons, obtained from hydrogen atoms, begin the chain in a linear accelerator called Linac2. The Linac2 accelerates the protons to 50 MeV. The protons are then injected in to the PS Booster, which accelerates them to 1.4 GeV. After the PS Booster, the protons are sent to the Proton Synchrotron where they are accelerated to 25 GeV. They are then sent to the Super Proton Synchrotron (SPS) where they are accelerated to 450 GeV. They are finally injected into

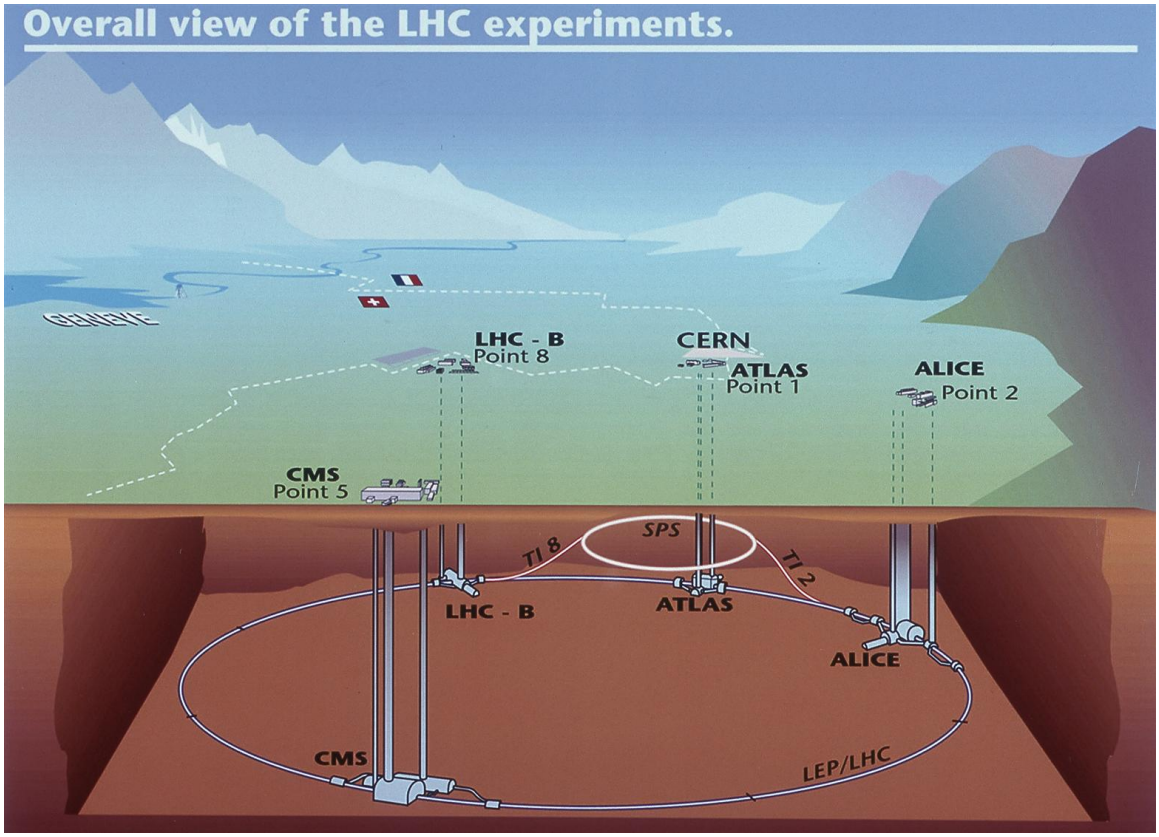

Figure 2.1: Diagram of the locations of the four main experiments (ALICE, ATLAS, CMS and LHCb) at the LHC. Located between 50 m and 150 m underground, huge caverns have been excavated to house the giant detectors. The SPS, the final link in the pre-acceleration chain, and its connection tunnels to the LHC are also shown.

the LHC where they are accelerated to their final energy. Under normal operating conditions, the colliding beams will circulate for many hours at a time.

As a consequence of the acceleration scheme, the proton beams circulate the ring in bunches. Under nominal operating conditions, each proton beam has 2808 bunches, with each bunch containing about 10^{11} protons. These bunches are a few centimeters long and about 16 μm wide when they collide. As a result, each bunch crossing produces many pp interactions. The 2012 running had as many as 30 interactions per bunch crossing.

2.2 The 2010-2012 LHC Data-Sets

From the physics point of view, the most important characteristics of a data-set provided by an accelerator are the energy and luminosity.

The LHC was designed to produce $\sqrt{s} = 14$ TeV collisions. During the initial turn on, in 2008, one of the links between super-conducting magnets failed, or "quenched", leading to an explosion that damaged several other magnets [43]. The source of the unexpected quench was determined to be a faulty solder connection. Problematic connections were found and repaired in several other magnets and additional quench protection was added. Until further repairs could be made it was decided to run the LHC at a reduced energy. In 2010 and 2011, the LHC was operated at 3.5 TeV per beam, producing $\sqrt{s} = 7$ TeV collisions. In 2012, the energy was increased to 4 TeV per beam, producing $\sqrt{s} = 8$ TeV collisions. The LHC will be shut down in 2013-2014 for a series of repairs, after which it is expected to be run at 6.5-7 TeV per beam.

The other important characteristic of the LHC data is the luminosity. The luminosity is proportional to the number of collisions produced by the accelerator. The performance is typically characterized by the "instantaneous" luminosity and the "integrated" luminosity. The instantaneous luminosity is proportional to the rate of collisions. Figure 2.2 shows the instantaneous luminosity of the 2010, 2011, and 2012 data sets [44]. The instantaneous luminosity has increased with time and is nearing the design of 10^{34} cm^{-2} s^{-1} or 10 nb^{-1}s^{-1}. The large number of interactions per bunch crossing is a direct consequence of the conditions required to produce high instantaneous luminosities.

The integrated luminosity, on the other-hand, is proportional to the total number of collisions collected. Figure 2.3 shows the integrated luminosity of the 2010, 2011, and 2012 data sets [44]. The total data set obtained in 2010 was 0.04 fb^{-1}, compared to 5 fb^{-1} collected in 2011, and around 30 fb^{-1} expected by the end of 2012. Large integrated luminosities correspond to large data sets, which allow for the study of rare processes, such as the production of the Higgs boson. The data sets shown in Figure 2.3 are the basis of the work presented in this thesis.

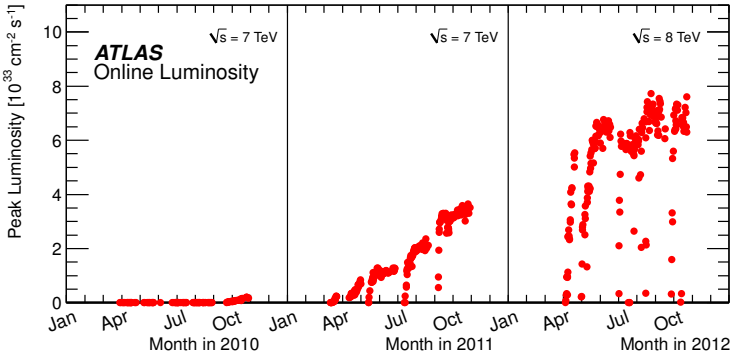

Figure 2.2: The peak instantaneous luminosity delivered to ATLAS per day versus time during the *pp* runs of 2010, 2011 and 2012.

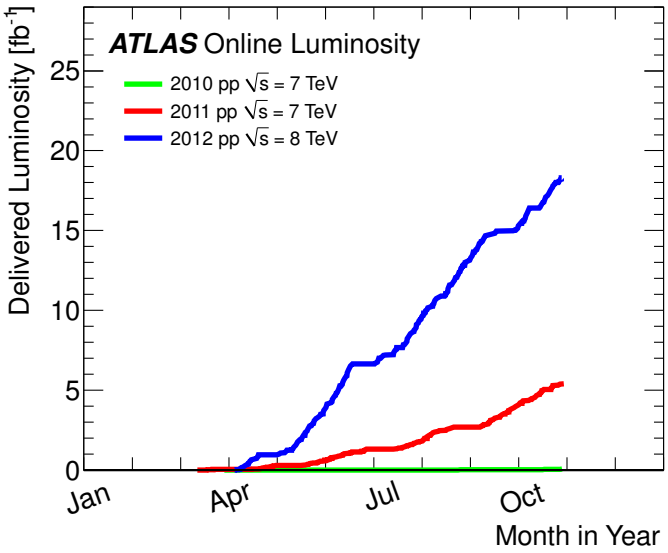

Figure 2.3: Cumulative luminosity versus day delivered to ATLAS during stable beams and for *pp* collisions. This is shown for 2010 (green), 2011 (red) and 2012 (blue) running. The relative amount of data accumulated in 2010 is so small that it does not show up on this scale.

Chapter 3

The ATLAS Experiment

This chapter provides a basic introduction to the ATLAS (**A** **T**oroidal **L**HC **A**pparatu**S**) detector. Focus is given to the detectors used in the work presented in this thesis. More information about the design, construction and operation of the ATLAS detector can be found in References [40, 45, 46, 47, 48].

The remainder of the chapter is organized as follows: Section 3.1 introduces the detector and the conventional coordinate system. Section 3.2 describes the Inner Detector tracking system. Section 3.3 describes the calorimeter system. Section 3.4 describes the Muon Spectrometer.

3.1 Overview

The ATLAS detector is centered on one of the LHC collision points. Shown in Figure 3.1, ATLAS is over 80 feet high and almost 150 feet long. It weighs approximately 7000 tons. ATLAS is built around the LHC beam pipe, 300 feet underground. The beam pipe is centered on the cylindrical axis of symmetry of the detector. Particles produced in the collisions emerge from the center of the detector in all directions. ATLAS has been designed to record the paths and energies of the particles emerging from the collisions.

ATLAS is composed of a series of concentric sub-systems, each sensitive to different types of particles produced in the collisions. The Inner Detector (ID) [49, 50] is closest to the interaction point and measures the trajectories of charged particles. The ID is composed of the Pixel Detector [51, 52], the Semiconductor Tracker (SCT) [53, 54, 55], and the Transition Radiation Tracker (TRT) [56, 57, 58]. The ID operates in a 2 Tesla magnetic field provided by the solenoid magnet [59].

Surrounding the ID is the calorimeter system [60]. The calorimeter system is composed of the liquid argon electromagnetic calorimeters [61], the tile calorimeters [62], the liquid argon hadronic end-cap calorimeters, and the forward calorimeters. These are each indicated in Figure 3.1. The

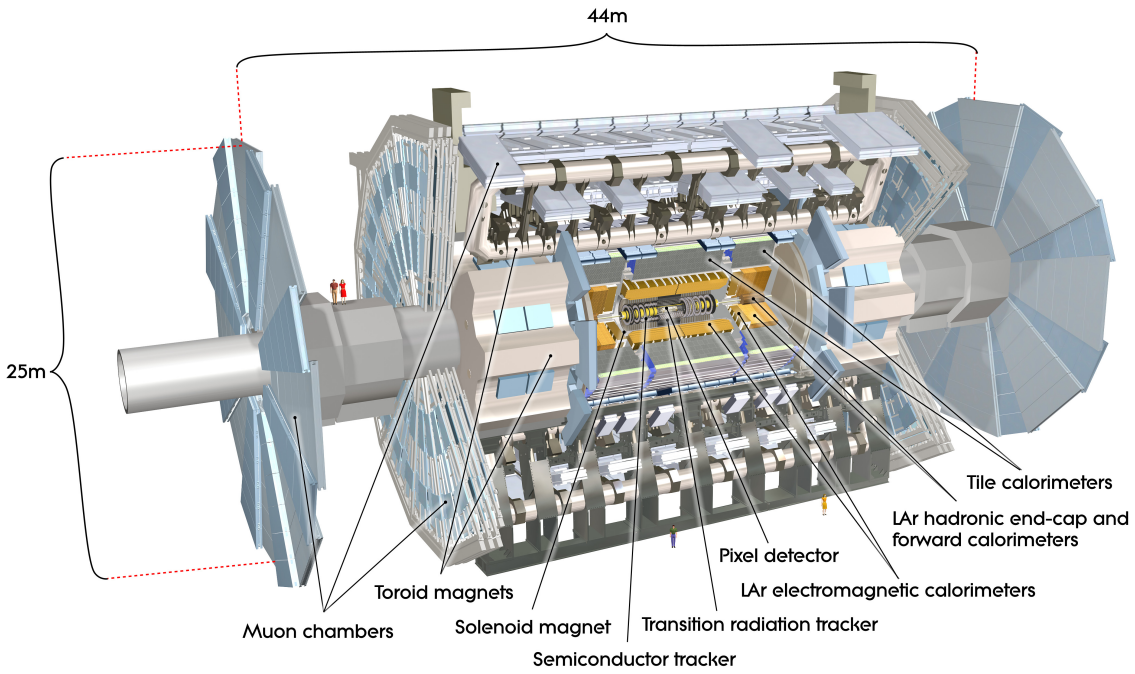

Figure 3.1: Cut-away view of the ATLAS detector.

calorimeters are designed to measure the energy of electrons, photons, and hadrons.

The Muon Spectrometer (MS) [63] surrounds the calorimeters. All particles except muons and neutrinos are stopped by the calorimeter system. The MS is designed to measure the trajectories of muons leaving the calorimeter. The MS is composed of muon chambers operating in a magnetic field, provided by the toroid magnetics [64, 65].

A common coordinate system is used throughout ATLAS. The interaction point is defined as the origin of the coordinate system. The z-axis runs along the beam line. The x-y plane is perpendicular to the beam line and is referred to as the transverse plane. Particle momenta measured in the transverse plane is referred to as the transverse momenta, p_{T}. The positive x-axis points from the interaction point to the center of the LHC ring; the positive y-axis points upward to the surface of the earth. The detector half at positive z-values is referred to as the "A-side", the other half the "C-side". The transverse plane is often described in terms of r-ϕ coordinates. The azimuthal angle ϕ is measured from the x-axis, around the beam. The radial dimension, r, measures the distance from the beam line. The polar angle θ is defined as the angle from the positive z-axis. The polar angle is often reported in terms of pseudorapidity, defined as $\eta = -\ln\tan(\theta/2)$. The distance ΔR is defined in $\eta - \phi$ space as $\Delta R = \sqrt{\Delta\eta^2 + \Delta\phi^2}$.

The remainder of the chapter describes the detector sub-systems important for the work in this thesis in more detail.

3.2 The Inner Detector

The ID measures the position of charged particles as they traverse the detector. In order to cope with the high particle densities produced by the LHC, the ID has been designed to make high-precision measurements with fine detector granularity. The ID operates in a 2 Tesla magnetic field provided by the solenoid magnet. This allows the ID to serve as a spectrometer in which the curved trajectories of charged particles can be reconstructed. Charged particles with transverse momentum above 500 MeV are reconstructed in the ID. Below 500 MeV, charged particles do not cross the full ID.

The ID consists of three sub-detectors built using two technologies: silicon sensors and straw drift tubes. When charged particles cross the silicon sensors, they generate electron-hole pairs that can be collected with an applied electric field. This charge is recorded locally in the sensor, identifying the position of the particle. A similar process occurs in the straw drift tubes. Charged particles traversing the drift tubes ionize gas contained within the straw. The liberated electrons are drifted, with an applied electron field, to the wire at the center of the straw, where they are recorded. Unlike the silicon sensors, in drift tubes, the primary ionization is multiplied before detection. Silicon pixels are used in the Pixel detector, and silicon strips are used in the SCT. Straw drift tubes are used in the TRT.

The ID is composed of modular collections of sensors. It is built around the beam pipe with a cylindrical geometry. The ID consists of central barrel layers, centered on the interaction point, and end-cap wheels or disks at either end of the barrel. Figure 3.2 shows a cut-away of the ID barrel, and Figure 3.3 shows a cut-away of one of the ID end-caps.

The Pixel detector is the closest sub-detector to the interaction point and provides the finest granularity. Comprised of over 80 million channels, the Pixel detector provides on average three measurements per charged particle and has a position resolution of 10 μm in the $r-\phi$ plane and 115 μm along z. The Pixel detector provides uniform coverage in ϕ, up-to $|\eta| = 2.5$.

The SCT surrounds the Pixel detectors. Each SCT layer is composed of a double layer of silicon strips, whose axes are tilted by 40 mrad with respect to one another. The pair of measurements at each SCT layer locates charged particles in $r-\phi$, with an accuracy of 17 μm, and along z, with an accuracy of 580 μm. The SCT provides between four and nine measurements per particle, with coverage up-to $|\eta| = 2.5$. In total, the SCT is comprised of $\sim$6 million channels.

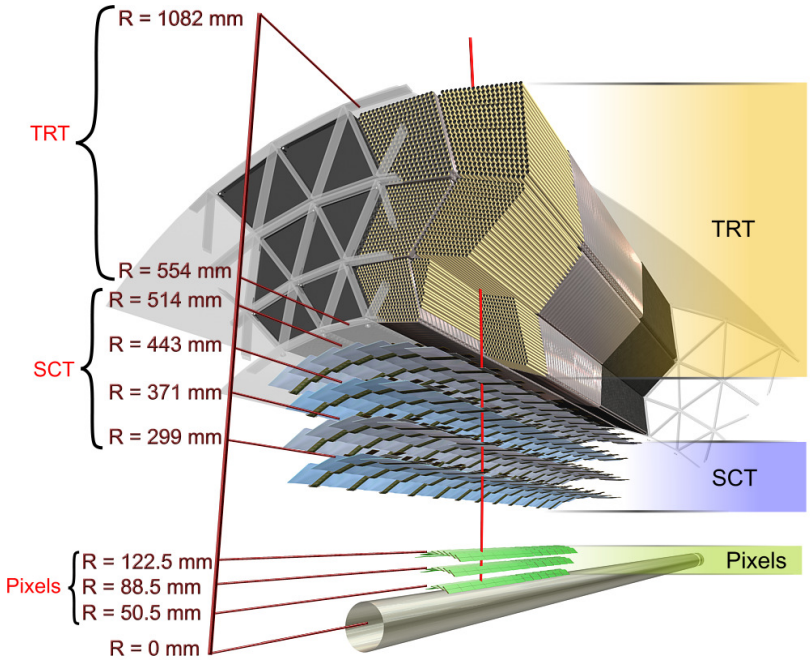

Figure 3.2: Drawing showing the detector elements crossed by a charged particle with 10 GeV p_{T} in the barrel of the Inner Detector. The particle emerges from the interaction point and traverses the beam-pipe, three pixel layers, four double layers of SCT sensors, and around 35 TRT straws.

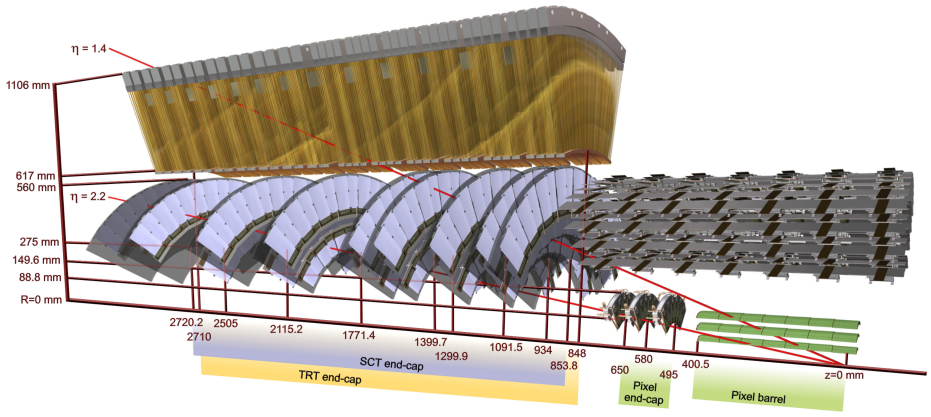

Figure 3.3: Drawing showing the detector elements crossed by two charged particles of 10 GeV p_{T} in the end-cap of the Inner Detector. A particle at $|\eta| = 1.4$ traverses the beam-pipe, three pixel layers, four SCT disks with double layers of sensors, and approximately 40 straws in the TRT end-cap. A particle at $|\eta| = 2.2$ traverses the beam-pipe, only the first layer of the pixel detector, two end-cap pixel disks and the last four disks of the SCT end-cap. The coverage of the end-cap TRT does not extend beyond $|\eta| = 2$.

The TRT is the largest of the sub-detectors in the ID. The TRT is composed of ∼300,000 straw drift tubes that provide position measurements with an accuracy of ∼130 μm in ϕ. A large number of hits, around 35 per particle, is provided, with coverage up to $|\eta| = 2.0$.

In addition to being a tracking detector, the TRT also provides particle identification through the detection of transition radiation. Charged particles emit transition radiation (TR) photons when traversing the TRT. The probability of emitting a TR photon is a function of the Lorentz factor-γ. At a fixed momentum, electrons will emit more transition radiation photons than charged hadrons. The number of TR photons detected in the TRT provides separation between electrons and charged hadrons. Particle identification with the TRT is discussed further in Chapter 7.

3.3 The Calorimeter System

The calorimeter system measures the energy of hadrons, electrons and photons. It provides coverage up-to $|\eta| = 4.9$, using several different technologies. An overview of the calorimeter system is shown in Figure 3.4. The calorimeter system provides containment for both electromagnetic and hadronic showers, stopping particles before they reach the muon system.

The ATLAS calorimeters are a type known as "sampling" calorimeters. Incident particles produce showers of energy in the calorimeter. Only a fraction of the energy produced by the particle is measured by active detector sensors. The energy of the full shower can be inferred from the observed energy.

The energies of electrons and photons are measured by the liquid-argon (LAr) electromagnetic (EM) barrel and end-cap calorimeters. The EM calorimeter is a lead-LAr detector with a specialized geometry that provides complete and uniform ϕ coverage and fast readout. These detectors provide high granularity measurements, critical for particle identification in the range $|\eta| < 2.5$. The EM calorimeter is segmented into three radial sections with different $\eta - \phi$ granularities. Figure 3.5 shows a cut-away of the different layers in the EM barrel calorimeter. The first layer, referred to as the "strips", provides very fine segmentation in η. The strips can separate between showers initiated by electrons or photons and showers initiated by neutral pions. The second sampling provides most of the energy measurement and has fine segmentation in both η and ϕ. The third sampling is coarser and adds additional depth to the calorimeter. The EM calorimeters cover the pseudorapidity range $|\eta| < 3.2$.

The Tile calorimeters and the LAr hadronic end-cap calorimeter are designed to measure the energy of hadrons. The range $|\eta| < 1.7$ is covered by the Tile calorimeter. The scintillator-tile calorimeter is separated into a barrel and two extended barrel cylinders. In the end-caps, $1.5 <$

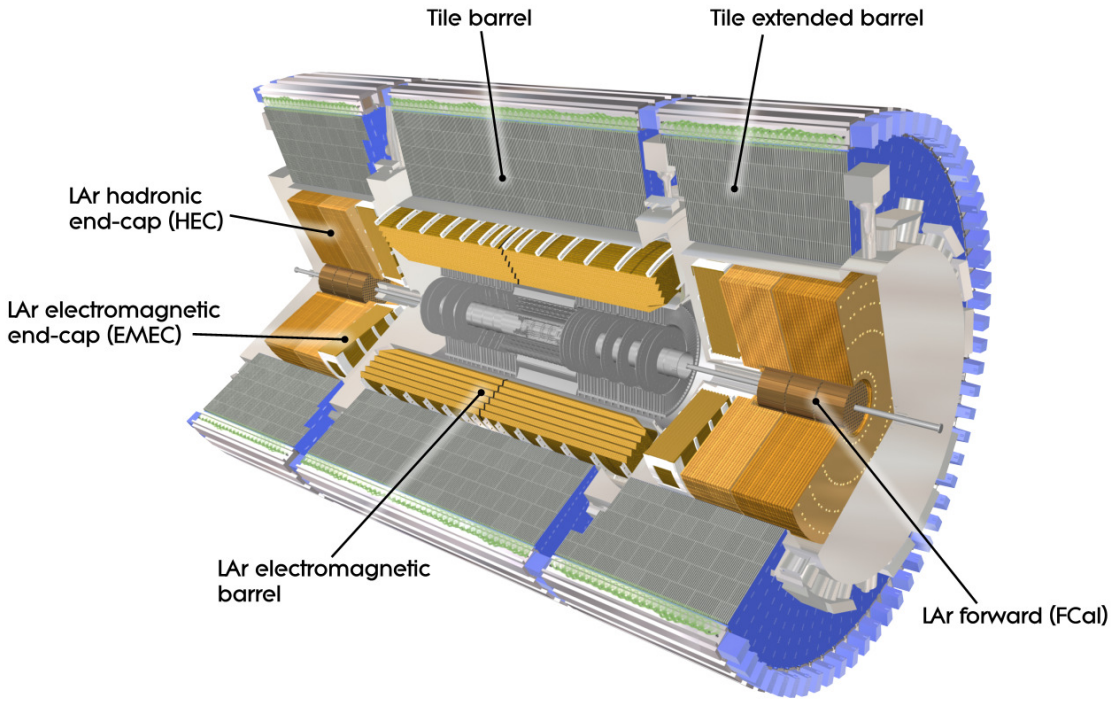

Figure 3.4: Cut-away view of the ATLAS calorimeter system.

$|\eta| < 3.2$, LAr technology is used for the hadronic calorimeters.

The LAr forward calorimeters provide both electromagnetic and hadronic energy measurements and extend the pseudorapidity coverage to $|\eta| = 4.9$.

3.4 The Muon Spectrometer

The calorimeter is surrounded by the muon spectrometer. The MS measures the position of muons as they traverse the detector. The layout of the MS is shown in Figure 3.6. The MS operates in a toroidal magnetic field. Over the range $|\eta| < 1.4$, magnetic bending is provided by the large barrel toroid. For $1.6 < |\eta| < 2.7$, muon tracks are bent by two smaller end-cap magnets inserted into both ends of the barrel toroid. In the region $1.4 < |\eta| < 1.6$, the bending is provided by a combination of the barrel and end-cap fields.

In the barrel region, the positions of the muons are measured in chambers arranged in three cylindrical layers around the beam axis. In the transition and end-cap regions, the chambers are arranged in three planes perpendicular to the beam. Over most of the η-range, the muon positions are measured by Monitored Drift Tubes [66]. In the range $2 < |\eta| < 2.7$, Cathode Strip Chambers [67]

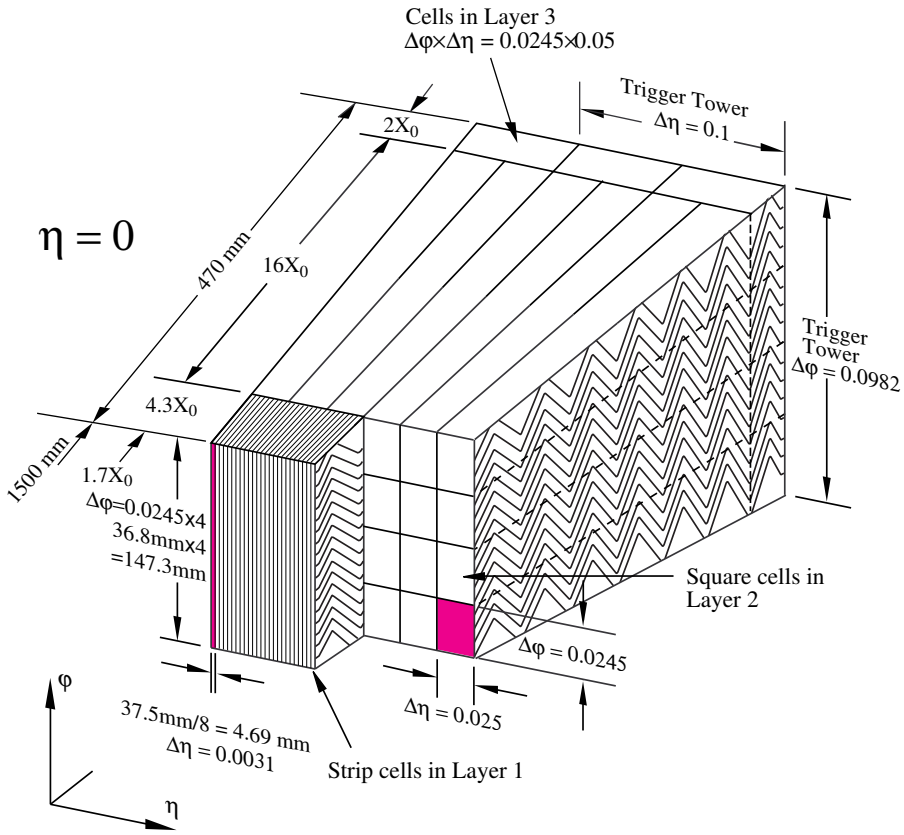

Figure 3.5: Sketch of section of the LAr EM barrel where the different layers are clearly visible. The granularity in η and ϕ of the cells of each of the three layers is shown.

are used.

The muon system includes chambers used in the trigger system described in Chapter 4. The muon trigger chambers cover the pseudorapidity range $|\eta| < 2.4$. Resistive Plate Chambers [68] are used in the barrel and Thin Gap Chambers [69] in the end-cap regions. The trigger chambers provide precise timing and well-defined p_{T} thresholds.

3.5 Conclusion

This chapter introduced the basic components of the ATLAS detector. More specific details are provided in further chapters as needed.

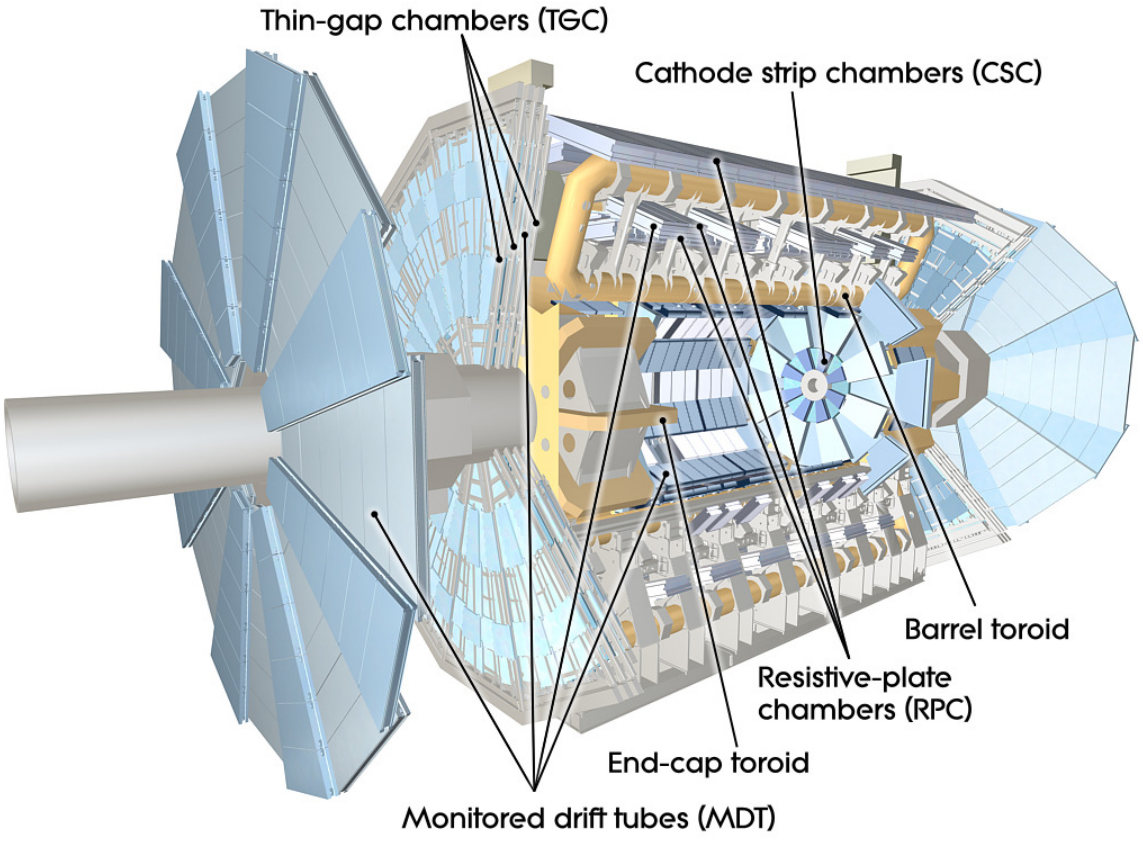

Figure 3.6: Cut-away view of the ATLAS muon system.

Chapter 4

Reconstruction and Commissioning

This chapter describes basic particle reconstruction and identification. The types of commissioning activities required to understand the detector and the performance of the particle reconstruction algorithms, are introduced. Several related concepts used throughout the thesis are also presented. The following chapters expand on the topics introduced here. Chapters 5 and 6 go into detail about a particular aspect of commissioning: detector alignment. Chapter 7 describes the details of electron reconstruction and identification.

The remainder of the chapter is organized as follows: Section 4.1 describes basic particle reconstruction and identification. Section 4.2 introduces the concept of triggering and discusses related issues. Section 4.3 describes pile-up. Section 4.4 introduces the detector commissioning.

4.1 Particle Reconstruction

Particle reconstruction, or simply reconstruction, is a general term that describes the process of converting the basic signals recorded by the detector into collections of measurements associated to particles produced in the collision. The reconstruction is performed by algorithms, implemented in standardized computer software, shared across the experiment. The output of a reconstruction algorithm is a collection of derived measurements corresponding to the properties of a given particle. There are several layers of reconstruction, such that the output of one reconstruction algorithm is often used as an input to another reconstruction algorithm. The ultimate purpose of reconstruction is to produce collection of objects associated to particles that can be used in a physics analyses.

The first level of particle reconstruction described here consists of "track" and "cluster" reconstruction. Reconstructed tracks and clusters are the basic inputs to the higher-level particle reconstruction algorithms. There are actually many levels of reconstruction prior to this stage, which are not described in this thesis. These lower levels convert signals read off of the detector

into measured positions or energies, that are input to track and cluster reconstruction. The reader is directed to References [70, 71, 72] for more information.

Track reconstruction identifies the trajectories of charged particles. These trajectories are referred to as "Tracks"; track reconstruction is also referred to as "Track Finding". A reconstructed track indicates the presence of a charged particle. The origin, direction, and momentum of a charged particle can be determined from its reconstructed track.

Track finding is performed using measurements made by both the Inner Detector (ID) and the Muon Spectrometer (MS). Charged particles traversing these detectors deposit energy, along their path, in the various detector sensors. The collection of sensor measurements, or "hits", from a single charged particle follows the path of the particle through space. Track reconstruction associates hits to individual particles and measures the trajectory from a three-dimensional fit to the position of the hits. Reconstructed tracks are critical for many aspects of particle reconstruction and identification. Details of how track reconstruction is performed in ATLAS can be found in References [70, 72].

Calorimeter clusters are the other basic input to particle reconstruction. Cluster reconstruction groups energies measured in the individual calorimeters cells into clusters of energy associated to incident particles. Electromagnetic and hadronic particles traversing the calorimeter will interact with the detector material and produce a cascade of additional electromagnetic or hadronic particles particles, which in turn interact and produce more particles. Occasionally, particles produced in this cascade will interact with the active material in the calorimeters, producing a signal in the calorimeter cells. Interacting particles incident to the calorimeter thus produce showers of particles whose energy is measured over many different calorimeter cells. Cluster reconstruction associates groups of neighboring cells to individual incident particles and provides a measurement of the initial particle's energy. Electromagnetic particles, *e.g.,* electrons and photons, tend to produce dense narrow showers, predominately contained in the electromagnetic (EM) calorimeter. Hadronically interacting particles, *e.g.,* pions and kaons, will produce broad showers, which penetrate deeply into the hadronic calorimeter. Cluster reconstruction is performed in both the electromagnetic and hadronic calorimeters. Based on the location and the energy density of the cluster, the algorithms can determine if they are predominately electromagnetic or hadronic. Details of how cluster reconstruction is performed in ATLAS can be found in Reference [71].

The remainder of this section describes the higher-level reconstruction of particles produced in the detector. A schematic of the different particle signatures is shown in Figure 4.1. The figure shows a cut-away of the various sub-detectors in ATLAS and the characteristics of the types of particles which traverse the detector. These different types of particles are described below.

One of the most important types of reconstructed particles are charged leptons. Charged leptons

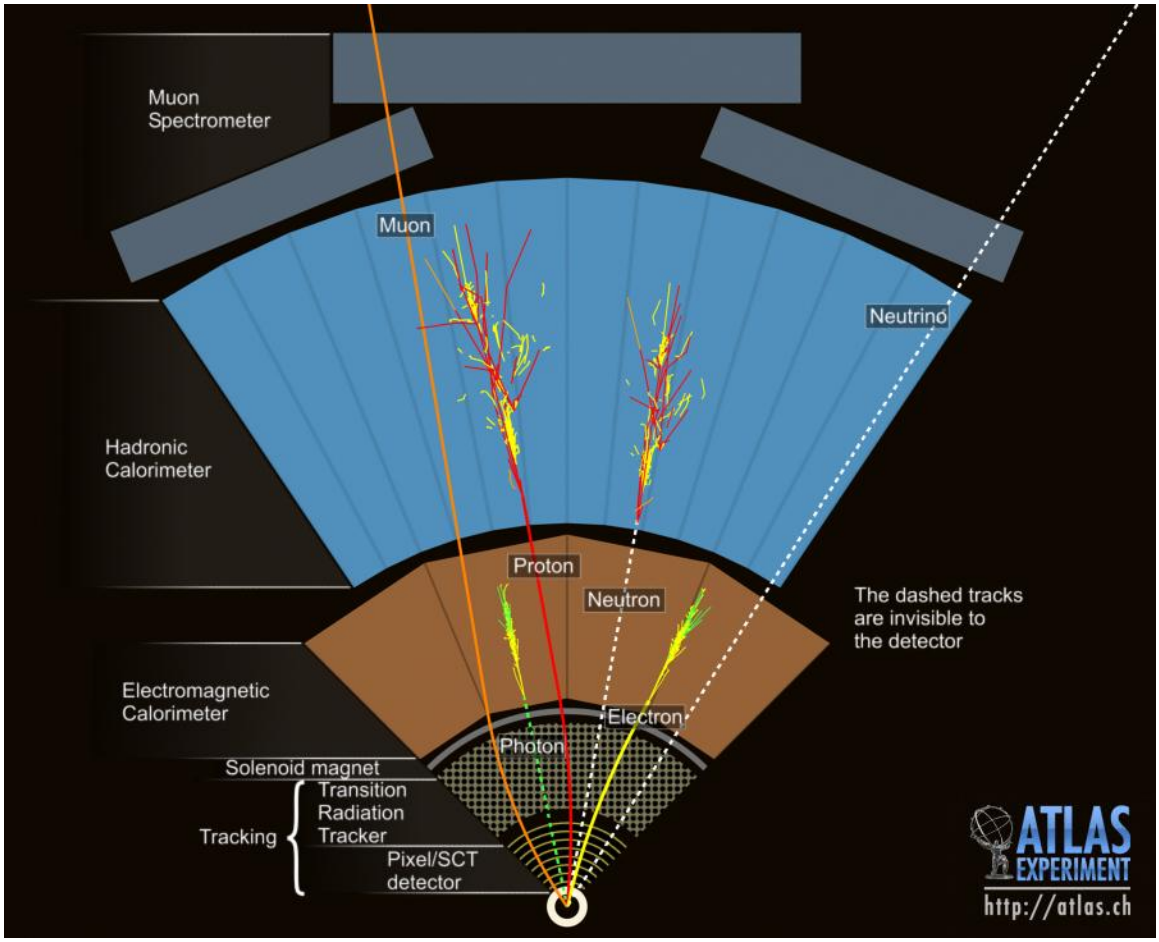

Figure 4.1: Schematic cut-away of the ATLAS detector. The different signatures of particles traversing the detector are shown.

are the signature of electro-weak processes in hadron colliders. They provide clear signals which can be accurately and efficiently reconstructed. Throughout this thesis, charged leptons usually only refers to electrons and muons.

Muons are one of the simplest particles to identify. As indicated in Figure 4.1, muons traverse the entire ATLAS detector. They are reconstructed as tracks in the ID matched to tracks in the MS. Muons leave little energy in the electromagnetic and hadronic calorimeters. Because all of the other interacting particles are stopped before reaching the MS, muons are identified simply by the fact that they made it to the MS. Muons produced from the decays of W and Z bosons tend to have relatively large momentum, above 15 GeV, and are produced in isolation, with little surrounding detector activity. When identifying isolated muons, a requirement is often made that the energy of the reconstructed tracks and clusters near the reconstructed muon not exceed a certain

value. This is referred to as an isolation requirement and is effective at suppressing muons produced from background processes such as meson decay in flight and heavy-flavor decay. As described in Chapter 8, reconstructed muons are critical for the analyses presented in this thesis.

Electrons are the other type of cleanly reconstructed charged leptons. The signature of an electron is shown in Figure 4.1. Electrons leave a track in the ID and initiate an electromagnetic shower in the EM calorimeter; almost all of the energy of the electron is absorbed before reaching the hadronic calorimeter. Electrons are reconstructed by matching reconstructed EM clusters to tracks reconstructed in the ID. This signature suffers from large backgrounds from other types of charged particles. The ATLAS detector provides an effective means of reducing these backgrounds. Like muons, electrons produced from the decays of W and Z bosons are often selected using an isolation criteria. Reconstructed electrons are central to the work presented in this thesis. Chapter 7 presents electron reconstruction and identification in detail.

Tau leptons are also charged leptons. However, from an experimental point of view, they are very different from electrons and muons. Taus are not depicted in Figure 4.1 because they decay into other types of particles before entering the detector. Around 40% of the time, taus decay to electrons or muons plus neutrinos. These decays are indistinguishable from the electron and muon signatures described above. The remainder of the time, taus decay to hadrons and a neutrino. The experimental signatures of these decays are multiple hadronic showers matched to tracks in the ID. This signature suffers from large backgrounds from other types of particles, which cannot be suppressed by experimental techniques as efficiently as backgrounds to electrons or muons. As a result, in the remainder of this thesis only the leptonic tau decays are used.

Neutrinos are also members of the lepton family. However they only interact via the weak force and are thus not directly detected by ATLAS. They are depicted in Figure 4.1 as passing directly through all of the sub-detectors. Although not directly observed, the presence of one or more neutrinos can be inferred from an overall transverse momentum imbalance of the measured energy in the event. This also provides a measurement of the neutrino transverse momentum. As the reconstruction of neutrinos relies on global properties of the entire event, the discussion of neutrino reconstruction is postponed until later in this section.

Photons are another type of particle that can be efficiently reconstructed and identified in ATLAS. As with leptons, photons produced by interesting physics processes are often produced in isolation. There are two experimental signatures of photons, depending on if the photon underwent a conversion into a e^+e^- pair in the detector material before entering the calorimeter. Photons which do not undergo such a conversion are referred to as un-converted. The signature of an un-converted photon is shown in Figure 4.1. Photons are neutral and thus leave no track in the ID.

They produce an electromagnetic shower upon entering the calorimeter. Un-converted photons are reconstructed as EM clusters which have no associated reconstructed track. Photons which undergo a conversion in the detector material are referred to as converted photons. A photon conversion produces oppositely-charged electrons whose tracks form a vertex displaced from the interaction point. Dedicated reconstruction algorithms identify photon conversions from pairs of reconstructed tracks. Details of how photon reconstruction is performed in ATLAS can be found in Reference [73]. For the analyses presented in this thesis, reconstructed converted photons are primarily used to suppress electron background from converted photons.

Jet reconstruction is another critical ingredient for physics analyses. High energy colored particles, quarks and gluons, undergo a process referred to as hadronisation, whereby they convert into sprays of colorless culminated hadrons that emerge from the interaction point. The collection of these culminated particles is referred to as a jet. The measured energy and direction of a jet provides information about the initial quarks or gluons that participate in the physics processes of interest. Jet reconstruction groups reconstructed clusters and tracks into larger collections using various clustering algorithms. These algorithms are described in detail in Reference [74, 75]. The reconstruction of a high p_{T} jet indicates the presence of a final state quark or gluon. The observed jet energy can also be used to infer the energy of the initiating parton. This is a particularly challenging aspect of jet reconstruction. The calibration of the jet energy is referred to as the determination of the "Jet Energy Scale" and the "Jet Energy Resolution" [76]. The uncertainties associated with the jet energy scale and resolution are often the largest source of experimental uncertainty. In the analyses presented in this thesis, reconstructed jets are primarily used to veto the presence of final state quarks and gluons.

In general, the jet reconstruction algorithms cannot determine the type of parton that initiated a given jet. The exception are jets initiated by b-quarks. Bottom-quark flavored hadrons are relatively long-lived; they decay primarily via suppressed weak interactions. Jets associated to b-quarks thus contain relatively long-lived particles with typical decay lengths of the order of millimeters. A millimeter displacement from the interaction region is large enough to be resolved by the ID. Jets initiated by b-quarks, "b-jets", can be identified from the reconstructed tracks associated to the jet. The process, referred to as "b-tagging", identifies jets as b-jets if they have several tracks consistent with coming from a long-lived particle. Details on "b-tagging" in ATLAS can be found in Reference [77]. Reconstructed b-jets are used in the analyses presented in this thesis to identify processes involving top quarks, which are a significant source of background.

As discussed above, neutrinos can be detected from an overall transverse momentum imbalance. The overall transverse momentum imbalance is referred to as the "missing transverse energy" or

$E_{\mathrm{T}}^{\mathrm{miss}}$. There are several ways the $E_{\mathrm{T}}^{\mathrm{miss}}$ can be determined. The most basic form of $E_{\mathrm{T}}^{\mathrm{miss}}$ is calculated by summing the p_{T} of all the reconstructed calorimeter clusters and the p_{T} of any reconstructed muons. Apart from neutrinos, all particles produced in a given interaction will deposit their energy in the calorimeters, or will be measured by the MS. Because the initial transverse momentum is known to be zero, any observed imbalance must be due to the presence of non-interacting particles: *i.e.,* neutrinos. When summing over many clusters, the intrinsic resolution, and the non-Gaussian tails of the detector response, leads to a substantial uncertainty on the reconstructed $E_{\mathrm{T}}^{\mathrm{miss}}$. A more precise estimate of $E_{\mathrm{T}}^{\mathrm{miss}}$ can be obtained by summing the transverse momenta of higher-level objects. The energy measurements associated to identified leptons, photons, and jets are improved by dedicated calibrations specific to each identified particle type. By using these refined estimates of the particles transverse momenta, a better measurement of the missing transverse energy can be made. As will be highlighted in Chapter 8, the detection of neutrinos through missing energy is critical to the analyses presented in this thesis.

An issue associated to particle reconstruction that often arises is duplicate objects. Different reconstruction algorithms may interpret input tracks and clusters in different ways. For example, the electromagnetic shower produced by an electron, may be reconstructed as an electron, a jet, and a photon. In reality, these reconstructed objects are different interpretations of the same thing. In physics analyses, a decision must be made on the proper interpretation of the measured energy. This processes is referred to as "overlap removal" and is done on a case-by-case basis depending on the physics analysis.

Figure 4.2 shows a visualization of a reconstructed event, illustrating many of the reconstructed objects discussed above. The transverse plane is shown in the upper left panel. Reconstructed tracks emerging from the collision are depicted as solid colored lines. Reconstructed clusters in the calorimeters are depicted as red and green bars, the height of which indicates the measured energy. The yellow blocks represent cell energies. The green bars correspond to EM clusters; the red bars correspond to hadronic clusters. The track shown in red passes through the calorimeters to the MS and corresponds to a reconstructed muon. The track shown in green matches a narrow EM cluster and corresponds to a reconstructed electron. Two jets have been reconstructed. One of the reconstructed jets has tracks shown in blue associated to it; the other jet has yellow tracks associated to it. The event also has large missing transverse energy, the direction of which is indicated by the dashed blue line. The lower left panel shows the same event in the z-y plane. The two reconstructed jets have been identified as b-jets. The upper right panel is a close up of the tracks emerging from the interaction point. The tracks associated to the jets have displaced vertices, indicated in orange. This event has the characteristics of a $t\bar{t}$ event which decays di-leptonically into an electron,

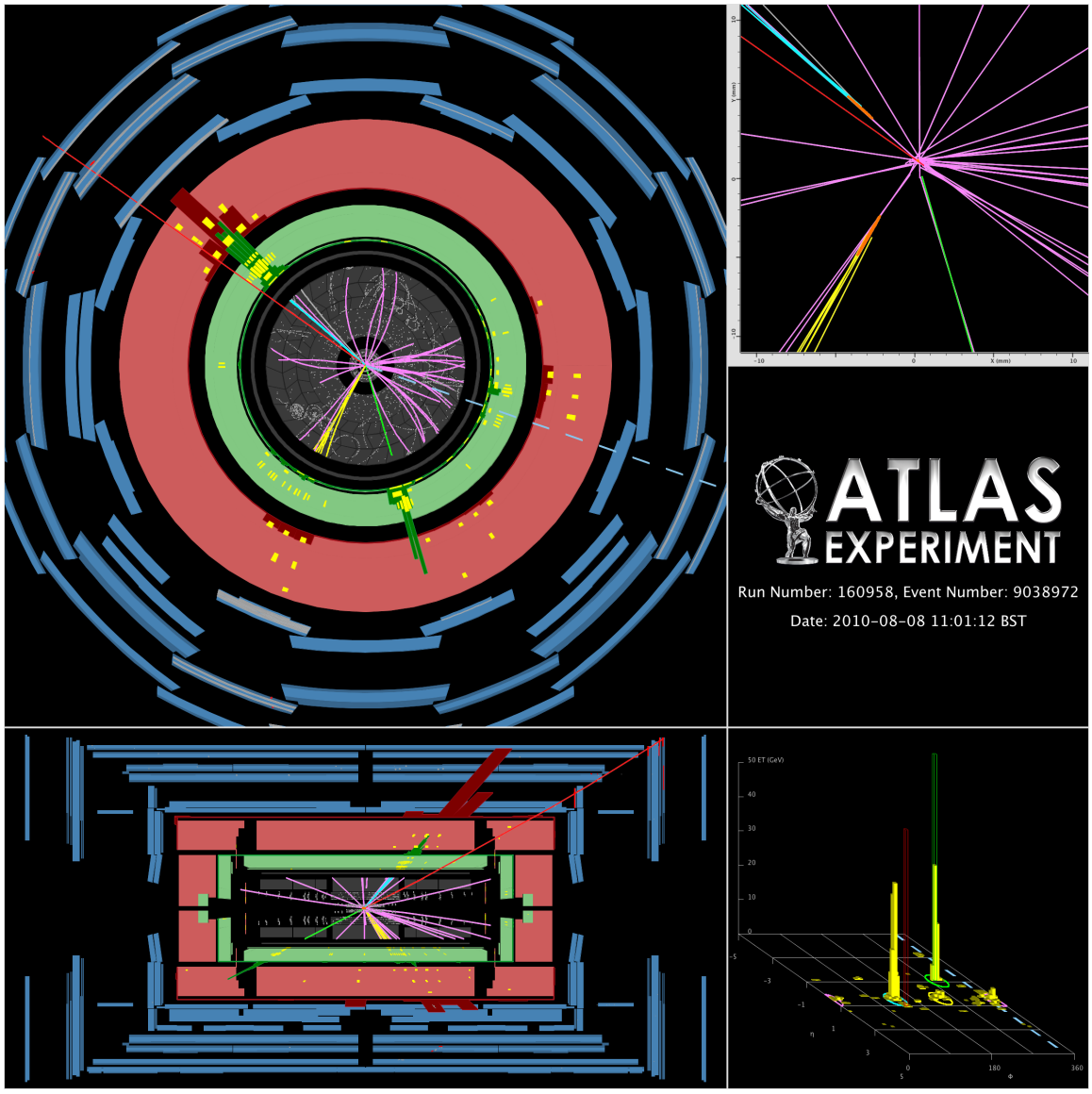

Figure 4.2: Event display of a $t\bar{t}$ di-lepton candidate in the $e\mu$-channel with two b-tagged jets. The electron is shown by the green track pointing to a calorimeter cluster, the muon by the long red track intersecting the muon chambers, and the $E_{\mathrm{T}}^{\mathrm{miss}}$ direction is indicated by the blue dotted line in the x-y view. The secondary vertices of the two b-tagged jets are indicated by the orange ellipses in the upper right.

a muon, neutrinos, and two b-jets. As discussed in Chapter 8, di-lepton top events are a substantial background to the analyses performed in this thesis.

A yet higher-level of reconstruction exists in which identified particles are combined to reconstruct short-lived particles that do not directly interact with the detector. For example, two reconstructed

electrons can be used to reconstruct a Z-boson. Z-bosons decay before leaving the interaction region, but can nevertheless be reconstructed by measuring their decay products. Various quantities associated to the Z-boson, *e.g.,* its mass or momentum, can be measured despite not directly observing it. In fact, particles reconstructed in this way can even be used as inputs to yet another level of reconstruction in which their kinematics are combined to infer the properties of a parent particle. This is done in the case of the Higgs searches presented in this thesis. In the $H \to ZZ^{(*)} \to llll$ and $H \to WW^{(*)} \to l\nu l\nu$ analyses, only the final products of the cascade are directly observed. These are used to infer the intermediate vector bosons, which are then used to reconstruct Higgs candidates.

4.2 Trigger

The trigger is a critical aspect of doing physics at a hadron collider. Many of the most interesting physics processes have very small cross sections. Large numbers of collisions are needed to produce significant quantities of these rare events. In order to produce these large numbers of collisions, the LHC operates at a high rate. Beam crossings, with many collisions per crossing, occur at a rate of 40 million per second. This high event rate posses a serious problem, as ATLAS can only afford to save around 400 events per second. The trigger system performs real-time event selection to reduce the number of recorded events to 400 per second. This amounts to saving one event for every 100,000 produced by the LHC. The trigger is optimized to select events in a way such that the interesting, rare events are not part of the 100,000.

The ATLAS trigger is composed of three levels: level one (L1), level two (L2), and the Event Filter (EF). The first level analyzes all 40 million events per second and selects 1 in $\sim$500 events to proceed to the next level. The L1 event selection is based on basic calorimeter clustering and track finding in the MS. The L1 trigger selects events with high p_{T} muons, or clusters consistent with high p_{T} objects. Because the L1 decisions need to be made extremely quickly, in 2.5 microseconds, the L1 reconstruction algorithms are implemented directly in hardware. The L1 selection reduces the event rate from 40 million per second to 75 thousand per second.

The L2 and EF stages of the trigger are performed using computer farms. L2 selects 1 in 15 events to proceed to the EF, reducing the event rate to 5 thousand per second. Event selection at L2 refines the reconstruction of objects selected at L1. Fast algorithms (50 ms per event) reconstruct leptons, photons, and jets around the objects found in L1. The L2 decisions are based on these reconstructed objects.

The EF selects 1 in 10 events to be written to tape for use in physics analyses. This reduces the

total event rate to 400 per second. The EF decisions are made using algorithms similar to those used to reconstruct objects in physics analyses.

The analyses presented in this thesis use events triggered by reconstructed electrons and muons. High p_{T} leptons, above around 20 GeV, can be efficiently identified and have relatively low levels of background. These leptons provide an effective way of selecting events in the trigger. Over half of the 400 events per second are selected on the basis of having a high p_{T} electron or muon. The generic selection of a single identified lepton supports a broad range of physics analyses. The details of the electron selection used in the trigger are described in Chapter 7. More information on the ATLAS trigger system can be found in Reference [78, 79].

4.3 Pile-Up

Overlapping signals from different pp collisions are a particularly challenging complication for reconstruction at the LHC. This phenomena is referred to as "Event Pile-up" or simply "Pile-up". There are two types of pile-up: in-time pile-up and out-of-time pile-up.

In-time pile-up occurs when multiple pp collisions take place in the detector simultaneously, during the same bunch crossing. The high luminosity LHC operating conditions give rise to many pp interactions per bunch crossing. Figure 4.3 shows the average number of interactions per crossing for the data used in the analyses presented in this thesis. Typical events in the $\sqrt{s}$= 7 TeV 2011 data set have 10 overlapping interactions; in the $\sqrt{s}$= 8 TeV 2012 data set, a typical event has around 20 overlapping interactions. The particles produced in these additional pile-up events obscure the reconstruction of the primary event of interest. The additional energy deposited in the detector as a result of pile-up will effect the measured energies in the calorimeter. This has a large effect on lepton isolation energies and the measurement of jet energies. As will be presented in Chapter 7, in-time pile-up also has a significant impact on the identification of electrons. In time pile-up significantly degrades the measurement of missing transverse energy. As discussed in Chapter 11, this has direct consequences for physics analyses.

Out-of-time pile-up is more benign. It occurs when signals from events in previous bunch crossings interfere with the current bunch crossing. Out-of-time pile-up is primarily an issue in the EM calorimeter. Because of its long signal shaping time, energy deposits from previous bunch crossings can affect the measured energy of EM clusters in the current crossing. Interestingly, out-of-time pile-up leads to negative energy contributions to clusters in the current event [61]. Although out-of-time pile-up can degrade energy resolution, it is typically less of a problem than in-time pile-up.

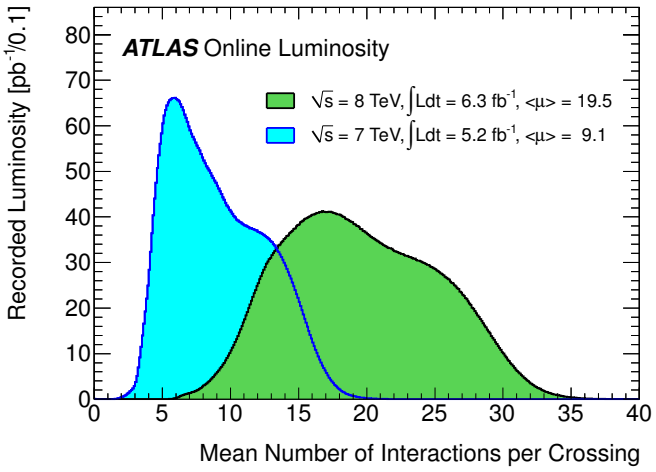

Figure 4.3: Mean number of interactions per bunch crossing, μ, for 2011 and 2012 data. The plot shows the full 2011 run and 2012 data taken between April and June.

4.4 Commissioning

Commissioning is a generic term that refers to the process of making the reconstruction algorithms work as they are intended and to understanding how what is reconstructed in the detector corresponds to what actually happened in the detector. Commissioning is one of the most important and challenging aspects of making an experiment such as ATLAS work. It effects all physics analyses. A significant portion of this thesis is devoted to commissioning activities.

Roughly speaking, commissioning is separated into two spheres: detector commissioning and the commissioning of the reconstructed objects. Detector commissioning involves understanding the real-world operating conditions of the detector and calibrating the lower-level reconstruction inputs. Converting voltages and times recorded by detector electronics into measured positions and energies is complicated. This process often relies on conditions which change with time or on detector specific parameters that must be precisely determined. One example is the detector alignment. Accurately determining the position of a measurement within ATLAS requires a precise knowledge of the positions of the individual detector elements making the measurements. Determining the in situ detector alignment is necessary for understanding the inputs to track finding, which as discussed above, is essential for all other reconstruction levels. Chapters 5 and 6, discuss detector alignment in detail.

Commissioning the reconstructed objects involves making the various reconstruction algorithms work properly and understanding their outputs. This involves: determining the energy scale and

resolution of reconstructed objects, tuning and measuring the efficiencies of various particle identification algorithms, and defining the event selection used in the trigger. These commissioning steps are critical for understanding reconstructed objects at a level that can be used in physics analyses. Chapter 7 describes the optimization of the electron identification algorithms and the various electron selections used in the trigger.

As mentioned above, leptons are crucial for doing physics at hadron colliders. In addition, the standard model provides clean sources of leptons which can serve as standard candles that can be used in commissioning. An example are Z bosons. Z bosons are an abundant, well-known source of leptons. They are used throughout this thesis in what is known as the "Tag-and-Probe" method. Requiring one fully identified lepton and a second basic object, *e.g.,* a reconstructed track or cluster, which form an invariant mass consistent with the known Z boson mass, gives a clean sample of unbiased leptons. This unbiased sample of leptons can then be used to commission the various levels of reconstruction. For example, the lepton identification efficiency can be optimized or measured, using this sample.

4.5 Conclusion

This chapter has provided a basic introduction to the particle reconstruction used throughout this thesis. The reconstructed particles are inputs to all physics analyses in ATLAS. They are the bridge from signals recorded in the detector to four-vectors of final state particles. Understanding these reconstructed objects is a prerequisite for all measurements, searches or discoveries.

The following three chapters are focused on understanding various aspects of the reconstruction, building on ideas introduced here. Chapters 5 and 6 are focused on detector alignment, crucial for understanding track reconstruction, one of the basic inputs to particle identification. Chapter 7 describes the reconstruction and identification of electrons, which are critical to the analyses presented in the remainder of this thesis.

Chapter 5

Detector Alignment

This chapter introduces detector alignment, a commissioning procedure critical for the reconstruction of charged particles with tracking detectors. Track-based alignment, a procedure for performing the detector alignment using the reconstructed trajectories of charged particles, or tracks, is described. The alignment of the ATLAS Inner Detector (ID) is presented. The ID alignment involves measuring the positions of over three hundred thousand detector elements, spanning meters in space, to an accuracy of tens of microns.

The remainder of this chapter is organized as follows: Section 5.1 introduces and motivates detector alignment, Section 5.2 describes the track-based alignment procedure, Section 5.3 discusses the validation of detector alignment, Section 5.4 describes the detector alignment in the ATLAS ID. Chapter 6 details the track-based alignment as applied to the TRT.

5.1 Introduction to Detector Alignment

Measuring charged particles efficiently and accurately is a crucial component of physics at high energy colliders. Precise track reconstruction is needed for a wide range of physics topics including; lepton identification, reconstruction of primary vertices, identification of b-quarks, and precise determination of invariant masses [49, 80, 81]. In ATLAS, the tracking requirements are met with a high resolution ID tracking system. The ID measures the trajectory of charged particles from signals recorded in the individual detector elements. Charged particles traversing the tracking detectors deposit energy that is translated into position measurements. The collection of these measurements, or "hits", from a single charged particle, follows the path of the particle through space. A helical trajectory can be fit to these spatial points to determine the origin, direction, and momentum[1]

[1] In the following the measured origin, direction and momentum of a charged particle are referred to as the "track parameters" of the particle.

of the particle that produced them. The high granularity of the ID provides precision position measurements, which allow for an accurate determination of the track parameters. This can be compromised by detector misalignment.

Tracking detectors measure the position of charged particles with respect to the detector elements making the measurements. The uncertainty on these local measurements is typically small, tens of microns for silicon detectors and is referred to as the intrinsic detector resolution. Several local measurements are combined in a fit to determine the path of the charged particle. In the track fit, the relative positions of the detector elements are needed to locate the individual local measurements with respect to one another in a global reference frame. The relative detector positions are determined from assumptions made about the detector geometry based on the design and construction of the detector. The uncertainties on the relative positions of the detector elements, introduced during construction and assembly, are often much larger than the intrinsic resolutions. These uncertainties will limit the overall precision of the track fit. Furthermore, differences in the assumed detector geometry and the actual installed detector geometry, can bias the measured positions used in the fit, which can bias the extracted track parameters. The accurate and precise measurement of the actual installed detector geometry is referred to as detector alignment. Detector alignment is needed in order to achieve the tracking performance required by the physics objectives.

A sketch of how misalignment can bias reconstructed track parameters and how detector alignment can recover the correct trajectory is given in Figures 5.1, 5.2, and 5.3. Figure 5.1 first shows the case of a perfectly aligned detector. The detector being perfectly aligned simply means that the actual installed detector positions, or true detector positions, correspond exactly to the assumed detector positions. Figure 5.1a shows the measurements induced by a passing charged particle. For simplicity, in this toy example the particle trajectories are assumed to be straight lines and the intrinsic resolutions is assumed to be negligible. Figure 5.1b shows the track reconstructed from the measurements created by the particle in Figure 5.1a. Because the assumed detector positions match the true detector positions, the correct relative positions of the local measurements are used in the fit. As a result, the trajectory is correctly reconstructed: the reconstructed trajectory in Figure 5.1b matches the true trajectory in Figure 5.1a.

The situation in the presence of detector misalignment is shown in Figure 5.2a. In this example, the second detector element from the top is misaligned, as indicated in the figure by α. The detector misalignment corresponds to the difference in actual detector position and assumed detector position. The passing charged particle creates locally measured track positions based on its distance to the actual detector positions. As a result of the misalignment, the second local measurement is larger than the corresponding measurement without misalignment in Figure 5.1a. The track recon-

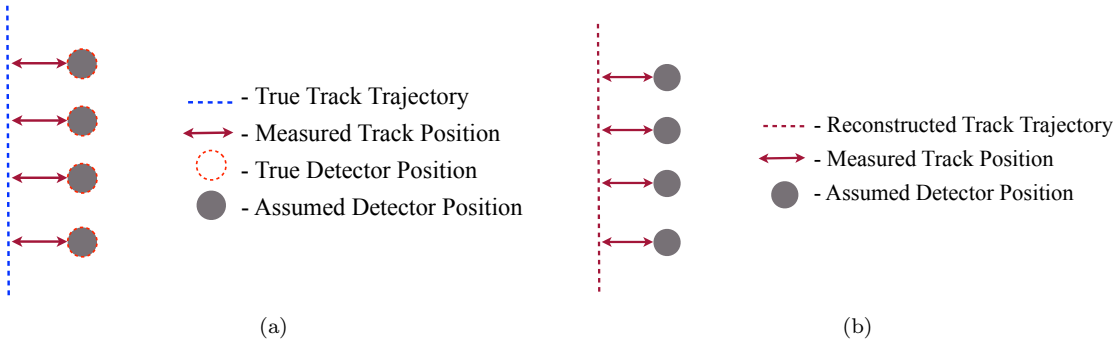

(a) (b)

Figure 5.1: Schematic of track reconstruction in the absence of detector misalignment. Figure (a) shows the measurements caused by the trajectory of a charged particle assuming no detector misalignment. Figure (b) shows the reconstructed trajectory using those measurements and assuming no misalignment. The correct trajectory is reconstructed.

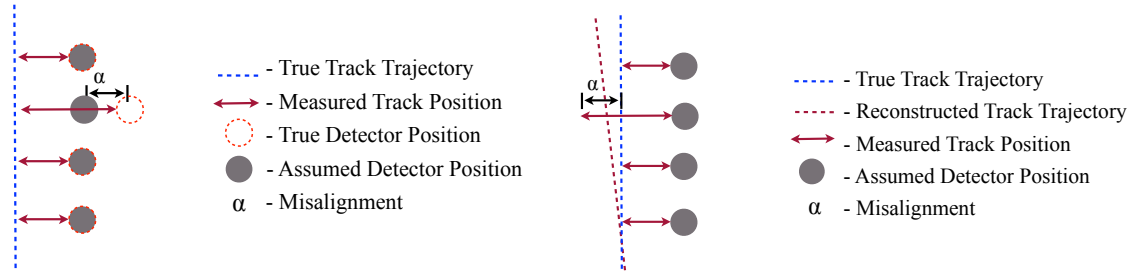

(a) (b)

Figure 5.2: Schematic of track reconstruction in the presence of detector misalignment. Figure (a) shows the measurements caused by the trajectory of a charged particle with detector misalignment indicated by α. Figure (b) shows the reconstructed trajectory using those measurements and assuming no misalignment. The reconstructed trajectory differs from the charged particle trajectory.

struction without performing detector alignment is shown in Figure 5.2b. The local measurements from Figure 5.2a are combined with the assumed detector positions. Because the assumed detector positions do not correspond to the true detector positions, the relative local measurement positions used in the fit are not correct. In particular, the reconstructed position of the second measurement is biased with respect to the path of the charged particle. As a result, the trajectory is incorrectly reconstructed: the reconstructed trajectory in Figure 5.2b is biased with respect to the true trajectory in Figure 5.2a. The presence of uncorrected detector misalignment biases the track parameters.

The corresponding track reconstruction with detector alignment is shown in Figure 5.3. Detector alignment measures the actual detector positions. In the example of Figure 5.2a, the difference in the

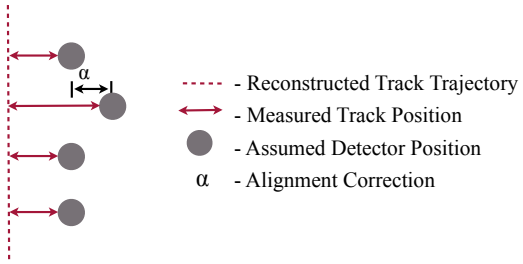

Figure 5.3: Schematic of the reconstructed trajectory using the measurements from 5.2a and correcting for detector misalignment. The correct trajectory is reconstructed.

assumed position of the second element and its true position would be determined by the detector alignment. The assumed detector position is then corrected with this difference in the geometry used for the track fit. What is changed by the detector alignment is our assumption of the detector positions, not the actual detector positions. The alignment procedure corrects the assumptions, so they are consistent with the actual detector. Figure 5.3 shows the local measurements from Figure 5.2a combined with the corrected detector positions. Because the assumed detector positions now match the true detector positions, the correct relative local measurement positions are used in the fit. As a result, the trajectory is correctly reconstructed: the reconstructed trajectory in Figure 5.3 matches the true trajectory in Figure 5.2a. Detector alignment removes the bias in the track parameters seen in Figure 5.2b.

The scenario in the example toy detector is played out on a larger scale in the ATLAS ID. In the ID the local measurements are made by silicon sensors or TRT drift tubes. The path of a typical charged particle in the ID gives around forty local measurements: three in the Pixel Detector (Pixel), eight in the SCT, and around thirty in the TRT. The intrinsic accuracy of the local measurements is 10 μm in the Pixel, 17 μm in the SCT, and 130 μm in the TRT. In order to provide full tracking coverage up to pseudorapidity of 2.5 many individual detector elements are needed. The Pixel is comprised of 1744 basic detector elements which span 12 cm radially and 1.3 m along z. The SCT is comprised of 4088 basic detector elements which span 56 cm radially and 5.5 m along z. Finally, the TRT is comprised of 350848 basic detector elements which span a meter radially and 5.5 m along z. The general layout of the detector elements in the ID is shown in Figure 5.4. Each of the sub-detectors in the ID consists of separate barrel and end-cap pieces that are themselves composed of smaller collections of detector elements. The barrels are made up of separate layers, and the end-caps are made up of individual wheels or disks. The basic detector elements are attached to the barrel layers and end-cap disks. Because the detector was constructed and assembled in a modular

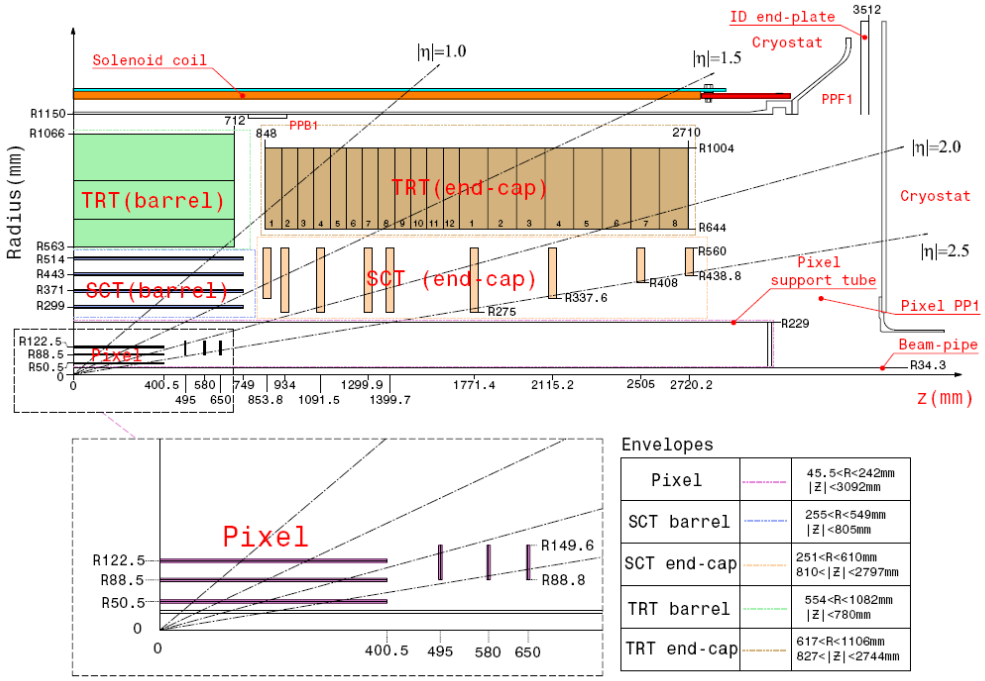

Figure 5.4: Layout of the Inner Detector. The division into barrel and end-caps can be seen. The further division of the barrels, into layers, and the end-caps, into disks is also shown. The full detector granularity is not given.

fashion, a hierarchy of misalignment is present. The ID sub-systems may be misaligned with respect to each other. The barrel and end-cap detectors within a subsystem may be misaligned. These, in turn, consist of yet smaller components that may be misaligned, etc. Different misalignments at each level are expected. The misalignment at a given level will correlate the misalignment of all the detector elements at a subsequent level. To address this, the ID alignment is performed in separate steps [47]. The misalignment of large structures is corrected first, removing the correlated misalignment of the lower-level substructures. The ID alignment is performed in three stages, or levels, with a granularity chosen to match that used in the detector assembly. The first level aligns the barrel and end-cap detectors of the individual subsystems with respect to one another. During the second alignment level, the barrel and end-caps are aligned internally at the level of the layers or rings. The final alignment level aligns each ID detector element individually.

The initially assumed detector positions, prior to alignment, come from the detector design and survey measurements made during assembly [82]. The initial detector positions and orientations have large, and in most cases unknown, uncertainties. These uncertainties are much larger than the intrinsic resolution. The detector positions are known to millimeters after assembly, versus intrinsic

resolutions of tens of microns. As a result, detector alignment is needed to recover the designed tracking performance of the ID. Measuring the positions and orientations of over a quarter million detector elements, spanning meters in space, to an accuracy of tens of microns, is an enormous challenge for the detector alignment.

The positions of detector elements are stored in a detector geometry database [83] and are used during track fitting just as in the toy example. Once the detector alignment has been performed, the measured differences in detector positions are used to update the detector geometry in the database. As in the example above, the alignment changes the assumed detector positions, not the actual geometry of the ID.

The remainder of this chapter is devoted to describing a method for determining the detector alignment and presenting the results of alignment of the ATLAS ID.

5.2 Track-Based Alignment

The method for determining the detector alignment used in ATLAS is known as track-based alignment [84, 85]. Track-based alignment uses properties of tracks reconstructed with the misaligned detector to infer the amount of misalignment. This alignment method is used because it is sensitive to detector misalignment at levels smaller than the intrinsic detector resolutions. It also has the advantage that it can be done in-situ, after detector installation, and can easily be applied to all detector elements in the ID.

The remainder of this section introduces track-based alignment. Sections 5.2.1 and 5.2.2 describe the mathematical formalism of track-based alignment. Section 5.2.3 discusses a potential pitfall when aligning the detector using a track-based approach.

The key to track-based alignment is the fact that track-fit qualities are worsened in the presence of detector misalignment. A fit quality can be assigned to each track. This fit quality describes how well the extracted charged particle trajectory agrees with the input local measurements. If the reconstructed track passes close to all the input hits, the fit quality is good. If there is a large scatter of the input hits around the fitted track, the fit quality is poor. The fit quality used for the ID alignment is called χ^2; it is defined as the square of the track-to-hit distance divided by the hit resolution, summed over hits on track:

$$\chi^2 = \sum_{\text{Hits on Track}} \left(\frac{\text{track-to-hit distance}}{\text{resolution}} \right)^2 .$$

The χ^2 is an observable quantity for all reconstructed tracks. Large values of χ^2 correspond to large track-to-hit distances and thus poor track qualities. Small values of χ^2 correspond to small

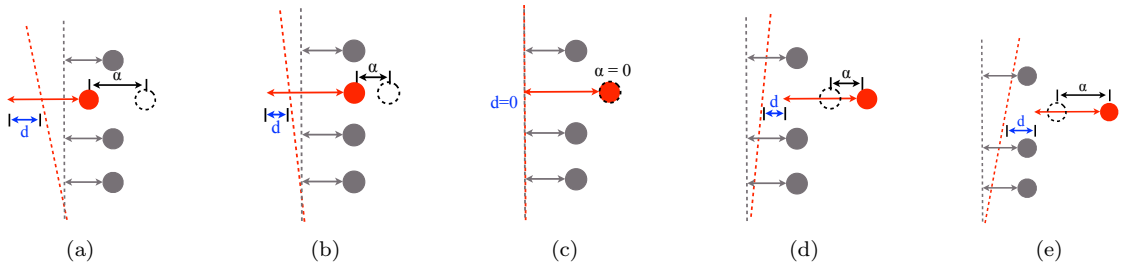

Figure 5.5: Sketch of how track quality is effected by detector misalignment. Figures (a)–(e) show various alignments of the second detector element and the resulting track fits, indicated by the dashed red line. When the detector misalignment, indicated by α, is larger, the distance of the track fit to the hits, indicated by d for the second hit, is correspondingly larger.

track-to-hit distances and thus good track qualities. To see how detector misalignment worsens the track-fit quality, it is best to return to the toy detector example.

The misaligned detector from Figure 5.2a is shown in Figure 5.5 with several choices of assumed position for the second detector. In the figure, the true position of the second detector element is indicated by the dashed circle. The misalignment is the difference in assumed detector position and true position and is indicated in the figure by α. As the assumed position of the second detector element changes, the corresponding track fit, indicated in the figure by the dashed red line, changes as a result. When the detector is further from its true position, the resulting distances between the track fit and the input measurements is increased. This is highlighted for the second detector measurement by the blue arrow labeled d in the figure. The track-hit distance has a minimum when there is no detector misalignment in Figure 5.5c. The distance increases as the assumed detector position moves from the true position in either direction, Figures 5.5b and 5.5d. The distance continues to increase as the misalignment becomes larger in Figures 5.5a and 5.5e. Although only explicitly shown for one measurement, this holds for all the hits in the figure. As a result, the track quality is a function of the assumed detector position and has a minimum at the value corresponding to the true detector position. The χ^2 as function of the misalignment in this example is sketched in Figure 5.6. The true detector alignment can be determined by scanning the assumed detector position until the minimum in observed χ^2 is reached. This procedure is referred to as track-based alignment.

The example above demonstrates the central idea of track-based alignment however, in practice, a few additional complications arise. First of all, in a more realistic detector all of the detector elements may be misaligned and in more than one dimension. In this case, the same reasoning as in the toy example applies, except that the χ^2 becomes a multi-dimensional function of all

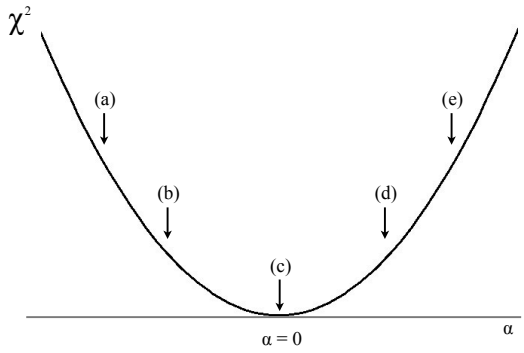

Figure 5.6: Sketch of the χ^2 as a function of detector misalignment α in Figure 5.5. The locations of the reconstructed tracks in Figures 5.5a–5.5e are indicated in the figure.

the possible detector element misalignments. Scanning the χ^2 over the multi-dimensional possible detector alignment space becomes prohibitive. Instead, the detector alignment is calculated by minimizing the χ^2 function with respect to the detector positions analytically. This is discussed further in the following section.

Detector resolution creates another complication. For a given track, there are often many different detector configurations that are consistent with giving the best track quality within the uncertainties of the local measurements. To cope with this, the χ^2 is calculated by summing over many different reconstructed tracks. The effects of the local measurement uncertainties are averaged out when considering many separate measurements.

The track-based alignment as described above is applied, on a much larger scale, to the alignment of the ID. The ID alignment is complicated by the large number of detector elements. The determination of detector positions, referred to as alignment parameters, for over 350,000 detector elements is computationally challenging. In total, there are over half a million sensitive alignment parameters in the ID [86]. Approximations are needed to minimize a function of this many parameters. These approximations require that the alignment procedure be iterated several times until the correct geometry is reached. The following section describes the mathematical formalism of the track-based alignment as applied in the ID.

5.2.1 Mathematical Formalism

When track-based alignment is performed on many detector elements, the χ^2 becomes a function of many alignment parameters. The multi-dimensional χ^2 has a minimum for the combination of alignment parameters corresponding to the true detector geometry. The detector alignment can be

determined by minimizing the χ^2.

The χ^2 is given by:

$$\chi^2 = \sum_{\text{Hits}} \left(\frac{m_i(\vec{\alpha}) - h_i(\vec{\alpha})}{\sigma_i} \right)^2, \tag{5.1}$$

where m_i are the positions of the input measurements; h_i is the position of the track fit closest to m_i; $\vec{\alpha}$ is the collection of alignment parameters; σ_i are the intrinsic detector resolutions. The sum is over the hits associated to reconstructed tracks. Both m_i and h_i depend on the alignment parameters. The positions of the input measurements depend directly on the position of the detector elements making the measurement. This dependence is known analytically. In the toy example above, m_i is simply α plus the value of the local measurement. In the case of the ID the dependence is more complicated, but known. The position of the track fit also depends on the alignment parameters. In the toy example, moving the second detector element changed the resulting track fit. In practice, with a large number of hits per track, this dependence is small and is typically ignored[2].

The true detector alignment is a minimum of the χ^2 and thus satisfies the condition:

$$\frac{d\chi(\vec{\alpha})^2}{d\vec{\alpha}} = 0. \tag{5.2}$$

This expression represents N constraints, where N is the number of alignment parameters. Expanding around the currently assumed detector geometry, $\vec{\alpha_0}$, gives:

$$\frac{d\chi^2(\vec{\alpha})}{d\vec{\alpha}} = \left.\frac{d\chi^2}{d\vec{\alpha}}\right|_{\vec{\alpha_0}} + \left.\frac{d^2\chi^2}{d\vec{\alpha}^2}\right|_{\vec{\alpha_0}} (\vec{\alpha} - \vec{\alpha_0}) + (\text{Higher Order Terms}). \tag{5.3}$$

In general, the χ^2 derivatives, $\frac{d\chi^2(\vec{\alpha})}{d\vec{\alpha}}$, are nonlinear functions of the alignment parameters. However, to make the problem tractable, a linear approximation is made:

$$\frac{d\chi^2(\vec{\alpha})}{d\vec{\alpha}} \approx \left.\frac{d\chi^2}{d\vec{\alpha}}\right|_{\vec{\alpha_0}} + \left.\frac{d^2\chi^2}{d\vec{\alpha}^2}\right|_{\vec{\alpha_0}} (\vec{\alpha} - \vec{\alpha_0}). \tag{5.4}$$

This linear approximation is accurate if the detector misalignments are small, if the current alignment parameters are close to the minimum. With the linear assumption, the alignment conditions reads:

$$\left.\frac{d\chi^2}{d\vec{\alpha}}\right|_{\vec{\alpha_0}} + \left.\frac{d^2\chi^2}{d\vec{\alpha}^2}\right|_{\vec{\alpha_0}} (\vec{\alpha} - \vec{\alpha_0}) = 0, \tag{5.5}$$

and the detector alignment can be determined from:

$$\Delta\vec{\alpha} = -\left(\left.\frac{d^2\chi^2}{d\vec{\alpha}^2}\right|_{\vec{\alpha_0}} \right)^{-1} \left.\frac{d\chi^2}{d\vec{\alpha}}\right|_{\vec{\alpha_0}}, \tag{5.6}$$

[2] Track-based alignment can be performed using an "unbiased" χ^2. This is another measure of the track quality that has less dependence of h_i on α. In the unbiased χ^2, for each hit in the sum, the hit in question is removed from the track fit when determining the track position at that measurement. The track position at the measurement is not influenced by the measurement itself. The track fit position is said to be unbiased with respect to that measurement. This trick further reduces the dependence of h_i on α.

where $\Delta\vec{\alpha} = (\vec{\alpha} - \vec{\alpha_0})$ represents the measured misalignment. The expression in the right-hand side of Equation 5.6 can be calculated with the tracks reconstructed using the current detector geometry.

In practice, the linear approximation of Equation 5.4 does not hold. In this case, Equation 5.2 can be solved iteratively with Equation 5.6 using the Newton-Raphson method. The detector misalignment is first calculated using Equation 5.6 with the initial detector geometry. These measured misalignments are used to update the detector geometry which is then used as input for the next iteration. The linear approximation becomes more accurate as the $\vec{\alpha_0}$ approaches the true detector alignment. This procedure is iterated until convergence is reached.

In Equation 5.6, $\vec{\alpha}$ is a vector of the alignment parameters with dimensionality equal to the number of alignment parameters, N. The χ^2 derivative, $\frac{d\chi^2}{d\vec{\alpha}}\Big|_{\vec{\alpha_0}}$, is an N-dimensional vector and the second derivative, $\frac{d^2\chi^2}{d\vec{\alpha}^2}\Big|_{\vec{\alpha_0}}$, is an $(N \times N)$-dimensional matrix. To determine the detector alignment, the χ^2 derivatives need to be calculated, and the $(N \times N)$-matrix needs to be inverted. In the ID, with N over 350,000, this inversion is non-trivial, both in terms of CPU and memory requirements. There are several methods of handling this matrix inversion. In ATLAS the two methods that are primarily used are known as matrix diagonalizing and the local-χ^2 method. These are the subject of the following section.

The track-based alignment as developed here has been implemented both for the toy example discussed in Figures 5.2– 5.5 above and in the ATLAS ID. The details of the implementation for the toy model are presented in Appendix A. The χ^2 derivatives are calculated and several studies of the performance of the track-based alignment with the toy model are presented. The track-based alignment for the ATLAS ID has been implemented in the `Athena` software framework [87]. It was first implemented separately for the TRT alignment in the `TRTAlignAlg` package as described in Reference [84] and for the Pixel and SCT alignment in the `SiAlignAlg` package as described in Reference [85]. It was later updated to integrate the full ID in the common packages, `InDetAlignment` and `TrkAlignment`, described in Reference [86].

5.2.2 Matrix Inversion

Determining the detector alignment involves inverting the $(N \times N)$-dimensional second derivative matrix in Equation 5.6. With a large number of alignment parameters this inversion can be computationally challenging. This section describes the two primary methods for inverting the second derivative matrix employed when aligning the ID. The first method, diagonalization, is the preferred method, but can only be used when the number of alignment parameters is below $\sim 10,000$. The second method, known as the local-χ^2 method, involves further approximation, but allows the

alignment of the full ID to be performed.

When aligning a subset of the ID, up to $\sim 10,000$ alignment parameters, directly inverting the second derivative matrix is feasible. This is done with singular value decomposition[88], referred to here as diagonalization. Diagonalization is used because it provides a straightforward way of regularizing $\frac{d^2\chi^2}{d\vec{\alpha}^2}\Big|_{\vec{\alpha_0}}$ in the presence of unconstrained degrees of freedom.

The condition for alignment, Equations 5.5, can be written[3] as

$$Ax = b, \tag{5.7}$$

where $A = \frac{1}{2}\frac{d^2\chi^2}{d\vec{\alpha}^2}\Big|_{\vec{\alpha_0}}$, $x = \Delta\vec{\alpha}$, and $b = -\frac{1}{2}\frac{d\chi^2}{d\vec{\alpha}}\Big|_{\vec{\alpha_0}}$. Because A is a second derivative, it is a symmetric matrix, and can be written in the form:

$$A = UDU^T, \tag{5.8}$$

where U is an orthogonal matrix, and D is a diagonal matrix. The matrix U is given by $U_{ij} = u_i^j$ where the u^js are the eigenvectors of A. The matrix D is given by $D_{ij} = d_i\delta_{ij}$ where the d_i are the corresponding eigenvalues. The alignment corrections are calculated as

$$x = UD^{-1}U^Tb, \tag{5.9}$$

$$x_i = U_{ij}D^{-1}_{jk}U^T_{kl}b_l = U_{ij}\frac{1}{d_j}U^T_{jl}b_l, \tag{5.10}$$

$$x_i = \sum_j \frac{(\vec{u^j}\cdot\vec{b})}{d_j}u_i^j, \tag{5.11}$$

The detector alignment can be represented as a linear combination of eigenvectors of $\frac{d^2\chi^2}{d\vec{\alpha}^2}\Big|_{\vec{\alpha_0}}$.

The uncertainties on the alignment parameters are given by the covariance matrix, $C = A^{-1}$:

$$C = UD^{-1}U^T \tag{5.12}$$

$$C_{ij} = U_{im}D^{-1}_{ml}U^T_{lj} \tag{5.13}$$

$$C_{ij} = \frac{U_{il}U^T_{lj}}{d_l} \tag{5.14}$$

$$C_{ij} = \sum_l \frac{u_i^l u_j^l}{d_l} \tag{5.15}$$

Equation 5.15 shows that each eigenvector contributes to the covariance matrix with a term that is proportional to the inverse of the corresponding eigenvalue. Eigenvectors with small eigenvalues give rise to large uncertainties. In fact, if the eigenvalue of a particular eigenvectors vanishes,

[3]The following uses the notation in Reference [84].

the uncertainty on the extracted alignment parameters becomes infinite. In this case the matrix $\frac{d^2\chi^2}{d\vec{\alpha}^2}\Big|_{\vec{\alpha_0}}$ is singular and a regularization procedure is needed to perform the alignment. Eigenvectors of $\frac{d^2\chi^2}{d\vec{\alpha}^2}\Big|_{\vec{\alpha_0}}$ with small or vanishing eigenvalues are referred to as weak modes. Weak modes pose a significant challenge to track-based alignment and are the subject of the following section.

When performing the detector alignment with more than $\sim 10,000$ alignment parameters the local-χ^2 method is used. The local-χ^2 method is the same as the track-based alignment procedure described above, except that a further approximation is made to simplify Equation 5.6. In the local-χ^2 method, terms that correlate different detector elements in the second derivative matrix, $\frac{d^2\chi^2}{d\vec{\alpha}^2}\Big|_{\vec{\alpha_0}}$, are neglected. This assumption amounts to aligning each detector element assuming all the others are fixed. The single large $(N \times N)$-dimensional matrix of Equation 5.6 is replaced with many separate equations, one for each detector element, each with a much smaller matrix. Inverting many small matrices is much easier computationally. In practice the assumption that the alignment of individual detector elements are uncorrelated does not hold. Iterations of the local-χ^2 alignment procedure are needed to recover the effect of correlations. As a result, the local-χ^2 alignment has slower convergence than alignment with direct inversion. For example, iterations would be needed even if $\frac{d\chi^2}{d\vec{\alpha}}$ was linear in the alignment parameters. The local-χ^2 method of alignment described above is used when aligning the ID with the full granularity.

5.2.3 Weak Modes

Weak modes are a major concern when performing track-based alignment [89]. Formally, weak modes are eigenvectors of $\frac{d^2\chi^2}{d\vec{\alpha}^2}\Big|_{\vec{\alpha_0}}$ with small or vanishing eigenvalues. Physically, weak modes correspond to coherent detector misalignments that have little or no effect on the overall χ^2. These class of misalignments are inherently problematic for the track-based alignment method, which exploits the dependence of the χ^2 on the detector alignment. The track-based alignment alone cannot account for detector displacements that correspond to weak modes.

There are two types of weak modes. The first type correspond to global movements of the ID as a rigid body. When aligning the full ID, there are six unconstrained degrees of freedom (DoF), three translations and three rotations of the entire ID. These DoF correspond to the global position and orientation of the ID within ATLAS and cannot be constrained from the reconstructed ID tracks alone. When performing the track-based alignment, these DoF are eigenmodes of $\frac{d^2\chi^2}{d\vec{\alpha}^2}\Big|_{\vec{\alpha_0}}$ with vanishing eigenvalue. As a result, the second derivative matrix is singular, and the inversion in Equation 5.6 cannot be carried out. In order to proceed with the alignment, this matrix needs to be regularized. This can be done when diagonalization is used by explicitly removing the six

lowest eigenmodes. The resulting matrix is non-singular, and the inversion can proceed. In this case, the DoF corresponding to the overall position and orientation of the ID within ATLAS must be determined elsewhere. This is typically done by requiring that orientation and center of gravity of the ID is unchanged by the alignment. When using the local-χ^2 method, this brute force regularization cannot be used. In this case, the tracks used in the alignment need to be reconstructed using an external reference. For example, the TRT can be aligned internally with the local-χ^2 method using tracks reconstructed while keeping the Pixel and SCT detectors fixed. Here, the fixed silicon detectors provide a fixed global reference frame for the tracks used in the alignment, removing the six unconstrained DoF in the TRT. This first type of weak mode is something that must be dealt with to properly define the alignment procedure, but is not a serious concern for the track-based alignment.

The second type of weak modes are potentially more dangerous. These correspond to coherent detector deformations that leave the χ^2 unchanged by biasing the reconstructed track parameters. There is a whole class of such distortions that plague detectors with cylindrical symmetry, such as the ID. An example, the curl deformation, is shown in Figure 5.7. This coherent misalignment results in a biasing of the p_{T} of charged particles. True charged particle trajectories, indicated in the figure by the dashed red and blue lines, are reconstructed with an incorrect curvature, indicated in the figure by the solid red and blue lines. The bias due to the curl deformation is opposite for oppositely charged tracks. In this example, the curvature of the negatively charged track (in red) is reduced by the curl, resulting in a reconstructed p_{T} that is larger than p_{T} of the original particle. One the other-hand, the curvature of the positively charged track (in blue) is increased by the curl, resulting in a reconstructed p_{T} that is smaller than the p_{T} of the original particle. The χ^2 of the incorrectly reconstructed tracks with curled geometry, is the same as the χ^2 of the correctly reconstructed tracks in the aligned geometry. As a result, the track-based alignment is unable to distinguish between the two.

The weak modes corresponding to detector deformations are especially problematic because they effect physics results. Unlike the first type of weak modes, which amount to a redefinition of the global coordinate frame, these weak modes bias the track parameters. These misalignments can be either deformations of the physical detector, or they can be introduced into the assumed detector geometry by the track-based alignment procedure. If the detector is built with a curl misalignment, the track-based alignment will not be able to remove it. On the other-hand, running the track-based alignment on a perfectly aligned detector may induce a curl as a result of the χ^2 minimization. In either case, the resulting misalignment will bias the reconstructed track p_{T}.

There are a few methods of handling weak modes. As mentioned above diagonalization provides

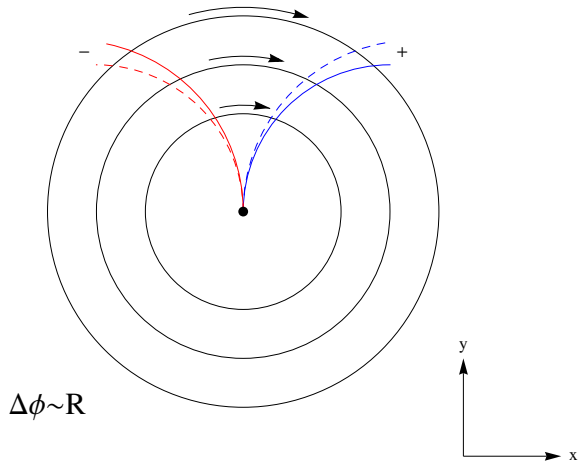

Figure 5.7: Sketch of the curl deformation, a weak mode that biases the reconstructed track p_{T}. The detector elements are misaligned in ϕ with a magnitude that is proportional the radial position, as indicated by the arrows. The effect on the curvature for a positively and negatively charged track are shown.

of means of identifying weak modes through the eigenvalue spectrum. Although simply removing eigenmodes with small eigenvalues can be used for eliminating the trivial, global ID DoF, it can be dangerous when applied to detector deformations. Unlike the six unconstrained DoF, the number of weak modes corresponding to detector deformations is not a priori known. The removal of eigenmodes with small eigenvalues is arbitrary and would not guarantee that the correct detector geometry is reached. This procedure can prevent the track-based alignment from inducing a weak mode deformation in an perfectly aligned detector, but it is helpless against removing real detector deformations. It can also not be used when aligning at the highest granularity with the local-χ^2 method.

Another potential means of eliminating weak modes is by adding external constraints beyond the track quality. If the direction or momentum of the charged particles can be independently measured, the track parameters of the corresponding tracks can be constrained. This would prevent the introduction of detector deformations which require the track parameters to be biased to preserve the χ^2. For example, tracks from electrons can be used in the alignment with the track p_{T} constrained from the measured energy in the calorimeter. This could remove detector deformation that bias the track p_{T}, as the case for the curl deformation. By adding additional constraints, the track-based alignment can gain sensitivity to weak modes.

The easiest and most effective method for eliminating potential weak modes is by combining tracks from events with different topologies. The χ^2 dependence on the alignment parameters is

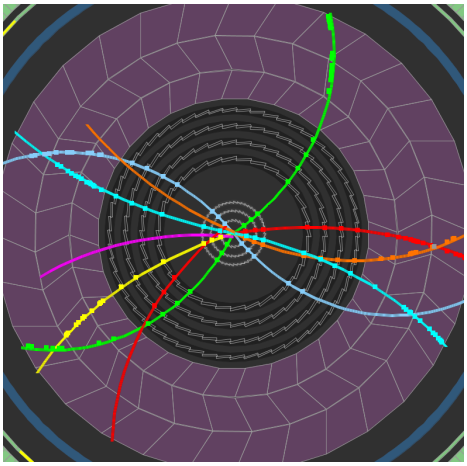

Figure 5.8: Typical track topologies from collision events. Tracks originate from the center of the detector. Different reconstructed tracks are shown in different colors.

highly dependent on the properties of the tracks used in the alignment: track origin, track direction, detector elements crossed. Different types of events will lead to different types of weak modes. An example of this used in the ID alignment is the combination of tracks from collision events and from cosmic-ray muons. Cosmic-ray muons provide a source of events with a wide range of track topologies different from those in collision events. Typical tracks from collision events are shown in Figure 5.8. Collision tracks originate at the interaction point and propagate outward, correlating detector elements radially. Examples of track topologies in cosmic-ray events are shown in Figure 5.9. Cosmic-ray muons originate from outside the detector, typically from above. Tracks from cosmic-ray muons can cross both halves of the ID barrel, correlating the positions of modules in opposite hemispheres of the detector, as in Figure 5.9a. They can also enter the detector with large impact parameters, Figure 5.9b, crossing detector elements not correlated by tracks in collision events. Weak modes of one type of event can be removed by adding events of a different type, for which the detector deformation is not weak. An example of this is the curl. As shown above in Figure 5.7, the curl deformation is a weak mode for collision-like tracks. However when considering tracks from cosmic-ray muons, the curl deformation is no longer a weak mode. This is illustrated in Figure 5.10. The p_{T} bias is opposite for the upper and lower half of the cosmic-ray track. Because a common p_{T} is fit to the full track, a consistent bias cannot be introduced which preserves the χ^2. By including tracks with different topologies, the presence of weak modes can be eliminated.

This concludes the general discussion of track-based alignment. The following section describes ways in which the detector alignment can be validated. The remainder of the chapter describes the track-based alignment as applied to the ATLAS ID.

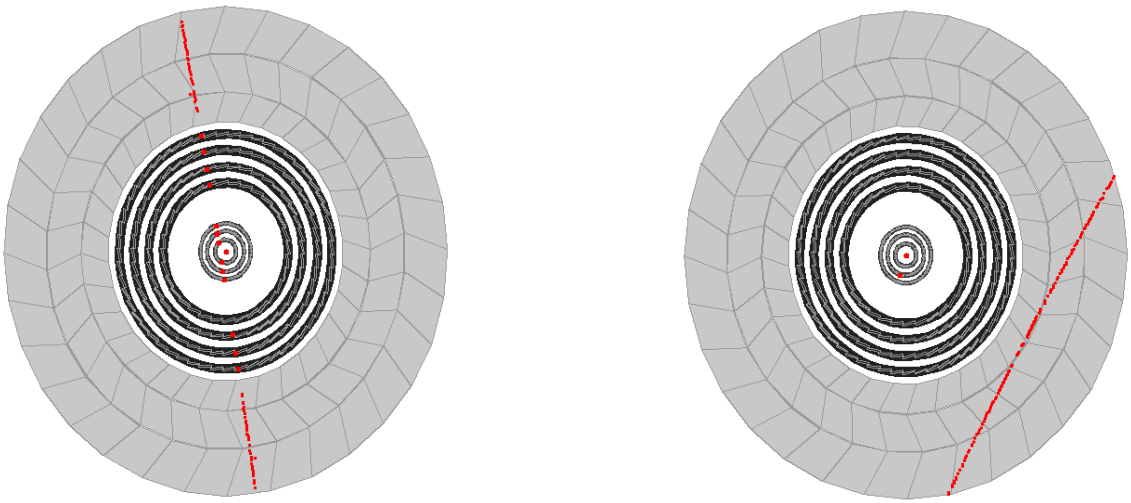

(a) (b)

Figure 5.9: Examples of tracks from cosmic-ray muons with track topologies different from that seen in collision events. Figure (a) shows an example of a cosmic-ray muon which correlates the upper and lower parts of the ID barrel. Figure (b) shows an example of a cosmic-ray muon which correlates detector elements in the TRT that are not correlated by tracks from collision events.

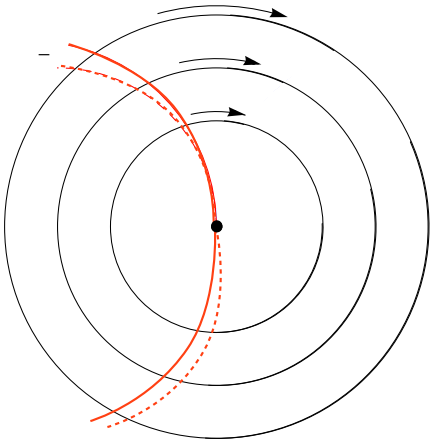

Figure 5.10: Sketch of the effect of a curl deformation on a track from a cosmic-ray muon. The detector elements are misaligned in ϕ with a magnitude that is proportional the radial position, as indicated by the arrows. For cosmic-ray muons this deformation is not a weak mode as the p_{T} bias is opposite for upper and lower half of reconstructed track. The effect on the curvature of a negatively charged track is shown.

5.3 Alignment Validation

The alignment of a detector with the size and complexity of the ID is a complicated procedure. Track-based alignment provides a mathematical formalism for determining the best fit detector positions from observed quantities using reconstructed tracks. As mentioned above, this procedure involves several approximations that are known to be incorrect in order to simplify the solution of Equation 5.2. The track-based procedure is also susceptible to systematic detector distortions, weak modes, which can directly effect the physics. Validating the results of the track-based alignment is a crucial step in the overall alignment procedure. Insuring that the χ^2 has been properly minimized, and that the resulting alignment is weak mode free, can be as challenging as the alignment itself. This section discusses general ways in which the detector alignment is validated. The following section and the next chapter present the alignment and validation of the ATLAS ID.

The first important check is that the minimum of the χ^2 has been reached. The overall χ^2 should decrease with alignment iteration, and the alignment corrections themselves should tend toward zero. In practice the alignment procedure is repeated for many iterations after χ^2 convergence to verify the stability of the alignment parameters. Basic track quantities, number of tracks, number of hits on track, should increase as a result of the alignment. Non-convergence of the alignment constants could indicate that the detector geometry is oscillating between local minima. In this case, adding tracks with different topologies can potentially resolve this ambiguity.

The other important check that the alignment has been correctly carried out is in the residual distributions. The residual is defined as the distance between the local input measurements and fitted track position. It is usually signed such that a bias in the position of the input measurements with respect to the track fit gives a bias in the residual. The residual distribution is the plot of the residual summed over many hits on track. If the alignment has been correctly performed the residual distribution should be a Gaussian centered on zero, with a width that represents the intrinsic detector resolution. Residual distributions should improve with alignment iteration. This means that any initial bias should decrease with iteration, and the overall residual width, or resolution, should improve. The overall residual will improve by construction as a result of the alignment, the χ^2 is proportional to the square of the residual. If the overall residual worsens, it is a sign that the alignment is not converging. Residual maps are often more useful in validating the alignment. Residual maps present the mean or width of individual residual distributions, binned in one or more detector coordinates. For example, the average residual as a function of ϕ or η can show regions of local misalignment. It is important to look for structure in the residual maps at the granularity at which the detector alignment is performed.

The validation plots discussed above are necessary but not sufficient to validate the alignment. The alignment can converge and the residuals improve despite the fact that weak mode detector deformations are present. The only robust way to validate the alignment against the presence of weak modes is by examining quantities sensitive to the reconstructed track parameters. Basic invariants can be used to spot problems. For example, track parameters should all be independent of ϕ. Known physical resonances can also serve as standard candles against which weak modes can be probed. For example, the invariant mass and width, of the K^0_S, J/ψ, Υ, and Z, should not depend on the direction or momentum of the decay daughters. Plotting reconstructed particle masses and widths as a function of detector coordinate will test against the presence of weak modes.

Tracks from cosmic-rays provide a unique class of validation plots for which the detector alignment can be checked. Unlike tracks from collision events, cosmic-ray muons can traverse the entire ID barrel, leaving hits in both the upper and lower halves of the ID. As shown in Figure 5.11, these tracks can be split in half and fit separately. The result is two collision-like tracks. These tracks should have the same track parameters, as they are created from a single physical particle. The differences in the upper and lower track parameters can be used to validate the quality of the alignment. In absence of misalignment, the differences in track parameters should be centered on zero with a width that is $\sqrt{2}$ times the track parameter resolution[4]. A Bias or a broadening in the width would signal the presence of misalignment. The split tracks thus provide an independent assessment of the quality of the alignment. This technique has been developed and used to validate the ID alignment.

5.4 ATLAS Inner Detector Alignment

The alignment of the ATLAS ID began in 2008 using tracks reconstructed from cosmic-ray muons. Over the following years the alignment has been completed using the first collision data, taken at 900 GeV in 2009, and 7 TeV collision data taken in 2010 and 2011. The quality of the detector alignment is continuously monitored and updated as needed. The ID alignment has been documented in References [47, 90, 86, 89]. This section summarizes the overall ID alignment. The results of the alignment are presented, and the impact on track reconstruction is discussed. The details of the TRT alignment are the subject of the next chapter.

The goal for the ID alignment is that the resolution of track parameters should be degraded by less than 20% with respect to the intrinsic detector resolution, and that there should be no significant biases of the measured track parameters [49]. This specification translates to the requirement that

[4] $\Delta P = P_{\text{Upper}} - P_{\text{Lower}}$ so $\sigma_{\Delta P} = \sqrt{(\sigma_{P_{\text{Upper}}})^2 + (\sigma_{P_{\text{Lower}}})^2} = \sqrt{2} \times \sigma_P$

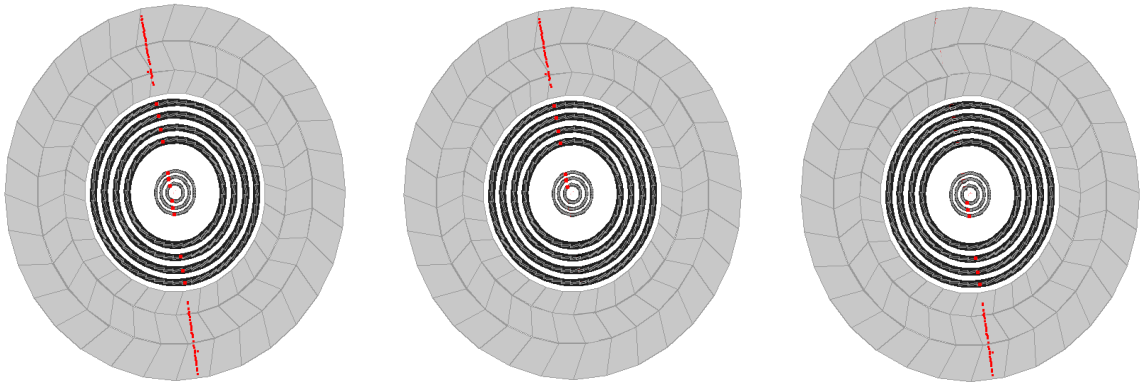

(a) (b) (c)

Figure 5.11: Illustration of track-splitting in cosmic-ray events. Cosmic-ray muons with low impact parameters crossing both halves of the ID (Figure (a)), can be split and reconstructed as two collision-like tracks (Figures (b) and (c)). The upper and lower track halves are from the same charged particle and should thus have the same track parameters.

the silicon sensors be measured with an accuracy of around ten microns, and that the position of TRT drift tubes be measured to tens of microns. This accuracy is an order of magnitude more precise than the positions are known after construction. In addition, weak modes leading to significant track parameter biases should be removed. With over 350,000 detector elements, meeting the goal of alignment in the ID poses a significant challenge for the track-based alignment.

As mentioned above, the ID alignment is performed in three levels using different granularity driven by the different stages in the detector construction and assembly. Table 5.1 summarizes the number of structures aligned and the active DoF for each alignment level. In the first alignment level (L1), the largest structures are aligned. This level is expected to have the largest misalignments and have the biggest impact on track reconstruction. During the second alignment level (L2), the barrel layers and end-cap disks are treated as separate align-able objects. This level has more structures and more alignment parameters than L1. In the final alignment level (L3), the individual detector elements are aligned with the highest granularity, module-level in the case of the Pixel and SCT and wire-level in the case of the TRT. The L3 alignment has the most structures and the highest number of alignment parameters.

At each level, each structure is treated as a rigid body. There are six degrees of freedom for a rigid body: three translations and three rotations. The DoF that are aligned at each level depends on the expected misalignment and the impact of the misalignment on tracking. In the first level of alignment, all six DoF of the L1 structures are aligned. The TRT wires are not sensitive to the track position along the wire. As a result, the TRT barrel is not aligned along z at L1. The same

Alignment Level	Detector	Structures	Degrees of Freedom Used	Number
Level 1	Pixel: whole detector	1	All	6
	SCT: barrel and 2 end-caps	3	All	18
	TRT: barrel	1	All (except T_z)	5
	TRT: 2 end-caps	2	All	12
	Total	7		41
Level 2	Pixel barrel: half shells	6	All	36
	Pixel end-caps: disks	6	$T_x,\ T_y,\ R_z$	18
	SCT barrel: layers	4	All	24
	SCT end-caps: disks	18	$T_x,\ T_y,\ R_z$	54
	TRT barrel: modules	96	All (except T_z)	480
	TRT end-caps: wheels	80	$T_x,\ T_y,\ T_z,\ R_z$	320
	Total	210		932
Level 3	Pixel: barrel modules	1456	All (except T_z)	7280
	Pixel: end-cap modules	288	$T_x,\ T_y,\ R_z$	864
	SCT: barrel modules	2112	$T_x,\ T_y,\ R_z$	6336
	SCT: end-cap modules	1976	$T_x,\ T_y,\ R_z$	5928
	TRT: barrel wires	105088	T_ϕ, R_r	210176
	TRT: end-cap wires	245760	T_ϕ, R_z	491520
	Total	356680		722104

Table 5.1: Summary of the different ID alignment levels. The number of structures aligned and the corresponding DoF used are given for each level in the alignment. "All" DoF corresponds to the six DoF of a rigid body: three translations and three rotations.

DoF are used to align the barrel layers at L2. The end-cap wheels at L2 are aligned in three DoF, translations along x and y, and rotations about z. Large misalignments of the TRT end-cap wheels were seen along z, so this DoF has also been included at L2. Because of the large number of L3 structures, only the most sensitive DoF are used in the L3 alignment. For the first two levels of alignment the track-based procedure using the full matrix inversion can be performed. At L3, the large number of DoF requires that the local-χ^2 method be used.

In the fall of 2008, ATLAS held a dedicated cosmic-ray data taking period, during which over seven million tracks from cosmic-ray muons were recorded in the ID [47]. This data set provided the first opportunity to perform the track-based alignment. Cosmic-rays entering the ID primarily originate from above and traverse the detector vertically. As a result, the reconstructed tracks in the end-caps and at large impact parameter in the barrel, cross the detector elements with large incident angles. These track are poorly reconstructed by the ID, which was optimized for tracks emerging from the interaction point and are not suitable for use in the alignment. The full L1 alignment was performed using cosmic-rays. The L2 alignment however, was only able to be done in the barrel. For the Pixel and SCT detectors a preliminary L3 alignment was also done for modules on the top

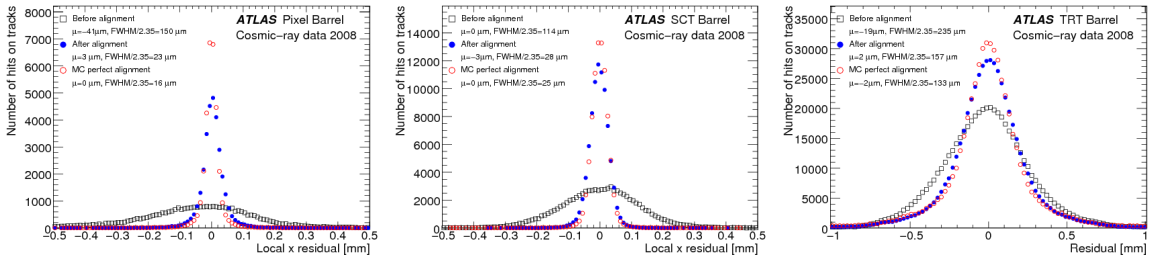

(a) (b) (c)

Figure 5.12: Residual distributions from cosmic-ray muon tracks in the Pixel (a), SCT (b), and TRT (c) barrels. Distributions are shown before and after the alignment from cosmic-rays. The result of using a perfectly aligned detector in MC is shown for comparison.

and bottom of the barrel. The results of this alignment have been reported in Reference [47].

Each level of alignment with cosmic-rays was repeated for several iterations until convergence was reached. The number of tracks and the number of hits on track increased as a result of the alignment. At L1, misalignments on the millimeter level were observed, with rotations around z of several milli-radians. The rotations around x and y were all consistent with zero. For the aligned L2 barrel modules, misalignments of hundreds of microns were measured.

The improvement in the residual distributions as a result of the alignment with cosmic-rays can be seen in Figure 5.12. The residual distributions in the barrel are shown for the Pixel (5.12a), SCT (5.12b), and TRT (5.12c), before the alignment in black, and after the alignment in blue. For comparison, the results using a perfectly aligned detector in MC are shown in red. Large improvements as a result of the alignment are seen for all subsystems. Initial biases present in the overall residual distributions are removed and the resolutions improve significantly.

The alignment validation using split cosmic-ray tracks can be seen in Figure 5.13. As described above, cosmic-rays crossing both halves of the detector are split, and two separate collision-like tracks are reconstructed. The figure shows the difference in d_0 (5.13a), ϕ_0 (5.13b), and z_0 (5.13c) for the upper and lower tracks reconstructed in the Pixel and SCT barrel. The distributions before the alignment are shown in black. Large biases, particularly in d_0 and ϕ_0, and poor track parameter resolutions are seen before the alignment. After the alignment, in blue, the biases are removed, and the track parameter resolutions approach that of the perfectly aligned detector, shown in red.

The first collision events were provided by the LHC during a commissioning run with a center-of-mass energy of 900 GeV in late 2009 [48]. This data set provided the first opportunity to perform the ID alignment using collision data. The L1 alignment was repeated using both collision and cosmic-ray data, and the L2 alignment was extended to the end-caps. A preliminary, statically

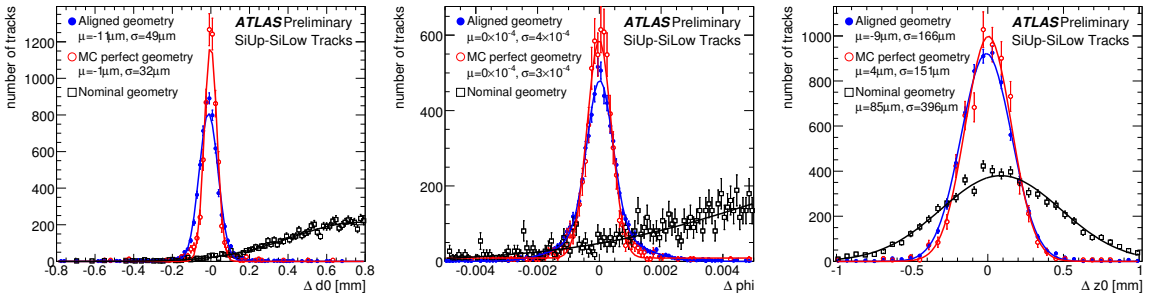

(a) (b) (c)

Figure 5.13: Difference in track parameters: d_0 (a), ϕ_0 (b), and z_0 (c), for split cosmic-ray tracks in the Pixel and SCT barrel. Distributions are shown before and after the alignment from cosmic-rays. The result of using a perfectly aligned detector in MC is shown for comparison.

limited, L3 alignment was also performed in the Pixel and SCT. The results of this alignment have been reported in Reference [90].

The alignment combining the 900 GeV collision and cosmic-ray data sets was repeated at each level for several iterations until convergence was reached. Increases in the number of reconstructed tracks and in the number of hits on track were seen with iteration, particularly in the end-caps. The measured misalignments with the initial alignment using cosmic-rays were confirmed with the collision data.

The improvement of the end-cap residual distributions as a result of the alignment with collision data is shown in Figure 5.14. These figures show the end-cap residual distributions before (black) and after (blue) the alignment using 900 GeV collision data. The results for the three ID subsystems are given separately. Large improvements are seen in the end-cap residual distributions after the alignment including collision data. Smaller improvements were seen from the updated alignment in the barrel, as was expected given the quality of the previous alignment with cosmic-rays.

It was only with the large statistics 7 TeV collision data sets provided by the LHC in 2010 that the full L3 alignment could be performed. Collision and cosmic-ray data collected during 2010 were used to repeat the L1 and L2 alignment and to complete the L3 alignment. The L3 alignment was performed using the local-χ^2 method. To improve convergence, the L3 alignment of the TRT was done separately from that of the Pixel and SCT. First the Pixel and SCT L3 alignment was performed, keeping the TRT fixed. Then the TRT L3 alignment was run, while keeping the silicon detectors fixed. Each step of the alignment was repeated for several iterations until convergence was reached. The results of this alignment have been reported in Reference [86].

The comparison of the residuals after the full L3 alignment to those of a perfectly aligned detector

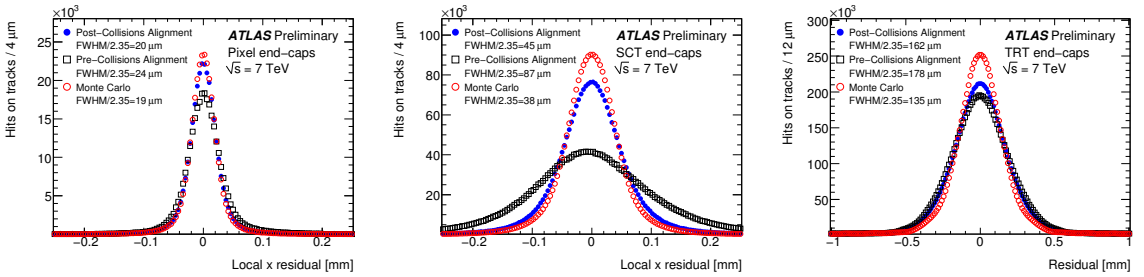

(a) (b) (c)

Figure 5.14: Residual distributions from collision tracks in the Pixel (a), SCT (b), and TRT (c) end-caps. Distributions are shown before and after the alignment from 900 GeV collisions. The result of using a perfectly aligned detector in MC is shown for comparison.

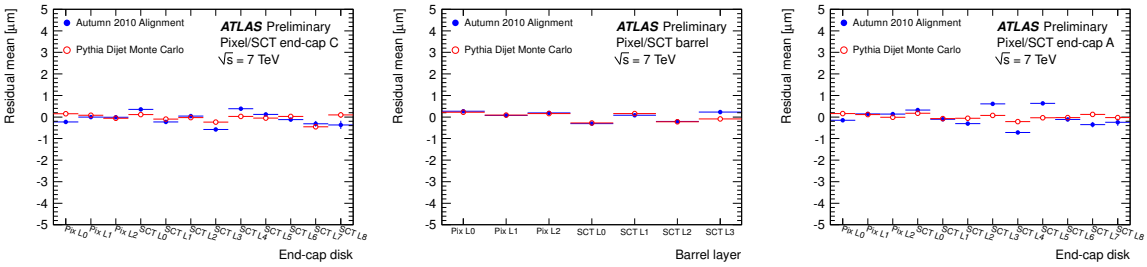

(a) (b) (c)

Figure 5.15: Average of the residual distribution as a function of Pixel or SCT barrel layer or end-cap disk for: end-cap C (a), barrel (b), and end-cap A (c). The result from data after the L3 alignment is shown in blue. The expectation from a perfectly aligned detector in MC is shown in red.

are shown in Figures 5.15 and 5.16. Figure 5.15 shows the average residual as a function of barrel layer and end-cap disk in the Pixel and SCT. The residuals after the L3 alignment are given in blue and agree with those of a perfectly aligned detector, shown in red, at the micron level. Figure 5.16 shows the barrel and end-cap residual distributions in the Pixel, SCT and TRT. The data after the L3 alignment is shown in blue. The expectation from a perfectly aligned detector in MC is shown in red. Overall good agreement is seen between the data after detector alignment and the simulation.

As discussed in Section 5.3, χ^2 convergence and improvement in residual distributions is not enough to ensure the correct detector alignment is reached. Weak modes may be present after alignment which bias the reconstructed track parameters. After the full ID alignment, using the 7 TeV data set, tests for the presence of weak modes were made using reconstructed $Z \to \mu\mu$ and $W \to e\nu$ events. Examples of these tests are given in Figure 5.17. Figure 5.17a is made using

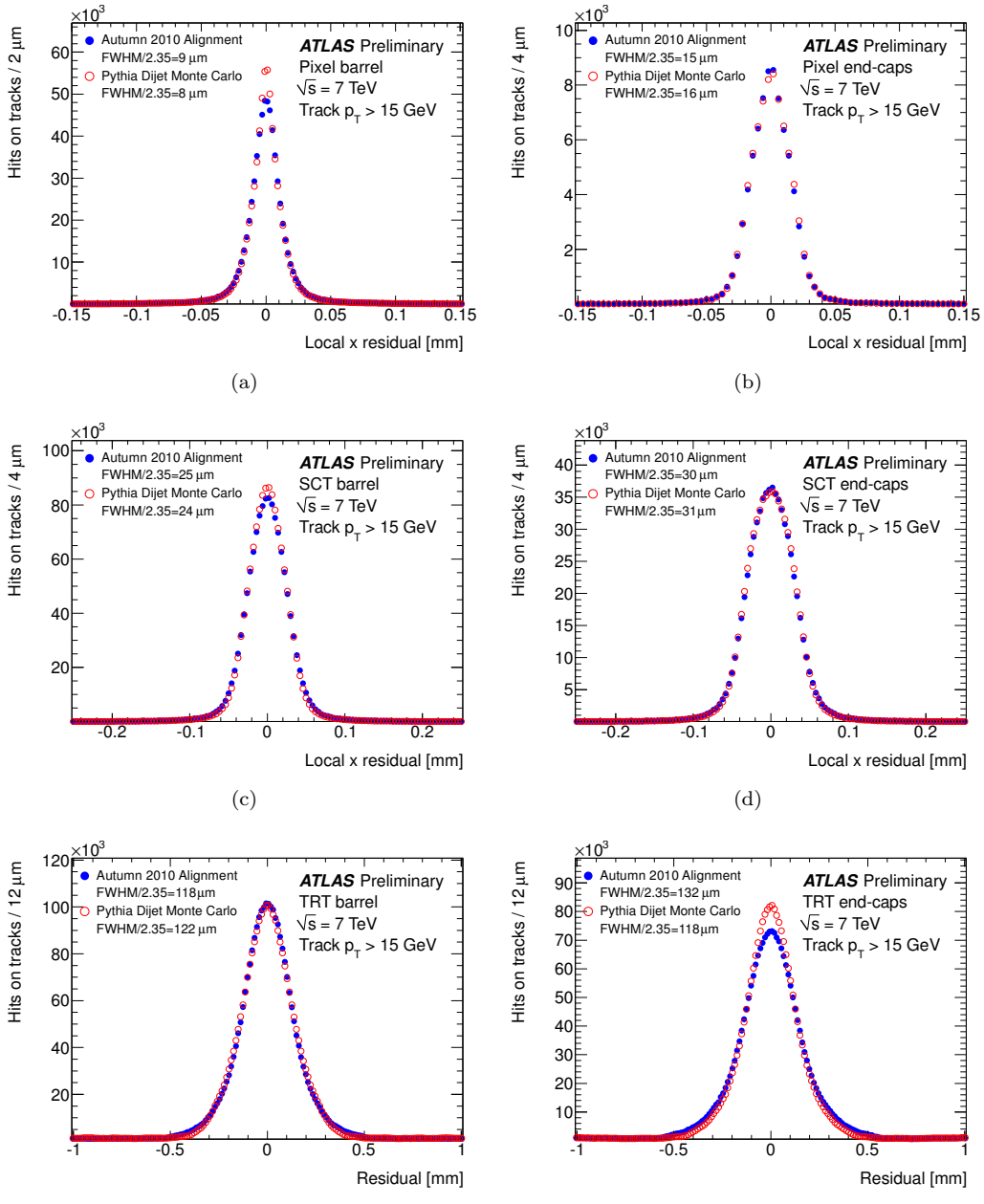

Figure 5.16: Residual distributions for Pixel, SCT and TRT. The results in data after the L3 alignment are shown in blue. The expectation from a perfectly aligned detector in MC is shown in red. The top row shows the Pixel detector, the middle shows the SCT, and the bottom row shows the TRT. The residual distributions in the barrel are given in the left-hand column, and those in the end-caps are given on the right.

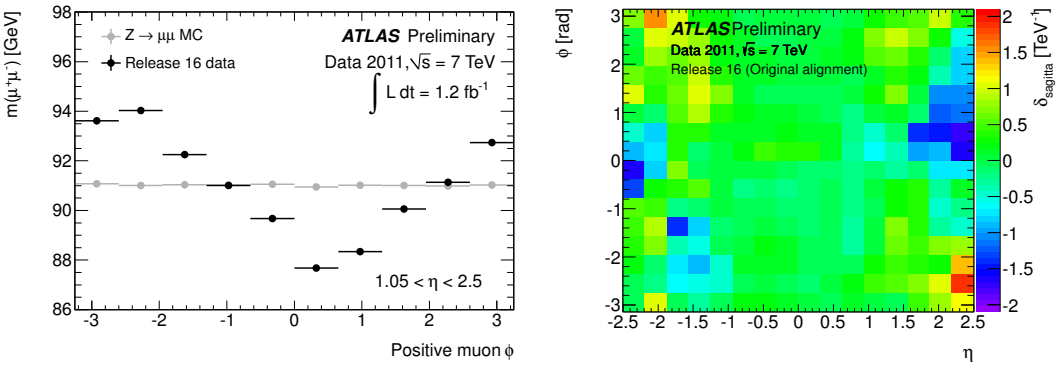

(a) (b)

Figure 5.17: Evidence for the presence of detector weak modes after alignment. Figure (a) shows the mean of the reconstructed Z invariant mass using ID tracks in $Z \to \mu\mu$ events as a function of the ϕ of the positive muon, for tracks in end-cap A. Figure (b) shows the measured sagitta bias using $W \to e\nu$ events as a function of the electron η and ϕ. No bias is expected from a properly aligned detector.

$Z \to \mu\mu$ events. It shows the reconstructed Z mass using the ID tracks as a function of the ϕ of the positive muon. In this plot both muons from the Z are required to be in end-cap A. A dependence of the reconstructed Z mass with muon-ϕ is seen in the data in black. This dependence is unexpected and not seen in the perfectly aligned MC, shown in gray. A similar result was also seen for tracks in end-cap C and, to a smaller extent, for tracks in the barrel. Another anomaly can be seen in Figure 5.17b. This figure shows the measured sagitta, or curvature bias,[5] in $W \to e\nu$ events as a function of the electron η and ϕ. The sagitta bias is measured by comparing the measured energy in the calorimeter (E), to the measured momentum in the ID (p), separately for positrons and electrons. No bias is expected from a properly aligned detector. These anomalies are present after the full ID alignment and are a sign of the presence of systematic detector deformations associated to weak modes.

To remove the weak modes the alignment must be done using constraints on the measured track parameters external to the ID. This will prevent a systematic deformation that biases the track parameters from being introduced. This was done using maps of the measured sagitta distortions from $W \to e\nu$ events, as shown Figure 5.17b. An iterative method was used to remove the biases. In the first step, the sagitta bias maps of the ID were calculated from $W \to e\nu$ events. In the second step, the measured biases were applied to correct the p_{T} of the ID tracks used in the alignment.

[5] The sagitta bias is measured as the difference in the average $\frac{E}{p}$ for positrons and electrons divided by twice the average E_T. The sagitta bias leads to a bias in the $\frac{E}{p}$ that is charge dependent and proportional to E_T: $\Delta\frac{E}{p} = E_T \times \delta_{\mathrm{sagitta}}$ for electrons and $\Delta\frac{E}{p} = -E_T \times \delta_{\mathrm{sagitta}}$ for positrons.

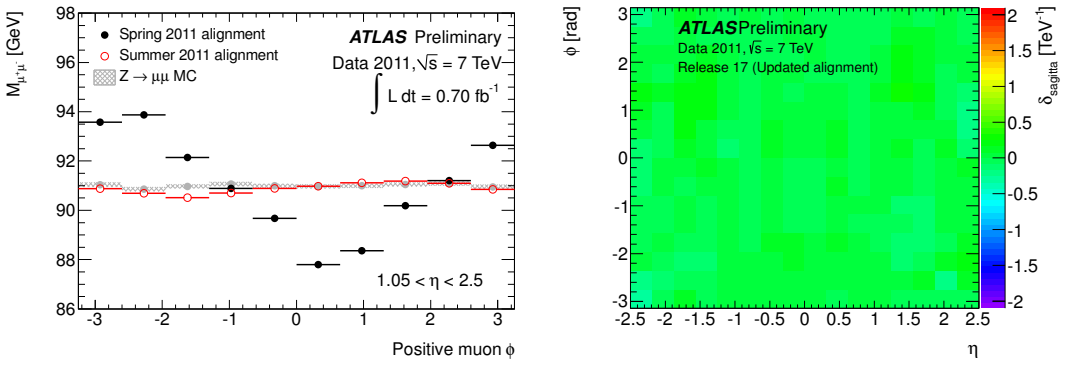

(a) (b)

Figure 5.18: Evidence for the removal of detector weak modes with the constrained alignment. Figure (a) shows the mean of the reconstructed Z invariant mass using ID tracks in $Z \to \mu\mu$ events as a function of the ϕ of the positive muon, for tracks in end-cap A. The data before the constrained alignment is shown in black. The data after the constrained alignment is shown in red. The expectation from a perfectly aligned detector is shown in gray. Figure (b) shows the measured sagitta bias using $W \to e\nu$ events as a function of the electron η and ϕ after the constrained alignment. No bias is seen after the constrained alignment.

The alignment was then performed with the input tracks constrained to the corrected p_{T}. After the alignment, the sagitta bias maps were recalculated using the updated detector geometry. The process was iterated until convergence was reached. Both the L2 and the L3 alignment was run using this procedure. The results of this alignment have been reported in Reference [89].

The updated alignment, using the p_{T} constraint, removed the biases in the $Z \to \mu\mu$ and $W \to e\nu$ events seen before. Figure 5.18a shows the reconstructed Z mass as a function of the ϕ of the positive muon. The result after the constrained alignment is shown in red. This is to be compared to the data prior to the alignment in black. The large biases are removed with the updated alignment and the data resemble the expectation from MC. The map of the sagitta bias using the updated alignment is shown in Figure 5.17b. Biases present before alignment in Figure 5.18b, are removed by the constrained alignment.

This section has summarized the ID alignment. The full ID alignment procedure has been performed at all levels using a combination of cosmic-ray data, 900 GeV collision data, and 7 TeV collision data. As a result of the ID alignment, biases in the residual distributions have been removed, and the detector resolution is approaching that of a perfectly aligned detector. Weak modes, biasing the reconstructed track p_{T}, have been discovered and removed. With the track-based alignment as presented here, the performance of the ID track reconstruction is close to that of the design. An example of this can be seen in Figure 5.19 which shows the constructed invariant mass using ID

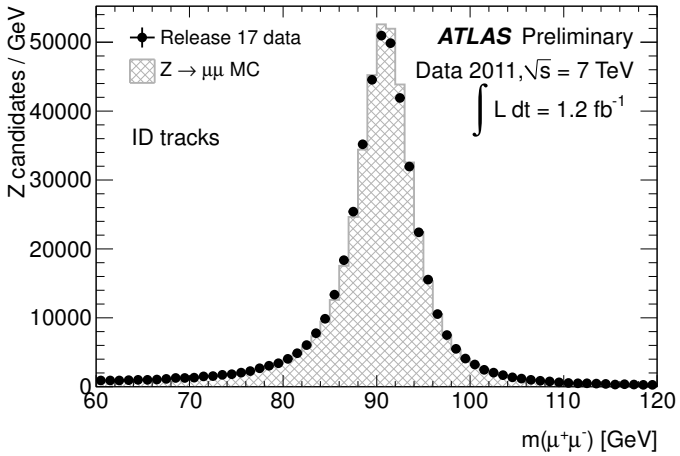

Figure 5.19: Reconstructed invariant mass using ID track for $Z \to \mu\mu$ events. The data after detector alignment is shown in black. The expectation from a perfectly aligned detector is shown in gray.

tracks in $Z \to \mu\mu$ events. The data is shown in black, the perfectly aligned MC is in gray. The resolution on the reconstructed Z-mass is approaching the MC expectation.

This chapter has introduced detector alignment and the track-based method of alignment. Methods of alignment validation have been discussed, and a summary of the detector alignment as applied to the ATLAS ID has been given. The following chapter presents the details of the track-based alignment as applied to the TRT.

Chapter 6

TRT Alignment

This chapter describes the alignment of the TRT. The TRT alignment began with the first recorded cosmic-ray data and continued through to the 7 TeV collision data, used to perform the wire-level alignment. The various stages of the alignment procedure are documented, and the results are presented.

The remainder of this chapter is organized as follows: Section 6.1 describes the aspects of the TRT construction that are relevant for the alignment. Section 6.2 describes the levels of the alignment procedure and the active degrees of freedom. Section 6.3 describes the alignment of the TRT barrel with respect to the Pixel and SCT detectors. Section 6.4 describes the alignment of the TRT end-caps with respect to the rest of the Inner Detector. Section 6.5 describes the internal module-level alignment of the TRT barrel. Section 6.6 describes the internal wheel-level alignment of the TRT end-caps. Section 6.8 describes the wire-level alignment of the TRT end-caps. Section 6.9 describes the wire-level alignment of the TRT Barrel. Section 6.10 describes the z alignment of the TRT end-cap wheels.

6.1 TRT Construction

The various steps of the TRT alignment procedure are driven by the different stages of the TRT construction [56, 57]. The TRT was constructed following a modular design. The TRT is composed of a barrel and two end-caps which were assembled independently and then later combined. Similarly, the barrel and end-caps were themselves assembled from smaller individual units that were constructed independently. This modular approach allowed the construction to proceed in parallel, at different sites and built in contingency during the assembly. Spare units were constructed which could be swapped into the detector if failures occurred. The remainder of this section describes the detector geometry and aspects of the assembly relevant to the alignment.

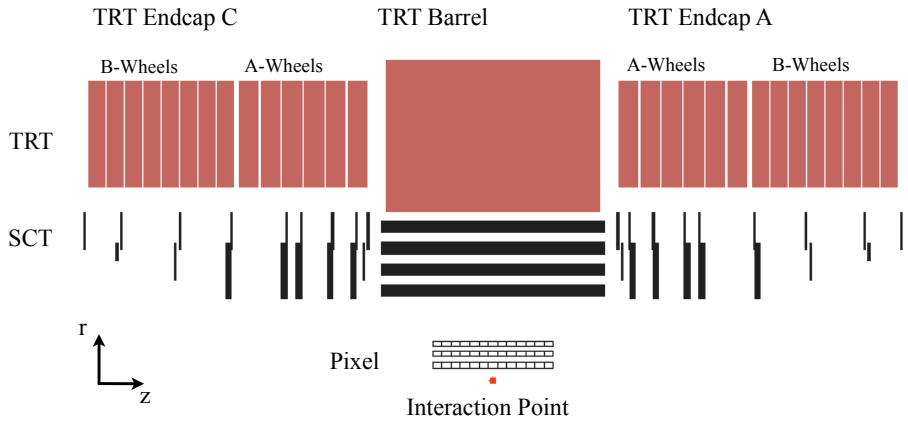

Figure 6.1: Schematic of TRT in the r-z plane. The TRT is composed of barrel and end-cap detectors. The division of the end-caps into A-wheels and B-wheels can be seen.

A schematic of the TRT is shown in Figure 6.1. The TRT is composed of three main detector pieces: barrel, end-cap A, and end-cap C. The barrel is located at the center of the detector along the z axis, with end-cap A (C) positioned at larger (smaller) values of z. The barrel and end-caps were each constructed independently and combined in the final stage of the detector construction.

The basic construction unit in the TRT barrel is the barrel module. The barrel modules each consist of a carbon-fiber shell, 400 μm thick, surrounding a collection of individual straw drift tubes. The straw drift tubes, or "straws", are the basic detector element in the TRT [58]. An example of the layout of the straws in a barrel module is shown in Figure 6.2. The straws are arranged parallel to one another and along the z-direction. Figure 6.3 shows the composition of the barrel modules along z. A wire joint electronically splits the wires within the straws near the center of the barrel modules. The halves of the wires are physically connected and are attached to the barrel modules at three wire supports: one at either end of the barrel module, and one in the center. Each wire is individually attached to the barrel modules, there is no physical substructure to the barrel modules beyond the individual wires. There are three types of barrel modules, Type I, Type II, and Type III, each of different size. Each of the barrel modules were constructed independently and later combined to form the TRT barrel. In the following, layers of straws, or "straw-layers", are discussed. This term denotes a logical collection of adjacent straws. A straw-layer does not represent a physically distinct structure within the barrel modules. An example group of straws making up a straw-layer are highlighted blue in Figure 6.2.

The Barrel Support System (BSS) [56], shown in Figure 6.4, supports the barrel modules and gives the barrel its shape. The BSS, is composed of wheel-like end-frames connected by two cylinders:

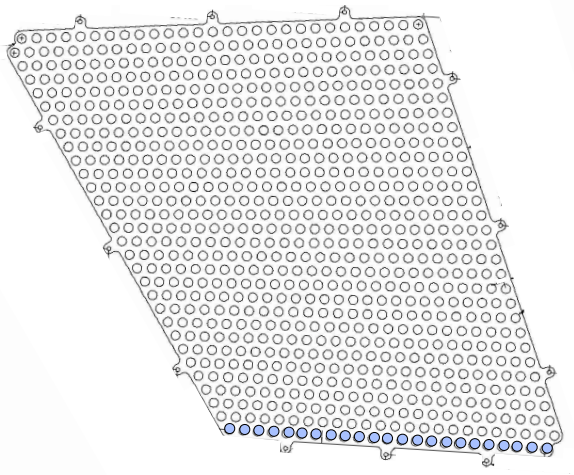

Figure 6.2: Schematic of a Type II TRT barrel module. The circles represent individual straws, which are all oriented parallel to the beam line. The z-axis (beam pipe) is in the direction coming out of the page. The first layer of straws is highlighted in blue at the bottom.

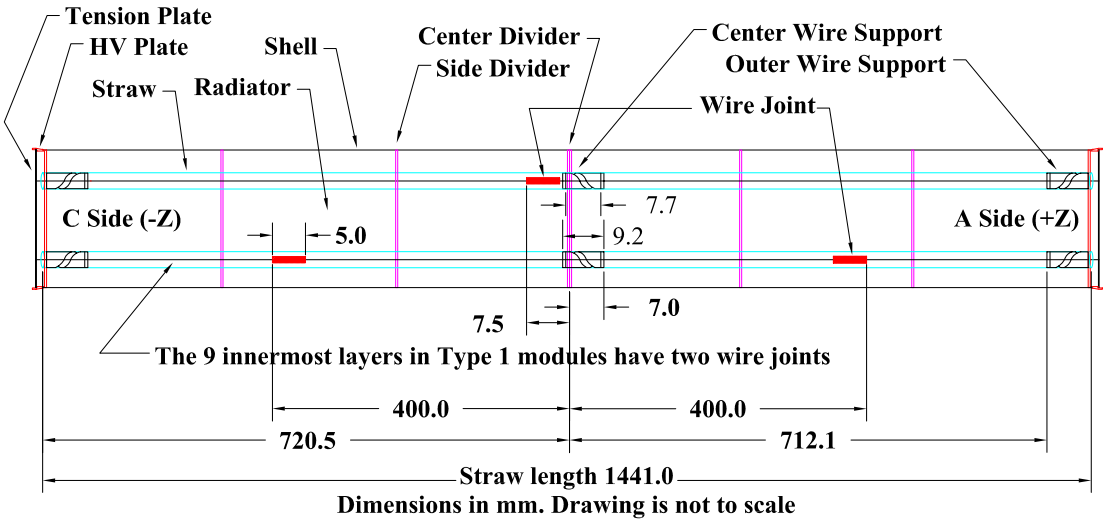

Figure 6.3: Schematic of a TRT barrel module along z. The wires are connected, but electronically split in the center of the barrel modules.

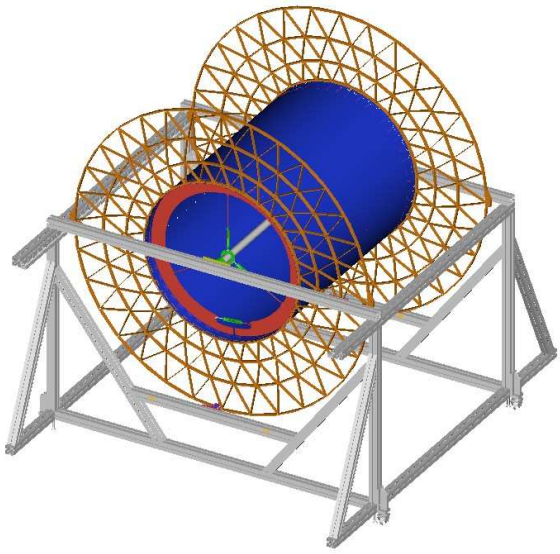

Figure 6.4: The Barrel Support System. Holds the TRT barrel modules in place forming the TRT barrel. The outer cylindrical shell is not shown.

one on the inner radius and one on the outer radius. As shown in Figure 6.5, the barrel is composed of three concentric layers of modules. Each layer is made up of 32 individual barrel modules. A radial group of modules at a given ϕ angle is referred to as a ϕ-sector. Each of these modules is connected to the BSS at either end by steel pins at opposite corners of the modules. Modules of Type I are the smallest and make up the first barrel layer, modules of Type II make up the second barrel layer, and modules of Type III are the largest and make up the outer barrel layer.

The basic construction unit in the TRT end-cap is the 4-plane wheel. The 4-plane wheels are composed of inner and outer carbon-fiber supporting rings attached by radially oriented straws. Figure 6.6 shows a picture of a 4-plane wheel during assembly. The inner and outer rings are visible, and one straw is shown connecting the rings. Four layers of straws planes are contained in a 4-plane wheel. The 4-plane wheels come in two varieties, Type-A and Type-B, which differ in the z-spacing of the straw planes. As with the barrel modules, there is no physical substructure to the 4-plane wheel beyond the individual wires. Each wire is individually connected to the 4-plane wheel. Straw planes are referred to in the following. This term simply denotes a logical collection of adjacent straws. The 4-plane wheels were each constructed independently using a custom-made aluminum alloy assembly table [57]. The table was specifically designed for flatness and was drilled with precision holes to position the rings during assembly.

Pairs of 4-plane wheels are combined back-to-back to form 8-plane end-cap wheels. The Type-B

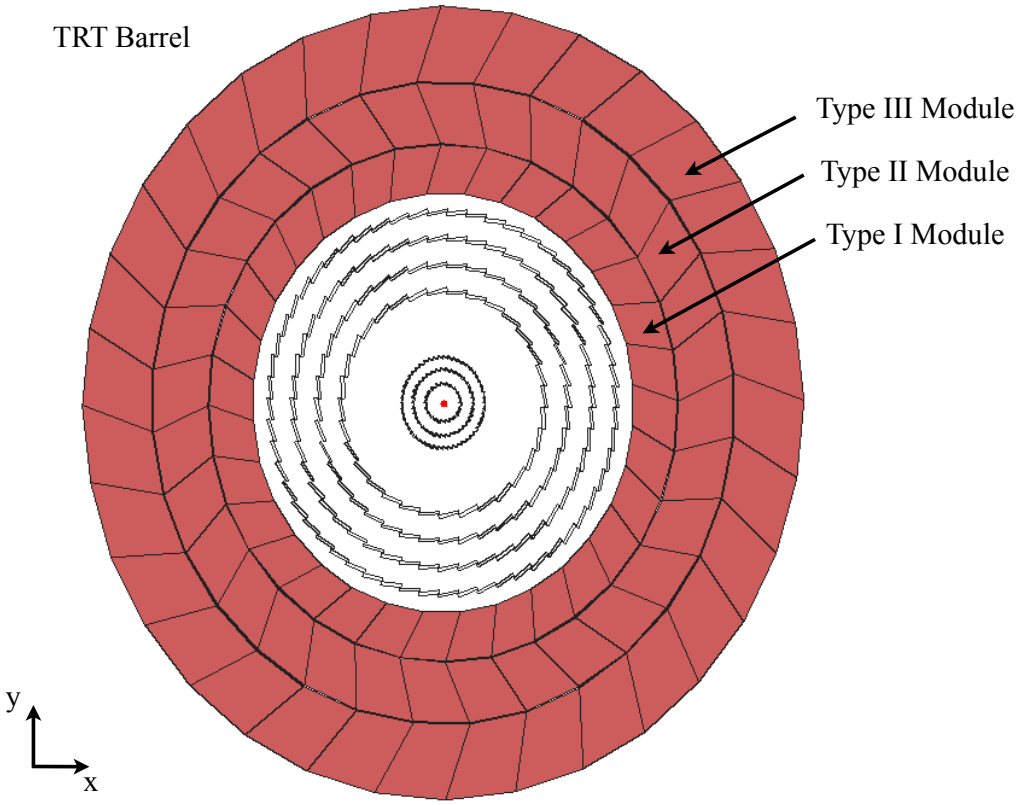

Figure 6.5: Schematic of the Inner Detector barrel, x-y view. The TRT barrel modules are the red shaded trapezoids. The three layers of module types are indicated.

8-plane wheels are referred to as Type-B end-cap wheels. Pairs of Type-A 8-plane end-cap wheels are further combined to create 16-plane end-cap wheels, these are referred to as Type-A end-cap wheels. Six Type-A end-cap wheels were stacked and combined with a stack of eight Type-B end-cap wheels to form an end-cap. In total each end-cap is comprised of 40 4-plane wheels: 24 (6×4) of Type-A and 16 (8×2) of Type-B . The end-caps are then positioned next to the barrel with the Type-A stack closest to the interaction point. The division of the end-caps into stacks of Type-A and Type-B wheels is visible in Figure 6.1.

6.2 TRT Alignment Levels

During each stage of the detector assembly, uncertainties on the detector positions are introduced as a result of the finite accuracy with which the components can be positioned. As a result of the modular construction, different levels of detector misalignment are expected. During each stage of the detector

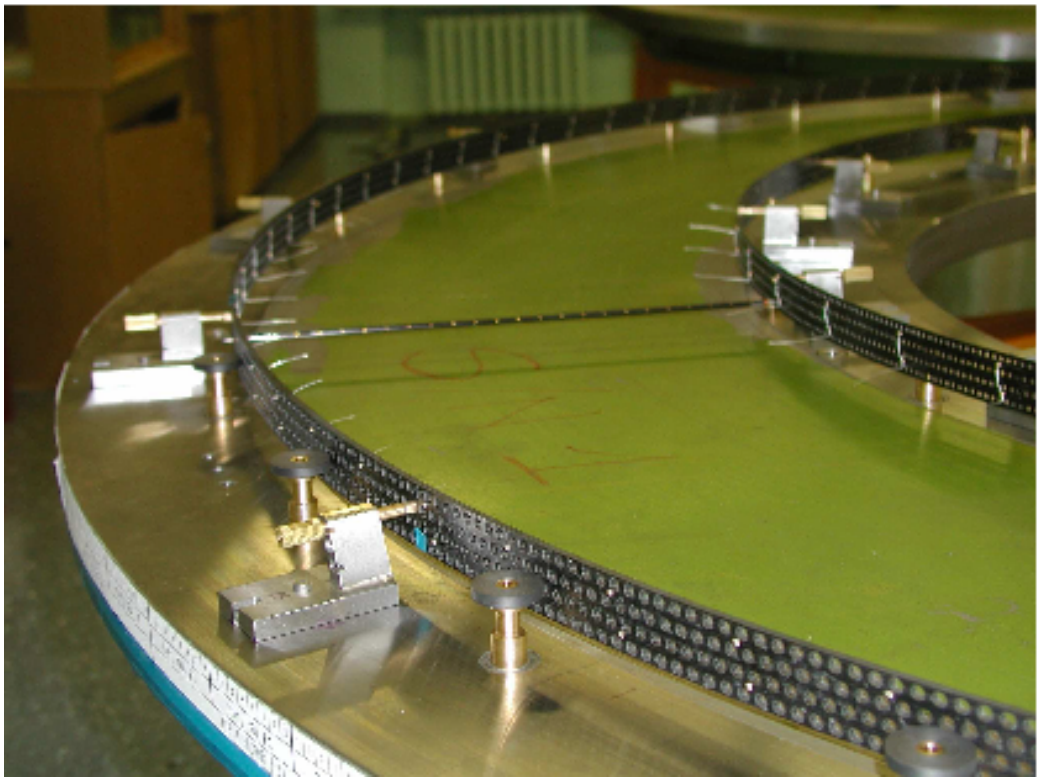

Figure 6.6: A picture of a TRT end-cap 4-plane wheel during construction. The inner and outer supporting rings are visible. One straw is shown connecting the rings.

assembly, misalignment will occur that correlates the misalignment of the constituent components. For example, an overall misalignment of the barrel will lead to a correlated misalignment of all barrel modules, which leads to the correlated misalignment of all straws within a given barrel module. This hierarchy of detector misalignment is exploited in the alignment procedure by performing the alignment separately at different levels. The misalignment of large structures are corrected first, removing the correlated misalignment of the lower level substructures. The TRT alignment is performed in three stages, or levels, with a granularity chosen to match that used in the detector assembly. The remainder of this section describes the different alignment levels.

In the first step of the TRT alignment, the barrel and each end-cap are aligned with respect to the rest of the Inner Detector (ID). This step is referred to in the following as the Level 1 (L1) alignment. During the L1 alignment the barrel and each end-cap are aligned as rigid bodies. The alignment of a rigid body is described by six degrees of freedom (DoF): three translations position the body in space and three rotations describe the orientation. The end-caps are each aligned with these six DoF at L1. The measurements in the barrel contain no information about the z-coordinate.

The track reconstruction is therefore insensitive to the barrel position along z. In the L1 alignment of the barrel, translations along z are ignored. The barrel is aligned in five DoF: two translations position the barrel in the x-y plane, and three rotations describe the orientation. In total, 17 DoF are corrected at L1. The relative misalignment of the L1 structures are expected to be larger than the internal module-level, or wheel-level, misalignment. Additionally, L1 misalignment represents the largest coherent displacement of straws. As a result, the L1 alignment has a larger impact on track reconstruction than the subsequent levels.

The barrel and end-caps are aligned internally during the second level of alignment. The Level 2 (L2) alignment treats the individual barrel modules and end-cap 4-plane wheels as rigid bodies. The 4-plane wheels are aligned with all six DoF. As the case in L1, displacements of the barrel along z are neglected. Each barrel module is aligned in five DoF. Although the wires inside of the barrel modules are separated into A and C-sides, the A-C distinction does not exists at the module level. In the L2 alignment the A and C-sides of the barrel modules are treated as a single rigid object. In total, 960 DoF are corrected at L2: (3 barrel layers $\times$ 32 modules per layer $\times$ 5 DoF per module) + (2 end-caps $\times$ 40 wheels per end-cap $\times$ 6 DoF per wheel)

The third and final step in the TRT alignment is the wire-level alignment. The Level 3 (L3) alignment positions the individual wires as rigid bodies. There are over 350,000 wires in the TRT. This large number of L3 objects poses a serious challenge to the alignment procedure. As a result of the large number of DoF, only the local-χ^2 alignment procedure[6] can be performed. To reduce the total number of DoF needed at L3, the individual wires are only aligned in the most sensitive DoF. The wire displacement perpendicular to the direction of tracks originating from the interaction point has the largest impact on track reconstruction. This misalignment can be described by two DoF: a translation in the straw plane, perpendicular to the direction along the wire and a rotation around the axis perpendicular to the straw plane. These L3 DoF are sketched in Figure 6.7. The L3 misalignment is described by the displacement at either end of the wire: dx1 and dx2. The wire translation and rotation are given by linear combinations of these displacements[7]. Measurements in the TRT do not contain information about the track position along wire, thus displacements along the wire are ignored. The wire misalignment out of the straw plane has a second order effect on track reconstruction and are also ignored in the TRT L3 alignment. In the barrel, the A-side and C-side wires are treated separately. Although attached physically, separating the wire sides allows a displacement of the center wire support to be corrected. In total there are 701696 DoF in the L3 alignment: (52544 straws in the barrel $\times$ 2 wires per straw $\times$ 2 DoF per wire) + (2 end-caps $\times$

[6] see Section 5.2.2.

[7] Translation = $\frac{1}{2}$(dx1 + dx2), Rotation $\approx \frac{1}{\text{straw length}}$(dx1 - dx2)

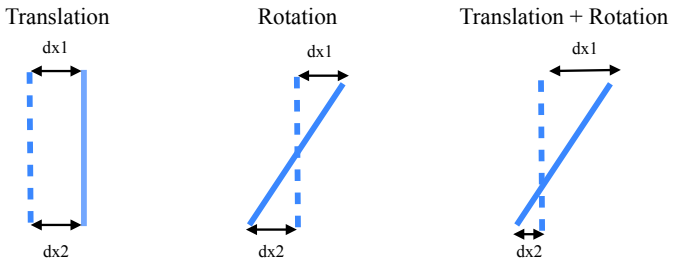

Figure 6.7: Wire-level DoF used in the L3 alignment. The plane of the page represents the straw plane. The direction of charged particles is into the page. The sensitive displacements in the straw plane can be represented by two DoF: a translation and a rotation.

122880 wires per end-cap $\times$ 2 DoF per wire). The L3 TRT alignment has over an order of magnitude more DoF than any another alignment level in ATLAS.

In the L3 alignment, the wires are aligned, not the straws. The position of the measured track is determined from the measured leading edge, which is sensitive to the wire position, not the position of the straw wall. As as result, the track-based alignment is sensitive to the position of the wire. In general, the wire may be offset with respect to the center of the straw. The wire-level corrections determined from the alignment are applied to both the wire and the straw. Wire-straw misalignment is currently not corrected in the TRT alignment[8].

Throughout the TRT alignment, deformations of detector modules are not explicitly corrected. Detector deformations at a given level are implicitly corrected by the alignment at the subsequent level. Distortions of L1 structures, *e.g.,* from the deformation of the BSS, would be corrected at L2 by a correlated movement of L2 structures. Similarly, distortions of barrel modules or end-cap wheels will be corrected at the wire-level and would be seen as coherent displacements of individual wires. Deformations of the individual wires are not corrected. No evidence of wire-level deformations has been found.

Each of the three levels of the TRT alignment has been performed using a track-based alignment procedure[9] and will be described in the remainder of this chapter. The L1 barrel and end-cap alignment, and the L2 barrel alignment were able to be performed before collision data taking using cosmic-ray muons ("cosmic-rays"). An initial L2 end-cap alignment was also performed with cosmic-rays. Collision data, taken in 2009 at 900 GeV, was used to finalize the L2 end-cap alignment. The L3 barrel and end-cap alignment was performed using large statistics samples of 7 TeV collision data. These are each described in the following.

[8] In principle, the time-over-threshold information could be used to determine the wire-straw offsets as it is sensitive to the position of the straw wall with respect to the wire. This is a topic for another thesis.

[9] see Chapter 5

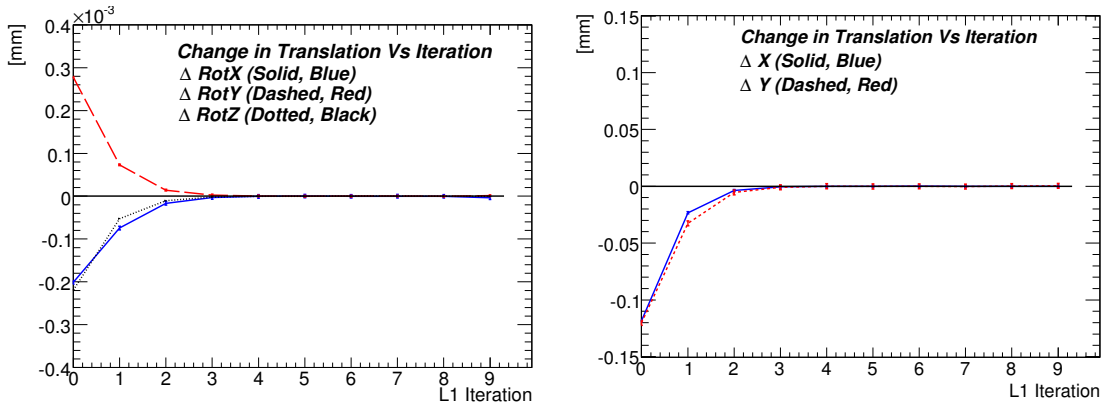

(a) (b)

Figure 6.8: Convergence of the L1 barrel alignment parameters. The changes in the alignment DoF vs iteration: (a) shows the convergence of the rotational DoF and (b) shows the convergence of the translation DoF.

6.3 L1 Barrel Alignment

In the fall of 2008, ATLAS held a dedicated cosmic-ray data taking period, during which over seven million tracks from cosmic-ray muons were recorded in the ID [47]. This data set was the first to be collected with the all of the ID subsystems participating in the running and was essential for understanding and commissioning the ID. The L1 TRT barrel alignment was performed using this data set. The L1 alignment presented here was performed using the track-based alignment as described in Section 5.2 and implemented in Reference [84]. An alignment of the Pixel and SCT detectors was performed prior to the TRT alignment. The initial L1 alignment was done with a data sample that had relatively large statistics, ≈250,000 events, the solenoid on, and the TRT operating with Xe gas mixture. Combined ID tracks, tracks containing both information from both the TRT and SCT, are needed for the L1 alignment.

The L1 alignment was run for ten iterations, the convergence can be seen in Figure 6.8. The Figures show the change in alignment parameter as a function of iteration. Figure 6.8a shows the rotational DoF, whereas the translational DoF can be seen in Figure 6.8b. The convergence is complete after four iterations. The number of reconstructed hits on track and the number of reconstructed tracks increased with iteration. The reconstructed L1 alignment parameters are given in Table 6.1.

To assess the quality of the L1 barrel alignment, validation plots produced with the ID geometry before and after the L1 barrel alignment were compared. Improvements in the distributions with

DoF	Misalignment
Translation x	-0.146 mm
Translation y	-0.159 mm
Rotation x	-0.300 mrad
Rotation y	0.369 mrad
Rotation z	0.285 mrad

Table 6.1: Results of the TRT L1 barrel alignment.

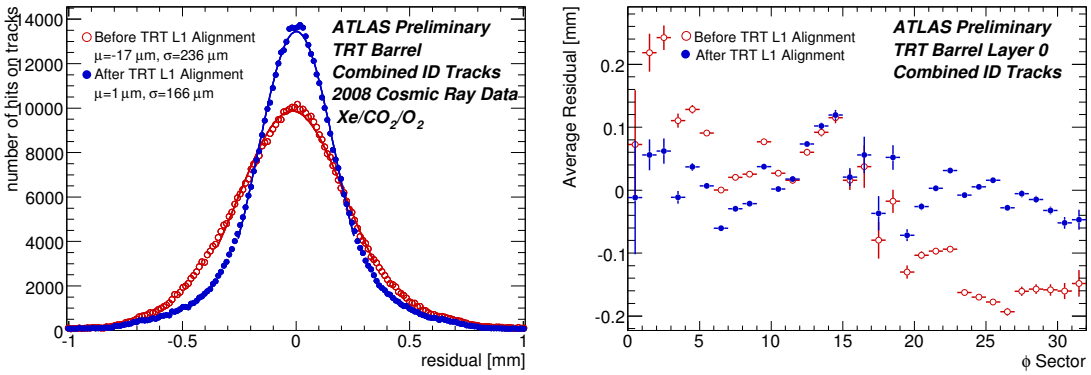

(a) (b)

Figure 6.9: (a) Comparison of the TRT residual for combined tracks before and after the L1 alignment. (b) Comparison of the average residual of combined tracks vs ϕ-sector for barrel modules in the first layer, before and after the L1 alignment.

the aligned geometry were seen uniformly across all quantities monitored. Examples are shown in Figures 6.9 and 6.10. Figure 6.9a shows the residual for all TRT barrel hits on track. This distribution is expected to be centered on zero with a width representing the TRT resolution. Figure 6.9a shows that the L1 alignment removes an initial bias present in the residual and improves the detector resolution by 60 μm. In Figure 6.9b the average residual in the first barrel layer is plotted as a function of ϕ-sector. Again improvement with the L1 alignment is seen; after alignment the residuals are closer to zero. The remaining scatter of the average residual in the aligned distribution is due to internal TRT misalignment, which cannot be removed at L1. The independent validation of the alignment from the split tracks[10] is shown in Figure 6.10. Figure 6.10a shows the matching in $\frac{q}{p_T}$ and Figure 6.10b shows the matching in ϕ_0. For both track parameters, the L1 alignment removes an initial bias and improves the resolution. The improvements seen in these validation plots provide confidence that the correct L1 barrel alignment was reached.

The L1 barrel alignment was repeated with collision data taken from the first 900 GeV commis-

[10] see Section 5.3 for discussion

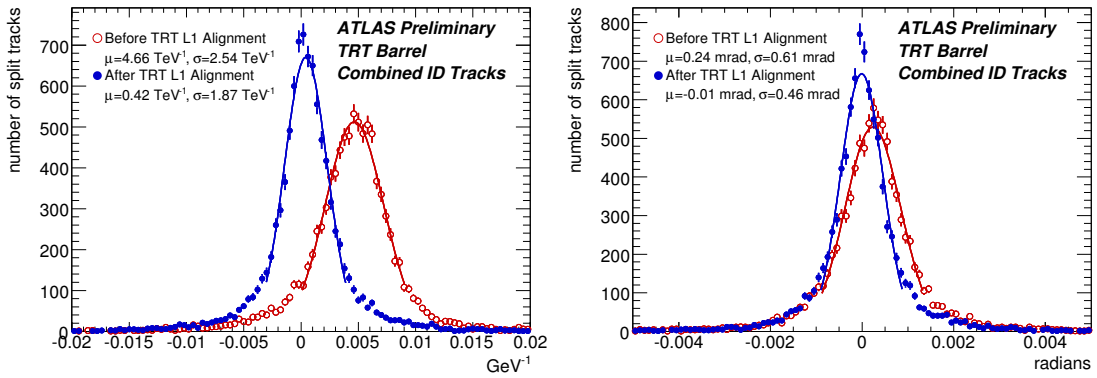

Figure 6.10: Validation of the L1 alignment with split tracks. Comparison of the $\frac{q}{p_T}$ (a) and the ϕ_0 (b), difference of split tracks before and after the L1 alignment.

DoF	End-cap A	End-cap C
Translation x	-1.03 mm	-0.20 mm
Translation y	-0.22 mm	1.49 mm
Translation z	-3.19 mm	1.82 mm
Rotation x	0.14 mrad	-0.33 mrad
Rotation y	0.87 mrad	0.51 mrad
Rotation z	-7.50 mrad	5.74 mrad

Table 6.2: Result of the L1 alignment derived from cosmic-ray data.

sioning run in the end of 2009 and with 7 TeV collision data taken in 2010 and 2011. No significant differences with the alignment presented here were seen.

6.4 L1 End-cap Alignment

The L1 end-cap alignment was also initially performed using the 2008 cosmic-ray data described in the previous section. For this alignment, reconstructed tracks crossing the TRT end-caps and the SCT barrel were used. The alignment was repeated for several iterations until the alignment parameters converged. The number of reconstructed hits on track increased, and the overall TRT resolution improved as a result of the alignment. The results of the L1 end-cap alignment are given in Table 6.2.

Unlike the barrel, the end-cap alignment greatly benefited from the first collision data collected during the 900 GeV commissioning run [48]. Collision data provides combined ID tracks that illuminate the end-caps much more uniformly than cosmic-rays. This can be seen by comparing

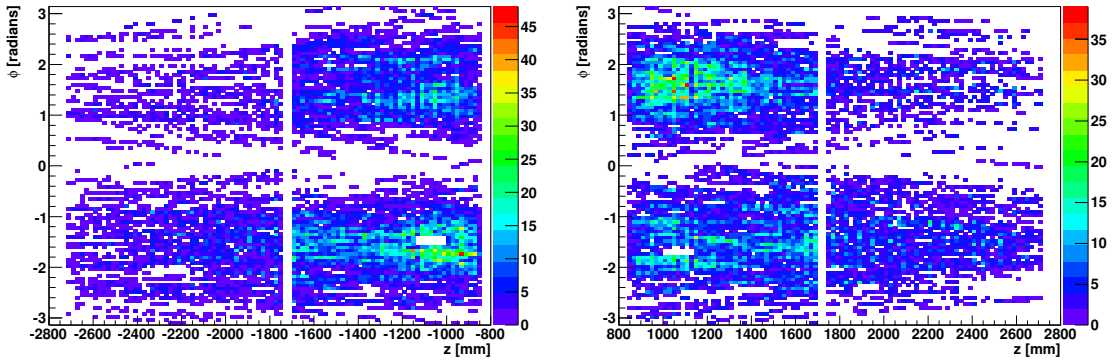

(a) (b)

Figure 6.11: Map of the TRT hits from combined ID tracks in cosmic-ray data. The figures show the number of hits on track as a function of z and ϕ, for end-cap C (a) and end-cap A (b).

DoF	End-Cap A	End-Cap C
Translation x	-1.49 mm	-1.05 mm
Translation y	0.24 mm	1.75 mm
Translation z	-3.38 mm	2.11 mm
Rotation x	0.06 mrad	-0.76 mrad
Rotation y	0.88 mrad	0.04 mrad
Rotation z	-6.39 mrad	6.98 mrad

Table 6.3: Result of the L1 alignment derived from collision data.

the hit maps for combined ID tracks in cosmic-ray data, Figure 6.11, to those from collision data, Figure 6.12. The L1 end-cap alignment was repeated with the 900 GeV collision data. The measured misalignment is given in Table 6.3. The differences in the measured L1 misalignment with the cosmic-ray data and the collision data, as seen in Tables 6.2 and 6.3, are not unexpected. The illumination of the TRT end-caps with combined ID tracks is different in the two cases. With the limited illumination in the case of the cosmic-ray data, the L1 alignment is effectively determining the average position of a subset of the end-cap, while with the more complete illumination in the collision data, the L1 alignment samples a much larger fraction of the end-caps.

The alignment using the 900 GeV collision data was used for the L1 end-cap alignment. The L1 end-cap alignment was repeated with 7 TeV collision data taken in 2010 and 2011. No significant differences with the 900 GeV alignment were seen.

To asses the quality of the L1 end-cap alignment, validation plots produced with the ID geometry before and after the L1 end-cap alignment, were compared. The improvement in the track residual

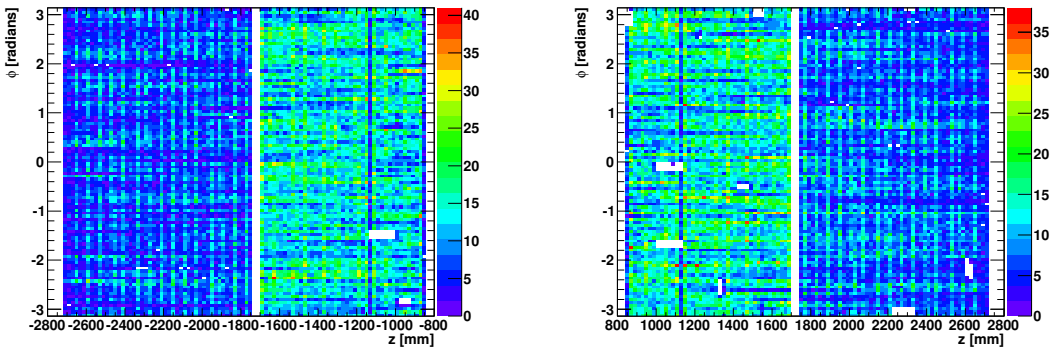

(a) (b)

Figure 6.12: Map of the TRT hits from combined ID tracks in collision data. The figures show the number of hits on track as a function of z and ϕ, for end-cap C (a) and end-cap A (b).

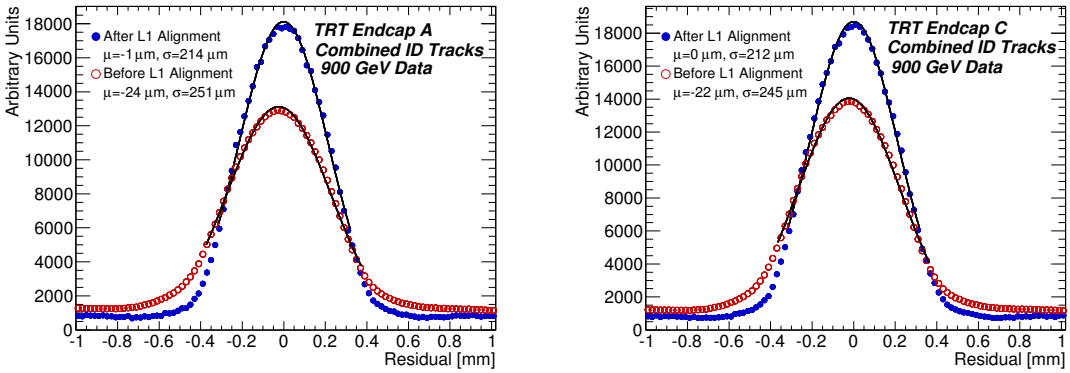

(a) (b)

Figure 6.13: The TRT end-cap residual distributions before and after the L1 end-cap alignment for end-cap A ((a)) and end-cap C ((b))

distributions can be seen in Figures 6.13 and 6.14. Figure 6.13 shows the impact of the L1 alignment on the overall residual distribution in the end-caps. The L1 alignment removes an initial bias and improves the residual width by over 30 μms in each end-cap. Figure 6.14 shows the mean of the fitted residual distribution as a function of end-cap 4-plane wheel before and after the L1 alignment. After the L1 alignment the average of the fitted residuals is centered on zero. The remaining scatter in the residual is due to internal end-cap misalignment, which cannot be corrected at L1. As for the L1 barrel alignment, the improvements seen in these validation plots provide confidence that the correct L1 end-cap alignment was reached.

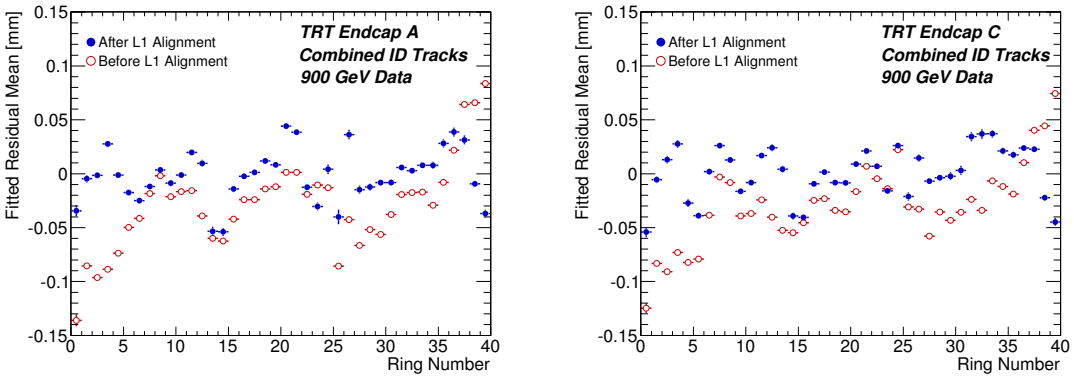

(a) (b)

Figure 6.14: Mean of the fitted TRT residual distribution as a function of end-cap 4-plane wheel (denoted ring in the figures) before and after the L1 alignment. End-cap A is shown in (a) and end-cap C is shown in (b).

6.5 L2 Barrel Alignment

The need for a L2 barrel alignment was seen above in Figure 6.9b. The residual scatter about zero indicated the presence of module-level misalignment of adjacent ϕ-sectors within a barrel layer. Figure 6.15 shows the presence of module-level misalignment of barrel modules in adjacent layers. In this figure the average residual of hits on track as a function of straw-layer is shown for hits in a single ϕ sector. Straw-layer is proportional to global $\hat{r}$ and increases with distance from the center of the ID. The first 19 straw-layers make up Type I barrel modules, Type II modules are composed of the next 23 straw-layers, and Type III modules are made up of the last 31 straw-layers. The difference of the average residuals from zero, indicates the presence of internal barrel misalignment, and the sharp discontinuities along the boundaries corresponding to barrel layers, indicate that the misalignment is present at the module-level.

In principle, the internal TRT barrel alignment is independent of the Pixel and SCT alignment and can be performed using either combined ID tracks or with TRT stand- alone tracks. In practice, an uncorrected Pixel and/or SCT misalignment can induce differences in the inferred internal TRT alignment when using combined ID tracks as opposed to TRT stand-alone tracks. The L2 barrel alignment using both of these approaches has been studied and is presented in following two sections.

6.5.1 L2 Barrel Alignment Using TRT Stand-Alone Tracks

The L2 barrel alignment was initially done using TRT stand-alone tracks. Unlike the alignment with combined ID tracks, the lack of knowledge of the z-coordinate in TRT stand-alone tracks

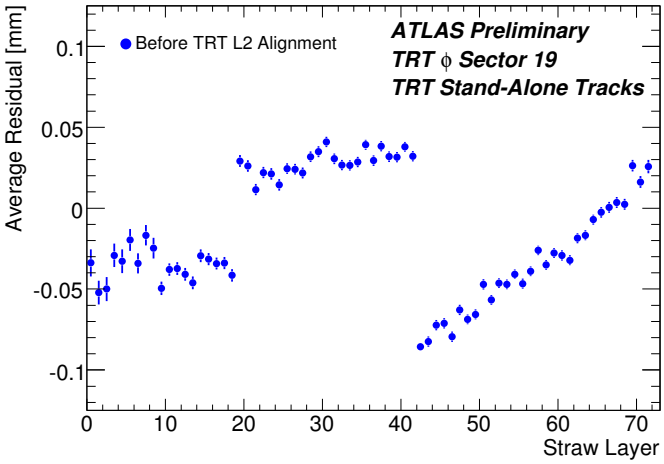

Figure 6.15: Average residual as a function of straw-layer for hits in ϕ sector 19. The discontinuities in the distribution are along module boundaries and indicate L2 barrel misalignment.

causes the rotational DoF around x and y to be under-constrained in the alignment. Attempting to align the barrel modules including these DoF, results in many unconstrained alignment solutions and prevents the alignment algorithm from converging. There is however sufficient information in the TRT stand-alone tracks to perform a L2 alignment using three DoF: translations along x and y, and rotations about z. The L2 barrel alignment with TRT stand-alone tracks was performed in these three DoF.

When aligning with TRT stand-alone tracks, the L2 alignment is independent of the rest of the ID. With the combined ID tracks, the Pixel and SCT measurements provide an overall frame of reference in which the tracks are located. Stand-alone TRT tracks provide no such reference; all the detector elements providing measurements are free to move. There will thus be trivially unconstrained DoF corresponding to coherent movements of all the modules as a rigid body, see Section 5.2.3. These correspond to the L1 barrel movements. When the L2 barrel alignment is done in three DoF, there will be a total of three unconstrained DoF. With these DoF, the χ^2 matrix of the alignment solution becomes singular, and the inversion fails. Identifying and removing these coherent movements is necessary for the L2 alignment to converge. The eigenvalue spectrum of the $\frac{d^2\chi^2}{d\vec{\alpha}^2}$ matrix is shown in Figure 6.16. The three unconstrained DoF are clearly identified as having eigenvalues near zero, orders of magnitude smaller than the others. The identification of these DoF is a consistency check of the L2 alignment procedure and a signal that the L2 alignment can proceed[11].

[11] To regularize the matrix the eigenmodes associated with the smallest eigenvalues were simply removed. A more formally correct treatment would be to add Lagrange multipliers, constraining these DoF to the measured L1 values.

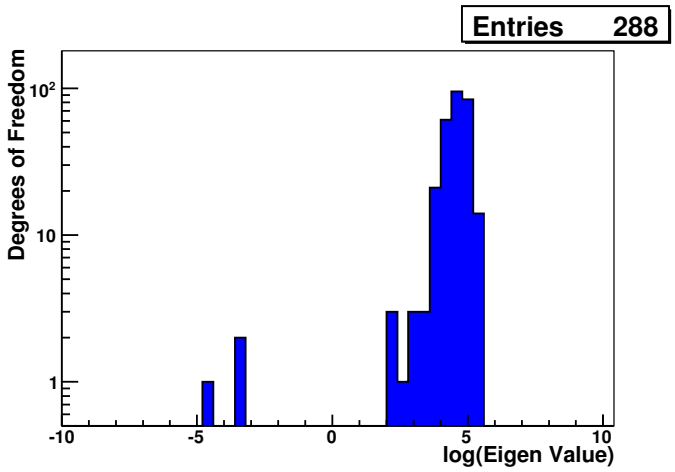

Figure 6.16: The eigenvalue spectrum of the second derivative matrix for the L2 alignment with TRT-Only tracks. The three trivially unconstrained DoF are identified as orders of magnitude smaller then the others.

The L2 barrel alignment using TRT stand-alone tracks was performed in three DoF, for five iterations. Examples of the convergence can be seen in Figure 6.17. Figure 6.17a shows the change in the rotations around z for all modules in the first barrel layer as a function of alignment iteration. Similarly, Figure 6.17b shows the change in translation of these modules along $\hat{\phi}$, as a function of iteration. The L2 convergence is complete after a few iterations. The number of hits on track and the number of reconstructed tracks increased with iteration. The result of the reconstructed barrel alignment is presented visually in Figure 6.18. The translational DoF are presented in Figure 6.18a. Each arrow represents a barrel module. The direction and size of the arrow indicates the direction and size of the measured misalignment. The rotational DoF are presented in Figure 6.18b. Again each arrow represents a barrel module. The size of the rotation is indicated by the angle the arrows make with respect to the positive x-axis.

To assess the L2 barrel alignment, validation plots using the ID geometry before and after the L2 alignment are compared. Improvements in the distributions with the aligned geometry were seen uniformly across all quantities monitored. Examples of this improvement are shown in Figures 6.19, 6.20, and 6.21. The resolution of barrel hits from TRT stand-alone tracks is shown in Figure 6.19a, before and after the L2 barrel alignment. The resolution improves with the L2 barrel alignment. Figure 6.19b shows the average residual in first module layer as a function of ϕ-sector before and after the L2 barrel alignment. The L2 barrel alignment corrects the residual bias between modules within a barrel layer. Figure 6.20 confirms that L2 alignment corrects the residual bias

This second method is not explored here.

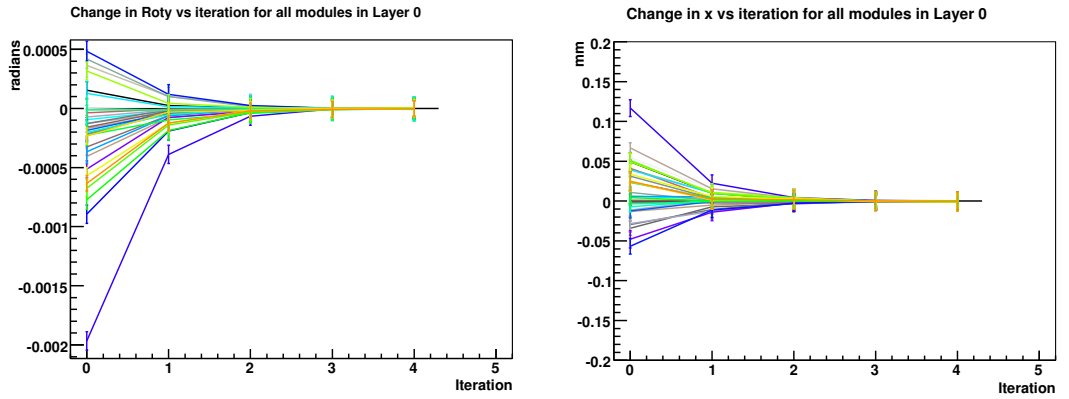

(a) (b)

Figure 6.17: Examples of convergence of the L2 alignment parameters. Changes in the rotations around y (a) and translations along x (b), as a function of alignment iteration for all modules in the first barrel layer. Each curve represents a different barrel module.

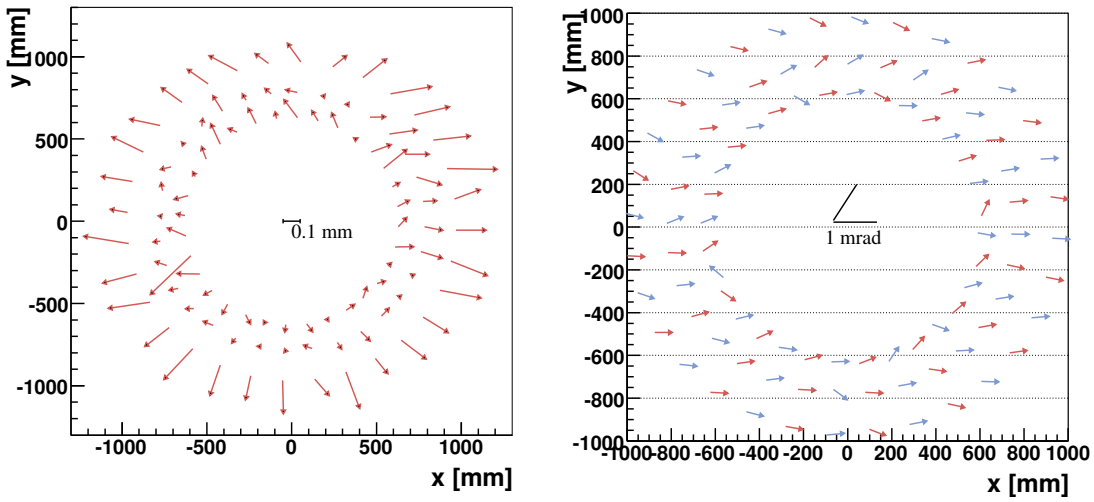

(a) (b)

Figure 6.18: Visual representation of the result of the L2 barrel alignment. (a) Visual representation of the translation alignment parameters. Each arrow represents a barrel module. The tail of the arrow is the nominal module position. The arrow length and direction represent the measured x and y alignment parameters. The arrow lengths are enlarged by a factor of 1000 relative to the axes. A scale is provided for reference. (b) Visual representation of the rotations about z. Each arrow represents a barrel module. The size of the rotation is given as the angle the arrows make with respect to the positive x-axis. The arrow length has no meaning. The size of the rotations are enlarged by a factor of 1000. A scale is provided for reference.

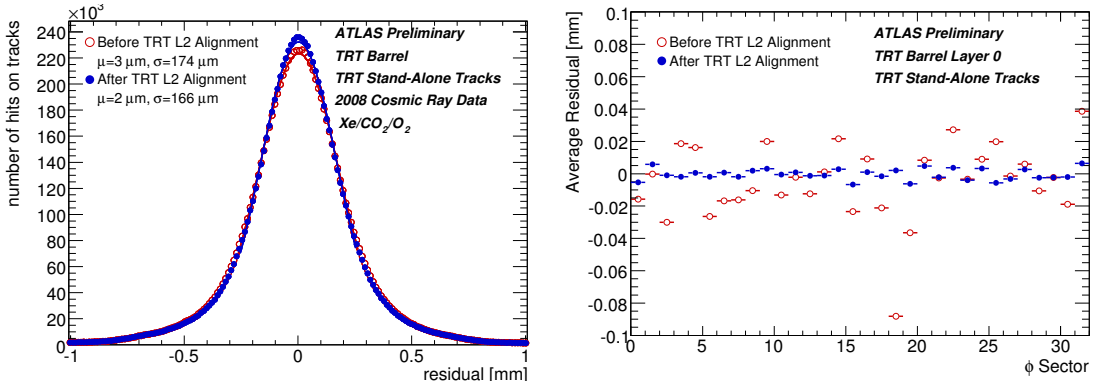

(a) (b)

Figure 6.19: TRT residuals before and after L2 alignment. (a) Comparison of TRT residual for TRT stand-alone tracks before and after L2 alignment. (b) Comparison of the average residual of TRT stand-alone tracks vs ϕ-sector for barrel modules in the first module layer, before and after L2 alignment.

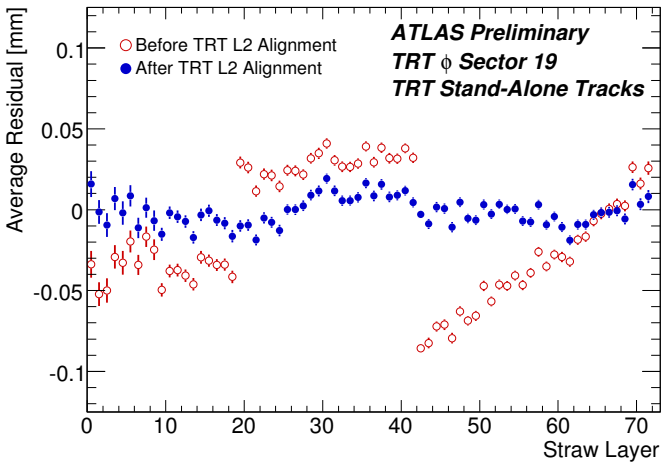

Figure 6.20: Average residual as a function of straw-layer for hits in ϕ-sector 19. The discontinuities in the distribution before L2 alignment are removed with the L2 alignment.

between module layers. Examples of the track segment validation plots are given in Figure 6.21. Both the matching in $\frac{q}{p_T}$, in Figure 6.21a, and in ϕ_0, in Figure 6.21b, show improvement with the L2 alignment.

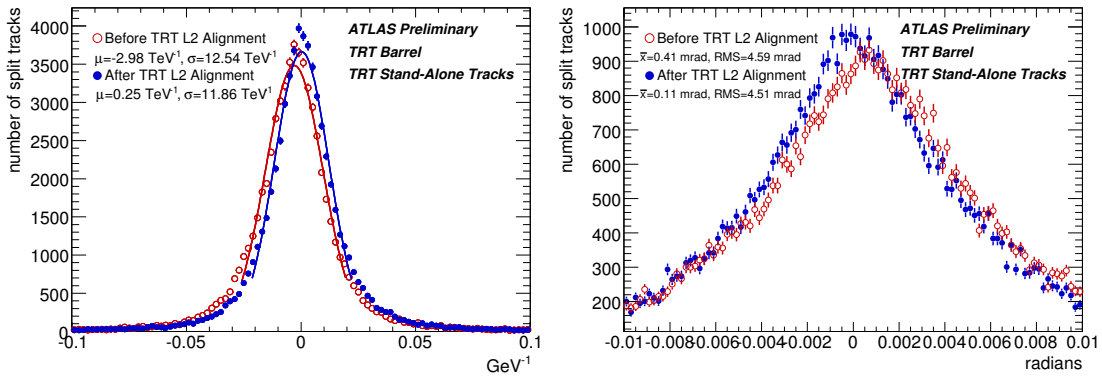

(a) (b)

Figure 6.21: Validation of the L2 alignment with split tracks. Comparison of the $\frac{q}{p_T}$ (a) and the ϕ_0 (b), difference of split tracks before and after the L2 barrel alignment.

6.5.2 L2 Barrel Alignment Using Combined ID Tracks

As an alternative approach to the L2 alignment as described in Section 6.5.1, the alignment was repeated using information from the Pixel and SCT detectors. Tracks were required to have a minimum of 45 TRT hits and a p_T greater than 2 GeV. Combined ID tracks were used when the cosmic muon entered the Pixel or SCT detectors. TRT stand-alone tracks were used when the muon was fully contained the TRT. With the L2 alignment performed in this way there is no need for regularization of the solution matrix, as the combined tracks fix the global reference frame. In addition, there is sufficient information to perform the L2 barrel alignment with all five module DoF.

The L2 barrel alignment was performed with the full five DoF and with three DoF, in order to compare to TRT stand-alone alignment. The convergence of the alignment and improvement in validation plots parallels that presented in Section 6.5.1. The differences in translations and in rotations around z in the alignment with three and five DoF was found to be negligible. The L2 alignment parameters when aligning in five DoF can be seen in Figures 6.22 and 6.23. An important thing to note in these figures is the absence of an overall offset in the L2 parameters. This lack of a common movement of the barrel modules provides another verification that L1 barrel alignment is correct. This conclusion could not have be drawn from Figure 6.18 because in this case the matrix regularization froze the effective L1 alignment DoF.

The misalignment measured in Section 6.5.1 and that shown in this section are similar in many ways. The movements are comparable in magnitude, are mainly radial, and are largest in the outer barrel layers. There are however significant, systematic differences between the two geometries. This

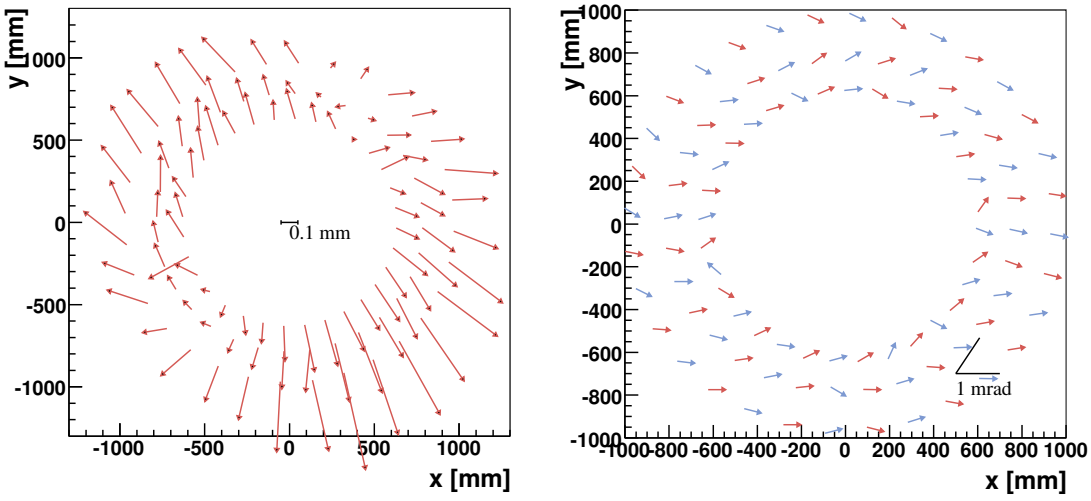

(a) (b)

Figure 6.22: L2 Alignment Parameters when using silicon Information. (a) Visual representation of the translation alignment parameters. Each arrow represents a barrel module. The tail of the arrow is the nominal module position. The arrow length and direction represent the global x and y alignment parameters. The arrow lengths are enlarged by a factor of 1000 relative to the axes. A scale is provided for reference. (b) Visual representation of the rotations about z. Each arrow represents a barrel module. The size of the rotation is given as the angle the arrows make with respect to the positive x-axis. The arrow lengths has no meaning. The size of the rotations are enlarged by a factor of 1000. A scale is provided for reference.

is the subject of the next section

6.5.3 Difference in L2 Alignment Constants

The differences in the L2 barrel alignment in 3 DoF with and without using silicon information can be seen in Figure 6.24. In all respects, other than the input track collection, the L2 alignment procedures are identical. The introduction of the Pixel and SCT information is driving the difference in alignment constants.

The validation plots using TRT stand-alone tracks with the two geometries are very similar. Small differences exist, but neither geometry performs systematically better. The differences in the validation plots using combined ID tracks are, on the other hand, much larger. One example is the average residual vs ϕ-sector for modules in the first barrel layer, shown in Figure 6.25. Figure 6.25a shows the residual distributions before and after the TRT stand-alone alignment, while Figure 6.25b shows the distributions before and after the alignment including silicon information. Both aligned

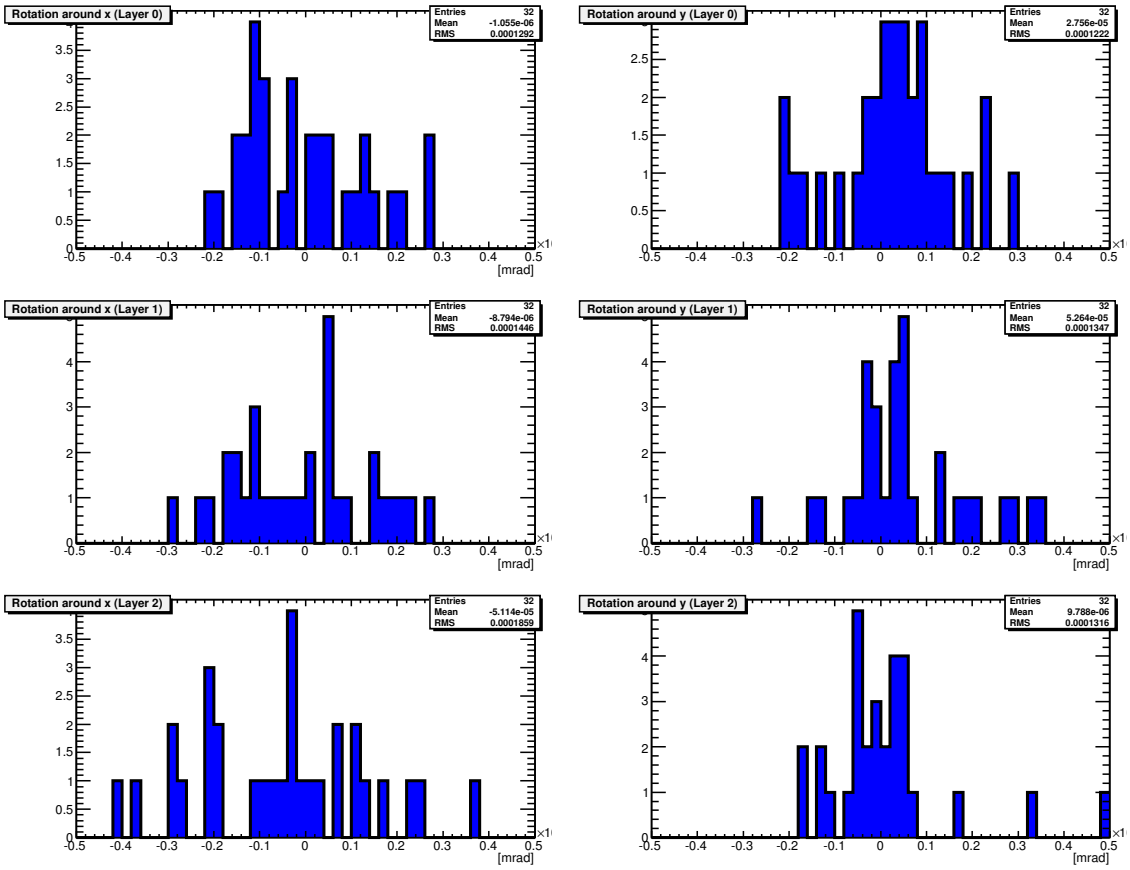

Figure 6.23: L2 alignment parameters for rotations around x and y when aligning with silicon information. The plots on the left give the rotation around x, whereas the plots on the right have the rotations around y. The parameters for barrel modules in layer zero are in the first row, those from layer one in the second, and those from layer two appear in the last row.

geometries bring improvement in the average residuals, however with the TRT stand-alone alignment, there is a larger remaining inconsistency in the residuals after the L2 alignment.

Only one set of alignment parameters can describe the correct internal position of the TRT barrel modules. At present evidence is lacking as to which geometry most accurately describes the TRT internal alignment. On one hand, Pixel or SCT misalignment can induce differences in the preferred internal TRT alignment when using Pixel and SCT information. On the other hand, the increased tracking precision from Pixel and SCT measurements allows the L2 alignment to be more sensitive to the internal TRT misalignment than when using only TRT stand-alone tracks. On the basis of providing a consistent ID geometry, the TRT L2 barrel alignment in 5 DoF derived with tracks including the Pixel and SCT information, was chosen.

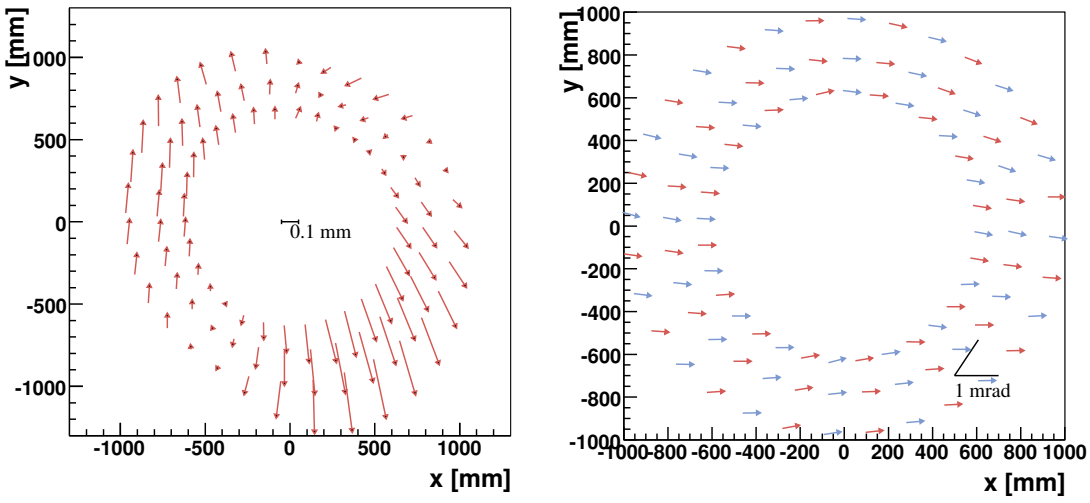

(a) (b)

Figure 6.24: Difference in L2 Alignment parameters with and without using silicon information. (a) Visual representation of the differences in translation alignment parameters after alignment with and without using silicon information. Each arrow represents a barrel module. The tail of the arrow is the module position after alignment with TRT stand-alone tracks. The arrow-head is the module position after alignment including silicon information. The arrow lengths are enlarged by a factor of 1000 relative to the axes. A scale is provided for reference. (b) Visual representation of the differences in rotations with and without using silicon information. Each arrow represents a barrel module. The difference in the rotation is given as the angle the arrows make with respect to the positive x-axis. The arrow lengths have no meaning. The size of the rotations are enlarged by a factor of 1000. A scale is provided for reference.

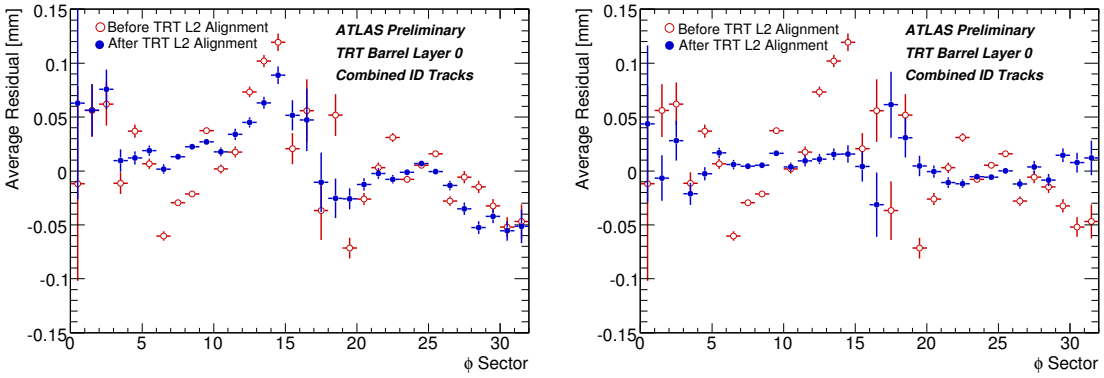

(a) (b)

Figure 6.25: Comparison of the average residual of combined tracks vs ϕ-sector for barrel modules in layer zero before and after the TRT stand-alone L2 barrel alignment (a), and before and after the L2 barrel alignment including silicon information (b) .

6.5.4 Barrel A/C Side Differences: "The ϕ Structure"

With all of the L2 barrel alignments described above, the average residual of TRT stand-alone tracks in each of the barrel modules is near zero, as seen in Figure 6.19b and 6.20. These residual plots include hits from both the A and C-sides of the barrel modules. When looking at these distributions separately for hits on the A and C-sides, remaining residual differences from zero are found. A striking pattern in the average residuals is seen in Figure 6.26, where the average residual vs ϕ-sector for each barrel layer, are shown separately for hits on the A and C-sides. The average residual alternates with both ϕ-sector and module layer, with a modulated amplitude that is smaller near the top and bottom of the detector, and is opposite in the two sides. This pattern is present in all of the L2 barrel alignments described above. Applying a d_0 cut of 500 mm removes this structure. It is thus not present for combined ID tracks.

The fact that the residual discrepancies persist after the L2 alignment, implies that the L2 alignment does not fully characterize the module-level misalignment. One way of extending the L2 barrel alignment to account for these differences is to align the barrel modules on sides A and C separately. To achieve this the alignment procedure described above was repeated once with the hits from the side-A masked off and once with hits from side-C masked off. The average residual vs ϕ-sector after these separate alignments is shown in Figure 6.27. The residual structure on the A-side (C-side) is removed when aligning with only hits from the A-side (C-side). The average of the alignment parameters derived from A-side and C-side alignment are identical to those shown in Figure 6.18. The differences between the A-side and C-side alignments can be seen in Figure 6.28. The same structure as was seen in Figure 6.26 is seen here. The radial detector positions alternate with both ϕ-sector and module layer and are opposite for the two sides. The structure seen in Figure 6.26 is that of an abstract quantity: track residuals. Through the separate A-side and C-side alignments, this structure is removed, and the pattern instead manifests itself in a much simpler quantity: the position of detector elements. The fact that the alignment differences in Figure 6.28 are dominantly radial explains why the amplitude of the ϕ structure in Figure 6.26 is smaller at the top and bottom of the detector. The detector misalignment is along the direction of the track for cosmic-rays crossing the top or bottom of the TRT. However, the radial misalignment with respect to a cosmic muons crossing the sides of the detector is perpendicular the track. Figure 6.28 also explains why the d_0 cut removed the residual discrepancy: to first order a radial misalignment has no impact on tracks passing into, or out-of, the center of the detector.

It is interesting that the barrel modules on side-A and side-C prefer separate L2 alignments. One possible explanation is the presence of gaskets which allow CO_2 to pass from one barrel module to

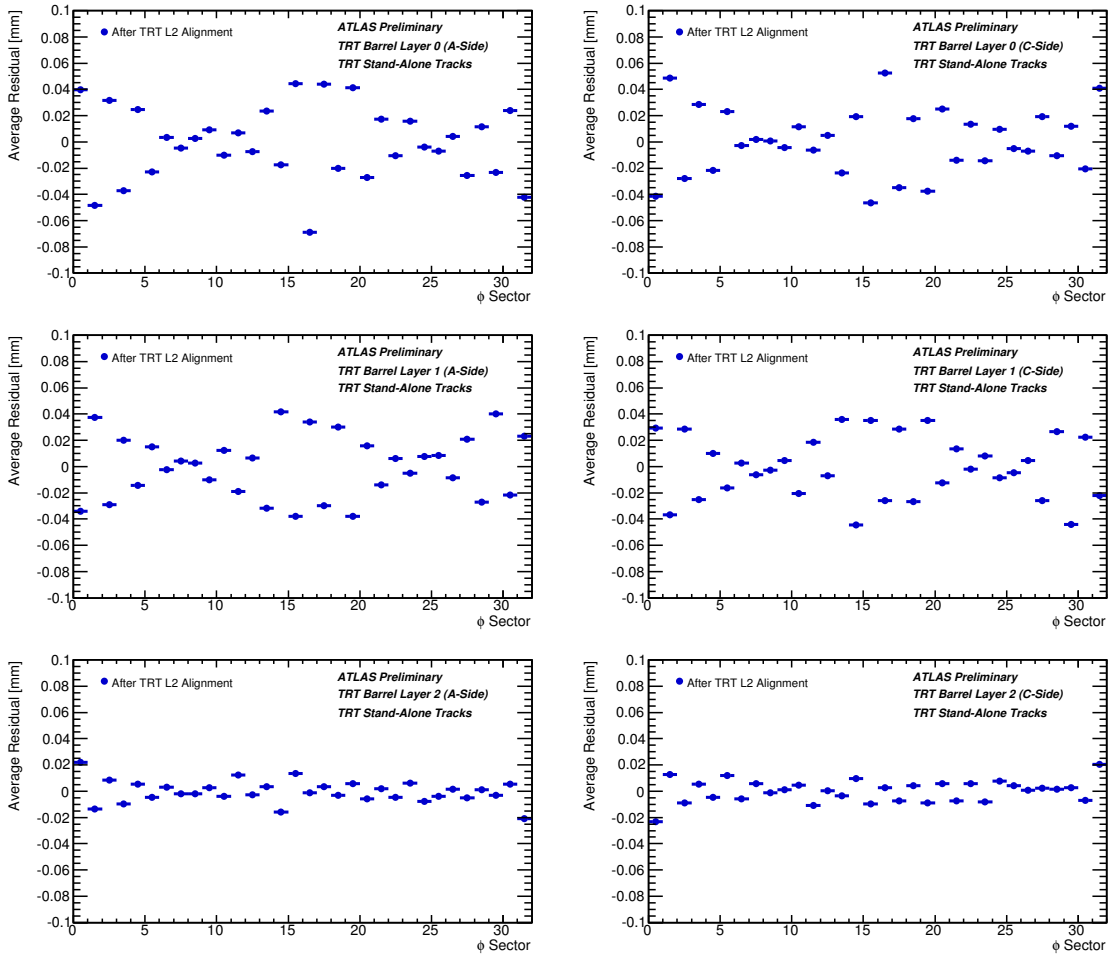

Figure 6.26: Average residual as a function of ϕ-sector for hits in barrel modules on side A (left plots) and C (right plots) separately. Modules in the first barrel layer are shown in the top row, those in the second are shown in the middle, and barrel modules in the third layer are shown in the bottom row.

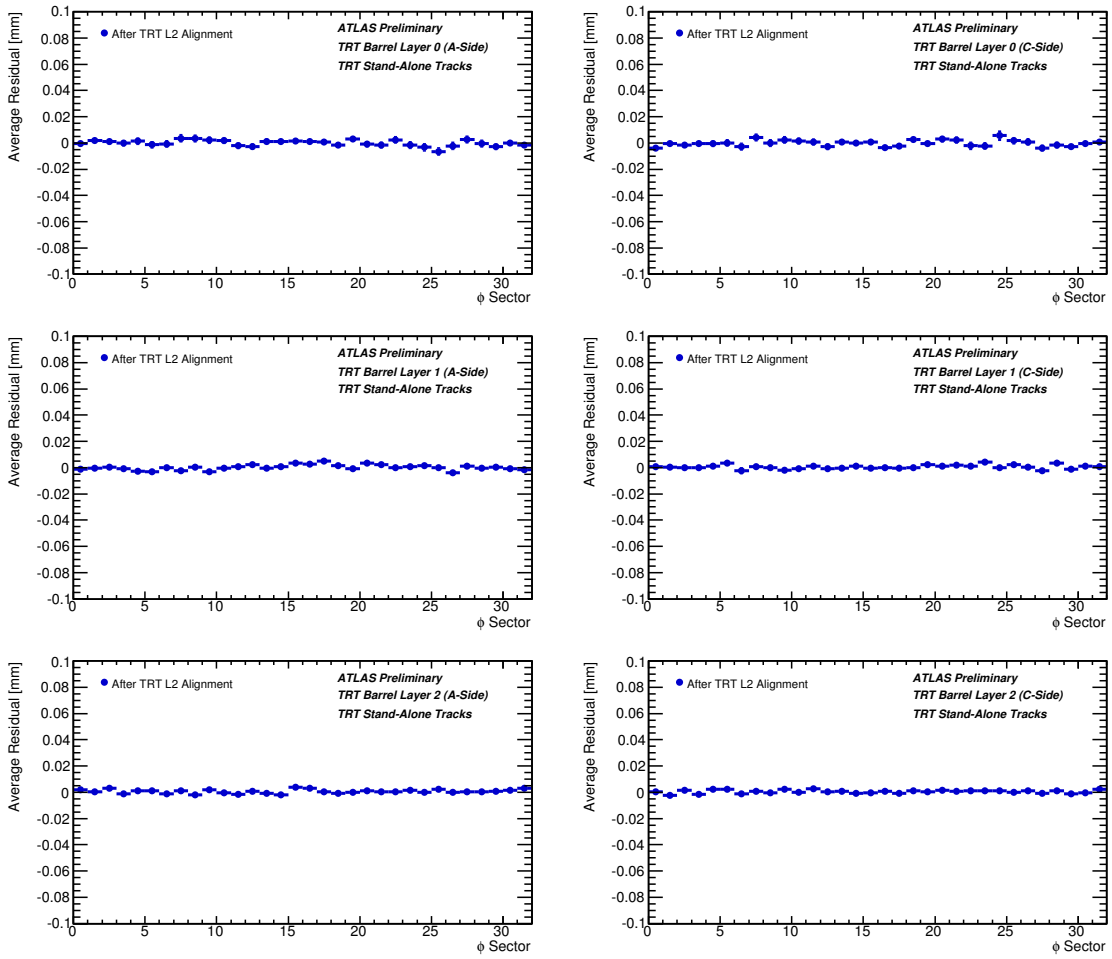

Figure 6.27: Average residual as a function of ϕ-sector for hits in barrel modules on sides A (left plots) and C (right plots) separately. Modules in the first barrel layer are in the top row, those in the second layer are shown in the middle, and barrel modules in the third layer are shown in the bottom row. For the residuals in side-A (side-C), the geometry after the L2 alignment with only the A-side (C-side) hits was used.

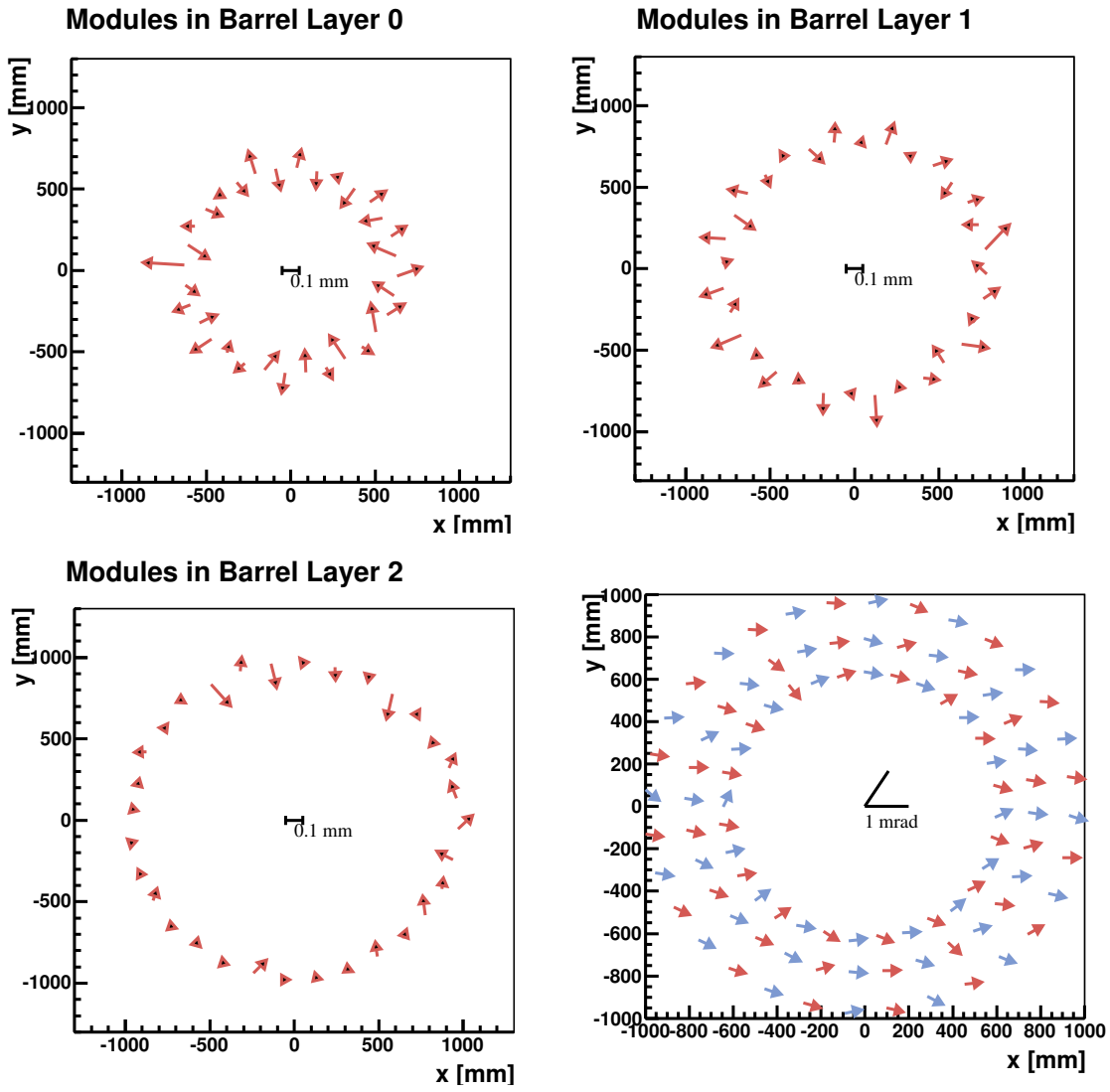

Figure 6.28: Visual representation of the differences in translation alignment parameters when aligning A-side only and C-side only. Each arrow represents a barrel module. For the upper two plots and for the one on the lower left, the tails of the arrows are the module position after alignment with C-side only. The arrow-heads are the module positions after alignment with A-side only. The arrow lengths are enlarged by a factor of 1000 relative to the axes. The modules in each layer are shown separately for clarity. Scales are provided for reference. The plot in the lower right is a visual representation of the differences in rotations. Each arrow represents a barrel module. The difference in the rotation is given as the angle the arrows make with respect to the positive x-axis. The arrow length has no meaning. The size of the rotations are enlarged by a factor of 1000. A scale is provided for reference.

another. The gaskets have a thickness of hundreds of microns and are located between barrel module layers on either the A or the C-side of each ϕ-module. The position of the gasket alternates with ϕ module and barrel layer with the same pattern as the misalignment seen in Figure 6.28. If the gaskets were the cause of the remaining misalignment responsible for the pattern in Figure 6.26, it would be expected that rotations of the barrel modules about the $\hat{\phi}$-axis could correct the misalignment. These rotational DoF were not included in the alignment because the lack of z-coordinate information in TRT-only tracks did not provide enough constraints on the χ^2 matrix. The fact that the separate A-side and C-side alignment can correct the residual discrepancy, suggests that the alignment could be performed with some of these DoF active. The current TRT L2 barrel alignment does not resolve the remaining A and C-side misalignment shown in Figure 6.28. This residual misalignment has a negligible impact on physics analysis, as the effect is only presence for TRT stand-alone tracks that have large (> 500 mm) impact parameters. Although the gaskets seem to be a likely cause for the source of the A and C-side differences and an explanation for appearance of the regular pattern seen in Figure 6.26, it is not further investigated here.

6.6 L2 End-cap Alignment

The need for an internal end-cap alignment was seen above in Figure 6.14. The residual scatter about zero indicated the presence of 4-plane wheel level misalignment within the end-caps. As with the barrel, the L2 alignment of the end-caps was first performed with cosmic-ray data. This alignment was initially performed using only one DoF per 4-plane wheel, rotations about z, which is the most sensitive to misalignment. The L2 end-cap alignment was later extended, using the higher statistics 900 GeV collision data, to include translations along x and y. This alignment is the subject of the following two sections. The rotational DoF about x and y were not seen to have a impact on tracking and have been ignored in the following. Translations along z were initially thought to have little impact on physics, but were later found to be important, particularly at low p_{T}. The alignment of these DoF is the subject of Section 6.10.

6.6.1 L2 End-cap Alignment with Cosmic-Ray Data

As a first step in the L2 end-cap alignment, each 4-plane wheel was aligned for rotations about z. This was performed with cosmic-ray data prior to the 900 GeV collision data taking. Initially only one DoF was used in order to validate the L2 algorithm in the end-caps and because of the limited end-cap statistics available in the cosmic-ray data. Rotations about z were chosen because they are the most sensitive to misalignment.

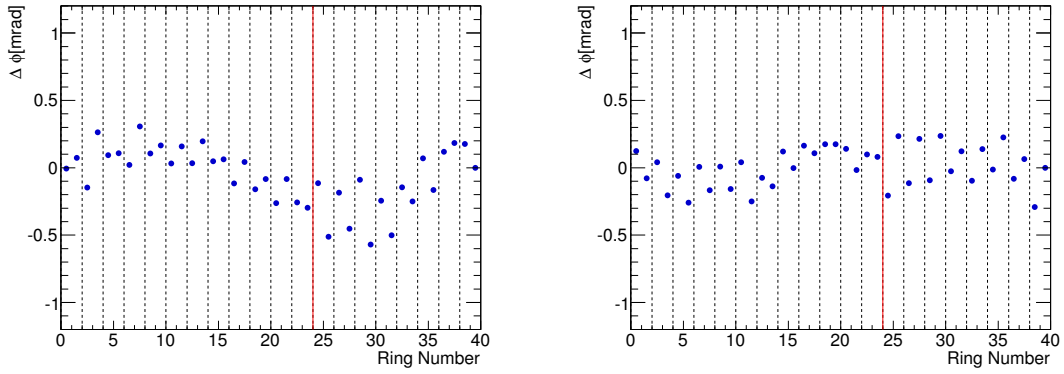

(a) (b)

Figure 6.29: Visualization of measured rotations about z with the alignment using cosmic-rays. The measured misalignment in ϕ is plotted as a function of 4-plane wheel number. The solid red lines give the separation of the Type-A and Type-B wheels, and the dashed vertical black lines give the separation of the 8-plane Type-A and Type-B type wheels. The results for end-cap C are shown on the left, whereas those for end-cap A are presented in the right.

The alignment was performed with tracks crossing the SCT barrel and the TRT end-caps. It was repeated for several iterations, until the constants converged. The number of hits on track increased with iteration and the overall resolution improved as a result of the alignment. The results of this L2 alignment are presented visually in Figure 6.29. The measured misalignment for all wheels is less than a milli-radian and is roughly continuous in z when considered at the level of the 8-plane wheels. At the level of the 4-plane wheels, systematic patterns in the alignment constants are seen. The pattern of relative misalignment of 4-plane wheels within an 8-plane wheel is systematically repeated across many 8-plane wheels. This pattern is believed to be a product of the construction procedure. Deviations in the table used to construct the 4-plane wheels could lead to an offset in the ϕ of the straw positions. This offset would be present in all 4-plane wheels. When the two 4-plane wheels are combined back-to-back to form 8-plane wheels, these offsets would give rise to the systematic misalignment within a wheel that is seen.

6.6.2 L2 End-cap Alignment with Collision Data

After the initial validation of the L2 alignment using one DoF with cosmic-ray data, the procedure was extended to include translations in the transverse plane, using 900 GeV collision data. The alignment procedure was again repeated for several iterations, resulting in an increased number of hits on track and an improved resolution. The results of the L2 alignment in 3 DoF are presented in Figures 6.30, 6.31, and 6.32. Figure 6.30 shows the differences in ϕ as a function of 4-plane wheel.

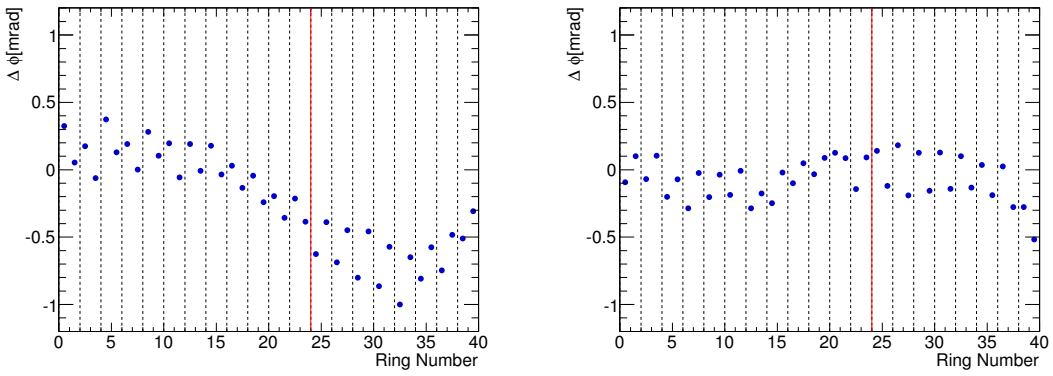

(a) (b)

Figure 6.30: Visualization of measured rotations about z with the alignment using collision data. The measured misalignment in ϕ is plotted as a function of 4-plane wheel number. The solid red lines give the separation of the Type-A and Type-B wheels, and the dashed vertical black lines give the separation of the 8-plane Type-A and Type-B wheels. The results for end-cap C are shown on the left, whereas those for end-cap A are presented in the right.

The measured misalignment seen in Figure 6.30 displays the same general features as was seen when only aligning this DoF in Figure 6.29. The measured misalignment is, apart for the B-wheels in end-cap C, less than a milli-radian, and continuous at the level of the 8-plane wheels. The same systematic shifts of the 4-plane wheels within the 8-plane wheels is seen again when aligning in 3 DoF. As for the case of the L1 alignment, the differences in the L2 constants seen when aligning with cosmic-ray vs collision data are not unexpected. The fact that the same pattern of misalignment is seen in the two cases provides confidence that real detector distortions are being measured. The measured misalignment in x and y is shown in Figures 6.31 and 6.32. The translations are all less than a millimeter. The y misalignment in end-cap C appears to be correlated wheel-to-wheel and suggests a detector deformation at the level of a millimeter. Smaller, hundreds of micron, correlations can also be seen in the A-wheels of end-cap A. The discontinuous change in the y alignment constants in end-cap C suggest that the stack of B-wheels was misaligned with respect to the stack of A-wheels. This "L1-like" misalignment is not corrected for explicitly, but is effectively corrected with the L2 alignment.

The improvement in the track residuals as a result of the L2 end-cap alignment can be seen in Figures 6.33 and 6.34. Figure 6.33 shows the mean of the fitted residual distribution as a function of 4-plane wheel. The remaining deviations in the residual distribution from zero, present after the L1 alignment, are removed at L2. After the L2 alignment the average residual of all 4-plane wheels is zero to within 10 microns. The effect of the L2 end-cap alignment on the overall TRT residual

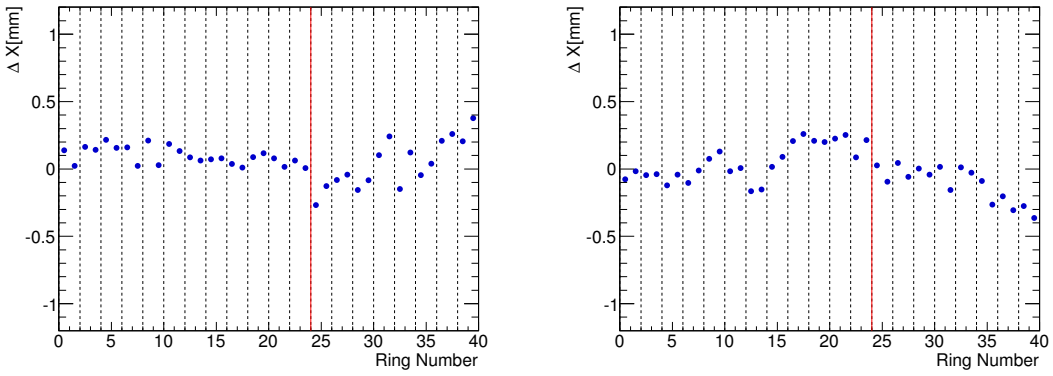

(a) (b)

Figure 6.31: Visualization of measured translations in x with the alignment using collision data. The measured misalignment in x is plotted as a function of 4-plane wheel number. The solid red lines give the separation of the Type-A and Type-B wheels, and the dashed vertical black lines give the separation of the 8-plane Type-A and Type-B wheels. The results for end-cap C are shown on the left, whereas those for end-cap A are presented in the right.

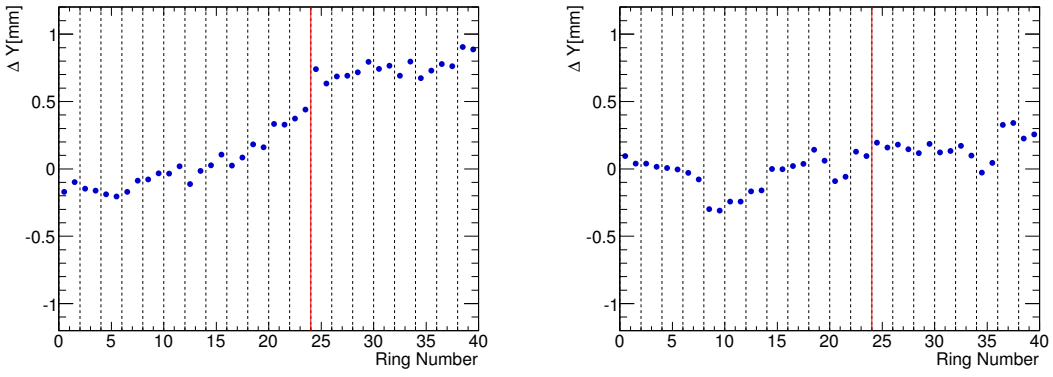

(a) (b)

Figure 6.32: Visualization of measured translations in y with the alignment using collision data. The measured misalignment in Y is plotted as a function of 4-plane wheel number. The solid red lines give the separation of the Type-A and Type-B wheels, and the dashed vertical black lines give the separation of the 8-plane Type-A and Type-B wheels. The results for end-cap C are shown on the left, whereas those for end-cap A are presented in the right.

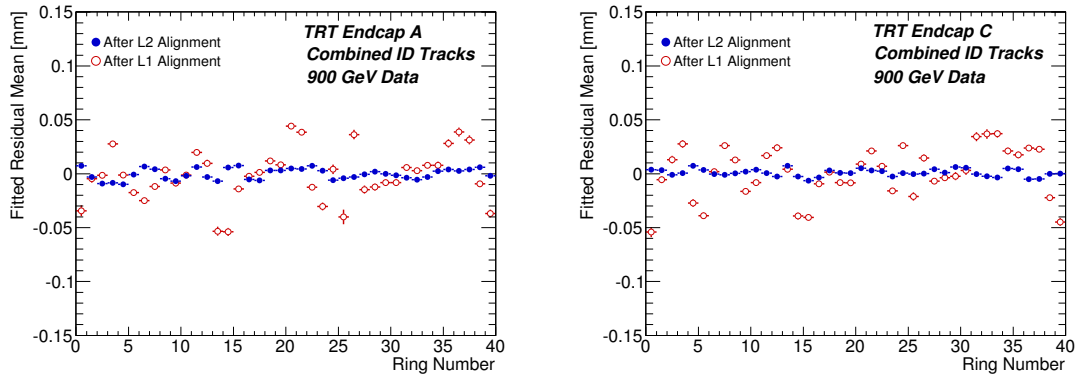

(a) (b)

Figure 6.33: Mean of the fitted TRT residual distribution a function of end-cap 4-plane wheel, before and after the L2 alignment. End-cap A is shown in (a) and end-cap C in (b)

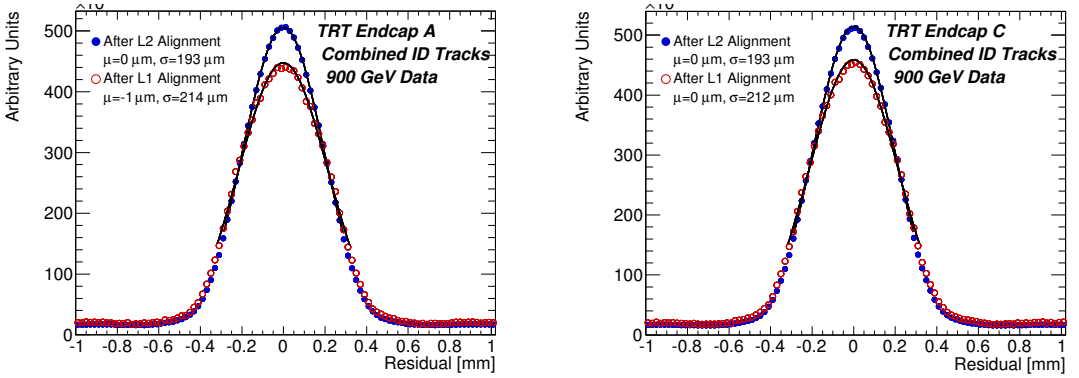

(a) (b)

Figure 6.34: TRT residual distributions before and after the L2 end-cap alignment for end-cap A Figure (a) and end-cap-C Figure (b)

distribution is shown in Figure 6.34. The L2 alignment improvement in resolution is nearly the same in each end-cap. The improvements seen in these validation plots provide confidence that the correct L2 end-cap alignment was reached.

6.7 Evidence for End-cap Wheel Distortions

In the course of validating the L2 end-cap alignment, systematic biases in the residual distributions within the end-cap wheels were seen. Residual maps[12] have been used to study the alignment in

[12]See Section 5.3

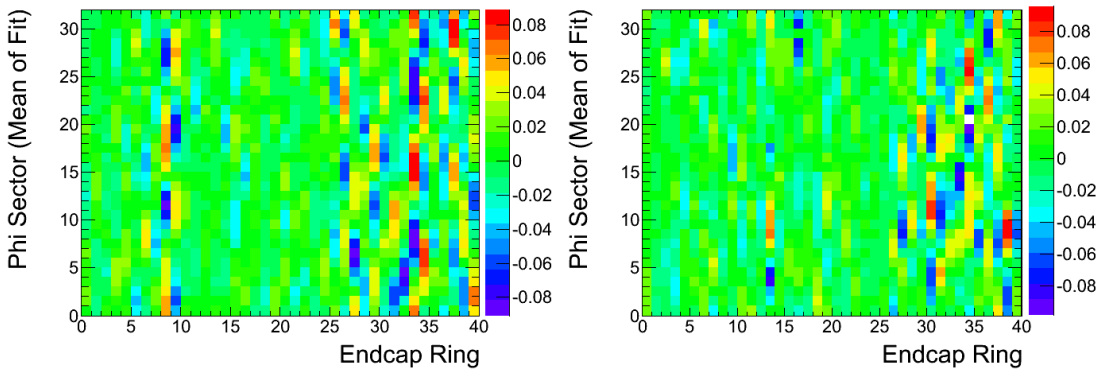

(a) (b)

Figure 6.35: Mean of the fitted residual distribution (in [mm] indicated by the color) vs end-cap 4-plane wheel (x-axis) and ϕ (y-axis). The results for end-cap C are shown on the left, whereas those for end-cap A are presented in the right.

the end-caps. The residual maps present the mean and width of a Gaussian fit of the residual distribution as a function of detector coordinates. The residual maps as a function of 4-plane wheel vs ϕ can be seen in Figure 6.35. Systematic deviations in the residual, of up to 100 microns, are seen along ϕ within many of the 4-plane wheels. These deviations vary continuously within the end-cap wheels and discontinuously across wheel boundaries. This indicates that the source of the effect is at the level of the 4-plane wheels. The residual variation in ϕ is periodic with a period of π. A residual misalignment rotationally about z would bias the overall residual uniformly in ϕ. A residual misalignment in the transverse plane would result in a ϕ oscillation of the residual distribution with period of 2π. Oscillations with a period of π are an indication that the 4-plane wheels are elliptically deformed. This deformation is sketched in Figure 6.37a and is not a DoF that can be removed with the L2 alignment.

A different effect can be seen in Figure 6.36. These maps show the fitted residual as a function of 4-plane wheel and radius. The results are presented with the detector radius binned with 32 equal divisions. Systematic structure in the average residuals is seen within many of the 4-plane wheels. The variation is again continuous within the 4-plane wheels and discontinuous across wheel boundaries. The average residual varies approximately linearly with radius, with residual deviations of up to 50 microns. These deviations occur predominately in the Type-A wheels and alternate sign with adjacent 4-plane wheel. This pattern in the residual structure is consistent with a ϕ rotation of the inner radius of the 4-plane wheel with respect to the outer radius: a twist deformation. The alternation with 4-plane wheels may again be an indication that the table used in production is the

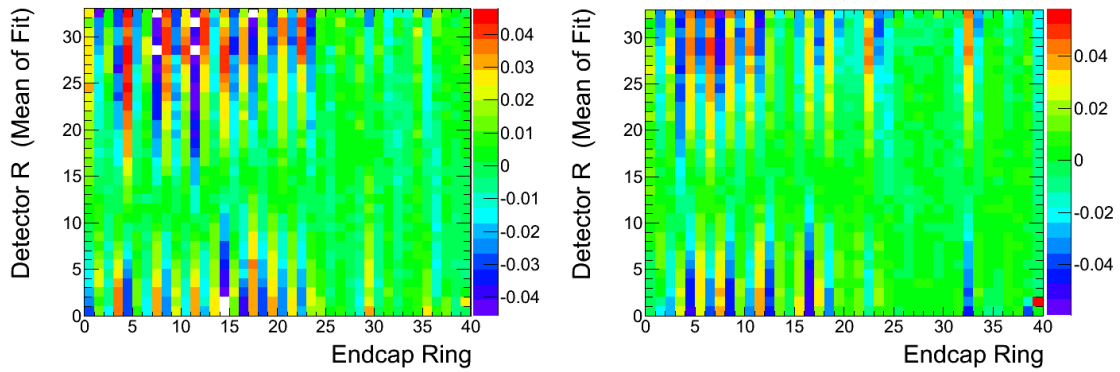

(a) (b)

Figure 6.36: Mean of the fitted residual distribution (in [mm] indicated by the color) vs 4-plane wheel (x-axis) and R (y-axis). The results for end-cap C are shown on the left, whereas those for end-cap A are presented in the right.

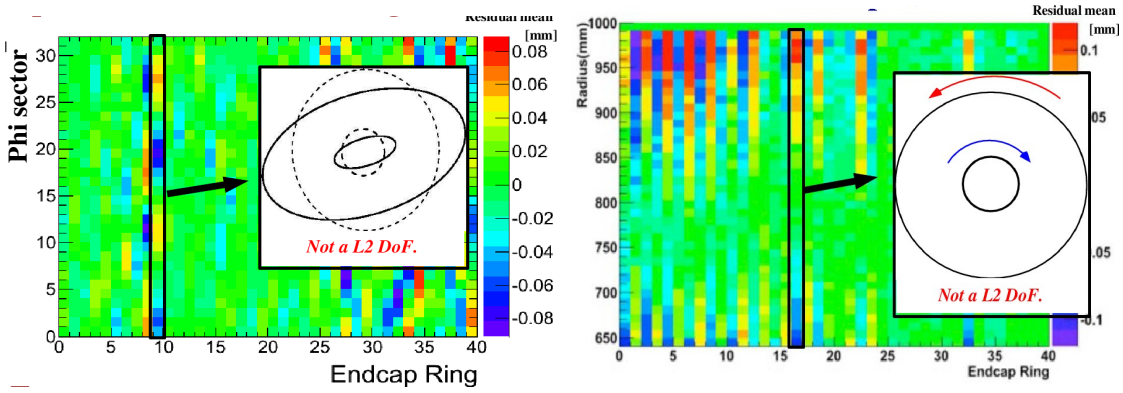

(a) (b)

Figure 6.37: Sketches of 4-plane wheel deformations indicated by systematic residual bias after the L2 alignment. The residual map of ϕ vs 4-plane wheel (left) shows signs of elliptical deformation. The residual map of r vs 4-plane wheel (right) shows signs of twist-like deformation.

cause of the distortions. This twist deformation is sketched in Figure 6.37b and is not a DoF that can be removed with the L2 alignment.

6.8 Wire-level End-cap Alignment

The wire-level alignment is the last step in the TRT alignment. Alignment at the wire-level will correct individual straw misplacement and will also account for deformations of the 4-plane wheels. The need for the wire level end-cap alignment was seen in the previous section, where residual

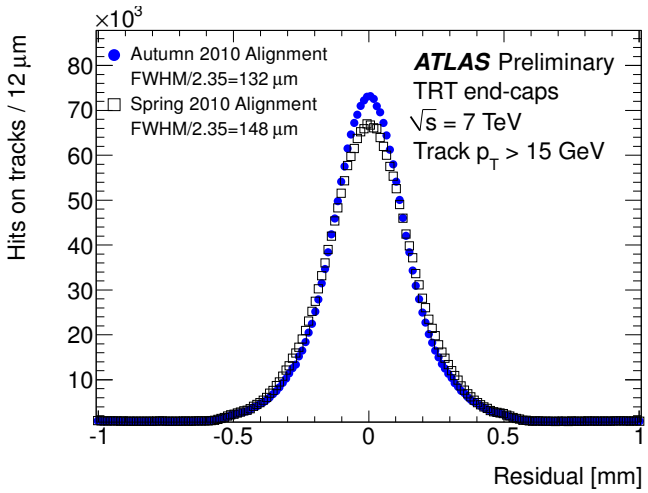

Figure 6.38: TRT residual distributions in the end-cap before and after the L3 end-cap alignment. The "Autumn 2010 Alignment" includes the L3 alignment, the "Spring 2010 Alignment" uses the TRT geometry before the L3 alignment.

structure after the L2 alignment indicated the presence of deformations in the 4-plane wheels.

The L3 end-cap alignment was performed using high statistics 7 TeV collision data samples collected in 2011. The alignment was repeated for several iterations, until convergence was reached. The number of reconstructed hits on track increased as a result of the alignment. The improvement in the TRT end-cap resolution as a result of the L3 alignment can be seen in Figure 6.38. The points labeled "Spring 2010 Alignment" are from before the L3 end-cap alignment, the points labeled "Autumn 2010 Alignment" are from after L3 alignment. The impact of the wire-level alignment on the residual maps presented in the previous section can be seen in Figures 6.39 and 6.40. The systematic residual biases in the 4-plane wheels along ϕ and r are removed as a result of the wire-level alignment. After the L3 alignment the residual maps are uniform in all detector coordinates. The results show the improvement for end-cap A, the results for end-cap C are very similar.

The patterns of wire-level misalignment derived by the alignment procedure confirm the hypothesis of 4-plane wheel deformations. Figure 6.41 presents a visual representation of the wire-level misalignment within a 4-plane wheel with residual biases indicative of the elliptical deformation. In Figure 6.41a, two lines are drawn for each straw in a straw-layer, depicting the wire-level DoF, dx1 and dx2, described in Section 6.2. The length of the lines indicate the size of the measured misalignment, the color indicates the direction of the displacement. Figure 6.41b, shows the measured wire displacement as a function of ϕ. A clear correlation of misalignment at the wire-level indicative of an elliptical deformation of up to 150 microns is visible. Figure 6.42 presents a visual representation

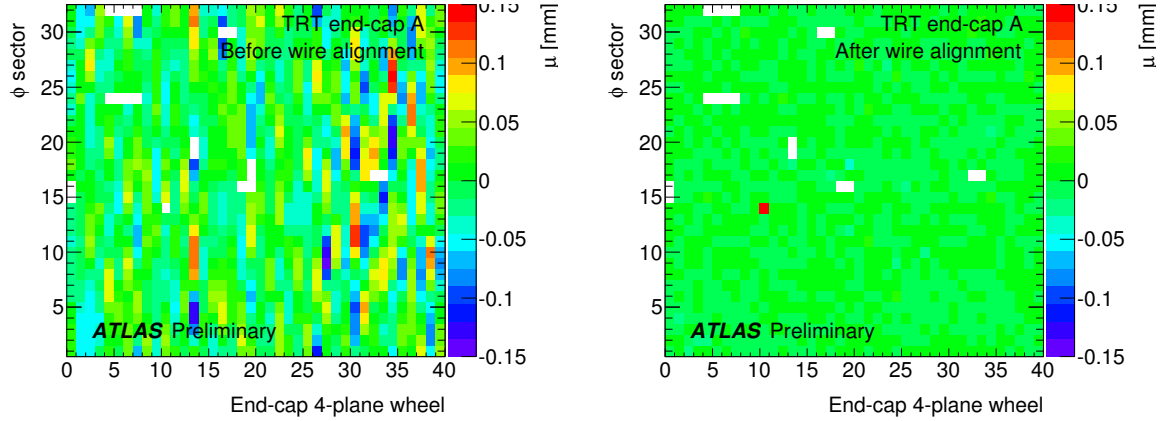

(a) (b)

Figure 6.39: Mean of a Gaussian fit to TRT residuals vs ϕ-sector and wheel before, (a), and after, (b), the wire-level alignment. The plots illustrate the results for end-cap A. The white bins are due to dead channels.

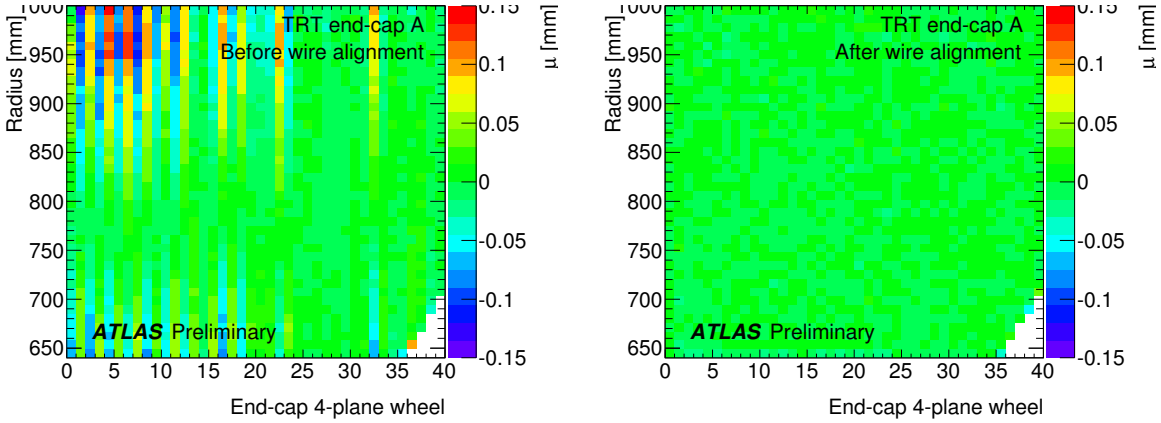

(a) (b)

Figure 6.40: Mean of a Gaussian fit to the TRT residuals vs radius and wheel before, (a), and after, (b), the wire-level alignment. The plots illustrate the results for end-cap A. The white area in the lower right corner is due to acceptance effects.

of the wire-level misalignment within a 4-plane wheel with residual biases indicative of the twist deformation. As before, Figure 6.42a gives the wire-level DoF. Figure 6.42b, shows the measured wire rotational DoF as a function of ϕ. A strong correlation at the wire level is seen corresponding to that expected from a twist deformation. The wire-level correlations presented above are similar for straw planes within a 4-plane wheel, and are different in adjacent 4-plane wheels, confirming that the deformations are at the wheel level.

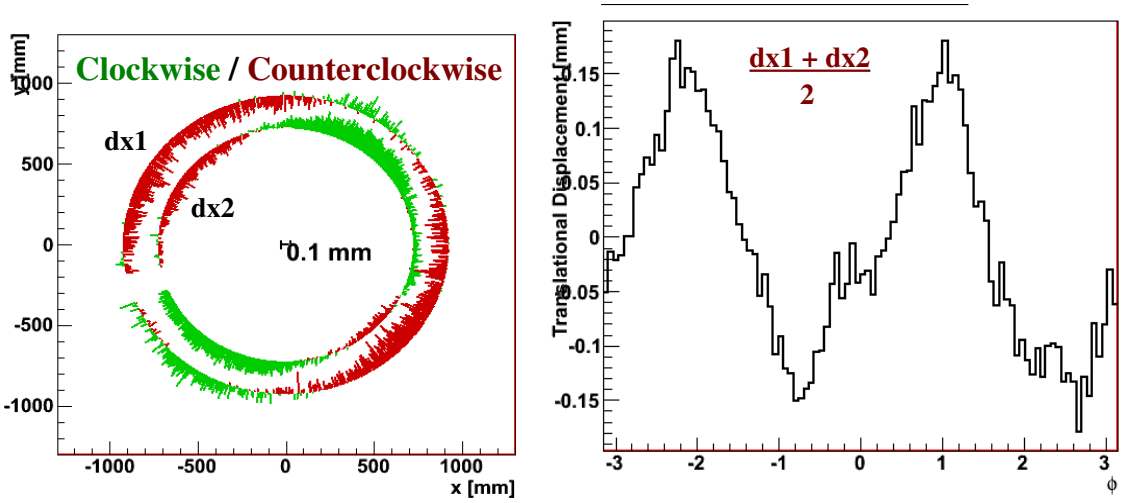

(a) (b)

Figure 6.41: Visual representation of wire-level misalignment in a 4-plane wheel with elliptical-deformation-like biases in the residual map. Figure (a) gives the measured alignment of each wire with respect to position in the wheel. Figure (b) shows the measured displacement of each wire as a function of ϕ position in the wheel. A correlation in the wire-level alignment indicative of an elliptical deformation is seen.

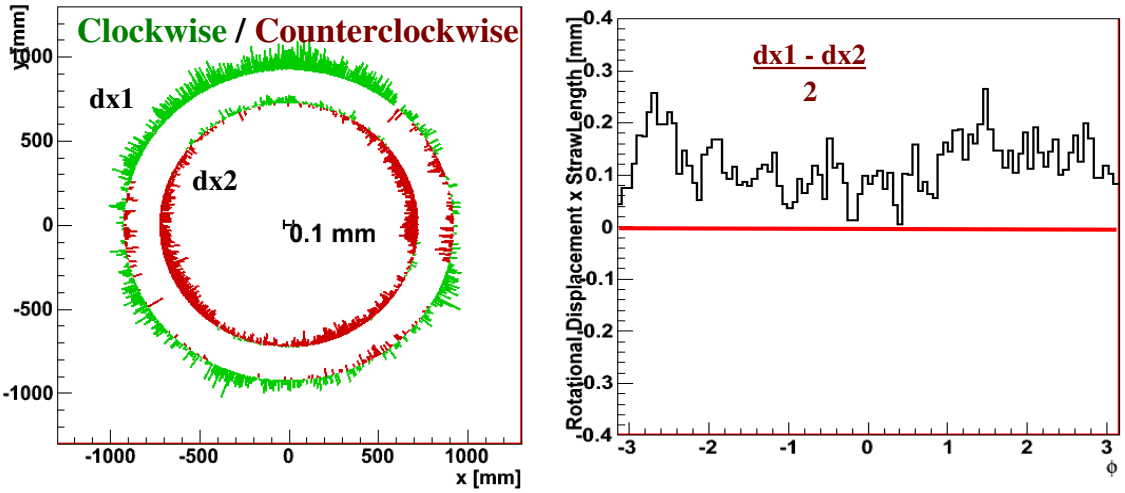

(a) (b)

Figure 6.42: Visual representation of wire-level misalignment in a 4-plane wheel with twist-deformation-like biases in the residual map. Figure (a) gives the measured alignment of each wire with respect to position in the wheel. Figure (b) shows the measured rotation of each wire as a function of ϕ position in the wheel. A correlation in the wire-level alignment indicative of an twist deformation is seen.

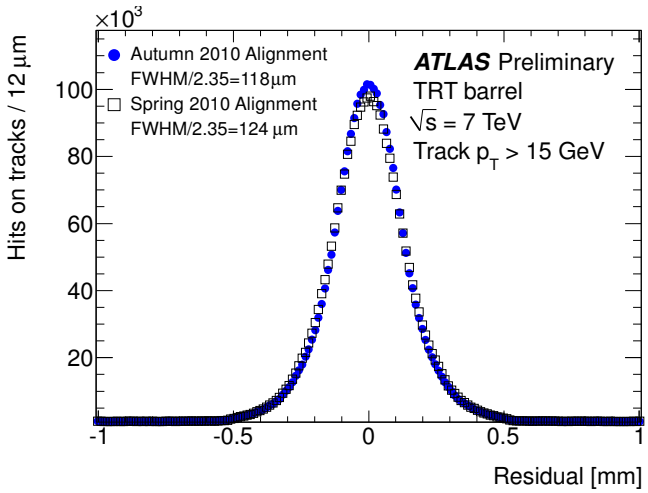

Figure 6.43: TRT residual distributions in the barrel before and after the L3 barrel alignment. The "Autumn 2010 Alignment" includes the L3 alignment, the "Spring 2010 Alignment" uses the TRT geometry before the L3 alignment.

6.9 Wire-level Barrel Alignment

The wire-level alignment was also performed in the TRT barrel. Alignment at the wire-level will correct individual straw misplacement and account for deformations of the barrel modules. The L3 barrel alignment was also performed using 7 TeV collision data and was repeated for several iterations, until convergence was reached. The number of reconstructed hits on track increased as a result of the alignment. The improvement in the TRT barrel resolution as a result of the L3 alignment can be seen in Figure 6.43. The impact of the wire-level alignment on residual maps in the barrel can be seen in Figure 6.39. Figure 6.44a displays the mean of the TRT residuals as a function of ϕ-sector and z for the innermost TRT barrel layer. Biases in the residuals of up to 80 μm are present before the L3 alignment. This residual structure in z is removed by the L3 alignment.

Unlike the end-caps, where the L3 wire-level alignment removed larger scale deformations, the primary corrections of the L3 barrel alignment account for wire-level misplacement within the modules. Therefore, the sizes of the measured misalignment provide an in-situ measurement of the wire placement accuracy in the TRT barrels during construction. Figure 6.45 shows the distribution of measured wire misalignment in the barrel. The distribution of measured translation displacements is given in the left, whereas the distribution of the measured rotation displacement, defined as $\frac{dx1-dx2}{2}$, is given on the right. The RMS from these distributions indicate that the wire placement accuracy in the barrel was better than 50 microns. This accuracy was found to be similar across ϕ modules and in the different barrel layers.

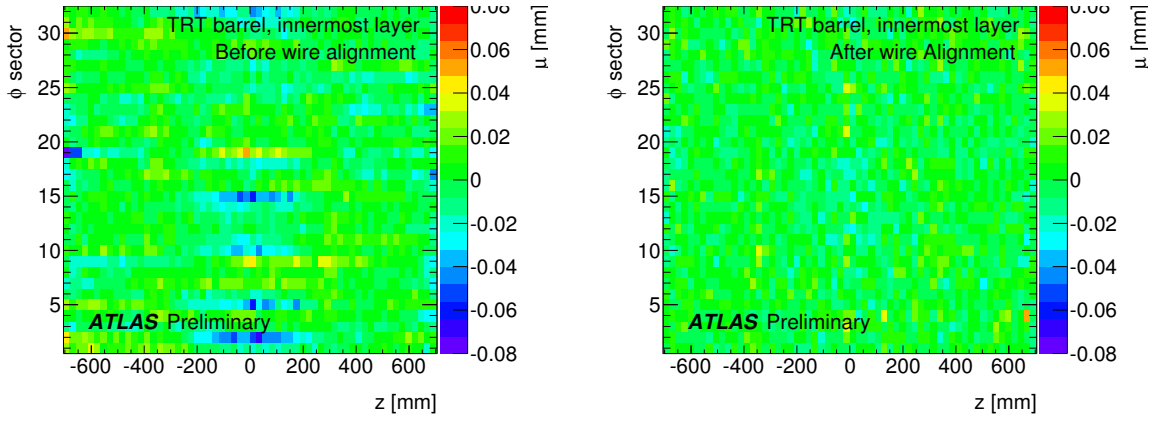

(a) (b)

Figure 6.44: Mean of a Gaussian fit to TRT residuals vs ϕ-sector and z for the first TRT barrel layer before, (a), and after, (b), the wire-by-wire alignment.

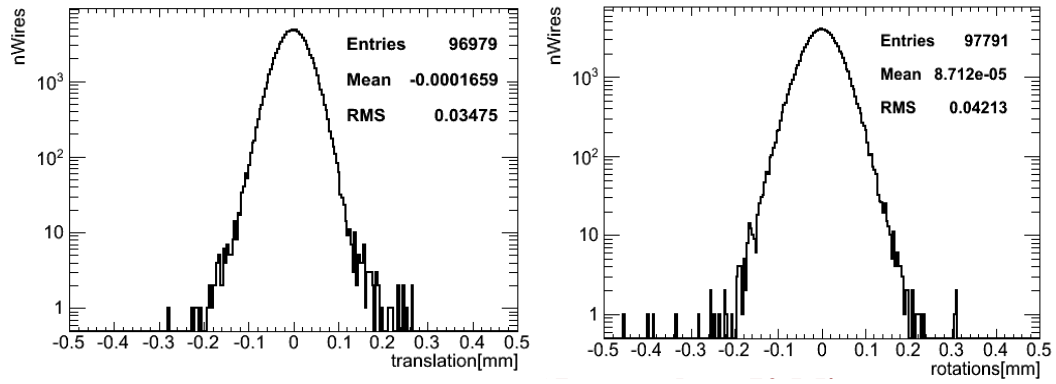

(a) (b)

Figure 6.45: Distribution of measured wire misalignment in the TRT Barrel. The measured translation displacements are given in the left. The measured rotation displacements, defined as $\frac{dx1-dx2}{2}$, are given on the right.

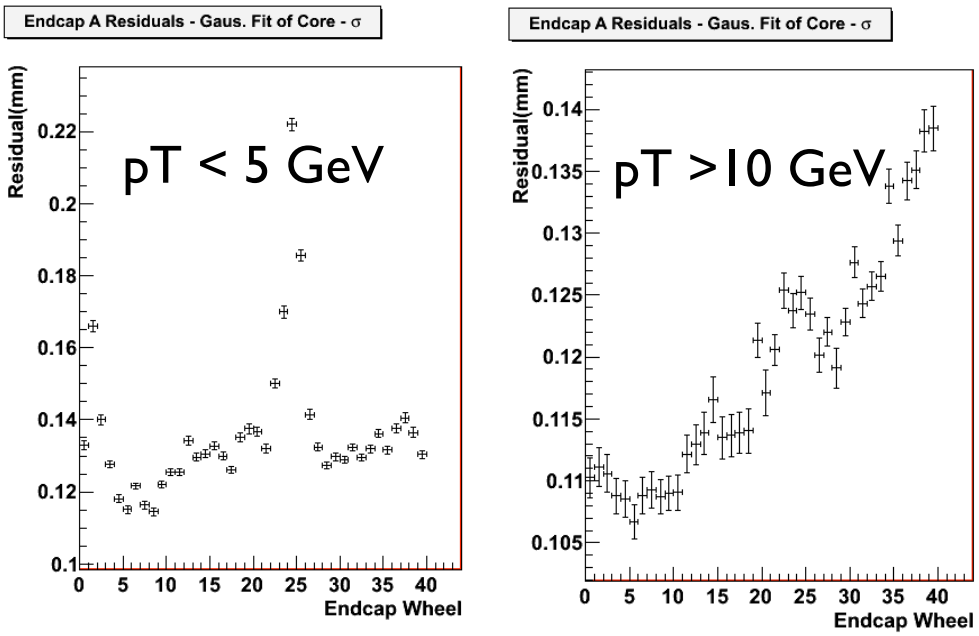

Figure 6.46: TRT resolution in end-cap A as a function of 4-plane wheel [91]. Left-hand plot uses tracks with p_{T} below 5 GeV. Right-hand plot is with tracks with p_{T} above 10 GeV. Note the scale difference.

6.10 End-cap Alignment along Z

Performance studies after the wire-level alignment revealed interesting anomalies in the end-cap residuals. Worsened resolution for low momentum tracks was seen in several 4-plane wheels. The corresponding resolution using high momentum tracks was as expected. Figure 6.46 shows the resolution as a function of end-cap wheel in end-cap A, separately for low p_{T} tracks ($p_{\mathrm{T}} < 5$ GeV), and high p_{T} tracks ($p_{\mathrm{T}} > 10$ GeV). Degradation of the TRT resolution in particular regions of the detector can be seen for the low p_{T} tracks. Looking further into lower momentum tracks, a charge-dependent bias in the residuals was found. Figure 6.47 shows the average residual vs wheel, separately for positively and negatively charged low p_{T} tracks. Biases of up to 100 microns are seen and are opposite for positive and negative tracks. The region in end-cap A most effected by the residual bias and resolution degradation was also associated to a bias in reconstructed the J/ψ mass. Figure 6.48 shows the reconstructed J/ψ mass as a function of η using silicon-only tracks and using combined ID tracks. A bias in the reconstructed J/ψ mass using combined tracks is seen around η of 1.4. This bias corresponds to tracks passing through end-cap wheels with the largest residual bias. It is only present when including TRT measurements.

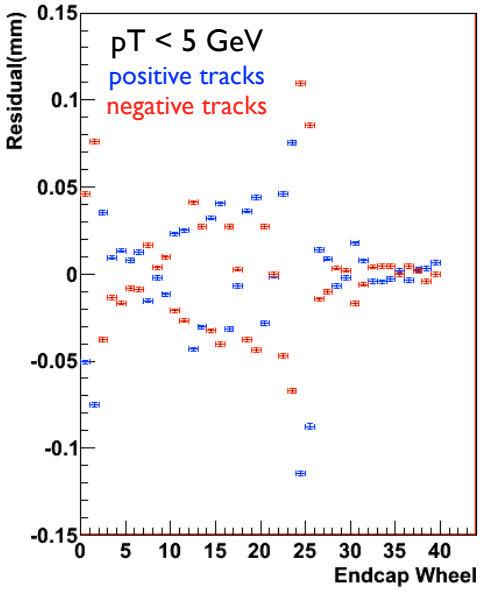

Figure 6.47: Average residual vs wheel in end-cap A [91]. Positively and negatively charged tracks are shown separately and are required to have p_{T} below 5 GeV.

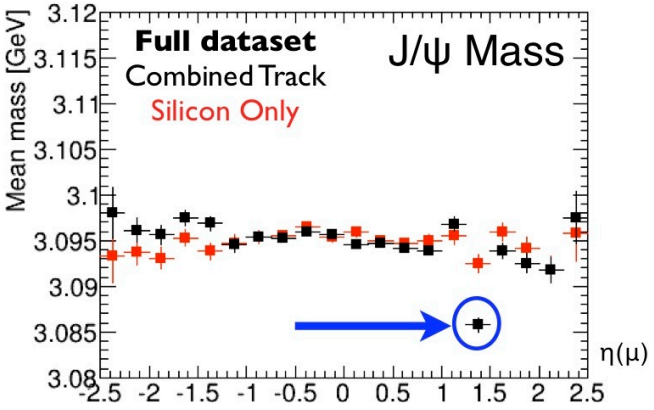

Figure 6.48: Reconstructed J/ψ mass as a function η from tracks with only Pixel and SCT measurements ("Silicon Only") and including TRT measurements ("Combined Tracks") [92].

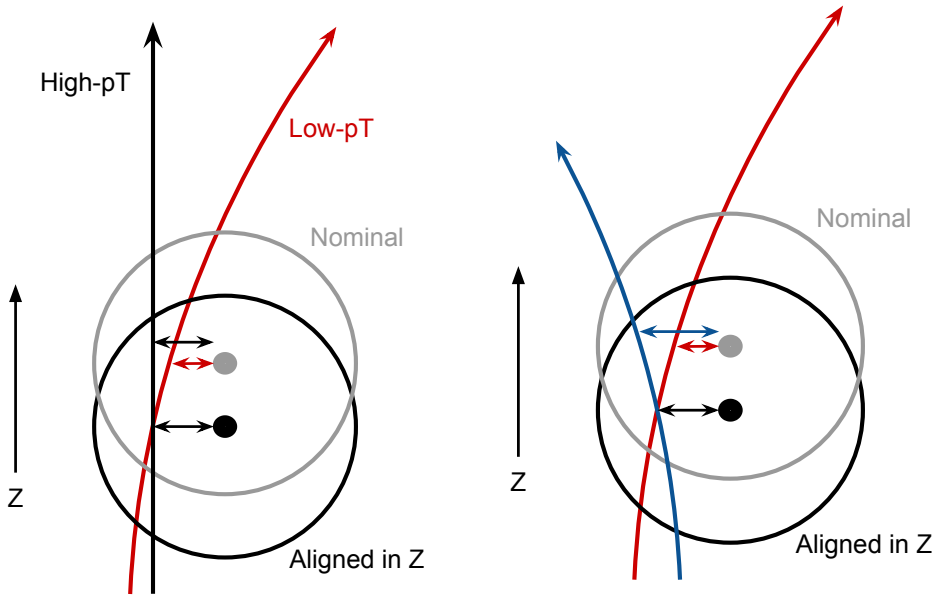

(a) (b)

Figure 6.49: Sketches of the effect of a z-misalignment in the end-caps [93]. The misalignment effects low p_{T} tracks, (a), and positively and negatively charged tracks in the opposite direction, (b).

The anomalies in the tracking performance of the end-caps presented above are the signature of end-cap misalignment along z. Misalignment along z will primarily effect low momentum tracks. Sketched in Figure 6.49a, the residual bias from the z-misalignment is a second order effect due to the track bending in the $z-\phi$ plane. Misalignment along z is a weak mode for high momentum tracks. Figure 6.49b shows the effect of the z-misalignment on positive and negative tracks. The residual bias caused by the track bending is opposite for positively and negatively charged tracks because the direction of deflection from the magnetic field is opposite. On the other hand, a z-misalignment will bias the p_{T} of oppositely charged tracks in the same direction resulting in a bias of the reconstructed mass of neutral particles.

Misalignment along z was not a DoF that was initially aligned during the L2 end-cap alignment, as it was thought to have a small effect on track performance. The size of the effects shown above suggest relatively large displacements in z and demonstrate the need to align this DoF. The alignment along z was performed using 7 TeV collision data for several iterations until convergence was reached. Large misalignment in z was measured by the alignment algorithm. Figure 6.50 shows the reconstructed z misalignment as a function of z. The misalignment in end-cap A shows

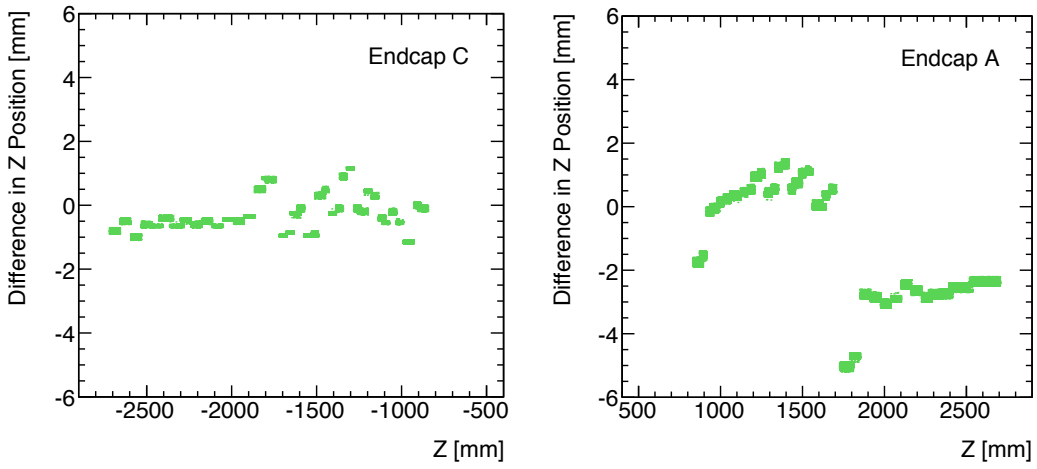

(a) (b)

Figure 6.50: Measured misalignment in z as a function of z, for end-cap C (left) and end-cap A (right). The division between A and B-wheels occurs around $|z|$ of 1700 mm.

strong correlations among Type-A and Type-B wheels, which displacements of up to 5 mm. The misalignment in end-cap C tends to be smaller and has less correlation among wheel type. The effect of the z-alignment on tracking performance is shown in Figures 6.51, 6.52, and 6.53. Figure 6.51 shows the residual RMS as a function of 4-plane wheel, before and after the z-alignment. The regions of poor resolution prior to alignment have been corrected by the z-alignment. Figure 6.52 shows the impact of the z-alignment on the residual distributions. The charge dependent residual biases are removed by the z-alignment. Finally, the effect of the z-alignment on the reconstructed J/ψ mass is shown in Figure 6.53. After z-alignment, the bias in J/ψ mass around η of 1.4 is removed. These validation plots are taken as a sign that the large z-misalignment correctly describe the detector geometry.

6.11 Conclusion

The TRT alignment has been performed and validated with data from cosmic-ray muons, 900 GeV collision data, and 7 TeV collision data. The alignment of large detector structures, down to the individual wires, has been presented. This alignment has brought large improvements to the TRT and combined ID tracking performance. The TRT alignment described in this section has been used for all ATLAS physics analyses. After the alignment presented here, the position resolution of the TRT is approaching that of the design. Figure 6.54 compares the TRT barrel and end-cap resolution

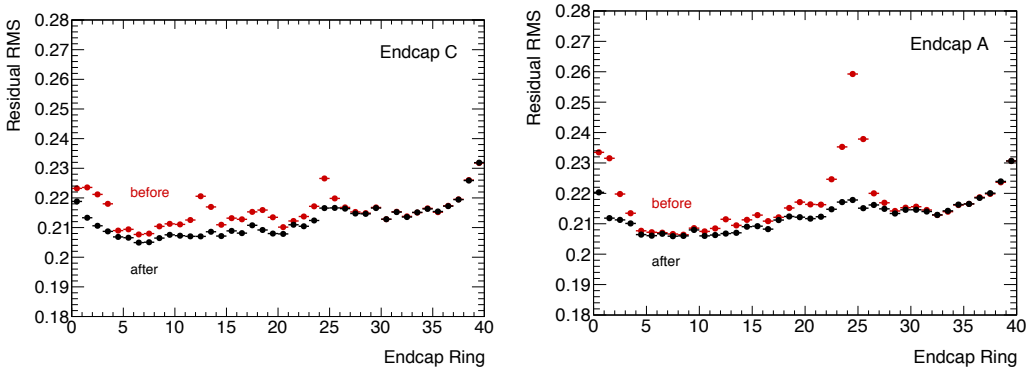

(a) (b)

Figure 6.51: RMS of the end-cap residuals as a function of 4-plane wheel, before (red) and after (black) the z-alignment. End-cap C is shown on the left. End-cap A is shown on the right.

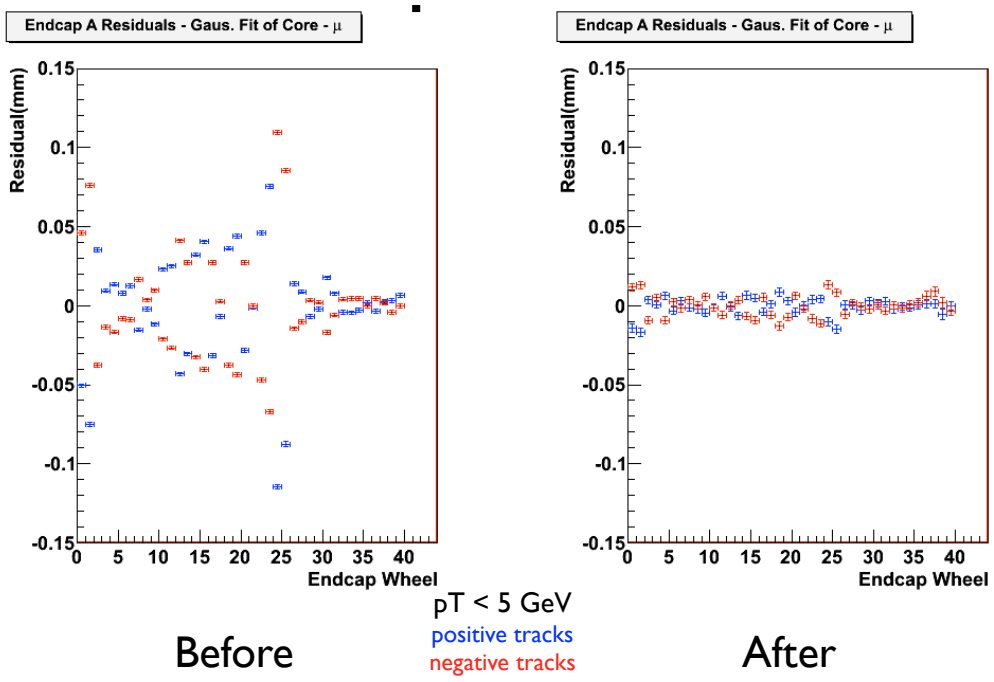

Figure 6.52: Average residual vs wheel in end-cap A [91]. Positively and negatively charged tracks are shown separately and are required to have p_{T} below 5 GeV. The result before the end-cap z-alignment are shown on the left, whereas, the result after the z-alignment is shown in the right.

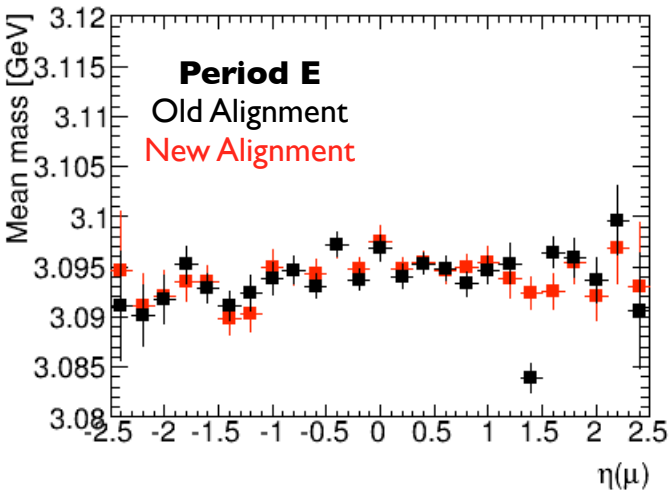

Figure 6.53: Reconstructed J/ψ mass as a function η using combined ID tracks before the end-cap z-alignment ("Old Alignment") and after the end-cap z-alignment ("New-Alignment") [92].

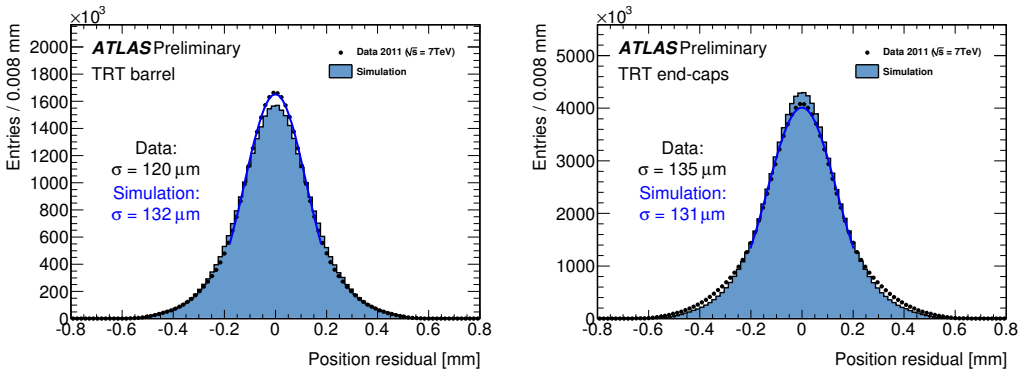

(a) (b)

Figure 6.54: TRT residual distribution after the alignment presented in this chapter for hits the barrel (left) and end-cap (right). The expectation from a perfectly aligned detector in simulation is provided.

to that expected from the simulation. In the barrel the data out performs the perfectly aligned MC, in the end-caps the resolution in data is within five microns of the ideal geometry.

Chapter 7

Electron Identification

The identification of electrons is of fundamental importance to the ATLAS physics program. Leptons are the primary signature of electro-weak processes. They are used in a wide range of physics analyses, from precision standard model measurements, to the search for exotic new physics. Many aspects of the overall design of ATLAS were driven by the requirement that electrons be well-reconstructed and efficiently identified. Efficient electron identification with large background rejection is achieved through the precision tracking and transition radiation detection in the Inner Detector and the fine segmentation of the electromagnetic calorimeter. In hadron colliders, high p_{T} electron production is rare compared to that of jets. Hight p_{T} As a result, electrons can be used to efficiently select interesting physics events on-line in the trigger. Electron identification is a critical component to the analyses presented in this thesis.

The remainder of this chapter is organized as follows: Section 7.1 describes the reconstruction of electron candidates. Section 7.2 describes the discriminating variables used in electron identification. Section 7.3 describes the development of standard operating points used to select electrons on-line, in the trigger, and offline, in physics analyses.

7.1 Electron Reconstruction.

The signature of an electron in ATLAS is a reconstructed track in the Inner Detector (ID) associated to a narrow, localized cluster of energy in the electromagnetic (EM) calorimeter. Figure 7.1 shows an event display of a reconstructed electron in a candidate $W \to e\nu$ event. The reconstructed electron track is shown in yellow. Measurements (hits) are present in all layers of the Pixel and SCT, and a large number of high-threshold hits, shown in red along the track, are seen in the TRT. The high-threshold hits in the TRT are an indication of the presence of transition radiation photons, expected to be emitted from electrons. The ID track points to a large energy deposit in the EM

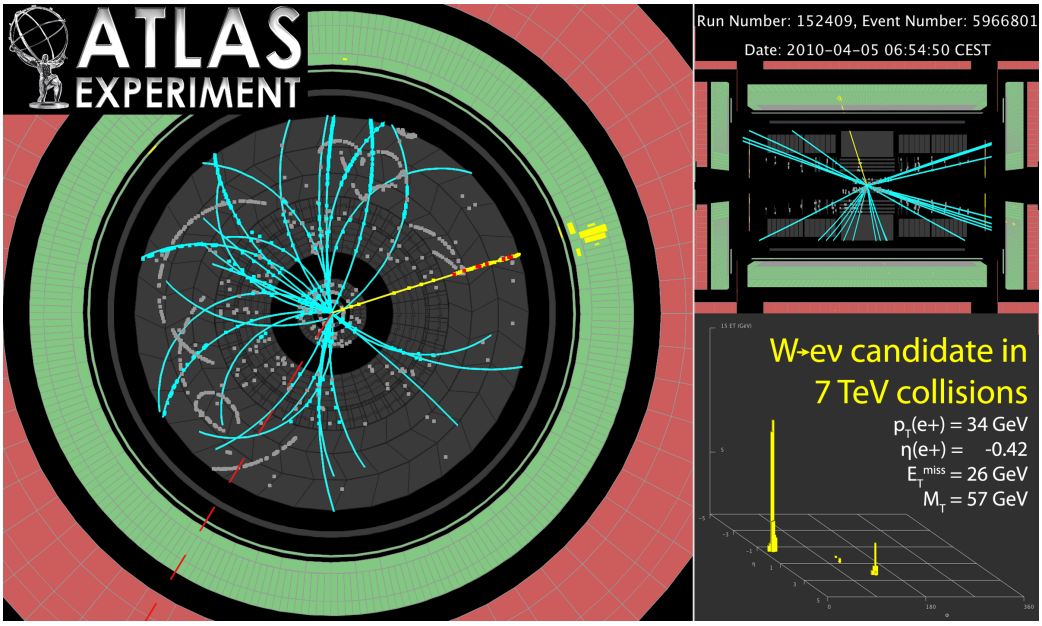

Figure 7.1: Event display of a reconstructed electron from a candidate W decay. The reconstructed electron track is indicated in yellow. The electron cluster is shown in yellow, in the green EM calorimeter. The red points along the electron track indicate detection of transition radiation. The red dashed line indicates the direction of the momentum imbalance.

calorimeter. This energy deposit is narrow in η and ϕ and is primarily contained in the first two layers of the EM calorimeter. There is little if any energy behind the electron cluster in the third EM calorimeter sampling, or in the hadronic calorimeter, shown in red. The reconstructed electron is isolated from the other activity in the event. The electron is isolated from the other reconstructed tracks in the ID and the other energy deposits in the calorimeter.

The ATLAS electron reconstruction algorithm begins with cluster finding in the EM calorimeter. When an electron interacts with the calorimeter, its energy is deposited in many different calorimeter cells. A clustering algorithm is used to group individual cells into clusters, which are associated to incident particles. A "sliding-window" clustering algorithm [71] is used to reconstruct electron clusters. The sliding-window algorithm scans a fixed-size rectangular window over the $\eta - \phi$ grid of calorimeter cells, searching for a local maxima of energy contained in the window. The reconstruction begins by a window of size 3×0.025 units in η-space, and 5×0.025 units in ϕ-space to form seed clusters. This window size is referred to as "3×5"; the unit size 0.025×0.025 corresponds to the granularity of the middle layer of the EM calorimeter. These seed clusters are required to have transverse energy of at least 2.5 GeV. This stage of the cluster finding is fully efficient for high p_{T} electrons.

In the next step of the electron reconstruction, the seed clusters are associated to tracks reconstructed in the ID. Tracks are extrapolated from the end of the ID to the middle layer of the calorimeter. To form an electron candidate, at least one track is required to fall within $\Delta\eta < 0.05$ and $\Delta\phi < 0.1(0.05)$ of the centroid of the reconstructed seed cluster. The matching in ϕ is loosened to account for the electron energy loss, via bremsstrahlung, in the ID. To increase efficiency of the The looser requirement is made on the side of the cluster to which the electron track is curving; a tighter 0.05 requirement is made on the side away from the direction of bending. If multiple tracks match the cluster, the track with the closest ΔR is chosen.

Beginning with the data taken in 2012, a dedicated track reconstruction algorithm was used to correct for electron energy losses in the ID due to bremsstrahlung. Tracks associated to the seed cluster are re-fit with a Gaussian Sum Filter (GSF) [94] algorithm. The GSF fitter allows for large energy losses when determining the electron trajectory, improving the estimated electron track parameters when a significant loss of energy due to bremsstrahlung has occurred. For electrons, the extrapolated track position in the calorimeter is more accurate using the GSF track parameters than the standard track fit. In some cases, the correct electron track will only be considered the best match to the seed cluster as a result of the improved GSF fit.

After track matching, the seed clusters of the electron candidates are rebuilt, and the electron energy is determined. The cluster size is enlarged to 3×7 in the barrel, and 5×5 in the endcap. The total electron energy is determined by adding four separate components [95]: the energy measured in the cluster, the energy estimated to have been lost in the material the electron traverse before entering the calorimeter, the energy estimated to have leaked laterally outside of the cluster, and the energy estimated to have leaked longitudinally behind the cluster. These components are parameterized as a function of the energies measured in the different longitudinal layers of the EM calorimeter. The parameterizations are determined from MC and are corrected in data based on electrons from $Z \to ee$ decays.

Electron candidates at this stage of the reconstruction are referred to as "reconstructed electrons" or as "container electrons". The efficiency for electrons to pass the cluster reconstruction and track matching requirements is high. Figure 7.2, shows the electron reconstruction efficiency as a function of E_{T} and η of the electron cluster. Included in the efficiency quoted is the efficiency of the "track-quality" requirement. The track-quality requirement is satisfied if the electron track has at least one hit in the Pixel detector and at least seven hits total in the Pixel and SCT detectors. The reconstruction and track-quality efficiency shown in the figure is measured with $Z \to ee$ events in data and MC using the "tag-and-probe" method, described in Chapter 4. The reconstruction efficiency is greater than 90% for E_{T} above 15 GeV and for all η. The increase in efficiency from

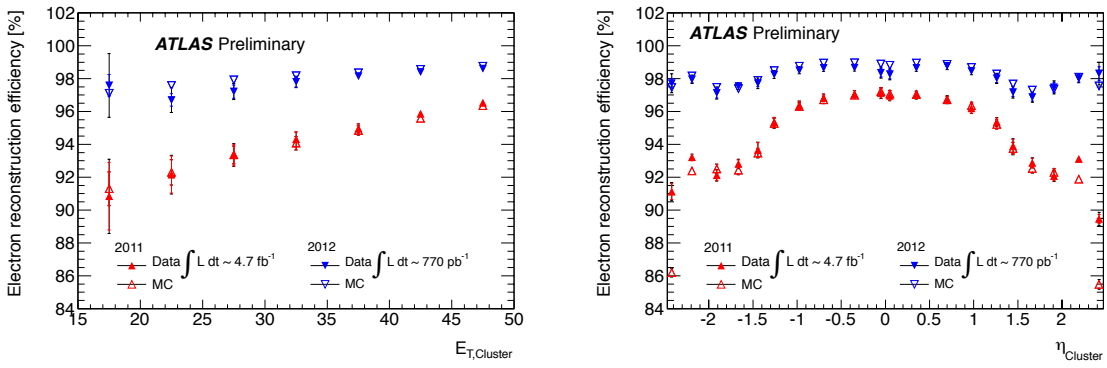

(a) (b)

Figure 7.2: Electron reconstruction efficiency, including the requirements on the track quality, ($N_{pix} \geq 1$ and $N_{Si} \geq 7$) as a function of (a) E_T and (b) η. The plot vs η is shown for electrons with E_T between 30 and 50 GeV.

2011 to 2012 is a result of the GSF fitting.

Particles satisfying the electron reconstruction consist primarily of hadrons and electrons from photon conversions (from π^0 decay) and electrons from heavy-flavor decay. In the case of photon conversions and semi-leptonic heavy-flavor decays, an actual electron is present in the final state. These electrons are still considered background in the sense that they are not produced in isolation as part of the prompt decay of a W, Z, or beyond the SM particle. In the following, both hadrons misidentified as electrons, and electrons from non-prompt sources will be considered as background. Prompt electrons produced in isolation, *e.g.,* from the decays of W or Z bosons, are referred to as "real", "true", or "signal" electrons. Figure 7.3 shows the composition of reconstructed electrons as function of E_T in MC [96]. Reconstructed electrons are dominated by misidentified electrons from hadrons and conversions. The following sections discuss efficient ways for increasing the signal to background of selected electrons.

One of the advantages of doing physics with electrons is that they provide striking trigger signals. In the first level of the trigger system, L1, electrons are selected by requiring adjacent EM trigger towers to exceed a certain E_T threshold [78]. For a given trigger, the L1 threshold varies as a function of η to reflect the η dependence of the detector E_T response. To reduce the large L1 rate at high instantaneous luminosities, a hadronic veto is applied to several of the L1 triggers. This hadronic veto requires the energy behind the electron in the hadronic calorimeter to be small because true electrons are expected to have very little energy in the hadronic calorimeter. Each L1 EM trigger defines a region of interest that seeds the electron reconstruction in the high level trigger (HLT).

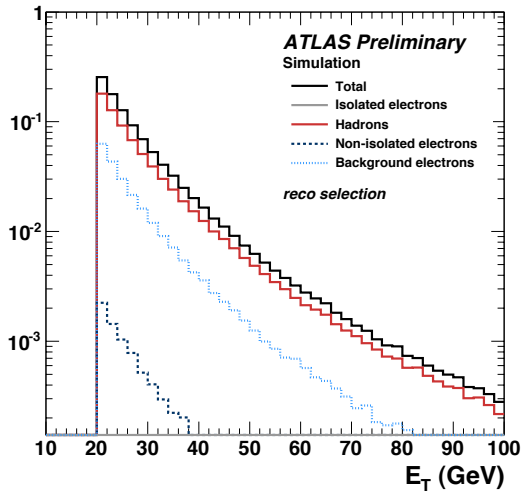

Figure 7.3: Composition of the reconstructed electrons as a function of E_{T}. The distribution is dominated by hadrons. Conversions are referred to in the figure as "Background" electrons. Electrons from semi-leptonic heavy-flavor decays are referred to as "Non-Isolated" electrons. The contribution from true electron, label "Isolated" in the figure, is not visible.

Fast, dedicated calorimeter reconstruction and track-finding algorithms are run on the regions of interest seeded by the L1 EM triggers [79]. These level 2 (L2) electron reconstruction algorithms are similar to those run offline. A more refined energy threshold than L1 is applied at L2, and several of the discriminating variables, described below, are used to reduce the L2 rate to an acceptable level.

The Event Filter uses the offline reconstruction and identification algorithms to apply the final electron selection in the trigger. An E_{T} threshold, similar to the calibrated offline value, is applied. Essentially all of the electron identification quantities are available to further reduce the HLT output rate to fit within the allocation of the trigger output bandwidth. Slight differences in configuration of the HLT electron algorithms lead to small inefficiencies of the trigger with respect to an equivalent offline selection.

There are two basic types of electron triggers: primary and supporting. Primary triggers are the main triggers used to collect signal events in analyses using electrons. The primary triggers are run without prescale and apply strict particle identification criteria to reduce the data rate to an acceptable level. Primary electron triggers are used by essentially all physics analyses that have an electron in the final state. A significant fraction of the total ATLAS trigger bandwidth is allocated to the single electron primary trigger. The following section will discuss the primary trigger operating points in more detail.

Another crucial class of triggers are the supporting triggers. The goal of the supporting triggers

is to collect a sample with less selection bias than the electrons selected with the primary electron trigger. Electrons selected by the primary trigger have many of the identification criteria already applied. The supporting triggers select electrons solely based on electron E_{T}, without any identification criteria beyond the container electron requirements. These supporting triggers are referred to as the "et-cut" triggers. This sample of electrons has several applications. They are used to build unbiased background probability distribution functions (PDFs) needed to optimize the electron identification selection. They are also used to predict background from electron misidentification using techniques based on reversing or relaxing particle identification criteria; Chapter 9 describes one such example. To reduce the large trigger rate without particle identification, the supporting triggers are subjected to a high prescale factor. There are a handful of "et-cut" triggers at different thresholds, each of which have an output rate of $\sim$ 1Hz.

The remainder of this chapter focuses on the determination of specific sets of electron identification selection criteria or "operating points". There are many aspects of the electron reconstruction that are not discussed in the following. Examples include electron reconstruction and identification in the forward $|\eta|$ region or at low E_{T}, below 5 GeV. There has also been considerable effort to determine the electron energy scale and resolution[95] and to measure of the inclusive electron transverse momentum spectrum [97], which is sensitive to heavy-flavor production. The reader is directed to [95] and references therein for a summary of the electron activity within ATLAS.

7.2 Discriminating Variables for Electron Identification.

Since the objects reconstructed as electrons are not very pure, additional selection criteria are necessary. These identification criteria provide a highly efficient electron selection, with large background rejection. Measured quantities that provide separation between real electrons and background are provided by both the ID and the calorimeter [96]. Discriminating variables used in the calorimeter are shown in Figure 7.4. These variables are generically referred to as "shower-shapes" and exploit the fine lateral and longitudinal segmentation of the ATLAS calorimeters. Each of the figures show the variable distribution for: true electrons labeled "Isolated electrons", hadrons, conversions labeled "Background electrons", and semi-leptonic heavy-flavor decays labeled "Non-isolated" electrons.

Figure 7.4a shows the hadronic leakage variable, R_{had1}. This variable is defined as the ratio of the energy in the first sampling of the hadronic calorimeter, behind the electron cluster, to the energy of the electron cluster. Real electrons deposit most of their energy in the EM calorimeter before reaching the hadronic calorimeter and thus have small values of R_{had1}. Large values of hadronic leakage indicate hadronic activity associated to the electron cluster. In the region of $|\eta|$ between 0.8

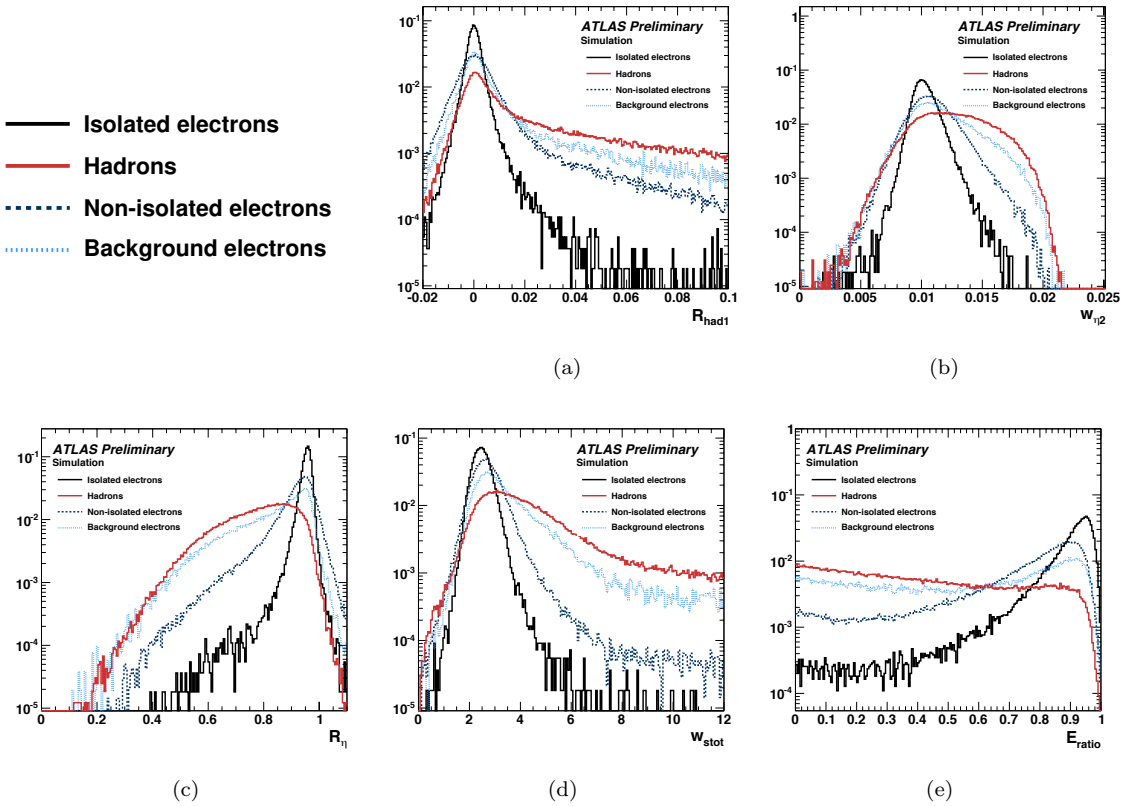

Figure 7.4: Electron identification variables in the calorimeter, "shower-shapes", shown separately for signal and the various background types. The variables shown are (a) hadronic leakage R_{had1}, (b) width in eta in the second sampling $w_{\eta 2}$, (c) R_{η}, (d) width in eta in the strips $w_{s,\mathrm{tot}}$, and (e) E_{ratio}.

and 1.37, the barrel hadronic calorimeter ends and the end-cap hadronic calorimeter begins. In this region, the hadronic leakage is calculated using all layers of the hadronic calorimeter to efficiently collect the hadronic energy and is denoted R_{had}. In the other $|\eta|$ regions, the energy in the first layer is sufficient.

The width in the second sampling, $w_{\eta 2}$, is shown in Figure 7.4b. $w_{\eta 2}$ measures the width of the shower in η as the energy-weighted RMS of the η distribution of cells in the second sampling. It is defined as

$$w_{\eta 2} = \sqrt{\frac{\sum_i (E_i \eta_i^2)}{\sum_i E_i} - \left(\frac{\sum_i E_i \eta_i}{\sum_i E_i}\right)^2}, \tag{7.1}$$

where $E_i(\eta_i)$ is the energy(η) of the i^{th} cell, and the sum runs over the cells in a 3×5 window of the second sampling, centered on the electron. Requiring narrow shower widths in η suppresses background from jets and photon conversions, which tend to have wider showers than true electrons.

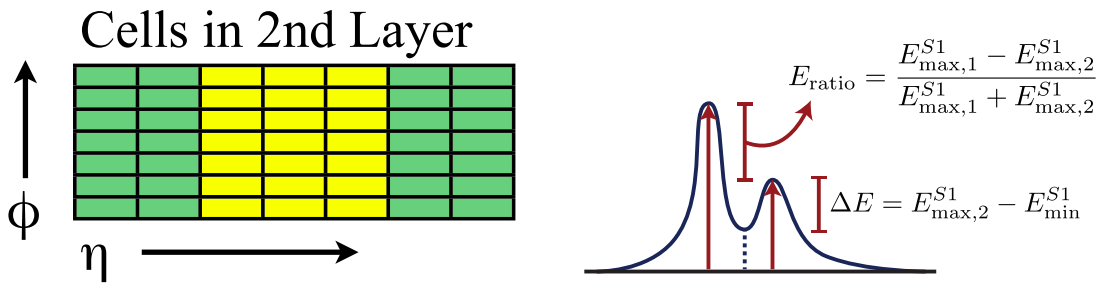

(a) (b)

Figure 7.5: Schematic diagrams of R_η and E_{ratio}. (a) R_η is calculated as the ratio of the sum of energy in the yellow cells to the sum of energy in the yellow and green cells. The yellow cells are centered on the reconstructed electron. (b) E_{ratio} is calculated as the ratio of the difference in energy of the two highest cells, to the sum the energy in the two highest cells. [98] E_{ratio} is calculated from the cells in the first layer of the calorimeter.

Another measure of the shower width is R_η, shown in figure 7.4c. R_η is defined as the ratio of cell energies in a 3×7 ($\eta\times\phi$) window to that of a 7×7 window, in the second sampling. A schematic of the R_η calculation is shown in Figure 7.5a. The yellow cells are centered on the reconstructed electron and represent the 3×7 core. The 7×7 window includes the 3×7 core, in addition to the green cells shown on either side. In the narrow showers associated to electrons, most of the energy is contained in the 3×7 window; as a result, the R_η variable peaks near one. The backgrounds to electrons tend to have a higher fraction of energy outside of the 3×7 core, resulting in lower values of R_η. R_η is one of the most powerful variables for background separation.

The width of the shower in the first layer of the calorimeter, or strips, is shown in Figure 7.4d. This variable is referred to as $w_{s,\text{tot}}$ and is defined as

$$w_{s,\text{tot}} = \sqrt{\frac{\sum_i E_i (i - i^{\text{max}})^2}{\sum_i E_i}}, \tag{7.2}$$

where, E_i is the energy in the i^{th} strip, i is the strip index, and i^{max} is the index of the strip with the most energy. The sum runs over the strips in a window of 0.0625×0.2 centered on the electron. This corresponds to 20×2 strips in $\eta\times\phi$. The shower width in the strips is larger for background than for signal, providing separation between signal and background with the $w_{s,\text{tot}}$ variable.

Another strip variable used to suppress background is E_{ratio}, shown in Figure 7.4e. E_{ratio} is defined using the cells corresponding to the two highest energy maxima in the strips. The difference in energy between the cells in the first and second maxima, is compared to their sum:

$$E_{\text{ratio}} = \frac{E^s_{1^{\text{st}}\text{-max}} - E^s_{2^{\text{nd}}\text{-max}}}{E^s_{1^{\text{st}}\text{-max}} + E^s_{2^{\text{nd}}\text{-max}}} \tag{7.3}$$

$\|\eta\|$-value	Detector Change
0.6	Change in depth of the 1st sampling
0.8	Change in absorber thickness (1.53 mm to 1.13 mm)
1.37	Beginning of Barrel-end-cap transition
1.52	End of Barrel-end-cap transition
1.81	Strips width changes from $\frac{0.025}{8}$ units in η to $\frac{0.025}{6}$
2.01	Strips width changes from $\frac{0.025}{6}$ units in η to $\frac{0.025}{4}$
2.37	Strips width changes from $\frac{0.025}{4}$ units in η to 0.025
2.47	Strips width changes from 0.025 units in η to 0.1

Table 7.1: Changes in the EM calorimeter geometry as a function $|\eta|$. These changes lead to an η-dependence in the electron identification variables.

Figure 7.5b shows a schematic of the E_{ratio} calculation. Jet background tends to have multiple incident particles associated to the reconstructed cluster. This background will have maxima comparable in size, and thus, lower values of E_{ratio} than for true electrons, which are dominated by a single maxima.

The fraction of energy in the third sampling of the EM calorimeter is another calorimeter variable, in addition to those shown in Figure 7.4, that is used to discriminate between electrons and background. Similar to R_{had}, the energy fraction in the third sampling, or f_3, tends to be smaller for electrons than for background, which penetrates deeper into the calorimeter.

The distributions of discriminating variables in the calorimeter are functions of both the η and the E_{T} of the reconstructed electrons. The η dependence is primarily driven by changes in the calorimeter geometry. For example, the region of $|\eta|$ between 1.37 and 1.52 is the transition of the barrel and end-cap calorimeters. Many of the calorimeter variables loose their power in this region as a result of the much poorer resolution. The electron selections used in most analyses exclude this crack region because of the relatively poor background rejection in this region. The physical size of the strips also change with $|\eta|$, leading to a strong η-dependence of the distributions of the strip-level variables. A table of relevant detector changes in $|\eta|$ is given in Table 7.1. The E_{T} dependence of the variables, on the other hand, is mainly due to the physics of the showering particles. For real electrons, the distributions of the shower-width variables defined above become narrower with increasing E_{T}; the background however, tends to have a smaller E_{T} dependence. For real electrons, the shower widths tend to narrow with increasing E_{T}; the background however, tends to have a smaller E_{T} dependence. As a result, the background separation of the calorimeter shower shapes improves with E_{T}.

The ID also provides discriminating variables used in electron identification. Examples of these ID variables are shown in Figure 7.6. Again the distributions for the various sources of electrons are

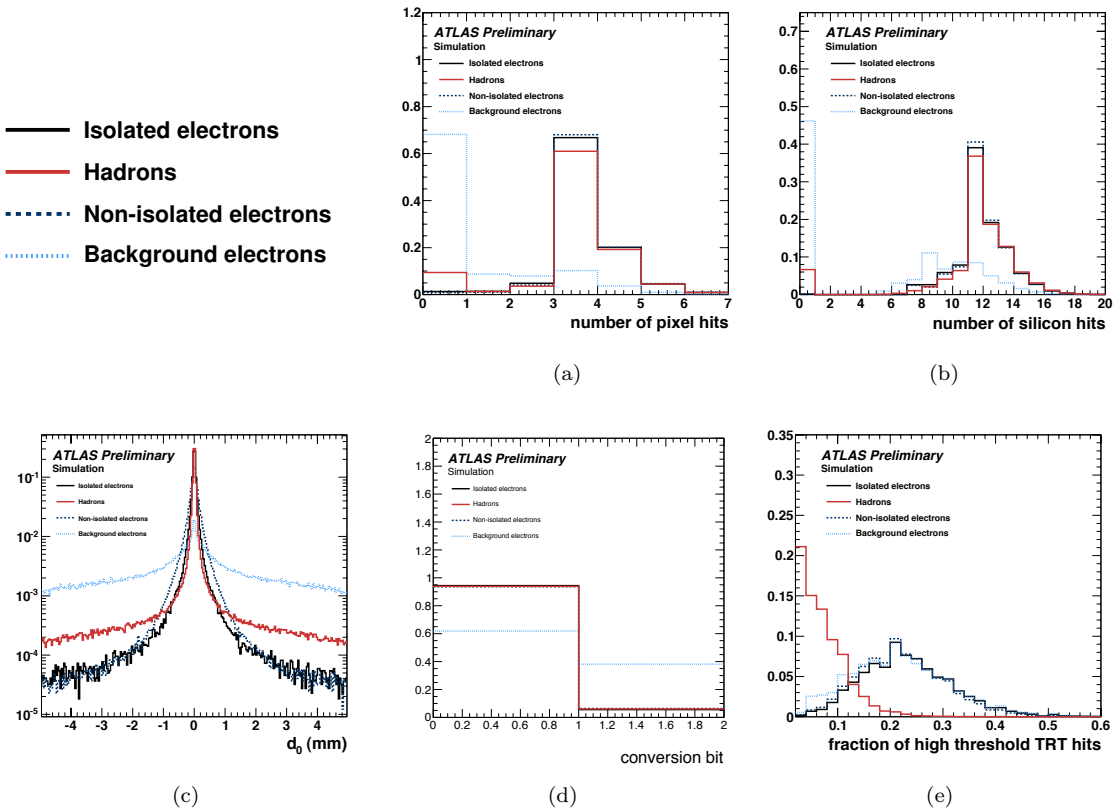

Figure 7.6: Electron identification variables in the ID, shown separately for signal and the various background types. The variables shown are (a) number of hits in the Pixel detector, (b) combined number of hits in the Pixel and SCT detectors, (c) transverse impact parameter d_0, (d) conversion flag, or "conversion bit", and (e) fraction of high-threshold hits in the TRT.

shown. The tracking variables are complementary to those in the calorimeter. For signal electrons, the ID variables are often uncorrelated from the calorimeter measurements. This allows the signal purity of the calorimeter (tracking) variables to be enhanced, in a unbiased way, by selection on the tracking (calorimeter) variables.

Figure 7.6a and Figure 7.6b shows the number of hits in the Pixel and SCT detectors associated to the electron track. By requiring electron tracks to have pixel hits and a significant number of SCT hits, *i.e.,* to satisfy the track-quality requirement, the background from conversions can be suppressed with little loss in signal efficiency. The detector layers that photons traverse before converting do not have hits associated to them. This results in a smaller number of hits in the Pixel and SCT detectors than for prompt electrons, which will have hits in all traversed layers. Another important ID variable is the number of hits in the first Pixel layer or b-layer. The b-layer

requirement is particularly effective at suppressing conversion background as it is sensitive to all conversions that occur after the first layer of the Pixel detector. When determining the number of b-layer hits, inactive detector elements crossed are treated as if a hit were present.

The transverse impact parameter distribution, d_0, is shown in Figure 7.6c. The impact parameter measures the distance of closest approach of the electron track to the primary vertex in the transverse plane. It primarily provides separation against conversions, which have tracks that can be significantly displaced from the interaction point; d_0 is also larger for heavy-flavor decays because of the large b-quark lifetime.

The conversion bit is shown in Figure 7.6d. The conversion bit is set if the electron track is matched to a conversion vertex [73]. Two types of conversion vertices are considered: single-leg and double-leg. Electrons are flagged as double-leg conversions if there is another ID track that forms a secondary vertex with the electron track consistent with coming from a photon conversion. The tracks forming the secondary vertex are required to have opposite electric charge, to have a small opening angle, and to be consistent with the basic geometry of a photon conversion. To increase the efficiency of the conversion finding, single-leg conversions are also used to set the conversion bit. An electron is flagged as a single-leg conversion if it is missing a hit in the b-layer. Requiring that the conversion bit is not set, removes a significant fraction of reconstructed electrons from conversions and has a relatively small inefficiency for signal electrons.

Figure 7.6e shows the fraction of high threshold hits in the TRT [99]. High threshold TRT hits indicate the presence of transition radiation (TR) photons. The probability of creating a high threshold hit depends on the Lorentz γ factor, $\frac{1}{\sqrt{1-\frac{v^2}{c^2}}}$. Figure 7.7 shows this dependence in the TRT barrel. The high threshold probability is flat around 0.05 below γ of 1000. At higher values of γ, the probability rises, or "turns on", to a value of around 0.2. The relatively heavy pions and other charged hadrons have Lorentz factors that lie in the low-probability region of the TR response. The Lorentz factors for electrons, on the other hand, lie at the top of the high threshold probability turn-on. As shown in Figure 7.6e, electron tracks have a higher fraction of high threshold hits then those from hadrons. Requiring TR photons along the track provides rejection against hadrons, but not conversions or semi-leptonic heavy-flavor decays, which also have final-state electrons. The high threshold fraction is one of the most powerful discriminating variables against background from hadrons. The TR requirement is particularly useful because it is largely uncorrelated from the discriminating variables used in the calorimeter. At the LHC, electron discrimination using TR is unique to ATLAS.

In general, the tracking requirements are independent of the electron η and E_{T}. The exception is the TR response, which is η dependent as a result of changes in the detector, *e.g.,* different radiator

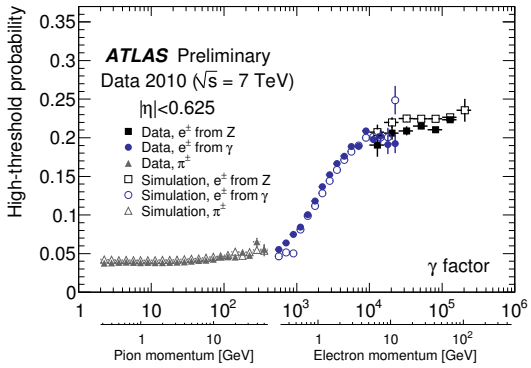

Figure 7.7: Probability of a high threshold TRT hit as a function of Lorentz γ factor in the TRT barrel. The corresponding momentum assuming the pion mass or the electron mass are shown.

material is used in the barrel and end-caps. In addition, the ID variables are mostly unaffected by pile-up. Out-of time pile-up is a non-issue due to the short readout windows of the ID subsystems. The highly granularity of the ID gives tracking efficiency and resolution that is robust against in-time pile-up.

Combining information from the ID and calorimeter provides additional background discrimination. Variables related to the track-cluster matching are shown in Figure 7.8. Figure 7.8a shows the difference in η of the track and the cluster. The comparison is made after extrapolating the track to the calorimeter. This distribution is narrowest for real electrons. The additional particles produced in association with the hadron and conversion background can bias the cluster position with respect to the matching track. Requiring small values of $|\Delta\eta|$ suppresses these backgrounds.

A similar variable, the track-cluster matching in ϕ, is shown in Figure 7.8b. The ϕ matching is less powerful than the matching in η because of bremsstrahlung. The radiation of bremsstrahlung photons will cause a difference in track and cluster ϕ for real electrons. The variable used is assigned to be positive or negative based on the electron charge such that the direction to which the track bends corresponds to negative values of $\Delta\phi$. This is done so that the difference in ϕ caused by bremsstrahlung is symmetric for electrons and positrons. Matching in ϕ, particularly on the positive side of the distribution, can be used to suppress background, analogously to $\Delta\eta$.

Another variable related to track-cluster matching is E/p, shown in Figure 7.8c. E/p is the ratio of the electron energy measured in the calorimeter to the track momentum determined from the ID. The distribution for signal electrons peaks at one and has a long tail in positive E/p. Without radiation, the electron energy measured by the ID and the calorimeter is similar. Photon radiation in the ID reduces the energy seen by the tracker with respect to the calorimeter, which absorbs

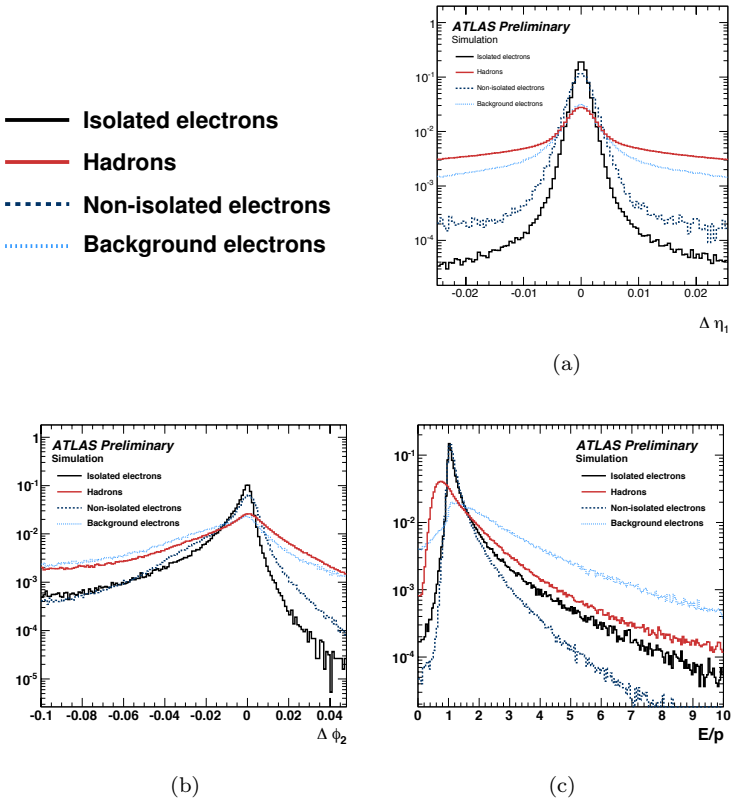

Figure 7.8: Track-Cluster matching variables, shown separately for signal and the various background types. The variables shown are (a) the difference in track and cluster η, (b) the difference in track and cluster ϕ, and (c) ratio of the energy measured in calorimeter to the momentum measured in the tracker.

the energy from both the electron and the radiated photon. Hadrons peak at lower values of E/p. Hadrons will not deposit all of their energy in the EM calorimeter, a significant fraction will be deposited in the hadronic calorimeter. The energy of the reconstructed EM cluster will not reflect the total energy of the incident particle. The total momentum of the hadron is measured in the ID, leading to an E/p distribution that peaks at lower values than electrons. Conversions tend to have larger values of E/p. In this case, the cluster measures the full energy of the photon, from both legs of the conversion, whereas only one of the legs gives rise to the track that is matched to the cluster. Requiring that E/p is consistent with the expectation from a real electron can suppress both hadron and conversion background.

The final class of identification variables used to discriminate between signal and background is isolation, shown in Figure 7.9. Isolation measures the amount of energy near the reconstructed

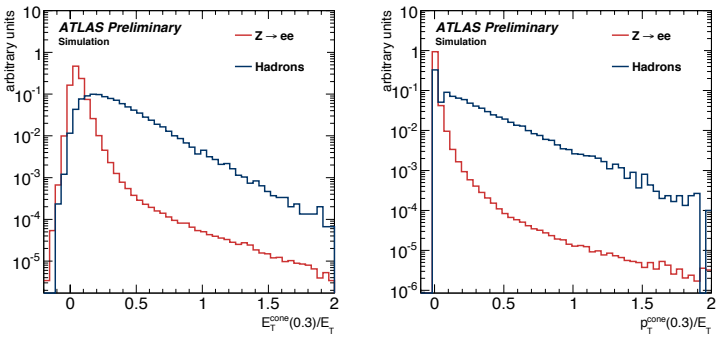

(a) (b)

Figure 7.9: Examples of electron isolation variables (a) relative calorimeter isolation in a cone of $\Delta R < 0.3$ (a) relative track isolation in a cone of $\Delta R < 0.3$. Signal electrons and hadron background are shown separately.

electron. Background electrons are produced in association with other particles, which lead to large values of isolation. Signal electrons tend to have low values of isolation as they are uncorrelated with other jet activity in the event. The isolation is calculated by summing the energy in a cone centered around the electron. The cone size is specified in terms of ΔR; typical cone sizes are 0.2, 0.3 or 0.4 units of ΔR. The isolation energy can be calculated using either the energy measured in the calorimeter or the momentum of tracks in the ID. Figure 7.9a shows the calorimeter isolation formed from the energy in the cone of $\Delta R = 0.3$ around the electron candidate divided by the E_{T} of the electron candidate. Figure 7.9b shows the relative track isolation, again, using a cone size of 0.3. The distributions are shown for signal electrons and the hadron background.

The track-based and calorimeter-based isolation are highly correlated, but offer different advantages. Calorimeter-based isolation is more sensitive to the surrounding particle activity because it measures the energy of both neutral and charged particles. Track-based isolation, on the other hand, can only detect the charged particle component. In this respect, calorimeter-based isolation provides more discriminating power. Track-based isolation, however, is less sensitive to pile-up. Both in-time and out-of-time pile-up degrade the performance of calorimeter-based isolation. Track-based isolation is unaffected by out-of-time pile, and the effect of in-time pile-up can be mitigated by only considering tracks consistent with originating from the same primary vertex as the electron candidate. In events with a large amount of pile-up, track-based isolation can often outperform calorimeter-based isolation.

This concludes the introduction of the electron identification variables used for background discrimination. The following sections describe the development of standard operating points using

these variables and how the electron identification has been commissioned using data.

7.3 Electron Operating Points

7.3.1 The isEM Menu

To standardize the electron selection used in the trigger and across analyses using high p_{T} electrons, the ATLAS has developed a set of identification requirements used to select electrons. The selection requires that the value of a particular selection criteria be larger or smaller than a particular value. This value is referred to as the "cut value". This common electron selection is a simple cut-based selection using the particle identification variables described in the previous section. It is referred to as the "isEM" menu or "isEM" selection. The use of common electron selection has the advantage of standardizing software used to select electrons. It also allows the electron efficiency measurements to be shared across analyses. The efficiency of a given electron selection is needed for essentially all physics analyses. To determine a cross section or a limit on a cross section you need the efficiency The isEM electron selection allows the efficiency measurements to be centrally handled within ATLAS.

To accommodate a broad range of physics topics, three separate operating points have been developed. They are referred to, in order of increasing background rejection, as Loose, Medium, and Tight. The operating points are inclusive, such that Loose is a subset of Medium, which in turn is a subset of Tight. The philosophy of the isEM menu is to tighten the selection at successive operating points by adding variables, not by tightening cut values. For example, the cut values for a particular selection criteria are the same for the Loose selection and the Tight selection.

Isolation is not used in the isEM menu. The isolation variables involve relatively large regions of the detector. Cone sizes of up to 0.4 are used for isolation, compared to the 0.1 size of the electron cluster. As a result, the isolation is not unique to all physics analyses involving electrons. The expected isolation from signal electrons can depend on the final state being considered. Because of this, isolation is not included directly in the standard electron definitions; individual analyses apply dedicated isolation requirements in addition to the standard isEM selection.

The isEM menu was developed before data taking began using MC. The cut values used in the menu were optimized to separate signal and background. In order to perform the optimization, probability distribution functions, PDFs, corresponding to the signal and background distributions are needed. The initial optimization was performed using input PDFs taken from simulation. The optimization was performed separately in bins of η and E_{T}. The binning uses the η boundaries listed in Table 7.1. For the TR requirement, the η binning is dictated by the TRT geometry, with bin boundaries at $|\eta|$ of 0.1, 0.625, 1.07, 1.30, 1.75, and 2.0. The E_{T} is binned in intervals of 5 GeV,

Loose
Middle-layer shower shapes: R_η, $w_{\eta 2}$
Hadronic leakage: R_{had1}(R_{had} for $0.8 < \lvert\eta\rvert < 1.37$)
Medium
Pass Loose selection
Strip-layer shower shapes: $w_{s,\text{tot}}$, E_{ratio}
Track quality
$\lvert\Delta\eta\rvert < 0.01$
$\lvert d0\rvert < 5$ mm
Tight
Pass Medium selection
$\lvert\Delta\eta\rvert < 0.005$
$\lvert d0\rvert < 1$ mm
Track matching: $\lvert\Delta\phi\rvert$ and E/p
High TRT HT fraction
$\text{N}_{\text{BL}} \geq 1$
Pass conversion bit

Table 7.2: Summary of the variables used in the Loose, Medium, and Tight operating points of the isEM menu.

up to 20 GeV, and then every 10 GeV up until 80 GeV, where the last E_{T} bin is used for all electrons above 80 GeV. The TMVA [100] software package was used to perform an initial, automated cut optimization. The cut values obtained from TMVA were treated as a starting point from which minor "by-hand" adjustments were made.

A summary of the variables used in each isEM operating point is given in Table 7.2. The first operating point is Loose. Loose uses only the variables defined in the second sampling, R_η and $w_{\eta 2}$, and the hadronic leakage, R_{had1}, or R_{had}. The Loose operating point was designed to yield around 95% signal efficiency, averaged over η and E_{T}. The expected jet rejection achieved with this operating point is around 500, *i.e.,* one in 500 jets will pass the Loose selection. The quoted jet rejection numbers should be treated as a guide to the relative rejection of the different operating points. There are large, unevaluated systematic uncertainties associated with these fake rates, see Chapter 9 for further discussion.

The next operating point is Medium. Medium includes the Loose selection and adds the strip-level shower shapes, $w_{s,\text{tot}}$ and E_{ratio}, and the track quality requirements. Relatively loose impact parameter and $\Delta\eta$ requirements are also included. Medium was designed to have a signal efficiency of around 90% in each η and E_{T} bin. With this signal efficiency, an expected jet rejection of around 5000 is achieved. The medium operating point serves as the identification criteria applied to the

single electron primary trigger. The medium isEM selection criteria are applied to the reconstructed electrons in the HLT.

The final operating point is Tight. The Tight selection includes the full power of electron identification at ATLAS, except, of course, for isolation. In addition to the Medium selection, cuts on the track-cluster matching, the transition radiation, and the conversion bit and number of b-layer hits are made. Stringent cuts are made on the impact parameter and $\Delta\eta$ variables. The Tight operating point was designed to achieve a high background rejection across η. A signal efficiency of 65-80% is achieved, with an η dependence of up to 15%. An expected jet rejection of around 50000 is achieved with the Tight operating point.

7.3.2 Data-Driven isEM Optimization

With the first data collected in 2009 and 2010, it became apparent that several of the shower shape variables were mis-modeled by the MC. Figure 7.10 shows a comparison of the R_η and $w_{\eta 2}$ distributions for signal electrons from $Z \to ee$ events. The distributions for data, in black, are shown after background subtraction using the technique described in reference [95]. Significant discrepancies between the data and MC distributions are seen. The differences are consistent with a broadening of the shower shapes in data with respect to the MC expectation. A similar effect is observed in other variables sensitive to the lateral width of the EM shower. Shower shapes not directly sensitive to the lateral width are modeled better by the MC. The equivalent plots for R_{had} and E_{ratio} are provided in Figure 7.11. Better agreement is seen in these variables.

An implication of the MC mis-modeling is a loss of signal efficiency in the first part of data taking in 2010. The isEM menu was optimized using the mis-modeled MC PDFs. The MC-optimized cut values are inefficient with respect to the broader showers observed in data. As a result, the efficiency of the isEM selection applied to data was significantly lower than the operating points targeted in the optimization. All of the isEM operating points were effected, as several of the mis-modeled variables were present in the Loose selection.

In order to cope with this loss of efficiency in the first data, the cut values of the mis-modeled variables were relaxed. The need for modifying the isEM menu was seen before a large sample of $Z \to ee$ events could be collected and used to determine the shower shape variable PDFs from data. A short-term menu, referred to as the "robust isEM" menu, was developed using electrons from $W \to e\nu$ events. $W \to e\nu$ events were selected by requiring large missing energy, a reconstructed electron, and a transverse mass consistent with a W. To increase the purity of the electron sample, all of the tight identification criteria were applied, except for the mis-modeled lateral shower shapes variables. The shower shapes from selected electrons were then used to revise the cut-values on

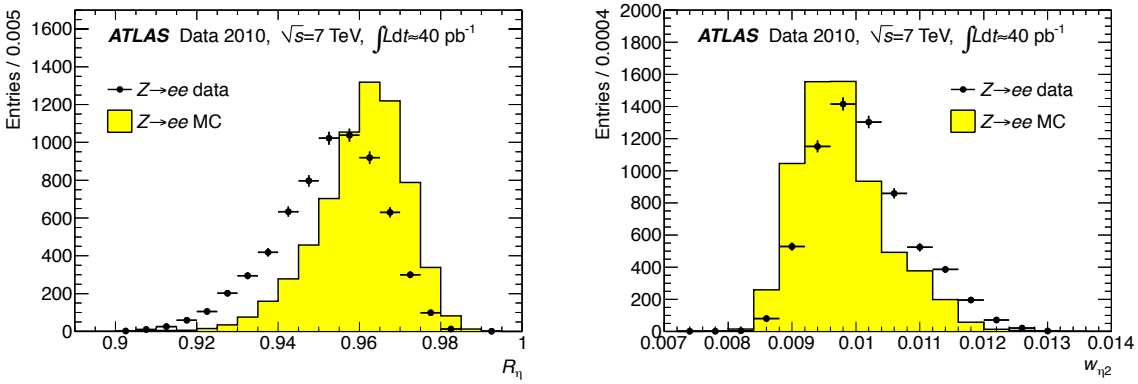

(a) (b)

Figure 7.10: Comparison of the shower shapes, R_η and $w_{\eta 2}$, of electrons from $Z \to ee$ events in data and MC. The electrons are required to have E_{T} between 40 and 50 GeV. The data distributions are shown after background subtraction. The uncertainties on the data include the systematic uncertainty from the background subtraction. The MC is normalized to the number of entries in data.

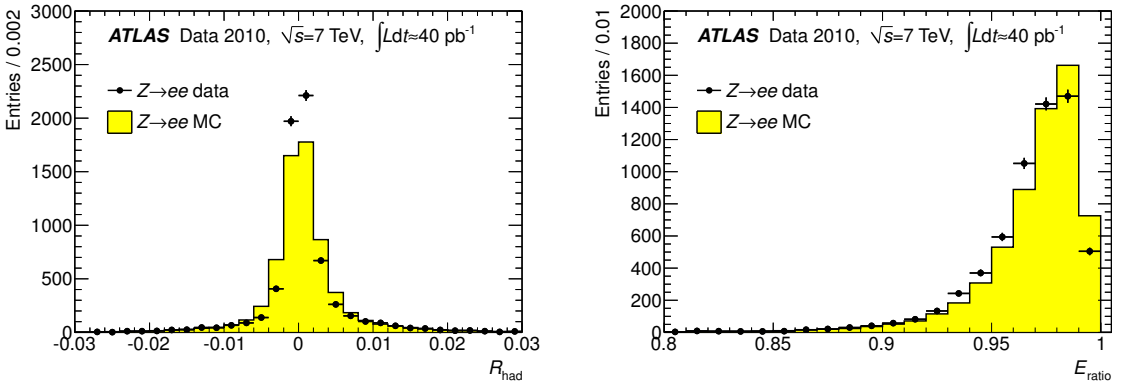

(a) (b)

Figure 7.11: Comparison of the shower shapes, R_{had} and E_{ratio}, of electrons from $Z \to ee$ events in data and MC. The electrons are required to have E_{T} between 40 and 50 GeV. The data distributions are shown after background subtraction. The uncertainties on the data include the systematic uncertainty from the background subtraction. The MC is normalized to the number of entries in data.

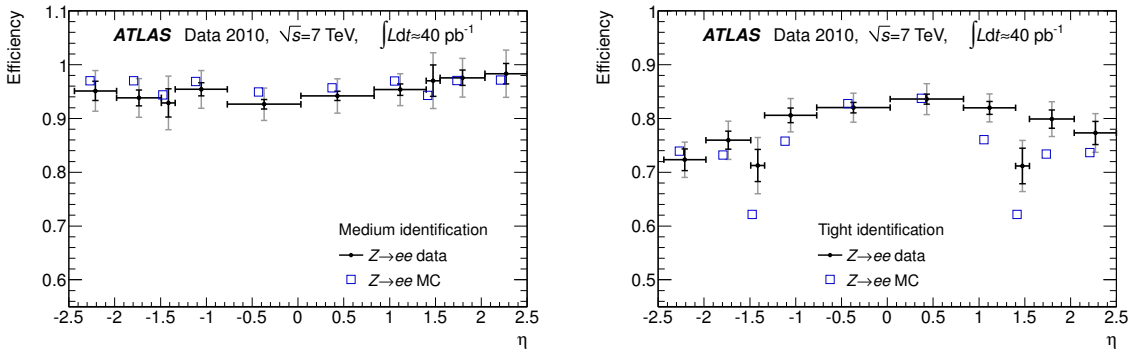

(a) (b)

Figure 7.12: Efficiencies of the medium and tight requirements in the "robust" isEM menu. The efficiencies are measured using $Z \rightarrow ee$ events and are shown for electrons with E_{T} between 20 and 50 GeV. The error bars provide the statistical (inner) and total (outer) uncertainties on the measured efficiencies.

mis-modeled distributions originally determined from MC using these PDFs observed in data.

The goal of the robust menu was to recover the efficiency loss from the MC mis-modeling. The loss in background rejection associated to the looser robust cuts was acceptable. With the relatively low instantaneous luminosities of the 2010 data taking, the loss in background rejection was tolerable in the trigger. The efficiencies of the tight and medium operating points of the robust isEM menu are shown in Figure 7.12. The quoted efficiencies are for electrons with E_{T} between 20 and 50 GeV. The efficiency of the robust medium (tight) requirement is around 95%(80%), somewhat higher than the target of the MC isEM optimization. The robust isEM menu was the basis of the electron selection for all 2010 ATLAS analyses.

The loss of background rejection incurred with the robust isEM menu became a problem with the higher luminosity data taking in 2011. To keep the single electron primary trigger rate within the bandwidth allocation, the background rejection of the electron selection had to be increased. It was critical that this be achieved while preserving most of the gains in signal efficiency provided by the robust isEM menu. To accomplish this, the isEM menu was re-optimized using input PDFs corresponding to electrons in data.

To re-optimize the isEM with electrons in data, unbiased signal and background PDFs were needed. The background PDFs were taken directly from data. With the full 2010 data sample, corresponding to 40 pb^{-1}, enough background statistics were collected with the unbiased etcut triggers to make adequate background PDFs in the different η and E_{T} bins. There is a small amount of signal contamination, but this signal in the tails of the distribution could compromise the

optimization. The background electrons were selected by applying electro-weak vetoes to suppress the signal contamination from Ws or Zs.

Generating adequate signal PDFs was more complicated. With the full 40 pb^{-1} data set, insufficient statistics for $Z \to ee$ decays were collected to fully populate the PDFs in all of the relevant phase space. This was especially true at lower E_{T} and high η, were the improved rejection for the trigger was most needed. To address this issue, a hybrid, data-corrected MC approach was taken. Mis-modeled PDFs in the MC were corrected, based on electrons observed in data, and were then used for the isEM optimization. This approach has the benefit of large MC statistics, while the data-driven corrections made the PDFs applicable to actual electrons found in data.

To correct the MC, the assumption was made that the MC mis-modeled the data by a simple shift in the lateral shower shape distributions. This assumption was motivated by observations made when creating the robust menu and was found to be a reasonable approximation. The shifted MC is only used to define the electron identification criteria. If the simple approximation is not completely accurate, the optimization is sub-optimal. The procedure would not lead to a bias of any kind but simply a loss of performance.

Although there was not enough data to construct the full PDFs, the data statistics were adequate enough to determine the value of the data-MC offset in each bin. Signal PDFs were obtained in data from $Z \to ee$ events using tag-and-probe. The data-MC shifts were determined, bin-by-bin in η and E_{T}, for the R_{η}, $w_{\eta 2}$, and $w_{s,\mathrm{tot}}$ variables. The shifts were determined by minimizing chi-square between the data and MC as a function of the shift.

Examples of the shifted MC are shown in Figure 7.13. The figure shows the R_{η} and $w_{\eta 2}$ distributions for signal electrons in a particular E_{T}-η bin. Data is shown in black, the nominal, uncorrected MC is shown in red, and the corrected MC is shown in blue. The corrected MC distributions are the same as the uncorrected distributions, except for the shift along the x-axis. The size of the MC corrections are substantial with respect to the width of the distributions. The results in Figure 7.13 were obtained using the 2010 data available at the time of the optimization. Here, the statistical advantage of the corrected MC over the data distribution is clearly visible. In the higher statistics data samples collected in 2011, the simple model of the MC correction could be better tested. Figure 7.14 shows a comparison of the PDFs with the 2011 data set to the corrected and uncorrected MC. The simple approximation is not perfect, but leads to a reasonable modeling of the data.

The data-driven signal and background PDFs were used to re-optimize the isEM selection. The re-optimization was performed in the same way as the original optimization of the isEM menu using MC. The required level of background rejection was achieved for the medium operating point, allowing a 20 GeV single medium-electron trigger to run in the HLT with a luminosity above 0.5 $\times$

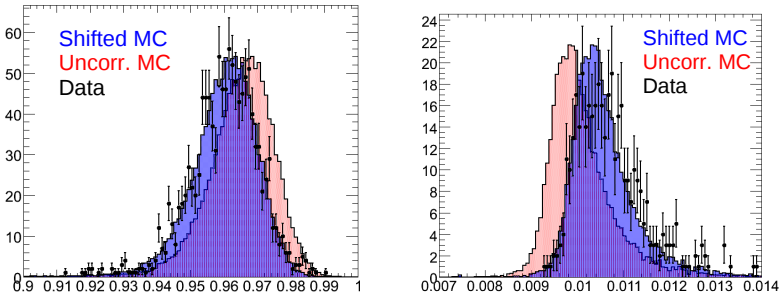

(a) (b)

Figure 7.13: Example of the MC correction procedure using statistics available in 2010. The R_η and $w_{\eta 2}$ distributions are shown for data (black), the uncorrected MC (red), and the corrected MC (blue). The results are shown for the bin with E_{T} between 30 and 40 GeV, and $|\eta|$ between 1.15 and 1.37.

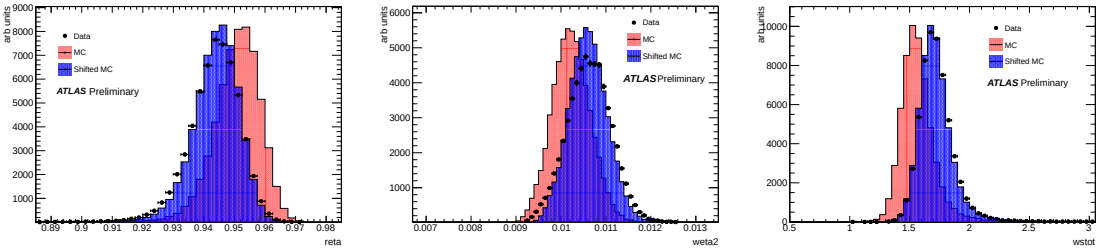

(a) (b) (c)

Figure 7.14: MC correction procedure using the high statistics 2011 data sample. The R_η, $w_{\eta 2}$, and $w_{s,\mathrm{tot}}$ distributions are shown for data (black), the uncorrected MC (red), and the corrected MC (blue). The results are shown for the bin with E_{T} between 30 and 40 GeV, and $|\eta|$ between 1.15 and 1.37.

10^{33} cm^{-2} s^{-1}. This trigger was used throughout the first half of the 2011 data taking, until the instantaneous luminosity reached 10^{33} cm^{-2} s^{-1}. The re-optimized isEM menu was the basis of the electron selection for 2011 ATLAS analyses using the first 2 fb^{-1}of 2011 data[13].

7.3.3 The isEM++ menu

With instantaneous luminosities of 10^{33} cm^{-2} s^{-1}, the background rejection provided by the re-optimized medium was not enough to provide sustainable rates in the trigger. A factor of three increase in background rejection was required for the 20 GeV single electron trigger to have an output rate of 20 Hz at 10^{33} cm^{-2} s^{-1}. At the time, 20 Hz represented 10% of the total ATLAS

[13]For the ATLAS aficionados, this corresponds to the 2011 "release 16" analyses.

trigger bandwidth.

It quickly became clear that re-optimizing isEM in the traditional way would require unacceptable efficiency losses to achieve the factor of three increase in the background rejection. The variables used at Medium already had stringent requirements; further tightening would cut into the bulk of the signal distributions. The only way to increase the rejection in an efficient manner was to add additional identification variables to the Medium operating point.

The need to reconsider the selection quantities used in the Medium selection was used as an occasion to break from the traditional isEM philosophy. Instead of using a subset of variables at Loose and adding variables to go to Medium and Tight, it was decided to used the all variables at all levels and tighten operating points by tightening the cut values used at subsequent levels. In 2011, the isEM menu was updated to follow this new paradigm. The updated menu is referred to as the "isEM++" menu.

A representation of the conceptual difference between the isEM and the isEM++ menu is shown in Figure 7.15. Var1 and Var2 represent two different identification variables. Electrons selected by the Loose definition, shown in red, are required to pass a cut on Var1, but not on Var2. Electrons selected by the Tight definition, shown in black, are required to pass cuts on both Var1 and Var2. The requirement on Var2 is the same in Loose and in Tight, as for the isEM menu. The Loose++ selection, the Loose operating point in the isEM++ menu, is indicated in blue. Electrons passing Loose++ are required to satisfy cuts on both Var1 and Var2. The requirements on Var1 and Var2 are however looser than in Tight, as the case for the isEM++ menu. By cutting hard on one variable and not at all on the other, Loose selects a strange region of PID space. Corners of PID space with electrons that look exactly like signal in one variable, but completely non-signal like in the other, are a part of the Loose selection. These electrons are far from the signal region. Loose++, on the other hand, selects a more natural region of electrons, surrounding the signal-like region in all dimensions. Electrons selected by Loose++ are closer to the signal region that those selected by Loose. An equivalent relationship holds for Medium and Medium++. The schematic can be extended to include Medium and Medium++ with another variable Var3, although the combined picture is harder to visualize in two dimensions.

There were two primary motivations to switch to the isEM++ menu. The first was to make the looser operating points more optimal. By relaxing the stringent cuts on the variables used in Loose and Medium, the signal inefficiency of these variables can be recovered. The corresponding operating points in the isEM++ menu could recuperate the background rejection by more efficiently using other variables. The other motivation for the isEM++ menu is the more natural regions of PID space selected by Loose++ and Medium++. The background electrons selected in these regions

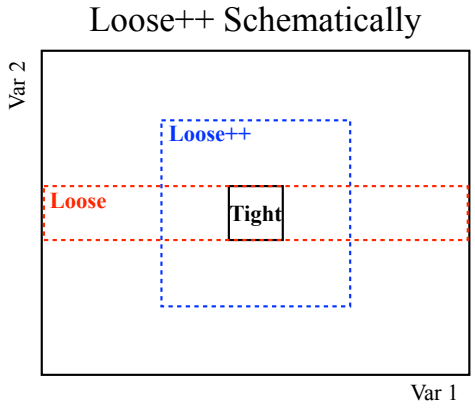

Figure 7.15: Conceptual difference in the isEM and isEM++ menu. The x and y-axis represent two different identification variables. Var2 is used in the isEM Loose definition, Var1 is not. The Tight definition uses both Var1 and Var2. Loose++ also selects on both Var1 and Var2, but looser than Tight.

correspond to less biased samples of background electrons than those selected by the isEM menu. Background near the signal region can be better selected by the isEM++ menu. This can be used for more efficiently determining background PDFs or for more robust estimates of background from misidentification using looser operating points.

The isEM++ menu was optimized using the same techniques as the isEM menu. Background PDFs were taken from data using the etcut triggers. High statistics signal PDFs were obtained from the MC using the data-driven corrections described above. The operating points were dictated by the trigger requirement. Medium++ was chosen such that the background rejection corresponded to a trigger rate of ∼20 Hz for 20 GeV electrons at 10^{33} cm^{-2} s^{-1}. This was achieved with a signal efficiency of around 85%. The Loose++ and Tight++ operating points were set with respect to Medium++. The cuts in Medium++ were relaxed to give ∼95% signal efficiency, to yield the Loose++ selection. Similarly, the Medium++ cuts were tightened to give a signal efficiency of ∼75%, to yield the Tight++ selection. A summary of the isEM++ operating points is given in Table 7.3.

A comparison of the performance of the isEM and isEM++ menus is given in Figure 7.16. The tight operating points are similar between the two menus. This is expected as both Tight and Tight++ were optimized using all identification variables. Medium++ gives a much higher background rejection than Medium, while keeping the signal efficiency around 85%. The efficiency of Loose++ is similar to Loose, but with a much larger background rejection.

The Medium++ operating point achieved the background rejection required to run a 22 GeV

Loose++
Shower shapes: R_η, $R_{\mathrm{had1}}(R_{\mathrm{had}})$, $w_{\eta 2}$, E_{ratio}, $w_{s,\mathrm{tot}}$
Track quality
$\lvert\Delta\eta\rvert < 0.015$

Medium++
Shower shapes: Same variables as Loose++, but at tighter values
Track quality
$\lvert\Delta\eta\rvert < 0.005$
$\mathrm{N_{BL}} \geq 1$ for $\lvert\eta\rvert < 2.01$
$\mathrm{N_{Pix}} > 1$ for $\lvert\eta\rvert > 2.01$
Loose TRT HT fraction cuts
$\lvert d0\rvert < 5$ mm

Tight++
Shower shapes: Same variables as Medium++, but at tighter values
Track quality
$\lvert\Delta\eta\rvert < 0.005$
$\mathrm{N_{BL}} \geq 1$ for all η
$\mathrm{N_{Pix}} > 1$ for $\lvert\eta\rvert > 2.01$
Tighter TRT HT fraction cuts
$\lvert d0\rvert < 1$ mm
E/p requirement
$\lvert\Delta\phi\rvert$ requirement
Conversion bit

Table 7.3: Summary of the variables used in the Loose++, Medium++ and Tight++ operating points in the isEM++ menu.

single Medium++ selection in the trigger throughout 2011, corresponding to luminosities of up to 3.5×10^{33} cm^{-2} s^{-1}. The isEM++ menu was the basis of electron identification for 2011 ATLAS analysis using the full 5fb^{-1}data set.

7.3.4 Coping with High Luminosity Running Conditions in the 2012 Data Taking.

The 2012 running brought another significant increase in the instantaneous luminosity. The LHC was expected to deliver data with an instantaneous luminosity of up to 7×10^{33} cm^{-2} s^{-1}. Associated to this increase was a jump in the average number of collisions per bunch crossing from up to 15 in 2011, to as high as 30 in 2012. These harsh running conditions posed further significant challenges for electron identification.

The first challenge was the single electron trigger rate. With an instantaneous luminosity of 7×10^{33} cm^{-2} s^{-1}, corresponding to a rate of $W \to e\nu$ events of about 70 Hz, there is a significant

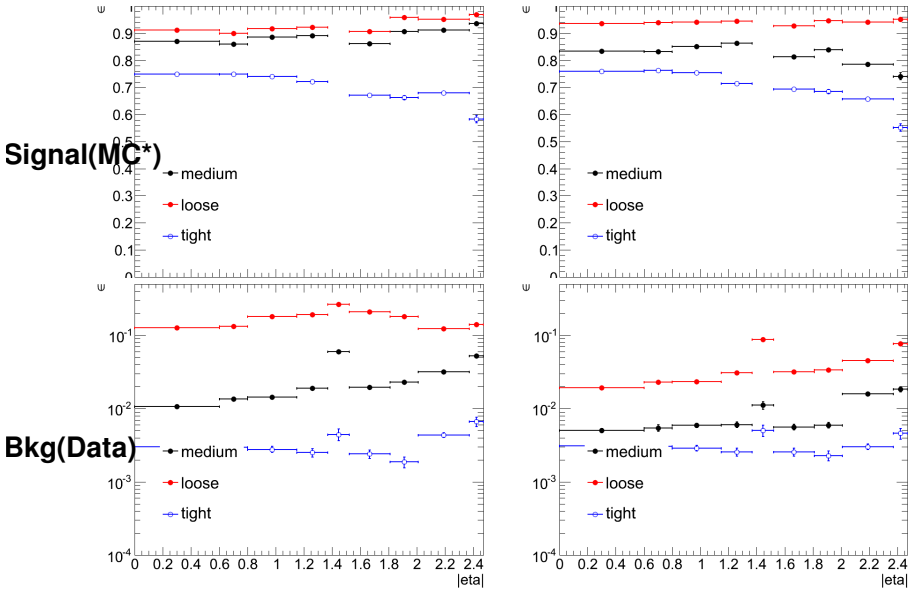

Figure 7.16: Comparison of the isEM and isEM++ menus. Signal efficiency and background rejection of the isEM menu is given on the left. The results for the isEM++ menu is given on the right. The upper two plots give the signal efficiency, as determined from the corrected MC. The lower plots show the background rejection with respect to reconstructed electrons. The results are shown for electrons candidates with $20 < E_{\mathrm{T}} < 30$ GeV.

amount of trigger rate from real electrons. This rate is irreducible in the sense that further increasing background rejection will not reduce the rate. The higher trigger rates in 2012 were partially addressed by increasing the overall ATLAS trigger output rate. The bandwidth allocated to the single electron trigger increased to 100 Hz, ∼25% of total bandwidth. Another measure taken to reduce the trigger rate was to increase the trigger threshold to 24 GeV. The final step was to add a track isolation requirement to the single electron trigger. The energy of tracks in a cone of 0.2 around the electron was required to be below 10% of the electron energy. This requirement is looser than most of the isolation criteria used in offline electron selection.

The other big challenge associated to the higher luminosity running is the increased level of pile-up. High pile-up events produce more energy in the detector. This higher energy tends to smear out the measured shower shapes in the calorimeter and can degrade the signal efficiency. A measure of the dependence of the signal efficiency on the amount of pile-up is shown in Figure 7.17. The signal efficiency of the various isEM++ operating points is shown as a function of the number of reconstructed vertices in the event. Pile-up events produce additional primary vertices so, ignoring vertex inefficiency, the number of reconstructed vertices scales with the amount of pile-up. The efficiencies of the 2011 isEM++ menu have significant pile-up dependence. Extrapolating the dependence for

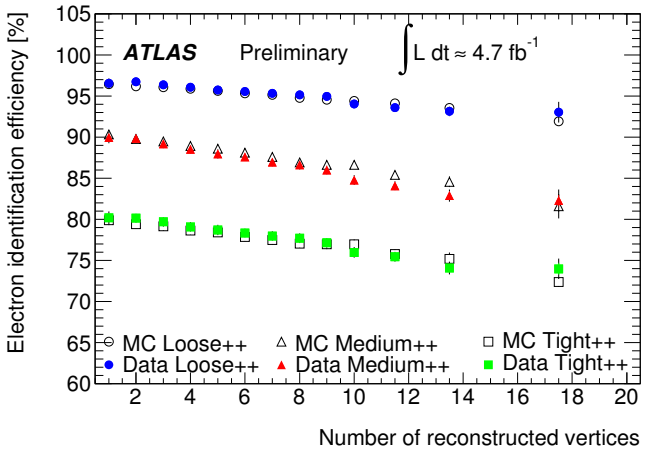

Figure 7.17: Efficiency of the isEM++ operating points as a function of the number of primary vertices. The efficiency was determined using the tag-and-probe technique in $Z \to ee$ events. Error bars include statistical and systematic uncertainties.

Medium++, this level of pile-up would lead to a decrease in signal efficiency of nearly ∼20%.

In order to cope with the expected levels of pile-up in 2012, the isEM++ menu was re-tuned to ameliorate the pile-up dependence. The pile-up dependence of the individual input variables was studied. The cuts on variables which suffered pile-up dependence were loosened, and the requirements on the pile-up independent variables were tightened to recoup background rejection. The variables with the most pile-up dependence were found to be R_{had} and R_{η}. The variable f_3, the fraction of energy in the third sampling, was found to have particularly low pile-up dependence. f_3 was added to the isEM++ menu to recover background rejection lost from the looser R_{had} and R_{η} requirements.

Figure 7.18 shows the results of the re-optimized isEM++ menu. The signal efficiency of the 2012 isEM++ menu has less pile-up dependence than seen with the 2011 menu. The re-optimized isEM++ menu maintains high signal efficiency in the presence of the large levels of pile-up seen in 2012. The re-tuned Medium++ operating point also preserved the background rejection required for a 24 GeV electron single electron trigger at 7×10^{33} cm^{-2} s^{-1}. The pile-up robust isEM++ menu is the basis of electron identification for 2012 ATLAS analyses.

7.3.5 The Future of Electron Identification

The cut-based approach to electron identification has reached a limit with the isEM++ menu. Any additional background rejection would come at the price of a significant loss of signal efficiency.

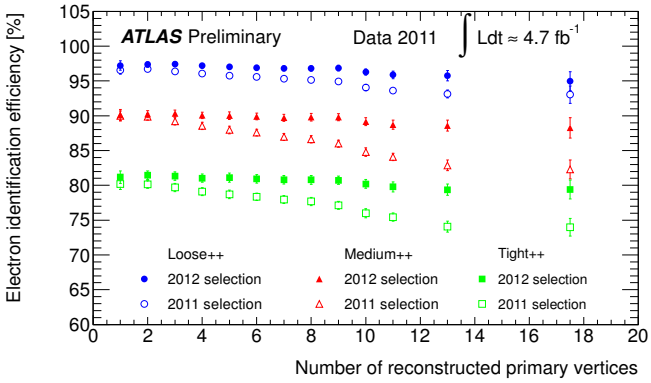

Figure 7.18: Efficiency of the 2011 and 2012 isEM++ operating points as a function of the number of primary vertices. The re-tuned 2012 isEM++ menu shows less pile-up dependence. The efficiency was determined using the tag-and-probe technique in $Z \to ee$ events. Error bars include statistical and systematic uncertainties.

Further improvements in electron identification can only be made by going beyond the cut-based approach.

The classification of signal and background electrons is a natural problem for a multi-variate analysis (MVA). There are many discriminating variables and several different classes of background. The electron identification variables provide a multi-dimensional space; which the different electron sources populate. Optimally selecting the region corresponding to signal electrons is a problem well suited for MVA classification algorithms. Furthermore, clean signal and background sources of electrons in data provide a straightforward means to train and validate an MVA electron selection.

Besides improving performance, an MVA electron identification has several advantages over a cut-based approach. By not applying a strict cut on the variables used, an MVA selection can include more discriminating variables. Variables for which signal and background electrons peak in the same place but have different shapes cannot efficiently be used in a cut-based selection. These variables provide discriminating power that can be extracted by an MVA selection.

Another advantage of an MVA selection is that, instead of providing a yes-no decision, it offers a continuous discriminating output value. This output discriminate provides increased flexibility in choosing an operating point. With the MVA, individual analyses can easily tailor the electron selection to their required level of background rejection. The MVA discriminate also provides a distribution that can be fit to determine the background level of a given selection.

At the time of writing, an electron selection using a likelihood method was being developed. The likelihood takes one dimensional signal and background PDFs as input and returns a likelihood discriminant. An example of the output discriminant for a preliminary version of the likelihood

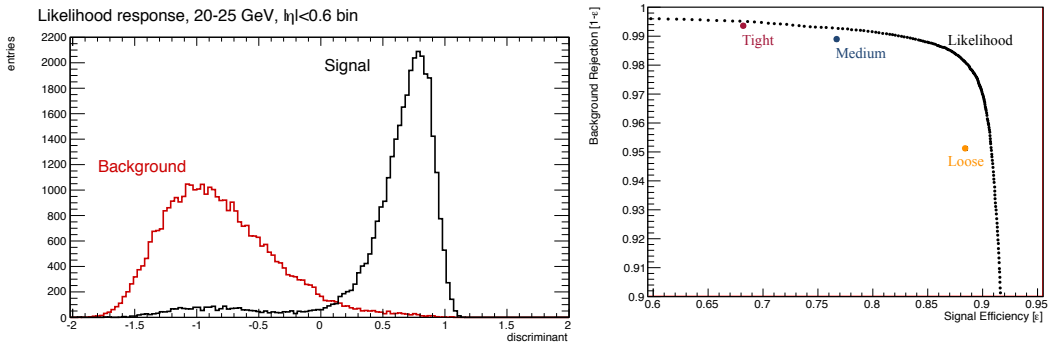

(a) (b)

Figure 7.19: Preliminary results from an implementation of a likelihood for electron selection. Left-hand plot shows the likelihood discriminate for signal and background electrons. Right-hand plot shows the performance of the likelihood with respect to the isEM++ operating points.

is shown in Figure 7.19a. The distributions for signal and background are shown separately. The discriminant can be cut on to reject background, or the signal and background shapes can be used to fit a sample of electrons to determine the purity.

An idea of the possible performance gains with an MVA electron identification can be seen in Figure 7.19b. The figure shows the background rejection as a function of signal efficiency when varying cut on the likelihood discriminate. This continuous set of operating point can be compared to the operating points of the isEM++ menu. The electron likelihood offers significant improvement, both in terms of background rejection and signal efficiency, over the cut-based menu.

The development of a multi-variate electron selection is an ongoing activity. There are several analyses that stand to gain considerably from improved electron identification, including the analyses presented in Chapters 10 and 11. The details of an MVA electron selection, and the documentation of the improvement over the isEM and isEM++ cut-based menus, will have wait for another thesis.

7.4 Conclusion

Electron reconstruction and identification is a critical component of the ATLAS physics program. Efficient signal selection, with large background rejection, is possible through the use of the many discriminating variables provided by the ATLAS detector. A standardized electron identification menu has been developed to harmonize electron selection across all ATLAS physics analyses. The operating points in this menu are used on-line in the trigger to select events.

Electron identification has faced several challenges in the first years of running. MC mis-

Season/Year	Inst. Lumi $[10^{33}s^{-1}cm^{-2}]$	E_{T} [GeV]	isEM	output rate [Hz]	Collisions per crossing
2010	0.1	15	"robust" Medium	20	1-4
spring 2011	0.5–1	20–22	Data-optimized Medium	20–40	1-10
fall 2011	1-3.5	22	Medium++	20–40	5-15
2012	6–7	24	Medium++ (w/Trk. Iso.)	100	15-30

Table 7.4: Table of changes in the single electron trigger.

modeling, high instantaneous luminosity running and large levels of pile-up have each provided unique obstacles. The electron identification has overcome these obstacles by evolving from the MC-optimized isEM menu, to a data-driven isEM menu, to ultimately the pile-up robust isEM++ menu.

The electron identification menu has maintained a highly efficient single electron trigger in the face of high instantaneous luminosity and large amounts of pile-up. A summary of the electron trigger evolution with time is given in Table 7.4. Throughout an order of magnitude change in the instantaneous luminosity and the number of collisions per crossing, ATLAS has maintained a single electron trigger below 25 GeV.

The electron reconstruction and identification presented in the section are critical to many ATLAS analyses including those presented in the remainder of this thesis.

Chapter 8

WW Physics

This chapter provides a general introduction to WW physics. The motivation for using the WW final state is outlined, and the basics of the signature and event selection are presented. The primary backgrounds to WW events are discussed, and the methods used to estimate them are introduced. This chapter is meant to serve as a basic introduction to the more detailed presentations of the WW cross section measurement of Chapter 10, and the search for $H \to WW^{(*)} \to l\nu l\nu$, documented in Chapter 11.

The remainder of this chapter is organized as follows: Section 8.1 introduces and motivates the study of WW production. Section 8.2 describes the WW signature and discusses the selection used to identify WW events. Section 8.3 presents the backgrounds to WW production and introduces the techniques used to estimate them. Section 8.4 describes how the continuum Standard Model WW production can be separated from $H \to WW^{(*)}$ events.

8.1 Introduction and Motivation

The primary motivation for studying the WW final state is to search for the Higgs boson. The Higgs boson (Higgs) can directly decay to pairs of oppositely charged W bosons. The most important $H \to WW$ production diagrams are shown in Figure 8.1. The gluon fusion (ggF) diagram, shown on the left-hand side, is the dominant $H \to WW$ production mode at the LHC. In ggF, initial state gluons are coupled to the Higgs through a top-quark loop, with the Higgs subsequently decaying to a pair of W bosons. The diagram on the right is referred to as vector-boson fusion (VBF). As described in Chapter 1, VBF has a production cross section that is roughly an order of magnitude smaller than ggF. In the VBF process, two initial state quarks radiate W or Z-bosons that fuse to form a Higgs. The Higgs then decays to a pair of W bosons. The VBF process results in a final state with two W bosons and two jets at large and opposite rapidities.

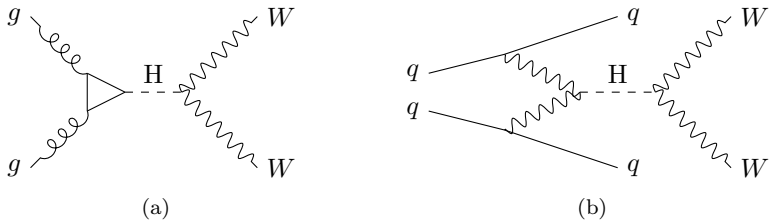

Figure 8.1: Leading-order Feynman diagrams for $H \to WW$ production. (a) The gluon-fusion diagram proceeds via top-quark loop. (b) The vector-boson fusion diagram results in a final state with WW+2 jets.

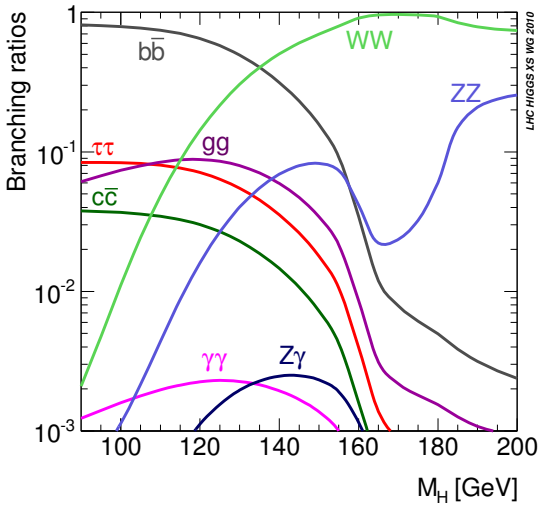

Figure 8.2: Higgs branching ratios as a function of Higgs mass.

The overall rate of $H \to WW$ production compared to other decay modes of the Higgs boson is dictated by the Higgs branching ratio to WW. The WW decay channel has the largest branching ratio (BR) over a wide range of Higgs mass. Figure 8.2 shows the Higgs BRs as a function of the Higgs mass (m_h) [34]. For m_h above $\sim$ 130 GeV, the BR to WW dominates. When the Higgs mass is below $2 \times m_W$, there is still a significant BR to WW. In this case, one of the Ws is produced off mass-shell, indicated in the following by W^*.

Wbosons have a relatively large branching fraction to $l\nu$, where $l = e$ or μ. When both W bosons decay leptonically, this provides a final state that can be exploited in the trigger and reconstructed with excellent signal to background. $H \to WW^{(*)} \to l\nu l\nu$ events contain two isolated, high p_{T} leptons in the final state. As discussed in Chapters 4 and 7, charged leptons can be efficiently identified, have low levels of background, and provide an effective signature for the trigger. Here,

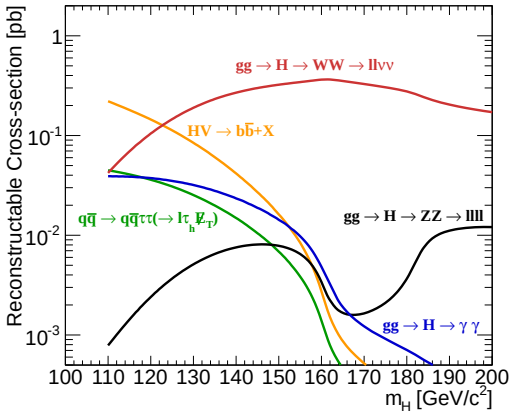

Figure 8.3: "Reconstructable" Higgs cross section as a function of Higgs m_h for $\sqrt{s} = 7$ TeV. The reconstructable Higgs cross sections include the BR to final states that can be reconstructed with high signal to background. The orange curve ($HV \to b\bar{b}+X$) is the sum of two production processes: the associated production of a Higgs boson with a W Boson and the associated production of a Higgs boson with a Z boson. The Higgs boson decays to $b\bar{b}$ and the W boson is required to decay to $e\nu$ or $\mu\nu$ and the Z boson is required to decay to e^+e^-, $\mu^+\mu^-$ or $\nu\bar{\nu}$.

and throughout this chapter, "leptons" refers only to electrons or muons.

Figure 8.3 shows the cross sections for "reconstructable" Higgs final states as a function of m_h, for $\sqrt{s} = 7$ TeV. A final state is considered reconstructable if it has a practical signature that can be used in the trigger and has a manageable signal-to-background ratio. The reconstructable cross sections include the appropriate Higgs production cross section, the BR of the Higgs, and any relevant BRs of the Higgs decay products that are required to make the channel efficiently observable. For example, the $gg \to H \to WW^{(*)} \to l\nu l\nu$ cross section is obtained from the ggF production cross section, times the Higgs BR to WW, times the BR for each W to decay to leptons. The figure shows the reconstructable cross sections for all of the important low-mass Higgs channels. The $H \to WW^{(*)} \to l\nu l\nu$ channel has a large reconstructable cross section over a wide and important range of values of m_h. This channel is particularly sensitive in the region of m_h favored by the electroweak fits, just above the LEP exclusion of 115 GeV. It has the strongest sensitivity, compared to the other Higgs searches, over broad range of m_h, from below 125 GeV to above 200 GeV. As a result, $H \to WW^{(*)} \to l\nu l\nu$ is one of the most important channels for the Higgs search at the LHC.

A complication with the Higgs search in the $H \to WW^{(*)} \to l\nu l\nu$ channel is the poor mass resolution resulting from the final state neutrinos. The individual momenta of the neutrinos cannot be fully reconstructed. Missing transverse energy, $E_{\mathrm{T}}^{\mathrm{miss}}$, is the only observable related to the neutrino momenta. $E_{\mathrm{T}}^{\mathrm{miss}}$ measures the transverse component of the sum of the neutrino momenta.

The individual transverse components and the longitudinal components of the neutrino momenta are undetected in the $H \to WW^{(*)} \to l\nu l\nu$ final state. This loss of information prevents the Higgs from being fully reconstructed and results in poor Higgs mass resolution.

Because of the poor resolution, there is no clear mass peak in the $H \to WW^{(*)} \to l\nu l\nu$ analysis. As a result, the $H \to WW^{(*)} \to l\nu l\nu$ search is primarily[14] a rate analysis, where an excess of observed events is searched for over a predicted amount of background. This type of analysis requires a high signal-to-background selection and an accurate modeling of the residual backgrounds; the signal to background cannot be improved with a narrow mass peak. Understanding other modes of WW production, and events that can mimic the $l\nu l\nu$ signature, is critical for the $H \to WW^{(*)} \to l\nu l\nu$ search.

The main background to the $H \to WW^{(*)}$ search is from the non-resonant, continuum Standard Model (SM) WW production. The leading order SM WW production diagrams are shown in Figure 8.4. At the LHC, WW production is dominated by $q\bar{q}$ annihilation. The leading order $q\bar{q}$ annihilation diagrams are the t-channel exchange, shown in the left-hand side of Figure 8.4, and the s-channel Z/γ exchange, shown in the center. The s-channel WW production is sensitive the WWZ and $WW\gamma$ triple gauge boson coupling (TGC) vertices indicated in the diagram. The next to leading-order prediction of the inclusive $q\bar{q}$ cross section is 44.4 ± 2.8 pb at $\sqrt{s}$= 7 TeV[101, 102]. Factoring in the $WW \to l\nu l\nu$ decay branching fraction, this corresponds to a reconstructable cross section of ∼3 pb [15], to be compared with ∼0.1 pb for $H \to WW^{(*)} \to l\nu l\nu$ at m_h= 125 GeV. The other non-resonant WW production mode is gluon-gluon fusion, shown on the right-hand side of Figure 8.4. Although gluon-gluon fusion is a next-to-next-to-leading order process, it is enhanced by the large gluon-gluon luminosities at the LHC. Gluon-gluon fusion contributes an additional 3% of the event rate to the total non-resonant WW production.

The $H \to WW^{(*)}$ search provides a clear motivation for studying SM WW production. It is necessary to understand the continuum WW production before searching for the Higgs in the WW final state. In addition, the backgrounds relevant to SM $WW \to l\nu l\nu$ production are shared by the $H \to WW^{(*)} \to l\nu l\nu$ search. Understanding the non-WW backgrounds in a $WW \to l\nu l\nu$ analysis is directly applicable to the $H \to WW^{(*)} \to l\nu l\nu$ analysis. By studying continuum WW production, many of the background estimation techniques can be tested in a place where the signal rate is known, before their application in a search for the unknown.

The continuum SM WW process is interesting in its own right. The WW process is one of the first observable di-boson final states at the LHC. In general, di-boson production provides an

[14] As will be discussed in the following, there is sensitivity to Higgs mass in the transverse mass, which is used to improve the sensitivity of the $H \to WW^{(*)} \to l\nu l\nu$ analysis.

[15] This includes the BR of W to τ with the τ decaying to an electron or muon

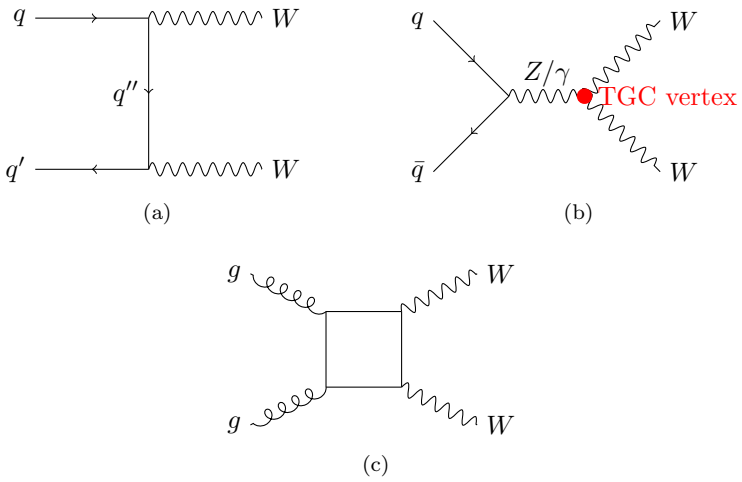

Figure 8.4: Feynman diagrams for the dominant production mechanisms for continuum WW production. (a) t-channel $q\bar{q}$ annihilation. (b) s-channel $q\bar{q}$ annihilation. (c) gluon-gluon fusion.

opportunity to test the predictions of the electro-weak sector of the SM at the TeV energy scale. The measurement of the SM WW production cross section is one such test. WW production is sensitive to TGCs and thus provides an important test of the gauge symmetry of the SM, which constrains the TGC vertices. Precise measurements of TGCs, through WW production, serve as a probe for possible new phenomena involving gauge bosons. SM WW measurements are thus a milestone of the ATLAS physics program.

The ultimate motivation of the work in this thesis is the Higgs; the goal is to discover or exclude the presence of the SM Higgs boson. This is the focus of the remainder of the thesis. LEP has excluded Higgs masses below 115 GeV. Fits to precision electro-weak data disfavor a Higgs mass above ∼200 GeV. Between these limits, $H \to WW^{(*)} \to l\nu l\nu$ is one of the most sensitive channels. With this analysis in mind, the continuum WW production has been studied. A measurement of the SM WW cross section, using the first 1 fb^{-1}of data, is the subject of Chapter 10. This measurement allowed for the development of analysis techniques that were carried over directly to the Higgs search. One such example, of particular importance to a low mass Higgs search, is the subject of Chapter 9. The WW cross section measurement provided the opportunity to produce a significant physics result with the first data, before having sensitivity to the Higgs. Chapter 11 turns to the search for $H \to WW^{(*)} \to l\nu l\nu$. An analysis using 4.7 fb^{-1}at $\sqrt{s}$= 7 TeV, and an analysis using 5.8 fb^{-1}at $\sqrt{s}$= 8 TeV, are both presented. Finally, Chapter 12 discusses the ATLAS Higgs search in broader terms and presents the results culminating in the paper [103] following the exciting discovery announced on the 4$^{\text{th}}$ of July, 2012.

8.2 Signature and Event Selection

This section describes the basic $WW \to l\nu l\nu$ signature and discusses the selection used to identify WW events.

For the SM WW cross section measurement and the $H \to WW^{(*)}$ search, WW events are reconstructed in the fully-leptonic final state. The fully-leptonic channel provides a signature that can be efficiently selected by the trigger and allows for a much higher signal to background than either the semi-leptonic or the fully hadronic channels, which are swamped by multi-jet background.

The basic WW signature is a pair of oppositely charged, high p_{T} leptons, with large missing transverse energy. However, events passing this basic selection are dominated by non-WW background. Further event-level requirements are applied to isolate WW events. These event-level requirements are dictated by the different sources of background. When requiring the Ws to decay to electrons or muons, there are three possible final states: ee, $e\mu$, and $\mu\mu$. The ee and $\mu\mu$ channels, collectively referred to as the "same-flavor" channels, have similar sources of background and are selected with similar event-level criteria. The background sources are different in the $e\mu$ channel, referred to as "opposite-flavor". For this reason, the WW event selection in the $e\mu$ channel differs from that used in the same-flavor channels.

The primary backgrounds to WW events are: Z/γ^* production, top-quark production, W+jet production, and other di-boson processes.

In the case of Z/γ^* production, a Z-boson or a virtual photon decays to a pair of opposite-sign, same-flavor leptons. These events can mimic the WW signature when there is $E_{\mathrm{T}}^{\mathrm{miss}}$ caused by a mis-measurement of the leptons or the other activity in the event. This type of $E_{\mathrm{T}}^{\mathrm{miss}}$ is referred to as "fake" in the sense that it is not caused by the presence of a final state neutrino; $E_{\mathrm{T}}^{\mathrm{miss}}$ from final state neutrinos is referred to as "real". The $Z/\gamma^* \to ll$ cross section is about a factor 1000 larger than $WW \to l\nu l\nu$ production. It is improbable that the $E_{\mathrm{T}}^{\mathrm{miss}}$ will be mis-measured at the level that it will produce a large enough $E_{\mathrm{T}}^{\mathrm{miss}}$ so that it will be background to the WW signature. However, the Z/γ^* background is primarily important in the same-flavor channels, but also contributes to the opposite-flavor channel through τ lepton decays. In this case, the Z/γ decays to a pair of τs, which in turn decay to an electron and a muon. These events have real $E_{\mathrm{T}}^{\mathrm{miss}}$ from the τ decays, but have a lower event rate from the additional BR for leptonic tau decays.

In top-quark production, two Ws are produced in association with b-quark jets. There are two primary sources of top-quark background: $t\bar{t}$ production, and Wt-channel single-top production. The leading-order Feynman diagrams for these processes are shown in Figure 8.5. In $t\bar{t}$ production, shown on the left, two b-quark jets, referred to as "b-jets", are produced in association with two Ws.

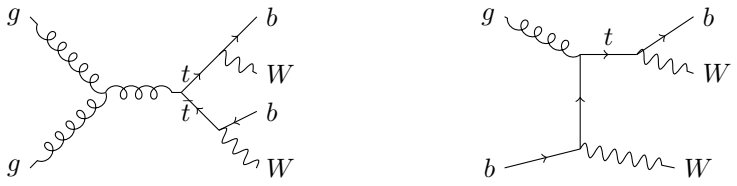

Figure 8.5: The dominant Feynman diagrams for (a) $t\bar{t}$ and (b) Wt production. $t\bar{t}$ production also includes a t-channel top quark exchange diagrams, which is not pictured. Wt production includes an s-channel b-quark exchange diagram which is not shown.

In the Wt process, shown on the right, the Ws are produced in association with one b-jet. These events can mimic the WW signature when the b-jet(s) are not identified, typically because they are either below the E_{T} threshold, or outside of the detector acceptance. These events can mimic the SM $WW \to l\nu l\nu$ or $H \to WW^{(*)} \to l\nu l\nu$ signature when the b-jet(s) are not identified, typically because they are either below the E_{T} threshold or outside of the detector acceptance. At $\sqrt{s}$= 7 TeV, the $t\bar{t}$ production cross section is about three and half times larger than SM WW production; Wt production is about a third of size of the SM WW production.

Events in which W bosons are produced in association with jets give rise to background to WW events when a jet is misidentified as a lepton. The jets are due to higher order diagrams, e.g., initial state radiation of a quark or gluon. These events contain a real lepton and real $E_{\mathrm{T}}^{\mathrm{miss}}$ from the W decay. The WW signature is mimicked if a jet is misidentified as a lepton. A reconstructed lepton is considered misidentified if it does not correspond to a prompt isolated lepton produced in an electroweak decay. These misidentified leptons are referred to as fake leptons; prompt leptons produced in isolation, *e.g.,* from the decays of W or Z bosons, are referred to as real leptons. QCD multi-jet events can also lead to WW background. Multi-jet background is generally much smaller than W+jet background, as it requires two fake leptons and fake $E_{\mathrm{T}}^{\mathrm{miss}}$ to mimic the WW signature. The W+jet and QCD multi-jet cross sections dwarf the SM WW production cross section. However the small lepton fake rates, provided by the lepton identification criteria, make this a manageable, yet challenging, background.

The final class of backgrounds are collectively referred to as "di-boson" background. This background arises from the SM production of the di-boson processes: $W\gamma$, $WZ/W\gamma^*$, and ZZ. Similar to W+jet background, $W\gamma$ events can give rise to WW background when the photon is misidentified as an electron. Photons are not misidentified as muons, so the $W\gamma$ background is only important in the ee and $e\mu$ channels. The production cross section for $W\gamma$ is much smaller than W+jet production, however the rate at which photons are misidentified as electrons is typically much higher than

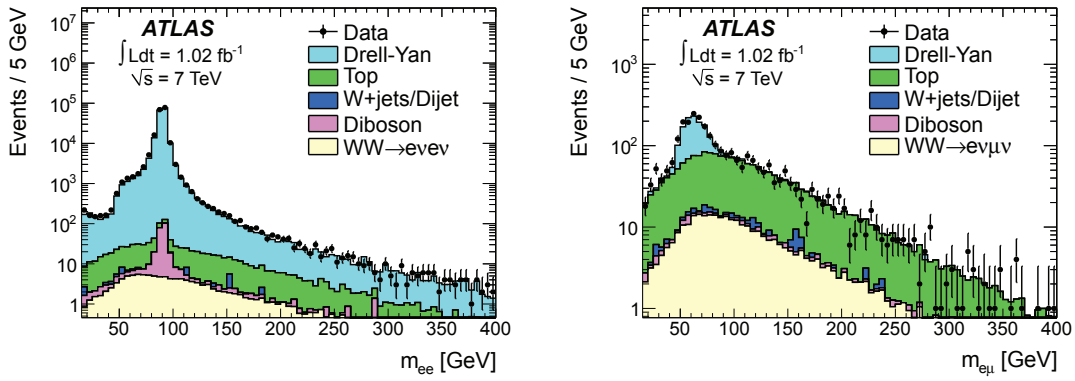

(a) (b)

Figure 8.6: m_{ll} distributions for same-flavor and opposite-flavor di-leptons before a missing energy requirement. Figure (a) shows the ee-channel, Figure (b) shows the $e\mu$-channel. The events are required to have one lepton with p_{T} above 25 GeV and one lepton with a p_{T} above 20 GeV.

for jets. The WZ and $W\gamma^*$ processes yield events with three real leptons and real $E_{\mathrm{T}}^{\mathrm{miss}}$. These events can mimic the WW signature when a lepton is not identified. Background from ZZ events arises when one of the Zs decays to leptons and the other Z decays to neutrinos. These events give two real leptons and real $E_{\mathrm{T}}^{\mathrm{miss}}$. This is an irreducible background in the same-flavor analysis.

The levels of the various WW background sources, after requiring two identified leptons, can be seen in Figure 8.6 [104]. Figure 8.6 shows the di-lepton invariant mass (m_{ll}) for events in the ee-channel, on the left, and in the opposite-flavor channel, on the right. The leptons are required to have transverse momentum (p_{T}) above 20 GeV and to pass tight identification criteria. For each di-lepton event, the lepton with highest p_{T}, referred to as the "leading lepton", is required to have p_{T} above 25 GeV.

After requiring two oppositely charged leptons, the selected events are dominated by Drell-Yan background. As discussed above, the Z/γ^* background is much larger in the same-flavor channels. In the same-flavor channel, the contribution from resonant Z decays peaks sharply at the Z mass. The next largest background is top. In the same-flavor channels, top is completely buried under the Z/γ^*. In the opposite-flavor channel, top is a significant fraction of the total background. At this point in the event selection, the contribution from the other sources of background, as well as from the WW signal, are a negligible fraction of the total events.

The first set of cuts in the WW event selection are designed to suppress the Z/γ^* background. Resonant Z production is removed in the same-flavor channels by rejecting events with m_{ll} consistent with the Z mass. In the $e\mu$-channel, the Z peak is broadened by the neutrinos in the τ decays,

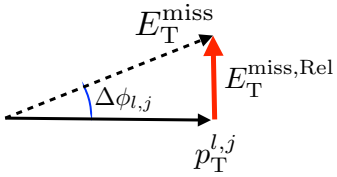

Figure 8.7: Schematic diagram of the $E_{\mathrm{T}}^{\mathrm{miss,Rel}}$ calculation. $E_{\mathrm{T}}^{\mathrm{miss,Rel}}$ uses the component of the $E_{\mathrm{T}}^{\mathrm{miss}}$ perpendicular to the nearest lepton or jet.

so no such requirement is made. After the Z veto, the selected events are still dominated by Z/γ^* background.

The Z/γ^* background is further suppressed by requiring large missing energy, consistent with the presence of a neutrino in the final state. The quantity used to impose the missing energy requirement is referred to as the "relative" missing energy, or $E_{\mathrm{T}}^{\mathrm{miss,Rel}}$. $E_{\mathrm{T}}^{\mathrm{miss,Rel}}$ is defined as

$$E_{\mathrm{T}}^{\mathrm{miss,Rel}} = \begin{cases} E_{\mathrm{T}}^{\mathrm{miss}} \times \sin(\Delta\phi_{l,j}) & \text{if } \Delta\phi_{l,j} < \pi/2 \\ E_{\mathrm{T}}^{\mathrm{miss}} & \text{otherwise,} \end{cases} \tag{8.1}$$

where $\Delta\phi_{l,j}$ is the difference in ϕ between the $\vec{E}_{\mathrm{T}}^{\ \mathrm{miss}}$ and the nearest lepton or jet. A schematic of the $E_{\mathrm{T}}^{\mathrm{miss,Rel}}$ calculation is shown in Figure 8.7. $E_{\mathrm{T}}^{\mathrm{miss,Rel}}$ de-weights missing energy that is in the direction of a reconstructed lepton or jet. When $\vec{E}_{\mathrm{T}}^{\ \mathrm{miss}}$ is close to a reconstructed object, only the component of $\vec{E}_{\mathrm{T}}^{\ \mathrm{miss}}$ perpendicular to the object is used. The motivation for using $E_{\mathrm{T}}^{\mathrm{miss,Rel}}$ is to suppress fake $E_{\mathrm{T}}^{\mathrm{miss}}$ from mis-measured leptons and jets and to remove $Z \to \tau\tau$ decays. Fake $E_{\mathrm{T}}^{\mathrm{miss}}$ can arise when the p_{T} of a lepton or jet is mis-measured. In this case, the resulting $\vec{E}_{\mathrm{T}}^{\ \mathrm{miss}}$ tends to either point along, or opposite to, the direction of the mis-measured object. The $E_{\mathrm{T}}^{\mathrm{miss,Rel}}$ variable is less sensitive to this type of fake $E_{\mathrm{T}}^{\mathrm{miss}}$. Similarly for $Z \to \tau\tau$, the lepton and neutrinos from the τ decay tend to be culminated and thus a significant component of $\vec{E}_{\mathrm{T}}^{\ \mathrm{miss}}$ is along the direction of the leptons. These events are suppressed by $E_{\mathrm{T}}^{\mathrm{miss,Rel}}$.

The $E_{\mathrm{T}}^{\mathrm{miss,Rel}}$ distribution for di-lepton events after the Z veto is shown in Figure 8.8. The Z/γ^* events populate low values of $E_{\mathrm{T}}^{\mathrm{miss,Rel}}$ in both the same-flavor and opposite-flavor channels. By requiring the events to have large $E_{\mathrm{T}}^{\mathrm{miss,Rel}}$, the dominant Z/γ^* component is removed. Typical $E_{\mathrm{T}}^{\mathrm{miss,Rel}}$ requirements are greater 45 GeV for the same-flavor channels and greater than 25 GeV for the opposite-flavor channel. These cut values are indicated in the figure. Because the Z/γ^* contribution is much larger in the same-flavor channels, the $E_{\mathrm{T}}^{\mathrm{miss,Rel}}$ requirement is stricter. As can be seen in figure, the $E_{\mathrm{T}}^{\mathrm{miss,Rel}}$ requirement results in a significant loss in WW acceptance, particularly in the same-flavor channels, but dramatically improves the signal to background.

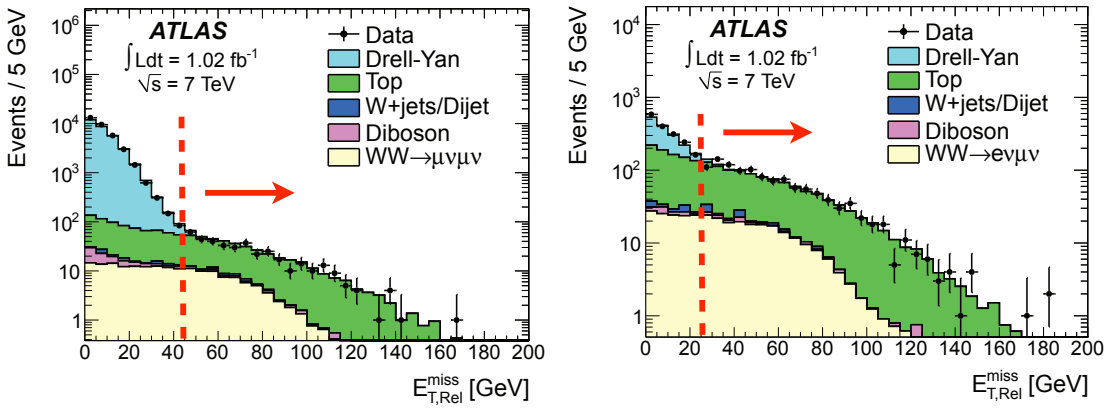

(a) (b)

Figure 8.8: $E_{\mathrm{T}}^{\mathrm{miss,Rel}}$ distributions for same-flavor and opposite-flavor di-leptons after the Z-mass veto. Figure (a) shows the same-flavor $\mu\mu$ channel. Figure (b) shows the $e\mu$-channel. Typical $E_{\mathrm{T}}^{\mathrm{miss,Rel}}$ requirements in the WW event selection are indicated in the figure.

After the requirement of large missing energy, the selected events are dominant by top-quark background. The majority of this is from $t\bar{t}$ production, with Wt contributing about 10%. Top events produce pairs of W bosons in association with b-jets. Thus, top background can be suppressed by removing events containing reconstructed jets. Figure 8.9 shows the distribution of the number of reconstructed jets after the $E_{\mathrm{T}}^{\mathrm{miss,Rel}}$ cut. Most of the top background has reconstructed jets in the final state. By vetoing events with reconstructed jets, the top background can be significantly reduced. This requirement, referred to as a "jet-veto", is effective in removing top and is fairly efficient for WW. As top is a major background for both same-flavor and opposite-flavor events, the jet-veto is applied to all channels. The top background surviving the jet-veto consists of roughly equal amounts of $t\bar{t}$ and Wt.

The events surviving the jet-veto define the basic WW event selection. This region is dominated by SM WW. Figure 8.10 shows the m_{ll} distribution for events passing the WW selection. At this point, there are roughly equal amounts of the different background sources. The large Z/γ^* and top backgrounds are suppressed by the WW event selection. The W+jet background is suppressed by the lepton identification criteria. It was a minor fraction of the background after the di-lepton selection, however, the W+jet background is not significantly reduced by the WW event selection. It has real $E_{\mathrm{T}}^{\mathrm{miss}}$ and tends to pass the jet-veto. The W+jet background is a significant contribution to both the opposite-flavor and same-flavor channels after the WW selection. The multi-jet background, on the other-hand, is small. This background is doubly suppressed by the lepton criteria and is further

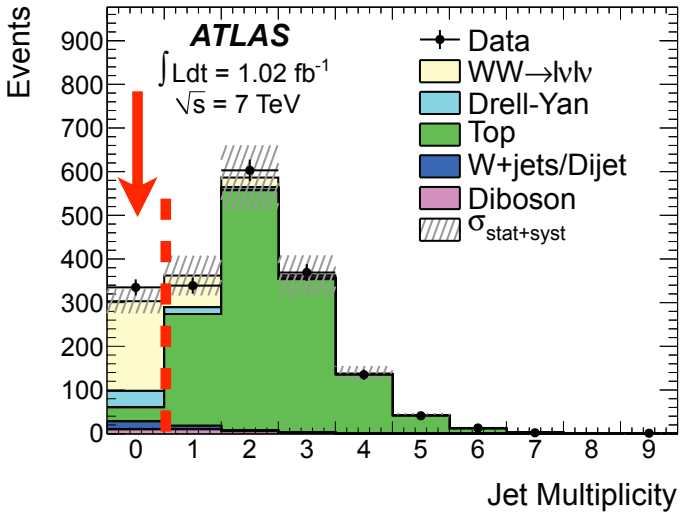

Figure 8.9: Distribution of the number of reconstructed jets after the $E_{\mathrm{T}}^{\mathrm{miss,Rel}}$ requirement. The plot combines the same-flavor and opposite-flavor channels. The jet veto of the WW signal selects events in the first bin, indicated by the arrow.

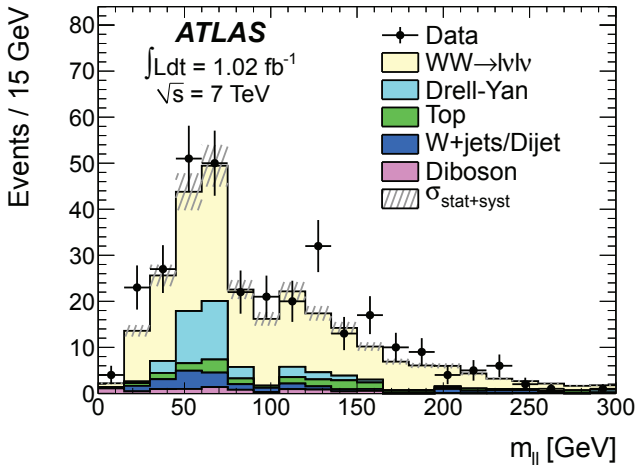

Figure 8.10: m_{ll} for events passing the WW signal selection. The same-flavor and opposite-flavor channels are combined.

reduced by the $E_{\mathrm{T}}^{\mathrm{miss,Rel}}$ requirement. After the WW selection, multi-jet background is roughly 1% of the W+jet background. Most of the di-boson contributions are suppressed by vetoing events with more than two leptons. The residual di-boson background in the WW event selection is small, but non-negligible.

This section has introduced the basic WW event selection. The actual implementation of this

selection varies slightly from analysis to analysis. These differences are small variations on the basic theme. Instead of using $E_{\mathrm{T}}^{\mathrm{miss}}$ as calculated from the energy in the calorimeter, the missing energy can be measured using the tracks in the ID. This quantity, referred to "track-met" or $p_{\mathrm{T}}^{\mathrm{miss}}$, can reduce the background with fake $E_{\mathrm{T}}^{\mathrm{miss}}$ coming from pile-up. In addition to $p_{\mathrm{T}}^{\mathrm{miss}}$, a cut on the transverse momentum of the di-lepton system, $p_{T_{ll}}$ can also be used to suppress events with fake $E_{\mathrm{T}}^{\mathrm{miss}}$ from pile-up. There are also variations on the top suppression. The E_{T} threshold of the of jet reconstruction can be lowered to become more efficient at jet finding. The $H \to WW^{(*)} \to l\nu l\nu$ analysis extends the signal acceptance by including events with one reconstructed jet. In this case, the large top background in the one jet bin can be reduced by vetoing jets identified as b-jets. The details of the implementation of the WW selection used in the WW cross section measurement and the $H \to WW^{(*)}$ analysis are presented in their respective chapters.

8.3 Background Estimation

Both the WW cross section measurement and the $H \to WW^{(*)}$ search require a precise determination of the amount of background passing the WW selection. The different sources of background fall into three general categories.

The first category includes Z/γ^* and top background. These backgrounds are initially large, but are easily suppressed with event-level criteria. In general, these backgrounds are well-modeled by the MC. Pure background control regions in data can be obtained by reversing the event-level criteria used to suppress them. These control regions can be used to validate or correct the MC background predictions.

The W+jet background falls into a different category. It is difficult to model in MC. An accurate modeling of the jet physics and of the small lepton fake rates, is not something the MC can be expected to do. It is thus critical that the W+jet background is measured directly with data. The W+jet background is small, but not readily reduced by the event selection. Because of this, it is not easy to define a W+jet control region using event-level criteria.

The final category is the di-boson background. These backgrounds are the easiest to cope with. They are small and efficiently suppressed by event selection. In general, the di-boson processes are well modeled by MC. An exception is $W\gamma$. $W\gamma$ is not suppressed by the event level-criteria and is sensitive to the rate at which photons fake electrons, which may not be accurately modeled in the simulation.

Determining the backgrounds is one of the most challenging aspects of a $WW \to l\nu l\nu$ analysis. The remainder of this section introduces the techniques used to estimate the various sources of back-

ground. The detailed background predictions, and the assessment of their systemic uncertainties, in the WW and $H \to WW^{(*)}$ analyses will be presented in their respective chapters.

8.3.1 Drell-Yan Background

Z/γ^* background arises from events which have fake $E_{\mathrm{T}}^{\mathrm{miss}}$. The $E_{\mathrm{T}}^{\mathrm{miss,Rel}}$ requirement suppresses cases when the fake $E_{\mathrm{T}}^{\mathrm{miss}}$ is from a mis-measurement of the leptons. However fake $E_{\mathrm{T}}^{\mathrm{miss}}$ can still arise from mis-measurement of the underlying event or from fluctuations in uncorrelated pile-up activity. The MC is expected to accurately model Z/γ^* events, however, these tails of the $E_{\mathrm{T}}^{\mathrm{miss}}$ distribution are not necessarily expected to be reproduced in the MC.

There are two primary techniques for estimating the Z/γ^* background [105, 106, 107, 108]. The first is referred to as the "Scale-Factor" method; the second is called the "ABCD" method.

The scale-factor method is simpler, but relies more heavily on the MC. In the scale-factor method, the MC Z/γ^* background estimate is used, with a correction factor to account for any MC mis-modeling of the $E_{\mathrm{T}}^{\mathrm{miss}}$ distribution. The correction factor, referred to as the scale-factor, is determined using same-flavor events that have m_{ll} consistent with the Z mass; these events are said to be "in the Z-peak". As a reminder, events in the Z-peak are dominated by resonant Z production and are excluded from the WW signal region. The scale-factor is determined by evaluating the data and MC agreement after applying the $E_{\mathrm{T}}^{\mathrm{miss,Rel}}$ cut used for the WW selection. All other analysis cuts are applied. The scale-factor is given by:

$$SF = \frac{N_{\mathrm{Data}} - N_{\mathrm{MC\ Non\text{-}}Z/\gamma^*}}{N_{\mathrm{MC}\ Z/\gamma^*}}, \tag{8.2}$$

where N_{Data} is the number of data events in the Z-peak passing the $E_{\mathrm{T}}^{\mathrm{miss,Rel}}$ cut, $N_{\mathrm{MC}\ Z/\gamma^*}$ is the MC prediction of Z/γ^* events in this region, and $N_{\mathrm{MC\ Non\text{-}}Z/\gamma^*}$ is the MC prediction of the non-Z/γ^* events in the region. The non-Z/γ^* events are mainly from di-boson processes. Figure 8.11a shows the $E_{\mathrm{T}}^{\mathrm{miss,Rel}}$ distribution for events in the Z-peak with all the other WW event selection applied. Any difference in absolute prediction above the $E_{\mathrm{T}}^{\mathrm{miss,Rel}}$ requirement in data and MC is assumed to be the result of a Z/γ^* mis-modeling. The measured scale-factor is used as a multiplicative correction to the MC prediction of Z/γ^* events in the WW region. The scale-factor method quantifies the MC modeling in a Z/γ^* control region and uses it to correct the Z/γ^* events in the signal region. The method assumes that all causes of discrepancies are the same inside and outside the Z mass window and that the other aspects of the Z/γ^* events are well modeled.

A similar technique is used in the ABCD method. However, instead of correcting the MC prediction in the WW region, the ABCD method uses an additional control region in data to estimate the Z/γ^* background. The ABCD method uses different regions of the m_{ll}-$E_{\mathrm{T}}^{\mathrm{miss,Rel}}$ plane,

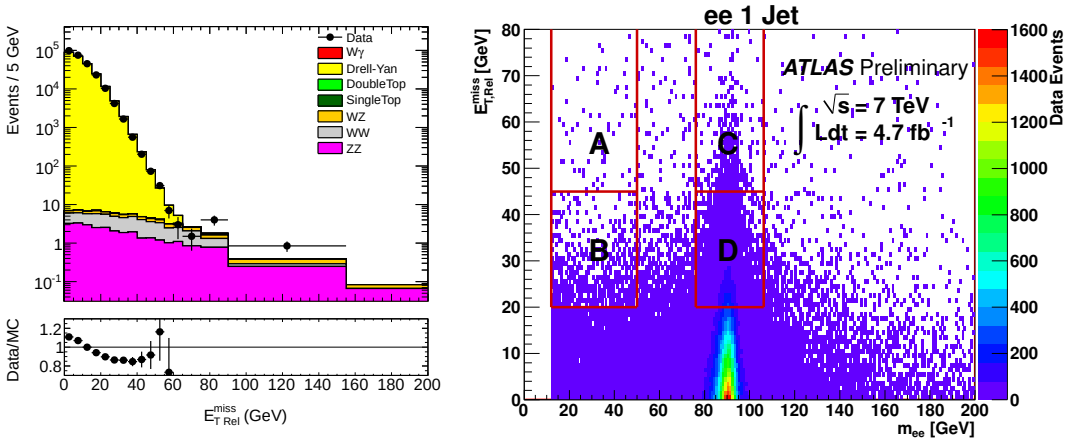

(a) (b)

Figure 8.11: Z/γ^* background estimation techniques. (a) $E_{\mathrm{T}}^{\mathrm{miss,Rel}}$ distribution in the Z-peak after applying the jet-veto in the $\mu\mu$-channel. The difference in absolute prediction above the $E_{\mathrm{T}}^{\mathrm{miss,Rel}}$ requirement is used in the scale-factor method. The 1.02 fb^{-1} data is shown. (b) m_{ll}-$E_{\mathrm{T}}^{\mathrm{miss,Rel}}$ plane used in the "ABCD" method. The distribution using 4.7 fb^{-1} of data is shown.

shown in Figure 8.11b. The regions labeled C and D in the figure are in the Z-peak. Events in region C pass the full $E_{\mathrm{T}}^{\mathrm{miss,Rel}}$ cut used in the WW event selection. Events in region D satisfy an intermediate $E_{\mathrm{T}}^{\mathrm{miss,Rel}}$ criteria; they pass a looser $E_{\mathrm{T}}^{\mathrm{miss,Rel}}$ requirement, but not the full $E_{\mathrm{T}}^{\mathrm{miss,Rel}}$ cut used in the WW event selection. The ratio of Z/γ^* events passing the full $E_{\mathrm{T}}^{\mathrm{miss,Rel}}$ cut to those in the intermediate $E_{\mathrm{T}}^{\mathrm{miss,Rel}}$ region is measured using the Z-peak as

$$R_{Z\text{-peak}} = \frac{C^{\mathrm{Data}} - C^{\mathrm{MC\ Non\text{-}}Z/\gamma^*}}{D^{\mathrm{Data}} - D^{\mathrm{MC\ Non\text{-}}Z/\gamma^*}}, \tag{8.3}$$

where $C^{\mathrm{Data}}(D^{\mathrm{Data}})$ is the data yield in region C(D), and $C^{\mathrm{MC\ Non\text{-}}Z/\gamma^*}(D^{\mathrm{MC\ Non\text{-}}Z/\gamma^*})$ is the MC estimate of the non-Z/γ^* background in region C(D). The Z-peak region is used because it is pure in Z/γ^*, so the non-Z/γ^* corrections are relatively small, and uncorrelated to the WW signal region. This ratio is assumed to characterize the Z/γ^* background outside of the Z-peak. The background in the WW region can then be determined by using the Z/γ^* events in the intermediate $E_{\mathrm{T}}^{\mathrm{miss,Rel}}$ region. For example, the Z/γ^* background in the region A, which is part of the WW signal region, would be calculated as

$$A_{\mathrm{Est.\ }Z/\gamma^*\mathrm{\ Bkg.}} = R_{Z\text{-peak}} \times \left(B^{\mathrm{Data}} - B^{\mathrm{MC\ Non\text{-}}Z/\gamma^*}\right), \tag{8.4}$$

where $A_{\mathrm{Est.\ }Z/\gamma^*\mathrm{\ Bkg.}}$ is the estimated Z/γ^* background in region A, and B^{Data} is the data yield in region B, and $B^{\mathrm{MC\ Non\text{-}}Z/\gamma^*}$ is the MC estimate of the non-Z/γ^* background in region B. The

ABCD method is a data-driven estimate of the Z/γ^* background that relies on the independence of m_{ll} and $E_{\mathrm{T}}^{\mathrm{miss,Rel}}$. This assumption is checked in the MC and appropriate systematics are assigned to account for the degree to which the assumption is valid.

The scale-factor and ABCD methods as presented above can be directly applied to the same-flavor channels. In the $e\mu$-channel, a technique similar to the scale-factor method is used. The data-MC agreement in a $Z \to \tau\tau$ control region is used to correct the MC Z/γ^* prediction in the signal region. The Z/γ^* background is less important the $e\mu$-channel and relatively large uncertainties can be tolerated.

8.3.2 Top Background

WW background from top-quark production arises when the jets associated to the final state b-quarks are not reconstructed. Top events are expected to be accurately modeled by the MC, however the precise rate at which jets are lost may not be accurately reproduced in the MC.

The method used to estimate the top background [106] is similar in spirit to the scale-factor method for the Z/γ^* background. The WW selection removes top background by requiring events to have no reconstructed jets. As shown in Figure 8.9, events with one or more reconstructed jets are dominated by top. Reversing the jet-veto gives a pure data sample of top events, referred to as the top control region[16]. As in the scale-factor method, the top background prediction is made using the estimated top background from MC, corrected by a scale-factor derived in the top control region. The top background is estimated as

$$N^{Est.}_{\text{Top 0-Jet}} = N^{\text{MC Top}}_{\text{0-Jet}} \times \left(\frac{N^{\text{Data}}_{\text{Top CR}} - N^{\text{MC non-Top}}_{\text{Top CR}}}{N^{\text{MC Top}}_{\text{Top CR}}} \right), \tag{8.5}$$

where $N^{Est.}_{\text{Top 0-Jet}}$ is the top background prediction, $N^{\text{MC Top}}_{\text{0-Jet}}$ is the top background from MC, $N^{\text{Data}}_{\text{Top CR}}$ is the data yield in the top control region, and $N^{\text{MC Top}}_{\text{Top CR}}$($N^{\text{MC non-Top}}_{\text{Top CR}}$) is the top (non-top) MC prediction in the top control region. Any difference in the top control region is assumed to be the result of a top mis-modeling. This method relies on the MC to correctly model the relative rate of $t\bar{t}$ and Wt production. An accurate modeling of the jet multiplicity in the top control region provides confidence in the MC prediction. The top background prediction as described here leads to a relatively large systematic uncertainty from the uncertainty on the jet energy scale. An additional scale factor, determined using events with a b-tagged jet, can be applied to reduce this uncertainty. The details of this correction are left to Chapters 10 and 11.

[16] For some reason, unbeknownst to the author, the full jet multiplicity, including the 0-jet bin, is used to define the top control region. In this section the method is described without the 0-jet bin in the top control region. This has the advantage that the MC correction is reduced, and the circularity coming from the overlap with the signal region is avoided. In the Chapters 10 and Chapters 11 the prediction including the 0-jet bin is presented.

In the WW analysis including the one jet bin, the top background is reduced by applying a b-jet veto. In this case, a 1-jet top control region can be defined by reversing the b-jet veto. These events are dominated by top production and have similar kinematics to the top background in the 1-jet WW region. This 1-jet top control region is used to constrain the top background in the 1-jet WW signal region analogously to the 0-jet case.

8.3.3 W+jet Background

Events in which W bosons are produced in association with jets can give background in the WW region when a jet is misidentified as a lepton. These events contain one real lepton, real $E_{\mathrm{T}}^{\mathrm{miss}}$, and one fake lepton. W+jet production and the rate at which jets are misidentified as leptons may not be accurately modeled in the MC.

The W+jet background is estimated using the "fake factor" method [105, 106, 107, 108]. The fake factor method is a data-driven procedure for modeling background from particle misidentification. The method provides a measurement of the yield and the kinematic distributions of background with fake leptons. The fundamental idea of the fake factor method is similar to that used in the Z/γ^* and top background. A control sample of W+jet events is selected, and an extrapolation factor is used to relate these events to the background in the signal region. The method is fully data-driven, as the control sample is selected in data, and the extrapolation factor is measured with data.

W+jet background arises from particle misidentification. The W+jet control region is thus defined using alternative lepton selection criteria, chosen such that the rate of misidentification is increased. The alternative lepton selection criteria is referred to as the "denominator" definition. An extrapolation factor relates the background misidentified with this criteria to background misidentified as passing the full lepton selection of the signal region. This extrapolation factor is referred to as the fake factor. The fake factor is measured and applied under the assumption that it is a local property of the leptons being misidentified and that it is independent of the event-level selection. The fact that the extrapolation is done in an abstract particle identification space can be conceptually challenging, but the underlying principle is straightforward.

The W+jet control region is selected by requiring one fully identified lepton and a reconstructed particle passing the denominator criteria. These events are treated as di-lepton events, where the denominator is considered a fully identified lepton. The full WW event selection is applied to the events in the W+jet control region. The background in the signal region is then calculated as

$$N_{\mathrm{W+Jet}}^{\mathrm{Est.}} = f \times \left(N_{W+\mathrm{jet\ CR}}^{\mathrm{Data}} - N_{W+\mathrm{jet\ CR}}^{\mathrm{MC\ non}\text{-}W+\mathrm{jet}} \right), \tag{8.6}$$

where $N_{\mathrm{W+Jet}}^{\mathrm{Est.}}$ is the estimated W+jet background, f is the fake factor, $N_{W+\mathrm{jet\ CR}}^{\mathrm{Data}}$ is the data yield

in the W+jet control region, and $N^{\text{MC non-}W\text{+jet}}_{W\text{+jet CR}}$ is the contribution of events in the W+jet control region that is not due to the W+jets process; this contribution is predicted by simulation.

The fake factor is calculated with multi-jet events as

$$f = \frac{N_{\text{Lepton}}}{N_{\text{Denominator}}}, \tag{8.7}$$

where N_{Lepton} is the number of identified leptons in the di-jet control region, and $N_{\text{Denominator}}$ is the number of identified denominators. The fake factor measures the ratio of the rate at which jets are misidentified as leptons to the rate at which they pass the denominator selection. It thus relates W+jet events in the control region to W+jet events in the WW signal region.

Separate denominator definitions are used for electrons and muons. In the ee-channel, the W+jet control region consists of a fully identified electron and an electron-type denominator. These events are weighted by the electron fake factor. The background in the $\mu\mu$-channel is calculated using the muon-type denominator and the muon fake factor. The $e\mu$-channel receives contributions from two terms: events with an identified electron and a muon-type denominator are scaled by the muon fake factor and are added to events with an identified muon and an electron-type denominator, which are scaled by the electron fake factor. These terms predict the contribution from fake muons and fake electrons separately.

Modeling background arising from misidentification is challenging. There are many subtleties associated with the fake factor method. Validating the background prediction and understanding the sources of systematic uncertainty can be complicated. As this is a difficult and critical background, particularly for the low mass $H \to WW^{(*)} \to l\nu l\nu$ search, the entirety of the following chapter is devoted to the fake factor method. Chapter 9 presents the method in detail, and discusses the various subtleties and sources of systematic uncertainty.

8.3.4 Di-boson Background

The di-boson background consists of the $W\gamma$, $W\gamma*$, WZ, and ZZ processes. $W\gamma$ background contributes to the WW signal region when the W decays leptonically and the photon is misidentified as an electron. Background from $W\gamma*$ and WZ arises when the bosons both decay leptonically and one of the leptons is lost. ZZ background can arise in the same-flavor channels when one Z decays leptonically and the other decays to neutrinos.

Di-boson production and the various lepton acceptances are expected to be accurately modeled by the MC. For this reason, the di-boson background passing the WW event selection is estimated from MC.

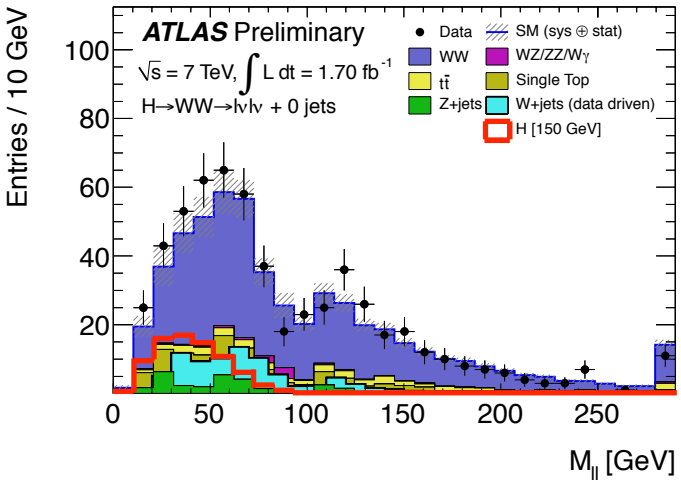

Figure 8.12: m_{ll} distribution after the WW selection. The distribution from the Higgs signal with a mass of 150 GeV is indicated in the figure.

One aspect of the MC modeling that may not be entirely accurate is the rate at which photons are misidentified as electrons in the $W\gamma$ background. The modeling of this background can be validated in a relatively pure sample in data. Events with an identified lepton and an electron failing the conversion rejection requirements, see Chapter 7 for details, are enriched in $W\gamma$ events. A MC mis-modeling, *e.g.,* from an inaccurate description of the detector material, could be spotted in this region. In the analyses reported in this thesis, the $W\gamma$ background is taken from the MC and cross checked in data. For future analyses, the fake factor method is being extended to include a data-driven estimate of the $W\gamma$ background. See Chapter 9 for more details.

8.4 Separating SM WW from $H \to WW^{(*)}$

The backgrounds discussed above are all backgrounds to the search for $H \to WW^{(*)} \to l\nu l\nu$. In the Higgs search, the WW event selection is applied to suppress these backgrounds, and the techniques described in the previous section are used to estimate their residual contribution. In addition to these non-WW backgrounds, the continuum SM WW production is a significant background in the Higgs search. SM WW production is the dominant background after the WW event selection. Figure 8.12 shows the m_{ll} distribution after the WW selection, including the expected distribution from the Higgs [109]. The $H \to WW^{(*)}$ signal is dwarfed by SM WW production. In order to have sensitivity to $H \to WW^{(*)} \to l\nu l\nu$, the SM $WW \to l\nu l\nu$ background must be suppressed.

The primary means of separating SM WW production from $H \to WW^{(*)}$ production comes from

the spin-zero nature of the Higgs boson. The Higgs boson is predicted to be a spin-zero particle. W bosons have spin one. In the $H \to WW^{(*)}$ decay, the spins of the Ws must be oppositely aligned to conserve angular momentum. The information of the oppositely-aligned W spins is preserved in the W decay products by the parity-violating weak interaction, which governs the W decays. This is illustrated in Figure 8.13. The figure shows the $H \to WW^{(*)} \to l\nu l\nu$ decay chain for two possible orientations of W spins. The solid red arrows indicate the direction of the decay products in the rest frame of the Higgs. The dashed black arrows indicate the direction of the spin component along the direction of the Higgs decay products. When the Ws decay to leptons, the matter-type particles, l^- and ν, emerge in the direction against the spin of the W, whereas the anti-matter-type particles, l^+ and $\bar{\nu}$, emerge in the direction along the W spin. As a result, the directions of the charged leptons are correlated, and the charged leptons emerge from the W decays in the same direction. The directions of the neutrinos are similarly correlated. This correlation produces a final state in which the angle between the leptons is smaller on average than for continuum SM WW production.

For Higgs masses below $2 \times m_W$, another kinematic difference between SM WW production and $H \to WW^{(*)}$ is the transverse momentum of the softer lepton. When the Higgs mass is below $2 \times m_W$, one of the Ws from the Higgs decay is off-shell. The leptons from these off-shell Ws tend to have a lower transverse momentum than the leptons produced from SM WW production, for which both leptons are on-shell. For the $H \to WW^{(*)}$ search, the lepton p_{T} requirement is lowered to 15 GeV to increase the acceptance for a low-mass Higgs.

The smaller lepton opening angles and softer lepton spectra in $H \to WW^{(*)} \to l\nu l\nu$ production are used to suppress the continuum background. The combination of these two effects leads to a smaller di-lepton invariant mass in $H \to WW^{(*)}$ decays. After the basic WW selection, events in the $H \to WW^{(*)}$ analysis are required to have a small m_{ll}. Figure 8.14a shows the low m_{ll} requirement used in the Higgs search. A significant fraction of the WW background is removed by the cut.

Selected events are also required to have small lepton opening angles. $\Delta\phi_{ll}$ is highly correlated to m_{ll}, but the additional requirement removes some additional WW background. Figure 8.14b shows the $\Delta\phi_{ll}$ distribution after the low m_{ll} requirement. The selection used in the $H \to WW^{(*)}$ analysis is indicated in the figure.

The final quantity used to distinguish SM WW and $H \to WW^{(*)}$ is an estimate of mass of the WW system. $H \to WW^{(*)}$ production proceeds via a resonance in m_{WW} at the value of the Higgs mass. Most of the mass information is lost by the final state neutrinos, for which the four-vectors cannot be reconstructed. However in the transverse plane, the combined neutrino momentum is

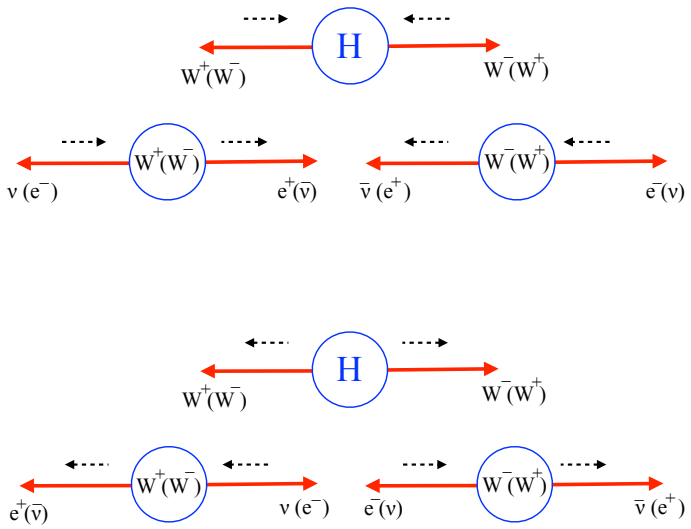

Figure 8.13: Schematic diagram illustrating the correlation in lepton direction resulting from the spin-zero nature of the Higgs and the parity violating weak decays of the Ws. Two Higgs decays, with different spin orientations of the Ws, are shown. The solid red arrows indicate the direction of the decay products in the rest frame of the Higgs. The dashed black arrows indicate the direction of the spin component along the direction of the Higgs decay products.

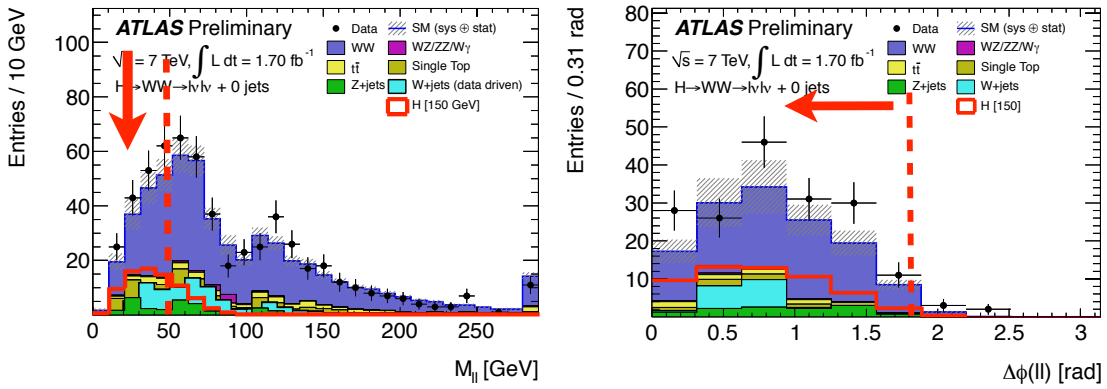

(a) (b)

Figure 8.14: Kinematic variables used to separate SM WW production from $H \to WW^{(*)}$ production. (a) m_{ll} distribution after the WW selection. The cut value used in the low-mass Higgs search is indicated in the figure. (b) $\Delta\phi_{ll}$ distribution after the low m_{ll} requirement. The cut value used in the low-mass Higgs search is indicated in the figure.

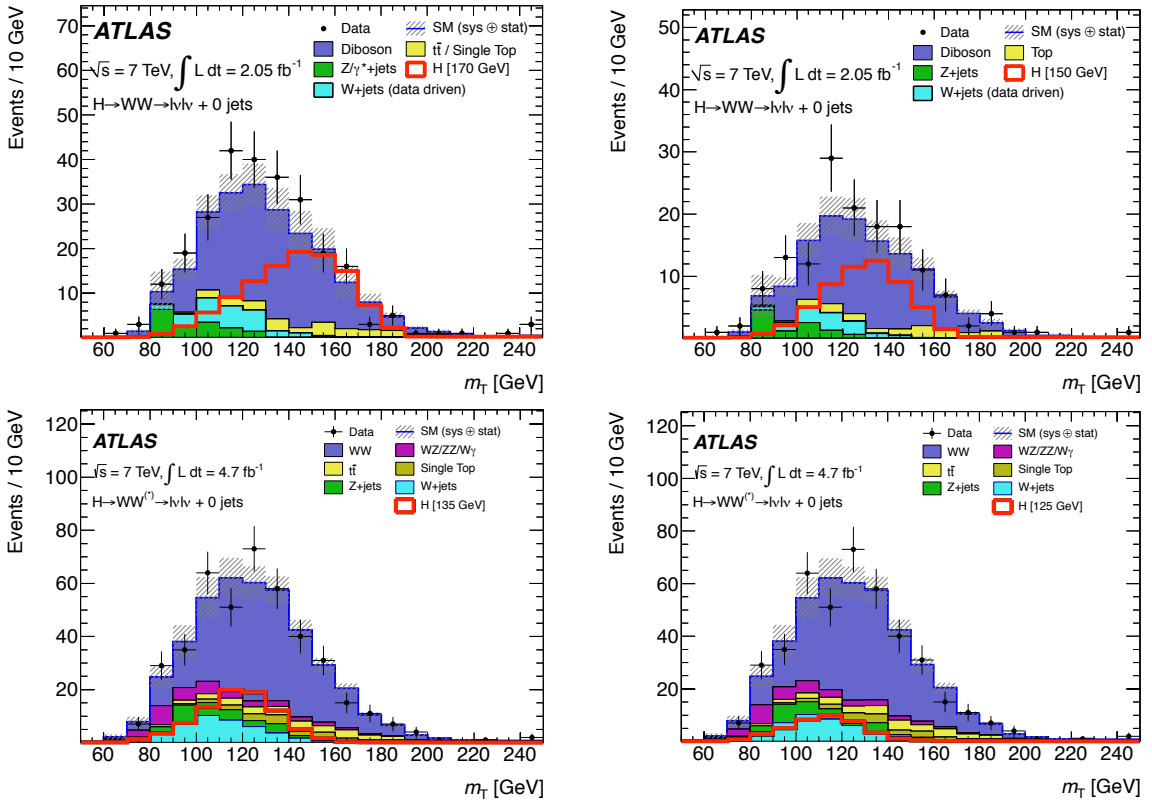

Figure 8.15: Transverse mass distribution after $H \to WW^{(*)}$ signal selection, for various values of Higgs mass. The result for a Higgs mass of 170 GeV is shown in the top left, 150 GeV in the top right, 135 GeV in the bottom left, and 125 GeV in the bottom right.

observable through $E_{\mathrm{T}}^{\mathrm{miss}}$. The transverse mass [110], defined as

$$m_{\mathrm{T}} = \sqrt{\left(E_{\mathrm{T}}^{ll} + E_{\mathrm{T}}^{\mathrm{miss}}\right)^2 - \left|\mathbf{p}_{\mathrm{T}}^{ll} + \mathbf{p}_{\mathrm{T}}^{\mathrm{miss}}\right|^2}, \tag{8.8}$$

where $E_{\mathrm{T}}^{ll} = \sqrt{|\mathbf{p}_{\mathrm{T}}^{ll}|^2 + m_{ll}^2}$, $|\mathbf{p}_{\mathrm{T}}^{\mathrm{miss}}| = E_{\mathrm{T}}^{\mathrm{miss}}$, and $|\mathbf{p}_{\mathrm{T}}^{ll}| = p_{T_{ll}}$, is a quantity that is sensitive to the mass of the WW system. Figure 8.15 [107, 108] shows the m_{T} distribution for the $H \to WW^{(*)}$ signal and the SM background, after the m_{ll} and $\Delta\phi_{ll}$ requirements. The distribution is shown for Higgs masses of 170 GeV (top left), 150 GeV (top right), 135 GeV (bottom left), and 125 GeV (bottom right). As the Higgs mass changes, the m_{T} distribution shifts, with a peak slightly below the corresponding value of m_H. The increase in signal to background with m_H is a result of the increase of the $H \to WW^{(*)}$ branching ratio with m_H.

The final step in the $H \to WW^{(*)} \to l\nu l\nu$ analysis is a fit to the m_{T} distribution. For m_H above around 135 GeV, there is considerable separation in the m_{T} shape of the $H \to WW^{(*)}$ signal and the various backgrounds. However, below m_H= 135 GeV, the signal distribution tends to peak in

the same place as the background. In particular, a Higgs with a mass of around of 125 GeV has an m_{T} distribution that peaks in the same place as the W+jet background. Understanding the W+jet background is thus of critical importance for the Higgs search in this region. The entire following chapter is devoted to the details of the fake factor method, which is used to model this W+jet background. The $H \to WW^{(*)} \to l\nu l\nu$ analysis can only have sensitivity to a 125 GeV Higgs if the background, particularly from W+jet, is understood.

This section has introduced the $H \to WW^{(*)} \to l\nu l\nu$ search in the 0-jet channel. The event selection described is used in the search for Higgs masses below ∼200 GeV. The $H \to WW^{(*)} \to l\nu l\nu$ analysis is also performed in the higher mass regime. The details of the high-mass Higgs selection will be presented in Chapter 11.

As mentioned above, the $H \to WW^{(*)} \to l\nu l\nu$ analysis is also carried out in the 1-jet channel. Almost all of the sensitivity to a low-mass Higgs comes from the 0-jet channel. The details of the event selection and background estimation in the 1-jet channel are given in Chapter 11.

In addition to the 0-jet and 1-jet analyses, there is also a dedicated search for $H \to WW^{(*)} \to l\nu l\nu$ via VBF production. With the current statistics, ∼10 fb^{-1}, we do not have sufficient statistics to isolate this production mechanism at low mass. For higher masses the VBF channel is important. The details of the VBF analysis are given in Chapter 11.

8.5 Conclusion

This chapter has introduced the WW final state and has described its event signature. The motivation for studying $WW \to l\nu l\nu$ is to search for the Higgs. The most important backgrounds for a Higgs with a mass of 125 GeV are the W+jet background and the continuum SM WW production. Chapter 9 presents the technique used to model the W+jet background, and Chapter 10 presents a measurement of the continuum SM WW production cross section. Chapter 11 presents the details and the results of the search for $H \to WW^{(*)} \to l\nu l\nu$. Chapter 12 discusses the role of the $H \to WW^{(*)} \to l\nu l\nu$ analysis in the discovery of the Higgs boson.

Chapter 9

The Fake Factor Method

Misidentification is an important source of background for physics analyses using particle-level identification criteria. In the case of the di-lepton analyses presented in this thesis, this background arises from W+jet events in which a jet is misidentified as a lepton. It is important to measure this type of background from data as the rate of misidentification may not be accurately modeled in the MC. The "fake factor" method is a data-driven procedure for modeling background from particle misidentification. This procedure is used both in the WW cross section measurement presented in Chapter 10 and in the $H \to WW^{(*)}$ search presented in Chapter 11. This chapter presents the fake factor method.

The remainder of this chapter is organized as follows: Section 9.1 introduces background from misidentification and the fake factor method. Section 9.2 describes the fake factor method. Section 9.3 describes the fake factor method as applied in a di-lepton analysis. Section 9.3.3 describes systematics associated with the method. Section 9.3.5 describes the validation of the fact factor predictions. Section 9.4 describes a procedure to extend the method to account for misidentified leptons from heavy-flavor decays.

9.1 Introduction

One of the primary motivations for using physics signatures with leptons in the final state is the large background rejection provided by the lepton identification of the ATLAS detector. The vast majority of QCD multi-jets can be suppressed by efficient lepton identification criteria. In ATLAS, the jet suppression is at the level of 10^{-5} [81, 96]; only jets in the tails of the detector response are misidentified as leptons. Despite the small lepton fake rates, a significant level of background from misidentification can be present due to the large production cross section of QCD jets at the LHC. Figure 9.1 compares the W+jet production cross section to those of standard model

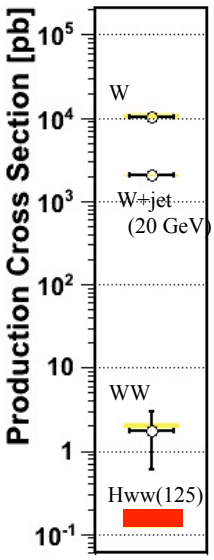

Figure 9.1: Production cross-sections in 7 TeV. The W+jet production cross section is contrasted against the WW and $H \to WW^{(*)}$cross sections.

$WW \to l\nu l\nu$ production and $H \to WW^{(*)} \to l\nu l\nu$ production. The sources of potential background from misidentification are produced at rates orders of magnitude higher than the signal processes. These large cross sections can lead to a significant amount of background from misidentification which needs to be properly estimated.

There are several different sources of lepton misidentification depending on lepton type. In the following misidentified leptons are referred to as "fake leptons", or "fakes". For electrons, fakes can arise from charged hadrons, photon conversions, or semi-leptonic heavy-flavor decays [96]. In the case of photon conversions and semi-leptonic heavy-flavor decays, an actual electron is present in the final state. These electrons are still considered fake in the sense that they are not produced in isolation as part of the prompt decay of a particle of interest. In the following, the term fake applies to both hadrons misidentified as leptons and to leptons from non-prompt sources. Prompt leptons produced in isolation, *e.g.,* from the decays of W or Z bosons, are referred to as "real" or "true" leptons. Figure 9.2 shows the contribution of the various sources of fake electrons passing a loose[17] electron identification criteria [97]. The contribution from true electrons is also shown as indicated by "$W/Z/\gamma* \to e$". The fake component is sharply peaked at lower p_{T}. At this level of selection, fake electrons are dominated by hadrons and conversions. With tighter identification criteria the contributions from all three sources are similar.

[17] In this figure a subset of the isEM medium cuts are used. The cuts on R_{had} and R_{η} are not applied.

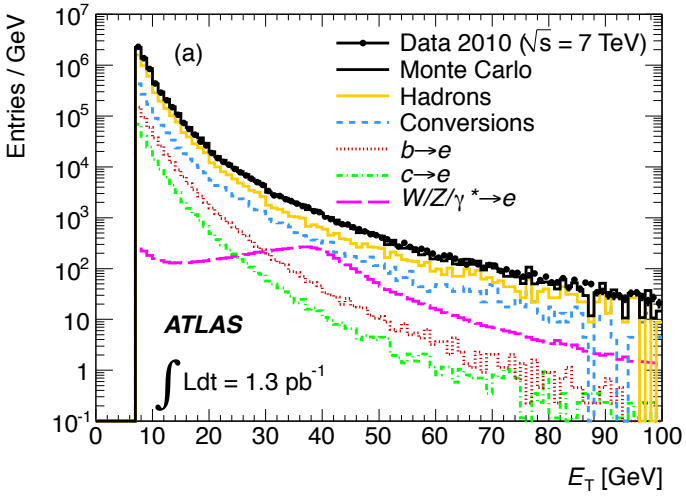

Figure 9.2: E_{T} distribution for reconstructed electrons passing a loose identification criteria. The data is shown along with the different sources of electrons. The electrons are required to pass a modified selection similar to medium but without the R_{had} and R_{η} requirements [97].

For muons the situation is simpler. Almost all fake muons come from either semi-leptonic heavy-flavor decays or meson decays in flight. As above, these muons are referred to as fake despite the fact that an actual muon is present in the final state. The relative contribution after a loose muon selection is shown in Figure 9.3 [111]. The fake component is sharply peaked at lower p_{T}. The fake muons are dominated by the heavy flavor contribution above 10 GeV. A tighter muon selection, requiring the muon to be well isolated and have a similar p_{T} measurement in the inner detector and muon spectrometer, suppresses the decay-in-flight fraction even further. Unlike electrons, most analyses requiring strict muon identification criteria only have misidentification from one source: semi-leptonic heavy-flavor decays.

Background from misidentification is not expected to be accurately modeled by the MC. An accurate prediction of the fake background would require correctly simulating the particles that are misidentified and a precise model of the rate of misidentification. Only a small fraction of jets fake leptons. Modeling this rate correctly would require an accurate modeling of the non-Gaussian tails of the detector response to jets. In addition, for electrons, several sources of misidentification would all need to be properly predicted. This level of detailed modeling is not expected from the MC. It is thus necessary to measure sources of background due to misidentification directly with data.

The fake factor method is a data-driven procedure for modeling background arising from misidentification [105, 106]. The method provides a measurement of the yield and the kinematic distributions of fake background. It is a general technique, applicable to any physics analysis in which particle-

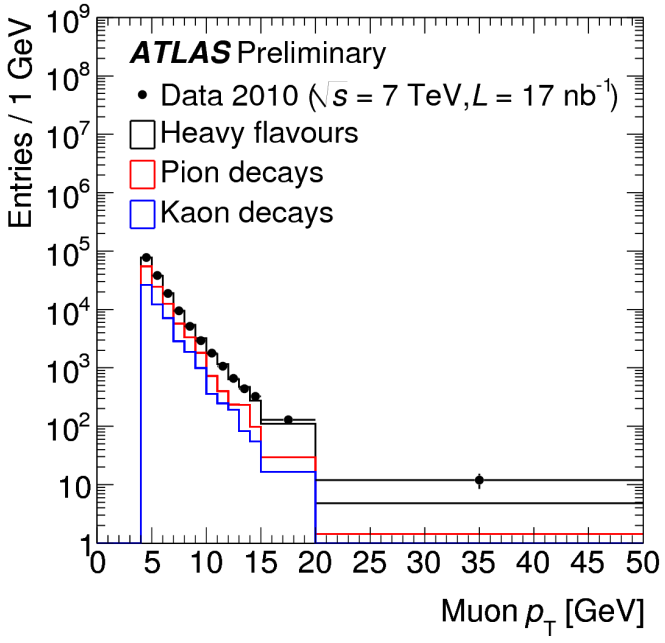

Figure 9.3: p_{T} distribution of reconstructed muons after a loose muon selection. The data is shown along with the different sources of "fake" muons.

level selection criteria are used to suppress background. The fake factor method can be used with any number of final state particles and is independent of the event selection. In the following, it is presented in the context of modeling the background to misidentified electrons and muons, referred to as "leptons", but the general discussion and techniques described are applicable to the background modeling of any particle with identification criteria: photons, hadronically-decaying taus, heavy-flavor jets, or more exotic objects such as lepton-jets.

The remainder of this chapter, presents the fake factor method in the context of a di-lepton + $E_{\mathrm{T}}^{\mathrm{miss}}$ analysis. This is motivated by the use of method in the $WW \to l\nu l\nu$ cross section measurement and the search for $H \to WW^{(*)} \to l\nu l\nu$ presented in Chapters 10 and 11. In the di-lepton + $E_{\mathrm{T}}^{\mathrm{miss}}$ analysis, referred to generically in the following as the "WW-analysis", the primary source of background from misidentification is W+jet. QCD multi-jet background is also present at a much smaller level. Events in which W bosons are produced in association with jets give rise to background to WW events when a jet is misidentified as a lepton. These events contain a real lepton and real missing energy from the W decay. With the jet misidentified as a lepton, the W+jet events have two identified leptons, missing energy, and no other significant event characteristics. As a result, the W+jet events cannot be readily suppressed by event selection. This background is particularly

important at low p_{T} and, as described in Chapter 8, is critical for the low mass Higgs search.

9.2 Fake Factor Method

The fundamental idea of the fake factor method is simple: select a control sample of events enriched in the background being estimated, and then use an extrapolation factor to relate these events to the background in the signal region. The method is data-driven provided the control sample is selected in data, and the extrapolation factor is measured with data. For background arising from particle misidentification, the extrapolation is done in particle identification space. The control sample is defined using alternative particle selection criteria that are chosen such that the rate of misidentification is increased. The extrapolation factor relates background misidentified with this criteria, to background misidentified as passing the full particle selection of the signal region. The extrapolation factor is referred to as the "fake factor". The fake factor is measured and applied under the assumption that it is a local property of the particles being misidentified and is independent of the event-level quantities. The fact that the extrapolation is done in an abstract particle identification space can be conceptually challenging, but the underlying procedure is straightforward.

The control region is defined in order to select the background being estimated. The type of background considered with the fake factor method arises from particle misidentification. To collect this type background more efficiently, the particle selection in the signal region is replaced with a particle selection for which the misidentification rate is higher. This alternative particle selection criteria is referred to as the "denominator selection" or the "denominator definition"; particles passing this criteria are referred to as "denominator objects" or simply "denominators". The control region is then defined to be the same as the signal region, except a denominator object is required in place of the full particle selection used in the signal region. For example, in the WW analysis, the control region is defined to select W+jet events in which the jet is misidentified as a lepton. A lepton denominator definition is chosen to enhance the misidentification rate from jets. The control region is then defined as events that contain one fully identified lepton, to select the real lepton from the W decay, and one denominator object, to select the fake lepton from the jet. These events are required to pass the full WW event selection, where the denominator is treated as if it were a fully identified lepton.

For analyses where there are multiple sources of fake background, multiple control regions are used. In the WW analysis, final states with both electrons and muons are considered: ee, $e\mu$, and $\mu\mu$. W+jet background can arise from misidentification of either an electron or a muon. To account for this, separate electron and muon denominator selections are defined and separate control regions

are used to predict the background from misidentification of the different lepton flavors.

Events in the control region are related to the background in the signal region by the fake factor. The fake factor relates background which is misidentified as denominators, to background which is misidentified as passing the full particle selection in the signal region. The full particle selection in the signal region is referred to as the "numerator selection"; particles passing this criteria are referred to as "numerator objects". The fake factor extrapolates from background misidentified as denominators, to background misidentified as numerators. It is important that the fake factor be measured in data. The fake factor measurement can be made in data using a pure sample of the objects being misidentified. For the case of the W+jet background, a pure sample of jets is needed. The fake factor can be measured in this sample by taking the ratio of the number of reconstructed numerators to the number of reconstructed denominators:

$$f = \frac{\mathrm{N}_{\mathrm{Numerator}}}{\mathrm{N}_{\mathrm{Denominator}}}. \tag{9.1}$$

Because the sample consists of background, the reconstructed numerators and denominators in the sample are due to misidentification. The ratio of the object yields measures the ratio of the misidentification rates. This is the quantity needed to relate the background in the control region to the background in the signal region. For the W+jet background in the WW analysis, the fake factor is defined separately for electrons and muons and measures the ratio of the rate at which jets pass the full lepton identification requirement to the rate at which they pass the denominator requirement. These fake factors are measured in data using a sample of di-jet events.

The sample used to measure the fake factor cannot be the same as the control region used to select the background being estimated. Events with numerators in the control region correspond to the events in the signal region. Attempting to measure the extrapolation factor into the signal region, from the signal region is circular. The amount of background in the signal region would need to be known in order to extract the fake factor, which is used to predict the amount of background in the signal region. The fake factor method requires two separate control regions in data: the control region used to select the background from which the extrapolation is made and a control region used to measure the fake factor. In the following, the first region is referred to as "the background control region", or in the case of the W+jet background, as "the W+jet control region". The region used to measure the fake factors is referred to as "the fake factor control region", or in the case of the W+jet background, as "the di-jet control region". The event selection used to define the background control region is dictated by the signal selection. There are no constraints on the event selection used to define the fake factor control region other than that it be dominated by background and distinct from the background control region.

After the control region is defined, and the fake factor measured, the background in the signal region is calculated by weighting the event yield in the control region by the fake factor:

$$\mathrm{N}_{\text{Background}} = f \times \mathrm{N}_{\text{Background Control}}. \tag{9.2}$$

The event yield in the control region measures the amount of background passing the event selection with a misidentified denominator instead of a misidentified numerator. This is related to the background passing the event selection with a misidentified numerator, i.e the background in the signal region, by the ratio of the misidentification rates, *i.e.,* the fake factor. This is expressed, colloquially, in equation form as

$$\begin{aligned} \mathrm{N}^{\text{Bkg.}}_{\text{X+N}} &= f \times \mathrm{N}^{\text{Bkg.}}_{\text{X+D}} \\ &= \left(\frac{\mathrm{N_N}}{\mathrm{N_D}}\right) \times \mathrm{N}^{\text{Bkg.}}_{\text{X+D}}, \end{aligned} \tag{9.3}$$

where N represents a numerator object, D a denominator object, and X stands for any object or event selection unrelated to the misidentification in question. In the background calculation, the rate of the background misidentification in the fake factor control region is assumed to be the same as the rate of background misidentification in the background control region. A systematic uncertainty is included to account for this assumption. This uncertainty is referred to as "sample dependence" and is often the dominant uncertainty on the background prediction. For the W+jet background, the fake factor is measured in di-jet events and is applied to events in the W+jet control region. The sample dependence uncertainty is the leading uncertainty in the W+jet background prediction.

The fake factor often has a dependence on the kinematics of the misidentified objects. This can be accounted for by measuring the fake factor separately in bins of the relevant kinematic variable and applying it based on the kinematics of the denominator in the background control sample. The total background yield is then calculated as

$$\mathrm{N}^{\text{Bkg.}}_{\text{X+N}} = \sum_i f^i \times \mathrm{N}^{i,\text{Bkg.}}_{\text{X+D}}, \tag{9.4}$$

where i labels the different kinematic bins. In the case of the W+jet background, the fake factor is measured in bins of lepton p_{T}. The W+jet background is then calculated as

$$\mathrm{N}^{W+\text{jet}}_{\text{Numerator+Numerator}} = \sum_i f^i \times \mathrm{N}^{i,W+\text{jet}}_{\text{Numerator+Denominator}}, \tag{9.5}$$

where i labels the p_{T} bin of the fake factor and the denominator object in the W+jet control region.

The fake factor method can model the event kinematics of the background due to misidentification. This is done by binning the background control region in the kinematic variable of interest.

The corresponding background distribution in the signal region is obtained by scaling with the fake factor, bin-by-bin:

$$\mathrm{N}_{\mathrm{X+N}}^{j,\mathrm{Bkg.}} = f \times \mathrm{N}_{\mathrm{X+D}}^{j,\mathrm{Bkg.}},$$

where j labels the bins of the kinematic distribution being modeled. A similar extension can be applied to Equation 9.4, in the case of a fake factor kinematic dependence:

$$\mathrm{N}_{\mathrm{X+N}}^{j,\mathrm{Bkg.}} = \sum_i f^i \times \mathrm{N}_{\mathrm{X+D}}^{i,j,\mathrm{Bkg.}}, \tag{9.6}$$

where i labels the kinematic dependence of the fake factor and the denominator object, and j labels the kinematic bins of the distribution being modeled.

In the discussion thus far the control regions have been assumed to consist purely of background. In practice, both the background control region and the fake factor control region will have contamination from sources other than the background of interest. To an extent, this can be mitigated by careful choice of denominator definition. For example, in the case of lepton misidentification from jets, the denominator definition can be chosen to explicitly exclude selection criteria that is efficient for true leptons. This reduces the contamination of true leptons in the denominator selection and thus the control regions. The residual sources of contamination have to be subtracted from the control regions. In many cases this subtraction can be done from MC, by running the control region selection on the contaminating samples. In some cases, the contamination in the control region arises from misidentification, in which case the fake factor method can be applied twice: once to predict the contamination in the control region, and once to predict the background in the signal region. Examples of these corrections for the WW analysis will be discussed in Section 9.3.

This concludes the introduction of the basic idea and methodology of the fake factor procedure. The following section motivates the fake factor method from another point of view. The rest of the chapter provides examples of the fake factor method in use. Subtleties that can arises in practice are discussed, systematic uncertainties associated with the method are described, and data-driven methods to validate the fake factor procedure are presented. Finally, an extension to the basic method that simultaneously accounts for several sources of background from misidentification is presented.

9.2.1 Motivation of Fake Factor Method

This section motivates the fake factor method in another way. The fake factor method is introduced as an extension of a simpler, more intuitive, background calculation. With this approach, the meaning of the fake factor and the major source of its systematic uncertainty are made explicit.

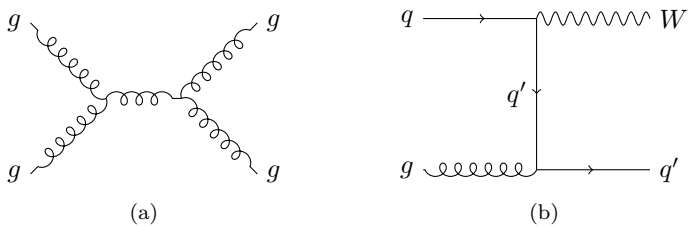

Figure 9.4: Leading order Feynman diagrams for (a) di-jet production and (b) W+jet production. The jets in the di-jet sample are gluon initiated, whereas jets in the W+jet sample are quark initiated.

The method is presented in the context of modeling misidentified leptons in W+jet events, but as mentioned above, the discussion is more generally applicable.

A simple, straightforward way to calculate the W+jet background is to scale the number of events with a reconstructed W and a reconstructed jet by the rate at which jets fake leptons:

$$N^{W+\text{jet}}_{(\text{Lepton+Lepton})} = F_{\text{Lepton}} \times N^{W+\text{jet}}_{(\text{Lepton+Jet})}, \tag{9.7}$$

where $N^{W+\text{jet}}_{(\text{Lepton+Lepton})}$ represents the W+jet background to di-lepton events passing a given event selection, F_{Lepton} is the jet fake rate, and $N^{W+\text{jet}}_{(\text{Lepton+Jet})}$ is the number of W+jet events with a lepton and a reconstructed jet passing the event selection. This method is simple: the number of reconstructed W+jet events is counted in data, and the rate at which jets are misidentified as leptons is used to predict the background in the signal region. The procedure would be fully data driven provided F_{Lepton} is determined from data.

The problem with this naive method is that the systematic uncertainty associated with the extrapolation from a reconstructed jet to a misidentified lepton is large. One source of systematic uncertainty comes from different jet types. There are a lot of different kinds of jets: quark jets, gluon jets, heavy-flavor jets, etc. Each of these different jet types will have a different fake rate. The fake rate, F_{Lepton}, is measured in a control sample with a particular mix of jet types and is only applicable for that specific mixture. For example, di-jet events are dominated by gluon jets. Figure 9.4a shows the leading order Feynman diagram for di-jet production at the LHC. If these events are used to measure F_{Lepton}, the fake rate will be mainly applicable to gluon jets. However, the jets in W+jet events tend to be quark-initiated jets. Figure 9.4b shows the leading order diagram for W+jet production. The gluon-jet fake rates may be substantially different from those of the quark jets they are used to model. Differences in composition between jets in the $N_{(\text{Lepton+Jet})}$ sample, and jets in the sample used to measure F_{Lepton}, is a large source of systematic uncertainty in Equation 9.7.

Differences between the reconstructed jet energy, and the reconstructed energy of the misidentified lepton, lead to another source of systematic uncertainty in the naive method. When extrapolating from reconstructed jets, there are two relevant energy scales: the energy of the jet and the energy of the misidentified lepton. A jet with a given energy can be misidentified as lepton with a different energy. For example, 100 GeV jets can be misidentified as 20 GeV electrons, or they can be misidentified as 100 GeV electrons. In general, the rate at which jets are misidentified as leptons depends on both the energy of the initial jet and the energy of the lepton it is misidentified as. The rate at which 100 GeV jets are misidentified as 20 GeV electrons will be different from the rate at which 100 GeV jets are reconstructed as 100 GeV electrons. This multidimensional kinematic dependence is not accounted for in Equation 9.7 and leads to a source of further systematic uncertainty.

A more precise calculation of the W+jet background can be made by extending the simple procedure to explicitly account for the effects mentioned above. An updated calculation of the background would be written as

$$N^{W+\text{jet}}_{(\text{Lepton+Lepton})} = \sum_{i,j,q'/g} F^{i,j}_{\text{Lepton}}(q'/g) \times N^{W+\text{jet } j}_{(\text{Lepton+Jet})}(q'/g), \tag{9.8}$$

where $N^{W+\text{jet}}_{(\text{Lepton+Lepton})}$ is the total W+jet background, $F^{i,j}_{\text{Lepton}}(q'/g)$ is the jet fake rate, and $N^{W+\text{jet } j}_{(\text{Lepton+Jet})}(q'/g)$ is the number of lepton plus jet events. The fake rate, $F^{i,j}_{\text{Lepton}}(q'/g)$, is binned according to the p_{T} of the reconstructed jet, denoted by the superscript j, and the p_{T} of the misidentified lepton, denoted by the superscript i. The fake rate is a function of the different types of jet: quark jet, gluon jet, etc, denoted by q'/g. The observed number of lepton plus jet events, $N^{W+\text{jet } j}_{(\text{Lepton+Jet})}(q'/g)$, is also binned in jet p_{T} and is a function of the reconstructed jet type. Calculating the total background requires summing over the different jet types, the p_{T} of the reconstructed jet, and the p_{T} of the misidentified lepton.

The updated W+jet prediction in Equation 9.8 is precise, but much more complicated. The fake rate is now a matrix. It maps reconstructed jets of p_{T} j into the misidentified leptons of p_{T} i. This matrix is awkward to work with in practice and is challenging to measure in data. The matrix elements F^{ij} can only be measured in events with a misidentified lepton, whereas, they are applied to jets in the control region without a corresponding misidentified lepton in the event. The correspondence between the p_{T} scale of jets misidentified as leptons and jets in the control region would have to be established and validated.

Another complication arises from the different jet types. Separate fake rate matrices are needed for each jet type. These are then applied based on the jet type seen in the control region. Associating jet types to reconstructed jets is not straightforward. Reconstructed jet observables that correlate to

jet type would have to be identified and validated. Uncertainties due to jet misclassification would need to be assigned. A procedure for measuring the separate fake rate matrices would also have to be established. Measuring the fake rate matrices and understanding the systematic uncertainties associated with the complications described above is not practical.

The fake factor method is designed to retain the precision of the updated W+jet calculation, while avoiding the complicated calculation in Equation 9.8. By defining an additional lepton criteria, referred to as the denominator selection, Equation 9.8 can be trivially rewritten as

$$N^{W+\text{jet}}_{(\text{Lepton+Lepton})} = \sum_{i,j,q'/g} \frac{F^{i,j}_{\text{Lepton}}(q'/g)}{F^{i,j}_{\text{Denominator}}(q'/g)} \times F^{i,j}_{\text{Denominator}}(q'/g) \times N^{W+\text{jet } j}_{(\text{Lepton+Jet})}(q'/g), \tag{9.9}$$

where $F^{i,j}_{\text{Denominator}}(q'/g)$ represents the rate at which jets are misidentified as denominators. As for leptons, the fake rate for denominators will depend on jet type and will be represented by a matrix: jets of a given p_{T} can be misidentified as denominators of a different p_{T}. Because the identification criteria for leptons and denominators are different, the corresponding jet fake rates will also be different. In general, the differences between lepton and denominator fake rates will be complicated. These differences will depend on the jet type, the jet p_{T}, and the misidentified lepton p_{T}.

The crux of the fake factor method is the assumption that the lepton and denominator fake rates are related by a single number[18] that is independent of all the other fake rate dependencies. The assumption is that the lepton fake rates can be expressed in terms of the denominator fake rates as

$$F^{i,j}_{\text{Lepton}}(q'/g) = f \times F^{i,j}_{\text{Denominator}}(q'/g), \tag{9.10}$$

where f is a constant number, referred to as the "fake factor". The assumption is that all the fake rate variation due to the underlying jet physics is the same for leptons and denominators, up to a numerical constant. This is an approximation. The degree to which the approximation is correct depends on the lepton and denominator definitions. In the fake factor method, a systematic uncertainty is needed to account for the extent to which this assumption is valid. This systematic uncertainty is the underlying cause of sample dependence.

With the fake factor assumption, the W+jet background in Equation 9.9, can be written as

$$\begin{aligned} N^{W+\text{jet}}_{(\text{Lepton+Lepton})} &= \sum_{i,j,q'/g} \frac{f \times F^{i,j}_{\text{Denominator}}(q'/g)}{F^{i,j}_{\text{Denominator}}(q'/g)} \times F^{i,j}_{\text{Denominator}}(q'/g) \times N^{W+\text{jet } j}_{(\text{Lepton+Jet})}(q'/g), \\ &= \sum_{i,j,q'/g} f \times F^{i,j}_{\text{Denominator}}(q'/g) \times N^{W+\text{jet } j}_{(\text{Lepton+Jet})}(q'/g). \end{aligned} \tag{9.11}$$

[18] In practice the dependence on lepton p_{T} is accounted for the fake factors, but this detail is ignored for now.

Because the fake factor is assumed to be independent of jet type and p_{T}, it can be factored out of the sum:

$$N^{W+\mathrm{jet}}_{(\mathrm{Lepton+Lepton})} = f \times \sum_{i,j,q'/g} F^{i,j}_{\mathrm{Denominator}}(q'/g) \times N^{W+\mathrm{jet}\ j}_{(\mathrm{Lepton+Jet})}(q'/g). \tag{9.12}$$

At first glance, the expression in Equation 9.12 is no simpler than the one started with in Equation 9.8. The denominator fake rate matrix has all the same complications as the lepton fake rate matrix. The dependence on jet type and all the associated complexity involved with observing it, is still present. However, the upshot of Equation 9.12 is that the sum on the right-hand side is observable in data. It is simply the number of reconstructed events with a lepton and a denominator. Equation 9.12 can be written as

$$N^{W+\mathrm{jet}}_{(\mathrm{Lepton+Lepton})} = f \times N^{W+\mathrm{jet}}_{(\mathrm{Lepton+Denominator})}. \tag{9.13}$$

where, $N_{(\mathrm{Lepton+Denominator})}$ is the number of observed lepton-denominator events. In a sense, by going through the denominator objects, the detector performs the complicated sums in Equations 9.8 and 9.12. In the fake factor method, the background extrapolation is made from reconstructed denominators instead of reconstructed jets. This provides a W+jet measurement with the precision of Equation 9.8, without having to perform the complicated calculation. This simplification comes at the cost of the added systematic uncertainty associated with the assumption in Equation 9.10.

In order for the fake factor method to be data-driven, the fake factor as defined in Equation 9.10, needs to be measured in data. This can be done by measuring the ratio of reconstructed leptons to denominators in a di-jet control sample. Assuming a pure di-jet sample, all the reconstructed leptons and denominators are due to misidentification. The ratio of leptons to denominators is then given by:

$$\frac{N_{\mathrm{Lepton}}}{N_{\mathrm{Denominator}}} = \frac{\sum\limits_{i,j,q'/g} F^{i,j}_{\mathrm{Lepton}}(q'/g) \times N^{j}_{\mathrm{Jet}}(q'/g)}{\sum\limits_{i,j,q'/g} F^{i,j}_{\mathrm{Denominator}}(q'/g) \times N^{j}_{\mathrm{jet}}(q'/g)} \tag{9.14}$$

where N_{Lepton} is the number of reconstructed leptons, $N_{\mathrm{Denominator}}$ is the number of reconstructed denominators, and $N^{j}_{\mathrm{jet}}(q'/g)$ is the number of jets of a given type and p_{T}. Using the fake factor definition, Equation 9.14 can be written as

$$\begin{aligned}
\frac{N_{\mathrm{Lepton}}}{N_{\mathrm{Denominator}}} &= \frac{\sum\limits_{i,j,q'/g} f \times F^{i,j}_{\mathrm{Denominator}}(q'/g) \times N^{j}_{\mathrm{Jet}}(q'/g)}{\sum\limits_{i,j,q'/g} F^{i,j}_{\mathrm{Denominator}}(q'/g) \times N^{j}_{\mathrm{jet}}(q'/g)} \\
&= \frac{f \times \sum\limits_{i,j,q'/g} F^{i,j}_{\mathrm{Denominator}}(q'/g) \times N^{j}_{\mathrm{Jet}}(q'/g)}{\sum\limits_{i,j,q'/g} F^{i,j}_{\mathrm{Denominator}}(q'/g) \times N^{j}_{\mathrm{jet}}(q'/g)} \\
&= f
\end{aligned} \tag{9.15}$$

The ratio of reconstructed leptons to reconstructed denominators in the di-jet control sample is a direct measurement of the fake factor. This provides a means for measuring the fake factor in data.

This section has provided an alternative motivation for the fake factor method. The fake factor method is similar to a naive extrapolation method, except the extrapolation is done from reconstructed objects that have a similar dependence on underlying jet physics as the particles being misidentified. By extrapolating from denominators reconstructed by the detector, a precise background prediction can be made without explicitly calculating the complicated effects of the underlying jet physics. Much of the challenge in the fake factor method is in defining a denominator definition for which the fake factor assumption holds and quantifying the degree to which it is valid. This is discussed throughout the remainder of this chapter.

9.3 Application of the Fake Factor Method to Di-Lepton Events

This section presents the fake factor method as applied to the WW analysis. The primary source of background from misidentification is from W+jet events, where one lepton is real, and one is from a misidentified jet. Background from QCD multi-jet events is also present at a smaller level. In the QCD multi-jet events, referred to in the following simply as "QCD", both leptons arise from misidentification. The fake factor method can be extended to model background resulting from multiple misidentified particles.

The background from QCD is a result of double fakes, and is given by:

$$N^{\mathrm{QCD}}_{\mathrm{Numerator+Numerator}} = f^2 \times N^{\mathrm{QCD}}_{\mathrm{Denominator+Denominator}}, \tag{9.16}$$

where $N^{\mathrm{QCD}}_{\mathrm{Denominator+Denominator}}$ is the number of events with two denominator objects, and f is the fake factor which is applied twice, for each denominator. However, QCD will also contribute to the W+jet control sample with a rate given by:

$$N^{\mathrm{QCD}}_{\mathrm{Numerator+Denominator}} = 2 \times f \times N^{\mathrm{QCD}}_{\mathrm{Denominator+Denominator}} \tag{9.17}$$

Here the fake factor is only applied once, as there is only one identified numerator in the W+jet control region. The factor of two is a combinatorial factor arising from the fact that either of the jets in a di-jet event can be misidentified as the numerator. Scaling the QCD contribution to the W+jet control region by the fake factor in the standard way gives:

$$\begin{aligned} f \times N^{\mathrm{QCD}}_{\mathrm{Lepton+Denominator}} &= 2 \times f^2 \times N^{\mathrm{QCD}}_{\mathrm{Denominator+Denominator}} \\ &= 2 \times N^{\mathrm{QCD}}_{\mathrm{Numerator+Numerator}}. \end{aligned} \tag{9.18}$$

The contribution from double fakes is double counted in the standard fake factor procedure. This double counting would have to be corrected when predicting misidentified background in a sample with a significant contribution from double fakes. The double fake contribution can be explicitly calculated from events containing two denominators by scaling by f^2. In this case, the background is calculated as

$$N^{\text{Total Background}}_{\text{Numerator+Numerator}} = f \times N^{W+\text{jet}}_{\text{Numerator+Denominator}} - f^2 \times N^{\text{QCD}}_{\text{Denominator+Denominator}}, \tag{9.19}$$

For the WW analysis, double fakes from QCD have been shown to contribute less than 5% of the total misidentified background. Given this small QCD contribution to the WW signal region, the W+jet prediction is not corrected for the QCD over-counting in the following. This leads to a slight, less than 5%, over prediction of the fake background. This difference is dwarfed by the systematic uncertainty associated to the background prediction.

The remainder of this section is organized as follows: Section 9.3.1 describes electron and muon denominator definitions. Section 9.3.2 discuses the di-jet control samples and the fake factor measurement. Section 9.3.3 presents the evaluation of the systematic uncertainties associated with the fake factors. Section 9.3.4 presents the background calculation in the signal region. Section 9.3.5 describes data-driven cross checks of the method.

9.3.1 Denominator Definitions

Implementation of the fake factor method begins with the denominator definition. This is often the most challenging aspect of the method. The denominator selection is chosen such that the contribution from real leptons is suppressed, and the contribution from misidentified jets is enhanced. This is achieved by relaxing or reversing identification criteria used to suppress misidentification. There is a trade off in terms of uncertainties when specifying these criteria. The tighter the denominator selection, or the closer the denominator definition is to that of the numerator, the smaller the systematic uncertainty associated with the extrapolation. As the denominator definition becomes more similar to the numerator definition, the fake factor approximation of Equation 9.10 becomes more accurate. A tighter denominator tends to reduce the systematic uncertainty on the predicted background. On the other hand, the tighter the denominator definition, the fewer number of jets are reconstructed as denominators. This decreases the size of the W+jet control region and increases the statistical uncertainty on the predicted background. Optimizing the overall background uncertainty requires balancing these competing effects.

The primary means to reduce electron misidentification is through the "isEM" requirements and isolation. As explained in Chapter 7, the electron isEM requirements represents a collection of selec-

Electron Numerator Definition
Electron Candidate
$\lvert z0\rvert < 10$mm, $d0/\sigma(d0) < 10$
$\frac{E_T^{Cone30}}{E_T} < 0.14$
$\frac{P_T^{Cone30}}{E_T} < 0.13$
Pass isEM Tight

Table 9.1: Example of an electron numerator definition. The numerator is required to pass tight isEM and be well isolated.

tion criteria based on the electromagnetic calorimeter shower shapes in a narrow cone, track quality, transition radiation, and track-cluster matching. Isolation, both track-based and calorimeter-based, are not a part of the isEM selection and provide an additional handle for suppressing misidentification. In the WW analysis, the electron numerator selection includes a requirement of tight isEM and requirements on both calorimeter-based and track-based isolation. An example of the numerator selection used in the $H \to WW^{(*)} \to l\nu l\nu$ analysis is given in Table 9.1. The numerator selection is dictated by the electron definition in the signal region. There is, however, freedom in choice of the denominator definition.

Electron denominators are chosen to be reconstructed electron candidates. This is a basic requirement that a reconstructed track has been associated to a cluster of energy in the calorimeter. Using electron candidates as the denominator objects unifies the numerator and denominator energy scales. The reconstructed energy of both the numerator and denominator is determined from the same reconstruction algorithm, using the same calibration scheme. The energy scale of the objects being extrapolated from is then the same as the energy scale of the objects being extrapolated to. This simplifies the kinematic dependencies of the fake factor.

The isEM and isolation requirements provide several choices of denominator definition. Examples of electron denominator definitions are given in Table 9.2. Each of these denominators reverses or loosens selection criteria with respect to the numerator definition in Table 9.1. The "PID"-denominator applies the same isolation requirement as the numerator selection, but requires the electron candidate to fail the medium isEM selection. Failing the medium isEM requirement makes the numerator and denominator definitions exclusive and suppresses the contribution from real electrons. Using exclusive numerator and denominator definitions simplifies the calculation of the statistical uncertainty on the background predictions. The "Isolation"-denominator does the opposite, applying the same isEM selection as the numerator, but reversing the isolation requirement. It is now the isolation requirement that makes the numerator and denominator definitions exclusive and suppresses the contribution from real electrons. The third definition, "PID-and-Iso"-denominator,

"PID"-Denominator	"Isolation"-Denominator	"PID-and-Iso"-Denominator
Electron Candidate	Electron Candidate	Electron Candidate
$\lvert z0\rvert < 10$mm, $d0/\sigma(d0) < 10$	–	$\lvert z0\rvert < 10$mm, $d0/\sigma(d0) < 10$
$\frac{E_T^{Cone30}}{E_T} < 0.14$	$0.14 < \frac{E_T^{Cone30}}{E_T} < 0.5$	$\frac{E_T^{Cone30}}{E_T} < 0.28$
$\frac{P_T^{Cone30}}{E_T} < 0.13$	–	$\frac{P_T^{Cone30}}{E_T} < 0.26$
Fails isEM Medium	Pass isEM Tight	Fails isEM Medium

Table 9.2: Examples of different electron denominator definitions. The denominator can be defined such that the extrapolation is done along isEM ("PID"), isolation, or both.

does a little of both. The electron candidate is required to fail the medium isEM selection, and the requirement on isolation is loosened. Relaxing the isolation results in a higher misidentification rate and a larger control sample. The relation of the different denominator definitions to that of the numerator is shown schematically in Figure 9.5. The y-axis represents isEM space, with larger values corresponding to tighter electron identification. The x-axis represents the isolation space; electrons with lower values are more isolated. The numerator selection is located in the region of tight electron identification and low values of isolation. Regions corresponding to the different denominator definitions in Table 9.2 are indicated in the figure. The "PID"-denominator extrapolates into the signal region along the isEM dimension, the "Isolation"-denominator extrapolates along the isolation dimension, and the "PID-and-Iso"-denominator extrapolates in both dimensions. The background prediction using the "Isolation"-denominator is statistically independent of that using the "PID" or "PID-and-Iso"-denominator. Predictions from the "PID" and "PID-and-Iso"-denominators are correlated but, as will be apparent in the following, are largely independent. The denominator definitions presented here will be returned to after a discussion of the di-jet control region used to measure the fake factors.

For muons there are less handles for choosing a denominator definition. Requirements on isolation and impact parameter are the primary ways that muon misidentification is reduced. In the WW analysis, the muon numerator selection includes requirements on both calorimeter-based and track-based isolation, as well on impact parameter. An example of the muon numerator selection used in the $H \to WW^{(*)} \to l\nu l\nu$ analysis is given in Table 9.3. Muon denominators are chosen to be reconstructed muons that have relaxed or reversed identification criteria. The requirement of a reconstructed muon unifies the numerator and denominator energy scales, but dramatically reduces the size of the control region. The misidentification rate for muon denominators is small because the jet rejection of a reconstructed muon, without any quality criteria, is already very small. As a result, both the isolation and impact parameter requirements are relaxed in the muon denominator definition in order to increase statistics. An example of a muon denominator definition is given in

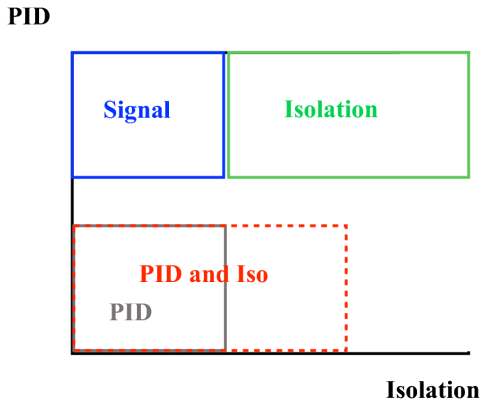

Figure 9.5: Schematic of the numerator selection in relation to the electron denominators given in Table 9.2. The denominator can be defined such that the extrapolation is done along isEM ("PID"), isolation, or both. The y-axis represents the isEM space, large values correspond to tighter electron identification. The x-axis represents the isolation space, lower values corresponds to more isolated.

Muon Numerator Definition
STACO Combined Muon
$\lvert\eta\rvert < 2.4$
Good ID Track
$\frac{E_T^{Cone30}}{E_T} < 0.14$
$\frac{P_T^{Cone30}}{E_T} < 0.13$
$d_0/\sigma_{d_0} < 3$
$\lvert z_0\rvert < 1$ mm

Table 9.3: Example of a muon numerator definition. The numerator is required to pass tight impact parameter cuts and be well isolated.

Table 9.4. Reconstructed muons passing the muon numerator selection are explicitly excluded from the denominator definition. This makes the numerator and denominator selections exclusive and reduces the contamination from real muons. The contamination of the denominator from real leptons tends to be a larger for muons because the definition is closer to the lepton selection. There are several ideas for increasing the size of the muon denominator definition. One is to use isolated tracks instead of reconstructed muons. Another is to use low p_{T} muon + track to model misidentification of higher p_{T} muons. These each pose unique challenges, but would allow the muon control regions to be dramatically increased. They are not investigated further here.

Muon Denominator Definition
STACO Combined Muon
$\lvert\eta\rvert < 2.4$
$\frac{E_T^{Cone30}}{P_T} < 0.3$
No Track-Based Isolation Requirement
No d_0 Impact Parameter Requirement
$\lvert z_0\rvert < 1$ mm
Fails the Muon Numerator Selection

Table 9.4: Example of a muon denominator definition. The denominator is required to satisfy looser impact parameter and calorimeter-based isolation criteria. The track-based isolation and the d_0 impact parameter criteria have been removed. Muons passing the numerator selection in Table 9.3 are explicitly vetoed.

9.3.2 Fake Factor Measurement

After the denominator selection has been defined, the fake factors can be measured. An unbiased sample of jets is needed to measure the electron and muon fake factors. The selection used to define the fake factor control sample cannot impose identification requirements on the jets which are stricter than denominator definitions. Finding jets at the LHC is easy, getting an unbiased sample is a challenge. Jets are most abundantly produced in multi-jet events. The ATLAS trigger rejects most of these events. The bandwidth dedicated to collecting samples of di-jet events is small and focused on collecting jets at high energies. Because the rate of lepton misidentification is so small, these di-jet samples are inefficient for selecting jets misidentified as leptons. The di-jet triggered samples provide few statistics with which to measure lepton fake factors.

ATLAS has dedicated supporting triggers that select unbiased samples of reconstructed electrons and muons. The reconstructed leptons are triggered without additional identification criteria. The requirement of a reconstructed lepton biases the jets selected by these triggers with respect to an inclusive jet sample, but the resulting jets are unbiased with respect to the numerator and denominator definitions, making them suitable for the fake factor measurement. Due to the lepton requirement, these samples avoid the inefficiency from the low rate of reconstructed leptons in the jet-triggered events. The samples collected by these supporting triggers are used to measure the fake factors.

An example of the fake factor measurement using the supporting triggers is shown in Figure 9.6. The electron fake factor corresponding to the numerator definition given in Table 9.1, and the "PID"-denominator definition given in Table 9.2, is shown as a function of electron E_{T}. Because many of the lepton identification criteria are E_{T} dependent, the fake factors are expected to depend on lepton E_{T}. This dependence is accounted for by measuring the fake factor separately in bins of

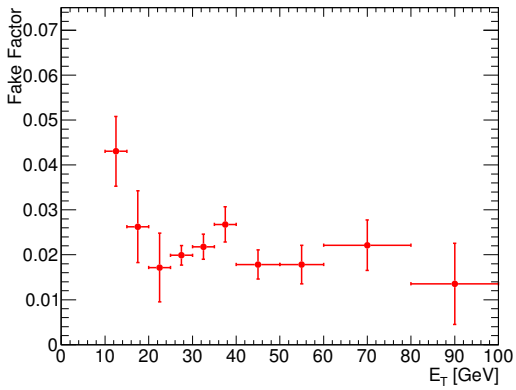

Figure 9.6: Example of the electron fake factor measurement using the electron supporting triggers. The error bars indicate the statistical uncertainty on the fake factor measurement. The "PID"-denominator definition is used the fake factor calculation.

E_T. Multiple supporting triggers are provided for different electron E_T ranges. The `EF_g11_etcut` trigger requires a reconstructed EM cluster with transverse energy above 11 GeV and makes no further requirement on the electron identification. The `EF_g20_etcut` trigger is the same, but with a E_T threshold of 20 GeV. These triggers will be collectively referred to as the "et-cut" triggers[19]. To avoid a possible bias from the trigger threshold, the fake factor for electrons below 25 GeV are calculated using the `EF_g11_etcut` triggered sample. The fake factors above 25 GeV are calculated using the sample triggered by `EF_g20_etcut`. The error bars in Figure 9.6 indicate the statistical uncertainty on the measured fake factors. Due to their large trigger rates, the et-cut triggers are heavily prescaled. This reduces the statistics available for the fake factor measurement and leads to relatively large statistical uncertainties.

The statistical uncertainty on the measured fake factors can be dramatically reduced by using a primary lepton trigger to collect the numerator sample used to measure the fake factor. The primary electron trigger, `EF_e20_medium`, requires a reconstructed electron with E_T above 20 GeV that satisfies the medium isEM requirements[20]. This trigger is run unprescaled at high rate. Electrons selected by the `EF_e20_medium` trigger are biased with respect to the isEM requirement, they pass medium isEM. This sample cannot be used for an electron selection with looser or reversed isEM requirements: *e.g.,* the "PID" or "PID-and-Iso"-denominators in Table 9.2. The primary trigger can however be used to collect electrons which have an isEM selection tighter than the trigger

[19] The E_T thresholds of the supporting triggers evolve with trigger menu. In the 2011 menu, 11 GeV and 20 GeV thresholds were used. In the 2012 menu, thresholds of 5 GeV, 11 GeV, and 24 GeV thresholds were available.

[20] The primary triggers also evolve with trigger menu. The trigger described here was used in the 2011 menu. In 2012, the primary electron trigger E_T threshold was raised to 24 GeV, and a loose track isolation requirement was added.

requirement. For example, the primary trigger is unbiased with respect to the electron numerator in Table 9.1. In this case, the fake factor can be calculated from a combination of the primary and supporting triggers. The primary trigger is used to collect the numerators, the et-cut trigger is used collect the denominators, and the fake factor is calculated correcting for the luminosity difference in the samples:

$$f = \frac{\mathrm{N}^{\text{Primary}}_{\text{Numerators}}/\mathcal{L}_{\text{Primary}}}{\mathrm{N}^{\text{et-cut}}_{\text{Denominators}}/\mathcal{L}_{\text{et-cut}}}, \tag{9.20}$$

where $\mathrm{N}^{\text{Primary}}_{\text{Numerators}}$ is the number of numerators in the primary electron sample, $\mathrm{N}^{\text{et-cut}}_{\text{Denominators}}$ is the number of denominators in the et-cut sample, and $\mathcal{L}_{\text{Primary}}(\mathcal{L}_{\text{et-cut}})$ is the luminosity collected with the primary (et-cut) trigger. The relative luminosity is known from the prescales set in the trigger menu. Because the primary trigger is run unprescaled, it will have more luminosity, and $\mathrm{N}^{\text{Primary}}_{\text{Numerators}}$ will be much larger than $\mathrm{N}^{\text{et-cut}}_{\text{Denominators}}$. When the fake factor is calculated using only the supporting trigger, the statistical uncertainty is limited by the number of numerators in the supporting trigger sample. When the fake factor is calculated as in Equation 9.20, the statistical uncertainty is now limited by the number of denominators in the supporting trigger sample. The statistical uncertainty is reduced by a factor of $\frac{1}{f} \approx 100$.

The fake factor measurement shown in Figure 9.6 is repeated in Figure 9.7, using the primary trigger to select the numerators. The blue points show the updated fake factor measurement. Above 25 GeV, the numerator sample is collected with the `EF_e20_medium` trigger, and the denominator sample is collected with the `EF_g20_etcut` trigger. There are no primary electron triggers below 20 GeV. Below 25 GeV, both the numerator and denominator samples are collected with the `EF_g11_etcut` trigger. The fake factors using only the et-cut trigger are shown for comparison in red. In the region with the primary electron trigger, above 25 GeV, the statistical uncertainty is dramatically reduced with the updated measurement. The trick of combining primary and supporting triggers is applicable to any type of object selection and is beneficial anytime there is a dedicated numerator trigger and the denominator sample is heavily prescaled. Throughout the following, this method is used when measuring the electron fake factors. For the muons, there is no need to reduced the statistical uncertainties as the supporting triggers have a much smaller prescales and adequate statistics.

The fake factor method assumes the denominator definition has been chosen such that the fake factor is independent of the p_{T} of the misidentified jet. To test the validity of this assumption, the fake factor is measured separately in several di-jet samples with different jet p_{T} spectra. The p_{T} of the jet being misidentified, referred to as "the near-side jet", is varied by selection on the p_{T} of the jet on the opposite side of the event, referred to as "the away-side jet". The assumption is that the p_{T} of the near-side jet is correlated to the p_{T} of the away-side jet. The measured p_{T} of the near-side

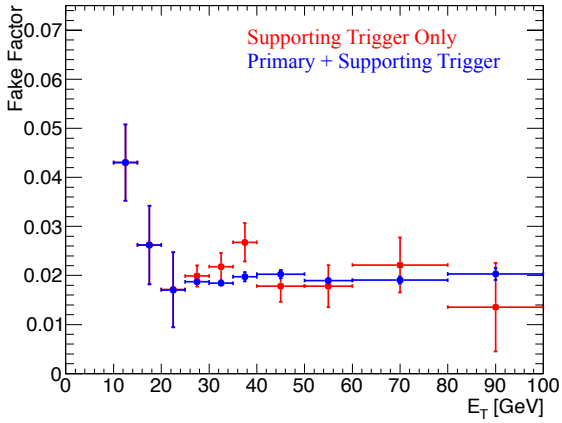

Figure 9.7: Comparison of electron fake factor using only the supporting triggered sample, in red, and using a combination of primary electron and supporting triggers, in blue. Using the combination of triggers reduces the statistical uncertainty on the fake factor. The "PID"-denominator definition is used the fake factor calculation.

jet cannot be used because it is biased by the requirement of an associated reconstructed lepton. The tiny fraction of jets that are reconstructed as lepton candidates may have a very different energy response than a typical jet. To avoid this bias, the p_{T} of the unbiased away-side jet is used as a proxy for the p_{T} of the near-side jet. Multiple fake factor control samples are created with different away-side jet p_{T} requirements. The fake factor is measured separately in each sample. The average across the samples is taken as the fake factor central value, and the spread among samples provides an indication of the systematic uncertainty associated with the dependence on jet p_{T}.

An example of the fake factor calculation using different away-side jet p_{T} bins is shown in Figure 9.8. The fake factor control region is divided into five sub-samples based on the p_{T} of the away-side jet. The measured fake factor in events with away-side jet greater than 20 GeV is shown in black, greater than 30 GeV in blue, and so on up to jets greater than 90 GeV in gray. The yellow band gives the average of the five measurements and shows a width of $\pm 30\%$ for scale. In the following, this away-side jet variation is used as a fast-and-loose estimate of the size of the systematic associated to the fake factor definition. It provides a lower limit on the extent to which the approximation in Equation 9.10 holds. Section 9.3.3 presents the more rigorous evaluation of the fake factor systematics used for the final background prediction.

The presence of real leptons from W or Z-bosons in the di-jet samples will bias the fake factor measurement. To suppress this contamination, events used in the fake factor calculation are vetoed if they have a transverse mass consistent with a W, or if they contain two reconstructed leptons with an invariant mass consistent with the Z. The residual W and Z contribution is subtracted from

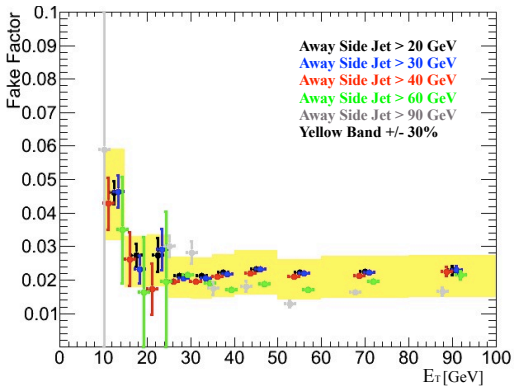

Figure 9.8: Example of the electron fake factor measurement using different away-side jet p_{T} bins. The fake factor measurements in the different away-side jet bins are shown in different colors. The yellow band shows the average ±30%. The "PID"-denominator definition is used the fake factor calculation.

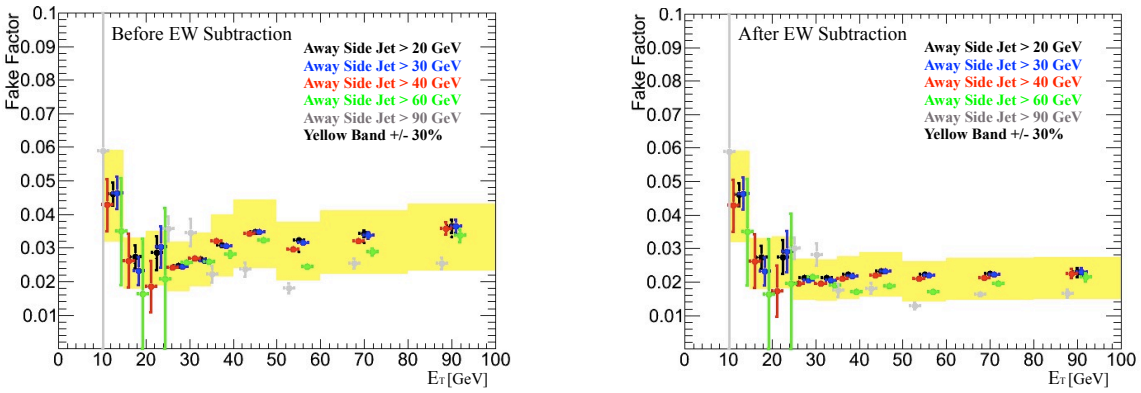

(a) (b)

Figure 9.9: Effect of electro-weak subtraction on measured fake factor. (a) shows the measured fake factor without the electro-weak correction. (b) shows the measured fake factor after making the electro-weak correction. The "PID"-denominator definition is used the fake factor calculation.

the di-jet sample using MC. The effect of the electro-weak subtraction can be seen in Figure 9.9. Figure 9.9a shows the measured fake factors before the electro-weak subtraction. Figure 9.9b shows the result after the electro-weak subtraction. The correction is mainly important at higher p_{T}, where the contribution of real leptons is larger. The magnitude of the measured fake factor decreases as a result of the electro-weak subtraction. Unless otherwise specified, the fake factors shown throughout this section are from after the electro-weak correction.

For electrons, an additional complication arises from γ+jet events. The γ+jet events produce

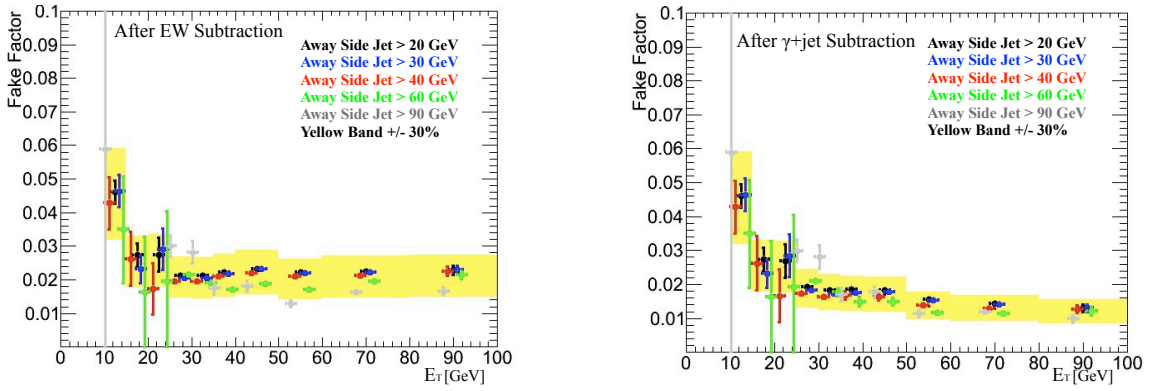

(a) (b)

Figure 9.10: Effect of γ+jet subtraction on measured fake factor. (a) shows the measured fake factor with the electro-weak correction, but not the γ+jet correction. (b) shows the measured fake factor after making both the electro-weak correction and the γ+jet correction. The "PID"-denominator definition is used the fake factor calculation.

prompt, isolated photons. When the photon undergoes a conversion it can be misidentified as an electron. If the photon converts early in the detector, and is relatively asymmetric, the misidentification cannot be suppressed by the isEM or the isolation requirements. As a result, the fake factor from isolated photons is much larger than that from jets. A significant contribution of prompt photons in the electron fake factor sample will bias the fake factor to higher values. The effect of γ+jet contamination in di-jet sample has been studied using γ+jet MC. Figure 9.10 shows the effect of the γ+jet subtraction on the measured fake factors. Figure 9.10a shows the measured fake factors after the electro-weak subtraction, but without the γ+jet correction, identical to Figure 9.9a. Figure 9.10b shows the result after the both the electro-weak subtraction and the γ+jet subtraction. The γ+jet correction is a relatively small correction for electrons with p_{T} below about 50 GeV, where the background from misidentification is most important. Given the size of the effect in the low p_{T} region, the γ+jet correction is not made in the following. There is however, a significant γ+jet correction at higher p_{T}. For analyses sensitive to high p_{T} fakes, it would be important to make this correction.

One interesting effect of the γ+jet correction is to reduce the differences in fake factor with the away-side jet variation. This may be an indication that some of the fake factor variation among the different away-side samples is due to differing levels of γ+jet contamination. The γ+jet correction is a potential avenue for reducing the away-side jet dependence. This effect is not further investigated here.

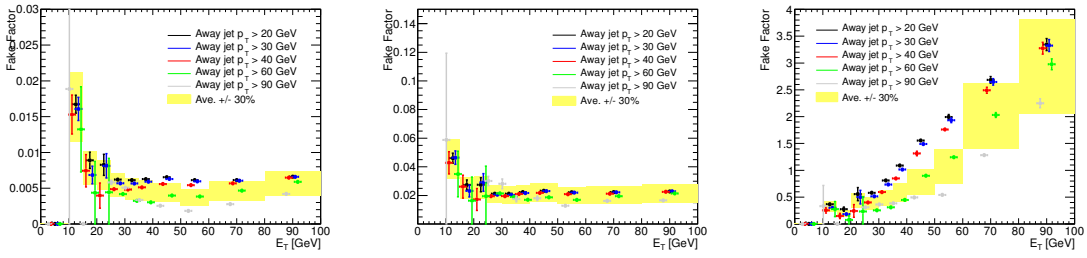

(a) (b) (c)

Figure 9.11: Measured fake factors corresponding to the denominator definitions in Table 9.2. (a) shows the "PID-and-Iso"-denominator, (b) shows the "PID"-denominator, and (c) uses the "Isolation"-denominator. The numerator selection is that given in Table 9.1.

The measured fake factors corresponding to the different denominator definitions in Table 9.2 are shown in Figure 9.11. Each of the fake factor measurements use the numerator definition in Table 9.1. The fake factor using the "PID-and-Iso"-denominator is shown in Figure 9.11a, the result with the "PID"-denominator is shown in Figure 9.11b, and the fake factor using the "Isolation"-denominator is shown in Figure 9.11c. The values of the fake factors differ considerably across the definitions. The "PID-and-Iso" fake factors start at ~ 0.01 and drop to ~ 0.005, the "PID"-denominator has fake factors which are about four times as large, and the "Isolation"-fake factors begin at ~ 0.2 and increase to values larger than one. Each of these fake factors is used to predict the same background, the background passing the common numerator definition. The measured value of the fake factor is not a direct indication of the size of the background in the signal region. The value of the fake factor only contains information about the size of the background in the signal region relative to the size of the control region. The fake factor can be larger than one. The fake factor is not the fake rate: it is a ratio of fake rates. If the fake factor is one, it does not mean every jet is misidentified as a numerator, but rather that the size of the W+jet control region is the same as the size of the background in the signal region. Having a fake factor above one means the misidentification rate for the numerators is larger than the misidentification rate for denominators. This is possible depending on the numerator and denominator definitions. Large fake factors, order unity or larger, are undesirable because the control region would then be smaller than the background being predicted in the signal region. In this case, the larger statistical uncertainties in the control region are amplified by fake factor in the signal region.

Another variation seen among the fake factors in Figure 9.11 is in the away-side jet dependence. The "PID" fake factors vary less than 30% among the different away-side jet samples. Moving to the looser isolation requirement in the "Pid-And-Iso"-denominator, the away-side variation increases

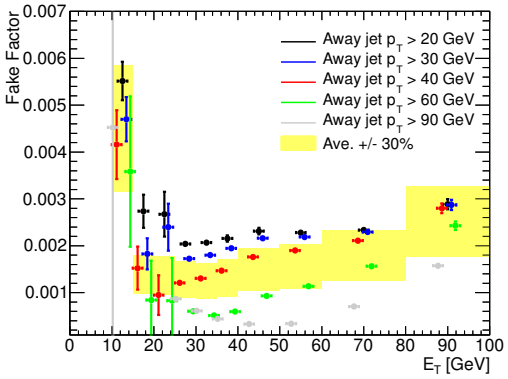

Figure 9.12: Measured electron fake factor with loosened isolation requirement in the denominator definition. The numerator selection is that given in Table 9.1. The denominator definition is: fail isEM medium and with an isolation requirement loosened to $\frac{E_T^{Cone30}}{E_T} < 0.5$.

to around 30%. And when the denominator isolation requirement is loosened further, as in the "Isolation" fake factors , the away-side jet variation increases to over 50%. Figure 9.12 shows the fake factor using a denominator that is required to fail medium isEM, as in the "PID" and "Pid-And-Iso" denominators, but has an even looser isolation requirement of $\frac{E_T^{Cone30}}{E_T} < 0.5$. Again, the away-side jet variation is seen to increase beyond 50%. The increase in away-side jet variation is an indication of the break down of the fake factor assumption in Equation 9.10. Without an isolation requirement in the denominator, the fake factor depends both on the p_{T} of the fake lepton and on the p_{T} of the jet being misidentified. This more complicated dependence is not accounted for in the fake factor method and leads to large systematic uncertainty on the background prediction. To avoid this increase in uncertainty, the fake factor denominators used in the WW analyses presented in Chapters 11 and 10 include isolation requirements.

The muon fake factor has been measured using a data sample triggered by the `EF_mu18` trigger. This trigger is an unprescaled primary trigger that requires a reconstructed muon with transverse energy above 18 GeV and makes no additional requirement on the muon impact parameter or isolation[21]. As for electrons, the contamination of muons from W-bosons or Z-bosons in the sample has been suppressed with m_{T} and Z-mass vetoes; the remaining contribution is subtracted using MC. The measured muon fake factor using the numerator and denominator definitions given in Section 9.3.1 is shown in Figure 9.13. The muon fake factor is larger than that of the electrons. This is a result of the tight requirement of a reconstructed muon in the denominator definition. Because

[21] In 2012, the primary muon trigger added a cut on track-based isolation which prevents the fake factor from being calculated from this trigger directly. However, muon supporting triggers without isolation were added that run at high rates. These are used in the 2012 analyses.

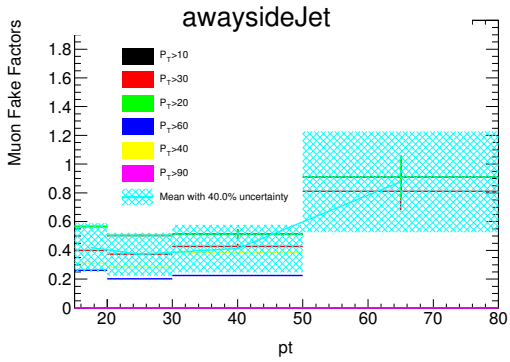

Figure 9.13: Measured muon fake factor as a function of p_{T}. The fake factors are measured in different away-side jet bins, as indicated by the different colored curves. The error band gives the average with the $\pm 40\%$ variation.

of the relatively large fake factors, the statistical uncertainty on the muon background prediction is larger than for the electrons. The isolation requirement in the muon denominator needs to be loosened in order to increase the misidentification rate. As discussed, this loosening of the isolation implies a larger systematic uncertainty, as can be seen from the away-side jet variation in Figure 9.13

This concludes the basic discussion of the fake factor measurement. There are several possible extensions to the method as was presented here. In addition to di-jet events, γ+jet and Z+jet events provide relatively pure sources of jets from which the fake factors can be measured. These events have the advantage of producing mainly quark-jets, similar to the W+jet background being modeled. There are additional complications associated with measuring the fake factor in these samples: smaller statistics, differences in flavor composition, larger electro-weak contamination, etc., but both provide promising ways to improve the measurement. The fake factor measurement in these samples is not further investigated here. The following section describes the systematic uncertainties associated with the fake factor measurement. The discussion of the fake factor measurement will be returned to in Section 9.4, where an extension to the fake factor method to include leptons from heavy-flavor is presented.

9.3.3 Fake Factor Systematics

This section presents the determination of the systematic uncertainty on the fake factors. This is the dominant source of uncertainty on the background prediction. The primary uncertainty associated with the fake factor measurement is from the sample dependence systematic uncertainty corresponding to the difference in fake factor between the di-jet and W+jet control regions, The

effect of additional, smaller uncertainties due to, pile-up, and the electro-weak subtraction, are also considered. The following sections discuss these various sources of systematic uncertainty and provide examples of how they are estimated. The examples use a particular choice of numerator and denominator definitions[22]. The actual values of the uncertainties will depend on the particular choice of definitions, but the methods presented are generally applicable. In Chapters 10 and 11, the systematic uncertainties on the fake factor specific to the definitions used in the analyses are provided.

9.3.3.1 Sample Dependence

The fake factor method assumes that the fake factor is a universal property of jets, independent of source, kinematics, or composition. This assumption was discussed in Section 9.2.1 when motivating the fake factor definition in Equation 9.10. The fake factor assumption leads to the assumption in the background calculation: that the rate of the background misidentification in the fake factor control region is the same as the rate of background misidentification in the background control region. In reality, the fake factor assumption is an approximation; different types of jets will have different fake factors. The fake factor is measured using jets in the di-jet control region and is applied to jets in the W+jet control region. Differences in fake factor between the jets in these samples will lead to a bias in the predicted background. A systematic uncertainty is needed to account for these potential differences. This uncertainty is the sample dependence uncertainty. The sample dependence is the dominant systematic uncertainty on the fake factor.

The systematic associated with sample dependence is closely related to the difference in fake factor due to away-side jet variation. Sample dependence uncertainty arises because the fake factor differs among different types of jets. The away-side jet variation is a measure of the uncertainty due to one type of possible difference: difference in jet p_{T}. This uncertainty is only one contributing factor to the overall sample dependence. Sample dependence arises from the difference in fake factors in two specific jet samples: the di-jet control region and the W+jet control region. The away-side jet variation can be larger or smaller than the sample dependence depending on the specific jet differences between the two samples. If the p_{T} spectra of jets in the two samples is similar, there can be a small sample dependence despite a large dependence on the away-side jet p_{T}. On the other hand, even if the away-side jet variation is small, there can be a large sample dependence due to differences other than jet kinematics, *e.g.,* flavor composition. In general, the away-side jet variation can be used as an estimate of the extent to which the fake factor assumption is violated, but the

[22] In this section, the results using systematics evaluated using the 2012 $H \to WW^{(*)} \to l\nu l\nu$ search are used as an example.

final sample dependence uncertainty needs to account for all the specific jet differences in the two control regions.

The sample dependence uncertainty is evaluated in MC using a closure test. The fake factor as measured in a di-jet MC is compared to the fake factor using a W+jet MC. The level of agreement in these samples provides a measurement of the fake factor sample dependence. As the fake factors may depend on the details of jet fragmentation and the underlying event model, it is important that the same MC generator be used for the di-jet MC and the W+jet MC. For electrons, an additional complication in the closure test arises due to the modeling of the heavy-flavor fraction. The discussion of sample depends begins with electrons and will then turn to muons.

As discussed in Section 9.1, for electrons, misidentification of both light-flavor jets and heavy-flavor jets is present at a significant level. The fake factor associated to heavy-flavor jets is different than that of light-flavor jets. This is shown in Figure 9.14, where the blue points give the fake factor from light-flavor jets, and the red points show the fake factor from heavy-flavor jets. Because these fake factors differ, the MC modeling of the total W+jet fake factor is sensitive to the MC modeling of the heavy-flavor fraction in W+jet events. The W+heavy-flavor modeling introduces an uncertainty in the closure test. Before the closure test is performed, the W+heavy-flavor component of the W+jet MC is corrected to reproduce the ATLAS W+heavy-flavor measurement [112], shown in Figure 9.15. A systematic on the W+heavy-flavor fraction is included by varying the W+heavy-flavor component by its measured uncertainty. The W+charm and W+bottom components are treated as 100% correlated. Figure 9.16 shows the effect of varying the W+heavy-flavor component within its measured uncertainties. The black points give the W+jet fake factor using the central value of the W+heavy-flavor measurement, the red (blue) points give the W+jet fake factor after varying the heavy-flavor fraction up (down) by its measured uncertainty. The heavy-flavor fraction of di-jet events has been found to be well modeled by the MC [113], so a similar correction for the di-jet MC is not needed.

Figure 9.17 shows the results of the electron closure test. The left-hand plot shows the fake factor in the di-jet MC in red, and in the W+jet MC, using the corrected value of the W+heavy-flavor fraction, in black. Only statistical uncertainties are shown. The right-hand plot gives the relative difference in di-jet and W+jet electron fake factor, $f_l^{di-jet} - f_l^{W+jets}/f_l^{di-jet}$, as a function of p_{T}. The yellow band shows the comparison using the nominal value of the W+heavy-flavor fraction, the red (blue) points show the comparison with the W+heavy-flavor fraction varied up (down) within the uncertainty. The fractional difference of the closure test, including the data-MC correction, is found to be within 40%.

For muons, the situation is simpler as only heavy-flavor contributes to the misidentified back-

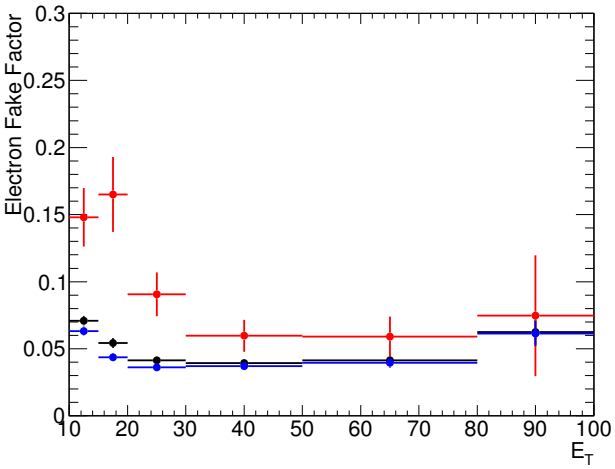

Figure 9.14: Fake Factor in W+jet MC. The black points show the total fake factor, the red points show the contribution from W+heavy-flavor and the blue points show the contribution from W+light-flavor.

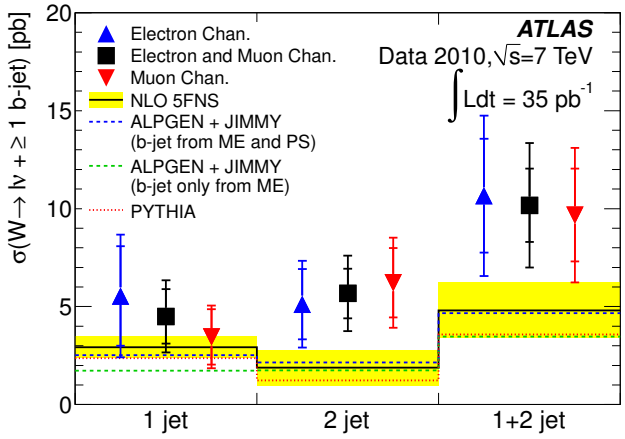

Figure 9.15: The measured W+b cross section in different jet bins.[112] The comparison of the data with the modeling of the MC is seen.

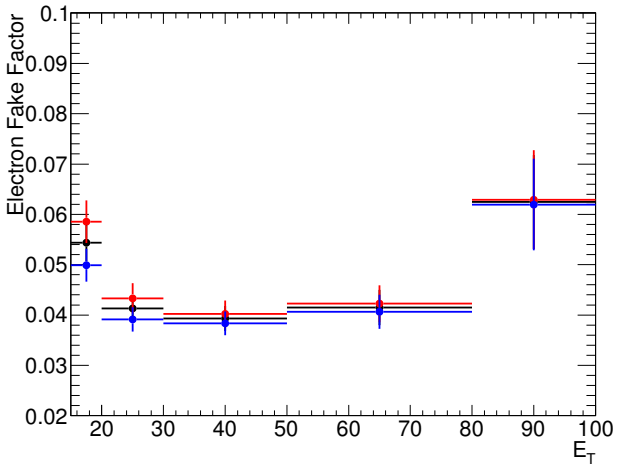

Figure 9.16: The variation of the W+jet fake factor with varying W+heavy-flavor fraction. The black points give the W+jet fake factor using the central value of the W+heavy-flavor measurement, the red (blue) points give the W+jet fake factor after varying the heavy-flavor fraction up (down) by its measured uncertainty.

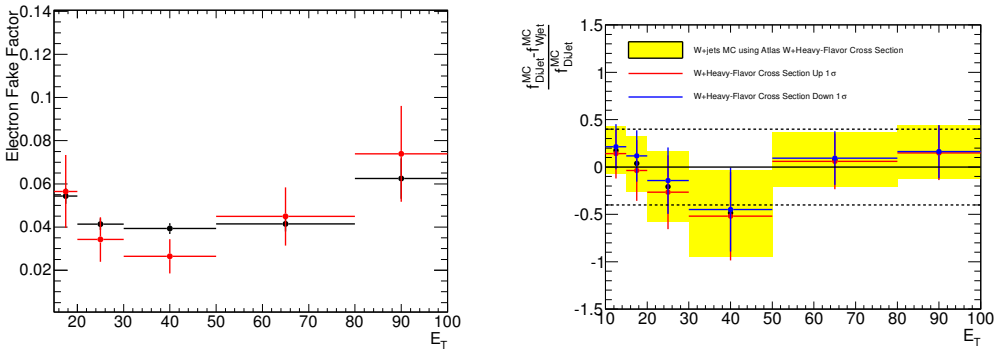

Figure 9.17: Comparison between di-jet and W+jet electron fake factors. The left-hand plot shows the electron fake factor in di-jet MC (red), and for the W+jet MC using the corrected value of the W+heavy-flavor fraction (black). The right-hand plot gives the relative difference in di-jet and W+jet electron fake factor. The yellow bands shows the central value of the closure test after correcting for the measured W+heavy-flavor fraction. The blue (red) points give the result of varying the W+heavy-flavor fraction down (up) by the measured uncertainty.

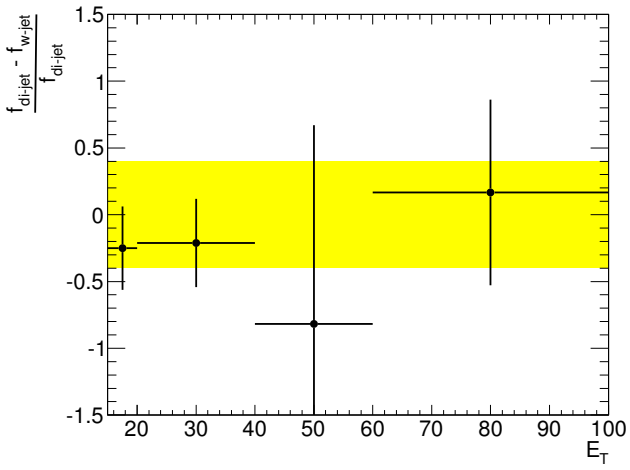

Figure 9.18: The fractional difference between the di-jet and W+jet muon fake factors.

ground at a significant level. A MC mis-modeling of the W+heavy-flavor cross section does not affect the modeling of the total W+jet fake factor. The cross section mis-modeling will give the wrong overall normalization of the W+jet background, but will not bias the fake factor modeling as for electrons. The closure test for muons is performed without correcting the W+heavy-flavor cross section. Figure 9.18 shows the comparison between the muon fake factor in the di-jet MC and in W+jets MC, $f_l^{di-jet} - f_l^{W+jets}/f_l^{di-jet}$, as a function of p_{T}. The fractional difference is found to be within 40%.

The determination of the sample dependence uncertainty is an aspect of the fake factor method that has potential for improvement. One issue with the current method is that the MC statistical uncertainty in the closure test is a significant contribution to the total sample dependence uncertainty. Significantly increasing the statistics of these high cross-section MC samples is not practical. Another issue with the closure test, is that it can only be done using the MC fake factors. However, the MC fake factors are not directly used to predict the background in the signal region. A better procedure for evaluating the sample dependence could lead to a significant improvement in the predicted background uncertainty.

The sample dependence uncertainty can potentially be improved by identifying the underlying causes of sample dependence and determining the appropriate systematic individually, for each cause. If the degrees of freedom responsible for sample dependence are known, the variation of the fake factor due to these underlying degrees of freedom can potentially be determined directly from data. This would avoid both of the shortcomings associated to the MC closure test. One example of this type of measurement, is the variation in fake factor due to the away-side jet variation.

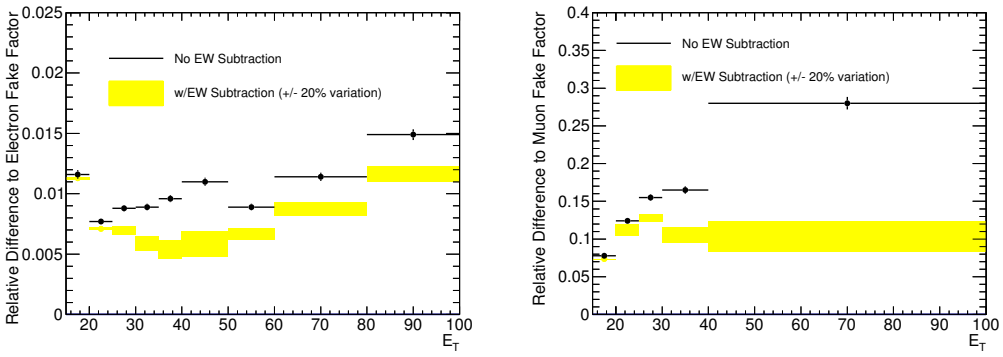

Figure 9.19: The electron (left) and muon (right) fake factor as a function of p_{T}. The black points show the fake factor before the subtraction of the EW contamination in the di-jet sample. The yellow band gives the fake factor after the subtraction and the change in fake factor by varying the amount of EW contamination by ± 20%

Here the variation from underlying jet p_{T} is measured directly in data with high statistics samples. Section 9.4 will discuss the determination of fake factors separately for heavy-flavor initiated jets. This method could prove useful in the measurement of the fake factor variation due to flavor content. Unfortunately, improving the procedure used do evaluate the sample dependence is not further considered here.

9.3.3.2 Lepton Contamination in the Di-Jet Control Sample

The di-jet control region is enriched in misidentified leptons. There is, however, some contamination from electro-weak (EW) processes, primarily W and Z-bosons. This real lepton contamination will bias the fake factor measurement. To reduce this bias, an EW veto is applied to the di-jet control sample as described in Section 9.3.2. This procedure rejects most of the W/Z events, while retaining almost all of the di-jet control region. The remaining W/Z contribution is subtracted from the observed data using the MC prediction. Figure 9.19 shows the estimated fake factor with and without the EW background subtraction. To evaluate the uncertainty due to the level of residual EW background, the cross section used in the MC subtraction is varied by ±20%. This variation accounts for both the systematics associated with the W and Z cross sections, and the uncertainty of the MC modeling of real leptons satisfying the denominator selection. The yellow bands in the figure show the variation in fake factors due to the 20% variation in the electron contamination. The lower p_{T} region, where the fake background is most important, has a small real lepton contribution and thus a small uncertainty due to lepton contamination.

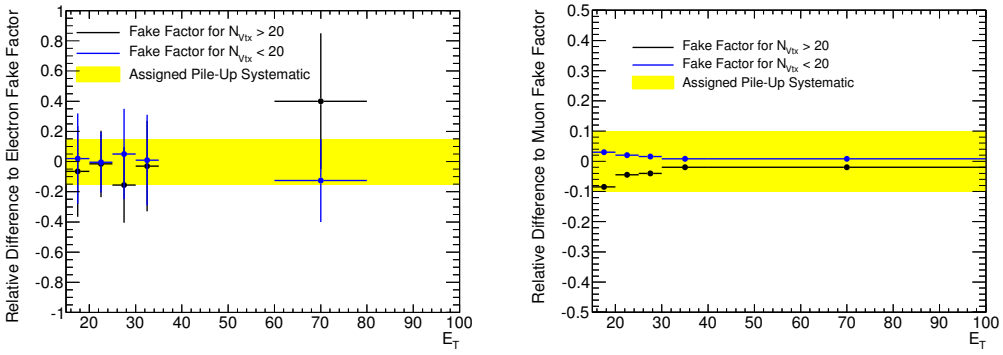

Figure 9.20: Relative difference in fake factor measured using a data sample with high pile-up (black) and low pile-up (blue). Electrons are shown on the left, muons on the right. The yellow band represents the assigned systematic uncertainty on the pile-up dependence.

9.3.3.3 Pile-Up Uncertainty

Pile-up a potential source of systematic. Pile-up affects misidentification rates and may be present at different levels in the di-jet control region and the W+jet control region. The systematic uncertainty resulting from variations in fake factor from differing levels of pile-up has been investigated by calculating the fake factor in a high pile-up and low pile-up di-jet sample. The di-jet sample has been divided in two subsets based on the number of primary vertices. If the number of primary vertices is above twenty, the event is assigned to the high pile-up sample. If the number of primary vertices is below twenty, the event is assigned to the low pile-up sample. These results of the fake factor calculated separately in the two samples is presented in Figure 9.20. The relative difference of the measured fake factor for the high (low) pile-up sample is shown in black (blue). The assigned systematic is shown in the yellow band. The result for electrons is shown on the left, muons on the right. As expected the fake factors decrease with increased pile up, which is primarily do to the increase in isolation energy from the higher event activity in the high pile-up events. A flat systematic of 15 %(10%) is applied for the electron (muon) fake factor.

9.3.3.4 Summary of Fake Factor Systematics.

A summary of the electron and muon fake factor systematic uncertainties is shown in Figure 9.21. The individual uncertainties are added in quadrature, and the uncertainty bands show the cumulative uncertainty. The actual values of the systematic will vary depending on the specific numerator and denominator definitions used, but the general trends can be seen. The final systematic uncertainties varies with p_{T} between 40%-50%. A table of the break down for the 15-20 GeV p_{T} bin, the bin with the largest amount of background, is given in Table 9.5. The largest source of uncertainty, for both

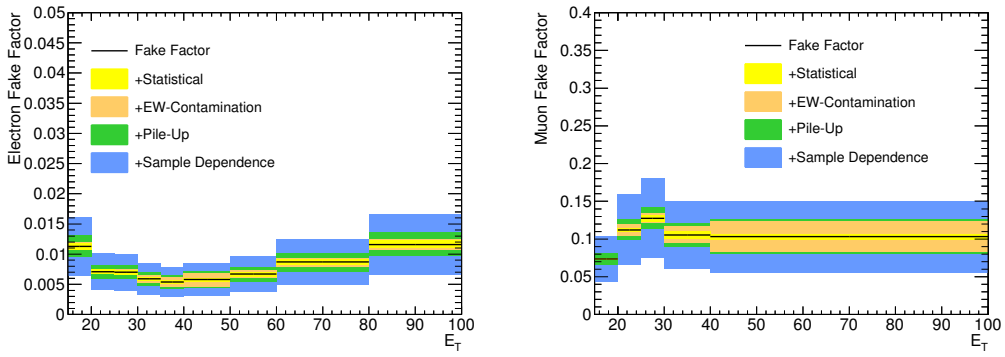

Figure 9.21: The fake factor as a function of p_{T} including the total systematic uncertainty for electrons (left) and muons (right). The uncertainty bands are cumulative and added in quadrature.

Source	Electron	Muon
Sample Dependence	40%	40%
Statistical Error	5%	2%
Pile-Up Error	15%	10%
EW-Contamination	1%	5%
Total Uncertainty	43%	41%

Table 9.5: Summary of the total fake factor uncertainties in the 15 - 20 GeV bin for electron and muons. The individual contributions are combined in quadrature to give to total uncertainty.

electrons and muons, is from the systematic due to sample dependence. The discussion of sample dependence will continue in Section 9.4, where an extension to the fake factor method that explicitly addresses the issue of sample dependence is presented.

9.3.4 Background Prediction

After the fake factor has been measured, and the systematic uncertainties have been evaluated, the background in the signal region can be calculated. The background is calculated by scaling the yield in the W+jet control region by the fake factor. The W+jet control region is created by selecting events containing a lepton and a denominator object. The full event selection in the signal region is applied to these events, where the denominator object is treated as a lepton. For example, to predict the background in the ee-channel, the W+jet control region is created by selecting events with an electron and an electron denominator. Any event selection involving the lepton kinematics, *e.g.*, m_{ll}, $p_{T_{ll}}$ or $\Delta\phi_{ll}$, is made using the denominator kinematics. In the $e\mu$-channel, two W+jet control regions are needed: one for the case when the electron is misidentified, and one for the case of a misidentified muon. The first control region is selected by requiring a muon and an electron

denominator; this region is then scaled by the electron fake factor to predict the background from a misidentified electron. The second control region is selected by requiring an electron and a muon denominator; this region is then scaled by the muon fake factor. In the $\mu\mu$ channel, only one control region is needed, similar to the ee-channel.

In data, the W+jet control regions will have contamination from non-W+jet processes. As discussed above, the QCD contamination is small and will be ignored. Contamination from other electro-weak processes that contain two real leptons, *e.g.,* Drell-Yan, fully leptonic top, di-bosons, will lead to an over prediction of the W+jet background. This contamination arises when a real lepton is identified as a denominator object. To correct this, the electro-weak contributions are subtracted from the W+jet control region using MC. The same W+jet control region selection is applied to the various electro-weak MC samples. The resulting MC yields are subtracted from the control region obtained in data. The result is a corrected control region, corresponding to only W+jet events which can used to correctly predict the W+jet background.

For electrons, the $W\gamma$ process provides an additional complication. $W\gamma$ events produce a real lepton, missing E_{T}, and an isolated photon. Background from $W\gamma$ arises when the photon undergoes a conversion and is misidentified as an electron. If the photon converts early in the detector and is relatively asymmetric, misidentification cannot be suppressed by the isEM or isolation requirements. As a result, the fake factor from isolated photons is much larger than that from jets. Attempting to predict the $W\gamma$ background using the fake factor measured in the di-jet control region, would lead to an under-prediction of the $W\gamma$ background. To avoid this, the $W\gamma$ background is estimated separately, from MC or using a dedicated data-driven estimate. The $W\gamma$ contribution to the W+jet control region is subtracted to avoid double counting. This contribution arises when the photon is identified as an electron denominator. $W\gamma$ is subtracted from the W+jet control region using MC in the same way as the other electro-weak contributions.

Examples of the W+jet background calculation in data are shown in Tables 9.6 – 9.8. The examples are taken from the 7 TeV $H \to WW^{(*)} \to l\nu l\nu$ search to illustrate the calculation. The specific background results for the analyses presented in Chapters 10 and 11 are provided individually in their respective chapters.

Table 9.6 shows the calculation in the ee-channel. The first row gives the uncorrected result in data. The yield in the W+jet control region, 116 events, is scaled by the electron fake factor to give the uncorrected W+jet prediction, 3.85 events. The fake factor is applied according to the p_{T} of the denominator and is on average 0.03. The uncertainty is broken down into two components. The first is statistical and is due to the statistical uncertainty on the yield in the W+jet control region, approximated by $f \times \sqrt{\mathrm{N}_{\mathrm{Event}}^{W\text{+jet CR}}}$. The second uncertainty is from the systematic uncertainty

ee-channel	$N_{\text{Event}}^{W+\text{jet CR}}$	N_{Event} ± (Stat.) ± (Sys.)
W+Jet Estimate from Data	116	3.85 ± 0.36 ± 1.15
W+Jet MC Correction from W+γ	-	-0.11 ± 0.04 ± 0.03
W+Jet MC Correction from Z	-	-0.12 ± 0.02 ± 0.04
W+Jet MC Correction from Top	-	-0.005 ± 0.001 ± 0.001
W+Jet MC Correction from WW	-	-0.10 ± 0.01 ± 0.03
W+Jet MC Correction from WZ	-	-0.004 ± 0.001 ± 0.001
Total MC Correction	-	-0.34 ± 0.05 ± 0.06
Total W+Jet Bkg Prediction	-	3.51 ± 0.36 ± 1.05

Table 9.6: Example of the W+jet background calculation in the ee-channel. The W+jet control yield in data and the various MC corrections are shown separately.

on the fake factor. For this example, a systematic of 30% has been assigned to the fake factor, which translates into a 30% systematic on the background yield. The following set of rows give the corrections for the various non-W+jet contributions to the W+jet control region. Corrections are made for the contamination due to: $W\gamma$, Z/γ^*, top, WW, and WZ; contributions from other electro-weak processes are found to be negligible. The total size of the MC correction to the W+jet prediction is about 10%, 0.34 events. The final W+jet prediction is given on the last line and is the result of subtracting the total MC correction from the data estimate. The statistical uncertainty on total prediction is obtained by adding the individual statistical uncertainties in quadrature, whereas the systematic uncertainties on the fake factor are treated as correlated. The uncertainty on the total background prediction is dominated by the systematic on the fake factor.

Table 9.7 shows the corresponding calculation in the $\mu\mu$-channel. The size of the W+jet control region is smaller for muons than electrons. This is because of the lower jet misidentification rate for the muon denominators. As a result, the statistical uncertainty is relatively larger. The fourteen events in the W+jet control region are scaled to 2.35, with an average fake factor of 0.17. The muon fake factor is much larger than the electrons because the muon denominator definition is closer to the numerator definition. This also results in a larger electro-weak correction. The total correction to the muon prediction is around 30%, 0.79 events. There is no contribution from $W\gamma$ in the $\mu\mu$-channel as photons do not fake muons. In this example, the statistical and systematic uncertainties on the final background prediction are comparable. With more luminosity, the statistical uncertainty decreases, and the systematic from the fake factor begins to dominant. The W+jet background prediction is smaller for muons than electrons. This agrees with the intuitive expectation that the muon fake rate is smaller than that of the electrons.

Table 9.8 shows the W+jet prediction in the $e\mu$-channel. In this case, the total W+jet prediction is the sum of contributions from separate e-fake and μ-fake control regions. The break down of the

$\mu\mu$-channel	$N_{\text{Event}}^{W+\text{jet CR}}$	N_{Event} ± (Stat.) ± (Sys.)
W+Jet Estimate from Data	14	2.35 ± 0.63 ± 0.71
W+Jet MC Correction from W+γ	-	0.0 ± 0.0 ± 0.0
W+Jet MC Correction from Z	-	-0.45 ± 0.08 ± 0.13
W+Jet MC Correction from Top	-	-0.09 ± 0.02 ± 0.03
W+Jet MC Correction from WW	-	-0.25 ± 0.03 ± 0.07
W+Jet MC Correction from WZ	-	-0.003 ± 0.001 ± 0.001
Total MC Correction	-	-0.79 ± 0.09 ± 0.16
Total W+Jet Bkg Prediction	-	1.57 ± 0.63 ± 0.47

Table 9.7: Example of the W+jet background calculation in the $\mu\mu$-channel. The W+jet control yield in data and the various MC corrections are shown separately.

$e\mu$-channel	$N_{\text{Event}}^{W+\text{jet CR}}$	N_{Event} ± (Stat.) ± (Sys.)
W+Jet Estimate from Data (e-fake)	334	11.98 ± 0.66 ± 3.60
W+Jet (e-fake) MC Correction from W+γ	-	-0.46 ± 0.09 ± 0.14
W+Jet (e-fake) MC Correction from Z	-	-0.50 ± 0.06 ± 0.15
W+Jet (e-fake) MC Correction from Top	-	-0.03 ± 0.004 ± 0.01
W+Jet (e-fake) MC Correction from WW	-	-0.24 ± 0.01 ± 0.07
W+Jet (e-fake) MC Correction from WZ	-	-0.006 ± 0.001 ± 0.002
Total (e-fake) MC Correction	-	-1.22 ± 0.11 ± 0.22
Total W+Jet (e-fake) Bkg Prediction	-	10.76 ± 0.67 ± 3.23
W+Jet Estimate from Data (μ-fake)	18	4.26 ± 1.00 ± 1.28
W+Jet (μ-fake) MC Correction from W+γ	-	-
W+Jet (μ-fake) MC Correction from Z	-	-0.78 ± 0.05 ± 0.23
W+Jet (μ-fake) MC Correction from Top	-	-0.17 ± 0.04 ± 0.05
W+Jet (μ-fake) MC Correction from WW	-	-0.40 ± 0.04 ± 0.12
W+Jet (μ-fake) MC Correction from WZ	-	-0.013 ± 0.004 ± 0.004
Total (μ-fake) MC Correction	-	-1.36 ± 0.08 ± 0.41
Total W+Jet (μ-fake) Bkg Prediction	-	2.90 ± 1.01 ± 0.87
Total W+Jet Bkg Prediction	-	13.66 ± 1.20 ± 4.10

Table 9.8: Example of the W+jet background calculation in the $e\mu$-channel. The W+jet control yields in data and the various MC corrections are shown separately. The $e\mu$-channel receives background contributions from two W+jet control regions.

calculation in each control region is shown separately in the table. The same trends between the e-fake and μ-fake control regions that were seen for the same flavor channels are evident for the $e\mu$-channel. Again, the contribution from electron fakes is seen to be larger than for muons, agreeing with the intuitive expectation. The W+jet background prediction is significantly larger in the $e\mu$-channel than the same flavor channels due to the different event-level selections. The W+jet acceptance is increased as a result of the looser missing E_{T} and $p_{T_{ll}}$ requirements of the $e\mu$-channel.

A couple of subtleties arise when selecting events in the W+jet control region. The first involves regions of the W+jet control region phase space that do not fire the trigger. The second involves

predicting jet counts in the presence of jet-lepton overlap. These are each discussed briefly below.

9.3.4.1 Non-Trigger-able W+jet Control Region

The first subtlety arises when triggers using particle identification criteria are used on-line to record events. There can be cases where misidentified background events are triggered, but the corresponding events in the background control region are not recorded. This is an issue when a jet misidentified as a numerator satisfies the trigger requirement, but a jet misidentified denominator does not. If the other objects in the event fail to fire the trigger, the background events in the signal region are not covered by the control region. This leads to an under-prediction of the background.

An example of this can be seen in the fake electron background in the $e\mu$-channel. W+jet events with a true muon with p_{T} below the trigger threshold can only be recorded if the misidentified jet satisfies the electron trigger. The electron trigger requires a reconstructed electron passing the medium isEM requirements. When the jet is misidentified as a numerator electron, which requires tight isEM, the event satisfies the electron trigger and is recorded. When the jet is misidentified as a denominator electron, which requires medium isEM to fail, the event does not satisfy the electron trigger, and the event is rejected on-line by the trigger. The fake factor method cannot account for these events, and the overall background is under-estimated.

The under-prediction due to non-trigger-able events in the background control region can be corrected by adding a contribution from a separate, trigger-able control region. The idea is to define a second alternative denominator selection that explicitly satisfies the lepton trigger requirement, referred to in the following as "trigger-able denominators". A second background control region is selected, consisting of events with a numerator which did not satisfy the trigger, and a trigger-able denominator which does. These events are then scaled by a separate fake factor, relating trigger-able denominators to numerators. The total background is given by:

$$\mathrm{N}^{\mathrm{Bkg.}}_{(\mathrm{N+N})} = f \times \mathrm{N}^{\mathrm{Bkg.}}_{(\mathrm{N_{Trig.}+D})} + f^{t} \times \mathrm{N}^{\mathrm{Bkg.}}_{(\mathrm{N_{!Trig.}+D_{Trig.}})}, \tag{9.21}$$

where N represents numerators, $\mathrm{N_{Trig.}}$ are numerators which fire the trigger, $\mathrm{N_{!Trig.}}$ are numerators which do not fire the trigger, D is the standard denominator definition, $\mathrm{D_{Trig.}}$ is the trigger-able denominator definition, f is the standard fake factor, and f^{t} is the trigger-able fake factor. The first term predicts background in which the real lepton satisfies the trigger; the second term predicts background that is only triggered by the misidentified object. The trigger-able fake factor can be calculated in the fake factor control sample in the typical way:

$$f^{t} = \frac{\mathrm{N_{Numerator}}}{\mathrm{N_{Trigger\text{-}able\ Denominator}}}. \tag{9.22}$$

Here, both the numerator and denominator samples can be collected from the high statistics primary trigger.

Returning to the example in the $e\mu$-channel, the trigger-able denominator can be defined as the "Isolation"-denominator in Table 9.2, which satisfies the single electron trigger. The second control region would then be selected by requiring a numerator muon which does not match the trigger and an "Isolation"-denominator. In the WW analyses, with the current single-lepton trigger thresholds, the non-trigger-able correction is around 10%, but can be a fairly large effect in certain regions of phase space, *e.g.,* low leading lepton p_{T} in the e-high/μ-low channel.

9.3.4.2 Jet Counting

The second subtlety involves correctly modeling the number of jets from fake background in cases where numerator objects can overlap with reconstructed jets. If numerator-jet overlap removal is not part of the signal selection, the signal region may contain events with numerators that have overlapping jets. This is not a concern for electrons. Almost all electrons are also reconstructed as jets, so most analyses include an explicit jet-electron overlap removal during jet selection. Muons are susceptible to jet overlaps. An isolation requirement on the muon will suppress muons with overlapping jets, but signal selections often do not explicitly exclude jet-muon overlaps. In this case, numerator muons in the signal region can overlap with reconstructed jets. To correctly model the number of jets in the signal region, the rate at which misidentified muons overlap with jets would need to be correctly modeled.

The jet counting complication with the fake factor method comes in because the rate of overlapping jets is different in the W+jet control region than in the signal region. Muon denominators are defined to have looser isolation criteria than numerators. This results in a larger overlapping-jet rate for muon denominators than for muon numerators. The different overlapping-jet rate in the control region leads to an incorrect prediction of the number of reconstructed jets in the signal region. This is a case where the assumption of event-level quantities, *i.e.,* the number of jets, being independent of the particle-level fake factor, has broken down. This issue is especially problematic when the signal selection includes a requirement on the number of jets. In this case, the difference in the overlapping-jet rate of numerators and denominators can result in an incorrect background prediction.

The problems associated to jet counting are illustrated in the example of the W+jet prediction in a WW analyses that includes a jet veto. The background modeling with the fake factor method for this example is sketched in Figure 9.22. Background in the signal region is represented by the two numerators on the left-hand side. The right-hand side represents the background modeling in the

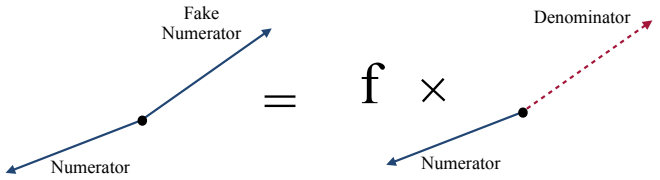

Figure 9.22: Schematic of the standard fake factor procedure for predicting background to events in which a jet veto is applied. The left-hand side represents the background in the signal region, the right-hand side represents the fake factor modeling of the background: W+jet control region times fake factor. None of the objects in the picture overlap with reconstructed jets.

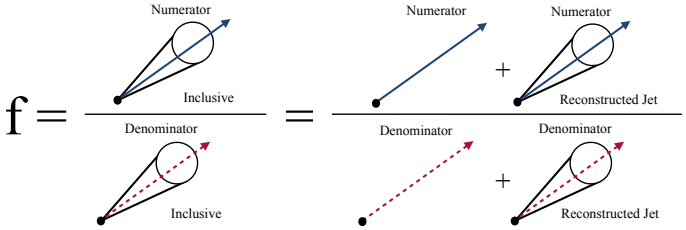

Figure 9.23: Schematic of the separation of the standard fake factor measurement into terms extrapolating to background with and without overlapping jets. f^0 extrapolates to fake background without overlapping jets. f^1 extrapolates to fake background with overlapping jets.

fake factor method: the W+jet control region, multiplied by the fake factor. The signal selection requirement of no reconstructed jets is applied both to the signal region and the W+jet control region; none of the depicted numerators or denominators overlap with reconstructed jets.

The problems with this background prediction stem from the fact that when the fake factor is measured in the di-jet control region, a jet veto is not applied. Inclusive numerator and denominator samples are used to measure the fake factor; no overlapping jet requirement is made. The fake factor measurement in the di-jet control region is sketched in Figure 9.23. The ratio of inclusive samples used to measure the fake factors is indicated in the figure by the ratio on the left-hand side. These inclusive samples consist of both objects which overlap reconstructed jets and those which do not. These separate contributions to the inclusive samples are indicated in the figure in the right-hand ratio.

There are two inconsistencies associated with using the inclusively measured fake factor to predict background in the zero-jet signal region. The first inconsistency is that different denominator definitions are used in the fake factor and in the W+jet control region. The denominators appearing in Figure 9.23 differ from those in Figure 9.22. Only denominators without overlapping jets are found in the W+jet control region, whereas the fake factor measurement includes all denominators,

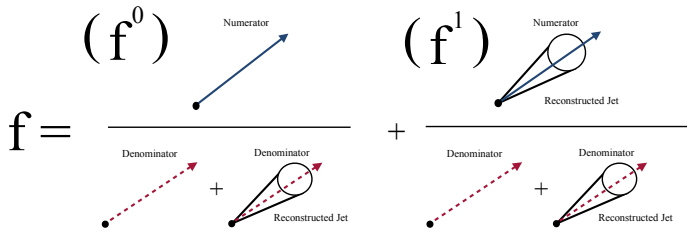

Figure 9.24: Schematic of the standard fake factor measurement in the di-jet control region. No overlapping jet requirement is made when measuring the fake factor. The inclusive sample of numerators and denominators are composed of those which overlap reconstructed jets and those which do not.

in particular, those with overlapping jets. In the zero-jet background prediction, the region extrapolated from is inconsistent with the applied extrapolation factor. This fake factor assumes a larger control region than it is being applied to, which leads to an under-prediction of the background.

The other inconsistency associated to the zero-jet background calculation, is that the inclusive fake factor extrapolates to a combination of zero-jet and one-jet events. As shown in Figure 9.24, the inclusive fake factor measurement can be separated into two terms: f^0 and f^1. The first term, f^0 extrapolates from denominators to numerators which do not overlap with jets. The second term, f^1 extrapolates from denominators to numerators which have overlapping jets. By applying f, the sum of these two terms, to the zero-jet control region in Figure 9.22, the background prediction includes events with misidentified numerators that overlap with jets. However, the actual background events that this prediction corresponds to are removed from the signal region by the jet veto. This leads to an over-estimate of the background prediction.

These effects can be corrected by applying the fake factor consistently, and by only extrapolating to the appropriate jet bin. The fake factor and background control region should use the same denominator definition. This can done by using the inclusive denominator definition of the fake factor measurement in the background control region. In practice, this is done by applying jet-denominator overlap removal in the background control region before making any event-level selection based on the number of jets. The choice to use the inclusive denominator as the common definition is preferred to the non-overlapping-jet denominator because it has a much larger misidentification rate from jets. Using the non-overlapping-jet denominator would suppress W+jet events, significantly reducing the size of the background control region and increasing the statistical uncertainty on the measurement.

The appropriate fake factor should be applied to the background control region. If predicting background events in which overlapping jets are excluded, the extrapolation should only be made with f^0. On the other hand, background with overlapping jets should be predicted using only f^1.

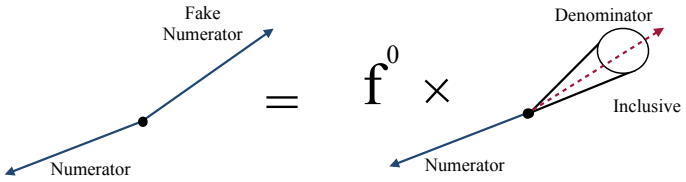

Figure 9.25: Schematic of corrected fake factor procedure for predicting background to events in which a jet veto is applied. The left-hand side represents the background in the signal region, the right-hand side represents the updated fake factor modeling of the background. The W+jet control region with the inclusive denominator sample is scaled by fake factor for no overlapping jets.

f^0 and f^1 can be determined from the standard fake factor, using the fraction of numerators in the fake factor control region that overlap with reconstructed jets, $\epsilon_{\text{overlap}}$:

$$\begin{aligned} f^0 &= (1 - \epsilon_{\text{overlap}}) \times f, \\ f^1 &= \epsilon_{\text{overlap}} \times f. \end{aligned}$$

As the numerator isolation requirement becomes tighter, the rate of overlapping jets, $\epsilon_{\text{overlap}}$, decreases. In this limit, the f^0 goes to f, and f^1 goes to 0, and scaling by the standard fake factor gives the correct prediction. Applying jet specific fake factors is thus more important when the numerator selection is relatively loose.

Returning to the example of the zero-jet W+jet background, the corrected W+jet prediction is sketched in Figure 9.25. In this updated calculation, the inclusive denominator definition is used in the W+jet control region, and the extrapolation to the signal region is done with f^0. Consistent denominator definitions are used in the fake factor and the control region, avoiding the inconsistency in the previous calculation. The updated prediction uses f^0 for the fake factor. This correctly extrapolates to only the zero-jet bin, consistent with the background being predicted.

To correctly predict background in a one-jet signal region, two terms are required: one to predict the background when the jet does not overlap the misidentified numerator, and one to predict the background where the misidentified numerator has an overlapping jet. These terms are sketched in Figure 9.26. The term on the left-hand side predicts the background when the jet does not overlap the misidentified numerator. This background is extrapolated from events in the W+jet control region containing an additional jet, using f^0. The denominator is extrapolated to a numerator without an overlapping jet; the other jet in the event satisfies the one-jet requirement. If this event was scaled by f^1, it would predict background in the two-jet bin, one jet overlapping the faked numerator plus the additional jet. The term on the right predicts the background for which the jet overlaps the faked numerator. This background is extrapolated from events in the W+jet control

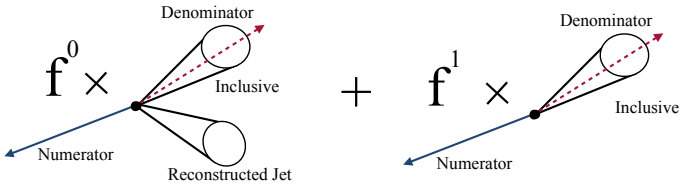

Figure 9.26: Schematic of background modeling in a one jet signal region. The left-hand term predicts background when the jet does not overlap the misidentified lepton. The right-hand term predicts background when the jet overlaps the misidentified lepton.

region with no additional jets, using f^1. This reasoning can be extended to correctly model the background with arbitrary number of jets.

This concludes the basic discussion of the W+jet background calculation. The following section describes ways in which the fake factor procedure can be validated in data.

9.3.5 Data-Driven Validation of the Background Modeling

The fake factor method can be validated by predicting the fake background in a region dominated by fake background. This serves as a data-driven closure test of fake factor procedure. The additional region dominated by fake background is referred to as the "validation region". This validation region is defined to be different from the background and fake factor control regions. The fake factor method can then be performed, treating the validation region as the signal region. The yield and the kinematics of events observed in the validation region is compared to the background model from the fake factor method. An accurate modeling of the validation region provides confidence that the fake factor extrapolation is valid. Major problems with the background prediction in the signal region can be seen through an inaccurate description of the observed validation region.

It is important that the source and characteristics of the misidentified background in the validation region is similar to the misidentified background in the signal region. The ultimate goal is in providing confidence in the background prediction in the signal region. If the validation region is too dissimilar from the signal region, there may be problems predicting background in the signal region, despite an accurate modeling of the validation region.

There is a trade-off when choosing a validation region. When the validation region is closer to the signal region, the test of the validation region modeling is more applicable to the background in the signal region. However, when the validation region is near the signal region, there are often significant contributions from sources other than misidentified background. Uncertainties on these other contributions compromise the precision of the background validation. The ideal validation

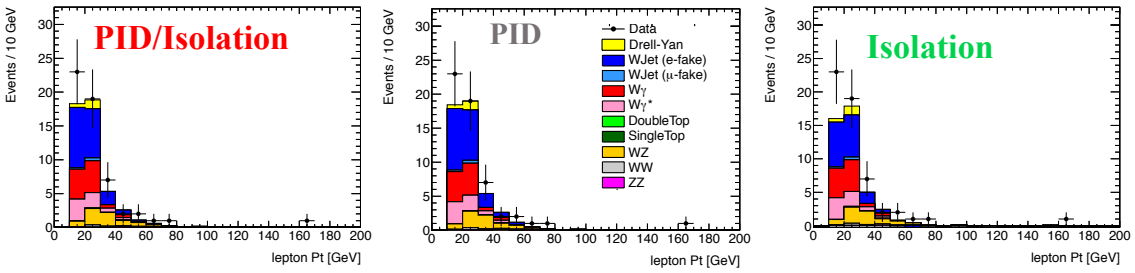

(a) (b) (c)

Figure 9.27: Test of W+jet modeling in same sign events. Sub-leading p_{T} distribution is shown for events in the μe-channel with a same sign requirement. The fake predictions are made with the fake factor procedure using: (a) the "Pid-And-Iso"-denominator definition. (b) the "Pid"-denominator definition (c) the "Isolation"-denominator definition. Results are from the 5.8 fb^{-1} 7 TeV data set.

region is dominated by the same type of misidentified background as is present in the signal region. Striking the balancing between, purity of the background in the validation region, and similarity of the validation region to background to the signal region, can be challenging.

For the W+jet background, a particularly nice validation region is provided by events with same-sign di-leptons. The same selection as in the signal region is applied, except the opposite charge lepton requirement is replaced with a same-charge lepton requirement. The same-sign requirement suppresses most electro-weak processes, leaving a data sample enriched in W+jet events. The fake factor procedure can be applied to the same-sign W+jet control region to predict the W+jet yield in the same-sign events. An example of the background modeling in the same sign region is shown in Figure 9.27. The figure shows the electron p_{T} distribution in same-sign μe events with a leading muon. The data are shown in the black points, and the background model is shown in the stacked histogram. The blue histogram, labeled "WJet (e-fake)", gives the misidentified electron background predicted by the fake factor procedure. Figure 9.27a shows the background prediction using the "Pid-And-Iso"-denominator, Figure 9.27b uses the "Pid"-denominator, and Figure 9.27c shows the prediction using the "Isolation"-denominator. The non-W+jet contribution to the same-sign region is estimated using MC. The same-sign region has a relatively large faction of W+jet events, particularly at low p_{T}. Overall, the observed same-sign data is well modeled by the different background predictions.

A drawback of the same-sign validation region is that it has a different heavy-flavor composition than the background in the signal region. Background from W+heavy-flavor arises from the semi-leptonic decay of the heavy-flavor quark which is misidentified as a true prompt lepton. The dominant source of W+heavy-flavor in the WW analysis is W+c production; W+b production is

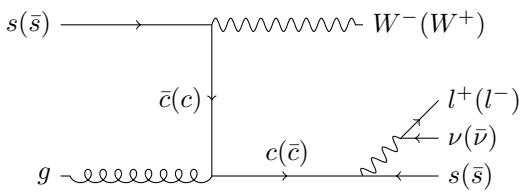

Figure 9.28: Feynman diagram for W+charm production where the charm quark decays semi-leptonically. The charge of the W is opposite that of the lepton from the charm quark decay.

CKM suppressed. The W+c production diagram, including the semi-leptonic decay of the charm-quark, is shown in Figure 9.28. The initial-state s-quark is correlated to the final-state c-quark, resulting in leptons with opposite charge. These W+c events are then suppressed by the same-sign requirement in the validation region. If only the W+heavy-flavor background component is mis-modeled, the background prediction in the signal region may be incorrect, despite an accurate modeling of the same-sign validation region.

To have sensitivity to the modeling of the W+heavy-flavor contribution, an opposite-sign validation is needed. The only separation between W+jet events and other electro-weak sources in an opposite-sign selection comes from the lepton identification criteria. The lepton identification criteria need to be reversed in order to define a validation region enriched in W+jet events. This is a little complicated because the lepton identification criteria are also used to define the W+jet control region. To avoid circularity, the validation region is defined to be independent of the background control region. To model the fake background in the validation region, separate fake factors need to be calculated to relate misidentification in the control region to misidentification in the validation region.

Examples of opposite-sign W+jet validation regions for the electron background are given in Table 9.9. In the "Tight-Inter-Iso" validation region, electrons are required to pass tight isEM and satisfy an intermediate isolation requirement. The intermediate isolation requirement enhances the rate of misidentification and suppresses the contribution from real leptons. Independent W+jet validation regions can be defined by reversing isolation criteria even further, by requiring isEM to be failed, or by doing both. In the "Medium-Not-Tight" validation region, electrons are required to pass the isolation and the medium isEM criteria, but to fail the tight isEM selection. Relaxing the isEM requirement to medium enhances the rate of misidentification, and reversing the tight isEM requirement suppresses the contribution from real leptons. For the "Medium-Not-Tight" validation region, independent W+jet control regions can be defined by reversing isEM even further, by requiring isolation to be failed, or by doing both. The "Tight-Inter-Iso" validation region tests the background prediction in a region with the same isEM requirement as the signal region, and the

"Tight-Inter-Iso"	"Medium-Not-Tight"
Electron Candidate	Electron Candidate
$0.14 < \frac{E_T^{Cone30}}{E_T} < 0.5$	$\frac{E_T^{Cone30}}{E_T} < 0.14$
–	$\frac{P_T^{Cone30}}{E_T} < 0.13$
Pass isEM Tight	Pass isEM Medium, but Fails isEM Tight

Table 9.9: Examples of opposite-sign W+jet validation regions. The validation region can be defined to test the extrapolation along the isEM or along the isolation dimension.

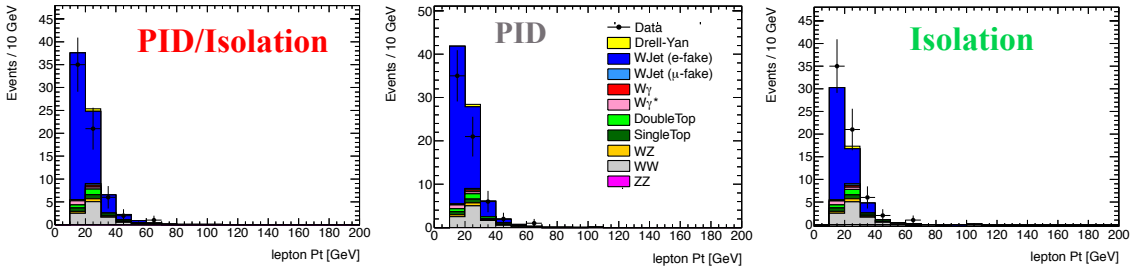

(a) (b) (c)

Figure 9.29: Test of W+jet modeling in the "Tight-Inter-Iso" validation region defined in Table 9.9. Sub-leading p_{T} distribution is shown for events in the μe-channel. The W+jet predictions are made with the fake factor procedure using: (a) the "Pid-And-Iso"-denominator definition, (b) the "Pid"-denominator definition, and (c) the "Isolation"-denominator definition. Results are from the 5.8 fb^{-1} 7 TeV data set.

"Medium-Not-Tight" validation region tests the background prediction in a region with the same isolation requirement as the signal region. Figures 9.29 and 9.30 show the modeling of the electron p_{T} in μe-channel for the "Tight-Inter-Iso" and "Medium-Not-Tight" validation regions. Figure 9.29a shows the "Tight-Inter-Iso" using the fake factor extrapolating in isEM and isolation, Figure 9.29b shows the prediction extrapolating in isEM, and Figure 9.29 shows the prediction extrapolating isolation. The corresponding regions for the "Medium-Not-Tight" validation region are shown in Figure 9.30. The non-W+jet contributions are estimated with MC. Overall, the data in the "Tight-Inter-Iso" and "Medium-Not-Tight" validation regions is well modeled by the various background predictions.

The downside to the opposite-sign W+jet validation region is that the background validation is not done with the same fake factors as used for the signal region. As the case with the same-sign control region, an accurate modeling of the opposite-sign validation regions provides confidence in the overall W+jet procedure, but cannot detect all potential failures.

Despite the lack of a perfect validation region, the background modeling in background dominated

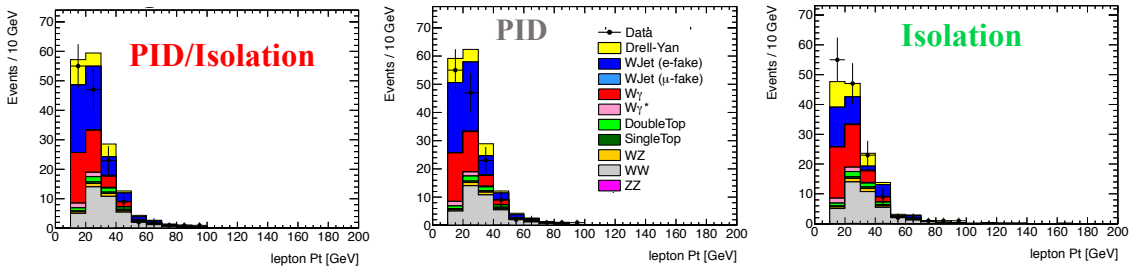

(a) (b) (c)

Figure 9.30: Test of W+jet modeling in the "Medium-Not-Tight" validation region defined in Table 9.9. Sub-leading p_{T} distribution is shown for events in the μe-channel. The fake predictions are made with the fake factor procedure using: (a) the "Pid-And-Iso"-denominator definition. (b) the "Pid"-denominator definition (c) the "Isolation"-denominator definition. Results are from the 5.8 fb^{-1} 7 TeVdata set.

regions is an important part of validation the fake factor method. The validation regions presented above provide data-driven cross checks of many of the aspects associated to the overall W+jet background prediction.

9.4 Extension of the Fake Factor Method for Multiple Sources of Background

Sample dependence is an issue that has been present throughout the discussion of the fake factor method. A particularly dangerous form of sample dependence arises when there are multiple sources of fake background which have different rates of misidentification. If these backgrounds are present in the fake factor and the background control regions at different levels, the background prediction from the fake factor method will be biased.

Electron misidentification is an example with multiple sources of fake background. Both light-flavor and heavy-flavor jets contribute to the electron background at significant levels. Because of the semi-leptonic decays, the misidentification rate from heavy-flavor jets can be much larger than that of light-flavor jets. Differences in heavy-flavor composition between the di-jet control region and the W+jet control region is a potential source of bias in the fake factor method.

This section discusses the bias associated to multiple sources of background and presents an extension to the fake factor method to account for these different sources. This extension is generally applicable to the modeling of any type of background with multiple sources of misidentification. In the following, the example of electron fakes from heavy-flavor decays will be used to illustrate the

idea, but it should be kept in mind that the formalism is widely applicable.

The remainder of the section is organized as follows: Section 9.4.1 discusses the potential bias associated to having different sources of background. Section 9.4.2 presents the extension to the fake factor method to account for multiple sources of background. Section 9.4.4 presents the application of the extended method to include heavy-flavor electron fakes in the WW analysis.

9.4.1 Bias From Multiple Sources of Background

A given particle selection can have multiple sources of fake background. If these sources contribute with different fake rates, there can be a bias in the background prediction from the fake fake method. To see how this bias comes about, consider an idealized the case of a numerator selection with two sources of background, denoted a and b. A corresponding denominator selection is defined, and the fake factor method is used to model the background. Background of types a and b can be misidentified as both numerator and denominator objects. In general, the rate of misidentification of the different background types will be different. A single fake factor is measured in the fake factor control region and is applied to denominators in the background control region.

In the fake factor control region, a fake factor corresponding to a particular mixture of the a and b backgrounds is measured. The measured fake factor is given by:

$$\begin{aligned} f &= \frac{\mathrm{N}}{\mathrm{D}} \\ &= \frac{\mathrm{N}^a + \mathrm{N}^b}{\mathrm{D}^a + \mathrm{D}^b}, \end{aligned} \tag{9.23}$$

where N represents the observed numerator objects, D represents the observed denominator objects, N^a (N^b) denotes numerators from background of type a (b), and D^a (D^b) denotes denominators from background of type a (b). Throughout this section, superscripts will denote truth-level quantities. Truth-level quantities are not observables. In the fake factor control region, only the total number of numerators and denominators are observable; the source of the misidentified objects cannot be directly determined. The truth-level factors are defined by:

$$F^a = \frac{\mathrm{N}^a}{\mathrm{D}^a} \text{ and } F^b = \frac{\mathrm{N}^b}{\mathrm{D}^b}. \tag{9.24}$$

The measured fake factor in Equation 9.23 is a mixture of the truth-level fake factors:

$$f = \frac{\mathrm{N}^a}{\mathrm{D}^a + \mathrm{D}^b} + \frac{\mathrm{N}^b}{\mathrm{D}^a + \mathrm{D}^b} \tag{9.25}$$

$$= F^a \left(\frac{1}{1 + \frac{\mathrm{D}^b}{\mathrm{D}^a}} \right) + F^b \left(\frac{1}{1 + \frac{\mathrm{D}^a}{\mathrm{D}^b}} \right) \tag{9.26}$$

Defining $\epsilon^b_{\text{ff-cr}}$ as the fraction of denominators from background type b in the fake factor control region, the fake factor can be written as

$$f = (1-\epsilon^b_{\text{ff-cr}})F^a + \epsilon^b_{\text{ff-cr}}F^b. \tag{9.27}$$

The measured fake factor corresponds to a mixture of the a-type and b-type fake factors. The relative size of the two contributions is determined by the fraction of b-type denominators in the fake factor control region.

The measured fake factor is used to predict the background in the signal region. The predicted amount of background is given by:

$$\begin{aligned} \mathrm{N}_{\mathrm{X+N}} &= f \times \mathrm{N}_{\mathrm{X+D}} && (9.28)\\ &= \left((1-\epsilon^b_{\text{ff-cr}})F^a + \epsilon^b_{\text{ff-cr}}F^b\right) \times \mathrm{N}_{\mathrm{X+D}} && (9.29)\end{aligned}$$

where $\mathrm{N}_{\mathrm{X+N}}$ is the background prediction, $\mathrm{N}_{\mathrm{X+D}}$ is the yield in the background control region, and f is the fake factor measured in the fake factor control region. Denominators from both a and b type backgrounds are present in the background control region, but again, only their sum is observable.

The true amount of background in the signal region, referred to as $\mathrm{N}^{\text{True}}_{\mathrm{X+N}}$, is given by the sum of background from each type:

$$\mathrm{N}^{\text{True}}_{\mathrm{X+N}} = F^a \times \mathrm{N}_{\mathrm{X+D}^a} + F^b \times \mathrm{N}_{\mathrm{X+D}^b}, \tag{9.30}$$

where $\mathrm{N}_{\mathrm{X+D}^a}(\mathrm{N}_{\mathrm{X+D}^b})$ represents the contribution to the background control region from background type $a(b)$. The true background can be written in terms of the total number of events in the background control region as

$$\begin{aligned} \mathrm{N}^{\text{True}}_{\mathrm{X+N}} &= F^a \times (1-\epsilon^b_{\text{bkg-cr}})\mathrm{N}_{\mathrm{X+D}} + F^b \times \epsilon^b_{\text{bkg-cr}}\mathrm{N}_{\mathrm{X+D}},\\ &= \left((1-\epsilon^b_{\text{bkg-cr}})F^a + \epsilon^b_{\text{bkg-cr}}F^b\right) \times \mathrm{N}_{\mathrm{X+D}}, && (9.31)\end{aligned}$$

where $\epsilon^b_{\text{bkg-cr}}$ is the fraction of denominators of from background of type b in the background control region.

The bias in the fake factor background prediction is the difference between what is predicted and the true amount of background. The relative bias of the fake factor estimate is given by:

$$\begin{aligned} \frac{\text{Bias}}{\mathrm{N}_{\mathrm{X+N}}} &= \frac{\mathrm{N}^{\text{True}}_{\mathrm{X+N}} - \mathrm{N}_{\mathrm{X+N}}}{\mathrm{N}_{\mathrm{X+N}}}\\ &= \frac{\left[\left((1-\epsilon^b_{\text{bkg-cr}})F^a + \epsilon^b_{\text{bkg-cr}}F^b\right) - \left((1-\epsilon^b_{\text{ff-cr}})F^a + \epsilon^b_{\text{ff-cr}}F^b\right)\right] \times \mathrm{N}_{\mathrm{X+D}}}{f \times \mathrm{N}_{\mathrm{X+D}}}\\ &= \left((\epsilon^b_{\text{ff-cr}} - \epsilon^b_{\text{bkg-cr}})F^a - (\epsilon^b_{\text{ff-cr}} - \epsilon^b_{\text{bkg-cr}})F^b\right) \times \frac{1}{f}\\ &= \Delta\epsilon \times \frac{\Delta f}{f} && (9.32)\end{aligned}$$

where Δf is the difference in fake factor between the two types of background, and $\Delta\epsilon$ is the difference in background fraction between the fake factor control region and the background control region. The fake factor estimate is unbiased if $\Delta f = 0$, *i.e.,* if both types of background have the same fake factor, or if $\Delta\epsilon = 0$, *i.e.,* if the relative contribution of the backgrounds is the same in the fake factor and the background control regions. In general, the different sources of background will have different fake factors and will contribute differently to the fake factor and background control regions. The general case will have a bias in the fake factor prediction given by Equation 9.32.

The sample dependence systematic is designed to cover potential biases in the fake factor prediction. The main problem with the bias due to multiple background sources is that it can be quite large. In the case of electron fakes, the relative difference in light-flavor and heavy-flavor fake factors, corresponding to the $\frac{\Delta f}{f}$ term in Equation 9.32, can be order 10, depending on the denominator definition. The systematic uncertainty associated to sample dependence is, in many cases, the leading source of uncertainty on the fake factor background prediction. Understanding and reducing the bias from multiple sources of background would lead to a significant reduction of the total uncertainty on the final background estimate.

The other potential problem associated to multiple sources of background is that a MC mismodeling can lead to an incorrect estimate of the sample dependence. Currently, the sample dependence is derived using a MC closure test. With multiple sources of background, this closure test depends on the relative fraction of the different backgrounds. If the relative background composition is mis-modeled, the closure test performed in MC may not be applicable to the background predicted in data. This could lead to the presence of a bias in data that is not covered by the sample dependence derived in MC. This is a potential failure mode in the fake factor method that could lead to a bias of physics results.

The following section presents an extension to the fake factor method to allow for multiple sources of background. This extension addresses the concerns associated to the bias described above. In addition, the techniques presented in the following may be able to be used to improve the determination of the sample dependence systematic by directly measuring the variation due to different sources of background.

9.4.2 Extending the Fake Factors Method to Account for Multiple Sources of Background

An extension to the fake factor method to include multiple sources of background was actually already made in Section 9.3 to predict the W+jet background in the $e\mu$-channel. There are two

sources of W+jet background in the $e\mu$-channel: $W \to e\nu$ with a fake muon, and $W \to \mu\nu$ with a fake electron. These background sources contribute to the same final state at different levels. The total W+jet background was calculated as

$$\mathrm{N}_{\mathrm{e}+\mu} \quad = \quad f_e \times \mathrm{N}_{(\mu+\mathrm{D}_e)} + f_\mu \times \mathrm{N}_{(e+\mathrm{D}_\mu)} \tag{9.33}$$

where, $\mathrm{N}_{\mathrm{e}+\mu}$ represents the total background prediction in the $e\mu$-channel, $f_e(f_\mu)$, represents the electron (muon) fake factor, and $\mathrm{N}_{(\mu+\mathrm{D}_e)}(\mathrm{N}_{(e+\mathrm{D}_\mu)})$ represents the number of events in the electron (muon) background control region. The multiple background sources are accommodated by defining a separate control region for each background and by applying a separate fake factor corresponding to the particular background source. The different background control regions are chosen to select the different sources of background. Here, the $\mathrm{N}_{(\mu+\mathrm{D}_e)}(\mathrm{N}_{(e+\mathrm{D}_\mu)})$ control region selects $W \to \mu\nu$ + fake electron ($W \to e\nu$ + fake muon) events. Separate fake factors are then used to relate the different control regions to the signal region.

The $e\mu$ example is a special case of a more the general scenario. The separate $e\mu$ sources of background differ in both the flavor of the lepton being faked and the flavor of the lepton in the W decay. The separate fake factors, used in Equation 9.33, extrapolate to different regions of particle identification space; f_e extrapolates to identified electrons, and f_μ extrapolates to identified muons. It is only by virtue of a symmetry that these events contribute to the same signal region. In this special case, the measurement of the two fake factors is decoupled. The electron and muon fake factors can be determined independently and applied separately without double counting. In this case, the fake factor predictions of the two background sources factorizes, and the extension to include both types of background is trivial.

The extension used in the $e\mu$ case cannot be applied when the different backgrounds arise from the same object being faked. For these backgrounds, the only difference is in the source of the object that is misidentified. The trivial extension used before fails because both backgrounds extrapolate to the same region of PID space. The fake factor extrapolates from denominators in the control region to the misidentified numerators in the signal region. If the fake factors were calculated independently and applied separately, the terms would extrapolate to the same background. Adding the contributions from the separate control regions would lead to an over estimate of the total background.

An example of this more complicated case is the light-flavor and heavy-flavor background to electrons. Both light-flavor and heavy-flavor jets can be misidentified as electrons. In the ee-channel, for example, W+jet background arises from either W+light-flavor or W+heavy-flavor events where, in both cases, the W decays to an electron. For each of these backgrounds, the object that is faked is an electron. If separate light-flavor and heavy-flavor denominators, $\mathrm{D}_{\mathrm{l.f.}}$ and $\mathrm{D}_{\mathrm{h.f.}}$, were defined,

and the background was estimated as

$$\mathrm{N}_{e+e} \quad = \quad f_{\mathrm{l.f.}} \times \mathrm{N}_{(e+\mathrm{D}_{\mathrm{l.f.}})} + f_{\mathrm{h.f.}} \times \mathrm{N}_{(e+\mathrm{D}_{\mathrm{h.f.}})}, \tag{9.34}$$

where the fake factors were calculated independently as

$$f_{\mathrm{l.f.}} = \frac{\mathrm{N}}{\mathrm{D}_{\mathrm{l.f.}}}, \text{ and } f_{\mathrm{h.f.}} = \frac{\mathrm{N}}{\mathrm{D}_{\mathrm{h.f.}}}, \tag{9.35}$$

the W+jet background in the signal region would be double counted. Both the light-flavor and heavy-flavor fake factors extrapolate to electron numerators. Each term in Equation 9.34 is an estimate of the total background, adding the two terms double counts.

The general case of multiple sources of background can be treated by generalizing the approach used in the $e\mu$ case. As before, separate control regions are defined for each source of background. However, the fake factors used to relate these control regions to the signal region are modified. Instead of extrapolating each control region to the full misidentified numerator sample in the signal region (and thus over-counting), fake factors are applied which only extrapolate to those numerators misidentified from the background source of the control region in question. The generalization comes from redefining the fake factors to avoid the over-counting. The modified fake factors will be referred to as the "corrected fake factors" in the following.

Returning to the example with the a and b-type backgrounds, the total background is predicted by the extended fake factor method as

$$\mathrm{N}_{\mathrm{X+N}} \quad = \quad f^a \times \mathrm{N}_{(X+\mathrm{D}_a)} + f^b \times \mathrm{N}_{(X+\mathrm{D}_b)}, \tag{9.36}$$

where f^a and f^b correspond to the corrected fake factors:

$$f^a = \frac{\mathrm{N}^a}{\mathrm{D}_a}, \text{ and } f^b = \frac{\mathrm{N}^b}{\mathrm{D}_b}. \tag{9.37}$$

Here, $\mathrm{D}_a(\mathrm{D}_b)$ is a denominator definition used to select $a(b)$-type background, and $\mathrm{N}^a(\mathrm{N}^b)$ represents misidentified numerators from $a(b)$-type background. Again, superscripts are used to indicated truth-level quantities. The denominator quantities, D_a and D_b, are observables; they are the number of reconstructed objects passing the denominator selection. However, the numerator terms in Equation 9.37 are not observables. Only the total number of objects passing the numerator selection is an observable; the source of the numerators cannot be directly determined. The corrected fake factors are written with superscripts because they rely on truth-level quantities. All of the complication with the extended method comes from determining the corrected fake factors. Double counting is avoided in Equation 9.36 because each term extrapolates only to those numerators misidentified by that type of background. The sum correctly gives the total background. Provided the corrected fake factors are known, the total background calculation is straightforward.

The corrected fake factors rely on truth-level quantities. They extrapolate denominators of a given definition, to numerators from a particular source. Because the source of a misidentified numerator is not observable, the corrected fake factors cannot be determined from the fake factor control region alone. They can, however, be extracted by the use of an additional fake factor control region. To see how this is done, it is easiest to start with an idealized case.

Assume for the moment that separate fake factor control regions could be defined that were each pure in a particular source of background. These are selections different from the background control regions that are composed of misidentified numerators and denominators from only one source of background. In this case, the corrected fake factors can easily be calculated in the separate fake factor control regions. In a given control region, all of the numerators are the result of misidentification from the background source corresponding to that control region. Although the source of the numerators is not observable, the fact that they are found in a particular control region indicates that they are from a particular source. The corrected fake factors can then be calculated from the ratio of numerators to the corresponding denominator definition in each fake factor control region.

For example, if separate a-type and b-type fake factor control regions can be selected, the corrected fake factors can be measured as

$$\begin{aligned} f_a &\equiv \left.\frac{\mathrm{N}}{\mathrm{D}_a}\right|_{a\text{-cr}} = f^a \\ f_b &\equiv \left.\frac{\mathrm{N}}{\mathrm{D}_b}\right|_{b\text{-cr}} = f^b \end{aligned} \tag{9.38}$$

where $f_a(f_b)$ is the ratio of numerators to $a(b)$-type denominators, measured in the $a(b)$-type control region as indicated by $|_{a(b)-\mathrm{cr}}$. The f_a and f_b quantities are written with subscripts because they are observables, with no dependence on truth-level information. Because the different control regions are pure, the observed f_a and f_b ratios are equivalent to the corrected fake factors. The separate fake factor control regions allow the corrected fake factors to be extracted. The total background can then be calculated using Equation 9.36.

The idealized case of pure fake factor control regions demonstrates the basic idea of how the corrected fake factors, which rely on truth-level quantities, can be obtained from separate control regions. In practice, the control regions are often cross contaminated. Even with impure control regions, the corrected fake factors can be extracted, provided the different control regions have different relative background contributions. Determining the corrected fake factors in the more realistic case is more complicated because the effects of the impurities need to be corrected. These corrections can be made using observable quantities in the different control regions.

The details of extracting the corrected fake factors in the more realistic case are provided in Appendix B.1. The upshot is that the observable quantities f_a and f_b, measured in the a and b-type

fake factor control regions, are related to the corrected fake factors, f^a and f^b, by ratios of the a and b-type denominators in the different control regions. The result is a system of two equations with two unknowns, $f^a$and f^b, which can be expressed in matrix form as

$$\begin{pmatrix} f_a|_{a\text{-cr}} \\ f_b|_{b\text{-cr}} \end{pmatrix} = \begin{pmatrix} 1 & \left(\frac{\mathrm{D}_b}{\mathrm{D}_a}\right)\Big|_{a\text{-cr}} \\ \left(\frac{\mathrm{D}_a}{\mathrm{D}_b}\right)\Big|_{b\text{-cr}} & 1 \end{pmatrix} \begin{pmatrix} f^a \\ f^b \end{pmatrix}. \tag{9.39}$$

The left-hand side, and the matrix elements are all observable quantities which can be measured in the fake factor control regions. The corrected fake factors can be solved for provided the matrix is non-singular, or equivalently, $\left(\frac{\mathrm{D}_b}{\mathrm{D}_a}\right)\Big|_{a\text{-cr}}$ is different than $\left(\frac{\mathrm{D}_b}{\mathrm{D}_a}\right)\Big|_{b\text{-cr}}$. As long as the control regions have different background compositions, the corrected fake factors can be extracted. The total background can then be predicted with Equation 9.36.

An example of the implementation of the fake factor procedure with two sources of background is presented in Section 9.4.4. In this example, the fake factor method is extended to model electron background from both light-flavor and heavy-flavor jets.

The formalism outlined in this section, and detailed in the appendix, to include an additional source of background can be further extended to accommodate multiple additional sources of background. Each additional background source requires: an additional denominator definition, an additional fake factor control sample, and an additional term in the total background prediction. Observable ratios are measured in the fake factor control regions. These are related to the corrected fake factors by a matrix, composed of ratios of the denominator definitions. An example with three sources of background is presented in Appendix B.2. In this example, the formalism to extend the fake factor method to model electron background from light-flavor, heavy-flavor, and prompt photons is given.

9.4.3 Bias in Extended Method

One of the advantages of the extended fake factor procedure is that the potential bias from sample dependence is reduced. To see this, the calculation of the bias in Section 9.4.1 is repeated here for the extended method.

In the extended fake factor method, the corrected fake factors, as determined in the different fake factor control region, are used to predict the background, see Appendix B.1 for details. The

corrected fake factors can be expressed in terms of the truth-level fake factors as

$$\begin{aligned} f^a\big|_{a\text{-cr}} &= \left.\frac{\mathrm{N}^a}{\mathrm{D}_a^a + \mathrm{D}_a^b}\right|_{a\text{-cr}} \\ &= F^a \times \frac{1}{1 + \left.\frac{\mathrm{D}_a^b}{\mathrm{D}_a^a}\right|_{a\text{-cr}}} \\ &= F^a \times \left(1 - \epsilon^{b\text{-in-D}_a}\big|_{a\text{-cr}}\right), \end{aligned} \tag{9.40}$$

where, $\mathrm{D}_a^a(\mathrm{D}_a^b)$ are type a denominators from background source $a(b)$, and $\epsilon^{b\text{-in-D}_a}\big|_{a\text{-cr}} = \frac{\mathrm{D}_a^b}{\mathrm{D}_a}$ is the fraction of a type denominators that are from the b-type background source. Similarly, f^b is given by:

$$f^b\big|_{b\text{-cr}} = F^b \times \left(1 - \epsilon^{a\text{-in-D}_b}\big|_{b\text{-cr}}\right). \tag{9.41}$$

The background prediction with the extended method is given by:

$$\begin{aligned} \mathrm{N}_{\mathrm{X+N}} &= f^a \times \mathrm{N}_{(X+\mathrm{D}_a)} + f^b \times \mathrm{N}_{(X+\mathrm{D}_b)}, \\ &= F^a \times \left(1 - \epsilon^{b\text{-in-D}_a}\big|_{a\text{-cr}}\right) \times \mathrm{N}_{(X+\mathrm{D}_a)} + F^b \times \left(1 - \epsilon^{a\text{-in-D}_b}\big|_{b\text{-cr}}\right) \times \mathrm{N}_{(X+\mathrm{D}_b)} \end{aligned} \tag{9.42}$$

The true background estimate is given by:

$$\mathrm{N}_{\mathrm{X+N}}^{\mathrm{True}} = F^a \times \mathrm{N}_{(\mathrm{X+D}_a^a)} + F^b \times \mathrm{N}_{(\mathrm{X+D}_b^b)}, \tag{9.43}$$

which can be written in terms of the inclusive D_a and D_b denominators as

$$\mathrm{N}_{\mathrm{X+N}}^{\mathrm{True}} = F^a \times (1 - \epsilon^{b\text{-in-D}_a}\big|_{\mathrm{bkg.\text{-}cr}})\mathrm{N}_{\mathrm{X+D}_a} + F^b \times (1 - \epsilon^{a\text{-in-D}_b}\big|_{\mathrm{bkg.\text{-}cr}})\mathrm{N}_{\mathrm{X+D}_b}, \tag{9.44}$$

where $\big|_{\mathrm{bkg.\text{-}cr}}$ indicates that the denominator fractions are evaluated the background control region.

The relative bias of the fake factor estimate is given by:

$$\begin{aligned} \frac{\mathrm{Bias}}{\mathrm{N}_{\mathrm{X+N}}} &= \frac{\mathrm{N}_{\mathrm{X+N}}^{\mathrm{True}} - \mathrm{N}_{\mathrm{X+N}}}{\mathrm{N}_{\mathrm{X+N}}} \\ &= (\epsilon^{b\text{-in-D}_a}\big|_{a\text{-cr}} - \epsilon^{b\text{-in-D}_a}\big|_{\mathrm{bkg.\text{-}cr}})\frac{F^a \mathrm{N}_{\mathrm{X+D}_a}}{\mathrm{N}_{\mathrm{X+N}}} + (\epsilon^{a\text{-in-D}_b}\big|_{b\text{-cr}} - \epsilon^{a\text{-in-D}_b}\big|_{\mathrm{bkg.\text{-}cr}})\frac{F^b \mathrm{N}_{\mathrm{X+D}_b}}{\mathrm{N}_{\mathrm{X+N}}}, \\ &= \Delta\epsilon^{b\text{-in-D}_a}\frac{F^a \mathrm{N}_{\mathrm{X+D}_a}}{\mathrm{N}_{\mathrm{X+N}}} + \Delta\epsilon^{a\text{-in-D}_b}\frac{F^b \mathrm{N}_{\mathrm{X+D}_b}}{\mathrm{N}_{\mathrm{X+N}}}, \end{aligned} \tag{9.45}$$

The background prediction is unbiased if, $\Delta\epsilon^{b\text{-in-D}_a} = 0$, *i.e.,* if there is the same fraction of a-type denominators from b-type background in the a-type control region as in the background control region, and if $\Delta\epsilon^{a\text{-in-D}_b} = 0$, *i.e.,* if there is the same fraction of b-type denominators from a-type background in the b-type control region as in the background control region. If however, the impurities of the a and b-type denominators are different in the different samples there will be a bias

given by Equation 9.45. The advantage of the extended method is that the bias no longer scales as the relative difference in fake factor, as in Equation 9.32. In addition, the bias no longer goes as the difference in background fraction, but as the difference in the impurity of the denominator definitions. This is advantageous because the denominators can be chosen such that the relative impurities are small. By choice of denominator definition, the bias can be made arbitrarily small, independently of differences in background fake factor or sample composition.

This concludes the general discussion of the formalism of the extended fake factor procedure. The remainder of the chapter discusses the implementation of this formalism to include electron background from heavy-flavor decays. The extended fake factor method was used in the W+jet background prediction of the WW cross section measurement presented in Chapter 10.

9.4.4 Application to Electron Heavy-Flavor Fakes

As discussed above, misidentified electrons have significant contributions from both light-flavor and heavy-flavor jets. In addition, the fake factor from heavy-flavor jets is expected to be significantly higher than that of light-flavor jets, given that heavy-flavor jets can contain real electrons from semi-leptonic c-quark and b-quark decays. With these different sources of background, contributing with different fake factors, the electron fakes provide a natural application for the extended fake factor procedure. This section presents the application of the extended fake factor method to include electron fakes from heavy-flavor decays in the W+jet background model.

Unlike electrons, nearly all high p_{T} fake muons are produced by heavy flavor jets. In this case, the standard fake factor procedure already accounts for heavy-flavor; muons from heavy-flavor decays constitute both the sample used to derive the fake factor, and the W+jet control sample to which it is applied. At lower p_{T}, there is a significant contribution of misidentified muons from meson decays in flight. Modeling these low p_{T} muons provides another potential application of the extended fake factor method. The extended fake factor procedure is not applied to muons in the following.

The example of electron background modeling presented here will follow closely that of the simple fake factor method presented in Section 9.3. The background being considered is W+jet background to a generic WW analysis. The numerator definition provided in Table 9.1 is used as the electron selection in the signal region. Many of the fake factor measurement techniques, described above, will be applied in the following.

In the extended fake factor method, the electron background is calculated as

$$\mathrm{N}_{\mathrm{X+N}} = f^{\mathrm{l.f.}} \times \mathrm{N}_{(\mathrm{X+D_{l.f.}})} + f^{\mathrm{h.f.}} \times \mathrm{N}_{(\mathrm{X+D_{h.f.}})}, \tag{9.46}$$

where $\mathrm{N}_{\mathrm{X+N}}$ represents the background in the signal region, $f^{\mathrm{l.f.}}(f^{\mathrm{h.f.}})$ is the corrected light-flavor

(heavy-flavor) fake factor, and $N_{(X+D_{l.f.})}(N_{(X+D_{h.f.})})$ represents the light-flavor(heavy-flavor) background control region. The "X" represents the other, unrelated event selection requirements. In the ee-channel "X" would include the presence of an additional identified electrons; in the $e\mu$-channel the "X" would include the presence of an additional identified muon. The first term on the right-hand side of Equation 9.46 predicts the background from W+light-flavor, whereas the second term predicts the W+heavy-flavor background. The corrected fake factors are defined as

$$f^{l.f.} = \frac{N^{l.f.}}{D_{l.f.}}, \tag{9.47}$$

$$f^{h.f.} = \frac{N^{h.f.}}{D_{h.f.}}, \tag{9.48}$$

where $D_{l.f.}(D_{h.f.})$ represents the light-flavor(heavy-flavor) denominator definition, and $N^{l.f.}(N^{h.f.})$ corresponds to numerators from light-flavor(heavy-flavor).

As in the simple fake factor method, the first step in the extended fake factor procedure is to define the denominator selections. Two electron denominator definitions are needed: one in which the misidentification rate from light-flavor jets is increased, and one in which the misidentification rate of heavy-flavor jets is enhanced. Examples of heavy-flavor denominator definitions are given in Table 9.10. Semi-leptonic heavy-flavor decays result in non-isolated electrons in the final state. These electrons are mainly suppressed by the isolation requirements. They tend to pass the isEM requirements. To select electrons from heavy-flavor decays, the "Isolation"-denominator requires the tight isEM selection and reverses the isolation requirement. Heavy-flavor decays are also associated with displaced vertices. The displaced vertices result in high b-tag weights associated to the reconstructed jets that overlap the electrons. The "Isolation–BTag" and "BTag"-denominators exploit this by requiring the electron to overlap with a reconstructed jet that is b-tagged. The "Isolation–BTag"-denominator adds the tagged jet requirement to the "Isolation"-denominator selection. This increases the purity of the heavy-flavor denominators, at a cost of a smaller sample size. The "BTag"-denominator requires an overlapping b-jet, reverses isolation, and makes no requirement on isEM selection. This denominator definition has a large misidentification rate due to the lack of isEM requirement. The heavy-flavor purity is achieved by the b-tag requirement.

Light-flavor decays are suppressed by both the isolation and isEM requirements. Examples of light-flavor denominator definitions are given in Table 9.11. In order to increase the misidentification rate from light-flavor jets, the isEM requirement has been reversed. An isolation requirement is kept in order to reduce the systematic associated to the underlying jet kinematics, seen by the away-side jet variation. The "Pid"-denominator makes the full isolation selection of the signal region, whereas the "Pid-And-Iso"-denominator loosens the isolation requirement to increase the misidentification rate.

"Isolation"-Denominator	"Isolation–BTag"-Denominator	"BTag"-Denominator
Electron Candidate	Electron Candidate	Electron Candidate
No Track Isolation Selection	No Track Isolation Selection	No Track Isolation Selection
$0.14 < \frac{E_T^{Cone30}}{E_T} < 0.5$	$0.14 < \frac{E_T^{Cone30}}{E_T} < 0.5$	$0.14 < \frac{E_T^{Cone30}}{E_T} < 0.5$
–	–	–
Pass isEM Tight	Pass isEM Tight	–
–	Has Overlapping B-Jet	Has Overlapping B-Jet

Table 9.10: Examples of heavy-flavor electron denominator definitions.

"Pid"-Denominator	"Pid-And-Iso"-Denominator
Electron Candidate	Electron Candidate
$\lvert z0\rvert < 10$mm, $d0/\sigma(d0) < 10$	$\lvert z0\rvert < 10$mm, $d0/\sigma(d0) < 10$
$\frac{E_T^{Cone30}}{E_T} < 0.14$	$\frac{E_T^{Cone30}}{E_T} < 0.28$
$\frac{P_T^{Cone30}}{E_T} < 0.13$	$\frac{P_T^{Cone30}}{E_T} < 0.26$
Fails isEM Medium	Fails isEM Medium

Table 9.11: Examples of light-flavor electron denominator definitions.

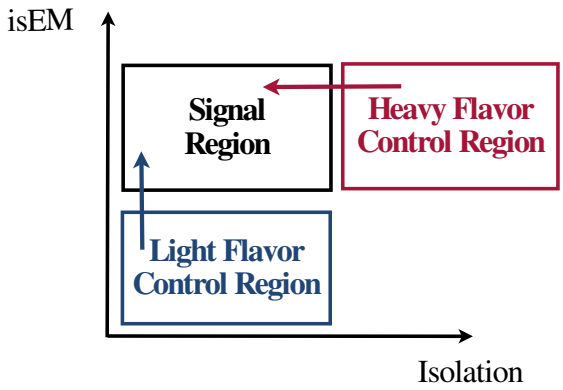

Figure 9.31: Conceptual description of the extended fake factor method using the "Pid"-denominator for $D_{l.f.}$ and the "Isolation"-denominator for $D_{h.f.}$. Each control region is extrapolated into the signal region along a different dimension of "PID"-space.

A conceptual representation of the electron background prediction using the extended fake factor method is shown in Figure 9.31. The example shown uses the "Isolation"-denominator for heavy-flavor and the "Pid"-denominator for the light-flavor. The heavy-flavor control region is shown in red. It extrapolates into the signal region using isolation. The light-flavor control region is shown in blue. The light-flavor background is extrapolated into the signal region along the isEM dimension. A similar picture applies when using the other denominator definitions, except the extrapolation is from different regions of PID space.

To extract the corrected fake factors, two di-jet control regions are needed: one enriched in misidentified electrons from light-flavor, and one enriched in misidentified electrons from heavy-flavor. As discussed in Section 9.4.2, the fake factor control regions are not required to be pure. What matters is that the control regions have different relative fractions of fakes from light-flavor and heavy-flavor. The fake factor control regions are selected using the same requirements as the electron fake factor control region described in Section 9.3, except for the requirement on the away-side jet. For the heavy-flavor control region, the away-side jet is required to be b-tagged. The idea is that in $b\bar{b}$ events the flavor of the away-side jet is correlated to that of the near side jet. By requiring an identified b-jet elsewhere in the event, the fraction of electrons from heavy-flavor decays will be increased. The light-flavor control region is selected by vetoing events with an away-side b-tagged jet. By suppressing b-jets elsewhere in the event, the fraction of electrons from heavy-flavor decays will be suppressed. The cross contamination of the control regions is corrected using the formalism presented in Section 9.4.2 and Appendix B.1.

The same general techniques used to measure the electron fake factors in Section 9.3 are applicable to the extended method. The numerator and denominator samples are collected using the primary electron trigger when the isEM selection is tighter than medium. Denominators that reverse, or do not select on, isEM are collected using the etcut supporting triggers. Both the light-flavor and the heavy-flavor control regions are corrected for electro-weak contamination. W and Z vetoes are applied, and the MC is used to subtract any residual contamination. As before, the variation in the measured fake factor when changing the away-side jet requirement is used as a guide to the associated systematic uncertainty.

The corrected light-flavor and heavy-flavor fake factors are shown in Figures 9.32 and 9.33. Figure 9.32 shows the light-flavor fake factors, $f^{\text{l.f.}}$, after correction for the heavy-flavor contamination using Equation 9.39. The corrected fake factor using the "Pid-And-Iso"-denominator is shown on the left, and the "Pid"-denominator is used on the right. The corrected light-flavor fake factors are similar to the electron fake factors using the "Pid" and "Pid-And-Iso"-denominators in Figure 9.11. Smaller values are measured for the corrected fake factors because the heavy-flavor contribution has been removed from the numerators.

The heavy-flavor corrected fake factors are shown in Figure 9.33. The result using the "Isolation"-denominator is shown on the left, the "Isolation–BTag"-denominator is shown in the center, and the fake factor using the "BTag"-denominator definition is shown on the right. The corrected fake factor using the "Isolation"-denominator is similar to the electron fake factor using the "Isolation"-denominator definition in Figure 9.11. The corrected fake factor is smaller because the contribution from light-flavor has been removed. It is interesting to note that the dependence on away-side jet is

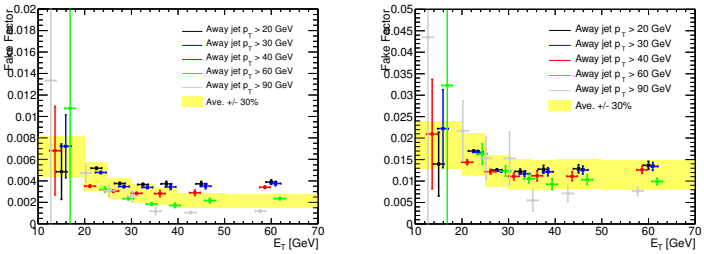

(a) (b)

Figure 9.32: Corrected light-flavor fake factors, $f^{\text{l.f.}}$, using the numerator selection defined in Table 9.1, and the "Pid"-denominator (b), and the "Pid-And-Iso"-denominator (a).

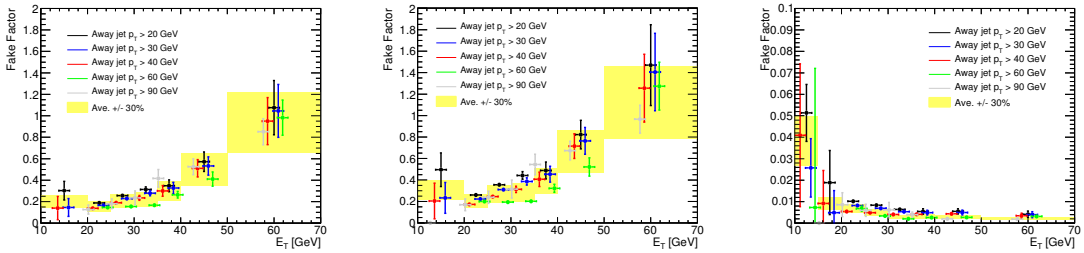

(a) (b) (c)

Figure 9.33: Corrected heavy-flavor fake factors, $f^{\text{h.f.}}$, using the numerator selection defined in Table 9.1, and the "Iso"-denominator (a), the "Isolation–BTag"-denominator (a), the "BTag"-denominator (c).

dramatically reduced after removing the light-flavor component. This is an indication that the strong away-side jet dependence seen before is a result of the light-flavor component of the fake factors. The corrected fake factor with the "Isolation–BTag"-denominator is slightly larger than that using the "Isolation"-denominator, as the control region is further reduced by the b-tag requirement. The heavy-flavor fake factor using the "BTag"-denominator is much smaller than the other two. This is a result of the increased misidentification rate from the loosened isEM selection in the denominator definition. This leads to a largely independent heavy-flavor background prediction.

The same data-driven validation techniques discussed in Section 9.3.5 are applicable to the W+jet prediction with the extended fake factor method. Figure 9.34 shows the electron background modeling in the same-sign control region. The figure shows the electron p_{T} distribution in same-sign μe events with a leading muon. The data are shown in the black points, and the background model is shown in the stacked histogram. The blue histogram, labeled "WJet (e-lf fake)", gives the misidentified electron background from light-flavor predicted by the fake factor procedure. The lighter

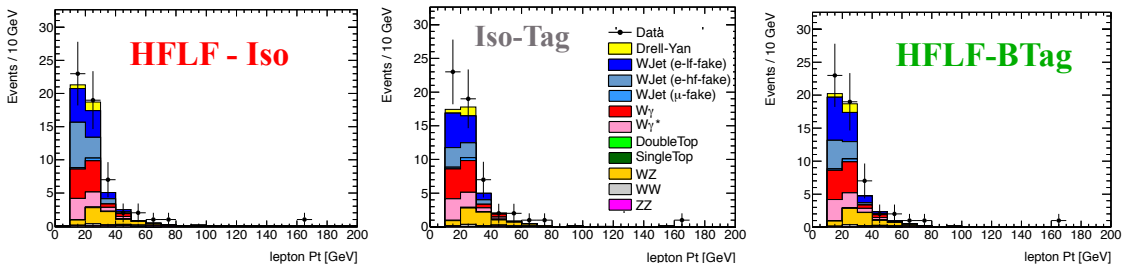

(a) (b) (c)

Figure 9.34: Test of the W+jet modeling in same sign events using separate light-flavor and heavy-flavor predictions. Sub-leading p_{T} distribution is shown for events in the μe-channel with a same sign requirement. The fake predictions are made with the fake factor procedure using: (a) the "Pid" light-flavor denominator definition and the "Isolation" heavy-flavor denominator definition. (b) the "Pid" light-flavor denominator definition and the "Isolation" heavy-flavor denominator definition. (c) the "Pid-And-Iso" light-flavor denominator definition and the "BTag" heavy-flavor denominator definition. Results are from the 5.8 fb^{-1} 7 TeV data set.

blue histogram, labeled "WJet (e-hf fake)", gives the misidentified background prediction from heavy-flavor. Figure 9.34a shows the background prediction using the "Pid"-denominator for the light-flavor prediction and the "Isolation"-denominator for the heavy-flavor prediction. Figure 9.34b uses the "Pid"-denominator for the light-flavor prediction and the "Isolation–BTag"-denominator for the heavy-flavor prediction. Figure 9.34c shows the prediction using the "Pid-And-Iso" for the light-flavor denominator and "BTag" for the heavy-flavor denominator. Overall, the observed same-sign data is well modeled by the various background predictions. The level of agreement is similar to inclusive electron prediction in Figure 9.27. The different denominator definitions give consistent results.

The opposite-sign validation regions are shown in Figures 9.35 and 9.36. The modeling of the electron p_{T} in μe-channel for the "Tight-Inter-Iso" region is shown in Figure 9.35. Figure 9.35a uses the "Pid" light-flavor denominator and the "Isolation" heavy-flavor denominator definition. The isolation requirements on the denominator definitions have been adjusted to treat the intermediate isolation region as the signal region, *e.g.,* the isolation requirement in the "Isolation"-denominator now reverses intermediate isolation. Figure 9.35b shows the prediction using the "Pid" light-flavor denominator and the "Isolation–BTag" heavy-flavor denominator. The prediction in Figure 9.35c is made with the "Pid-And-Iso" light-flavor denominator and the "BTag" heavy-flavor denominator. A higher fraction of heavy-flavor background is predicted in the "Tight-Inter-Iso" opposite-sign validation region. This is expected from the charge correlation in W+heavy-flavor events discussed above. Overall, the data is well modeled in the "Tight-Inter-Iso" validation region. The combination

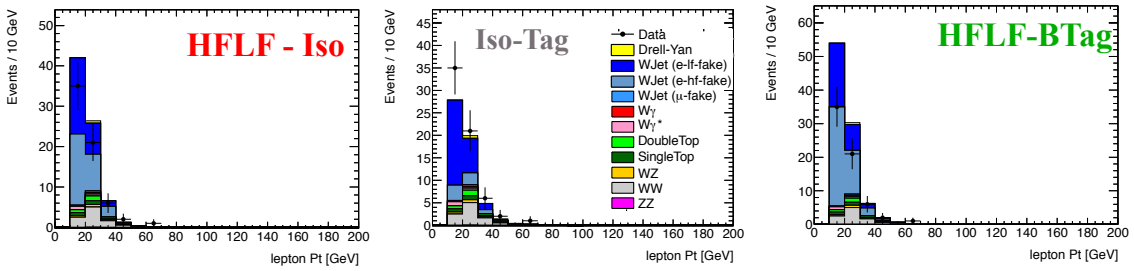

(a) (b) (c)

Figure 9.35: Test of the W+jet modeling in the "Tight-Inter-Iso" validation region using separate light-flavor and heavy-flavor predictions. Sub-leading p_{T} distribution is shown for events in the μe-channel. The W+jet predictions are made using: (a) the "Pid" light-flavor denominator definition and the "Isolation" heavy-flavor denominator definition. (b) the "Pid" light-flavor denominator definition and the "Isolation" heavy-flavor denominator definition. (c) the "Pid-And-Iso" light-flavor denominator definition and the "BTag" heavy-flavor denominator definition. Results are from the 5.8 fb^{-1} 7 TeV data set.

with the "Pid-And-Iso" light-flavor denominator and "BTag" heavy tends to over predict, but is consistent with the observed data with a systematic uncertainty of around 40%.

Similar distributions for the "Medium-Not-Tight" validation region are shown in Figure 9.36. Here, the denominator definitions have been adjusted to treat the "Medium-Not-Tight" region as the signal region. Again, a reasonable modeling of the validation region is seen. A smaller fraction of heavy-flavor background is expected from reversing the tight isEM in the signal region, which suppresses the semi-leptonic heavy-flavor decays. This expectation is born out in the relative background predictions.

Overall, the W+jet background modeling using simple fake factor method and the extended procedure gives consistent results. This supports the conclusion that sample dependence uncertainty from differences in heavy-flavor composition is not limiting the W+jet background prediction. In other analyses with significantly different heavy-flavor fractions, it will be more important to correctly model the light-flavor and heavy-flavor components individually. The extended fake factor procedure provides a framework in which this can be done. Longer term, it should be possible to use the separate heavy-flavor and light-flavor predictions in a data-driven assessment of the sample dependence systematic. This is left for the subject of another thesis.

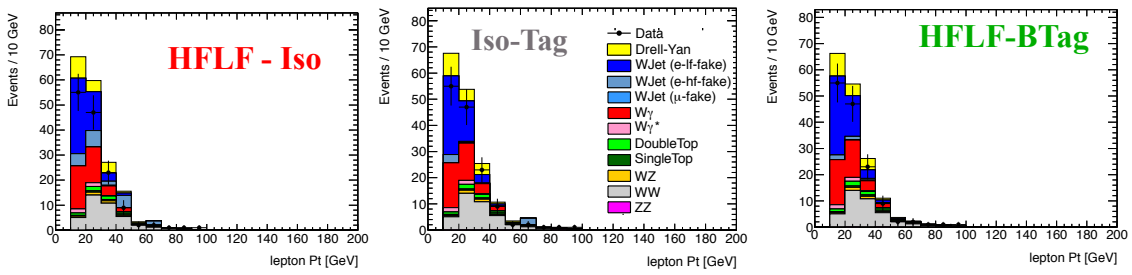

(a) (b) (c)

Figure 9.36: Test of the W+jet modeling in the "Medium-Not-Tight" validation region using separate light-flavor and heavy-flavor predictions. Sub-leading p_{T} distribution is shown for events in the μe-channel. (a) the "Pid" light-flavor denominator definition and the "Isolation" heavy-flavor denominator definition. (b) the "Pid" light-flavor denominator definition and the "Isolation" heavy-flavor denominator definition. (c) the "Pid-And-Iso" light-flavor denominator definition and the "BTag" heavy-flavor denominator definition. Results are from the 5.8 fb^{-1} 7 TeV data set.

9.5 Conclusion

This concludes the presentation and discussion of the fake factor method. Modeling background arising from misidentification is important for many analyses. It is critical that this can be done in a data-driven way. The fake factor method provides a generic, flexible approach to modeling background from misidentification. Although the details can be complicated, the underlying idea is straightforward. The fake factor method as described in this chapter has been used in both the WW cross-section measurement and the $H \to WW^{(*)} \to l\nu l\nu$ search presented in Chapters 10 and 11 of this thesis.

Chapter 10

WW Cross Section Measurement

This chapter presents a measurement of the WW production cross section in pp collisions with $\sqrt{s}$= 7 TeV [106]. The measurement is performed using data corresponding to an integrated luminosity of 1.02 fb^{-1}. The total measured cross section is $\sigma(pp \to WW) = 54.4 \pm 4.0$ (stat.) ± 3.9 (syst.) ± 2.0 (lumi.) pb, consistent with the Standard Model prediction of $\sigma(pp \to WW) = 44.4 \pm 2.8$ pb [101, 102]. As discussed in Chapter 8, a precise measurement of the WW cross section provides an important test of the Standard Model and is an important step in the search for the Higgs boson.

The remainder of this chapter is organized as follows: Section 10.1 provides a brief overview of the analysis. Section 10.2 describes the data set used for the measurement and the MC samples used to model the background. Section 10.3 describes the WW event selection. Section 10.4 presents the estimation of the backgrounds. Section 10.5 describes the WW acceptance and the associated systematic uncertainties. Section 10.6 presents the results.

10.1 Analysis Overview

A general introduction to the $WW \to l\nu l\nu$ final state, and the various sources of background is given in Chapter 8. The dominant Standard Model WW production mechanisms, shown in Figure 8.4, are s-channel and t-channel quark-anti-quark annihilation. The gluon-gluon fusion process contributes an additional 3% to the total production cross section. For this measurement, WW events from Higgs production via the gluon-gluon fusion process, Figure 8.1a, are not included in the simulation of the WW production and would contribute an additional $\sim$5% to the overall event rate, assuming a Higgs mass of 130 GeV. WW production through vector-boson fusion/scattering has also not been included in the WW modeling. The production cross-section for these processes is an order of magnitude smaller than the gluon-gluon fusion production mechanism [114, 115, 116].

The WW cross section measurement is performed in the fully leptonic decay channel $WW \to$

$l\nu l\nu$, using final states with electrons and muons. Throughout this chapter, "lepton" refers to an electron or a muon. After a basic selection of di-leptons events with large $E_{\mathrm{T}}^{\mathrm{miss}}$, the dominant contribution is from $t\bar{t}$ events. The $t\bar{t}$ process also produces a final state with two W bosons. For the cross section measurement, this process is not considered signal and is suppressed by vetoing events containing reconstructed jets. After the jet veto, no one single background dominates. There are significant sources of background from Z/γ^*, top ($t\bar{t}$ and Wt), W+jet, and other di-boson processes.

The cross section measurement is performed as a counting experiment in the fiducial phase space of the detector. This fiducial phase space includes geometric and kinematic acceptance requirements. The fiducial cross section is then extrapolated to the total phase space. The total production cross section is measured using the equation [117]:

$$\sigma(pp \to WW) = \frac{N_{\mathrm{Data}} - N_{\mathrm{Bkg}}}{A_{WW} C_{WW} \mathcal{L} \mathcal{B}}, \tag{10.1}$$

where N_{Data} is the number of observed data events, N_{Bkg} is the number of estimated background events, A_{WW} is the kinematic and geometric acceptance, C_{WW} is the ratio of the number of selected events to the number of events produced in the fiducial phase space, $\mathcal{L}$ is the integrated luminosity of the data sample, and $\mathcal{B}$ is the branching ratio for the Ws to decay to leptons. The branching ratio includes W decays to electrons or muons through tau leptons, $W \to \tau\nu_{\bar{\tau}} \to l\bar{\nu}_l\nu_{\bar{\tau}}$.

The total cross section extrapolates from the kinematic region selected by the measurement to the full phase space. This extrapolation introduces an additional systematic uncertainty, associated to the theoretical modeling of the WW signal. To avoid this additional uncertainty, a fiducial cross section is also reported. The fiducial cross section is defined [117] as

$$\sigma_{\mathrm{fid}}(pp \to WW) = \frac{N_{\mathrm{Data}} - N_{\mathrm{Bkg}}}{C_{WW} \mathcal{L}}. \tag{10.2}$$

The fiducial cross section allows for easier comparisons with alternative theoretical predictions and has a reduced theoretical uncertainty.

10.2 Data Set and MC Samples

The data set used for this analysis corresponds to 1.02 ± 0.04 fb^{-1} [118] of pp collisions at $\sqrt{s}$= 7 TeV, recorded between April and June of 2011. The uncertainty of the integrated luminosity obtained from Van der Meer scans is 3.7% and is dominated by the knowledge of the LHC beam currents.

The data set was collected using inclusive single-muon and single-electron triggers. Events were selected requiring either a single electron with $p_{\mathrm{T}} > 20$ GeV and $|\eta| < 2.5$, or a single muon with $p_{\mathrm{T}} > 18$ GeV and $|\eta| < 2.4$. The triggering electron is required to pass the medium isEM

requirement, see Chapter 7. This combination of triggers results in $\approx 100\%(98\%)$ trigger efficiency for WW events in the $e\mu$ and ee ($\mu\mu$) channels, passing the WW event selection described below.

All of the detector sub-systems were required to be operating under nominal conditions during the taking of the data used in this analysis. Overall quality criteria are applied in order to suppress non-collision backgrounds. In addition, events are rejected if an electron or jet is found within a region of the detector that was not fully operational.

Backgrounds are estimated using a combination of Monte Carlo (MC) samples including a full GEANT [119] simulation of the ATLAS detector and control samples from data. The simulation includes the modeling of multiple pp interactions in the same bunch crossing (pile-up), as well as corrections determined from data to improve the modeling of reconstructed objects. The corrections applied to the MC are:

MC Corrections
Lepton trigger efficiency
Lepton identification efficiency
Lepton p_{T} smearing
Pile-up re-weighting
Jet veto efficiency
b-Jet veto efficiency

The Z/γ^* background is modeled using the Alpgen [120] Monte Carlo generator interfaced to Pythia [121] for parton showering. The $t\bar{t}$ background is modeled using MC@NLO [122], and AcerMC [123] is used to model Wt production. Monte Carlo estimates of the $W\gamma$, WZ, and ZZ backgrounds are obtained using a combination of Alpgen and Pythia, for $W\gamma$, and `HERWIG` [124] with `JIMMY` [125], for the others. The di-boson cross sections are normalized to the next-to-leading order (NLO) cross sections calculated with `MCFM` [126].

10.3 Event Selection

The electron and muon identification criteria are an input to the basic event selection.

Electrons are reconstructed and identified as described in Chapter 7. Electrons are required to lie within the fiducial regions of the calorimeters, $|\eta| < 1.37$ or $1.52 < |\eta| < 2.47$, and have $p_{\mathrm{T}} > 25$ GeV. The lower p_{T} electron in the ee-channel is required to have $p_{\mathrm{T}} > 20$ GeV. The tight isEM requirement[23] is used to select electrons. In addition to the tight isEM requirement, electrons are required to be isolated in the calorimeter and tracker and to satisfy longitudinal and transverse

[23] The isEM menu used in this analysis corresponds to the 2011 data-optimized menu described in Chapter 7.

Electron Identification Criteria
Tight isEM requirement
Calorimeter Isolation: $E_T^{\text{Cone }0.3} < 4$ GeV
Track Isolation: $p_T^{\text{Cone }0.3}/p_{\text{T}} < 0.1$
Transverse Impact Parameter: $\frac{d_0}{\sigma_{d_0}} < 10$
Longitudinal Impact parameter: $\lvert z_0\rvert < 10$ mm

Table 10.1: Electron identification criteria.

Muon Identification Criteria
Basic Track Quality.
Calorimeter Isolation Requirement: $E_T^{\text{Cone }0.2}/p_{\text{T}} < 0.15$
Track Isolation Requirement: $p_T^{\text{Cone }0.2}/p_{\text{T}} < 0.1$
Transverse Impact parameter requirement: $\frac{d_0}{\sigma_{d_0}} < 10$
Longitudinal Impact parameter requirement: $\lvert z_0\rvert < 10$ mm

Table 10.2: Muon identification criteria.

impact parameter requirements. The specific selection used is listed in Table 10.1. The calorimeter isolation energy is corrected for the lateral leakage of the electron shower into the isolation cone and for the increased isolation energy due to in-time pile-up. The overall electron selection efficiency is ∼80% for the central region, $|\eta| < 0.8$ and decreases to ∼65% in the forward region, $2.0 < |\eta| < 2.47$.

The muon reconstruction algorithm combines Inner Detector tracks with tracks from the Muon Spectrometer. The combined muons are required to have a $p_{\text{T}} > 20$ GeV and $|\eta| < 2.4$. In the $\mu\mu$-channel, at least one muon must have $p_{\text{T}} > 25$ GeV. Muons from decays in flight or semi-leptonic heavy-flavor decays are suppressed by calorimeter-based and track-based isolation criteria and by requirements on the transverse and longitudinal impact parameters. The specific selection used in listed in Table 10.2. The overall muon selection efficiency is ∼95%.

A basic pre-selection is used to select di-lepton events. The di-lepton pre-selection criteria are given in Table 10.3. Events are required to have two, and only two, identified leptons. Removing events with more than two leptons suppresses the contribution from WZ events. In the $e\mu$-channel, the electron is required to have p_{T} above 25 GeV, whereas the muon is only required to have p_{T} above 20 GeV. The asymmetric requirement is justified by the higher electron fake rate.

After the pre-selection, the dominant contribution to same flavor events is from $Z/\gamma* \to \ell^+\ell^-$. At this point, the WW signal contributes only ∼0.1% to the selected events. For the $e\mu$-channel final state, the WW signal contributes ∼10%, where the major background contributions come from top production, ∼50%, and $Z \to \tau\tau$, 35%. Figure 10.1 shows the di-lepton invariant mass distributions after the di-lepton pre-selection.

1) Primary Vertex Selection:
Events are required to have a reconstructed primary vertex with at least three tracks.

2) Di-leptons:
Events must have two, and only two, selected, oppositely charged leptons of $p_{\mathrm{T}} > 20$ GeV. In the ee-channel, at least one electron must have $p_{\mathrm{T}} > 25$ GeV, in the $\mu\mu$-channel, at least one muon must have $p_{\mathrm{T}} > 25$ GeV, in the $e\mu$-channel, the electron must have $p_{\mathrm{T}} > 25$ GeV.

3) Trigger/Trigger matching:
One of the single lepton triggers must be fired, and at least one of the selected leptons must match the trigger.

Table 10.3: Basic di-lepton pre-selection criteria.

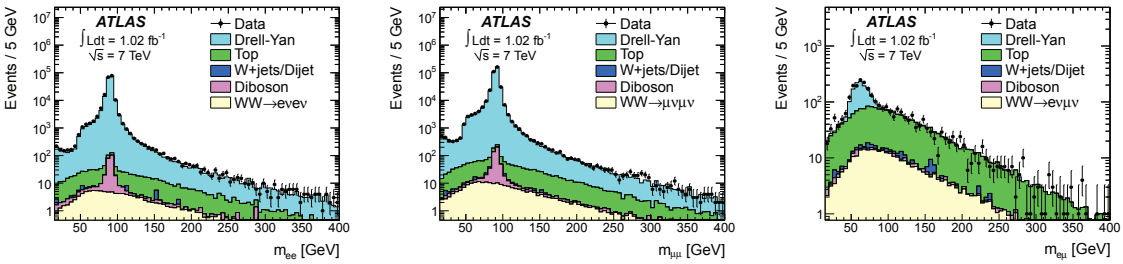

Figure 10.1: Invariant mass in the three channels after the pre-selection requirements. The left-hand plot shows the ee-channel, the middle plot the $\mu\mu$-channel, and the right-hand plot the $e\mu$-channel. The points show the observed data and the stacked histograms represent the signal and background expectation. Scale factors as outlined in Section 10.2 are applied to MC.

Requirement	ee-channel	$\mu\mu$-channel	$e\mu$-channel
Pre-selection	Basic pre-selection in Table 10.3		
low m_{ll}	$m_{ll} > 15$ GeV	$m_{ll} > 15$ GeV	$m_{ll} > 10$ GeV
Z-veto	$\lvert m_{ll} - m_Z \rvert > 15$ GeV	$\lvert m_{ll} - m_Z \rvert > 15$ GeV	-
$E_{\mathrm{T}}^{\mathrm{miss,Rel}}$	$E_{\mathrm{T}}^{\mathrm{miss,Rel}} > 40$ GeV	$E_{\mathrm{T}}^{\mathrm{miss,Rel}} > 45$ GeV	$E_{\mathrm{T}}^{\mathrm{miss,Rel}} > 25$ GeV
Jet-veto	No reconstructed jets above 25 GeV and $\lvert\eta\rvert < 4.5$.		
b-Jet-veto	No identified b-jets above 20 GeV and $\lvert\eta\rvert < 2.5$.		

Table 10.4: WW Event Selection.

A summary of the event selection used for the WW cross section measurement is given in Table 10.4. The invariant mass of the di-lepton pair is required to be greater than 15 (10) GeV for same-flavor (opposite-flavor) events to remove low mass resonances and the low mass spectrum not modeled by MC. In addition, the large Z boson contribution in the same-flavor channels is reduced by requiring the di-lepton invariant mass to satisfy $|M_{\ell\ell} - M_Z| > 15$ GeV.

The selected di-lepton events are required to have large missing energy, consistent with the

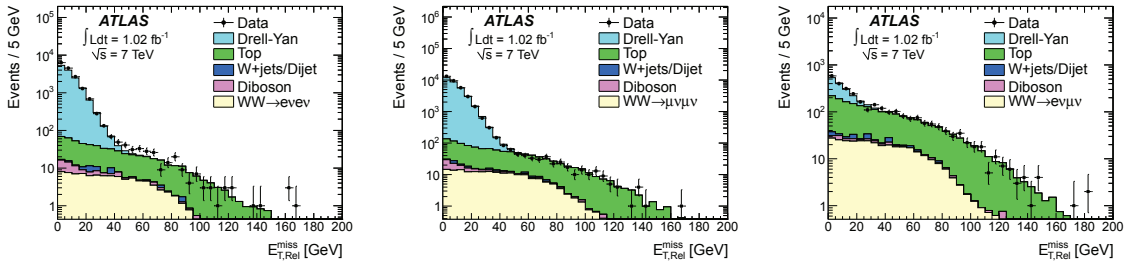

Figure 10.2: $E_{\mathrm{T}}^{\mathrm{miss,Rel}}$distributions for ee(left), $\mu\mu$(middle) and $e\mu$ channels after the Z-veto cut. The points show the observed data and the stacked histograms represent the signal and background expectation. Scale factors as outlined in Section 10.2 are applied to MC.

presence of final state neutrinos. A requirement is made on the relative missing energy, $E_{\mathrm{T}}^{\mathrm{miss,Rel}}$,

$$E_{\mathrm{T}}^{\mathrm{miss,Rel}} = \begin{cases} E_{\mathrm{T}}^{\mathrm{miss}} \times \sin(\Delta\phi_{l,j}) & \text{if } \Delta\phi_{l,j} < \pi/2 \\ E_{\mathrm{T}}^{\mathrm{miss}} & \text{otherwise.} \end{cases} \tag{10.3}$$

$E_{\mathrm{T}}^{\mathrm{miss,Rel}}$ suppresses $E_{\mathrm{T}}^{\mathrm{miss}}$ coming from mis-reconstructed leptons or τ-lepton decays, see Chapter 8 for more details. The $E_{\mathrm{T}}^{\mathrm{miss,Rel}}$ is required to be above 25 GeV in $e\mu$-channel, above 40 GeV in ee-channel, and above 45 GeV in the $\mu\mu$-channel. The cut value is increased by 5 GeV in the $\mu\mu$-channel relative to the ee-channel to account for the wider $E_{\mathrm{T}}^{\mathrm{miss,Rel}}$ distribution. The $E_{\mathrm{T}}^{\mathrm{miss,Rel}}$ distributions before the $E_{\mathrm{T}}^{\mathrm{miss,Rel}}$ requirement are shown in Figure 10.2

Background from top-quark production is rejected by vetoing events containing reconstructed jets. Jets are reconstructed from calorimeter clusters using the anti-k_{T} algorithm [127] with a radius parameter of $R = 0.4$. Events are rejected if they contain a reconstructed jet with $p_{\mathrm{T}} > 25$ GeV and $|\eta| < 4.5$. The calorimeter clusters associated with an electron will also be reconstructed as part of a jet. To remove this double counting, jets that overlap with selected electrons are not considered. The jet multiplicity distributions before the jet veto are shown in Figure 10.3.

A further 30% reduction of the top-quark background is achieved by rejecting events with a lower p_{T} jet, $p_{\mathrm{T}} > 20$ GeV, identified as a b-jet. The identification of b-jets combines information from the impact parameters and the reconstructed vertices of tracks within the jet [77]. The additional b-jet rejection reduces the WW acceptance by 1.3%.

The cut-flow for the WW event selection is shown in Table 10.5. The complete event selection yields 202 events in the $e\mu$-channel, 59 events in the ee-channel, and 64 events in the $\mu\mu$-channel. Kinematic distributions of the selected events are shown in Figure 10.4. Overall the kinematics of the selected signal events is consistent with WW production.

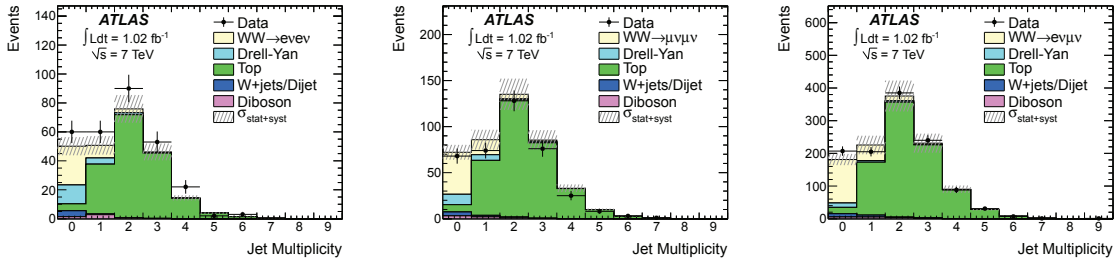

Figure 10.3: Jet multiplicity distributions for the ee-channel (left-hand side), the $\mu\mu$-channel (middle) and $e\mu$-channel (right-hand side) before the jet veto. The points show the observed data and the stacked histograms represent the signal and background expectation. Scale factors as described in Section 10.2 are applied to MC.

Cuts	ee-channel	$\mu\mu$-channel	$e\mu$-channel
Pre-selection	198273	376437	2872
low m_{ll}	197957	374644	2867
Z-mass veto	16296	34330	2867
$E_{\mathrm{T}}^{\mathrm{miss,Rel}}$cut	290	383	1165
Jet veto	60	68	207
b-jet veto	59	64	202

Table 10.5: Cut-flow for the WW selection Cut-flow for data collected in 2011 at 7 TeV for 1.02 fb^{-1} in the three di-lepton channels.

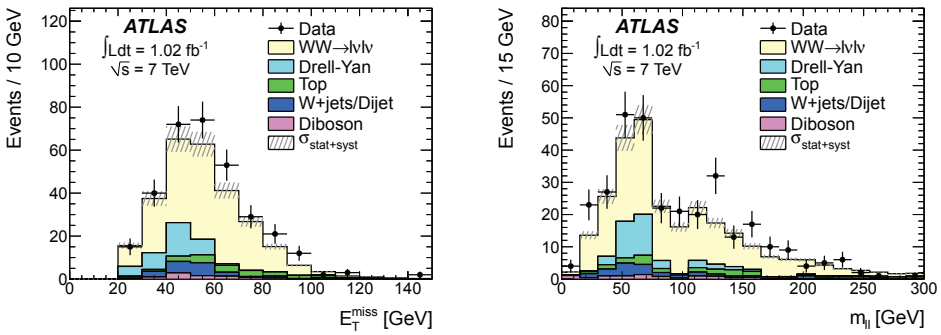

Figure 10.4: Kinematic distributions of selected events in the WW signal region. The $E_{\mathrm{T}}^{\mathrm{miss}}$ is shown on the left-hand side, m_{ll} is shown on the right-hand side. The same-flavor and opposite-flavor channels have been combined. The points show the observed data and the stacked histograms represent the signal and background expectation.

Background Process	$e\mu$-channel	ee-channel	$\mu\mu$-channel
DY	$13.0 \pm 2.1 \pm 1.6$	$12.5 \pm 2.3 \pm 1.4$	$10.9 \pm 2.5 \pm 1.4$
Top	$11.9 \pm 1.8 \pm 2.4$	$3.1 \pm 0.5 \pm 0.6$	$3.8 \pm 0.6 \pm 0.8$
W+jet	$10.0 \pm 1.6 \pm 2.1$	$4.1 \pm 1.3 \pm 0.9$	$4.2 \pm 1.1 \pm 1.3$
Di-boson	$5.1 \pm 1.0 \pm 0.7$	$2.1 \pm 0.8 \pm 0.3$	$2.9 \pm 0.4 \pm 0.4$
Total background	$40.0 \pm 3.3 \pm 3.6$	$21.7 \pm 2.8 \pm 1.8$	$21.8 \pm 2.8 \pm 2.1$
(Data Yields)	(202)	(59)	(64)

Table 10.6: The estimated background yields in the WW data sample. The first uncertainty is statistical, the second systematic.

10.4 Background Estimation

The selected data sample contains ∼25% background. A summary of the estimated backgrounds in the WW event selection is given in Table 10.6. In decreasing order of size, the main background processes are: Z/γ^* production, $t\bar{t}$ and Wt production, W+jet production, and di-boson production. The background estimation methods are each summarized in turn below.

10.4.1 Z/γ^* Background

The Z/γ^* background is estimated by running the WW event selection on the simulated Z/γ^* events. The Alpgen MC generator, interfaced to Pythia for parton showering, is used to model Z/γ^* events. However, the causes of fake $E_{\mathrm{T}}^{\mathrm{miss}}$ may not be accurately reproduced by the Monte Carlo. To address this issue, a data-driven method is used to determine a systematic uncertainty on the background prediction.

The MC modeling of the $E_{\mathrm{T}}^{\mathrm{miss,Rel}}$ distribution is tested using same-flavor events for which the Z-veto is reversed, $|m_{ll} - m_Z| < 15$ GeV. The systematic uncertainty is evaluated by quantifying the data-MC agreement after the $E_{\mathrm{T}}^{\mathrm{miss,Rel}}$ requirement. All of the other WW event selection is applied. Non-Z/γ^* contributions from other backgrounds are subtracted using the Monte Carlo prediction. Any MC mis-modeling is attributed to only the Z/γ^* process. The method assumes that all causes of discrepancies are the same inside and outside the Z-mass window.

The $E_{\mathrm{T}}^{\mathrm{miss,Rel}}$ distributions in the Z-mass window for the ee and $\mu\mu$ channels are shown in Figure 10.5. The data-MC agreement is quantified using the S ratio, defined as

$$S = \frac{N_{\mathrm{Data}} - N_{\mathrm{MC}}}{N_{\mathrm{MC}\ Z/\gamma^*}}, \tag{10.4}$$

where N_{Data} is the number of data events in the Z-peak passing the $E_{\mathrm{T}}^{\mathrm{miss,Rel}}$ cut, N_{MC} is the MC prediction for the number of events in this region, and $N_{\mathrm{MC}\ Z/\gamma^*}$ is the MC prediction of Z/γ^* events in this region. The method is applied using the same $E_{\mathrm{T}}^{\mathrm{miss,Rel}}$ cut that is applied to the

Channel	N_{Data}	N_{MC}	N_{DY}	S ratio	Assigned Systematic (fractional)
ee	166 ± 13	162 ± 8	142 ± 9	0.03 ± 0.11	11%
$\mu\mu$	136 ± 12	134 ± 6	102 ± 8	0.02 ± 0.13	13%

Table 10.7: Z/γ^* background systematic results. All errors are statistical. The statistical uncertainty on S is applied as the systematic uncertainty on the Z/γ^* background.

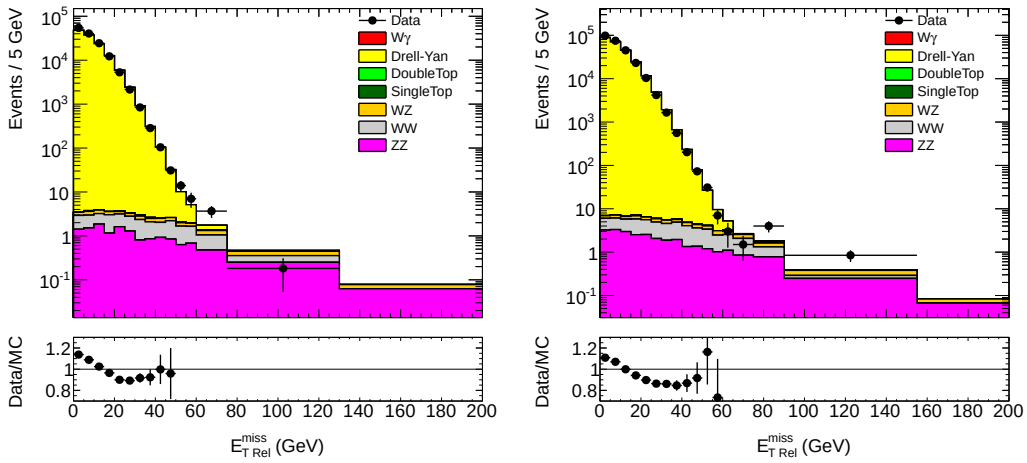

Figure 10.5: Missing energy distributions in the Z mass window for the ee (left) and $\mu\mu$(right) channels.

signal region. Table 10.7 shows the measured S values. Measured S ratios are consistent with zero to within statistical uncertainties. Because Z/γ^* MC accurately models the number of events above the $E_{\text{T}}^{\text{miss,Rel}}$ thresholds, no correction is applied to the MC Z/γ^* estimate. The statistical uncertainty on S is used as a relative systematic uncertainty on the MC prediction. An 11% uncertainty is applied in the ee-channel, and a 13% uncertainty is applied in the $\mu\mu$-channel.

A pure Z/γ^* control sample, independent of the signal region, does not exist for the $e\mu$-channel; no mass-window cut is made on the invariant mass of the pair. The method used in the same-flavor channels cannot be applied. Instead, the results obtained from the ee and $\mu\mu$ channels are averaged and applied to the $e\mu$ channel. This assumes that any sources of disagreement in the $E_{\text{T}}^{\text{miss}}$ distribution are common between the channels. Although the $E_{\text{T}}^{\text{miss,Rel}}$ cut in the $e\mu$-channel is smaller than the same-flavor channels, the $E_{\text{T}}^{\text{miss,Rel}}$ distributions in the opposite-flavor and same-flavor channels in MC is similar. This agreement is shown in Figure 10.6. A fractional systematic uncertainty of 12% is assigned in the $e\mu$-channel.

The Z/γ^* background estimated from the MC, with the systematic uncertainty described in this

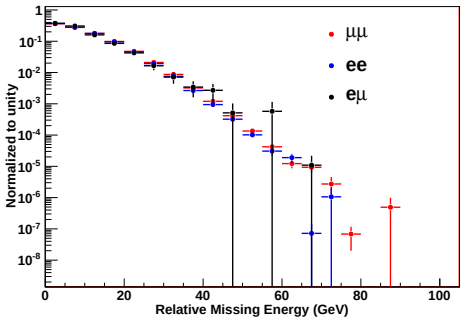

Figure 10.6: Comparison between the MC $E_{\mathrm{T}}^{\mathrm{miss,Rel}}$ distributions for Z/γ^* events in the ee, $e\mu$, and $\mu\mu$ channels. The distributions are normalized to unity.

section, is listed in Table 10.6.

10.4.2 Top Background

Background from top-quark production can arise either when the final-state b-jets have $p_{\mathrm{T}} < 20$ GeV, when they have p_{T} between 20 and 25 GeV but are not identified as b-jets, or when they are in the far forward region $|\eta| > 4.5$. The top background is modeled with MC@NLO, for $t\bar{t}$, and AcerMC, for Wt. Corrections to the MC are applied to improve the overall normalization and the modeling of jet veto efficiency.

An overall normalization factor is determined by comparing the data in the WW selection before the jet-veto, to the corresponding MC prediction. This sample is dominated by top production, as shown in Figure 10.3. The contribution from other processes, ∼25%, is subtracted. The subtraction of the WW component is based on the SM prediction of WW production, with an uncertainty that covers the difference between the prediction and the cross section measurement reported here. The relative cross sections of $t\bar{t}$ to Wt are set by the generator calculations: $\sigma_{t\bar{t}} = 164.6$ pb and $\sigma_{Wt} = 15.6$ pb.

A second correction factor is applied to correct the modeling of the jet veto efficiency. This correction is derived using a top-quark control region, defined by requiring at least one b-jet with $p_{\mathrm{T}} > 25$ GeV. This region is dominated by top events. The fraction of events in this sample with only one reconstructed jet above 25 GeV is sensitive to the top jet energy spectrum. This faction is defined as P1. Figure 10.7 shows the jet multiplicity distributions in data compared to MC in the b-tagged control region. A multiplicative correction based on the ratio of P1 as measured in data, to P1 as measured in MC, is applied to reduce the uncertainties resulting from the jet veto requirement.

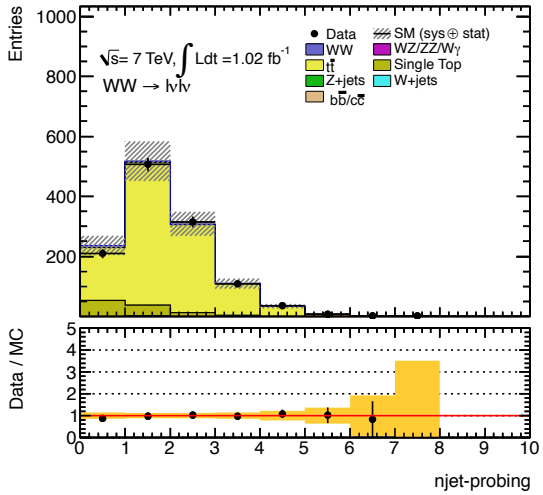

Figure 10.7: Jet multiplicity distributions in the b-tagged control sample.

The estimated number of top background events in the signal region is calculated as

$$N^{\text{Est}}_{\text{Top 0-jets}} = \left(\frac{P_1^{\text{Data}}}{P_1^{\text{MC}}}\right)^2 \times \left(\frac{N^{\text{Data}}_{\text{Top All jets}}}{N^{\text{MC}}_{\text{Top All jets}}}\right) \times N^{\text{MC}}_{\text{Top 0-jets}}, \tag{10.5}$$

The P1 factor is applied twice. This is motivated by the fact that there are typically two b-jets in top production. The top correction scheme has been validated with a MC closure test.

The leading sources of systematic uncertainty on the top background prediction come from: jet energy scale and resolution 4%, b-quark identification efficiency 6%, parton showering model 12%, statistical uncertainty on the P1/P2 correction 12%, and on un-modeled higher order QCD corrections and interference effects 15%. The number of top background events surviving the jet veto cut is estimated to be $26.6 \pm 3.9(\text{stat}) \pm 5.4(\text{syst})$, to be compared with the corresponding MC prediction of 32.1 events. After the b-jet veto, the top background is reduced to $18.8 \pm 2.7(\text{stat}) \pm 3.8(\text{syst})$ in data, and 22.7 in MC. The channel-by-channel break down of the top background is given in Table 10.6.

10.4.3 W+jet Background

Events in which W bosons are produced in association with QCD jets give rise to background to WW events when the jet is misidentified as a lepton. The rate at which QCD jets are misidentified as leptons may not be accurately described in the MC. The fake factor method, described in detail in Chapter 9, is used to estimate the W+jet background. For electrons, the fake factor method is extended, as described in Section 9.4, to explicitly include fakes from heavy-flavor decays. The

Muon Denominator Definition
STACO Combined Muon
$\|\eta\| < 2.4$
$p_T > 20$ GeV
$\|z0\| < 10$ mm
$p_T(MS) > 4$ GeV
$p_T^{\text{Cone } 0.2}/p_T < 0.3$
Fail WW Muon Selection

Table 10.8: Muon denominator definition.

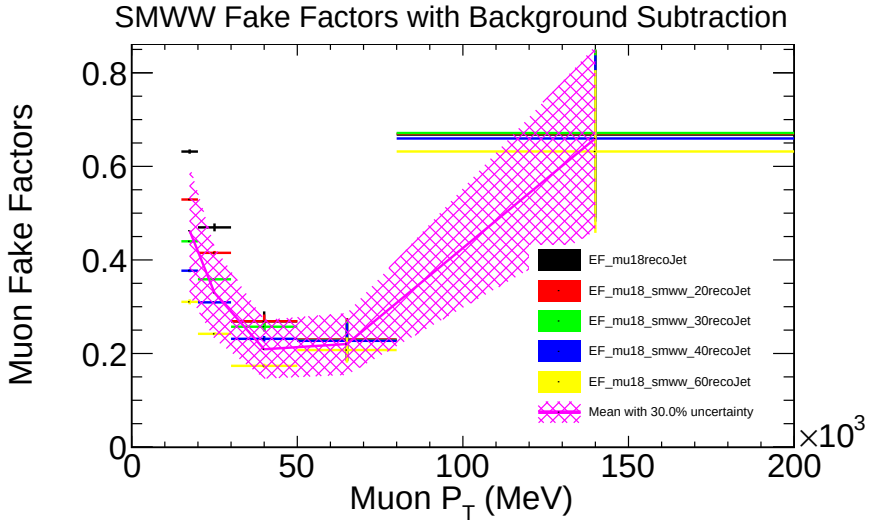

Figure 10.8: Muon fake factors measured in the di-jet sub-samples. The purple line shows the weighted average of the fake factors and the hashing indicates the ±30% band. The statistical and the systematic error from electro-weak MC subtraction are included in the error bars.

remainder of this section only provides the details of the fake factor method specific to the selection used in the WW cross section measurement. The reader is referred to Chapter 9 for details on the method.

The muon denominator definition is given in Table 10.8. The corresponding muon fake factor, after the electro-weak subtraction, is shown in Figure 10.8. The muon fake factors have been calculated as described in Chapter 9 using the `EF_mu20` trigger. The purple line shows the weighted average of the fake factor measurements and the hashing indicates the ±30% band.

Including heavy-flavor requires two electron denominator definitions, one enriched in light flavor and one enriched in heavy flavor. These definitions are given in Table 10.9. The light-flavor denominators pass the isolation requirement but fail the isEM requirements. The heavy-flavor de-

Light-Flavor Denominator	Heavy-Flavor Denominator
Fails isEM Medium Selection	Passes isEM Tight Selection
$E_T^{Cone0.3} < 4$ GeV	4GeV $< E_T^{Cone0.3} < 7$ GeV
$\|z0\| < 10$ mm	$\|z0\| < 10$ mm
$d0/\sigma(d0) < 10$	-
B-Layer Hit (if expected)	B-Layer Hit (if expected)

Table 10.9: Electron denominator definitions.

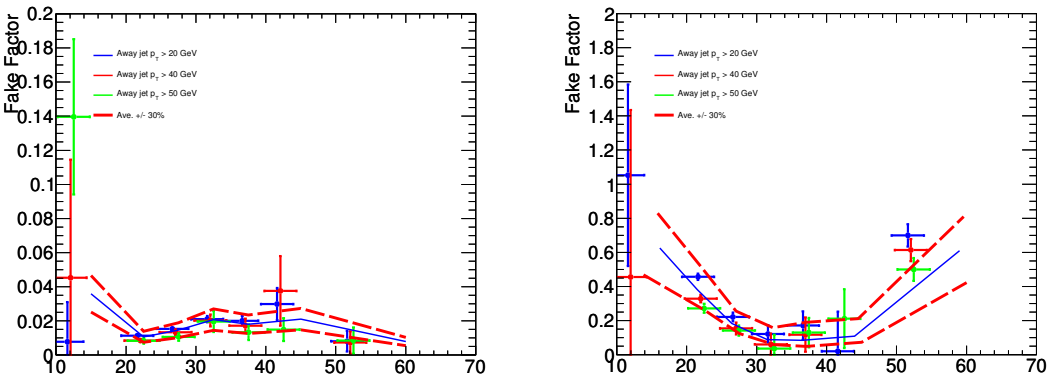

(a) (b)

Figure 10.9: Extracted light-flavor $f_{\text{l.f.}}$ (left) and heavy-flavor $f_{\text{h.f.}}$ (right) fake factors.

nominators pass the isEM requirements, but fail the isolation requirement. The light-flavor and heavy-flavor fake factors have been extracted as presented in Chapter 9. The results are shown in Figures 10.9. The blue lines show the weighted average of the fake factor measurements, and the dotted red lines indicate the ±30% band.

The dominate source of systematic uncertainty on the W+jet prediction is the sample dependence of the fake factor. This systematic is studied with the away-side jet variation in data and using a closure test in MC. Other sources of systematic uncertainty, described in Chapter 9, were also considered. Based on these studies, a 30% systematic uncertainty has been assigned to the fake factors.

The W+jet background in the WW signal region estimated by the fake factor procedure is presented in Table 10.6. The systematic uncertainty is from the uncertainty associated to the measured fake factor.

The W+jet modeling in the same sign validation region has been checked. To increase the statistics of the same-sign control region, the jet veto was removed. Figure 10.10 shows the modeling of these same sign events. Agreement between the observed and predicted number of events in the

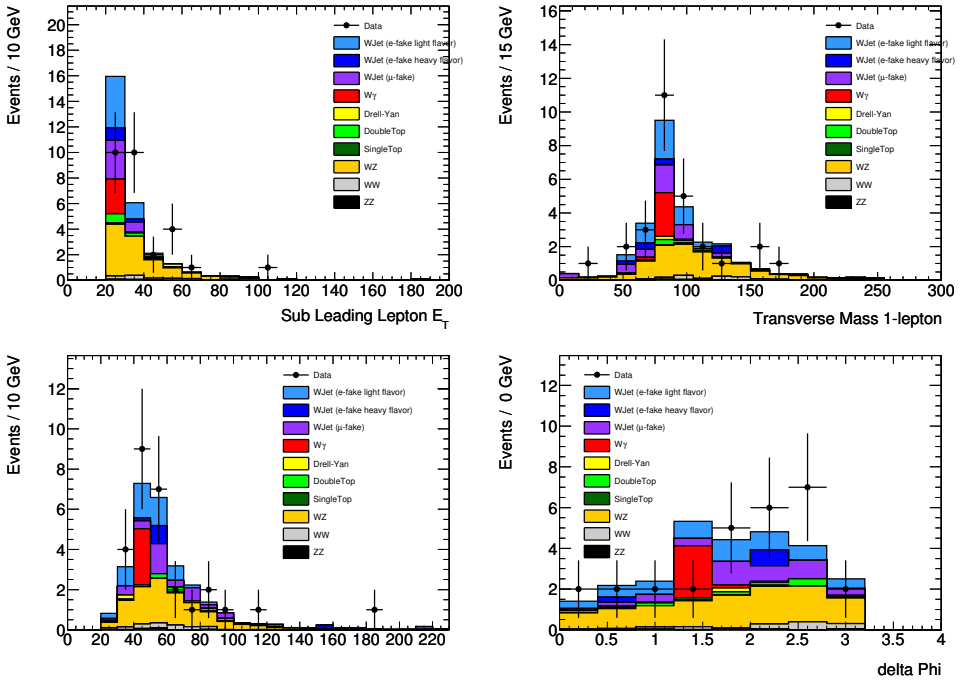

Figure 10.10: Kinematics for events in the same-sign control region without applying the jet veto. The observed data is shown with the background modeling including the data-driven W+jet prediction. The sub-leading lepton p_{T} is shown in the upper left, the transverse mass ($m_{\mathrm{T}} = \sqrt{2p_{\mathrm{T}}E_{\mathrm{T}}^{\mathrm{miss}}(1 - cos(\Delta\phi))}$) is shown in the upper right, The $E_{\mathrm{T}}^{\mathrm{miss}}$ is shown in the lower left, and $\Delta\phi_{ll}$ is shown in the lower right

same-sign control region is found.

10.4.4 Di-boson Background

The di-boson background is estimated from MC. The $W\gamma$ process, is modeled using Alpgen and Pythia. The WZ and ZZ backgrounds are estimated from `HERWIG` with `JIMMY`. A breakdown of the background yields and statistical uncertainties is given in Table 10.10. Various sources of systematic uncertainty on the di-boson background have been considered. The overall uncertainty on these backgrounds is dominated by the uncertainty on the jet energy scale. The total systematic uncertainty is ∼10%, as shown in Table 10.6.

10.5 WW acceptance

In addition to the background estimation, the WW cross section measurement requires an estimate of the A_{WW} and C_{WW} factors in Equation 10.1. The acceptance factor A_{WW} is defined as the

Process	ee-channel	$\mu\mu$-channel	$e\mu$-channel
WZ	0.50±0.18	1.95±0.38	3.48±0.51
ZZ	0.64±0.11	0.97±0.13	0.16±0.05
Wγ	0.97±0.76	-	1.47±0.83
Di-boson Background	2.10±0.79	2.92±0.41	5.12±0.97

Table 10.10: Di-boson background yields with their associated statistical uncertainties as determined from MC. Scale factors as described above are applied to the MC.

- Muon $p_{\mathrm{T}} > 20$ GeV and $|\eta| < 2.4$
  ($p_{\mathrm{T}} > 25$ GeV for at least one muon in the $\mu\mu$-channel).
- Electron $p_{\mathrm{T}} > 20$ GeV and either $|\eta| < 1.37$ or $1.52 < |\eta| < 2.47$
  ($p_{\mathrm{T}} > 25$ GeV in the $e\mu$-channel and for at least one electron in the ee-channel).
- No anti-k_{t} jet ($R = 0.4$) with $p_{\mathrm{T}} > 25$ GeV, $|\eta| < 4.5$, and $\Delta R(e,\mathrm{jet}) > 0.3$.
- No jet with $p_{\mathrm{T}} > 20$ GeV, $|\eta| < 2.5$ and $\Delta R(e,\mathrm{jet}) > 0.3$ within $R = 0.3$ of a b-quark with $p_{\mathrm{T}} > 5$ GeV.
- Neutrino $|\sum \vec{p}_{\mathrm{T}}|$ or $|\sum \vec{p}_{\mathrm{T}}| \times \sin\Delta\phi$ (for $\Delta\phi < \pi/2$) $> 45, 40, 25$ GeV in the $\mu\mu$, ee, and $e\mu$ channels respectively ($\Delta\phi$ is the azimuthal angle between the neutrino $\sum \vec{p}_{\mathrm{T}}$ and the nearest charged lepton).
- $m_{ll} > 15$ (10) GeV in the same-flavor (opposite-flavor) channel.
- $|m_{ll} - m_Z| > 15$ GeV in the $\mu\mu$-channel and ee-channel channels.

Table 10.11: Definition of the fiducial phase space used in the WW cross section measurement.

ratio of generated WW events in the fiducial phase space to those in the total phase space. The correction factor C_{WW} is defined as the ratio of measured events to generator-level events in the fiducial phase space. The fiducial phase space used for the cross section measurement is given in Table 10.11. The A_{WW} and C_{WW} factors are estimated using MC@NLO to model $q\bar{q} \to WW$ and gg2ww [102] to model $gg \to WW$.

A correction to the $q\bar{q} \to WW$ modeling of the jet veto efficiency is derived using $Z \to \ell\ell$ events. The fraction of Z events with no additional jets is compared between data and the MC@NLO prediction. The correction factor is measured as $\epsilon_Z^{data}/\epsilon_Z^{MC}$, where $\epsilon_Z = \mathrm{N}_{0\ \mathrm{jet}}/\mathrm{N}_{\geq 0\ \mathrm{jet}}$. This correction is found to be 0.963 and is applied as a multiplicative correction to the WW MC. This reduces the uncertainty associated to the jet veto efficiency due to jet energy scale and resolution.

The acceptances are determined separately for each channel. The results are shown in Table 10.12, including the statistical and systematic uncertainties. A breakdown of the systematic uncertainties on the acceptance is given in Table 10.13. The theoretical uncertainty on the jet veto acceptance is the largest uncertainty. The efficiencies relating to leptons are measured as a function

	$e\mu$-channel	ee-channel	$\mu\mu$-channel
C_{WW}	$0.541 \pm 0.005 \pm 0.022$	$0.396 \pm 0.005 \pm 0.019$	$0.721 \pm 0.005 \pm 0.025$
A_{WW}	$0.161 \pm 0.001 \pm 0.008$	$0.089 \pm 0.001 \pm 0.005$	$0.082 \pm 0.001 \pm 0.004$
$A_{WW} \times C_{WW}$	$0.087 \pm 0.001 \pm 0.005$	$0.035 \pm 0.001 \pm 0.003$	$0.059 \pm 0.001 \pm 0.004$

Table 10.12: Acceptances in the various channels. The first uncertainty is statistical and the second systematic.

	Relative uncertainty (%)		
Source of uncertainty	$e\mu$-channel	ee-channel	$\mu\mu$-channel
Trigger efficiency	1.0	1.0	1.0
Lepton efficiency	2.3	4.1	1.8
Lepton p_{T} scale and resolution	0.4	1.0	0.1
$E_{\mathrm{T}}^{\mathrm{miss}}$ modeling	0.6	1.0	2.2
Jet energy scale and resolution	1.1	1.1	1.1
Lepton acceptance	2.0	2.1	1.6
Jet veto acceptance	5.0	5.0	5.0
PDFs	1.4	1.2	1.2
Total	6.2	7.2	6.2

Table 10.13: Relative uncertainties, in percent, on the estimate of the product $A_{WW} \times C_{WW}$ for the individual WW decay channels. The uncertainty on A_{WW} (C_{WW}) receives contributions from the last three (first six) sources.

of lepton p_{T} and η using tag-and-probe, See Chapter 4 for details. The total acceptance uncertainty in the ee and $e\mu$ channels is 6.2%, in the ee-channel the uncertainty is 7.2%.

10.6 Results

The WW cross section is measured in the fiducial phase space and extrapolated to the total phase space. The fiducial cross section is measured using Equation 10.2. The measured values are reported in Table 10.14. The measurements are consistent with the SM predictions, differing by $+1.7\sigma$ ($e\mu$-channel), $+1.3\sigma$ (ee-channel) and 0.1σ ($\mu\mu$-channel). Contributions from a SM Higgs boson would be small. For a Higgs boson of mass 125 GeV, 2.9 events are expected in the $e\mu$-channel, 0.9 in the ee-channel, and 1.8 events in the $\mu\mu$ channel. The uncertainties on the fiducial cross section measurement arising from the C_{WW} term are due to the lepton modeling, jet energy scale and resolution, and $E_{\mathrm{T}}^{\mathrm{miss}}$ modeling. These uncertainties are listed in the first five rows of Table 10.13.

The extrapolation to the total cross section is made with A_{WW}. The uncertainty on A_{WW} comes from PDFs and scale variations affecting the lepton and jet veto acceptances. These are shown in the last three rows of Table 10.13. The total cross section is measured combining the three channels. The combined measurement is performed by minimizing a likelihood fit to the WW cross-section

	$e\mu$-channel	ee-channel	$\mu\mu$-channel
σ_{fid} [fb]	$294 \pm 26 \pm 15 \pm 11$	$92.0 \pm 18.9 \pm 9.4 \pm 3.4$	$57.2 \pm 10.8 \pm 5.2 \pm 2.1$
σ_{fid}^{SM} [fb]	230 ± 19	63.4 ± 5.3	59.0 ± 4.7

Table 10.14: The measured fiducial cross sections (σ_{fid}) and the SM predictions (σ_{fid}^{SM}). The first uncertainty is statistical and the second systematic. The 3.7% relative uncertainty on the integrated luminosity is the third uncertainty on the measured cross sections. The uncertainties on σ_{fid}^{SM} are highly correlated between the channels.

using the observed data and background predictions in each channel. The combined cross section measurement gives:

$$\sigma(pp \to WW) = 54.4 \pm 4.0(\text{stat}) \pm 3.9(\text{syst}) \pm 2.0(\text{lumi}) \text{ pb},$$

to be compared with the NLO SM prediction of $\sigma(pp \to WW) = 44.4 \pm 2.8$ pb.

10.7 Conclusion

The $pp \to WW$ cross section has been measured in the fully leptonic decay channel using the first 1.02 fb^{-1} of $\sqrt{s}$= 7 TeV data collected in 2011. The measured cross section of 54.4 ± 5.9 pb is consistent with the SM prediction of 44.4 ± 2.8 pb. The measurement of the WW cross section in the fiducial phase space has also been reported.

Chapter 11

Search for $H \to WW^{(*)}$

This chapter presents the search for the Standard Model Higgs boson using the $H \to WW^{(*)} \to l\nu l\nu$ decay mode. The analysis has been performed using 4.7 fb^{-1} of $\sqrt{s} = 7$ TeV data collected in 2011 [128] and 5.8 fb^{-1} of $\sqrt{s} = 8$ TeV data collected in the first half of 2012 [129]. In the 2011 analysis, no significant excess of events over the expected background was observed, and the Standard Model Higgs boson with mass in the range between 133 GeV and 261 GeV has been excluded at 95% confidence level. In the 2012 analysis, an excess of events over the expected background is observed, corresponding to a local significance of 3.2 standard deviations. The 2011 and 2012 results are combined, and the observed excess corresponds to a local significance of 2.8 standard deviations.

The remainder of the chapter is organized as follows: Section 11.1 provides a brief overview of the analyses. Section 11.2 describes the data sets and the MC samples used to model the signal and backgrounds. Section 11.3 describes the event selection used in the various channels. Section 11.4 presents the background estimates. Section 11.5 describes the main sources of systematic uncertainty. Section 11.6 describes the fitting procedure and the statistical model. Section 11.7 presents the results.

11.1 Analysis Overview

The $H \to WW^{(*)} \to l\nu l\nu$ search is performed in three signal regions defined according to jet multiplicity, referred to as the 0-jet analysis, 1-jet analysis, and the 2-jet analysis. The different channels are combined in a global fit using a transverse mass variable to fit for the presence of signal. The large continuum Standard Model (SM) WW and top backgrounds are constrained by including dedicated control regions in the fit. The other backgrounds are estimated using the techniques described in Chapter 8 and used in the SM WW cross section measurement presented

in Chapter 10.

The 0-jet and 1-jet analysis are designed to select $H \to WW^{(*)}$ events produced through the dominant gluon-gluon fusion process shown in Figure 8.1a. Most of the Higgs events produced via ggF will not have final state jets and will be selected by the 0-jet analysis. However, a significant fraction of Higgs events will have a final state jet produced from radiation of quark or gluon off of the initial state gluons. These events are recovered in the 1-jet analysis.

The signal selection in the 0-jet bin begins with a basic WW selection, as described in Chapter 8, to remove non-WW backgrounds. Further event selection, as described in Section 8.4, is then applied to separate the SM WW production from $H \to WW^{(*)}$ events. The transverse mass distribution, defined in Section 8.4, is used as the final discriminate in the combined fit. The 0-jet bin dominates the $H \to WW^{(*)}$ sensitivity.

The 1-jet bin suffers from a significant amount of background from top production. After the 1-jet requirement, event selection is applied to suppress both the SM WW and top backgrounds. The final 1-jet selection contains roughly equal amounts of SM WW and top backgrounds. As in the 0-jet analysis, the transverse mass distribution is used as the final discriminate in the fit.

The 2-jet bin is designed to select $H \to WW^{(*)}$ events produced through vector boson fusion (VBF), shown in Figure 8.1b. The VBF process tends to produce two widely separated, high p_{T} jets, with little central hadronic activity. The large top background in the 2-jet bin is suppressed by requiring jets consistent with the VBF process. After the full 2-jet selection the statistics are not large enough to fit m_{T}; only the event yields in the 2-jet signal region are used in the fit.

The analysis using 4.7 fb^{-1} of $\sqrt{s} = 7$ TeV data collected in 2011, referred to in the following as the "2011 Analysis", is performed using both opposite-flavor and same-flavor final states. The opposite-flavor final states suffer from much less Z/γ^{*}background and provide the majority of the sensitivity. The opposite-flavor channel is separated according to the flavor of the higher p_{T} lepton. This separation improves the overall sensitivity because of the different signal-to-background ratios in the different channels. In W+jet events, it is primarily the softer lepton that is the result of misidentification. Events with sub-leading muons have a lower W+jet background because of the smaller muon fake rate. The 2011 analyses has been separately optimized for three different regions of Higgs mass: $m_h < 200$ GeV, 200 GeV $\leq m_h \leq 300$ GeV, and 300 GeV $< m_h < 600$ GeV. These mass regions are referred to in the following as low m_h, intermediate m_h, and high m_h.

The analysis using 5.8 fb^{-1} of $\sqrt{s} = 8$ TeV data collected in 2012, referred to as the "2012 analysis", benefits from the increase of Higgs production cross section with $\sqrt{s}$. The Higgs cross section at m_h= 125 GeV increases by about 30% with the increase of $\sqrt{s}$ from 7 TeV to 8 TeV. The analysis techniques used in the 2012 analysis are largely the same as those of the 2011 analysis, with

two main exceptions.

The first fundamental difference with the 2012 analysis is the result of the increased pile-up of the $\sqrt{s}$= 8 TeV data set. The average number of interactions per bunch crossing doubled from around ten in the 2011 analysis, to around twenty in the 2012 analysis. This increased level of pile-up results in a significantly larger Z/γ^* background from fake $E_{\mathrm{T}}^{\mathrm{miss}}$ in the same-flavor channels. As a result, only the opposite-flavor final states are used in the 2012 analysis. Dropping the same-flavor channels degrades the $H \to WW^{(*)} \to l\nu l\nu$ sensitivity by less than 10%.

The other main difference with the 2012 analysis is that it has been specifically designed to search in the region of m_h between 110 and 140 GeV. The 2011 combined Higgs searches [130], including the 2011 $H \to WW^{(*)}$ analysis presented here, excluded almost all of the relevant region of m_h. The mass region from 110 GeV to over 500 GeV, was excluded at the 95% confidence level, apart from the region between ∼120 GeV to ∼130 GeV. The 2012 $H \to WW^{(*)}$ analysis was optimized for this un-excluded region. As a result, the lepton identification criteria were significantly tightened to reduce the W+jet background, which is critical at low m_h, see Section 8.4 for further discussion. In addition, data in the region expected to have the highest signal-to-background for signal with m_h between 110 and 140 GeV was blinded during the optimization of the event selection. Only after agreement between observed data and the background model in various control regions was judged to be reasonable, was the signal region un-blinded. Blinding the signal region helps to prevent against unintended biases introduced based on the observed data. The blinding also helped to focus the analysis on the understanding of the background modeling in the control regions.

Both the 2011 and 2012 analyses are presented in the following. Because many aspects of the analyses are similar, they are described together in the following. The background estimates and final results will be presented separately for the two analyses. The results of combining the analyses are also presented.

11.2 Data Sets and MC Samples

The data used in the 2011 analysis was collected using inclusive single-lepton triggers. The single-muon trigger required a reconstructed muon with p_{T} greater 18 GeV, with no requirement on isolation. The single-electron trigger threshold varied from 20 to 22 GeV throughout the data taking. The electrons were required to pass the medium isEM requirement in the beginning of the year and to pass medium++ during the second half of the year. The trigger object requirements were tightened throughout the data taking to cope with the increasing instantaneous luminosity.

The data used in the 2012 analysis was taken from the beginning of April to the middle of June

Process at $\sqrt{s}$= 7 TeV	Generator	m_h [GeV]	$\sigma\times$Br [pb]
ggF	POWHEG+Pythia	125	0.347
ggF	POWHEG+Pythia	240	0.265
VBF	POWHEG+Pythia	125	2.7×10^{-2}
VBF	POWHEG+Pythia	240	3.4×10^{-2}
WH/ZH	Pythia	125	2.0×10^{-2}
WH/ZH	Pythia	240	0.6×10^{-2}

Process at $\sqrt{s}$= 8 TeV	Generator	m_h [GeV]	$\sigma\times$Br [pb]
ggF	POWHEG+Pythia8	125	0.441
VBF	POWHEG+Pythia8	125	3.5×10^{-2}
WH/ZH	Pythia8	125	2.5×10^{-2}

Table 11.1: MC generators used to model the Higgs signal processes for $\sqrt{s}$= 7 TeV (upper table) and $\sqrt{s}$= 8 TeV (lower table). Cross sections are quoted for m_h = 125 GeV and 240 GeV. The quoted signal production cross sections include the $H \to WW^{(*)} \to l\nu l\nu$ branching fractions but not the branching fractions for the W and Z boson in the associated production.

2012. It was also collected using inclusive single-lepton triggers. The single-electron and single-muon triggers each required a reconstructed lepton with p_{T} greater 24 GeV. In addition, the 2012 single-lepton triggers have a track-based isolation requirement. The single-electron trigger required the track energy in a cone of $\Delta R < 0.2$ to be less than 10% of the electron p_{T}. For the single-muon trigger the requirement is loosened to 12% of the muon p_{T}.

The Monte Carlo (MC) generators used to model signal are listed in Table 11.1. For both analyses, the signal contribution includes the dominant ggF production process, VBF, and the associated production of the Higgs with a W or Z boson. Only the fully leptonic decays of the Higgs are considered, including W decays to electrons or muons through tau leptons, $W \to \tau\nu_{\bar{\tau}} \to l\bar{\nu}_l\nu_{\bar{\tau}}$. For the 2012 analysis, only the opposite-flavor final states are modeled. The signal cross section is computed to next-to-next-to-leading order (NNLO) [131, 132, 133]. in QCD for the ggF process. Next-to-leading order (NLO) electro-weak (EW) corrections are also applied, as well as QCD soft-gluon re-summations up to next-to-next-to-leading log (NNLL) [134, 135]. These calculations are detailed in Reference [136, 137, 138] and assume factorization between QCD and EW corrections. The ggF Higgs boson p_{T} spectrum is re-weighted to agree with the prediction from HqT [139]. Full NLO QCD and EW corrections [140, 141, 115] and approximate NNLO QCD corrections [142] are used to calculate the cross sections for VBF signal production. The WW branching fractions are taken from the HDECAY [143] program.

The MC generators used to model the background processes are listed in Table 11.2. The MC samples include a full GEANT simulation of the ATLAS detector. For most processes, separate

Process	Generator	σ [pb]
$q\bar{q}/g \to WW$	MC@NLO+HERWIG	4.68
$gg \to WW$	gg2ww+HERWIG	0.14
$t\bar{t}$	MC@NLO+HERWIG	167
$Wt/tb/tq$	AcerMC+Pythia	85
Inclusive Z/γ^*	Alpgen+Pythia	1.5×10^4
$W\gamma$	Alpgen	345
WZ	MC@NLO	18.0
$W\gamma^*$	Alpgen	6.5
ZZ	SHERPA	5.6

Process	Generator	σ [pb]
$q\bar{q}/g \to WW$	MC@NLO+HERWIG	5.68
$gg \to WW$	gg2ww+HERWIG	0.16
$t\bar{t}$	MC@NLO+HERWIG	238
Wt/tb	AcerMC+Pythia	28
tq	AcerMC+Pythia	88
Inclusive Z/γ^*	Alpgen+Pythia	1.6×10^4
$W\gamma$	Alpgen	369
$WZ \to 3l + \nu$	MC@NLO	1.54
$W\gamma^*$	Alpgen	9.26
$ZZ \to 4l$	SHERPA	0.73

Table 11.2: MC generators used to model the background processes for $\sqrt{s}$= 7 TeV (upper table) and $\sqrt{s}$= 8 TeV (lower table). The number quoted for the inclusive Z/γ^* process is for $m_{ll} >$ 10 GeV. Kinematic criteria are also applied in the generation of $W\gamma$ events (the photon must have $p_{\mathrm{T}} > 10(8)$ GeV and be separated from the charged lepton by $\Delta R > 0.1(0.25)$ for the 7 (8) TeV sample) and $W\gamma^*$ events (the higher and lower transverse momenta of the leptons from the γ^* decay must exceed 15 GeVand 5 GeV, respectively). The $ZZ \to 4l$ samples are generated with an invariant mass cut of $m_{ll} > 4\ GeV$. For the $W\gamma^*$ a lower invariant mass cut of $m_{ll} > 2m_e$ is applied. Leptonic decay modes are summed over, except for the 7 TeV $t\bar{t}$, WZ, and ZZ samples and the 8 TeV $t\bar{t}$ sample; in which the inclusive cross sections are quoted.

programs are used to generate the hard scattering process and to model the parton showering and hadronisation stages. Wherever HERWIG is used for the parton showering, JIMMY is used for the simulation of the underlying event. The simulation includes the modeling of multiple pp interactions in the same bunch crossing (pile-up), as well as corrections determined from data to improve the modeling of reconstructed objects. The corrections applied to the MC are listed in Table 11.3.

11.3 Event Selection

The event selection begins with the lepton selection.

The electron identification criteria used for the 2011 and 2012 analyses are given in Table 11.4.

MC Corrections
Lepton trigger efficiency
Lepton identification efficiency
Lepton p_{T} smearing
Pile-up re-weighting
Jet veto efficiency
b-Jet veto efficiency
Higgs p_{T}

Table 11.3: List of MC corrections

	2011 Electron Selection	2012 Electron Selection
isEM requirement	Tight++ (2011 menu)	Tight++ (2012 menu)
Calorimeter Isolation	$E_T^{\mathrm{Cone\ 0.3}}/p_{\mathrm{T}} < 0.14$	"topo" $E_T^{\mathrm{Cone\ 0.3}}/p_{\mathrm{T}} < 0.16$
Track Isolation	$p_T^{\mathrm{Cone\ 0.3}}/p_{\mathrm{T}} < 0.13$	$p_T^{\mathrm{Cone\ 0.3}}/p_{\mathrm{T}} < 0.12$ ($p_{\mathrm{T}} < 25$ GeV) $p_T^{\mathrm{Cone\ 0.3}}/p_{\mathrm{T}} < 0.16$ ($p_{\mathrm{T}} > 25$ GeV)
Transverse impact parameter	$d_0/\sigma_{d_0} < 10$	$d_0/\sigma_{d_0} < 3$
Longitudinal impact parameter	$\lvert z_0 \rvert < 1$ mm	$\lvert z_0 \sin(\theta) \rvert < 0.4$ mm

Table 11.4: Electron identification criteria used in the $H \to WW^{(*)} \to l\nu l\nu$ analysis.

Electrons are required to satisfy the Tight++ isEM requirement and to pass a track-based and a calorimeter-based isolation requirement. In 2012, the isEM menu was re-optimized to be robust against pile-up, see Chapter 7. The re-optimized Tight++ menu is used in the 2012 analysis. The calorimeter isolation is corrected for both the lateral leakage of the electron energy into the isolation cone and the contribution from pile-up. In the 2011 analysis, the calorimeter-based isolation variable was calculated by summing the energy from individual calorimeter cells. To reduce pile-up dependence, the calorimeter isolation variable used in the 2012 analysis sums the energy in reconstructed topological clusters, referred to as"topo"-clusters. The energy thresholds applied in the topo-cluster reconstruction reduces the dependence on both in-time and out-of-time pile-up. As described in Chapter 7, the electron reconstruction in 2012 was improved by the use of a dedicated track fitter to account for energy loss due to bremsstrahlung. The improved track resolution provided by the GSF fitter allowed for tighter impact parameter requirements. In the 2012 analysis, the isolation and impact parameter operating points were optimized for m_h= 125 GeV. This resulted in a tighter electron operating point than used in the 2011 analysis. The tighter cuts reduce the expected background contribution from W+jet by ∼50% with respect to the 2011 analysis, with a relatively small loss in signal efficiency.

The muon identification criteria are given in Table 11.5. As with the electrons, the calorimeter isolation variable used for muons is corrected for the contribution from pile-up. In the 2012 analysis,

	2011 Muon Selection	2012 Muon Selection
Track Quality	Pass Basic Track Quality	Pass Basic Track Quality
$\|\eta\|$ Acceptance	$\|\eta\| < 2.4$	$\|\eta\| < 2.5$
Calorimeter Isolation	$E_T^{\text{Cone }0.3}/p_{\text{T}} < 0.14$	$E_T^{\text{Cone }0.3}/p_{\text{T}} < 0.014 p_{\text{T}} - 0.15$ and $E_T^{\text{Cone }0.3}/p_{\text{T}} < 0.2$
Track Isolation	$p_T^{\text{Cone }0.3}/p_{\text{T}} < 0.13$	$p_T^{\text{Cone }0.3}/p_{\text{T}} < 0.01 p_{\text{T}} - 0.105$ and $p_T^{\text{Cone }0.3}/p_{\text{T}} < 0.15$
Transverse Impact parameter	$d_0/\sigma_{d_0} < 3$	$d_0/\sigma_{d_0} < 3$
Longitudinal Impact parameter	$\|z_0\| < 1$ mm	$\|z_0 \sin(\theta)\| < 1$ mm

Table 11.5: Muon identification criteria used in the $H \to WW^{(*)} \to l\nu l\nu$ analysis.

the muon isolation operating points were optimized for m_h= 125 GeV. This optimization favored tighter operating points at lower p_{T}, reducing the expected W+jet contribution with respect to the 2011 analysis.

The separation of the analysis into jet bins depends on the jet definition. Jets are reconstructed using the anti-kt algorithm, with a distance parameter of 0.4. The calorimeter clusters associated with an electron will also be reconstructed as part of a jet. To remove this double counting, jets that overlap with selected electrons are not considered. In the 2011 analysis, identified jets are required to have $p_{\text{T}} > 25$ GeV, $|\eta| < 4.5$, and jet vertex fraction, or JVF, greater than 0.75. The JVF is the fraction of the jet energy associated to the primary vertex. JVF is defined using tracks associated to the jet in the ID. It is the p_{T} sum of the tracks associated to the jet that originate from the primary vertex, divided by the p_{T} sum of all tracks associated to the jet. JVF is only defined in the region of $|\eta|$ with ID acceptance. The JVF requirement suppresses jets that are produced in pile-up collisions and are not associated to the interaction producing the reconstructed leptons. In the 2012 analysis, identified jets are required to have $p_{\text{T}} > 25$ GeV, $|\eta| < 4.5$, and JVF greater than 0.5. The jet p_{T} threshold is increased to 30 GeV in the forward region, $2.5 < |\eta| < 4.5$, to reduce the contribution from jets produced by pile-up in the region without ID acceptance.

A basic pre-selection is used to select di-lepton events. The di-lepton pre-selection criteria are given in Table 11.6. Events are required to have two and only two identified leptons of opposite charge. Removing events with more than two leptons suppresses the contribution from WZ events. In the 2012 analysis, the leptons must also be of opposite flavor. The highest p_{T} lepton is required to have p_{T} above 25 GeV, and the sub-leading lepton is required to have p_{T} above 15 GeV. The lower bound on the invariant mass removes the low mass resonances and the Z/γ^* spectrum not modeled by MC.

After the pre-selection, the dominant contribution to same-flavor events is from $Z/\gamma* \to \ell^+\ell^-$. In the opposite-flavor final states, the dominant backgrounds are from $Z/\gamma^* \to \tau\tau$ and top-quark

1) Primary Vertex Selection:
Events are required to have a reconstructed primary vertex with at least three tracks.

2) Di-leptons:
Events must have two, and only two, selected, oppositely charged leptons.
For the 2012 analysis, the leptons must be of opposite flavor.
The highest p_{T} lepton must be above 25 GeV.
The second lepton must be above 15 GeV.

3) Trigger/Trigger matching:
One of the single lepton triggers must be fired, and at least one of the selected leptons must match the trigger.

4) m_{ll}:
The invariant mass of the di-lepton pair is required to be greater than 12 (10) GeV for same-flavor (opposite-flavor) events.

Table 11.6: Basic di-lepton pre-selection criteria.

production. The large Z/γ^* background is suppressed by removing same-flavor events consistent with the Z mass, and by requiring large relative missing energy. The relative missing energy, $E_{\mathrm{T}}^{\mathrm{miss,Rel}}$ is defined as

$$E_{\mathrm{T}}^{\mathrm{miss,Rel}} = \begin{cases} E_{\mathrm{T}}^{\mathrm{miss}} \times \sin(\Delta\phi_{l,j}) & \text{if } \Delta\phi_{l,j} < \pi/2 \\ E_{\mathrm{T}}^{\mathrm{miss}} & \text{otherwise.} \end{cases} \tag{11.1}$$

$E_{\mathrm{T}}^{\mathrm{miss,Rel}}$ suppresses $E_{\mathrm{T}}^{\mathrm{miss}}$ coming from mis-reconstructed leptons or τ-lepton decays, see Chapter 8 for discussion. Figures 11.1 and 11.2 show the $E_{\mathrm{T}}^{\mathrm{miss,Rel}}$ distribution after the di-lepton pre-selection. In the same-flavor channels, the $E_{\mathrm{T}}^{\mathrm{miss,Rel}}$ is required to be greater than 45 GeV. In the opposite-flavor channels, of both the 2011 and 2012 analyses, the $E_{\mathrm{T}}^{\mathrm{miss,Rel}}$ is required to be greater than 25 GeV.

After the $E_{\mathrm{T}}^{\mathrm{miss,Rel}}$ requirement, the selected events are dominated by top-quark production. Figure 11.3 shows the jet multiplicity distributions after the $E_{\mathrm{T}}^{\mathrm{miss,Rel}}$ cut for the two analysis. The different background sources and overall signal-to-background vary considerably across the different jet bins. As a result, the analysis is divided according to jet multiplicity. A jet veto is applied in the 0-jet analysis. The 1-jet analysis requires exactly one reconstructed jet. The 2-jet analysis selects events which have two or more reconstructed jets. These analysis are described in turn below.

11.3.1 0-Jet Analysis

The 0-jet analysis applies a jet veto after the $E_{\mathrm{T}}^{\mathrm{miss,Rel}}$ requirement. The jet veto removes most of the top background. As can be seen in Figure 11.3, after the jet veto the background is dominated

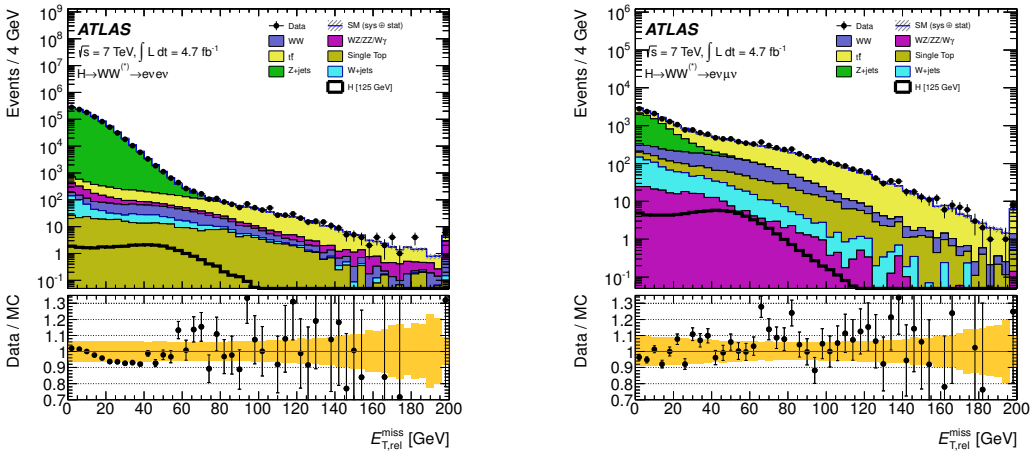

Figure 11.1: $E_{\mathrm{T}}^{\mathrm{miss,Rel}}$distributions after the di-lepton pre-selection in the 2011 analysis. The same-flavor (ee) channel is shown on the left. The opposite-flavor channel is shown on the right. The points show the observed data and the stacked histograms represent the signal and background expectation.

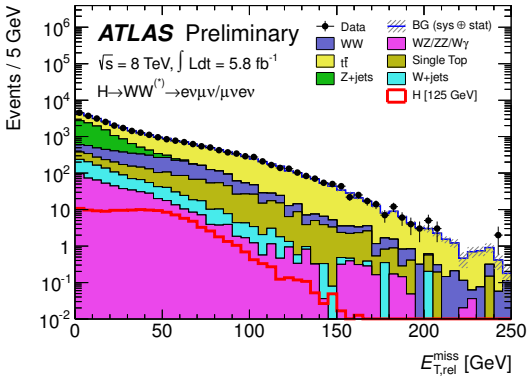

Figure 11.2: $E_{\mathrm{T}}^{\mathrm{miss,Rel}}$distributions after the di-lepton pre-selection in the 2012 analysis. The points show the observed data and the stacked histograms represent the signal and background expectation.

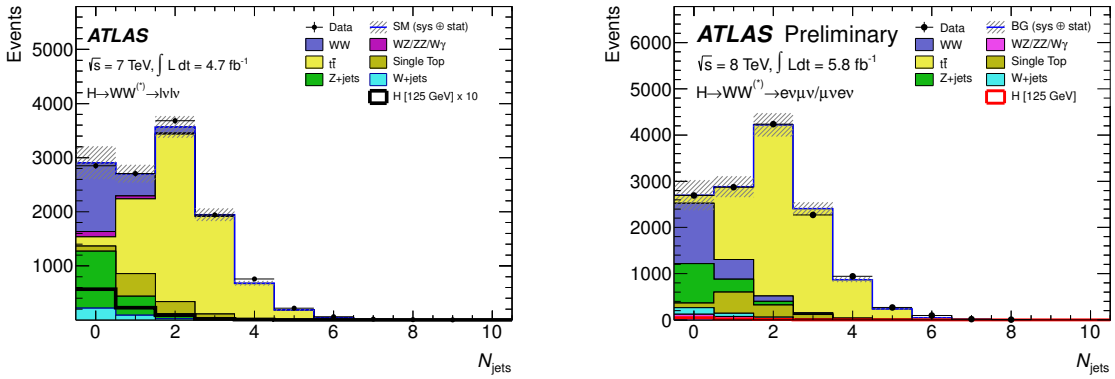

Figure 11.3: Jet multiplicity distributions after the $E_{\mathrm{T}}^{\mathrm{miss,Rel}}$ requirement for 2011 analysis (left-hand side) and the 2012 analysis (right-hand side). The points show the observed data and the stacked histograms represent the signal and background expectation. The signal distribution in the left-hand plot has been scale up by a factor of 10 for clarity.

2011 Analysis Low m_h	2011 Analysis Intermediate m_h	2011 Analysis High m_h	2012 Analysis
$p_{T_{ll}} > 30$ GeV OF	$p_{T_{ll}} > 30$ GeV OF	$p_{T_{ll}} > 30$ GeV OF	$p_{T_{ll}} > 30$ GeV
$p_{T_{ll}} > 45$ GeV SF	$p_{T_{ll}} > 45$ GeV SF	$p_{T_{ll}} > 45$ GeV SF	-
$m_{ll} < 50$ GeV	$m_{ll} < 150$ GeV	-	$m_{ll} < 50$ GeV
$\Delta\phi_{ll} < 1.8$	-	-	$\Delta\phi_{ll} < 1.8$

Table 11.7: Summary of the 0-jet event selection after the jet veto. For the 2011 analysis, a different $p_{T_{ll}}$ requirement is made in the opposite-flavor (OF) and same-flavor (SF) channels.

by SM WW and Z/γ^*. Additional event selection is applied in the 0-jet analysis to suppress these backgrounds. A summary of the 0-jet selection is given in Table 11.7

The transverse momentum of the di-lepton system, $p_{T_{ll}}$, is sensitive to the presence of final state neutrinos. For 0-jet events, small values of $p_{T_{ll}}$ indicate the lack of a neutrinos associated with the di-lepton system; the measured momentum imbalance is not a result of the lepton system. Figure 11.4 shows the $p_{T_{ll}}$ distribution after the jet veto. Requiring large values of $p_{T_{ll}}$ suppresses the majority of the Z/γ^* background with little loss in signal efficiency.

After the $p_{T_{ll}}$ requirement, the dominant background in the 0-jet analysis is SM WW. The remainder of the 0-jet event selection is meant to separate SM WW from $H \to WW^{(*)}$. As discussed in Section 8.4, the m_{ll} and $\Delta\phi_{ll}$ distributions are sensitive to the spin-0 nature of the Higgs decays. Figure 11.5 shows the m_{ll} distribution after the $p_{T_{ll}}$ cut in the 2012 analysis. In the 2011 analysis, the m_{ll} requirement is actually made before applying the $p_{T_{ll}}$ selection, so Figure 11.5 shows the 2011 m_{ll} distribution before the $p_{T_{ll}}$ requirement. Requiring low m_{ll} and $\Delta\phi_{ll}$ suppresses SM WW

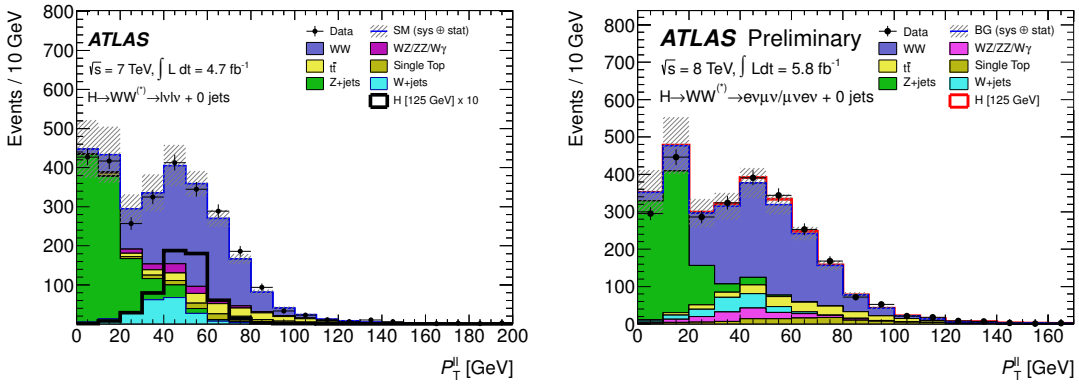

Figure 11.4: $p_{T_{ll}}$ distribution after the jet veto for 2011 analysis (left-hand side) and the 2012 analysis (right-hand side). The points show the observed data and the stacked histograms represent the signal and background expectation. The signal distribution in the left-hand plot has been scale up by a factor of 10 for clarity.

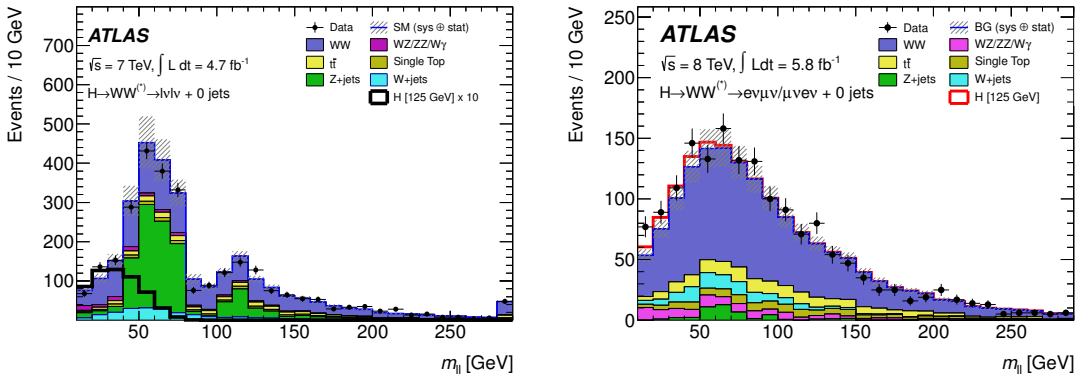

Figure 11.5: m_{ll} distribution before the $p_{T_{ll}}$ requirement for the 2011 analysis (left-hand side) and after the $p_{T_{ll}}$ requirement for 2012 analysis (right-hand side). The 2011 analysis is shown before the $p_{T_{ll}}$ because in that analysis the m_{ll} cut is made before the $p_{T_{ll}}$ requirement. The points show the observed data and the stacked histograms represent the signal and background expectation. The signal distribution in the left-hand plot has been scale up by a factor of 10 for clarity.

relative to $H \to WW^{(*)}$. For the intermediate and high mass search in 2011, the m_{ll} and $\Delta\phi_{ll}$ cuts are relaxed as the leptons from a higher mass Higgs tend to have higher p_{T} and larger angular separation.

The cut flow for the low m_h 0-jet 2011 analysis and the 0-jet 2012 analysis are shown in Tables 11.8 and 11.9. The tables give the observed number of events, along with the signal and background predictions. The tables are meant to provided a feel for the different levels of the various sources of background, at each stage of the analysis. Only the statistical uncertainties are quoted. Further

0-jet	Signal	WW	Di-boson	$t\bar{t}$	Single Top	Z/γ^*	$W+$jets	Total Bkg.	Obs.
Jet Veto	56.7 ± 0.2	1273 ± 79	97 ± 4	174 ± 12	95 ± 7	1039 ± 28	217 ± 4	2893 ± 115	2849
$m_{\ell\ell} < 50$ GeV	45.2 ± 0.2	312 ± 20	41 ± 3	29 ± 2	19 ± 2	168 ± 10	70 ± 2	639 ± 28	645
$p_{\mathrm{T}}^{\ell\ell}$ cut	40.1 ± 0.2	282 ± 18	35 ± 3	28 ± 2	18 ± 2	28 ± 6	49 ± 2	439 ± 26	443
$\Delta\phi_{\ell\ell} < 1.8$	39.0 ± 0.2	276 ± 17	33 ± 2	27 ± 2	18 ± 2	28 ± 6	44 ± 1	425 ± 26	429

Table 11.8: The observed and expected numbers of signal and background events in the low m_h selection of the 0-jet 2011 analysis. The signal is for $m_H = 125$ GeV. The W+jets background is estimated entirely from data, whereas MC predictions normalized to data in control regions are used for WW, Z/γ^*+jets, and top processes. Contributions from other background sources are taken directly from MC. Only statistical uncertainties associated with the number of events in the MC samples and the data control regions are shown.

0-jet	Signal	WW	Di-boson	$t\bar{t}$	Single Top	Z/γ^*	$W+$jets	Total Bkg.	Obs.
Jet Veto	47.5 ± 0.4	1308 ± 9	125 ± 4	184 ± 4	109 ± 6	850 ± 32	138 ± 4	2714 ± 34	2691
$p_{\mathrm{T}}^{\ell\ell} > 30$ GeV	43.4 ± 0.4	1077 ± 8	99 ± 4	165 ± 4	98 ± 5	47 ± 8	102 ± 2	1589 ± 14	1664
$m_{\ell\ell} < 50$ GeV	34.9 ± 0.4	244 ± 4	33 ± 2	28 ± 2	17 ± 2	5 ± 2	29 ± 1	356 ± 6	421
$\Delta\phi_{\ell\ell} < 1.8$	33.6 ± 0.4	234 ± 4	32 ± 2	27 ± 2	17 ± 2	4 ± 2	25 ± 1	339 ± 6	407

Table 11.9: The observed and expected numbers of signal and background events in the 0-jet 2012 analysis. The signal is for $m_H = 125$ GeV. The W+jets background is estimated entirely from data, whereas MC predictions normalized to data in control regions are used for SM WW and top processes. Contributions from other background sources are taken directly from MC. Only statistical uncertainties associated with the number of events in the MC samples and the data control regions are shown.

details on the background predictions and the associated systematic uncertainties are provided below.

The transverse mass, m_{T}, of events passing the 0-jet selection is used in the final fit. The transverse mass is defined as

$$m_{\mathrm{T}} = \sqrt{\left(E_{\mathrm{T}}^{ll} + E_{\mathrm{T}}^{\mathrm{miss}}\right)^2 - \left|\mathbf{p}_{\mathrm{T}}^{ll} + \mathbf{p}_{\mathrm{T}}^{\mathrm{miss}}\right|^2}, \tag{11.2}$$

where $E_{\mathrm{T}}^{ll} = \sqrt{|\mathbf{p}_{\mathrm{T}}^{ll}|^2 + m_{ll}^2}$, $|\mathbf{p}_{\mathrm{T}}^{\mathrm{miss}}| = E_{\mathrm{T}}^{\mathrm{miss}}$, and $|\mathbf{p}_{\mathrm{T}}^{ll}| = p_{T_{ll}}$. As discussed is Section 8.4, m_{T} is sensitive to the Higgs mass in the resonant $H \to WW^{(*)}$ production. The m_{T} distribution after the full 0-jet selection is shown in Figure 11.6. For m_h= 125 GeV, the Higgs signal distribution has the same shape as the W+jet background. The final fit cannot constrain the relative amount of W+jet in the signal region. It is thus critical that the W+jet background is well understood.

11.3.2 1-Jet Analysis

After the $E_{\mathrm{T}}^{\mathrm{miss,Rel}}$ requirement, events containing one reconstructed jet are dominated by top background and have significant contributions from SM WW and Z/γ^* background. The relative contri-

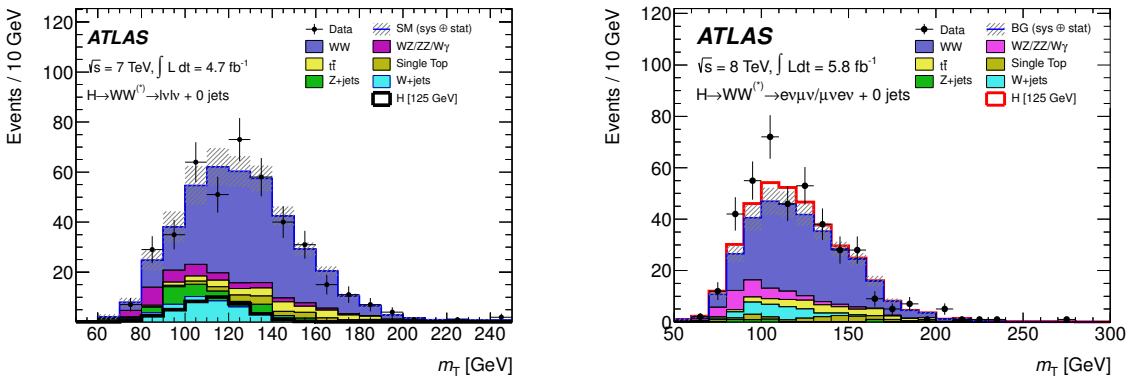

Figure 11.6: m_{T} distribution after the full 0-jet selection for the 2011 analysis (left-hand side) and the 2012 analysis (right-hand side). The points show the observed data and the stacked histograms represent the signal and background expectation. The signal distribution in the left-hand plot has not been scale up.

2011 Analysis Low m_h	2011 Analysis Intermediate m_h	2011 Analysis High m_h	2012 Analysis
b-jet veto	b-jet veto	b-jet veto	b-jet veto
$\lvert\mathbf{p}_{\mathrm{T}}^{\mathrm{tot}}\rvert < 30$ GeV	$\lvert\mathbf{p}_{\mathrm{T}}^{\mathrm{tot}}\rvert < 30$ GeV	$\lvert\mathbf{p}_{\mathrm{T}}^{\mathrm{tot}}\rvert < 30$ GeV	$\lvert\mathbf{p}_{\mathrm{T}}^{\mathrm{tot}}\rvert < 30$ GeV
$Z \to \tau\tau$ veto	$Z \to \tau\tau$ veto	$Z \to \tau\tau$ veto	$Z \to \tau\tau$ veto
$m_{ll} < 50$ GeV	$m_{ll} < 150$ GeV	-	$m_{ll} < 50$ GeV
$\Delta\phi_{ll} < 1.8$	-	-	$\Delta\phi_{ll} < 1.8$

Table 11.10: Summary of the event selection in the 1-jet analysis after requiring one reconstructed jet.

butions of the various backgrounds after the 1-jet requirement can be seen in Figure 11.3. Additional event selection is applied in the 1-jet analysis to remove these backgrounds. A summary of the 1-jet selection is given in Table 11.10

Top background has jets from b-quarks in the final state. A significant fraction of the top background can be removed by vetoing events in which the selected jet is identified as a b-jet. This b-jet veto removes over half of the top background with little loss in signal efficiency.

After the b-jet veto, a requirement is made on the magnitude of the "total" p_{T} in the event. The total p_{T}, referred to as $\mathbf{p}_{\mathrm{T}}^{\mathrm{tot}}$, is defined as the vector sum of the p_{T} of the lepton system, the p_{T} of the jet, and the p_{T} assigned to the neutrino(s), *i.e.*, $E_{\mathrm{T}}^{\mathrm{miss}}$:

$$\mathbf{p}_{\mathrm{T}}^{\mathrm{tot}} = \mathbf{p}_{T_{ll}} + \mathbf{p}_T(\mathrm{jet}) + \mathbf{E}_T^{miss}. \tag{11.3}$$

Events with fake $E_{\mathrm{T}}^{\mathrm{miss}}$ not associated to the leptons or jet have large values of $|\mathbf{p}_{\mathrm{T}}^{\mathrm{tot}}|$. $|\mathbf{p}_{\mathrm{T}}^{\mathrm{tot}}|$ is also sensitive to events in which a second jet balances the leptons-jet-$E_{\mathrm{T}}^{\mathrm{miss}}$ system but was not identified.

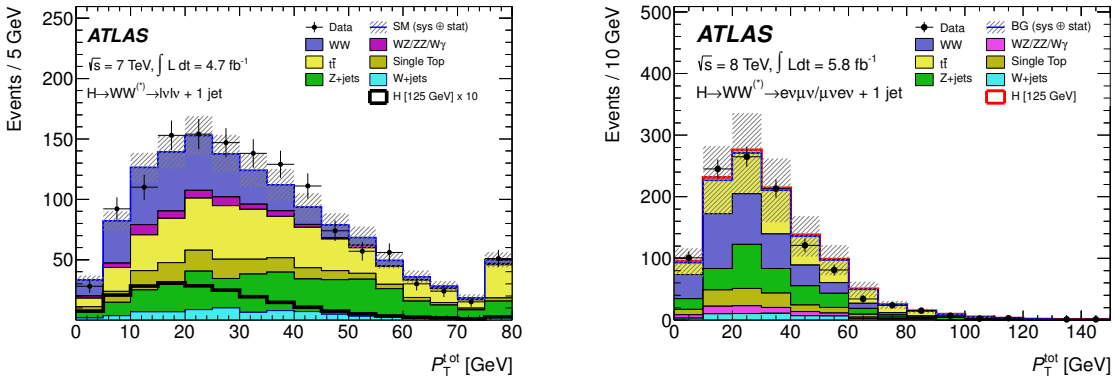

Figure 11.7: $|\mathbf{p}_{\mathrm{T}}^{\mathrm{tot}}|$ distribution after the b-jet veto in the 2011 analysis (left-hand side) and the 2012 analysis (right-hand side). The points show the observed data and the stacked histograms represent the signal and background expectation. The signal distribution in the left-hand plot has been scale up by a factor of 10 for clarity.

The $|\mathbf{p}_{\mathrm{T}}^{\mathrm{tot}}|$ distribution after the b-jet veto in the 1-jet analysis is shown in Figure 11.7. Requiring $|\mathbf{p}_{\mathrm{T}}^{\mathrm{tot}}|$ below 30 GeV suppresses both Z/γ^* and $t\bar{t}$ relative to signal.

A $Z \to \tau\tau$ veto is applied after the $|\mathbf{p}_{\mathrm{T}}^{\mathrm{tot}}|$ cut. The di-tau invariant mass, $m_{\tau\tau}$, is reconstructed using the collinear approximation [144]. This approximation assumes that the reconstructed leptons are τ decay products and that all the $E_{\mathrm{T}}^{\mathrm{miss}}$ is due to the neutrinos in the τ decays which are produced collinear to the reconstructed leptons. Events are rejected if the reconstructed di-tau invariant mass is within 25 GeV of the Z mass. The $Z \to \tau\tau$ veto removes a significant fraction of $Z/\gamma^* \to \tau\tau$ events, with essentially no loss in signal efficiency.

The remainder of the 1-jet event selection is designed to suppress the SM WW background. The same m_{ll} and $\Delta\phi_{ll}$ requirements used to remove SM WW in the 0-jet analysis are applied in the 1-jet analysis. Figure 11.8 shows the m_{ll} distribution after the $Z \to \tau\tau$ veto. The low m_{ll} and $\Delta\phi_{ll}$ requirements suppress the residual SM WW and top backgrounds with respect to the 1-jet $H \to WW^{(*)}$ events.

After the full 1-jet selection, there are roughly equal amounts of SM WW and top background. The cut flow for the low m_h 1-jet 2011 analysis and the 1-jet 2012 analysis are shown in Tables 11.11 and 11.12. As before, the tables are meant to provided a feel for the different levels of the various sources of background, and only the statistical uncertainties are quoted. Further details on the background predictions and the associated systematic uncertainties are provided below.

The transverse mass of events passing the 1-jet selection is used in the final fit. The m_{T} distribution after the full 1-jet selection is shown in Figure 11.9. The m_{T} shape provides additional separation of SM WW and top background, but not against the W+jet background.

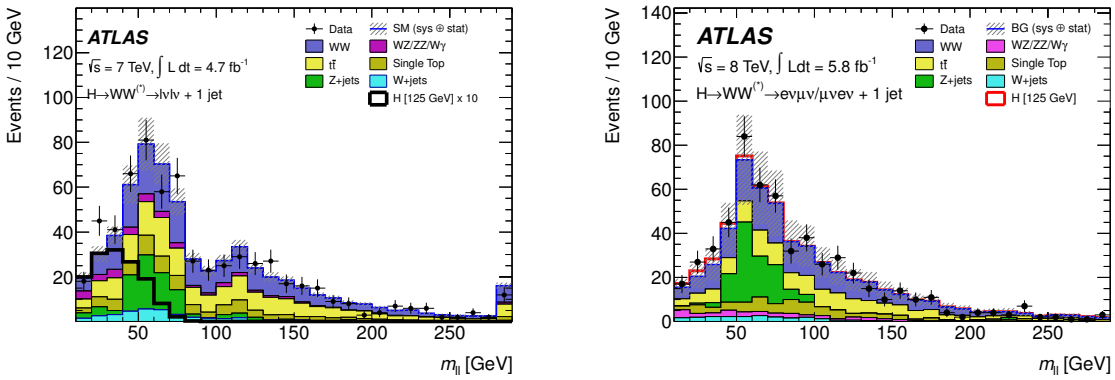

Figure 11.8: m_{ll} distribution after the $Z \to \tau\tau$ veto for the 2011 analysis (left-hand side) and the 2012 analysis (right-hand side). The points show the observed data and the stacked histograms represent the signal and background expectation. The signal distribution in the left-hand plot has been scale up by a factor of 10 for clarity.

1-Jet	Signal	WW	Di-boson	$t\bar{t}$	Single Top	Z/γ^*	W + jets	Total Bkg.	Obs.
1 jet	22.7 ± 0.1	343 ± 54	56 ± 3	1438 ± 60	436 ± 19	357 ± 17	85 ± 3	2715 ± 142	2706
b-jet veto	20.9 ± 0.1	319 ± 50	52 ± 3	412 ± 18	139 ± 7	332 ± 16	76 ± 3	1330 ± 84	1369
$\lvert\mathbf{p}_{\mathrm{T}}^{tot}\rvert < 30$ GeV	14.0 ± 0.1	226 ± 35	34 ± 2	181 ± 8	80 ± 4	108 ± 8	37 ± 2	666 ± 51	684
$Z \to \tau\tau$ veto	14.0 ± 0.1	220 ± 34	34 ± 2	173 ± 8	77 ± 4	85 ± 7	37 ± 2	627 ± 50	644
$m_{\ell\ell} < 50$ GeV	10.9 ± 0.1	49 ± 8	14 ± 2	33 ± 2	18 ± 1	24 ± 3	12 ± 1	148 ± 12	170
$\Delta\phi_{\ell\ell} < 1.8$	10.1 ± 0.1	44 ± 7	13 ± 2	31 ± 2	17 ± 1	10 ± 2	10 ± 1	126 ± 10	145

Table 11.11: The observed and expected numbers of signal and background events in the low m_h selection of the 1-jet 2011 analysis. The signal is for $m_H = 125$ GeV. The W+jets background is estimated entirely from data, whereas MC predictions normalized to data in control regions are used for WW, Z/γ^*+jets, and top processes. Contributions from other background sources are taken directly from MC. Only statistical uncertainties associated with the number of events in the MC samples and the data control regions are shown.

1-Jet	Signal	WW	Di-boson	$t\bar{t}$	Single Top	Z/γ^*	W + jets	Total Bkg.	Obs.
1 jet	24.9 ± 0.3	396 ± 5	74 ± 3	1652 ± 12	479 ± 12	283 ± 20	68 ± 3	2953 ± 27	2874
b-jet veto	21.1 ± 0.3	334 ± 4	56 ± 2	349 ± 6	115 ± 6	236 ± 18	53 ± 2	1144 ± 21	1115
$\lvert\mathbf{p}_{\mathrm{T}}^{tot}\rvert < 30$ GeV	12.2 ± 0.2	210 ± 3	30 ± 2	139 ± 4	63 ± 5	124 ± 14	23 ± 2	590 ± 15	611
$Z \to \tau\tau$ veto	12.2 ± 0.2	204 ± 3	29 ± 2	133 ± 3	61 ± 5	98 ± 12	23 ± 2	547 ± 14	580
$m_{\ell\ell} < 50$ GeV	9.2 ± 0.2	37 ± 1	10 ± 1	21 ± 1	12 ± 2	16 ± 5	8.0 ± 0.9	104 ± 6	122
$\Delta\phi_{\ell\ell} < 1.8$	8.6 ± 0.2	34 ± 1	9 ± 1	20 ± 1	11 ± 2	3 ± 2	6.4 ± 0.7	84 ± 4	106

Table 11.12: The observed and expected numbers of signal and background events in the 1-jet 2012 analysis. The signal is for $m_H = 125$ GeV. The W+jets background is estimated entirely from data, whereas MC predictions normalized to data in control regions are used for SM WW and top processes. Contributions from other background sources are taken directly from MC. Only statistical uncertainties associated with the number of events in the MC samples and the data control regions are shown.

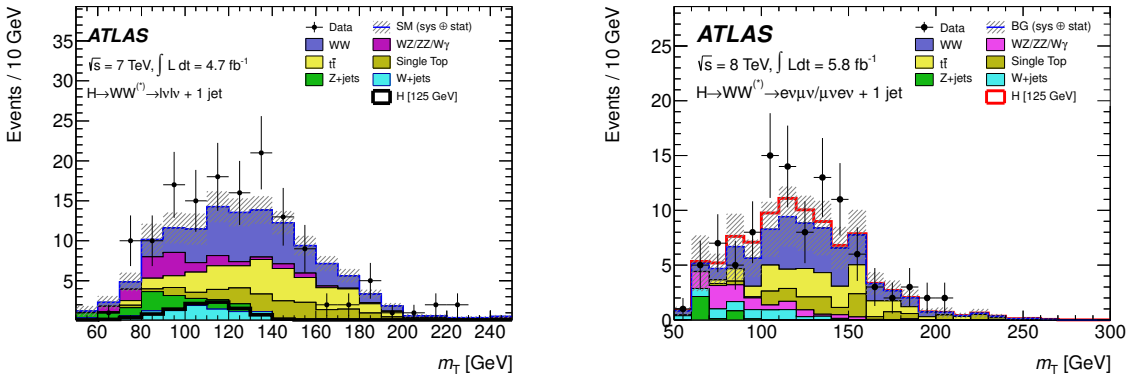

Figure 11.9: m_{T} distribution after the full 1-jet selection for the 2011 analysis (left-hand side) and the 2012 analysis (right-hand side). The points show the observed data and the stacked histograms represent the signal and background expectation. The signal distribution in the left-hand plot has not been scale up.

2011 Analysis Low m_h	2011 Analysis Intermediate m_h	2011 Analysis High m_h	2012 Analysis
b-jet veto	b-jet veto	b-jet veto	b-jet veto
$\lvert\Delta\eta_{jj}\rvert > 3.8$	$\lvert\Delta\eta_{jj}\rvert > 3.8$	$\lvert\Delta\eta_{jj}\rvert > 3.8$	$\lvert\Delta Y_{jj}\rvert > 3.8$
Opp. hemispheres	Opp. hemispheres	Opp. hemispheres	-
central-jet veto	central-jet veto	central-jet veto	central-jet veto
$m_{jj} > 500$ GeV	$m_{jj} > 500$ GeV	$m_{jj} > 500$ GeV	$m_{jj} > 500$ GeV
$\lvert\mathbf{p}_{\mathrm{T}}^{\mathrm{tot}}\rvert < 30$ GeV	$\lvert\mathbf{p}_{\mathrm{T}}^{\mathrm{tot}}\rvert < 30$ GeV	$\lvert\mathbf{p}_{\mathrm{T}}^{\mathrm{tot}}\rvert < 30$ GeV	$\lvert\mathbf{p}_{\mathrm{T}}^{\mathrm{tot}}\rvert < 30$ GeV
-	-	-	$Z \to \tau\tau$ veto
$m_{ll} < 80$ GeV	$m_{ll} < 150$ GeV	-	$m_{ll} < 80$ GeV
$\Delta\phi_{ll} < 1.8$	-	-	$\Delta\phi_{ll} < 1.8$

Table 11.13: Summary of the event selection in the 2-jet analysis after the requiring ≥ 2 reconstructed jets.

11.3.3 2-Jet Analysis

Events with two or more reconstructed jets have little signal from ggF and an enormous amount of top background. Figure 11.3 shows the large top background in the high jet multiplicity bins after the $E_{\mathrm{T}}^{\mathrm{miss,Rel}}$ requirement. The 2-jet analysis is designed to select Higgs events produced via vector boson fusion, VBF. VBF events produce high p_{T} jets widely separated in η, with little hadronic activity between the jets. Requiring jets consistent with VBF production reduces the large top background. A summary of the 2-jet selection is given in Table 11.13

The 2-jet analysis makes several requirements on the two highest p_{T} jets, referred to as the "tagging jets". The tagging jets are required to be separated by 3.8 units in η and have an invariant mass greater than 500 GeV. In the 2011 analysis, the jets were required to be on opposite

2-Jet	Signal	WW	Di-boson	$t\bar{t}$	Single Top	Z/γ^*	$W+$jets	Total Bkg.	Obs.
≥ 2 jets	11.4 ± 0.1	142 ± 2	26 ± 2	5939 ± 17	339 ± 5	120 ± 7	40 ± 4	6605 ± 20	6676
Central jet veto (20 GeV)	9.0 ± 0.1	113 ± 2	20 ± 1	3279 ± 13	238 ± 4	89 ± 6	25 ± 3	3765 ± 15	3811
b-jet veto	7.6 ± 0.1	98 ± 1	18 ± 1	353 ± 4	51 ± 2	77 ± 5	19 ± 2	615 ± 8	667
Opp. hemispheres	4.2 ± 0.1	46 ± 1	7 ± 1	149 ± 3	21 ± 1	32 ± 3	9 ± 1	264 ± 5	269
$\lvert\Delta\eta_{\rm jj}\rvert > 3.8$	1.8 ± 0.1	8.4 ± 0.4	0.9 ± 0.2	23.2 ± 1.0	2.2 ± 0.4	5.8 ± 1.7	1.7 ± 0.4	42.2 ± 2.1	40
$m_{\rm jj} > 500$ GeV	1.3 ± 0.1	3.9 ± 0.3	0.4 ± 0.1	10.4 ± 0.6	1.0 ± 0.3	0.7 ± 0.4	0.9 ± 0.3	17.3 ± 0.9	13
$m_{\ell\ell} < 80$ GeV	0.9 ± 0.1	1.1 ± 0.2	0.1 ± 0.1	1.4 ± 0.2	0.4 ± 0.1	0.2 ± 0.2	0.2 ± 0.2	3.2 ± 0.4	2
$\Delta\phi_{\ell\ell} < 1.8$	0.8 ± 0.1	0.8 ± 0.1	0.1 ± 0.1	0.9 ± 0.2	0.1 ± 0.1	-	-	1.8 ± 0.3	1

Table 11.14: The observed and expected numbers of signal and background events in the low m_h selection of the 2-jet 2011 analysis. The signal is for $m_H = 125$ GeV. The W+jets background is estimated entirely from data, whereas MC predictions normalized to data in control regions are used for WW, Z/γ^*+jets, and top processes. Contributions from other background sources are taken directly from MC. Only statistical uncertainties associated with the number of events in the MC samples and the data control regions are shown.

hemispheres of the detector ($|\eta_{j1}\eta_{j2}| < 0$). Events in which an additional jet, with $p_{\rm T} > 20$ GeV, is produced between the two tagging jets are rejected; this is referred to as a "central jet veto". These requirements select jets consistent with VBF production.

Aside from the tagging jet selection, the 2-jet analysis follows selection of the 1-jet analysis. A b-jet veto is applied to remove top background. The total $p_{\rm T}$, now defined to include all selected jets, is required to be below 30 GeV, suppressing top and Z/γ^* background.

Finally, the m_{ll} and $\Delta\phi_{ll}$ requirements are applied in the 2-jet analysis to suppresses SM WW. The upper bound on m_{ll} is increased to 80 GeV.

After the full event selection the signal-to-background is roughly 0.5 in the 2-jet bin. The cut flow for the low m_h 2-jet 2011 analysis and the 2-jet 2012 analysis are shown in Tables 11.14 and 11.15. The dominant sources of background are SM WW and top production. Because of the poor statistics in the 2-jet analysis, only event yields are used in the final fit.

11.4 Background Estimation

In general, the various backgrounds to the selected events are estimated using the MC predictions corrected by control regions in data. The major exception to this is the W+jet background which is estimated using a fully data-driven method. The small backgrounds from non-WW di-boson processes are estimated directly from MC. In the 2-jet analysis, statistically adequate control regions for SM WW and Z/γ^* cannot be defined. As a result, in the 2-jet analysis, these backgrounds are estimated directly from MC.

A summary of the backgrounds in the signal region is given in Table 11.16 for the 2011 analysis, and in Table 11.17 for the 2012 analysis. The background results are quoted for the signal-rich

2-Jet	Signal	WW	Di-boson	$t\bar{t}$	Single Top	Z/γ^*	$W+$jets	Total Bkg.	Obs.
≥ 2 jets	14.5 ± 0.2	139 ± 3	30 ± 2	7039 ± 24	376 ± 11	104 ± 12	71 ± 4	7759 ± 29	7845
b-jet veto	9.6 ± 0.2	95 ± 2	19 ± 1	356 ± 6	44 ± 4	62 ± 9	21 ± 2	597 ± 12	667
$\lvert\Delta Y_{jj}\rvert > 3.8$	2.0 ± 0.1	8.3 ± 0.6	2.0 ± 0.4	31 ± 2	5 ± 1	4 ± 2	1.4 ± 0.5	52 ± 3	44
Central jet veto (20 GeV)	1.6 ± 0.1	6.5 ± 0.5	1.3 ± 0.3	16 ± 1	4 ± 1	1 ± 1	0.5 ± 0.3	29 ± 2	22
$m_{jj} > 500$ GeV	1.1 ± 0.0	3.2 ± 0.4	0.7 ± 0.2	6.2 ± 0.7	1.8 ± 0.6	-	< 0.2	12 ± 1	13
$\lvert\mathbf{p}_T^{tot}\rvert < 30$ GeV	0.8 ± 0.0	1.7 ± 0.3	0.3 ± 0.1	2.5 ± 0.5	0.8 ± 0.4	-	< 0.2	5.4 ± 0.7	6
$Z \to \tau\tau$ veto	0.7 ± 0.0	1.8 ± 0.3	0.3 ± 0.1	2.4 ± 0.4	0.8 ± 0.4	-	< 0.2	5.2 ± 0.7	6
$m_{\ell\ell} < 80$ GeV	0.7 ± 0.0	0.6 ± 0.2	0.1 ± 0.1	0.8 ± 0.3	0.3 ± 0.2	-	< 0.2	1.9 ± 0.5	3
$\Delta\phi_{\ell\ell} < 1.8$	0.6 ± 0.0	0.5 ± 0.2	0.1 ± 0.1	0.5 ± 0.3	0.3 ± 0.2	-	< 0.2	1.4 ± 0.4	2

Table 11.15: The observed and expected numbers of signal and background events in the 2-jet 2012 analysis. The signal is for $m_H = 125$ GeV. The W+jets background is estimated entirely from data, whereas MC predictions normalized to data in control regions are used for SM WW and top processes. Contributions from other background sources are taken directly from MC. Only statistical uncertainties associated with the number of events in the MC samples and the data control regions are shown.

		Signal	WW	Di-boson	$t\bar{t}$	Single Top	Z/γ^*	$W+$jets	Total Bkg.	Obs.
0-jet	$m_H = 125$ GeV	26 ± 7	108 ± 12	12 ± 2	7 ± 2	5 ± 1	14 ± 6	27 ± 16	172 ± 21	174
	$m_H = 240$ GeV	61 ± 17	450 ± 49	24 ± 3	73 ± 15	42 ± 9	6 ± 2	36 ± 24	632 ± 63	627
1-jet	$m_H = 125$ GeV	6 ± 2	16 ± 5	5 ± 2	8 ± 2	4 ± 2	5 ± 2	5 ± 3	42 ± 7	56
	$m_H = 240$ GeV	24 ± 9	95 ± 21	9 ± 1	84 ± 21	39 ± 15	5 ± 1	8 ± 7	241 ± 41	232
2-jet	$m_H = 125$ GeV	0.5 ± 0.2	0.2 ± 0.2	-	0.2 ± 0.1	-	0.0 ± 0.1	-	0.4 ± 0.2	0
	$m_H = 240$ GeV	2.6 ± 0.4	1.2 ± 0.8	0.1 ± 0.1	2.2 ± 1.0	0.3 ± 0.2	-	0.1 ± 0.1	3.9 ± 1.4	2

Table 11.16: The expected numbers of signal ($m_H = 125$ GeV and 240 GeV) and background events after the full low m_H and intermediate m_H selections in the 2011 analysis. The results are quoted in the signal-rich region of m_T, defined by of $0.75\,m_H < m_T < m_H$ for $m_H = 125$ GeV and $0.6\,m_H < m_T < m_H$ for $m_H = 240$ GeV. The observed numbers of events are also displayed. The uncertainties shown are the combination of the statistical and all systematic uncertainties, taking into account the constraints from control samples. Note that these results differ from those discussed earlier due to the application of the additional m_T requirements. All numbers are summed over lepton flavors. Backgrounds with fewer than 0.01 events expected are marked as negligible using a '-'.

region of m_T, defined by of $0.75\,m_H < m_T < m_H$ for $m_H = 125$ GeV and $0.6\,m_H < m_T < m_H$ for $m_H = 240$ GeV. The uncertainties quoted in the tables are the combination of the statistical and all systematic uncertainties, taking into account the constraints from the various control regions defined below. The remainder of this section describes the estimation of these various backgrounds.

11.4.1 Standard Model WW Background

The SM WW MC background predictions in the 0-jet and 1-jet analyses are normalized using SM WW control regions. The control regions are defined using the same selection as the signal regions except that the $\Delta\phi_{ll}$ requirement is removed and the upper bound on m_{ll} is replaced with a lower bound of 80 GeV, *i.e.,* $m_{ll} > 80$ GeV. Tables 11.18 and 11.19 show the yields in the SM WW

	Signal	WW	Di-boson	$t\bar{t}$	Single Top	Z/γ^*	W + jets	Total Bkg.	Obs.
0-jet	20 ± 4	101 ± 13	12 ± 3	8 ± 2	3.4 ± 1.5	1.9 ± 1.3	15 ± 7	142 ± 16	185
1-jet	5 ± 2	12 ± 5	1.9 ± 1.1	6 ± 2	3.7 ± 1.6	0.1 ± 0.1	2 ± 1	26 ± 6	38
2-jet	0.34 ± 0.07	0.10 ± 0.14	0.10 ± 0.10	0.15 ± 0.10	-	-	-	0.35 ± 0.18	0

Table 11.17: The expected numbers of signal ($m_H = 125$ GeV) and background events after the full selections in the 2012 analysis. The results are quoted in the signal-rich region of m_{T}, defined by $0.75\, m_H < m_{\mathrm{T}} < m_H$ for $m_H = 125$ GeV. The observed numbers of events are also displayed. The uncertainties shown are the combination of the statistical and all systematic uncertainties, taking into account the constraints from control samples. These results differ from those discussed earlier due to the application of the additional m_{T} requirement. All numbers are summed over lepton flavors. Backgrounds with fewer than 0.01 events expected are marked as negligible using a '-'.

	Signal	WW	Di-boson	$t\bar{t}$	Single Top	Z/γ^*	W + jets	Total Bkg.	Obs.
WW 0-jet	0.3 ± 0.1	471 ± 3	26 ± 1	87 ± 2	42 ± 2	7 ± 2	49 ± 2	682 ± 5	697
WW 1-jet	0.1 ± 0.1	128 ± 2	12 ± 1	89 ± 2	34 ± 2	9 ± 2	11 ± 1	282 ± 4	270

Table 11.18: The observed and expected numbers of signal and background events in the 0-jet and 1-jet WW control region for the 2011 analysis. The W+jets background is estimated entirely from data, the top background is normalized to data in the top control region. Contributions from other background sources are taken directly from MC. Only statistical uncertainties associated with the number of events in the MC samples and the data control regions are shown.

	Signal	WW	Di-boson	$t\bar{t}$	Single Top	Z/γ^*	W + jets	Total Bkg.	Obs.
WW 0-jet	0.3 ± 0.0	531 ± 5	43 ± 2	104 ± 3	62 ± 4	11 ± 4	38 ± 1	789 ± 9	820
WW 1-jet	0.1 ± 0.0	112 ± 3	13 ± 1	80 ± 3	34 ± 3	9 ± 4	7.7 ± 0.8	256 ± 6	255

Table 11.19: The observed and expected numbers of signal and background events in the 0-jet and 1-jet WW control region for the 2012 analysis. The W+jets background is estimated entirely from data, the top background is normalized to data in the top control region. Contributions from other background sources are taken directly from MC. Only statistical uncertainties associated with the number of events in the MC samples and the data control regions are shown.

control regions for the 2011 and 2012 analyses. In the 0-jet analysis, the WW control region is ~70% pure. In the 1-jet analysis, there is significant contamination from top production; the purity is only around 45%. The yields predicted by the MC agree well with the observed data for both the 0-jet and 1-jet analysis in 2011 and 2012. Figure 11.10 shows the m_{T} modeling in the WW control regions. The MC prediction accurately describes the m_{T} shape in the region enriched in SM WW background.

The overall SM WW normalization is floated in the final fit, which includes the constraint from the WW control regions. Because of relatively large theoretical uncertainties on the cross section predictions in different jet multiplicities, the normalization is fit separately in the 0-jet and 1-jet

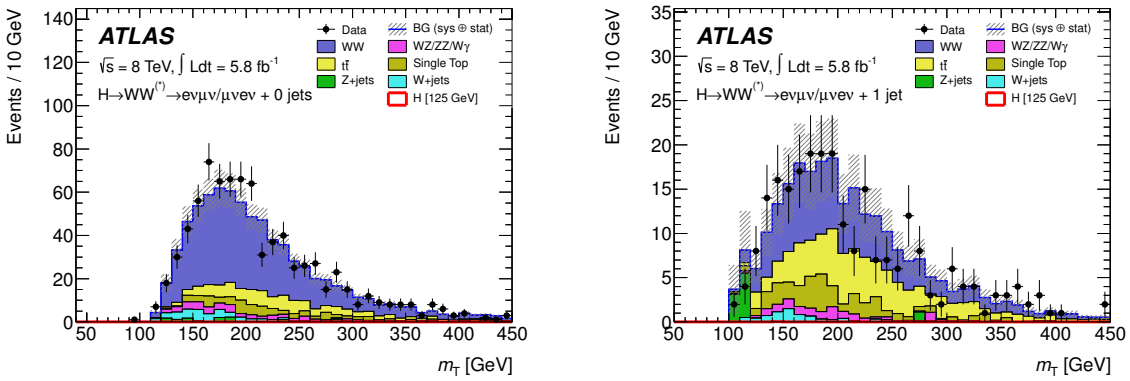

Figure 11.10: m_{T} distribution in the WW control region for the 0-jet 2012 analysis (left-hand side) and the 1-jet 2012 analysis (right-hand side). The points show the observed data and the stacked histograms represent the signal and background expectation.

bins. The WW normalization receives an additional constraint from the m_{T} side bands in the signal regions.

In the 2011 analysis, the WW control region is only used in the low m_h search. For intermediate and high m_h, the WW control regions have a large signal contamination. These analyses use the SM WW prediction directly from MC. In the 2-jet analysis, a statistically adequate WW control region cannot be defined, so the prediction is also taken from MC.

The total uncertainty on the predicted WW background in the signal region is discussed in the following section.

11.4.2 Top Background

The top background in the 0-jet analysis is estimated from MC using corrections derived with data. Corrections to the MC are applied to improve the overall normalization and the modeling of jet veto efficiency. The method is the same as was used in the WW cross section measurement, described in Chapter 10. As a reminder, the method normalizes the MC prediction using the event yield before the jet veto. An additional correction factor is applied to reduce the systematic uncertainty associated to the jet energy scale. See Section 10.4 for more details.

In the 1-jet and 2-jet analyses, the top background prediction is normalized using control regions. The top control regions are defined by reversing the b-jet veto and dropping the $\Delta\phi_{ll}$ and m_{ll} requirements. Tables 11.20 shows the yields in the 1-jet and 2-jet top control regions for the 2011 analyses. Top production is the dominant contribution to both the 1-jet and 2-jet control regions. The yields predicted by the MC agree well with the observed data for both the 1-jet and 2-jet

	Signal	WW	Di-boson	$t\bar{t}$	Single Top	Z/γ^*	W + jets	Total Bkg.	Obs.
Top 1-jet	1.2 ± 0.1	20 ± 1	1.9 ± 0.5	434 ± 4	169 ± 4	7 ± 2	4 ± 1	635 ± 6	676
Top 2-jet	0.1 ± 0.1	0.4 ± 0.1	-	10.0 ± 0.7	1.0 ± 0.3	-	-	11.4 ± 0.7	10

Table 11.20: The observed and expected numbers of signal and background events in the 1-jet and 2-jet top control region for the 2011 analysis. The W+jets background is estimated entirely from data. Contributions from other background sources are taken directly from MC. Only statistical uncertainties associated with the number of events in the MC samples and the data control regions are shown.

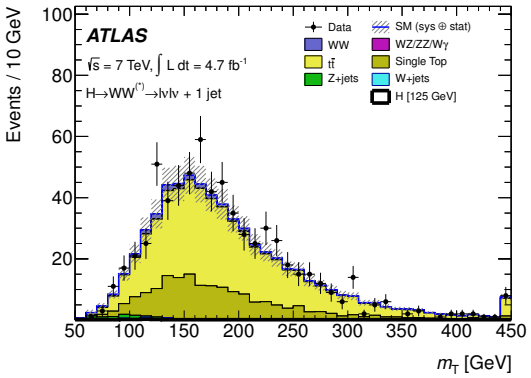

Figure 11.11: m_{T} distribution in the Top control region for the 1-jet 2011 analysis. The distribution for the 2-jet analysis is not shows as the statistics are too poor to make a meaningful shape comparison. The points show the observed data and the stacked histograms represent the signal and background expectation.

analysis. Figure 11.11 shows the m_{T} modeling in the 1-jet top control region. The MC prediction accurately describes the m_{T} shape in the region enriched in top background. The m_{T} distribution for the 2-jet analysis is not shown as the statistics are too poor to make a meaningful shape comparison.

In the 0-jet bin, the top background estimate, with its associated uncertainty, is included as a nuisance parameter in the final fit. In the 1-jet and 2-jet bins, the top normalization is floated in the final fit using the control regions. Separate top normalizations are used in the 1-jet and 2-jet bins. The top background is also a significant contribution to the 1-jet WW control region. The correlation among control regions is properly handled in the fit.

11.4.3 Z/γ^* Background

The "ABCD" method, described in Chapter 8, is used to predict the Z/γ^* background in the same-flavor channels of the 2011 analysis. A Z/γ^* control region is defined as the full selection criteria except $\Delta\phi_{ll}$ and with $E_{\mathrm{T}}^{\mathrm{miss,Rel}}$ between 20 and 45 GeV. Events in this intermediate $E_{\mathrm{T}}^{\mathrm{miss,Rel}}$ region

are used to estimate the background passing the full $E_{\mathrm{T}}^{\mathrm{miss,Rel}}$ requirement using an extrapolation factor measured in the Z peak. The acceptance of the $\Delta\phi_{ll}$ cut is taken from simulation. The method is performed separately in the 0-jet and 1-jet analyses. The resulting uncertainty on the Z/γ^* background in the signal region is 38%, in the 0-jet analysis, and 33%, in the 1-jet analysis. The "ABCD" method is also used to predict the Z/γ^* background in the WW control regions. In this case, the WW selection is used with an intermediate $E_{\mathrm{T}}^{\mathrm{miss,Rel}}$ requirement.

The relatively small $Z/\gamma^* \to \tau\tau$ background in the opposite-flavor analyses is estimated using MC. The overall MC modeling is checked in regions enriched in Z/γ^*, but these regions are not used as constraints in the background prediction.

The Z/γ^* predictions, in the signal and control regions, are included with their associated systematic uncertainties as nuisance parameters in the final fit.

11.4.4 W+jet Background

The rate at which jets are misidentified as leptons may not be accurately described in the MC. The fake factor method, described in detail in Chapter 9, is a data-driven procedure for estimating background arising from misidentification. It is used to estimate the W+jet background in various $H \to WW^{(*)}$ signal regions. The remainder of this section only provides the details of the fake factor method specific to the selection used in the 2011 and 2012 $H \to WW^{(*)}$ search. The reader is referred to Chapter 9 for details on the method.

The muon denominators are defined to have looser isolation and impact parameters requirements than used in the full selection. In addition, muons selected as denominators are required to fail the full muon identification criteria of the signal region. The electron denominators are required to fail the medium isEM requirement and to satisfy a looser isolation requirement. The measured electron and muon fake factors, with the corresponding uncertainties, for the 2011 and 2012 analyses are shown in Figures 11.12 and 11.13.

The total uncertainty on the W+jet background prediction is dominated by the uncertainties on the fake factors. The systematic uncertainties are given in Figures 11.12 and 11.13. Sample dependence is the dominant source of uncertainty on the fake factors, see Chapter 9 for further discussion. The sample dependence has been evaluated with a closure test using W+jet and di-jet MC. The systematic uncertainty assigned to the sample dependence is ∼40% for both the 2011 and 2012 analyses.

The background predictions in 0-jet and 1-jet signal regions are given in Table 11.21. The 2011 results are broken down by lepton channel. The W+jet prediction in the 2012 analysis is nearly a factor two smaller than the $e\mu$-channel of the 2011 analysis when one corrects for the luminosities

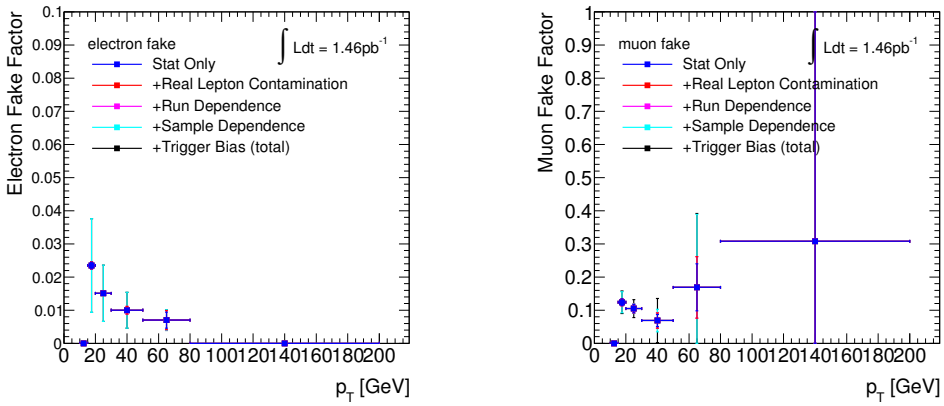

Figure 11.12: Measured electron (left) and muon (right) fake factors for the 2011 analysis. The systematic uncertainties are included in the error bands.

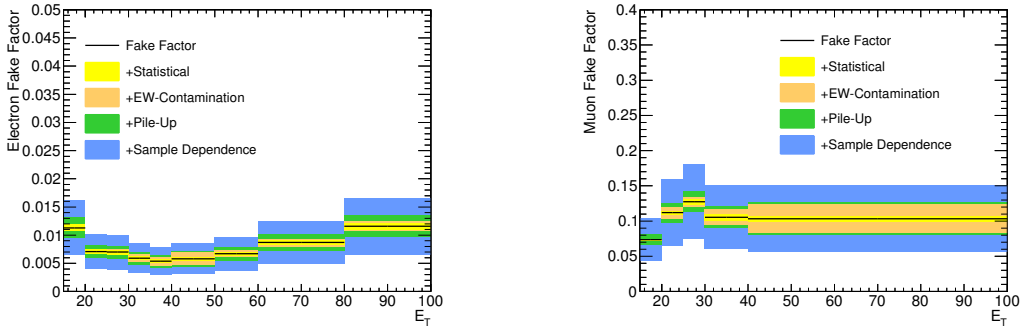

Figure 11.13: Measured electron (left) and muon (right) fake factors for the 2011 analysis. The systematic uncertainties are included in the error bands.

and the increased W+jet cross section at 8 TeV with respect to 7 TeV. This reduction reflects the tighter lepton identification operating points chosen for the 2012 analysis. The reduction in W+jet background is probably the single most significant improvement with the 2012 analysis.

As described in Chapter 9, the W+jet background modeling can be validated in events with same-sign leptons. The predictions in the same-sign validation regions for the 2011 and 2012 analyses are shown in Figures 11.14 and 11.15. The W+jet prediction is obtained from the fake factor method, the other background contributions are estimated from MC. Because of the tighter lepton identification criteria, the W+jet background is a smaller contribution in the same-sign validation region in the 2012 analysis. In both the 2011 and 2012 analyses, the agreement in the same-sign control region provides confidence in the W+jet modeling.

The fake factor method is used to predict the W+jet background in the various signal and control

	2011 low m_h ee-channel	2011 low m_h $\mu\mu$-channel	2011 low m_h $e\mu$-channel	2012 $e\mu$-channel
0-jet	$4.83 \pm 0.30 \pm 2.79$	$1.19 \pm 0.42 \pm 0.39$	$21.4 \pm 0.72 \pm 11.20$	$15.43 \pm 0.80 \pm 6.61$
1-jet	$1.17 \pm 0.15 \pm 0.68$	$0.45 \pm 0.28 \pm 0.09$	$3.26 \pm 0.30 \pm 1.60$	$2.31 \pm 0.40 \pm 1.03$

Table 11.21: Prediction of the W+jet background in the 2011 and 2012 analysis, for the 0-jet and 1-jet bins. The first uncertainty is the statistical uncertainty from the W+jet control region. The second uncertainty is the systematic uncertainty from the uncertainty associated to the fake factors. The background results are quoted for the signal-rich region of m_{T}, defined by of $0.75\,m_H < m_{\mathrm{T}} < m_H$ with $m_H = 125$ GeV.

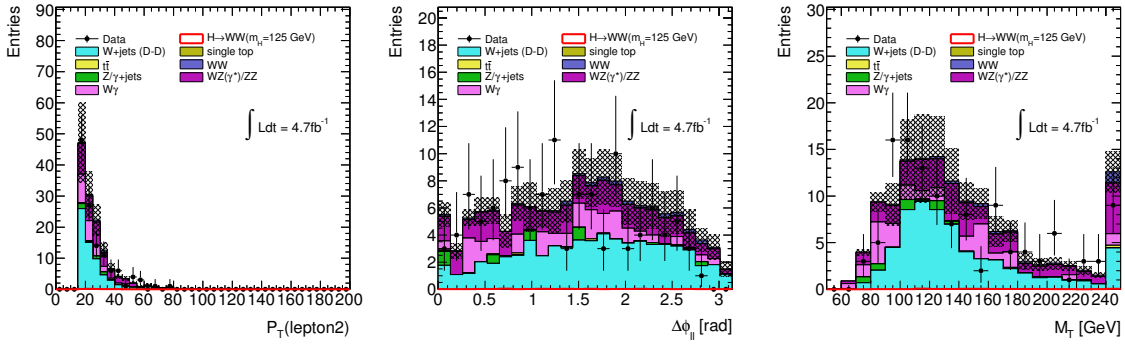

Figure 11.14: Modeling of the same sign validation region after the jet-veto in the 2011 0-jet analysis. The sub-leading lepton p_{T} is shown on the left, $\Delta\phi_{ll}$ is shown in the middle, and m_{T} is given on the right. The W+jet prediction is obtained from the fake factor method, the other background contributions are estimated from MC. The error band represents the systematic uncertainty associated to the W+jet prediction.

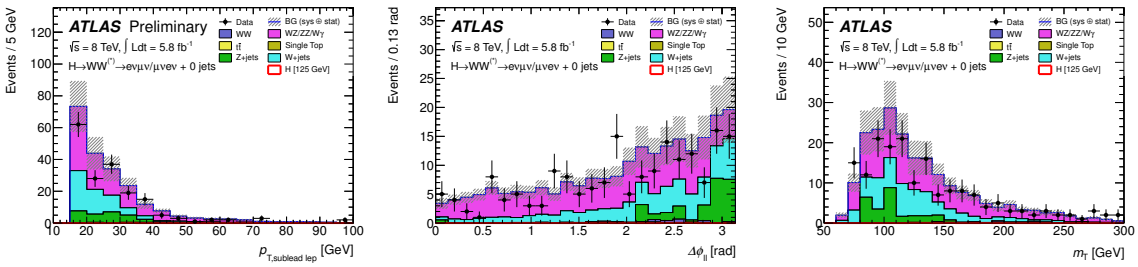

Figure 11.15: Modeling of the same sign validation region after the jet-veto in the 2012 0-jet analysis. The sub-leading lepton p_{T} is shown on the left, $\Delta\phi_{ll}$ is shown in the middle, and m_{T} is given on the right. The W+jet prediction is obtained from the fake factor method, the other background contributions are estimated from MC. The error band represents the systematic uncertainty associated to the W+jet prediction.

regions. The predictions, with their associated systematic uncertainties, are included as nuisance parameters in the final fit.

11.4.5 Di-boson Background

The relatively small non-WW di-boson backgrounds are estimated directly from MC. The overall MC modeling of the $W\gamma$ background is checked in dedicated control regions enriched in $W\gamma$. These regions show good modeling, but are not used as constraints in the background prediction.

Uncertainties on the $W\gamma$ background normalization are evaluated for each jet bin using the procedure described in Reference [145]. The uncertainty relative to the predicted $W\gamma$ background is 11% for the 0-jet bin and 50% for the 1-jet bin. For $W\gamma^*$ with $m_{ll} < 7$ GeV, a K-factor of 1.3 ± 0.3 is applied to the MadGraph LO prediction based on the comparison with the `MCFM` NLO calculation. The corresponding K-factor and uncertainty for WZ^* with $m_{ll} > 7$ GeV is 1.51 ± 0.45.

The di-boson predictions, in the signal and the control regions, are included with their associated systematic uncertainties as nuisance parameters in the final fit.

11.5 Systematics

The main sources of systematic uncertainty are summarized in Table 11.22, for the 2011 analysis, and Table 11.23, for the 2012 analysis. These are each described in turn below.

The dominant uncertainties on the predicted signal yield is from the theoretical uncertainties on the production cross section. These uncertainties are determined following References [34, 35]. The QCD renormalization and factorization scales are varied up and down independently by a factor of two. Independent uncertainties on the ggF signal production are assumed for the inclusive cross section and for the production cross section for events with at least one jet or at least two jets. The relative 0-jet (1-jet) cross section uncertainties depend on m_h, rising from 21% (31%) at m_h= 125 GeV and m_h= 240 GeV to 42% (31%) at m_h= 600 GeV [35, 145, 146]. Further uncertainties on the modeling of the ggF signal process are estimated by using MC@NLO as an alternative generator. The uncertainties associated with the underlying event and the parton showering are taken into account in the acceptance uncertainty, but are small compared to the scale uncertainties on the cross sections in exclusive jet bins.

The PDF uncertainties are estimated, following References [147, 148, 149, 150], by the envelopes of error sets as well as different PDF sets, applied separately to quark-quark, quark-gluon, and gluon-gluon initiated processes. The relative PDF uncertainty on the ggF signal process is about 8%; the VBF uncertainty varies from 2% at $m_h = 125$ GeV to 4% at $m_h = 600$ GeV.

Source (0-jet)	Signal (%)	Bkg. (%)
Inclusive ggF signal ren./fact. scale	19	-
1-jet incl. ggF signal ren./fact. scale	10	-
W+jets fake factor	-	10
Parton distribution functions	8	2
WW normalization	-	6
Jet energy scale	6	-
Source (1-jet)	Signal (%)	Bkg. (%)
1-jet incl. ggF signal ren./fact. scale	27	-
2-jet incl. ggF signal ren./fact. scale	15	-
$E_{\mathrm{T}}^{\mathrm{miss}}$ modeling	8	3
W+jets fake factor	-	7
b-tagging efficiency	-	7
Parton distribution functions	7	1

Table 11.22: Main systematic uncertainties on the predicted numbers of signal ($m_H = 125$ GeV) and background events for the low m_h 2011 analyses. The percentages are quoted relative to the total signal and background expectations. All numbers are summed over lepton flavors. The results are given for the signal-rich region of m_{T}, defined by $0.75\,m_H < m_{\mathrm{T}} < m_H$ for $m_H = 125$ GeV. Sources of uncertainty that are negligible or not applicable are marked with a '-'.

Source (0-jet)	Signal (%)	Bkg. (%)
Inclusive ggF signal ren./fact. scale	13	-
1-jet incl. ggF signal ren./fact. scale	10	-
Parton distribution functions	8	2
Jet energy scale	7	4
WW normalization	-	7
WW modeling and shape	-	5
W+jets fake factor	-	5
QCD scale acceptance	4	2
Source (1-jet)	Signal (%)	Bkg. (%)
1-jet incl. ggF signal ren./fact. scale	28	-
WW normalization	-	25
2-jet incl. ggF signal ren./fact. scale	16	-
b-tagging efficiency	-	10
Parton distribution functions	7	1
W+jets fake factor	-	5

Table 11.23: Main systematic uncertainties on the predicted numbers of signal ($m_H = 125$ GeV) and background events for the 2012 0-jet and 1-jet analyses. The percentages are quoted relative to the total signal and background expectations. The results are given for the signal-rich region of m_{T}, defined by $0.75\,m_H < m_{\mathrm{T}} < m_H$ for $m_H = 125$ GeV. Sources of uncertainty that are negligible or not applicable are marked with a '-'.

The main experimental uncertainties are related to the jet energy scale and the uncertainty on the fake factor used in the W+jet prediction. The fake factor uncertainty has been described in Section 11.4 and Chapter 9. The jet energy scale is determined from a combination of test beam, simulation, and in-situ measurements. The uncertainty on the jet energy scale varies from 2% to 14% as a function of jet $p_{\mathrm{T}}$and η [151]. An additional contribution to the jet energy scale uncertainty arises from pile-up and is estimated to vary between 1% and 5% for in-time pile-up, and up to 10% for out-of-time pile-up. The jet energy resolution varies from 5% to 25% as a function of jet p_{T} and η, and the relative systematic uncertainty on it ranges from 17% to 25%.

Uncertainties on the modeling of background processes are estimated by using alternative generators: MC@NLO is used for SM WW production, POWHEG for $t\bar{t}$ production, and Pythia for Z/γ^*. For the backgrounds normalized using control regions, the systematic uncertainties are evaluated on the relative normalization between the backgrounds in the signal and control regions and on the m_{T} shape in the signal region. The theoretical uncertainty on the extrapolation to the signal region from the control regions has been evaluated according to the prescription of [35]. In the 2012 analysis, an additional modeling uncertainty has been added to take into account differences in the number of extrapolated events obtained with MC@NLO+`HERWIG` and POWHEG+Pythia8.

The jet energy scale and lepton momentum scale uncertainties are propagated to the $E_{\mathrm{T}}^{\mathrm{miss}}$ computation. Additional contributions arise from low-energy calorimeter deposits, not associated with reconstructed physics objects. Their effect on the total background event yield ranges from 1% to 8%. Uncertainties on the modeling of pile-up contributions are estimated by varying their effect on low-energy calorimeter deposits. The impact on the background yield varies between 1% and 5%.

The efficiency of the b-tagging algorithm is calibrated using samples containing muons reconstructed in the vicinity of jets. The resulting uncertainty on the b-jet tagging efficiency varies between 5% and 14% as a function of jet p_{T}. The uncertainty on the integrated luminosity is 3.9%.

In the final fit, the m_{T} distribution is used to obtain the signal yield for each mass hypothesis. The m_{T} shapes for the individual backgrounds and signal do not exhibit a statistically significant dependence on most of the uncertainties. The uncertainties that do produce statistically significant variations have no appreciable effect on the final results, except for the SM WW background. Here, an uncertainty is included to take into account differences in the m_{T} shape observed between the MC@NLO and POWHEG generators. The uncertainty on the shape of the total background is dominated by the uncertainties on the normalizations of the individual backgrounds.

The 2-jet analysis is mainly sensitive to the VBF process. The impact of the scale variations on the combined VBF signal cross section and jet veto acceptance is 4% [35]. In the 2-jet analysis,

around 25% of the signal events are produced via ggF, where the relative uncertainty is around 25%. Additional 7% uncertainties are included to account for the effect of the underlying event modeling on the signal acceptance for VBF signal events after jet tagging and central jet veto cuts.

11.6 Statistical Model

The event yields in the selected regions are statistically analyzed using a binned likelihood function, $\mathcal{L}(\mu, \theta)$, defined as the product of separate Poisson probability terms:

$$P(\mathrm{N_{obs}}|\mu s + \sum_{i}^{\mathrm{N_{bkg}}} b_i), \tag{11.4}$$

where, P is the Poisson distribution: $P(x|y) = \frac{y^x e^{-y}}{x!}$, $\mathrm{N_{obs}}$ is the number of observed events, μ is the "signal strength" parameter, s is the number of predicted signal events, and b_i is number of predicted background events of type i. The signal strength parameter is the parameter of interest. It multiplies the expected signal yield in each bin, acting like a scale factor on the total number of predicted Higgs events. The signal strength is defined such that $\mu = 0$ corresponds to the background-only hypothesis and a value of 1 corresponds to the background plus Higgs signal, predicted with the expected SM cross section.

The signal and background predictions depend on the systematic uncertainties. These are parameterized in the fit by nuisance parameters denoted $\vec{\theta}$. The nuisance parameters are constrained by their respective uncertainties in the fit using Gaussian functions: $N(\theta|\vec{\theta})$. For example, the W+jet background depends on the fake factor. The fake factor is included as a nuisance parameter in the fit, constrained by its measured uncertainty. The expected signal and background event counts in each region are functions of $\vec{\theta}$.

The full likelihood is written as

$$\mathcal{L}(\mu, \theta) = \left(\prod_{\mathrm{l}}^{\mathrm{ch}} \prod_{\mathrm{j}}^{\mathrm{N_{jets}}} \prod_{k}^{m_{\mathrm{T}}} P(\mathrm{N_{obs}}_{ljk}|\mu s_{ljk}(\vec{\theta}) + \sum_{i}^{\mathrm{N_{bkg}}} b_{ljki}(\vec{\theta})) \right) \times \prod_{m}^{\mathrm{N}_\theta} N(\vec{\theta}_m), \tag{11.5}$$

where the product of Poisson terms is over lepton channels (l), jet bins (j), and the binning used in the m_{T} distribution (k). The binned m_{T} distribution is used in the 0-jet and 1-jet analyses. In the 2-jet analysis, shape information is not used due to the small number of events remaining after the event selection. The likelihood function includes all the parameters that describe the systematic uncertainties and their correlations.

Values of μ are tested with a statistic, $q_\mu = -2\ln(\lambda(\mu))$, based on the profile likelihood ratio [152].

The test statistic is defined using:

$$\lambda(\mu) = \frac{\mathcal{L}(\mu, \hat{\vec{\theta}}_\mu)}{\mathcal{L}(\hat{\mu}, \hat{\vec{\theta}})}, \tag{11.6}$$

where $\hat{\mu}$ and $\hat{\theta}$ are the parameters that maximize the likelihood[24] and $\hat{\vec{\theta}}_\mu$ are the nuisance parameter values that maximize the likelihood for a given μ. This test statistic extracts the information on the signal strength from fitting to the data. The level of disagreement of the data with a particular signal strength hypothesis is quantified with the p-value, p_μ, defined as

$$p_\mu = \int_{q_\mu^{\text{obs.}}}^{\infty} f(q_\mu|\mu) dq_\mu, \tag{11.7}$$

where $q_\mu^{\text{obs.}}$ is the value of the test statistic observed in data, and $f(q_\mu|\mu)$ is the probability distribution function of q_μ for the given signal strength hypothesis. The modified frequentest method, referred to as CL_s [153, 152] is used to compute exclusion limits. The quantity CL_s is defined as

$$CL_s(\mu) = \frac{p_\mu}{1 - p_b}, \tag{11.8}$$

where $1 - p_b = \int_{q_\mu^{\text{obs.}}}^{\infty} f(q_\mu|\mu = 0) dq_\mu$. A value of μ is regarded as excluded at 95% confidence level (CL) when CL_s is less than 5%. A SM Higgs boson with mass m_h is considered excluded at 95% CL when $\mu = 1$ is excluded at that mass.

The significance of an excess in the data is quantified with p_0, the probability that the background can produce a fluctuation greater than or equal to the excess observed in data. p_0 is defined using the test statistic $q_0 = -2\ln(\lambda(0))$ as

$$p_0 = \int_{q_0^{\text{obs.}}}^{\infty} f(q_0|\mu) dq_0. \tag{11.9}$$

11.7 Results

This section presents the results of the individual 2011 and 2012 analyses. The combination of the two analyses is also given.

11.7.1 Results of the 2011 Analysis

The number of observed events, and the predicted signal and background yields, for the 2011 analysis were presented in Sections 11.3 and 11.4. The statistical analysis described in the previous section has been performed. Figure 11.16 shows the resulting p_0, the probability of the background-only hypothesis, as a function of m_h, for the combined 0-jet, 1-jet and 2-jet analyses. No significant

[24] with the constraint that $0 \leq \hat{\mu} \leq \mu$

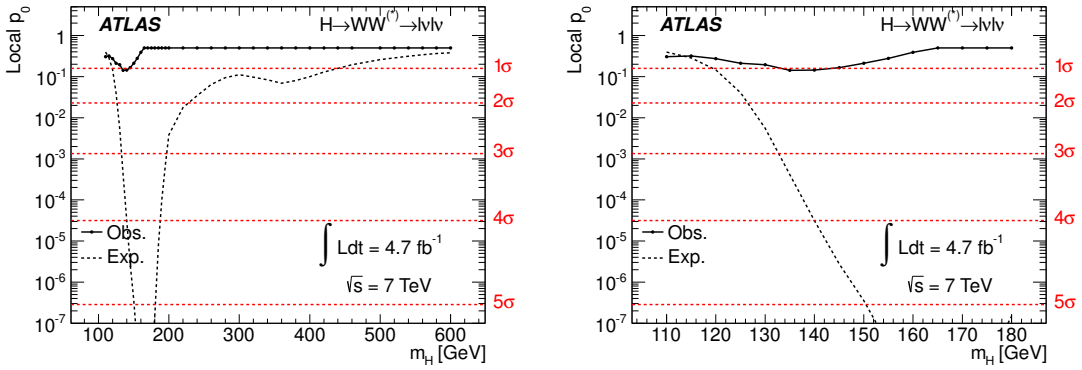

Figure 11.16: Probabilities for the background-only hypothesis, p_0, as a function of m_h, for the 2011 analysis. The left-hand plot shows m_h in the range 110 - 600 GeV, the right-hand plot focuses on m_h between 110 and 180 GeV. The solid line shows the observed probability. The dashed line shows the corresponding expectation for the signal+background hypothesis at the given value of m_h. The red, horizontal dashed lines indicate the corresponding significance.

excess of events over the expected background is observed over the entire mass range; the lowest p-value observed is 0.15. The observed data is then used to set limits on the Higgs production cross section.

Figure 11.17 shows the observed and expected cross section upper limits at 95% CL, as a function of m_h for the combined 0-jet, 1-jet and 2-jet analyses. The limits exclude the SM Higgs boson with a mass in the range from 133 GeV to 261 GeV; the expected exclusion range in the absence of a signal is 127 GeV to 233 GeV.

The breakdown of the observed and expected limits by jet bin is shown in Figure 11.18. The majority of the sensitivity comes from the 0-jet analysis.

The 2011 $H \to WW^{(*)} \to l\nu l\nu$ analysis was combined with several other Higgs searches performed using the 2011 $\sqrt{s}$= 7 TeV data set[130]. The combined result excluded the presence of a Higgs boson in the mass range of around 110 to 120 GeV, and from about 130 GeV to over 500 GeV, at the 95% confidence level. An excess of events was observed at Higgs masses of around 125 GeV. The excess corresponded to a local significance of 2.9 standard deviations. The probability for the background to produce an excess at least as significant anywhere in the entire mass range, 110 – 600 GeV, was estimated to be 15%, corresponding to a global significance of approximately 1 standard deviation.

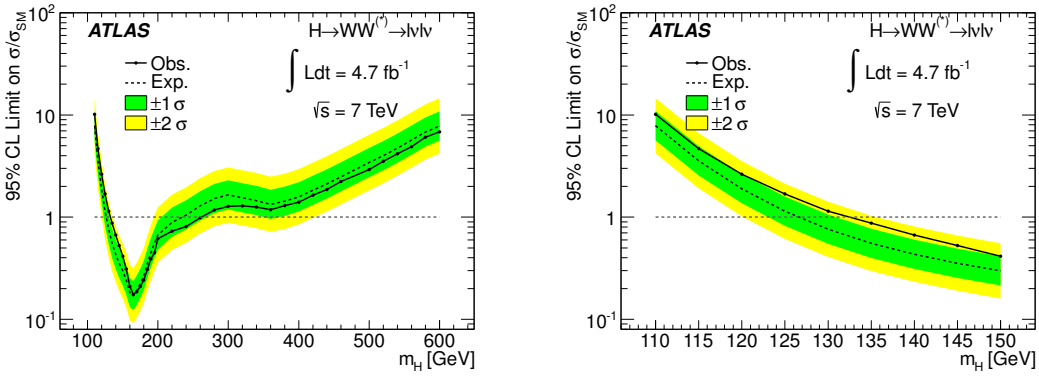

Figure 11.17: Observed and expected limits on the Higgs production cross section as a function of m_h, for the 2011 analysis. The left-hand plot shows m_h in the range 110 - 600 GeV, the right-hand plot focuses on m_h between 110 and 150 GeV. The curves show the 95% CL upper limits. The green and yellow regions indicate the 1σ and 2σ uncertainty bands on the expected limit.

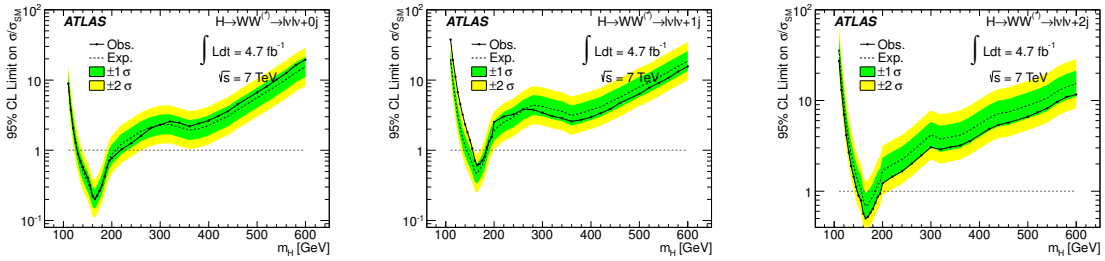

Figure 11.18: Observed and expected limits on the Higgs production cross section for the 0-jet (left), 1-jet (middle), and 2-jet (right) 2011 analyses.

11.7.2 Results of the 2012 Analysis

The number of observed events, and the predicted signal and background yields, for the 2012 analysis were presented in Sections 11.3 and 11.4. The statistical analysis described in the previous section has been performed. Figure 11.19 shows the p_0 as a function of m_h, for the combined 0-jet, 1-jet and 2-jet analyses. An excess of events is observed over the expected background, reflected by a low observed p_0. Due to the limited mass resolution, the p_0 distribution is fairly flat with a broad minimum around $m_h = 125$ GeV. The value of p_0 at $m_h = 125$ GeV is 8×10^{-4} , corresponding to a significance of 3.1 standard deviations. The expected p_0 for a Higgs with $m_h = 125$ GeV is 0.05, or 1.6 standard deviations.

Figure 11.20 shows the distribution of the transverse mass of the selected events in the 2011 0-jet and 1-jet analyses, after subtracting the total estimated background. The predicted $m_h = 125$ GeV

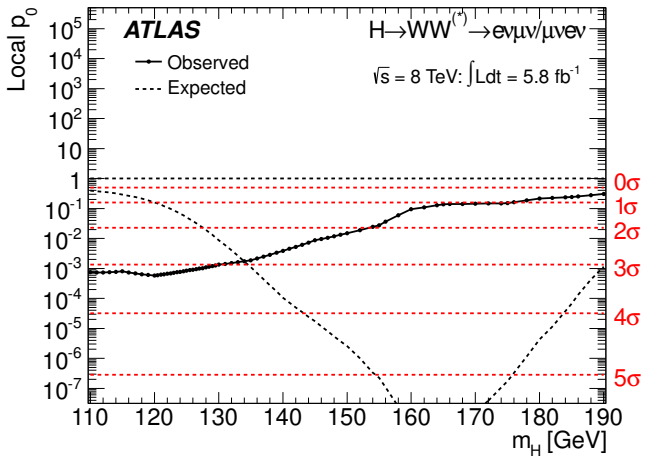

Figure 11.19: Probabilities for background-only hypothesis, p_0, as a function of m_h, for the 2012 analysis. The solid line shows the observed probability. The dashed line shows the corresponding expectation for the signal+background hypothesis at the given value of m_h. The red, horizontal dashed lines indicate the corresponding significance.

signal is superimposed. No systematic uncertainties are included. The observed excess of events is consistent with a SM Higgs boson of $m_h = 125$ GeV.

As a result of the observed excess of events over the expected background, the observed data is used to make a measurement of the signal strength parameter. The fitted signal strength is shown in Figure 11.21 as a function of m_h. At 126 GeV, the measured value of μ is 1.9 ± 0.7, consistent with the SM expectation of 1. The increase of the fitted signal strength at lower m_h is due to the decreasing expected $\sigma \cdot$ Br for the signal.

11.7.3 Combined Results

The results obtained with the 5.8 fb^{-1} 8 TeV dataset are combined with the results of the 4.7 fb^{-1} 7 TeV analysis. The 7 TeV analysis resulted in a signal strength of $\mu = 0.5 \pm 0.6$ at $m_h = 126$ GeV. The signal strengths measured with the 7 TeV and 8 TeV analyses separately are compatible within 1.5 standard deviations.

Figure 11.22a shows the p_0 value as a function of m_h for the combined 2011 and 2012 analyses. An excess of events is observed over the expected background, reflected by a low observed p_0. Due to the limited mass resolution, the p_0 distribution is fairly flat with a broad minimum around $m_h = 125$ GeV. The minimum value of p_0, found at $m_h = 125$ GeV, is 3×10^{-3} , corresponding to a significance of 2.8 standard deviations. The expected p_0 for a Higgs with $m_h = 125$ GeV is 0.01, or

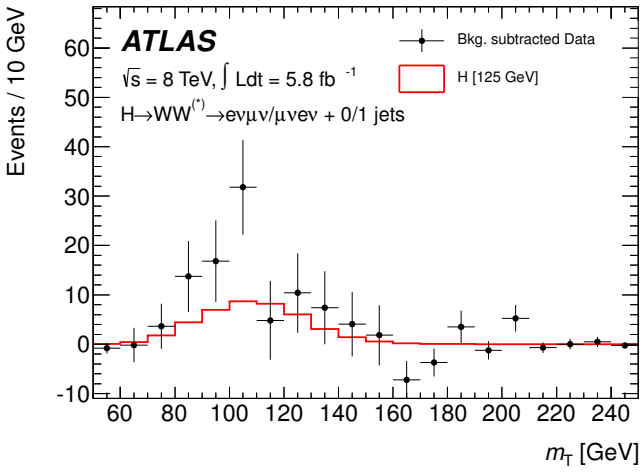

Figure 11.20: The m_{T} distribution in data with the estimated background subtracted, overlaid with the predicted signal for $m_h = 125$ GeV. The distributions are summed for the 0-jet and 1-jet analyses and for the 2012 analysis. The statistical errors of both the data and the subtracted background are reflected in the data points. The systematic uncertainty on the background estimate is not included.

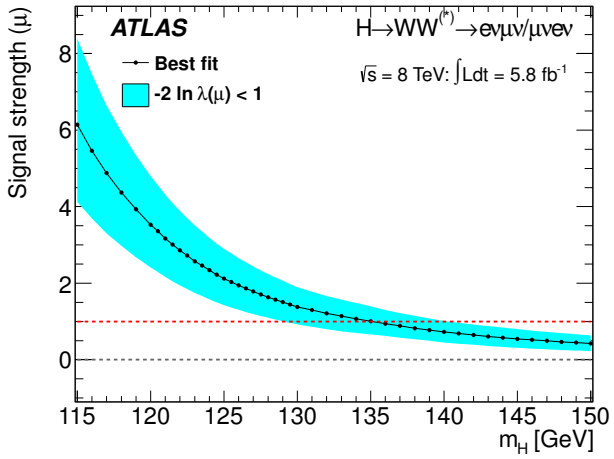

Figure 11.21: Fitted signal strength parameter (μ) as a function of m_h for the 2012 analysis.

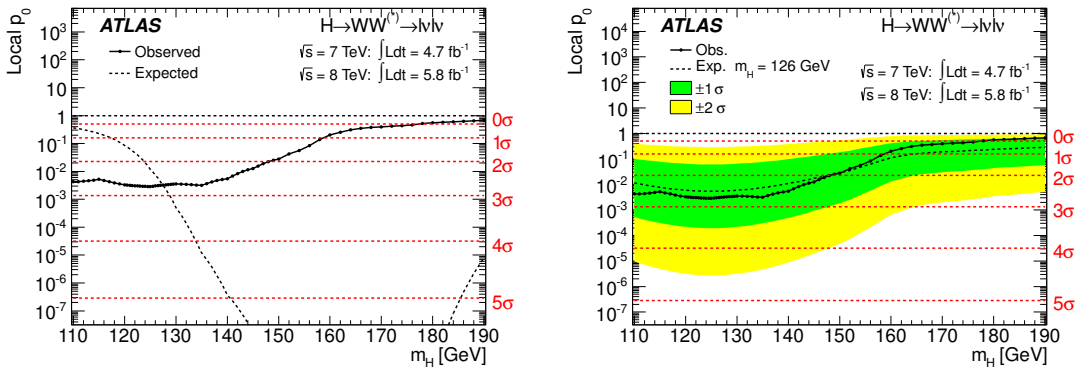

(a) (b)

Figure 11.22: Probabilities for background-only hypothesis, p_0, as a function of m_h, for the combined 2011 and 2012 analysis. The solid lines show the observed probability. The dashed line in the left-hand plot shows the corresponding expectation for the signal+background hypothesis at the given value of m_h. In the right-hand plot, the dashed line shows the corresponding expectation for the $m_h = 126$ GeV hypothesis. The green and yellow regions indicate the 1σ and 2σ uncertainty bands on the expected p_0. The red, horizontal dashed lines indicate the corresponding significance.

2.3 standard deviations. Figure 11.22b shows the observed p_0 compared to the expectation in the presence of a signal at $m_h = 126$ GeV. The shape and normalization of the p_0 curves as a function of m_h are in agreement.

Figure 11.23 shows the distribution of the transverse mass of the selected events in the 2011 and 2012 0-jet and 1-jet analyses, after subtracting the total estimated background. The predicted $m_h = 125$ GeV signal is superimposed. No systematic uncertainties are included. The observed excess of events is consistent with a SM Higgs boson of $m_h = 125$ GeV.

As a result of the observed excess of events over the expected background, the observed data is used to make a measurement of the signal strength parameter. The fitted signal strength is shown in Figure 11.24 as a function of m_h. At 126 GeV, the measured value of μ is 1.3 ± 0.5, consistent with the SM expectation of 1. The increase of the fitted signal strength at lower m_h is due to the decreasing expected $\sigma \cdot$ Br for the signal. The expectation of the measured μ in the presence of a signal at $m_h = 126$ GeV is shown for comparison. The shape and normalization of the curves as a function of m_h are in agreement.

11.8 Conclusion

A search for the SM Higgs boson has been performed in the $H \to WW^{(*)} \to l\nu l\nu$ channel using 4.7 fb^{-1} of 7 TeV data collected in 2011, and 5.8 fb^{-1} of 8 TeV data collected in 2012. A combined

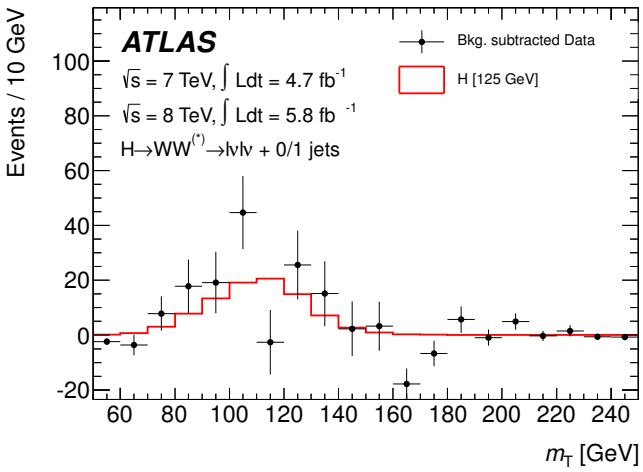

Figure 11.23: The m_{T} distribution in data with the estimated background subtracted, overlaid with the predicted signal for $m_h = 125$ GeV. The distributions are summed for the 0-jet and 1-jet analyses and for the 2011 and 2012 analyses. The statistical errors of both the data and the subtracted background are reflected in the data points. The systematic uncertainty on the background estimate is not included.

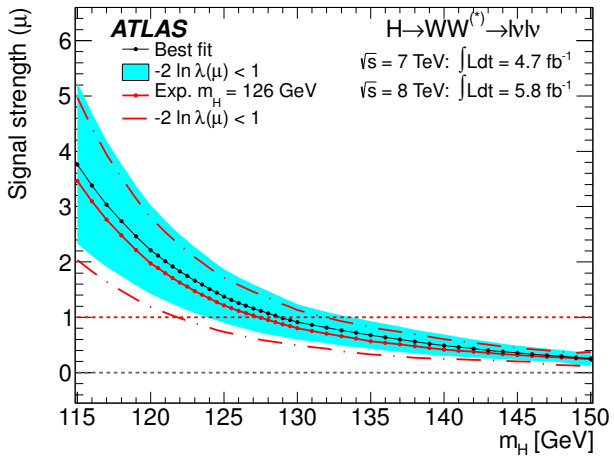

Figure 11.24: Fitted signal strength parameter, indicated in the solid black line with cyan band, as a function of m_h for the combined 2011 and 2012 analysis. The expected result for a signal hypothesis of $m_h = 126$ GeV is shown in the red lines for comparison.

analysis of the two datasets results in an observed excess of events consistent with $m_h = 125$ GeV. The probability for a background fluctuation to produce an excess as large as the one observed is 3×10^{-3}, corresponding to a significance of 2.8 standard deviations. The best fit signal strength at $m_h = 126$ GeV is $\mu = 1.3 \pm 0.5$, consistent with the SM prediction.

The $H \to WW^{(*)} \to l\nu l\nu$ analysis presented here has been combined with several other Higgs searches performed using equivalent data sets [103]. The results of this combined Higgs search are the subject of the following chapter.

Chapter 12

Combined Higgs Results

This chapter presents the combined ATLAS search for the Standard Model Higgs boson. The analysis has been performed using 4.7 fb^{-1} of $\sqrt{s} = 7$ TeV data collected in 2011, and 5.8 fb^{-1} of $\sqrt{s} = 8$ TeV data collected in the first half of 2012. The results of the $H \to WW^{(*)} \to l\nu l\nu$ analyses presented in Chapter 11 are combined with searches in the $H \to ZZ^{(*)} \to llll$ [154] and $H \to \gamma\gamma$ [155] channels, using both the 7 TeV and 8 TeV data sets, and with several other Higgs searches using the 7 TeV data set [130]. Clear evidence for the production of a neutral boson with a mass of around 126 GeV is found [103]. This observation has a significance of 5.9 standard deviations and is compatible with the production and decay of the Standard Model Higgs boson.

The remainder of the chapter is organized as follows: Section 12.1 provides a brief overview of the main Higgs searches used in the combination. Section 12.2 describes the procedure for combining the individual analyses. Section 12.3 presents the combined results.

12.1 Overview of other Higgs searches at ATLAS

12.1.1 $H \to ZZ^{(*)} \to llll$

The search for the SM Higgs boson through the decay $H \to ZZ^{(*)} \to llll$, where l is an electron or muon, provides sensitivity over a wide mass range, from 110 to 600 GeV. The $H \to ZZ^{(*)} \to llll$ analysis selects Higgs boson candidates by selecting two pairs of isolated high p_{T} leptons. Each pair is required to be of same flavor and opposite charge. A visualization of an event selected by the $H \to ZZ^{(*)} \to llll$ analysis is shown in Figure 12.1.

An excess of observed events is searched for in the four lepton invariant mass distribution, m_{4l}, which would peak at the value of m_h for resonant Higgs production. The largest background is from continuum $Z(\gamma^*)Z(\gamma^*)$ production, referred to as SM ZZ. For low masses, there are also important

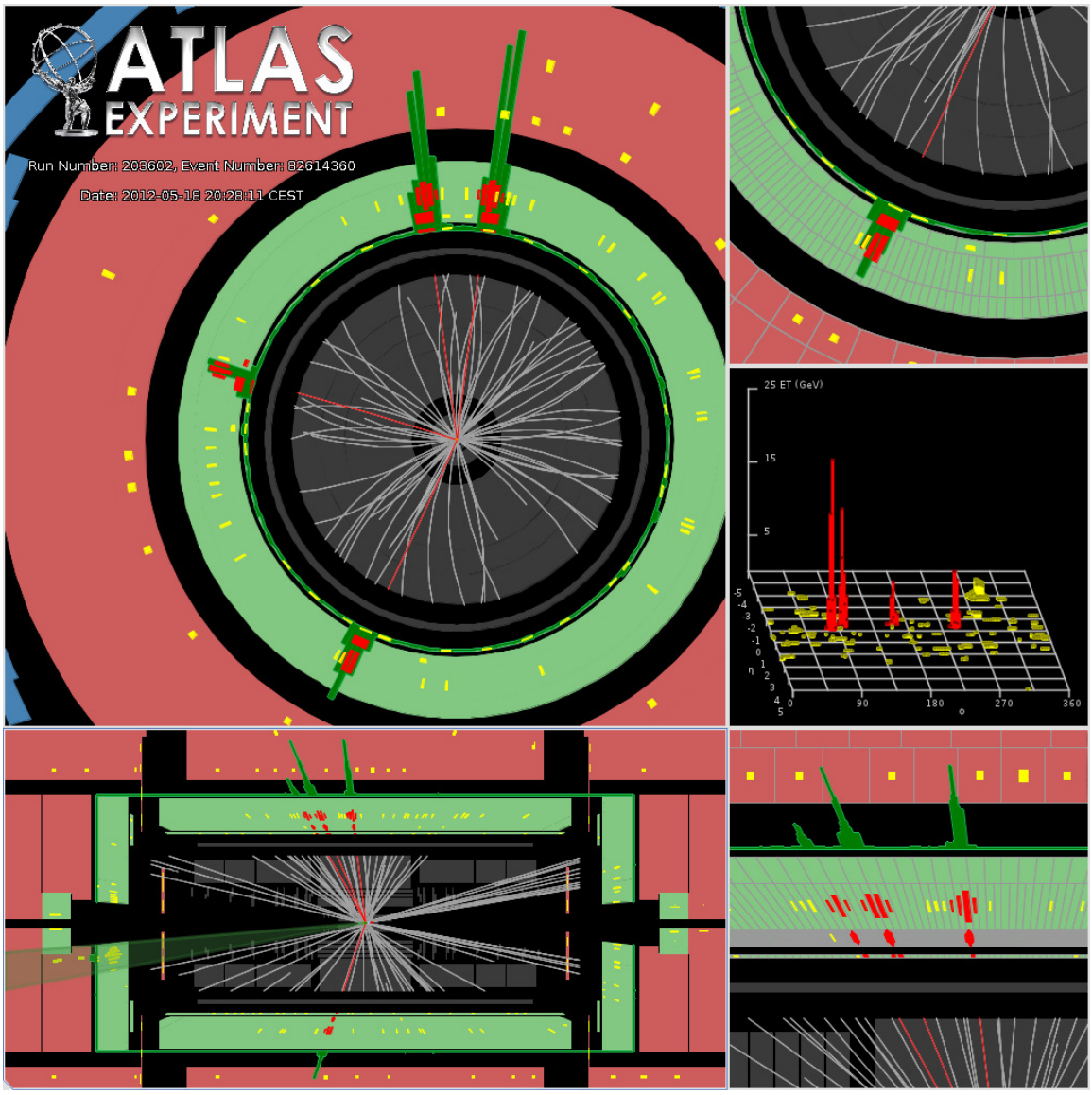

Figure 12.1: Event display of a selected $H \to ZZ^{(*)} \to llll$ event with four identified electrons. The electrons are shown in red and correspond to localized high energy deposits in the calorimeter matched to tracks in the inner detector, indicated by the red lines. The electrons have a combined invariant mass of 124.6 GeV. The upper-left panel shows the projection of the detector in the plane perpendicular to the beam line. The lower-left panel shows the projection of the detector along the beam line, running left to right in the panel. The upper-right and lower-right panels are zoom-ins of interesting regions. The middle-right panel depicts the energy deposited in the calorimeters as a function of ϕ and η.

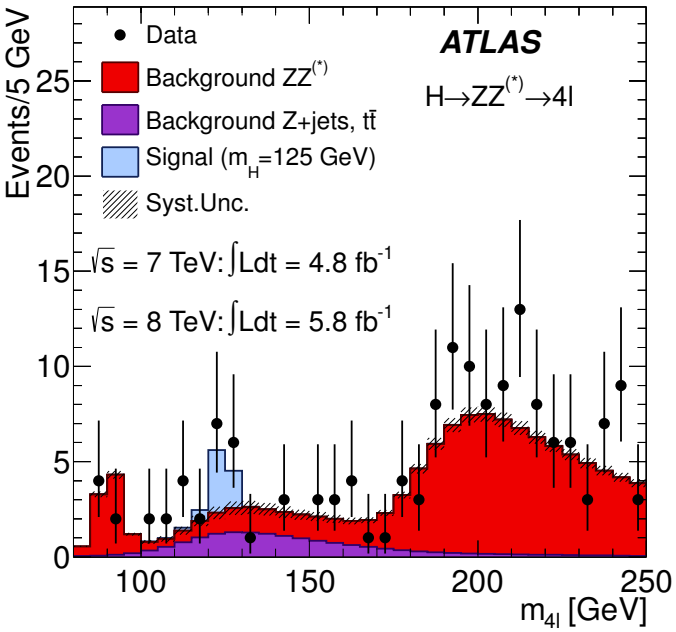

Figure 12.2: The four-lepton invariant mass distribution, m_{4l}, for selected events in the $H \to ZZ^{(*)} \to llll$ analysis using the combined 7 TeV and 8 TeV data sets. The observed data is compared to the background expectation. The signal expectation for a SM Higgs with m_H= 125 GeV is shown.

background contributions from Z/γ^*+ jets and $t\bar{t}$ production, where two of the leptons arise from misidentification.

Figure 12.2 shows the four-lepton invariant mass for selected events. The expected background and observed data are shown along with the expected signal for m_h= 125 GeV. The SM ZZ background is predicted from MC simulation normalized to the theoretical cross section. The reducible Z/γ^*+jets and $t\bar{t}$ backgrounds are estimated using dedicated control regions in data. An observed excess of events over the predicted background is seen in the m_{4l} distribution in the region corresponding to signal with m_h = 125 GeV.

The results are interpreted statistically using a fit of signal and background models to the observed m_{4l} distribution. The fit accounts for the various sources of systematic uncertainty. The significance of an excess is given by p_0, the probability that the observed data is a result of a fluctuation of the background in absence of signal. Figure 12.3 shows the observed p_0, as a function of the tested Higgs mass, using the combined 8 TeV and 7 TeV data sets. The results using the individual 7 TeV and 8 TeV data sets are also shown separately. In the combined analysis, the lowest observed p_0 value is at m_h = 125 GeV, with a value of 2.9×10^{-4}, corresponding to a statistical significance of 3.4 standard deviations.

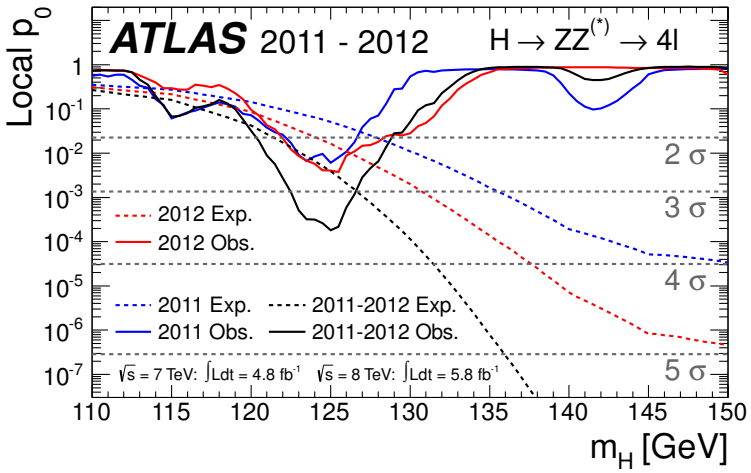

Figure 12.3: The observed p_0 as a function of m_h for the $H \to ZZ^{(*)} \to llll$ channel. The dashed line shows the corresponding expectation for the signal+background hypothesis at the given value of m_h. Results are shown separately for the $\sqrt{s}$= 7 TeV data (dark, blue), the $\sqrt{s}$= 8 TeV data (light, red), and their combination (black).

As a result of the observed excess of events over the expected background and the consistency of the excess with a potential Higgs signal, the observed data is used to perform a measurement of m_h and the production cross section. The cross section is reported in terms of the signal strength parameter, μ. The signal strength parameter multiplies the expected signal yield, acting like a scale factor on the total number of predicted signal events. It is defined such that $\mu = 0$ corresponds to the background-only hypothesis and a value of 1 corresponds to background plus Higgs signal produced with the expected SM cross section. The measurements are made using the profile likelihood ratio, see Section 11.6 for more details. Figure 12.4 shows the best fit values for μ and m_H, with the contours that correspond to the 68% and 95% confidence levels. The observed excess at 125 GeV has an observed production cross section consistent with that of the SM Higgs boson, *i.e.*, $\mu = 1$.

The combined 7 TeV and 8 TeV $H \to ZZ^{(*)} \to llll$ analyses shows a 3.4 standard deviation excess at m_h= 125 GeV with a production cross section that is consistent with the SM Higgs expectation.

12.1.2 $H \to \gamma\gamma$

The search for the SM Higgs boson through the decay $H \to \gamma\gamma$ is performed in the mass range between 110 GeV and 150 GeV. The $H \to \gamma\gamma$ analysis selects Higgs boson candidates by selecting pairs of isolated high p_{T} photons. A visualization of an event selected by the $H \to \gamma\gamma$ analysis is shown in Figure 12.5.

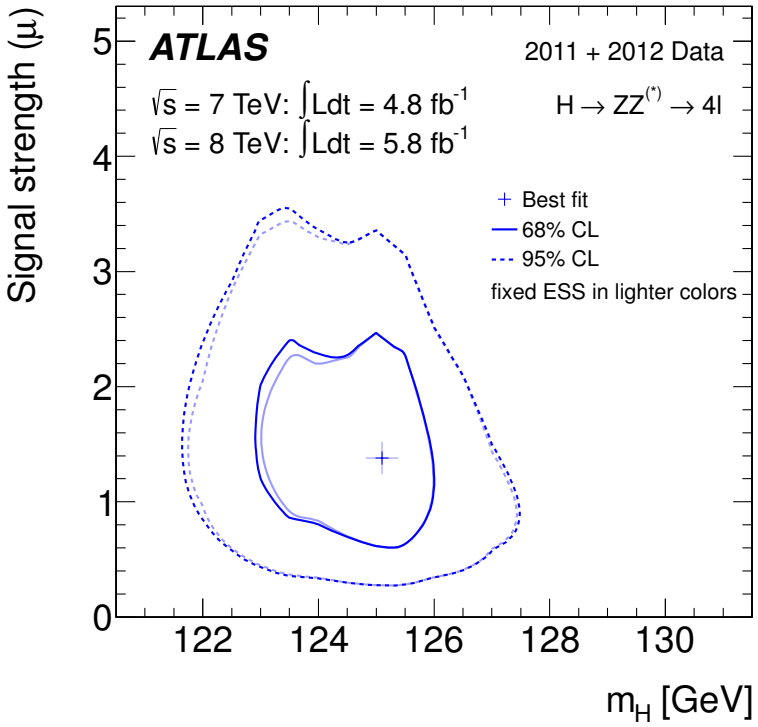

Figure 12.4: Best fit values for μ and m_h in the combined $H \to ZZ^{(*)} \to llll$ analysis. The contours that correspond to the 68% and 95% confidence levels are shown. The lighter lines indicate the effect of important systematic uncertainties effecting the measurements.

An excess of observed events is searched for in the di-photon invariant mass distribution which would peak at the value of m_h for resonant Higgs production. The dominant background is from continuum $\gamma\gamma$ production. Smaller contributions also arise from γ+jet and jet+jet production with one or two jets mis-identified as photons. The level of background is constrained by a fit to the observed data. To improve sensitivity, the selected events are divided into categories according to the expected signal-to-background ratio and mass resolution.

Figure 12.6 shows the di-photon invariant mass for the selected events. The upper panel, marked a), shows the di-photon invariant mass spectrum, $m_{\gamma\gamma}$, of all selected events. The fit to the background-only model is shown in the dotted line. The panel marked b) shows the background-subtracted data. The lower-panel, marked c), shows the combined $m_{\gamma\gamma}$ after properly weighting the different events according to their respective categories. Again, the fit of the background-only model is shown in the dotted line. The bottom panel, marked d), gives the weighted data, after background subtraction. An observed excess of events over the fitted background is seen in the $m_{\gamma\gamma}$

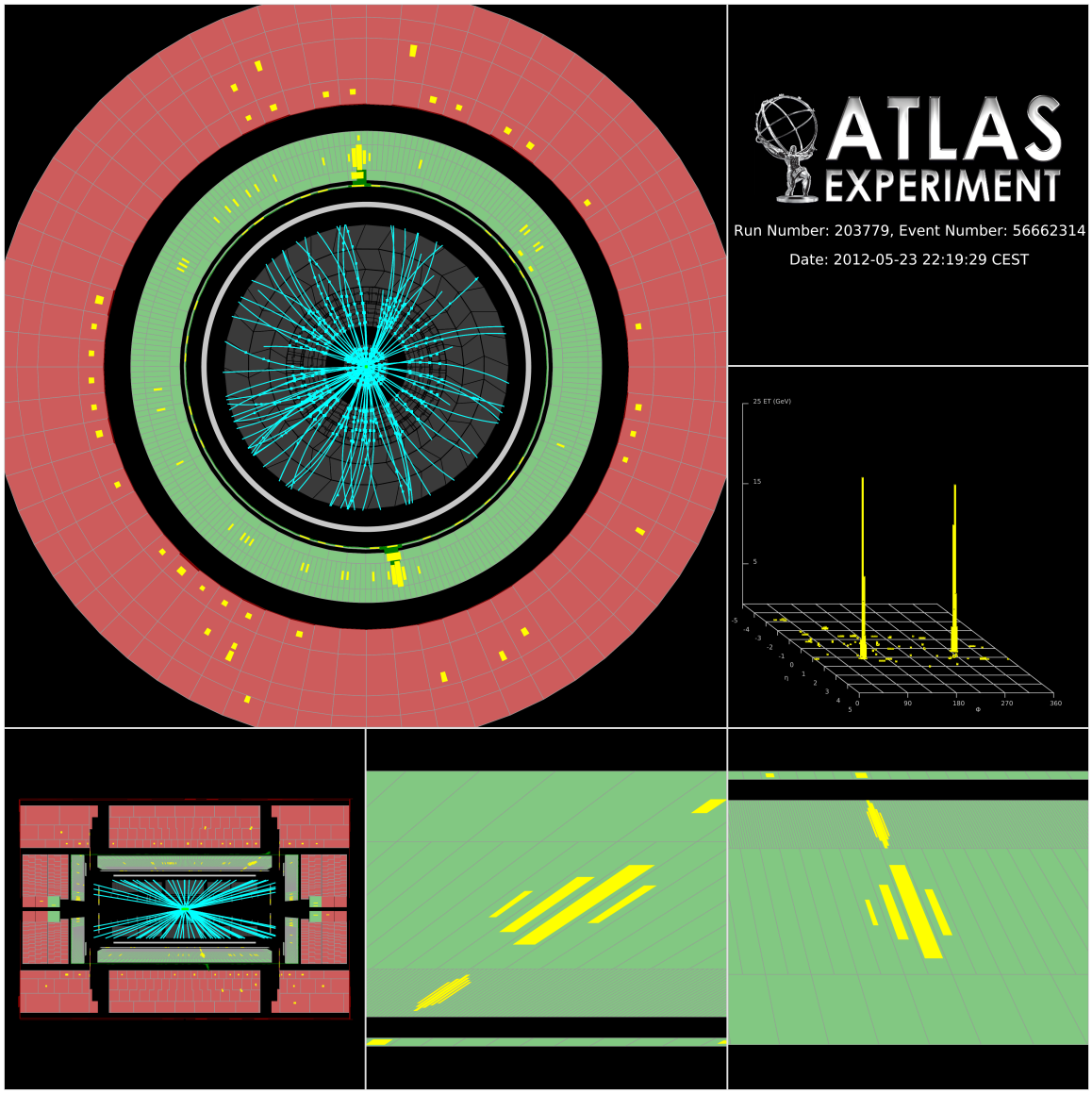

Figure 12.5: Event display of a selected $H \to \gamma\gamma$ event. The photons are shown in yellow and correspond to localized high energy deposits in the calorimeter not matched to tracks in the inner detector. The photons have a combined invariant mass of 126.9 GeV. The upper-left panel shows the projection of the detector in the plane perpendicular to the beam line. The lower-left panel shows the projection of the detector along the beam line, running left to right in the panel. The lower-middle and lower-right panels are zoom-ins of interesting regions. The middle-right panel depicts the energy deposited in the calorimeters as a function of ϕ and η.

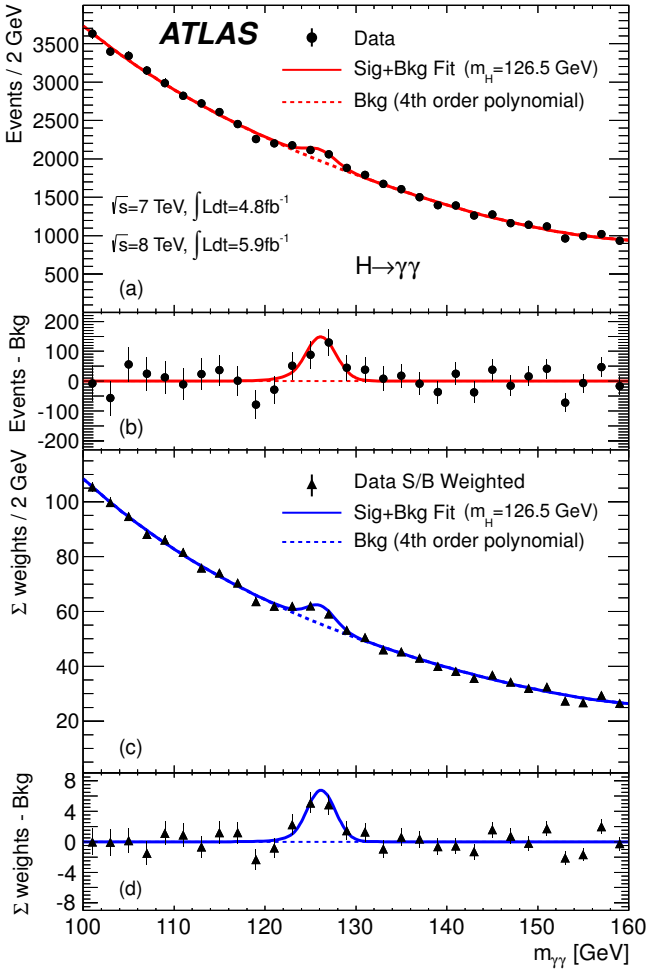

Figure 12.6: The distributions of the invariant mass of di-photon candidates after all selections for the combined 7 TeV and 8 TeV data sample. The inclusive sample is shown in upper figure, marked a). The distribution weighted according to the event categories is shown in the lower figure marked c). The result of a fit using a m_h= 126.5 GeV signal component and the background component is superimposed. The excess of data with respect to the background fit are displayed in panels marked b) and d).

distribution in the region corresponding to signal with m_h = 125 GeV. The fit including signal with m_h= 126.5 GeV, shown in the solid lines, accurately models the observed data.

The results are interpreted statistically as described above for the $H \to ZZ^{(*)} \to llll$ analysis. Figure 12.7 shows the observed p_0, as a function of the tested Higgs mass, using the combined 8 TeV and 7 TeV data sets. The results using the individual 7 TeV and 8 TeV data sets are also shown separately. In the combined analysis, the lowest observed p_0 value is at m_h = 126.5 GeV, with a value of 2×10^{-6}, corresponding to a statistical significance of 4.7 standard deviations.

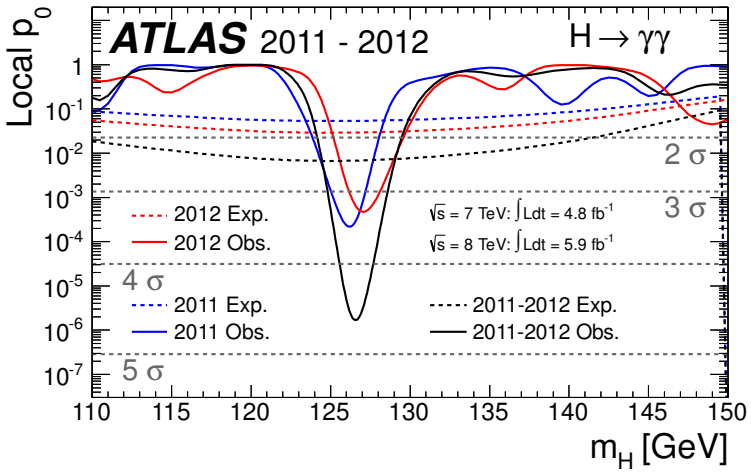

Figure 12.7: The observed p_0 as a function of m_h for the $H \to \gamma\gamma$ channel. The dashed line shows the corresponding expectation for the signal+background hypothesis at the given value of m_h. Results are shown separately for the $\sqrt{s}$= 7 TeV data (dark, blue), the $\sqrt{s}$= 8 TeV data (light, red), and their combination (black).

As a result of the observed excess of events over the expected background and the consistency of the excess with a potential Higgs signal, the observed data is used to perform a measurement of m_h and the production cross section. The measurements are made analogously to those of the $H \to ZZ^{(*)} \to llll$ analysis described above. Figure 12.8 shows the best fit values for μ and m_H, with the contours that correspond to 68% and 95% confidence levels. The observed excess at 126.5 GeV has an observed production cross section consistent with that of the SM Higgs boson, *i.e.,* $\mu = 1$.

12.1.3 $H \to WW^{(*)}$

The $H \to WW^{(*)}$ analysis was described in detail in Chapter 11. This section provides a brief review with the same level of detail as the other channels described above. The reader is directed to Chapters 8 and 11 for more information.

The search for the SM Higgs boson through the decay $H \to WW^{(*)} \to l\nu l\nu$, where l is an electron or muon, provides sensitivity over a wide mass range, from 110 to 600 GeV, and is particularly important in the region below 200 GeV. The $H \to WW^{(*)}$ analysis selects Higgs boson candidates by selecting events with pairs of isolated high p_{T} leptons, with large momentum imbalance, due to the un-detected neutrinos. A visualization of a WW candidate event is shown in Figure 12.9.

The $H \to WW^{(*)}$ analysis is particularly challenging because the un-detected neutrinos prevent

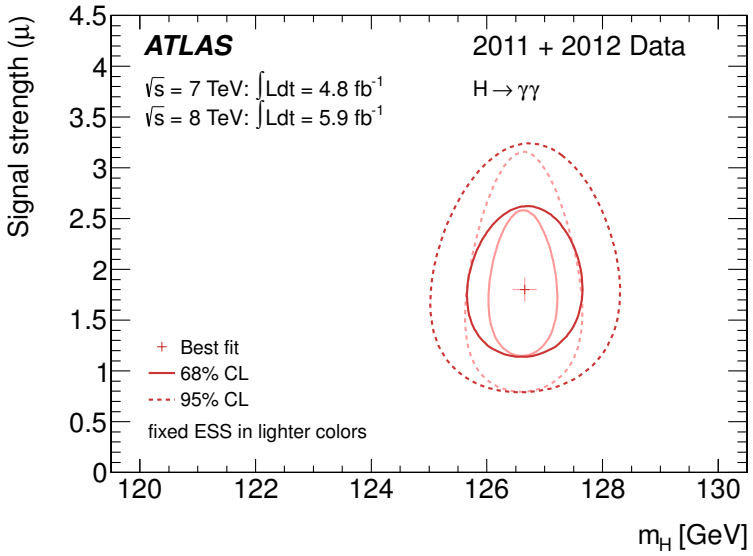

Figure 12.8: Best fit values for μ and m_h in the combined $H \to \gamma\gamma$ analysis. The contours that correspond to the 68% and 95% confidence levels are shown. The lighter lines indicate effect of the important systematic uncertainties effecting the measurements.

the Higgs invariant mass from being fully reconstructed. Most of the $H \to WW^{(*)}$ sensitivity comes from comparing the total event yield with the predicted background. This type of analysis requires a high signal-to-background selection and an accurate modeling of the residual backgrounds. Meeting this challenge has been the subject of this thesis.

The dominant backgrounds are continuum WW production and top-quark production, each of which have real W pairs in the final state. Other important backgrounds include Z/γ^* and W+jet events. Figure 12.10 shows the best estimate of the Higgs mass for selected events using the observed leptons and the measured momentum imbalance. The data is shown after subtracting the estimated backgrounds, along with the corresponding signal distribution with $m_h = 125$ GeV. An observed excess of events over the predicted background is seen. The observed excess is consistent with the expectation of a signal with $m_h = 125$ GeV.

The results are interpreted statistically as described above. Figure 12.11 shows the observed p_0, as a function of the tested Higgs mass, using the combined 8 TeV and 7 TeV data sets. The results using the individual 7 TeV and 8 TeV data sets are also shown separately. A broad distribution of p_0 values, consistent with the poor mass resolution in the $H \to WW^{(*)}$ analysis, is observed around 3×10^{-3}, corresponding to a statistical significance of 2.8 standard deviations.

As a result of the observed excess of events over the expected background and the consistency of

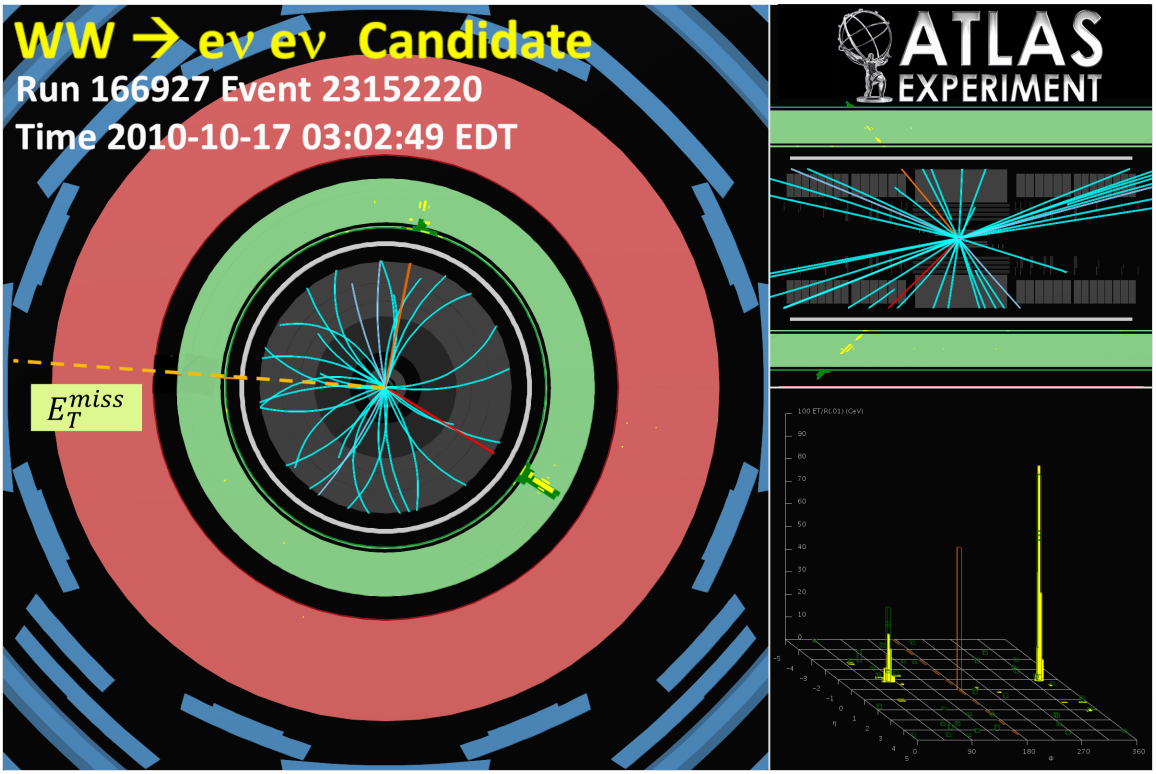

Figure 12.9: Event display of a WW event in the $e\nu e\nu$ channel. The electrons are shown in yellow and correspond to localized high energy deposits in the calorimeter matched to tracks in the inner detector, indicated by the red and orange lines. The dashed line, label $E_{\mathrm{T}}^{\mathrm{miss}}$, indicates the direction of the measured momentum imbalance. The left panel shows the projection of the detector in the plane perpendicular to the beam line. The upper-right panel shows the projection of the detector along the beam line, running left to right in the panel. The lower-right panel depicts the energy deposited in the calorimeters and the direction of the $E_{\mathrm{T}}^{\mathrm{miss}}$, as a function of ϕ and η.

the excess with a potential Higgs signal, the observed data is used to perform a measurement of the production cross section. Figure 12.12 shows the best fit values for μ and m_H, with the contours that correspond to 68% and 95% confidence levels. The results from the $H \to WW^{(*)} \to l\nu l\nu$ analysis are given in green. The large uncertainty on m_h in the $H \to WW^{(*)} \to l\nu l\nu$ analysis is a result of the poor mass resolution from the un-measured neutrinos. The results from the $H \to ZZ^{(*)} \to llll$ and $H \to \gamma\gamma$ analyses shown above are repeated in the figure for comparison. The measured cross sections for the observed excesses at $m_h = 125$ GeV are consistent among the three analyses. The observed excess in $H \to WW^{(*)} \to l\nu l\nu$ analysis has a measured production cross section consistent with that of the SM Higgs boson at m_h= 125 GeV.

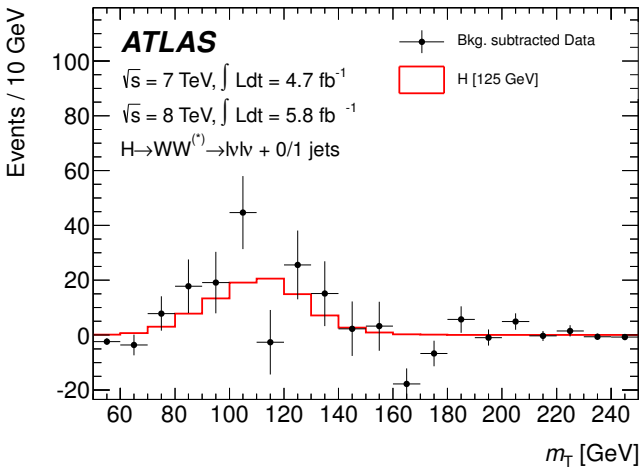

Figure 12.10: Estimated Higgs mass distribution, m_{T}, in data with the estimated background subtracted. The predicted signal for m_h= 125 GeV is overlaid.

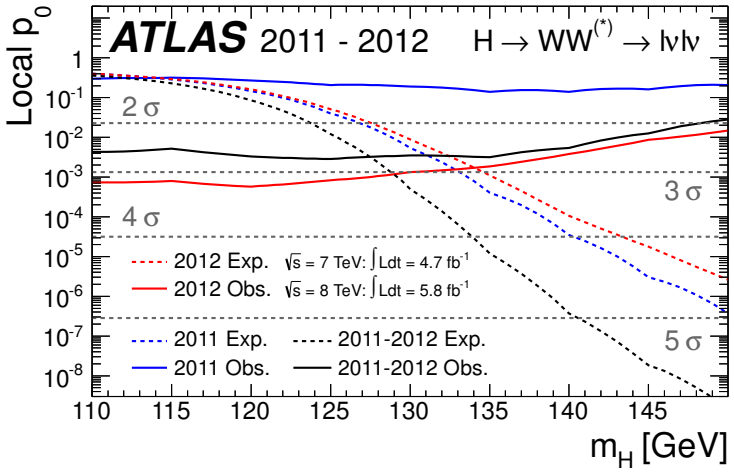

Figure 12.11: The observed p_0 as a function of m_h for the $H \to WW^{(*)}$ channel. The dashed line shows the corresponding expectation for the signal+background hypothesis at the given value of m_h. Results are shown separately for the $\sqrt{s}$= 7 TeV data (dark, blue), the $\sqrt{s}$= 8 TeV data (light, red), and their combination (black).

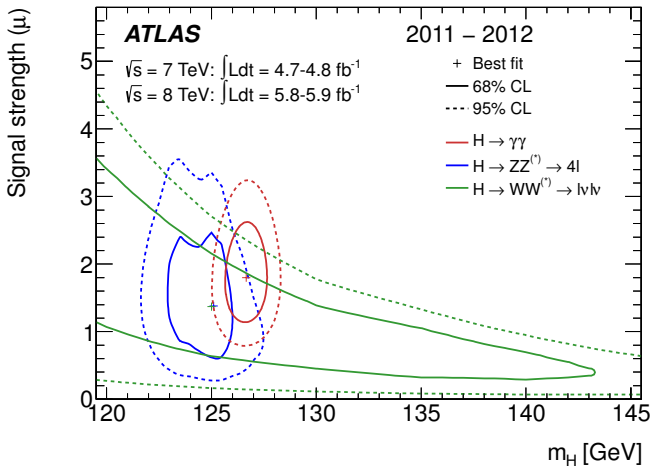

Figure 12.12: Best fit values for μ and m_h in the $H \to WW^{(*)} \to l\nu l\nu$ analysis. The results from the $H \to ZZ^{(*)} \to llll$ and $H \to \gamma\gamma$ analyses shown above are repeated for comparison. The contours that correspond to the 68% and 95% confidence levels are shown.

Channel	m_h range [GeV]	Data Set
$H \to WW^{(*)} \to l\nu l\nu$	110 - 600	7 TeV and 8 TeV
$H \to ZZ^{(*)} \to llll$	110 - 600	7 TeV and 8 TeV
$H \to \gamma\gamma$	110 - 150	7 TeV and 8 TeV
$H \to \tau\tau$	110 - 150	7 TeV
$VH \to Vb\bar{b}$	110 - 130	7 TeV
$H \to ZZ \to ll\nu\nu$	200 - 600	7 TeV
$H \to ZZ \to llq\bar{q}$	200 - 600	7 TeV
$H \to WW \to l\nu q\bar{q}$	300 - 600	7 TeV

Table 12.1: Analyses used in the Higgs combination, where l stands for an electron or muon.

12.2 Higgs Combination

The ultimate Higgs sensitivity comes from the combination of all of the individual search channels. The most sensitive channels at low mass, $m_h < 200$ GeV, are the $H \to WW^{(*)} \to l\nu l\nu$, $H \to ZZ^{(*)} \to llll$, and $H \to \gamma\gamma$ channels presented in the previous section. For these channels, the full 7 TeV and 8 TeV data sets are used. The full combination includes additional channels that are important in the mass range above 200 GeV and channels that add sensitivity at low mass. The analysis of these additional channels has only been performed using the 7 TeV data set. Table 12.1 lists the individual search channels that enter the final combination. The additional channels are briefly summarized below.

The additional channels designed for the low mass region are $H \to \tau\tau$ and $H \to b\bar{b}$. These

channels have relatively low sensitivity, but are important because they are sensitive to the Higgs couplings to fermions.

The $H \to \tau\tau$ analysis is categorized according to the τ decays [156]. It is performed in the mass range from 110 to 150 GeV. The sub-channels are triggered using electrons or muons, except for the fully hadronic channel, which is triggered using the two hadronic τ decays. The dominant backgrounds are from $Z \to \tau\tau$ and multi-jet events. The di-tau invariant mass distribution is used as the final discriminating variable.

The $H \to b\bar{b}$ analyses select Higgs events produced in association with a W or Z boson [157]. These associated production modes are used to improve the signal to background and to provide a source of trigger. The search is performed in the $ZH \to llb\bar{b}$, $ZH \to \nu\bar{\nu}b\bar{b}$, and $WH \to l\nu b\bar{b}$ channels, where l represents an electron or muon. These analyses are performed for m_h between 110 and 130 GeV. The sub-channels are triggered using the leptons, except for the $ZH \to \nu\bar{\nu}b\bar{b}$ channel, which is triggered by the missing transverse momentum. All three analyses require two b-tagged jets. The invariant mass of the two b-jets is used as the final discriminating variable.

The remaining additional channels improve the search sensitivity in the high mass range. The $H \to ZZ^{(*)} \to ll\nu\nu$ analysis is performed for m_h between 200 and 600 GeV[158]. The transverse mass, computed from the di-lepton transverse momentum and the missing transverse momentum, is used as the final discriminating variable.

The $H \to ZZ^{(*)} \to llq\bar{q}$ search is also performed in the mass range between 200 and 600 GeV[159]. The dominant background arises from Z+jet production. The sensitivity is improved by adding a dedicated ll$b\bar{b}$ sub-channel. The invariant mass of the $llq\bar{q}$ system is used as the final discriminating variable.

The final analysis included in the combined Higgs result is $H \to WW^{(*)} \to l\nu q\bar{q}$. This analysis is performed for m_h from 300 to 600 GeV[160]. The mass of the two selected jets are required be consistent with a W boson. This mass constraint allows for an event-by-event estimate of the Higgs mass. The reconstructed Higgs mass is then used as the final discriminating variable.

To provide a feeling for the relative sensitivity of the various Higgs searches, in the different mass ranges, Figure 12.13 shows the expected limits of the individual channels as a function of m_h. At the lowest masses the sensitivity is driven by the $H \to \gamma\gamma$ analysis; the $H \to \tau\tau$ and $H \to b\bar{b}$ analyses provide additional sensitivity. From 125 to 200 GeV, the sensitivity is driven by the $H \to WW^{(*)} \to l\nu l\nu$ and $H \to ZZ^{(*)} \to ll\nu\nu$ analyses. Above 200 GeV, $H \to ZZ^{(*)} \to llll$ is the strongest channel. The $H \to ZZ^{(*)} \to ll\nu\nu$, $H \to ZZ^{(*)} \to llq\bar{q}$, and $H \to WW^{(*)} \to l\nu q\bar{q}$ analyses provide additional sensitivity at high mass.

The analyses introduced above are combined using a statistical procedure similar to that de-

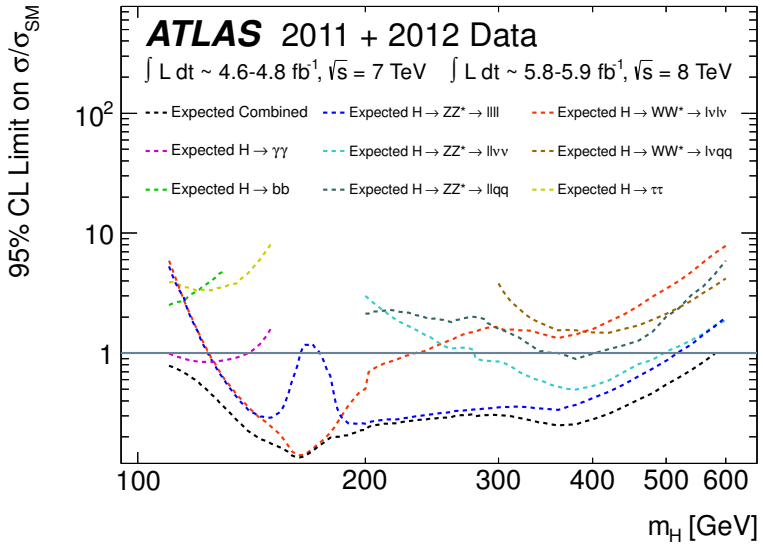

Figure 12.13: The expected 95% CL cross section upper limits as a function of m_h for the individual search channels and their combination. The expected limits are those for the background-only hypothesis, in the absence of a Higgs boson signal.

scribed in previous section. Different values of μ are tested with a statistic described in Chapter 11, based on the profile likelihood ratio. The likelihood function includes all the parameters that describe the systematic uncertainties and their correlations. Uncertainties on background normalizations or background model parameters from control regions or sidebands are uncorrelated among channels. The uncertainties due to: luminosity, lepton efficiency and energy scale, jet energy scale, and theoretical uncertainties on the Higgs production mechanisms are properly correlated among the different analyses.

The CL_s prescription is used to extract 95% exclusion limits. A SM Higgs boson with mass m_h is considered excluded at the 95% confidence level (CL) when $\mu = 1$ is excluded at that mass. The combined significance of an excess in the data is quantified using p_0, which represents the probability that the background can produce a fluctuation greater than or equal to the excess observed in data.

12.3 Results

An excess of events is observed around 125 GeV in both the $H \to ZZ^{(*)} \to llll$ and $H \to \gamma\gamma$ analyses. The $H \to WW^{(*)} \to l\nu l\nu$ channel saw an consistent excess in this region. The combined p_0 is shown in Figure 12.14. The largest significance for the combination of channels is found at m_h = 126.5 GeV, with a p_0 value corresponding to a significance of 6.0σ. The expected significance is

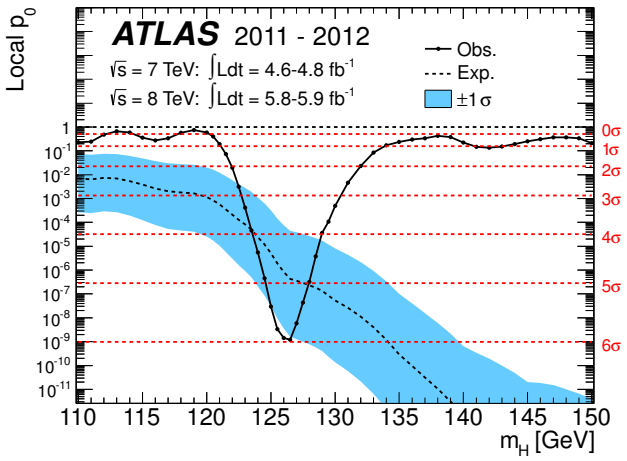

Figure 12.14: The observed and expected p_0 as a function of m_h in the low mass range for the combined Higgs search. The dashed curve shows the corresponding expectation for p_0 for the signal+background hypothesis at the given values of m_h; the blue band gives the ± 1 one sigma region. The horizontal dashed lines indicate the p-values corresponding to significances of 1 to 6 sigma.

4.9σ, with an uncertainty band indicated in the figure. The global significance for an excess of this size to occur anywhere in the mass range 110-600 GeV is estimated to be 5.1 σ. This corresponds to the observation of new particle.

The mass of the newly observed particle as measured using $H \to ZZ^{(*)} \to llll$ and $H \to \gamma\gamma$ channels is $126.0 \pm 0.4(\text{stat.}) \pm 0.4(\text{sys.})$ GeV. The leading sources of systematic uncertainty come from the electron and photon energy scales and resolutions.

A summary of the measured signal strengths in the combined and individual channels is shown in Figure 12.15. The combined signal strength of the observed excess is $\mu = 1.4 \pm 0.3$ at $m_h = 126$ GeV. The measured cross section is consistent with the SM Higgs boson prediction of $\mu = 1$.

The observed decays to pairs of vector bosons, with zero net charge, indicates that the new particle is a neutral boson. The observation in the di-photon channel disfavors the spin-1 hypothesis [161, 162].

Figure 12.16 shows the observed p_0 in full search range. The only significant excess is observed at 126 GeV. The data is consistent with the background only hypothesis throughout the rest of the mass range. The observed data is used to set limits on the Higgs production cross section. Figure 12.17 shows the combined 95% CL exclusion limits, in terms of the signal strength parameter, as a function of m_h. The expected exclusion region is from 110 GeV to 582 GeV. Apart from the region between 122 and 131 GeV, corresponding to the observed excess, the mass range from 110 to

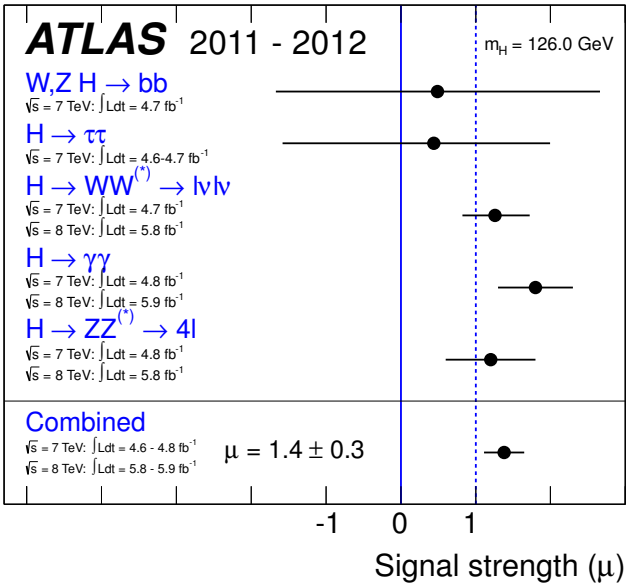

Figure 12.15: Measurements of the signal strength parameter μ for $m_h = 126$ GeV for the individual channels and their combination.

560 GeV is excluded at the 95% CL level. Figure 12.18 shows the break down of the observed limits according to channel.

12.4 Conclusions

Excesses consistent with the production of the Standard Model Higgs boson have been observed in the $H \to WW^{(*)} \to l\nu l\nu$, $H \to ZZ^{(*)} \to llll$, $H \to \gamma\gamma$ decay channels. The combined excess corresponds to a significance of 5.9 standard deviations. These results provide conclusive evidence for the discovery of a new neutral boson with mass of $126.0 \pm 0.4(\text{stat}) \pm 0.4(\text{sys})$ GeV. The measured signal strength is consistent with the SM Higgs prediction. While all of the current observations are consistent with new particle being the Standard Model Higgs boson, the relatively large uncertainties of the current data set cannot exclude significant deviations from the Standard Model hypothesis. More precise tests the compatibility of the new particle with the Standard Model Higgs boson will be the subject of future work.

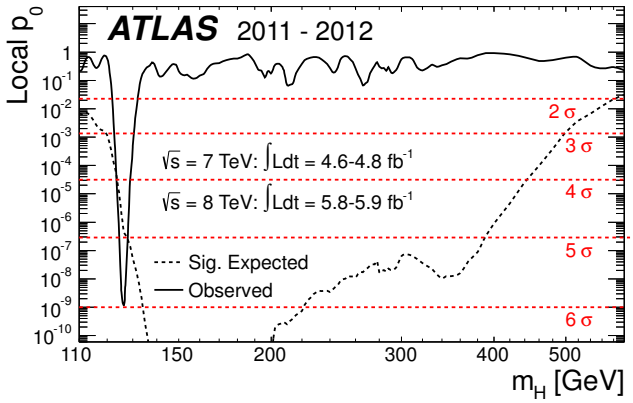

Figure 12.16: The observed and expected p_0 as a function of m_h for the entire search range for the combined analysis. The dashed curve shows the corresponding expectation for p_0 for the signal+background hypothesis at the given values of m_h. The horizontal dashed lines indicate the p-values corresponding to significances of 2 to 6 sigma.

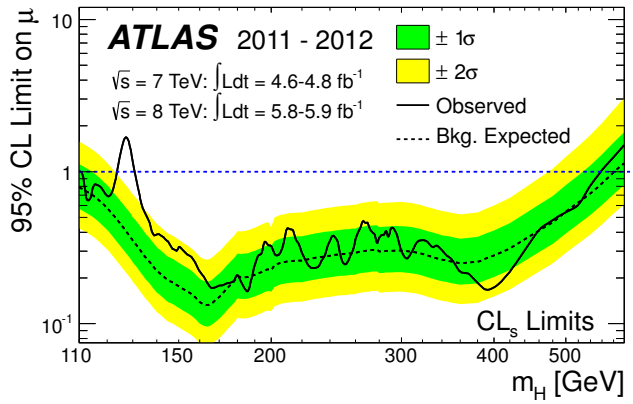

Figure 12.17: The observed (solid) 95% CL upper limit on the signal strength as a function of m_h. The dashed line gives the expected exclusion under the background-only hypothesis. The green and yellow shaded bands give the one and two sigma uncertainties on the expected exclusion.

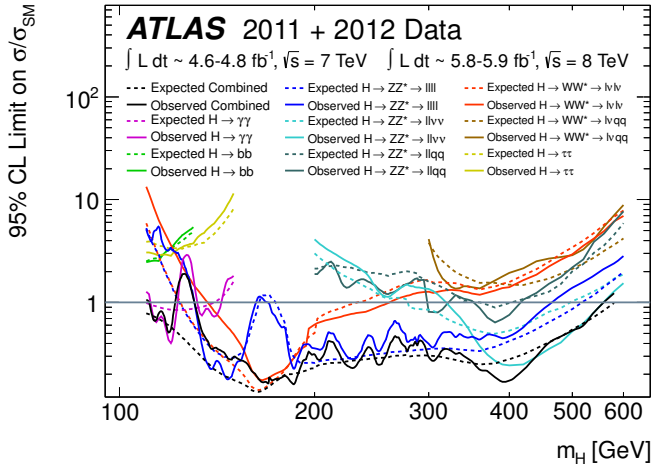

Figure 12.18: The observed (solid) and expected (dashed) 95% CL cross section upper limits for the individual search channels and the combination as a function of m_h.

Appendix A

Alignment Toy

The toy model used to introduce detector alignment in Chapter 5 is developed in detail in this section. This model is directly applicable to the study of single wire alignment in the TRT. It is in that context that it is presented in the following.

The aim is to get a feel for the different ways this alignment can be done and to get an estimate for the precision that can be reached. The wire alignment has been studied as a function of: number hits used, single hit resolution, spread of initial misalignment, and phi spread in tracks used. This toy model will hopefully serve as a setting in which future studies can quickly be carried out.

Straws are described by a circle of radius 2 mm representing the straw, with a point at the center, representing the wire. The nominal position of the straw is the origin. Misalignments are introduced by shifting the straw in the x-y plane, see Figure A.1.

Tracks traversing the straws are simulated as straight lines. The tracks can be represented by $y = mx+b$, however to relate more directly with track coming from cosmic-ray muons, the tracks are parametrized in terms of the quantities x_0 and ϕ_0. As can be seen in Figure A.2, x_0 is the distance of the track from the origin on the x-axis. ϕ_0 is angle of the track with respect to the x-axis.[25]

Tracks are generated at random with x_0 drawn from a flat distribution from -3 mm to 3 mm and with ϕ_0 drawn from a Gaussian distribution centered on $\frac{\pi}{2}$, along the y axis, with a width of **PhiSpread** which is set 0.1 radians as a default.

For each track crossing the straw there are two quantities of interest: **measR** and **trkR**. **measR** is the distance of closest approach of the track to the wire as measured by the straw. This quantity depends on the true wire alignment and the measurement resolution. In this toy **measR** is simulated as the distance of closest approach of the track to the true wire center plus a random number drawn from a Gaussian centered on zero with width of **hitError**, set to 0.13 mm as a default, to simulate

[25]The relation between the two parametrization is $m = tan(\phi_0)$, $b = -mx_0$

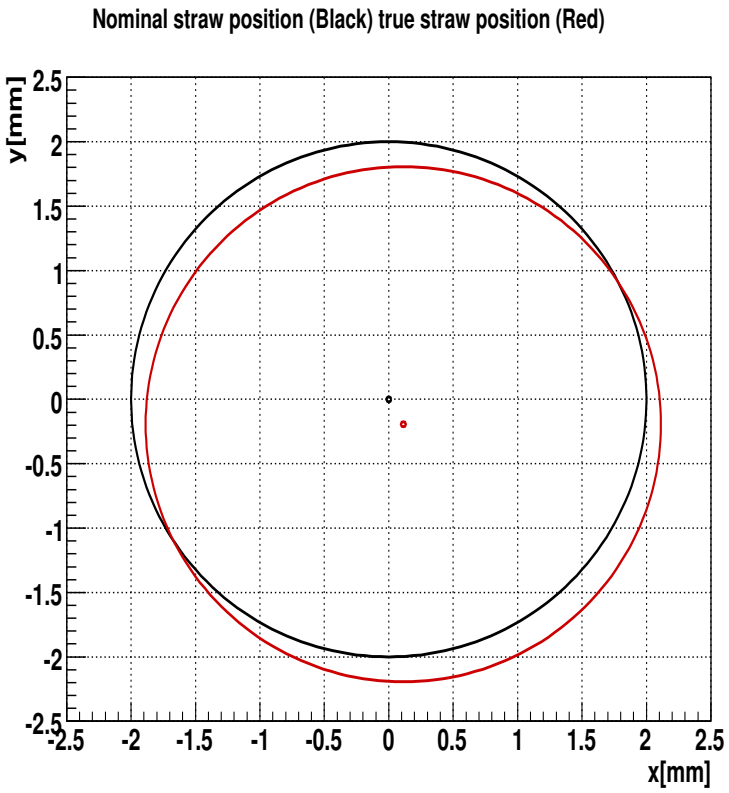

Figure A.1: Description of a straw. The nominal position is at the origin, misalignment is seen in red.

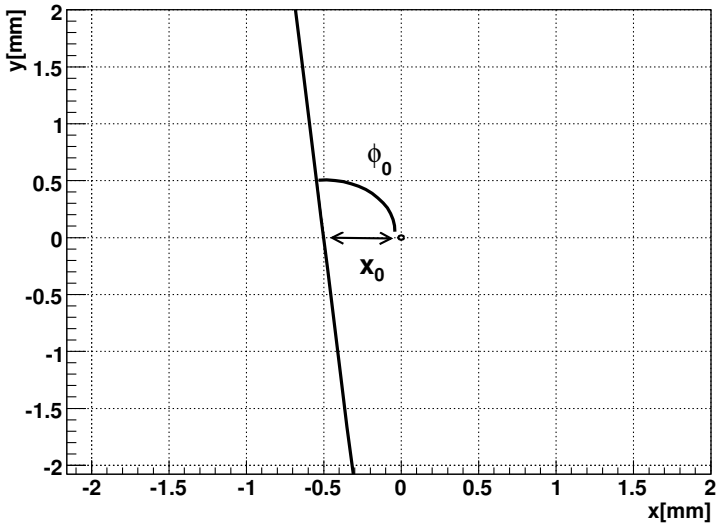

Figure A.2: Track parameters x_0 and ϕ_0.

the measurement uncertainty. **trkR** is the distance of closest approach of the track fit to the nominal wire center. For this toy the track fit is assumed to be perfect, i.e. the track fit is the same as the true track making the measurement **measR**, and is independent of straw under consideration, i.e. the **measR** of the straw plays no role in the track fit. Both **measR** and **trkR** are signed quantities. They always have the same sign which is determined from the point at which the track fit crosses the x-axis. If it is on the positive side, the sign is taken to be positive, otherwise the sign is negative.

Given these definitions one can form a residual. In this note two definitions of the residual are used:

$$\mathbf{res} = |\mathbf{trkR}| - |\mathbf{measR}| \tag{A.1}$$

and

$$\mathbf{res} = \mathbf{trkR} - \mathbf{measR} \tag{A.2}$$

Equation A.1 is used in the χ^2 minimization discussed below in Section A.5 and is chosen for ease of calculating derivatives. Equation A.2 is the traditional residual used when monitoring alignment and will be the definition used when aligning the straw based on the average residual.

A.1 Alignment Procedures.

There are a few ways one might go about calculating wire alignments. The first is to simply treat the mean of the residual distribution as the measure of the misalignment. The second is χ^2 minimization, described in Section A.5 which is the method used when aligning the TRT at L1 and L2. In this study the performance of reconstructed alignments using the two methods will be compared. The χ^2 formalism for wire alignment is discussed then the alignment is assessed.

A.1.1 Performance of Alignment.

In order to test the different methods of alignment one thousand misaligned straws were simulated with one thousand tracks each. The straws were randomly misaligned in both x and y according to a Gaussian distribution centered on zero with a width of 100 μm, which is roughly the order of magnitude expected. The straw misalignments can be seen in Figure A.3.

The χ2 minimization described in Section A.5 was preformed and the results can be seen in Figure A.4, where the reconstructed value of the alignment parameter is plotted against the true value of the misalignment.

We see in the figure that the χ^2 alignment is able to recover the initial misalignments. As expected the alignment in X is much better than in Y due to the track topology (tracks come

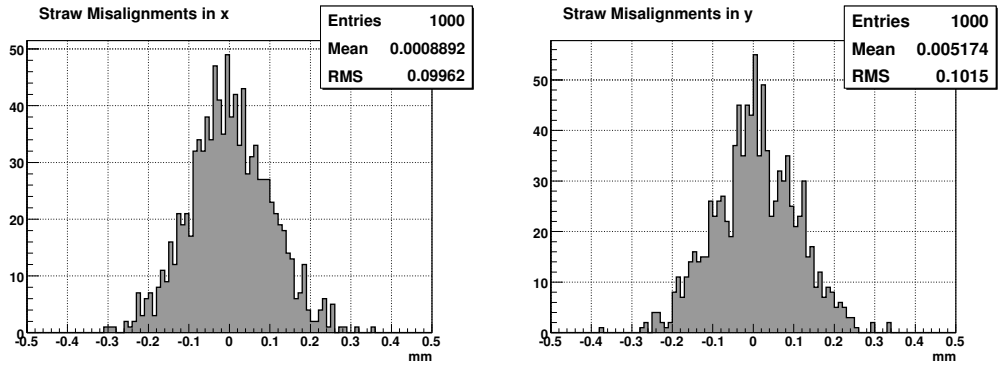

Figure A.3: Straw misalignments.

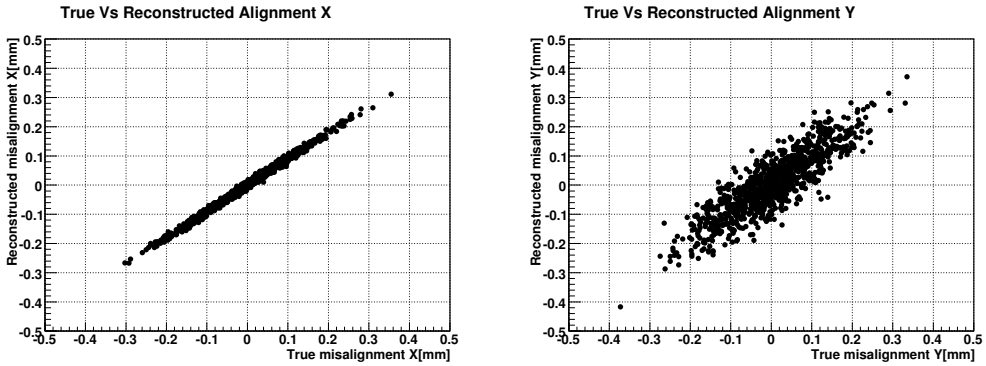

Figure A.4: Reconstructed Vs True Alignment.

"down" along the y axis with a spread of 0.1). Figure A.5 shows the residual misalignments in X and Y. Here we see the alignment is unbiased and the scale of the residual misalignments, given by the RMS of the residual misalignments, is $\approx 10\mu$m in X and $\approx 52\mu$m in Y.

As mentioned above, the alignment can also be "read off" from the residual distribution. The residual distribution given in Equation A.2 is a residual in the distance of the track to the wire, however because the tracks are coming dominantly from above, this residual approximates a residual in X. Figure A.6 shows the comparison of the average residual of tracks with the true misalignment in X.

Here we see that, as in the case of the χ^2 minimization, the alignment is unbiased with the residual misalignment on the order of 10μm.

Having validated the simple alignment techniques for this particular situation:

hitError = 0.13 mm,

PhiSpread = 0.1 radians,

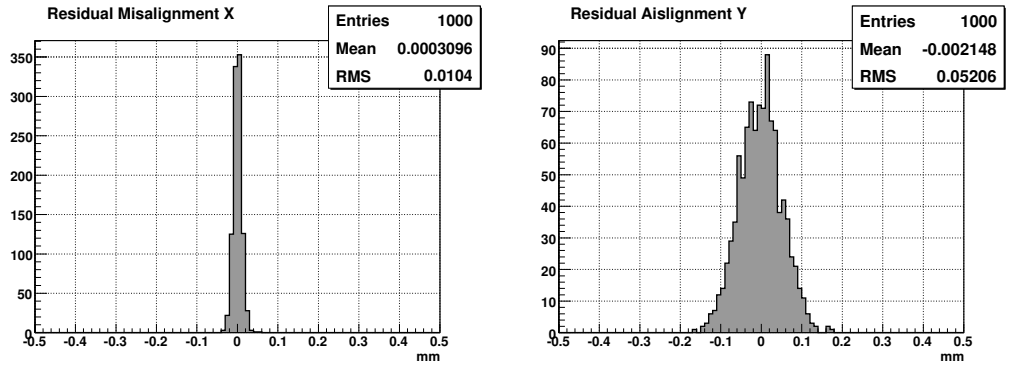

Figure A.5: Residual Misalignment.

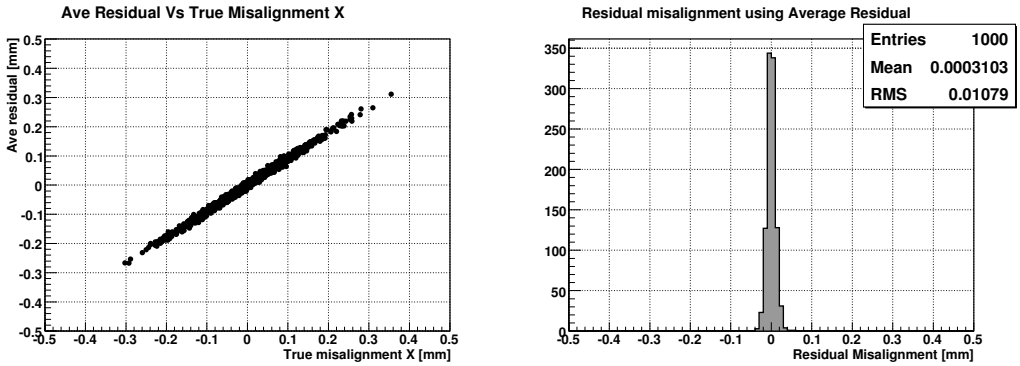

Figure A.6: Residual Misalignment.

nTrack/straw = 1000,

we study the alignment as a function of these parameters.

A.2 Study vs nHits.

The alignment was preformed as described above while varying the number of hits used. The results are shown in Figure A.7, where the RMS of residual misalignments are shown vs the number of the hits used. As expected the alignment improves with increase in number of hits used, with an asymptotic value around 10μm. The two methods of alignment show similar performance with the χ^2 method slightly better for larger numbers of hits.

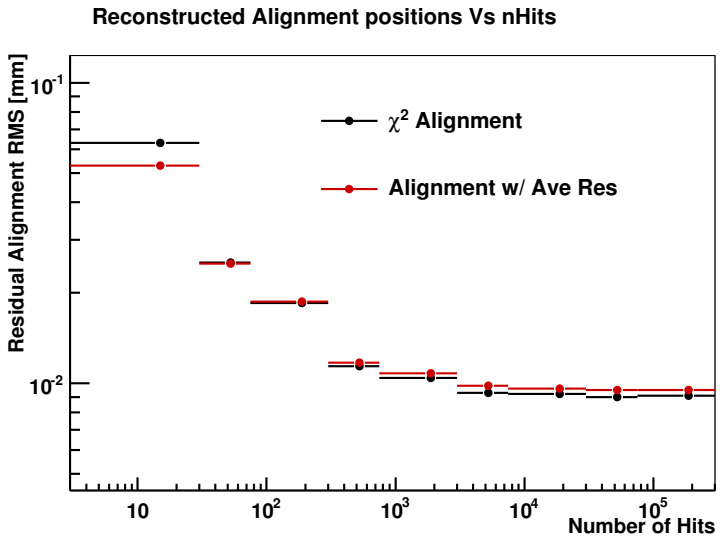

Figure A.7: RMS of residual misalignments as a function of number of hits used in alignment

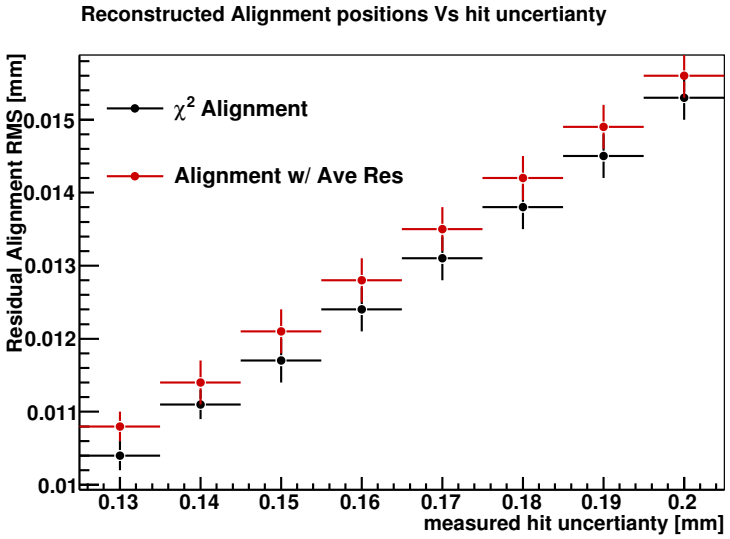

Figure A.8: RMS of residual misalignments as a function of the hit resolution used.

A.3 Study vs resolution.

The alignment was preformed as described above (1000 hits per straw) as a function of the resolution of hits used. The results are shown in Figure A.8, where the RMS of residual misalignments are shown vs the measured hit uncertainty. As expected the alignment degrades with worsening of the measured hit resolution. Again, the two methods of alignment show similar performance with the χ^2 method slightly better.

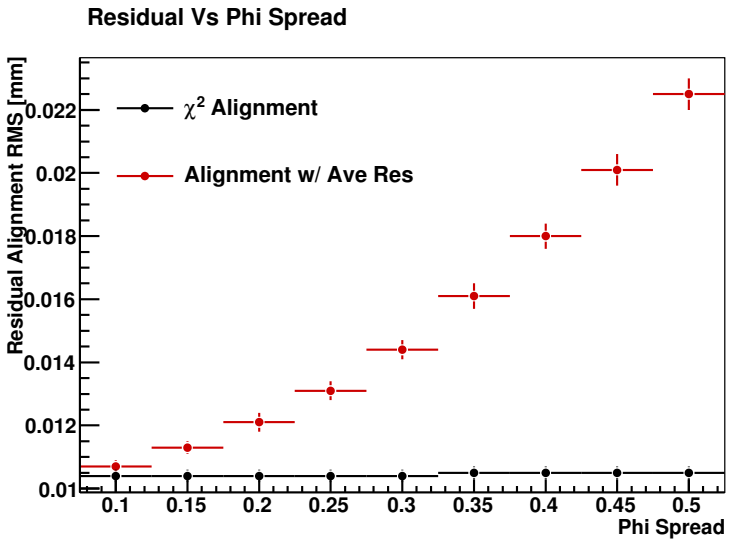

Figure A.9: RMS of residual misalignments as a function of phi spread of tracks used in alignment.

A.4 Study vs phi Spread.

The alignment was preformed as described above (0.13 mm hit resolution) as a function of **PhiSpread** of the tracks simulated. The results are shown in Figure A.9 where the RMS of residual misalignments are shown vs the measured hit uncertainty. . As expected the alignment using the average residual degrades as the spread in phi distribution of the tracks increases. As this happens the approximation of the residual in R being a residual in X degrades and the alignment worsens. However by redefining the residual such that the residual contains information about the reconstructed phi of the track I suspect that we can remove a similar performance to the χ^2 for larger phi spreads.

A.5 χ^2 minimization.

With χ^2 defined as, $\chi^2 = \frac{\mathbf{res}^2}{\sigma^2}$, the alignment solution is characterized by:

$$\frac{d\chi^2(x,y)}{dx} = 0 \tag{A.3}$$

and

$$\frac{d\chi^2(x,y)}{dy} = 0. \tag{A.4}$$

We approximate the solution with a Taylor expansion:

$$\frac{d\chi^2(x,y)}{dx} \approx \frac{d\chi^2(x,y)}{dx}|_{x_0,y_0} + \frac{d^2\chi^2(x,y)}{dx^2}|_{x_0,y_0}(x-x_0) + \frac{d^2\chi^2(x,y)}{dydx}|_{x_0,y_0}(y-y_0) = 0 \tag{A.5}$$

$$\frac{d\chi^2(x,y)}{dy} \approx \frac{d\chi^2(x,y)}{dy}|_{x_0,y_0} + \frac{d^2\chi^2(x,y)}{dxdy}|_{x_0,y_0}(x-x_0) + \frac{d^2\chi^2(x,y)}{dy^2}|_{x_0,y_0}(y-y_0) = 0 \tag{A.6}$$

These equations can be written in matrix notation as

$$\begin{pmatrix} \frac{d\chi^2}{dx} \\ \frac{d\chi^2}{dy} \end{pmatrix} + \begin{pmatrix} \frac{d^2\chi^2}{dx^2} & \frac{d^2\chi^2}{dydx} \\ \frac{d^2\chi^2}{dxdy} & \frac{d^2\chi^2}{dy^2} \end{pmatrix} \begin{pmatrix} x-x_0 \\ y-y_0 \end{pmatrix} = 0,$$

and solved as,

$$\begin{pmatrix} x-x_0 \\ y-y_0 \end{pmatrix} = - \begin{pmatrix} \frac{d^2\chi^2}{dx^2} & \frac{d^2\chi^2}{dydx} \\ \frac{d^2\chi^2}{dxdy} & \frac{d^2\chi^2}{dy^2} \end{pmatrix}^{-1} \begin{pmatrix} \frac{d\chi^2}{dx} \\ \frac{d\chi^2}{dy} \end{pmatrix}$$

Now we need to calculate the derivatives:

$$\chi^2 = \frac{\mathbf{res}^2}{\sigma^2} \tag{A.7}$$

Thus,

$$\frac{d\chi^2}{dx} = \frac{2\mathbf{res}}{\sigma^2}\frac{d\mathbf{res}}{dx} \tag{A.8}$$

$$\frac{d\chi^2}{dy} = \frac{2\mathbf{res}}{\sigma^2}\frac{d\mathbf{res}}{dy} \tag{A.9}$$

and,

$$\frac{d^2\chi^2}{dx^2} = \frac{2}{\sigma^2}\left(\frac{d\mathbf{res}}{dx}\right)^2 \tag{A.10}$$

$$\frac{d^2\chi^2}{dy^2} = \frac{2}{\sigma^2}\left(\frac{d\mathbf{res}}{dy}\right)^2 \tag{A.11}$$

$$\frac{d^2\chi^2}{dxdy} = \frac{d^2\chi^2}{dydx} = \frac{2}{\sigma^2}\left(\frac{d\mathbf{res}}{dx}\right)\left(\frac{d\mathbf{res}}{dy}\right) \tag{A.12}$$

Now,

$$\mathbf{res} = |\mathbf{trkR}| - |\mathbf{measR}| \tag{A.13}$$

$|\mathbf{measR}|$ is a number that is recorded by the straw, (which depends on the true wire position). $|\mathbf{trkR}|$ is the distance of closest approach of the track to the wire, given by:

$$\mathbf{trkR} = \frac{1}{\sqrt{m^2+1}}(mx - y + b) \tag{A.14}$$

if $\mathbf{trkR} > 0$:

$\mathbf{res} = \mathbf{trkR} - \mathbf{measR}$,

$\frac{d\mathbf{res}}{dx} = \frac{m}{\sqrt{m^2+1}}$

$\frac{d\mathbf{res}}{dy} = \frac{-1}{\sqrt{m^2+1}}$

if $\mathbf{trkR} < 0$:

$\mathbf{res} = -\mathbf{trkR} - \mathbf{measR}$,

$\frac{d\mathbf{res}}{dx} = \frac{-m}{\sqrt{m^2+1}}$

$\frac{d\mathbf{res}}{dy} = \frac{1}{\sqrt{m^2+1}}$

Appendix B

Fake Factor Derivations

B.1 Calculation of Corrected Fake Factors in the General Case.

This section presents the details of extracting the corrected fake factors discussed in Section 9.4.2, in the general case of control region impurities. The result with two sources of background is given. The logic to include additional sources is analogous.

Consider the example with a and b-type backgrounds and two, a and b-type, fake factor control regions. In the general case it is assumed that the control regions are impure, i.e. there is a contribution from both background types in each control region. In the a-type control region, the observable f_a corresponds to:

$$\begin{aligned} f_a &\equiv \left.\frac{\mathrm{N}}{\mathrm{D}_a}\right|_{a\text{-cr}} \text{(dropping the } |_{a-\mathrm{cr}}) \\ &= \frac{\mathrm{N}^a + \mathrm{N}^b}{\mathrm{D}_a} = f^a + \epsilon^{b\text{-in-}a}\left(\frac{\mathrm{N}}{\mathrm{D}_a}\right) = f^a + \epsilon^{b\text{-in-}a} f_a \end{aligned} \tag{B.1}$$

where $\epsilon^{b\text{-in-}a} = \frac{\mathrm{N}^b}{\mathrm{N}}$ is the fraction of b-type numerators in the a-type control region. The result is similar to the case of the pure control region, Equation 9.38, except there is an additional term that corrects for the impurity of the fake factor control region. The correction term contains a factor of $\epsilon^{b\text{-in-}a}$, a truth-level quantity. The observable f_b, measured in the a-type fake factor control region, is related to the impurity $\epsilon^{b\text{-in-}a}$. It is given by:

$$\begin{aligned} f_b &\equiv \left.\frac{\mathrm{N}}{\mathrm{D}_b}\right|_{a\text{-cr}} \text{(dropping the } |_{a-\mathrm{cr}}) \\ &= \frac{\mathrm{N}^a + \mathrm{N}^b}{\mathrm{D}_b} = (1 - \epsilon^{b\text{-in-}a}) f_b + f^b. \end{aligned} \tag{B.2}$$

This can be solved for $\epsilon^{b\text{-in-}a}$ as:

$$\epsilon^{b\text{-in-}a} = \frac{f^b}{f_b}. \tag{B.3}$$

Substituting $\epsilon^{b\text{-in-}a}$ back into Equation B.1 gives:

$$\begin{aligned} f_a &= f^a + \left(\frac{f^b}{f_b}\right) f_a, \\ &= f^a + \left(\frac{f_a}{f_b}\right) f^b = f^a + \left(\frac{\mathrm{D}_b}{\mathrm{D}_a}\right) f^b. \end{aligned} \tag{B.4}$$

or, more explicitly,

$$f_a|_{a\text{-cr}} = f^a|_{a\text{-cr}} + \left(\frac{\mathrm{D}_b}{\mathrm{D}_a}\right)\Big|_{a\text{-cr}} f^b|_{a\text{-cr}}\,. \tag{B.5}$$

The same logic can be applied in the b-type fake factor control region leading to:

$$f_b|_{b\text{-cr}} = f^b|_{b\text{-cr}} + \left(\frac{\mathrm{D}_a}{\mathrm{D}_b}\right)\Big|_{b\text{-cr}} f^a|_{b\text{-cr}}\,. \tag{B.6}$$

Now,

$$f^a = \frac{\mathrm{N}^a}{\mathrm{D}^a_a + \mathrm{D}^b_a} \text{ and } f^b = \frac{\mathrm{N}^b}{\mathrm{D}^a_b + \mathrm{D}^b_b},$$

where $\mathrm{D}^a_a(\mathrm{D}^a_b)$ are $a(b)$-type denominators from background of type a, and $\mathrm{D}^b_a(\mathrm{D}^b_b)$ are $a(b)$-type denominators from background of type b. In general, the corrected fake factors, f^a and f^b, will differ in the a and b factor control regions because the composition of a and b-type denominators will differ in the samples. The quantities that are invariant among samples are the truth-level ratios:

$$F^a = \frac{\mathrm{N}^a}{\mathrm{D}^a_a} \text{ and } F^b = \frac{\mathrm{N}^b}{\mathrm{D}^b_b}. \tag{B.7}$$

Using these, $f^b|_{a\text{-cr}}$ can be written as:

$$f^b|_{a\text{-cr}} = r^{b\text{-in-}\mathrm{D}_a}\, f^b|_{b\text{-cr}}\,, \tag{B.8}$$

where:

$$r^{b\text{-in-}\mathrm{D}_a} = \frac{1 - \epsilon^{b\text{-in-}\mathrm{D}_a}|_{b\text{-cr}}}{1 - \epsilon^{b\text{-in-}\mathrm{D}_a}|_{a\text{-cr}}}, \tag{B.9}$$

and:

$$\epsilon^{b\text{-in-}\mathrm{D}_a} = \frac{\mathrm{D}^b_a}{\mathrm{D}_a}. \tag{B.10}$$

Similarly, $f^a|_{b\text{-cr}}$ can be expressed in terms of $f^a|_{a\text{-cr}}$, using $r^{a\text{-in-}\mathrm{D}_b}$, defined analogously to $r^{b\text{-in-}\mathrm{D}_a}$. This leads to the following system of equations:

$$\begin{aligned} f_a|_{a\text{-cr}} &= f^a|_{a\text{-cr}} + r^{b\text{-in-}\mathrm{D}_a} \left(\frac{\mathrm{D}_b}{\mathrm{D}_a}\right)\Big|_{a\text{-cr}} f^b|_{b\text{-cr}}\,, \\ f_b|_{b\text{-cr}} &= f^b|_{b\text{-cr}} + r^{a\text{-in-}\mathrm{D}_b} \left(\frac{\mathrm{D}_a}{\mathrm{D}_b}\right)\Big|_{b\text{-cr}} f^a|_{a\text{-cr}} \end{aligned} \tag{B.11}$$

The $r^{b\text{-in-D}_a}$ and $r^{a\text{-in-D}_b}$ terms are related to the difference in impurity of the a and b-type denominator definitions. Taylor expanding $r^{b\text{-in-D}_a}$ gives:

$$r^{b\text{-in-D}_a} = 1 + \left(\epsilon^{b\text{-in-D}_a}\big|_{a\text{-cr}} - \epsilon^{b\text{-in-D}_a}\big|_{b\text{-cr}}\right) + \dots \tag{B.12}$$

The a and b-type denominators are defined such that the impurity is small. The impurity difference between control samples is smaller still. In practice, the corrections to $r^{b\text{-in-D}_a}$ and $r^{a\text{-in-D}_b}$ terms are second-order corrections and can be neglected. In the following, $r^{b\text{-in-D}_a}$ and $r^{a\text{-in-D}_b}$ are set to one.

Equation B.11 gives a system of equations which can be written as:

$$\begin{pmatrix} f_a|_{a\text{-cr}} \\ f_b|_{b\text{-cr}} \end{pmatrix} = \begin{pmatrix} 1 & \left(\frac{\mathrm{D}_b}{\mathrm{D}_a}\right)\Big|_{a\text{-cr}} \\ \left(\frac{\mathrm{D}_a}{\mathrm{D}_b}\right)\Big|_{b\text{-cr}} & 1 \end{pmatrix} \begin{pmatrix} f^a \\ f^b \end{pmatrix}, \tag{B.13}$$

where the $|_{a\text{-cr}}$ and $|_{b\text{-cr}}$ on the corrected fake factors have been dropped. These corrected fake factors are then used in Equation 9.36 to predict the total background. The matrix and the left-hand side can be measured directly in the fake factor control samples. The equations have a solution provided the matrix can be inverted. In which case, the corrected fake factors are given by:

$$\begin{pmatrix} f^a \\ f^b \end{pmatrix} = \frac{1}{1 - \left(\frac{\mathrm{D}_a}{\mathrm{D}_b}\right)\Big|_{b\text{-cr}} \left(\frac{\mathrm{D}_b}{\mathrm{D}_a}\right)\Big|_{a\text{-cr}}} \begin{pmatrix} 1 & -\left(\frac{\mathrm{D}_a}{\mathrm{D}_b}\right)\Big|_{b\text{-cr}} \\ -\left(\frac{\mathrm{D}_b}{\mathrm{D}_a}\right)\Big|_{a\text{-cr}} & 1 \end{pmatrix} \begin{pmatrix} f_a|_{a\text{-cr}} \\ f_b|_{b\text{-cr}} \end{pmatrix}. \tag{B.14}$$

The matrix can be inverted if $\left(\frac{\mathrm{D}_a}{\mathrm{D}_b}\right)\Big|_{b\text{-cr}} \left(\frac{\mathrm{D}_b}{\mathrm{D}_a}\right)\Big|_{a\text{-cr}}$ is not equal to one. This amounts to the requirement that the control regions have different background compositions. The corrected fake factors can be extracted so long as control regions with different background compositions can be constructed; purity of the control regions is not required.

B.2 Extending the Fake Factor Method to Include Electron Background from W+light-flavor, W+heavy-flavor, and Wγ

The extension of the fake factor method to separately predict W+light-flavor and W+heavy-flavor fakes was described in Section 9.4.2 and presented in Section 9.4.4. This section extends the two component background model to also include $W\gamma$.

The electron fake factor from prompt photons will, in general, differ from that of light-flavor jets and heavy-flavor jets. Typically this is dealt with by taking the $W\gamma$ background prediction from MC. However, the fake factor procedure can also be extended to include a data-driven $W\gamma$

prediction. This can be done by determining the corrected fake factors:

$$\begin{aligned} f^{\text{l.f.}} &= \frac{\text{N}^{\text{l.f.}}}{\text{D}_{\text{l.f.}}}, \\ f^{\text{h.f.}} &= \frac{\text{N}^{\text{h.f.}}}{\text{D}_{\text{h.f.}}}, \\ f^{\gamma} &= \frac{\text{N}^{\gamma}}{\text{D}_{\gamma}}, \end{aligned} \tag{B.15}$$

where: $\text{D}_{\text{l.f.}}(\text{D}_{\text{h.f.}}/\text{D}_{\gamma})$ is a light-flavor (heavy-flavor/prompt photon) denominator definition, and $\text{N}^{\text{l.f.}}(\text{N}^{\text{h.f.}}/\text{N}^{\gamma})$ are numerators from light-flavor (heavy-flavor/prompt photon). $\text{D}_{\text{l.f.}}$, $\text{D}_{\text{h.f.}}$, and D_{γ} are definitions that are chosen and correspond to observables in a given sample. $\text{N}^{\text{l.f.}}$, $\text{N}^{\text{h.f.}}$, and N^{γ} are truth-level quantities, which are not observable; only the sum $\text{N} = \text{N}^{\text{l.f.}} + \text{N}^{\text{h.f.}} + \text{N}^{\gamma}$ is observable. If the corrected fake factors are determined, the W+jet background can be calculated as:

$$\text{N}_{\text{X}+e} = f^{\text{l.f.}} \times \text{N}_{(\text{X}+\text{D}_{\text{l.f.}})} + f^{\text{h.f.}} \times \text{N}_{(\text{X}+\text{D}_{\text{h.f.}})} + f^{\gamma} \times \text{N}_{(\text{X}+\text{D}_{\gamma})}, \tag{B.16}$$

where the first term on the right-hand side predicts the background from W+light-flavor, the second term predicts W+heavy-flavor, and the last term gives the background from $W\gamma$. To predict background in the ee-channel X is an identified electron, in the $e\mu$-channel X corresponds to an identified muon.

To determine the corrected fake factors, three fake factor control regions, with different relative amounts of light-flavor, heavy-flavor, and prompt photons, are required. The heavy-flavor control region can be a di-jet selection with an away-side b-tag; the light-flavor control region can be a di-jet selection with an away-side b-veto; $Z\gamma$ events are used for the photon control region. For the photon control region, $Z\gamma$ events in which the Z decays to muons with final state radiation are selected by requiring the 3-body mass, $m_{\mu\mu\text{N}}$ or $m_{\mu\mu\text{D}_{\gamma}}$, to be consistent with a Z. This allows a pure sample of photons to be selected. The restriction to the muon decays of the Z removes the potential ambiguity present in the electron channel.

In the light-flavor control region, $f_{\text{l.f.}}$ is given by:

$$\begin{aligned} f_{\text{l.f.}} &= \frac{\text{N}}{\text{D}_{\text{l.f.}}} \\ &= \frac{\text{N}^{\text{l.f.}} + \text{N}^{\text{h.f.}} + \text{N}^{\gamma}}{\text{D}_{\text{l.f.}}} = f^{\text{l.f.}} + \epsilon^{\text{h.f.}} \frac{\text{N}}{\text{D}_{\text{l.f.}}} + \epsilon^{\gamma} \frac{\text{N}}{\text{D}_{\text{l.f.}}} = f^{\text{l.f.}} + \epsilon^{\text{h.f.}} f_{\text{l.f.}} + \epsilon^{\gamma} f_{\text{l.f.}} \end{aligned} \tag{B.17}$$

where $\epsilon^{\text{h.f.}} = \frac{\text{N}^{\text{h.f.}}}{N}$ and $\epsilon^{\gamma} = \frac{\text{N}^{\gamma}}{N}$. All of the observable quantities are as measured in the light-flavor control region. The specifier $|_{\text{l.f.}}$ has been suppressed. The heavy-flavor fraction in the numerator

sample $\epsilon^{\text{h.f.}}$ can be determined from measuring $f_{\text{h.f.}}$:

$$\begin{aligned} f_{\text{h.f.}} &= \frac{\text{N}}{\text{D}_{\text{h.f.}}} \\ &= \frac{\text{N}^{\text{l.f.}} + \text{N}^{\text{h.f.}} + \text{N}^{\gamma}}{\text{D}_{\text{h.f.}}} = (1 - \epsilon^{\text{h.f.}} - \epsilon^{\gamma}) f_{\text{h.f.}} + f^{\text{h.f.}} + \epsilon^{\gamma} f_{\text{h.f.}}, \end{aligned} \tag{B.18}$$

which leads to the relation:

$$\epsilon^{\text{h.f.}} = \frac{f^{\text{h.f.}}}{f_{\text{h.f.}}} \tag{B.19}$$

The measurement of $f_{\gamma} = \frac{\text{N}}{\text{D}_{\gamma}}$ leads to relation $\epsilon^{\gamma} = \frac{f^{\gamma}}{f_{\gamma}}$. Substituting into Equation B.17 gives:

$$f_{\text{l.f.}} = f^{\text{l.f.}} + \frac{f_{\text{l.f.}}}{f_{\text{h.f.}}} f^{\text{h.f.}} + \frac{f_{\text{l.f.}}}{f_{\gamma}} f^{\gamma} \tag{B.20}$$

$$= f^{\text{l.f.}} + \frac{\text{D}_{\text{h.f.}}}{\text{D}_{\text{l.f.}}} f^{\text{h.f.}} + \frac{\text{D}_{\gamma}}{\text{D}_{\text{l.f.}}} f^{\gamma} \tag{B.21}$$

or more explicitly,

$$f_{\text{l.f.}}|_{\text{l.f.}} = f^{\text{l.f.}}|_{\text{l.f.}} + \left.\frac{\text{D}_{\text{h.f.}}}{\text{D}_{\text{l.f.}}}\right|_{\text{l.f.}} f^{\text{h.f.}}|_{\text{l.f.}} + \left.\frac{\text{D}_{\gamma}}{\text{D}_{\text{l.f.}}}\right|_{\text{l.f.}} f^{\gamma}|_{\text{l.f.}} \tag{B.22}$$

where the $|_{\text{l.f.}}$ indicates that the quantities are as evaluated in the light-flavor control region.

The same logic works in the heavy-flavor and prompt photon control region giving;

$$f_{\text{h.f.}}|_{\text{h.f.}} = \left.\frac{\text{D}_{\text{l.f.}}}{\text{D}_{\text{h.f.}}}\right|_{\text{h.f.}} f^{\text{l.f.}}|_{\text{h.f.}} + f^{\text{h.f.}}|_{\text{h.f.}} + \left.\frac{\text{D}_{\gamma}}{\text{D}_{\text{h.f.}}}\right|_{\text{h.f.}} f^{\gamma}|_{\text{h.f.}} \tag{B.23}$$

$$f_{\gamma}|_{\gamma} = \left.\frac{\text{D}_{\text{l.f.}}}{\text{D}_{\gamma}}\right|_{\gamma} f^{\text{l.f.}}|_{\gamma} + \left.\frac{\text{D}_{\text{h.f.}}}{\text{D}_{\gamma}}\right|_{\gamma} f^{\text{h.f.}}|_{\gamma} + f^{\gamma}|_{\gamma}\,. \tag{B.24}$$

The argument used in Equation B.12 can be applied here to relate the corrected fake factors in the different control regions. This results in a system of equations which can be written as:

$$\begin{pmatrix} f_{\text{l.f.}}|_{\text{l.f.}} \\ f_{\text{h.f.}}|_{\text{h.f.}} \\ f_{\gamma}|_{\gamma} \end{pmatrix} = \begin{pmatrix} 1 & \left.\frac{\text{D}_{\text{h.f.}}}{\text{D}_{\text{l.f.}}}\right|_{\text{l.f.}} & \left.\frac{\text{D}_{\gamma}}{\text{D}_{\text{l.f.}}}\right|_{\text{l.f.}} \\ \left.\frac{\text{D}_{\text{l.f.}}}{\text{D}_{\text{h.f.}}}\right|_{\text{h.f.}} & 1 & \left.\frac{\text{D}_{\gamma}}{\text{D}_{\text{h.f.}}}\right|_{\text{h.f.}} \\ \left.\frac{\text{D}_{\text{l.f.}}}{\text{D}_{\gamma}}\right|_{\gamma} & \left.\frac{\text{D}_{\text{h.f.}}}{\text{D}_{\gamma}}\right|_{\gamma} & 1 \end{pmatrix} \begin{pmatrix} f^{\text{l.f.}}|_{\text{l.f.}} \\ f^{\text{h.f.}}|_{\text{h.f.}} \\ f^{\gamma}|_{\gamma} \end{pmatrix}. \tag{B.25}$$

The matrix and left-hand side can be measured directly in the fake factor control samples. The equation has a solution provided the matrix can be inverted.

The final state radiation requirement in the $Z\gamma$ fake factor control region results in a very pure sample of photons. This can be used to simplify the system of equations for the corrected fake factors. If the $Z\gamma$ control region is assumed to be pure, the $\left.\frac{\text{D}_{\text{l.f.}}}{\text{D}_{\gamma}}\right|_{\gamma}$ and $\left.\frac{\text{D}_{\text{h.f.}}}{\text{D}_{\gamma}}\right|_{\gamma}$ terms can be neglected. Equation B.25 reduces to:

$$\begin{pmatrix} f_{\text{l.f.}}|_{\text{l.f.}} \\ f_{\text{h.f.}}|_{\text{h.f.}} \\ f_{\gamma}|_{\gamma} \end{pmatrix} = \begin{pmatrix} 1 & \left.\frac{\text{D}_{\text{h.f.}}}{\text{D}_{\text{l.f.}}}\right|_{\text{l.f.}} & \left.\frac{\text{D}_{\gamma}}{\text{D}_{\text{l.f.}}}\right|_{\text{l.f.}} \\ \left.\frac{\text{D}_{\text{l.f.}}}{\text{D}_{\text{h.f.}}}\right|_{\text{h.f.}} & 1 & \left.\frac{\text{D}_{\gamma}}{\text{D}_{\text{h.f.}}}\right|_{\text{h.f.}} \\ 0 & 0 & 1 \end{pmatrix} \begin{pmatrix} f^{\text{l.f.}}|_{\text{l.f.}} \\ f^{\text{h.f.}}|_{\text{h.f.}} \\ f^{\gamma}|_{\gamma} \end{pmatrix}. \tag{B.26}$$

This leads to $f^{\gamma} = f_{\gamma}|_{\gamma}$. The remaining two equations can then be written as,

$$\begin{pmatrix} f_{\text{l.f.}}|_{\text{l.f.}} - \frac{\text{D}_{\gamma}}{\text{D}_{\text{l.f.}}}\Big|_{\text{l.f.}} f_{\gamma}|_{\gamma} \\ f_{\text{h.f.}}|_{\text{h.f.}} - \frac{\text{D}_{\gamma}}{\text{D}_{\text{h.f.}}}\Big|_{\text{h.f.}} f_{\gamma}|_{\gamma} \end{pmatrix} = \begin{pmatrix} 1 & \frac{\text{D}_{\text{h.f.}}}{\text{D}_{\text{l.f.}}}\Big|_{\text{l.f.}} \\ \frac{\text{D}_{\text{l.f.}}}{\text{D}_{\text{h.f.}}}\Big|_{\text{h.f.}} & 1 \end{pmatrix} \begin{pmatrix} f^{\text{l.f.}}|_{\text{l.f.}} \\ f^{\text{h.f.}}|_{\text{h.f.}} \end{pmatrix}. \tag{B.27}$$

This is the same equation for the light-flavor and heavy-flavor case with a correction for the photon contamination on the left hand side.

Appendix C

Appendix with List of Tables

List of Tables

5.1 Summary of the different ID alignment levels. The number of structures aligned and the corresponding DoF used are given for each level in the alignment. "All" DoF corresponds to the six DoF of a rigid body: three translations and three rotations. 53

6.1 Results of the TRT L1 barrel alignment. 70
6.2 Result of the L1 alignment derived from cosmic-ray data. 71
6.3 Result of the L1 alignment derived from collision data. 72

7.1 Changes in the EM calorimeter geometry as a function $|\eta|$. These changes lead to an η-dependence in the electron identification variables. 113
7.2 Summary of the variables used in the Loose, Medium, and Tight operating points of the isEM menu. 120
7.3 Summary of the variables used in the Loose++, Medium++ and Tight++ operating points in the isEM++ menu. 128
7.4 Table of changes in the single electron trigger. 133

9.1 Example of an electron numerator definition. The numerator is required to pass tight isEM and be well isolated. . . . 170
9.2 Examples of different electron denominator definitions. The denominator can be defined such that the extrapolation is done along isEM ("PID"), isolation, or both. . . . 171
9.3 Example of a muon numerator definition. The numerator is required to pass tight impact parameter cuts and be well isolated. . . . 172
9.4 Example of a muon denominator definition. The denominator is required to satisfy looser impact parameter and calorimeter-based isolation criteria. The track-based isolation and the d_0 impact parameter criteria have been removed. Muons passing the numerator selection in Table 9.3 are explicitly vetoed. . . . 173
9.5 Summary of the total fake factor uncertainties in the 15 - 20 GeV bin for electron and muons. The individual contributions are combined in quadrature to give to total uncertainty. . . . 189
9.6 Example of the W+jet background calculation in the ee-channel. The W+jet control yield in data and the various MC corrections are shown separately. . . . 191
9.7 Example of the W+jet background calculation in the $\mu\mu$-channel. The W+jet control yield in data and the various MC corrections are shown separately. . . . 192
9.8 Example of the W+jet background calculation in the $e\mu$-channel. The W+jet control yields in data and the various MC corrections are shown separately. The $e\mu$-channel receives background contributions from two W+jet control regions. . . . 192
9.9 Examples of opposite-sign W+jet validation regions. The validation region can be defined to test the extrapolation along the isEM or along the isolation dimension. . . . 201
9.10 Examples of heavy-flavor electron denominator definitions. . . . 213
9.11 Examples of light-flavor electron denominator definitions. . . . 213

10.1 Electron identification criteria. . . . 222
10.2 Muon identification criteria. . . . 222
10.3 Basic di-lepton pre-selection criteria. . . . 223
10.4 WW Event Selection. . . . 223
10.5 Cut-flow for the WW selection Cut-flow for data collected in 2011 at 7 TeV for 1.02 fb^{-1} in the three di-lepton channels. . . . 225
10.6 The estimated background yields in the WW data sample. The first uncertainty is statistical, the second systematic. . . . 226

10.7 Z/γ^* background systematic results. All errors are statistical. The statistical uncertainty on S is applied as the systematic uncertainty on the Z/γ^* background. 227
10.8 Muon denominator definition. 230
10.9 Electron denominator definitions. 231
10.10 Di-boson background yields with their associated statistical uncertainties as determined from MC. Scale factors as described above are applied to the MC. 233
10.11 Definition of the fiducial phase space used in the WW cross section measurement. . . . 233
10.12 Acceptances in the various channels. The first uncertainty is statistical and the second systematic. 234
10.13 Relative uncertainties, in percent, on the estimate of the product $A_{WW} \times C_{WW}$ for the individual WW decay channels. The uncertainty on A_{WW} (C_{WW}) receives contributions from the last three (first six) sources. 234
10.14 The measured fiducial cross sections (σ_{fid}) and the SM predictions (σ_{fid}^{SM}). The first uncertainty is statistical and the second systematic. The 3.7% relative uncertainty on the integrated luminosity is the third uncertainty on the measured cross sections. The uncertainties on σ_{fid}^{SM} are highly correlated between the channels. 235

11.1 MC generators used to model the Higgs signal processes for $\sqrt{s}$= 7 TeV (upper table) and $\sqrt{s}$= 8 TeV (lower table). Cross sections are quoted for $m_h = 125$ GeV and 240 GeV. The quoted signal production cross sections include the $H \to WW^{(*)} \to l\nu l\nu$ branching fractions but not the branching fractions for the W and Z boson in the associated production. 239
11.2 MC generators used to model the background processes for $\sqrt{s}$= 7 TeV (upper table) and $\sqrt{s}$= 8 TeV (lower table). The number quoted for the inclusive Z/γ^* process is for $m_{ll} > 10$GeV. Kinematic criteria are also applied in the generation of $W\gamma$ events (the photon must have $p_T > 10(8)$GeV and be separated from the charged lepton by $\Delta R > 0.1(0.25)$ for the 7 (8) TeV sample) and $W\gamma^*$ events (the higher and lower transverse momenta of the leptons from the γ^* decay must exceed 15 GeVand 5 GeV, respectively). The $ZZ \to 4l$ samples are generated with an invariant mass cut of $m_{ll} > 4\ GeV$. For the $W\gamma^*$ a lower invariant mass cut of $m_{ll} > 2m_e$ is applied. Leptonic decay modes are summed over, except for the 7 TeV $t\bar{t}$, WZ, and ZZ samples and the 8 TeV $t\bar{t}$ sample; in which the inclusive cross sections are quoted. 240
11.3 List of MC corrections 241
11.4 Electron identification criteria used in the $H \to WW^{(*)} \to l\nu l\nu$ analysis. 241

11.5 Muon identification criteria used in the $H \to WW^{(*)} \to l\nu l\nu$ analysis. 242
11.6 Basic di-lepton pre-selection criteria. 243
11.7 Summary of the 0-jet event selection after the jet veto. For the 2011 analysis, a different $p_{T_{ll}}$ requirement is made in the opposite-flavor (OF) and same-flavor (SF) channels. . . 245
11.8 The observed and expected numbers of signal and background events in the low m_h selection of the 0-jet 2011 analysis. The signal is for $m_H = 125$GeV. The W+jets background is estimated entirely from data, whereas MC predictions normalized to data in control regions are used for WW, Z/γ^*+jets, and top processes. Contributions from other background sources are taken directly from MC. Only statistical uncertainties associated with the number of events in the MC samples and the data control regions are shown. . . . 247
11.9 The observed and expected numbers of signal and background events in the 0-jet 2012 analysis. The signal is for $m_H = 125$GeV. The W+jets background is estimated entirely from data, whereas MC predictions normalized to data in control regions are used for SM WW and top processes. Contributions from other background sources are taken directly from MC. Only statistical uncertainties associated with the number of events in the MC samples and the data control regions are shown. . . . 247
11.10Summary of the event selection in the 1-jet analysis after requiring one reconstructed jet. 248
11.11The observed and expected numbers of signal and background events in the low m_h selection of the 1-jet 2011 analysis. The signal is for $m_H = 125$GeV. The W+jets background is estimated entirely from data, whereas MC predictions normalized to data in control regions are used for WW, Z/γ^*+jets, and top processes. Contributions from other background sources are taken directly from MC. Only statistical uncertainties associated with the number of events in the MC samples and the data control regions are shown. . . . 250
11.12The observed and expected numbers of signal and background events in the 1-jet 2012 analysis. The signal is for $m_H = 125$GeV. The W+jets background is estimated entirely from data, whereas MC predictions normalized to data in control regions are used for SM WW and top processes. Contributions from other background sources are taken directly from MC. Only statistical uncertainties associated with the number of events in the MC samples and the data control regions are shown. . . . 250
11.13Summary of the event selection in the 2-jet analysis after the requiring ≥ 2 reconstructed jets. . . . 251

11.14The observed and expected numbers of signal and background events in the low m_h selection of the 2-jet 2011 analysis. The signal is for $m_H = 125$GeV. The W+jets background is estimated entirely from data, whereas MC predictions normalized to data in control regions are used for WW, Z/γ^*+jets, and top processes. Contributions from other background sources are taken directly from MC. Only statistical uncertainties associated with the number of events in the MC samples and the data control regions are shown. . . . 252

11.15The observed and expected numbers of signal and background events in the 2-jet 2012 analysis. The signal is for $m_H = 125$GeV. The W+jets background is estimated entirely from data, whereas MC predictions normalized to data in control regions are used for SM WW and top processes. Contributions from other background sources are taken directly from MC. Only statistical uncertainties associated with the number of events in the MC samples and the data control regions are shown. 253

11.16The expected numbers of signal ($m_H = 125$GeV and 240 GeV) and background events after the full low m_H and intermediate m_H selections in the 2011 analysis. The results are quoted in the signal-rich region of m_{T}, defined by of $0.75\,m_H < m_{\mathrm{T}} < m_H$ for $m_H = 125$GeV and $0.6\,m_H < m_{\mathrm{T}} < m_H$ for $m_H = 240$GeV. The observed numbers of events are also displayed. The uncertainties shown are the combination of the statistical and all systematic uncertainties, taking into account the constraints from control samples. Note that these results differ from those discussed earlier due to the application of the additional m_{T} requirements. All numbers are summed over lepton flavors. Backgrounds with fewer than 0.01 events expected are marked as negligible using a '-'. 253

11.17The expected numbers of signal ($m_H = 125$GeV) and background events after the full selections in the 2012 analysis. The results are quoted in the signal-rich region of m_{T}, defined by $0.75\,m_H < m_{\mathrm{T}} < m_H$ for $m_H = 125$GeV. The observed numbers of events are also displayed. The uncertainties shown are the combination of the statistical and all systematic uncertainties, taking into account the constraints from control samples. These results differ from those discussed earlier due to the application of the additional m_{T} requirement. All numbers are summed over lepton flavors. Backgrounds with fewer than 0.01 events expected are marked as negligible using a '-'. 254

11.18 The observed and expected numbers of signal and background events in the 0-jet and 1-jet WW control region for the 2011 analysis. The W+jets background is estimated entirely from data, the top background is normalized to data in the top control region. Contributions from other background sources are taken directly from MC. Only statistical uncertainties associated with the number of events in the MC samples and the data control regions are shown. . . . 254

11.19 The observed and expected numbers of signal and background events in the 0-jet and 1-jet WW control region for the 2012 analysis. The W+jets background is estimated entirely from data, the top background is normalized to data in the top control region. Contributions from other background sources are taken directly from MC. Only statistical uncertainties associated with the number of events in the MC samples and the data control regions are shown. . . . 254

11.20 The observed and expected numbers of signal and background events in the 1-jet and 2-jet top control region for the 2011 analysis. The W+jets background is estimated entirely from data. Contributions from other background sources are taken directly from MC. Only statistical uncertainties associated with the number of events in the MC samples and the data control regions are shown. . . . 256

11.21 Prediction of the W+jet background in the 2011 and 2012 analysis, for the 0-jet and 1-jet bins. The first uncertainty is the statistical uncertainty from the W+jet control region. The second uncertainty is the systematic uncertainty from the uncertainty associated to the fake factors. The background results are quoted for the signal-rich region of m_{T}, defined by of $0.75\,m_H < m_{\mathrm{T}} < m_H$ with $m_H = 125$GeV. . . . 259

11.22 Main systematic uncertainties on the predicted numbers of signal ($m_H = 125$GeV) and background events for the low m_h 2011 analyses. The percentages are quoted relative to the total signal and background expectations. All numbers are summed over lepton flavors. The results are given for the signal-rich region of m_{T}, defined by $0.75\,m_H < m_{\mathrm{T}} < m_H$ for $m_H = 125$GeV. Sources of uncertainty that are negligible or not applicable are marked with a '-'. . . . 261

11.23 Main systematic uncertainties on the predicted numbers of signal ($m_H = 125$GeV) and background events for the 2012 0-jet and 1-jet analyses. The percentages are quoted relative to the total signal and background expectations. The results are given for the signal-rich region of m_{T}, defined by $0.75\,m_H < m_{\mathrm{T}} < m_H$ for $m_H = 125$GeV. Sources of uncertainty that are negligible or not applicable are marked with a '-'. . . . 261

12.1 Analyses used in the Higgs combination, where l stands for an electron or muon. 283

Appendix D

Appendix with List of Figures

List of Figures

1.1 The hadronic cross-section in electron-positron collisions as a function of center-of-mass energy. The solid line is the prediction of the SM, and the points are the experimental measurements. Also indicated are the energy ranges of various e^+e^- accelerators. The cross-sections have been corrected for the effects of photon radiation. 4

1.2 Summary of several Standard Model total production cross section measurements compared to the corresponding theoretical expectations. The dark error bar represents the statistical uncertainly. The red error bar represents the full uncertainty, including systematics and luminosity uncertainties. The W and Z vector-boson inclusive cross sections were measured with 35 pb^{-1} of integrated luminosity. All other measurements were performed using the 2011 data-set. The top quark pair production cross-section is based on a statistical combination of measurements in the single-lepton, di-lepton and all-hadronic channels using up to 0.7$\text{fb}^{-1}$of data. The single-top measurement uses 0.7$\text{fb}^{-1}$of data. The WW and WZ and ZZ measurements were made using 1.02fb^{-1}. 5

1.3 Results on the mass of the top quark. The direct measurements of m_t from Run-II of the Tevatron (top) are compared with the indirect SM predictions (bottom) 6

1.4 The comparison of the indirect constraints on m_W and m_t based on LEP-I/SLD data (dashed contour) and the direct measurements from the LEP-II/Tevatron experiments (solid contour). In both cases the 68% CL contours are given. The shaded band shows the SM relationship for the masses as a function of the Higgs mass. The regions excluded by direct searches, < 114GeV and 158GeV $- 175$GeV, or disfavored by theory, > 1TeV, are not shown. The arrow labeled $\Delta\alpha$ shows the variation of this relation with one of the SM parameters. This variation gives an additional uncertainty to the SM band shown in the figure. 7

1.5 Standard Model prediction of the Higgs mass. The line is the result of the fit using data at the Z pole, and the direct determinations of m_t,m_W, Γ_w. The band represents an estimate of the theoretical error due to missing higher order corrections. The vertical band shows the 95% CL exclusion limit on m_h from the direct searches at LEP-II (up to 114 GeV) and the Tevatron (158 to 175 GeV). The dashed curve shows the result of using a different values of $\Delta\alpha^{(5)}_{\text{had}}$. The dotted curve corresponds to a fit including lower energy data. 8

1.6 Leading order Feynman diagrams for Higgs production at the LHC. (a) The gluon fusion diagram proceeds via top-quark loop. (b) The vector-boson fusion diagram results in a final state with the Higgs and two jets. (c) The associated production diagram results in a final state with the Higgs and a W or Z boson. The relative size of the cross-sections of the different processes is shown in Figure 1.7. 9

1.7 Standard Model Higgs boson cross sections for the various production mechanisms shown in Figure 1.6. The process in Figure 1.6a is shown in blue, Figure 1.6b in red, and the processes corresponding to Figure 1.6c are shown in green and black. The lowest band is an additional Higgs production mode not discussed in this thesis. 10

2.1 Diagram of the locations of the four main experiments (ALICE, ATLAS, CMS and LHCb) at the LHC. Located between 50 m and 150 m underground, huge caverns have been excavated to house the giant detectors. The SPS, the final link in the pre-acceleration chain, and its connection tunnels to the LHC are also shown. 12

2.2 The peak instantaneous luminosity delivered to ATLAS per day versus time during the pp runs of 2010, 2011 and 2012. 14

2.3 Cumulative luminosity versus day delivered to ATLAS during stable beams and for pp collisions. This is shown for 2010 (green), 2011 (red) and 2012 (blue) running. The relative amount of data accumulated in 2010 is so small that it does not show up on this scale. . . . 14

3.1 Cut-away view of the ATLAS detector. . . . 16
3.2 Drawing showing the detector elements crossed by a charged particle with 10 GeV p_{T} in the barrel of the Inner Detector. The particle emerges from the interaction point and traverses the beam-pipe, three pixel layers, four double layers of SCT sensors, and around 35 TRT straws. . . . 18
3.3 Drawing showing the detector elements crossed by two charged particles of 10 GeV p_{T} in the end-cap of the Inner Detector. A particle at $|\eta| = 1.4$ traverses the beam-pipe, three pixel layers, four SCT disks with double layers of sensors, and approximately 40 straws in the TRT end-cap. A particle at $|\eta| = 2.2$ traverses the beam-pipe, only the first layer of the pixel detector, two end-cap pixel disks and the last four disks of the SCT end-cap. The coverage of the end-cap TRT does not extend beyond $|\eta| = 2$. . . . 18
3.4 Cut-away view of the ATLAS calorimeter system. . . . 20
3.5 Sketch of section of the LAr EM barrel where the different layers are clearly visible. The granularity in η and ϕ of the cells of each of the three layers is shown. . . . 21
3.6 Cut-away view of the ATLAS muon system. . . . 22

4.1 Schematic cut-away of the ATLAS detector. The different signatures of particles traversing the detector are shown. . . . 25
4.2 Event display of a $t\bar{t}$ di-lepton candidate in the $e\mu$-channel with two b-tagged jets. The electron is shown by the green track pointing to a calorimeter cluster, the muon by the long red track intersecting the muon chambers, and the $E_{\mathrm{T}}^{\mathrm{miss}}$ direction is indicated by the blue dotted line in the x-y view. The secondary vertices of the two b-tagged jets are indicated by the orange ellipses in the upper right. . . . 29
4.3 Mean number of interactions per bunch crossing, μ, for 2011 and 2012 data. The plot shows the full 2011 run and 2012 data taken between April and June. . . . 32

5.1 Schematic of track reconstruction in the absence of detector misalignment. Figure (a) shows the measurements caused by the trajectory of a charged particle assuming no detector misalignment. Figure (b) shows the reconstructed trajectory using those measurements and assuming no misalignment. The correct trajectory is reconstructed. . . . 36

5.2 Schematic of track reconstruction in the presence of detector misalignment. Figure (a) shows the measurements caused by the trajectory of a charged particle with detector misalignment indicated by α. Figure (b) shows the reconstructed trajectory using those measurements and assuming no misalignment. The reconstructed trajectory differs from the charged particle trajectory. 36

5.3 Schematic of the reconstructed trajectory using the measurements from 5.2a and correcting for detector misalignment. The correct trajectory is reconstructed. 37

5.4 Layout of the Inner Detector. The division into barrel and end-caps can be seen. The further division of the barrels, into layers, and the end-caps, into disks is also shown. The full detector granularity is not given. 38

5.5 Sketch of how track quality is effected by detector misalignment. Figures (a)–(e) show various alignments of the second detector element and the resulting track fits, indicated by the dashed red line. When the detector misalignment, indicated by α, is larger, the distance of the track fit to the hits, indicated by d for the second hit, is correspondingly larger. 40

5.6 Sketch of the χ^2 as a function of detector misalignment α in Figure 5.5. The locations of the reconstructed tracks in Figures 5.5a–5.5e are indicated in the figure. 41

5.7 Sketch of the curl deformation, a weak mode that biases the reconstructed track p_{T}. The detector elements are misaligned in ϕ with a magnitude that is proportional the radial position, as indicated by the arrows. The effect on the curvature for a positively and negatively charged track are shown. 47

5.8 Typical track topologies from collision events. Tracks originate from the center of the detector. Different reconstructed tracks are shown in different colors. 48

5.9 Examples of tracks from cosmic-ray muons with track topologies different from that seen in collision events. Figure (a) shows an example of a cosmic-ray muon which correlates the upper and lower parts of the ID barrel. Figure (b) shows an example of a cosmic-ray muon which correlates detector elements in the TRT that are not correlated by tracks from collision events. 49

5.10 Sketch of the effect of a curl deformation on a track from a cosmic-ray muon. The detector elements are misaligned in ϕ with a magnitude that is proportional the radial position, as indicated by the arrows. For cosmic-ray muons this deformation is not a weak mode as the p_{T} bias is opposite for upper and lower half of reconstructed track. The effect on the curvature of a negatively charged track is shown. 49

5.11 Illustration of track-splitting in cosmic-ray events. Cosmic-ray muons with low impact parameters crossing both halves of the ID (Figure (a)), can be split and reconstructed as two collision-like tracks (Figures (b) and (c)). The upper and lower track halves are from the same charged particle and should thus have the same track parameters. . . . 52

5.12 Residual distributions from cosmic-ray muon tracks in the Pixel (a), SCT (b), and TRT (c) barrels. Distributions are shown before and after the alignment from cosmic-rays. The result of using a perfectly aligned detector in MC is shown for comparison. . 54

5.13 Difference in track parameters: d_0 (a), ϕ_0 (b), and z_0 (c), for split cosmic-ray tracks in the Pixel and SCT barrel. Distributions are shown before and after the alignment from cosmic-rays. The result of using a perfectly aligned detector in MC is shown for comparison. 55

5.14 Residual distributions from collision tracks in the Pixel (a), SCT (b), and TRT (c) end-caps. Distributions are shown before and after the alignment from 900 GeV collisions. The result of using a perfectly aligned detector in MC is shown for comparison. 56

5.15 Average of the residual distribution as a function of Pixel or SCT barrel layer or end-cap disk for: end-cap C (a), barrel (b), and end-cap A (c). The result from data after the L3 alignment is shown in blue. The expectation from a perfectly aligned detector in MC is shown in red. 56

5.16 Residual distributions for Pixel, SCT and TRT. The results in data after the L3 alignment are shown in blue. The expectation from a perfectly aligned detector in MC is shown in red. The top row shows the Pixel detector, the middle shows the SCT, and the bottom row shows the TRT. The residual distributions in the barrel are given in the left-hand column, and those in the end-caps are given on the right. 57

5.17 Evidence for the presence of detector weak modes after alignment. Figure (a) shows the mean of the reconstructed Z invariant mass using ID tracks in $Z \to \mu\mu$ events as a function of the ϕ of the positive muon, for tracks in end-cap A. Figure (b) shows the measured sagitta bias using $W \to e\nu$ events as a function of the electron η and ϕ. No bias is expected from a properly aligned detector. 58

5.18 Evidence for the removal of detector weak modes with the constrained alignment. Figure (a) shows the mean of the reconstructed Z invariant mass using ID tracks in $Z \to \mu\mu$ events as a function of the ϕ of the positive muon, for tracks in end-cap A. The data before the constrained alignment is shown in black. The data after the constrained alignment is shown in red. The expectation from a perfectly aligned detector is shown in gray. Figure (b) shows the measured sagitta bias using $W \to e\nu$ events as a function of the electron η and ϕ after the constrained alignment. No bias is seen after the constrained alignment. 59

5.19 Reconstructed invariant mass using ID track for $Z \to \mu\mu$ events. The data after detector alignment is shown in black. The expectation from a perfectly aligned detector is shown in gray. 60

6.1 Schematic of TRT in the r-z plane. The TRT is composed of barrel and end-cap detectors. The division of the end-caps into A-wheels and B-wheels can be seen. 62

6.2 Schematic of a Type II TRT barrel module. The circles represent individual straws, which are all oriented parallel to the beam line. The z-axis (beam pipe) is in the direction coming out of the page. The first layer of straws is highlighted in blue at the bottom. . 63

6.3 Schematic of a TRT barrel module along z. The wires are connected, but electronically split in the center of the barrel modules. 63

6.4 The Barrel Support System. Holds the TRT barrel modules in place forming the TRT barrel. The outer cylindrical shell is not shown. 64

6.5 Schematic of the Inner Detector barrel, x-y view. The TRT barrel modules are the red shaded trapezoids. The three layers of module types are indicated. 65

6.6 A picture of a TRT end-cap 4-plane wheel during construction. The inner and outer supporting rings are visible. One straw is shown connecting the rings. 66

6.7 Wire-level DoF used in the L3 alignment. The plane of the page represents the straw plane. The direction of charged particles is into the page. The sensitive displacements in the straw plane can be represented by two DoF: a translation and a rotation. 68

6.8 Convergence of the L1 barrel alignment parameters. The changes in the alignment DoF vs iteration: (a) shows the convergence of the rotational DoF and (b) shows the convergence of the translation DoF. 69

6.9 (a) Comparison of the TRT residual for combined tracks before and after the L1 alignment. (b) Comparison of the average residual of combined tracks vs ϕ-sector for barrel modules in the first layer, before and after the L1 alignment. 70

6.10 Validation of the L1 alignment with split tracks. Comparison of the $\frac{q}{p_T}$ (a) and the ϕ_0 (b), difference of split tracks before and after the L1 alignment. 71

6.11 Map of the TRT hits from combined ID tracks in cosmic-ray data. The figures show the number of hits on track as a function of z and ϕ, for end-cap C (a) and end-cap A (b). 72

6.12 Map of the TRT hits from combined ID tracks in collision data. The figures show the number of hits on track as a function of z and ϕ, for end-cap C (a) and end-cap A (b). 73

6.13 The TRT end-cap residual distributions before and after the L1 end-cap alignment for end-cap A ((a)) and end-cap C ((b)) 73

6.14 Mean of the fitted TRT residual distribution as a function of end-cap 4-plane wheel (denoted ring in the figures) before and after the L1 alignment. End-cap A is shown in (a) and end-cap C is shown in (b). 74

6.15 Average residual as a function of straw-layer for hits in ϕ sector 19. The discontinuities in the distribution are along module boundaries and indicate L2 barrel misalignment. . 75

6.16 The eigenvalue spectrum of the second derivative matrix for the L2 alignment with TRT-Only tracks. The three trivially unconstrained DoF are identified as orders of magnitude smaller then the others. 76

6.17 Examples of convergence of the L2 alignment parameters. Changes in the rotations around y (a) and translations along x (b), as a function of alignment iteration for all modules in the first barrel layer. Each curve represents a different barrel module. 77

6.18 Visual representation of the result of the L2 barrel alignment. (a) Visual representation of the translation alignment parameters. Each arrow represents a barrel module. The tail of the arrow is the nominal module position. The arrow length and direction represent the measured x and y alignment parameters. The arrow lengths are enlarged by a factor of 1000 relative to the axes. A scale is provided for reference. (b) Visual representation of the rotations about z. Each arrow represents a barrel module. The size of the rotation is given as the angle the arrows make with respect to the positive x-axis. The arrow length has no meaning. The size of the rotations are enlarged by a factor of 1000. A scale is provided for reference. 77

6.19 TRT residuals before and after L2 alignment. (a) Comparison of TRT residual for TRT stand-alone tracks before and after L2 alignment. (b) Comparison of the average residual of TRT stand-alone tracks vs ϕ-sector for barrel modules in the first module layer, before and after L2 alignment. 78

6.20 Average residual as a function of straw-layer for hits in ϕ-sector 19. The discontinuities in the distribution before L2 alignment are removed with the L2 alignment. 78

6.21 Validation of the L2 alignment with split tracks. Comparison of the $\frac{q}{p_T}$ (a) and the ϕ_0 (b), difference of split tracks before and after the L2 barrel alignment. 79

6.22 L2 Alignment Parameters when using silicon Information. (a) Visual representation of the translation alignment parameters. Each arrow represents a barrel module. The tail of the arrow is the nominal module position. The arrow length and direction represent the global x and y alignment parameters. The arrow lengths are enlarged by a factor of 1000 relative to the axes. A scale is provided for reference. (b) Visual representation of the rotations about z. Each arrow represents a barrel module. The size of the rotation is given as the angle the arrows make with respect to the positive x-axis. The arrow lengths has no meaning. The size of the rotations are enlarged by a factor of 1000. A scale is provided for reference. 80

6.23 L2 alignment parameters for rotations around x and y when aligning with silicon information. The plots on the left give the rotation around x, whereas the plots on the right have the rotations around y. The parameters for barrel modules in layer zero are in the first row, those from layer one in the second, and those from layer two appear in the last row. 81

6.24 Difference in L2 Alignment parameters with and without using silicon information. (a) Visual representation of the differences in translation alignment parameters after alignment with and without using silicon information. Each arrow represents a barrel module. The tail of the arrow is the module position after alignment with TRT stand-alone tracks. The arrow-head is the module position after alignment including silicon information. The arrow lengths are enlarged by a factor of 1000 relative to the axes. A scale is provided for reference. (b) Visual representation of the differences in rotations with and without using silicon information. Each arrow represents a barrel module. The difference in the rotation is given as the angle the arrows make with respect to the positive x-axis. The arrow lengths have no meaning. The size of the rotations are enlarged by a factor of 1000. A scale is provided for reference. 82

6.25 Comparison of the average residual of combined tracks vs ϕ-sector for barrel modules in layer zero before and after the TRT stand-alone L2 barrel alignment (a), and before and after the L2 barrel alignment including silicon information (b) 82

6.26 Average residual as a function of ϕ-sector for hits in barrel modules on side A (left plots) and C (right plots) separately. Modules in the first barrel layer are shown in the top row, those in the second are shown in the middle, and barrel modules in the third layer are shown in the bottom row. 84

6.27 Average residual as a function of ϕ-sector for hits in barrel modules on sides A (left plots) and C (right plots) separately. Modules in the first barrel layer are in the top row, those in the second layer are shown in the middle, and barrel modules in the third layer are shown in the bottom row. For the residuals in side-A (side-C), the geometry after the L2 alignment with only the A-side (C-side) hits was used. 85

6.28 Visual representation of the differences in translation alignment parameters when aligning A-side only and C-side only. Each arrow represents a barrel module. For the upper two plots and for the one on the lower left, the tails of the arrows are the module position after alignment with C-side only. The arrow-heads are the module positions after alignment with A-side only. The arrow lengths are enlarged by a factor of 1000 relative to the axes. The modules in each layer are shown separately for clarity. Scales are provided for reference. The plot in the lower right is a visual representation of the differences in rotations. Each arrow represents a barrel module. The difference in the rotation is given as the angle the arrows make with respect to the positive x-axis. The arrow length has no meaning. The size of the rotations are enlarged by a factor of 1000. A scale is provided for reference. 86

6.29 Visualization of measured rotations about z with the alignment using cosmic-rays. The measured misalignment in ϕ is plotted as a function of 4-plane wheel number. The solid red lines give the separation of the Type-A and Type-B wheels, and the dashed vertical black lines give the separation of the 8-plane Type-A and Type-B type wheels. The results for end-cap C are shown on the left, whereas those for end-cap A are presented in the right. 88

6.30 Visualization of measured rotations about z with the alignment using collision data. The measured misalignment in ϕ is plotted as a function of 4-plane wheel number. The solid red lines give the separation of the Type-A and Type-B wheels, and the dashed vertical black lines give the separation of the 8-plane Type-A and Type-B wheels. The results for end-cap C are shown on the left, whereas those for end-cap A are presented in the right. 89

6.31 Visualization of measured translations in x with the alignment using collision data. The measured misalignment in x is plotted as a function of 4-plane wheel number. The solid red lines give the separation of the Type-A and Type-B wheels, and the dashed vertical black lines give the separation of the 8-plane Type-A and Type-B wheels. The results for end-cap C are shown on the left, whereas those for end-cap A are presented in the right. 90

6.32 Visualization of measured translations in y with the alignment using collision data. The measured misalignment in Y is plotted as a function of 4-plane wheel number. The solid red lines give the separation of the Type-A and Type-B wheels, and the dashed vertical black lines give the separation of the 8-plane Type-A and Type-B wheels. The results for end-cap C are shown on the left, whereas those for end-cap A are presented in the right. 90

6.33 Mean of the fitted TRT residual distribution a function of end-cap 4-plane wheel, before and after the L2 alignment. End-cap A is shown in (a) and end-cap C in (b) 91

6.34 TRT residual distributions before and after the L2 end-cap alignment for end-cap A Figure (a) and end-cap-C Figure (b) 91

6.35 Mean of the fitted residual distribution (in [mm] indicated by the color) vs end-cap 4-plane wheel (x-axis) and ϕ (y-axis). The results for end-cap C are shown on the left, whereas those for end-cap A are presented in the right. 92

6.36 Mean of the fitted residual distribution (in [mm] indicated by the color) vs 4-plane wheel (x-axis) and R (y-axis). The results for end-cap C are shown on the left, whereas those for end-cap A are presented in the right. 93

6.37 Sketches of 4-plane wheel deformations indicated by systematic residual bias after the L2 alignment. The residual map of ϕ vs 4-plane wheel (left) shows signs of elliptical deformation. The residual map of r vs 4-plane wheel (right) shows signs of twist-like deformation. 93

6.38 TRT residual distributions in the end-cap before and after the L3 end-cap alignment. The "Autumn 2010 Alignment" includes the L3 alignment, the "Spring 2010 Alignment" uses the TRT geometry before the L3 alignment. 94

6.39 Mean of a Gaussian fit to TRT residuals vs ϕ-sector and wheel before, (a), and after, (b), the wire-level alignment. The plots illustrate the results for end-cap A. The white bins are due to dead channels. 95

6.40 Mean of a Gaussian fit to the TRT residuals vs radius and wheel before, (a), and after, (b), the wire-level alignment. The plots illustrate the results for end-cap A. The white area in the lower right corner is due to acceptance effects. 95

6.41 Visual representation of wire-level misalignment in a 4-plane wheel with elliptical-deformation-like biases in the residual map. Figure (a) gives the measured alignment of each wire with respect to position in the wheel. Figure (b) shows the measured displacement of each wire as a function of ϕ position in the wheel. A correlation in the wire-level alignment indicative of an elliptical deformation is seen. 96

6.42 Visual representation of wire-level misalignment in a 4-plane wheel with twist-deformation-like biases in the residual map. Figure (a) gives the measured alignment of each wire with respect to position in the wheel. Figure (b) shows the measured rotation of each wire as a function of ϕ position in the wheel. A correlation in the wire-level alignment indicative of an twist deformation is seen. 96

6.43 TRT residual distributions in the barrel before and after the L3 barrel alignment. The "Autumn 2010 Alignment" includes the L3 alignment, the "Spring 2010 Alignment" uses the TRT geometry before the L3 alignment. 97

6.44 Mean of a Gaussian fit to TRT residuals vs ϕ-sector and z for the first TRT barrel layer before, (a), and after, (b), the wire-by-wire alignment. 98

6.45 Distribution of measured wire misalignment in the TRT Barrel. The measured translation displacements are given in the left. The measured rotation displacements, defined as $\frac{dx1-dx2}{2}$, are given on the right. 98

6.46 TRT resolution in end-cap A as a function of 4-plane wheel [91]. Left-hand plot uses tracks with p_{T} below 5 GeV. Right-hand plot is with tracks with p_{T} above 10 GeV. Note the scale difference. 99

6.47 Average residual vs wheel in end-cap A [91]. Positively and negatively charged tracks are shown separately and are required to have p_{T} below 5 GeV. 100

6.48 Reconstructed J/ψ mass as a function η from tracks with only Pixel and SCT measurements ("Silicon Only") and including TRT measurements ("Combined Tracks") [92]. . 100

6.49 Sketches of the effect of a z-misalignment in the end-caps [93]. The misalignment effects low p_{T} tracks, (a), and positively and negatively charged tracks in the opposite direction, (b). 101

6.50 Measured misalignment in z as a function of z, for end-cap C (left) and end-cap A (right). The division between A and B-wheels occurs around $|z|$ of 1700 mm. 102

6.51 RMS of the end-cap residuals as a function of 4-plane wheel, before (red) and after (black) the z-alignment. End-cap C is shown on the left. End-cap A is shown on the right. . . 103

6.52 Average residual vs wheel in end-cap A [91]. Positively and negatively charged tracks are shown separately and are required to have p_{T} below 5 GeV. The result before the end-cap z-alignment are shown on the left, whereas, the result after the z-alignment is shown in the right. 103

6.53 Reconstructed J/ψ mass as a function η using combined ID tracks before the end-cap z-alignment ("Old Alignment") and after the end-cap z-alignment ("New-Alignment") [92]. 104

6.54 TRT residual distribution after the alignment presented in this chapter for hits the barrel (left) and end-cap (right). The expectation from a perfectly aligned detector in simulation is provided. 104

7.1 Event display of a reconstructed electron from a candidate W decay. The reconstructed electron track is indicated in yellow. The electron cluster is shown in yellow, in the green EM calorimeter. The red points along the electron track indicate detection of transition radiation. The red dashed line indicates the direction of the momentum imbalance. . . 106

7.2 Electron reconstruction efficiency, including the requirements on the track quality, ($N_{pix} \geq 1$ and $N_{Si} \geq 7$) as a function of (a) E_T and (b) η. The plot vs η is shown for electrons with E_T between 30 and 50 GeV. 108

7.3 Composition of the reconstructed electrons as a function of E_T. The distribution is dominated by hadrons. Conversions are referred to in the figure as "Background" electrons. Electrons from semi-leptonic heavy-flavor decays are referred to as "Non-Isolated" electrons. The contribution from true electron, label "Isolated" in the figure, is not visible. 109

7.4 Electron identification variables in the calorimeter, "shower-shapes", shown separately for signal and the various background types. The variables shown are (a) hadronic leakage R_{had1}, (b) width in eta in the second sampling $w_{\eta 2}$, (c) R_η, (d) width in eta in the strips $w_{s,tot}$, and (e) E_{ratio}. 111

7.5 Schematic diagrams of R_η and E_{ratio}. (a) R_η is calculated as the ratio of the sum of energy in the yellow cells to the sum of energy in the yellow and green cells. The yellow cells are centered on the reconstructed electron. (b) E_{ratio} is calculated as the ratio of the difference in energy of the two highest cells, to the sum the energy in the two highest cells. [98] E_{ratio} is calculated from the cells in the first layer of the calorimeter. 112

7.6 Electron identification variables in the ID, shown separately for signal and the various background types. The variables shown are (a) number of hits in the Pixel detector, (b) combined number of hits in the Pixel and SCT detectors, (c) transverse impact parameter d_0, (d) conversion flag, or "conversion bit", and (e) fraction of high-threshold hits in the TRT. 114

7.7 Probability of a high threshold TRT hit as a function of Lorentz γ factor in the TRT barrel. The corresponding momentum assuming the pion mass or the electron mass are shown. 116

7.8 Track-Cluster matching variables, shown separately for signal and the various background types. The variables shown are (a) the difference in track and cluster η, (b) the difference in track and cluster ϕ, and (c) ratio of the energy measured in calorimeter to the momentum measured in the tracker. 117

7.9 Examples of electron isolation variables (a) relative calorimeter isolation in a cone of $\Delta R < 0.3$ (a) relative track isolation in a cone of $\Delta R < 0.3$. Signal electrons and hadron background are shown separately. 118

7.10 Comparison of the shower shapes, R_η and $w_{\eta 2}$, of electrons from $Z \to ee$ events in data and MC. The electrons are required to have E_{T} between 40 and 50 GeV. The data distributions are shown after background subtraction. The uncertainties on the data include the systematic uncertainty from the background subtraction. The MC is normalized to the number of entries in data. 122

7.11 Comparison of the shower shapes, R_{had} and E_{ratio}, of electrons from $Z \to ee$ events in data and MC. The electrons are required to have E_{T} between 40 and 50 GeV. The data distributions are shown after background subtraction. The uncertainties on the data include the systematic uncertainty from the background subtraction. The MC is normalized to the number of entries in data. 122

7.12 Efficiencies of the medium and tight requirements in the "robust" isEM menu. The efficiencies are measured using $Z \to ee$ events and are shown for electrons with E_{T} between 20 and 50 GeV. The error bars provide the statistical (inner) and total (outer) uncertainties on the measured efficiencies. 123

7.13 Example of the MC correction procedure using statistics available in 2010. The R_η and $w_{\eta 2}$ distributions are shown for data (black), the uncorrected MC (red), and the corrected MC (blue). The results are shown for the bin with E_{T} between 30 and 40 GeV, and $|\eta|$ between 1.15 and 1.37. 125

7.14 MC correction procedure using the high statistics 2011 data sample. The R_η, $w_{\eta 2}$, and $w_{s,\mathrm{tot}}$ distributions are shown for data (black), the uncorrected MC (red), and the corrected MC (blue). The results are shown for the bin with E_{T} between 30 and 40 GeV, and $|\eta|$ between 1.15 and 1.37. 125

7.15 Conceptual difference in the isEM and isEM++ menu. The x and y-axis represent two different identification variables. Var2 is used in the isEM Loose definition, Var1 is not. The Tight definition uses both Var1 and Var2. Loose++ also selects on both Var1 and Var2, but looser than Tight. 127

7.16 Comparison of the isEM and isEM++ menus. Signal efficiency and background rejection of the isEM menu is given on the left. The results for the isEM++ menu is given on the right. The upper two plots give the signal efficiency, as determined from the corrected MC. The lower plots show the background rejection with respect to reconstructed electrons. The results are shown for electrons candidates with $20 < E_{\mathrm{T}} < 30$GeV. . . . 129

7.17 Efficiency of the isEM++ operating points as a function of the number of primary vertices. The efficiency was determined using the tag-and-probe technique in $Z \to ee$ events. Error bars include statistical and systematic uncertainties. 130

7.18 Efficiency of the 2011 and 2012 isEM++ operating points as a function of the number of primary vertices. The re-tuned 2012 isEM++ menu shows less pile-up dependence. The efficiency was determined using the tag-and-probe technique in $Z \to ee$ events. Error bars include statistical and systematic uncertainties. 131

7.19 Preliminary results from an implementation of a likelihood for electron selection. Left-hand plot shows the likelihood discriminate for signal and background electrons. Right-hand plot shows the performance of the likelihood with respect to the isEM++ operating points. 132

8.1 Leading-order Feynman diagrams for $H \to WW$ production. (a) The gluon-fusion diagram proceeds via top-quark loop. (b) The vector-boson fusion diagram results in a final state with WW+2 jets. 135

8.2 Higgs branching ratios as a function of Higgs mass. 135

8.3 "Reconstructable" Higgs cross section as a function of Higgs m_h for $\sqrt{s} = 7$ TeV. The reconstructable Higgs cross sections include the BR to final states that can be reconstructed with high signal to background. The orange curve ($HV \to b\bar{b}+X$) is the sum of two production processes: the associated production of a Higgs boson with a W Boson and the associated production of a Higgs boson with a Z boson. The Higgs boson decays to $b\bar{b}$ and the W boson is required to decay to $e\nu$ or $\mu\nu$ and the Z boson is required to decay to e^+e^-, $\mu^+\mu^-$ or $\nu\bar{\nu}$. 136

8.4 Feynman diagrams for the dominant production mechanisms for continuum WW production. (a) t-channel $q\bar{q}$ annihilation. (b) s-channel $q\bar{q}$ annihilation. (c) gluon-gluon fusion. 138

8.5 The dominant Feynman diagrams for (a) $t\bar{t}$ and (b) Wt production. $t\bar{t}$ production also includes a t-channel top quark exchange diagrams, which is not pictured. Wt production includes an s-channel b-quark exchange diagram which is not shown. 140

8.6 m_{ll} distributions for same-flavor and opposite-flavor di-leptons before a missing energy requirement. Figure (a) shows the ee-channel, Figure (b) shows the $e\mu$-channel. The events are required to have one lepton with p_{T} above 25 GeV and one lepton with a p_{T} above 20 GeV. 141

8.7 Schematic diagram of the $E_{\mathrm{T}}^{\mathrm{miss,Rel}}$ calculation. $E_{\mathrm{T}}^{\mathrm{miss,Rel}}$ uses the component of the $E_{\mathrm{T}}^{\mathrm{miss}}$ perpendicular to the nearest lepton or jet. 142

8.8 $E_{\mathrm{T}}^{\mathrm{miss,Rel}}$ distributions for same-flavor and opposite-flavor di-leptons after the Z-mass veto. Figure (a) shows the same-flavor $\mu\mu$ channel. Figure (b) shows the $e\mu$-channel. Typical $E_{\mathrm{T}}^{\mathrm{miss,Rel}}$ requirements in the WW event selection are indicated in the figure. . 143

8.9 Distribution of the number of reconstructed jets after the $E_{\mathrm{T}}^{\mathrm{miss,Rel}}$ requirement. The plot combines the same-flavor and opposite-flavor channels. The jet veto of the WW signal selects events in the first bin, indicated by the arrow. 144

8.10 m_{ll} for events passing the WW signal selection. The same-flavor and opposite-flavor channels are combined. 144

8.11 Z/γ^* background estimation techniques. (a) $E_{\mathrm{T}}^{\mathrm{miss,Rel}}$ distribution in the Z-peak after applying the jet-veto in the $\mu\mu$-channel. The difference in absolute prediction above the $E_{\mathrm{T}}^{\mathrm{miss,Rel}}$ requirement is used in the scale-factor method. The 1.02 fb^{-1} data is shown. (b) m_{ll}-$E_{\mathrm{T}}^{\mathrm{miss,Rel}}$ plane used in the "ABCD" method. The distribution using 4.7 fb^{-1} of data is shown. 147

8.12 m_{ll} distribution after the WW selection. The distribution from the Higgs signal with a mass of 150 GeV is indicated in the figure. 151

8.13 Schematic diagram illustrating the correlation in lepton direction resulting from the spin-zero nature of the Higgs and the parity violating weak decays of the Ws. Two Higgs decays, with different spin orientations of the Ws, are shown. The solid red arrows indicate the direction of the decay products in the rest frame of the Higgs. The dashed black arrows indicate the direction of the spin component along the direction of the Higgs decay products. 153

8.14 Kinematic variables used to separate SM WW production from $H \to WW^{(*)}$ production. (a) m_{ll} distribution after the WW selection. The cut value used in the low-mass Higgs search is indicated in the figure. (b) $\Delta\phi_{ll}$ distribution after the low m_{ll} requirement. The cut value used in the low-mass Higgs search is indicated in the figure. 153

8.15 Transverse mass distribution after $H \to WW^{(*)}$ signal selection, for various values of Higgs mass. The result for a Higgs mass of 170 GeV is shown in the top left, 150 GeV in the top right, 135 GeV in the bottom left, and 125 GeV in the bottom right. 154

9.1 Production cross-sections in 7 TeV. The W+jet production cross section is contrasted against the WW and $H \to WW^{(*)}$cross sections. 157

9.2 E_{T} distribution for reconstructed electrons passing a loose identification criteria. The data is shown along with the different sources of electrons. The electrons are required to pass a modified selection similar to medium but without the R_{had} and R_{η} requirements [97]. 158

9.3 p_{T} distribution of reconstructed muons after a loose muon selection. The data is shown along with the different sources of "fake" muons. 159

9.4 Leading order Feynman diagrams for (a) di-jet production and (b) W+jet production. The jets in the di-jet sample are gluon initiated, whereas jets in the W+jet sample are quark initiated. 164

9.5 Schematic of the numerator selection in relation to the electron denominators given in Table 9.2. The denominator can be defined such that the extrapolation is done along isEM ("PID"), isolation, or both. The y-axis represents the isEM space, large values correspond to tighter electron identification. The x-axis represents the isolation space, lower values corresponds to more isolated. 172

9.6 Example of the electron fake factor measurement using the electron supporting triggers. The error bars indicate the statistical uncertainty on the fake factor measurement. The "PID"-denominator definition is used the fake factor calculation. 174

9.7 Comparison of electron fake factor using only the supporting triggered sample, in red, and using a combination of primary electron and supporting triggers, in blue. Using the combination of triggers reduces the statistical uncertainty on the fake factor. The "PID"-denominator definition is used the fake factor calculation. 176

9.8 Example of the electron fake factor measurement using different away-side jet p_{T} bins. The fake factor measurements in the different away-side jet bins are shown in different colors. The yellow band shows the average $\pm 30\%$. The "PID"-denominator definition is used the fake factor calculation. 177

9.9 Effect of electro-weak subtraction on measured fake factor. (a) shows the measured fake factor without the electro-weak correction. (b) shows the measured fake factor after making the electro-weak correction. The "PID"-denominator definition is used the fake factor calculation. 177

9.10 Effect of γ+jet subtraction on measured fake factor. (a) shows the measured fake factor with the electro-weak correction, but not the γ+jet correction. (b) shows the measured fake factor after making both the electro-weak correction and the γ+jet correction. The "PID"-denominator definition is used the fake factor calculation. 178

9.11 Measured fake factors corresponding to the denominator definitions in Table 9.2. (a) shows the "PID-and-Iso"-denominator, (b) shows the "PID"-denominator, and (c) uses the "Isolation"-denominator. The numerator selection is that given in Table 9.1. 179

9.12 Measured electron fake factor with loosened isolation requirement in the denominator definition. The numerator selection is that given in Table 9.1. The denominator definition is: fail isEM medium and with an isolation requirement loosened to $\frac{E_T^{Cone30}}{E_T} < 0.5$. . . . 180

9.13 Measured muon fake factor as a function of p_{T}. The fake factors are measured in different away-side jet bins, as indicated by the different colored curves. The error band gives the average with the $\pm$40% variation. 181

9.14 Fake Factor in W+jet MC. The black points show the total fake factor, the red points show the contribution from W+heavy-flavor and the blue points show the contribution from W+light-flavor. 184

9.15 The measured W+b cross section in different jet bins.[112] The comparison of the data with the modeling of the MC is seen. 184

9.16 The variation of the W+jet fake factor with varying W+heavy-flavor fraction. The black points give the W+jet fake factor using the central value of the W+heavy-flavor measurement, the red (blue) points give the W+jet fake factor after varying the heavy-flavor fraction up (down) by its measured uncertainty. 185

9.17 Comparison between di-jet and W+jet electron fake factors. The left-hand plot shows the electron fake factor in di-jet MC (red), and for the W+jet MC using the corrected value of the W+heavy-flavor fraction (black). The right-hand plot gives the relative difference in di-jet and W+jet electron fake factor. The yellow bands shows the central value of the closure test after correcting for the measured W+heavy-flavor fraction. The blue (red) points give the result of varying the W+heavy-flavor fraction down (up) by the measured uncertainty. 185

9.18 The fractional difference between the di-jet and W+jet muon fake factors. 186

9.19 The electron (left) and muon (right) fake factor as a function of p_{T}. The black points show the fake factor before the subtraction of the EW contamination in the di-jet sample. The yellow band gives the fake factor after the subtraction and the change in fake factor by varying the amount of EW contamination by $\pm$ 20% 187

9.20 Relative difference in fake factor measured using a data sample with high pile-up (black) and low pile-up (blue). Electrons are shown on the left, muons on the right. The yellow band represents the assigned systematic uncertainty on the pile-up dependence. 188
9.21 The fake factor as a function of p_{T} including the total systematic uncertainty for electrons (left) and muons (right). The uncertainty bands are cumulative and added in quadrature. 189
9.22 Schematic of the standard fake factor procedure for predicting background to events in which a jet veto is applied. The left-hand side represents the background in the signal region, the right-hand side represents the fake factor modeling of the background: W+jet control region times fake factor. None of the objects in the picture overlap with reconstructed jets. 195
9.23 Schematic of the separation of the standard fake factor measurement into terms extrapolating to background with and without overlapping jets. f^0 extrapolates to fake background without overlapping jets. f^1 extrapolates to fake background with overlapping jets. 195
9.24 Schematic of the standard fake factor measurement in the di-jet control region. No overlapping jet requirement is made when measuring the fake factor. The inclusive sample of numerators and denominators are composed of those which overlap reconstructed jets and those which do not. 196
9.25 Schematic of corrected fake factor procedure for predicting background to events in which a jet veto is applied. The left-hand side represents the background in the signal region, the right-hand side represents the updated fake factor modeling of the background. The W+jet control region with the inclusive denominator sample is scaled by fake factor for no overlapping jets. 197
9.26 Schematic of background modeling in a one jet signal region. The left-hand term predicts background when the jet does not overlap the misidentified lepton. The right-hand term predicts background when the jet overlaps the misidentified lepton. 198
9.27 Test of W+jet modeling in same sign events. Sub-leading p_{T} distribution is shown for events in the μe-channel with a same sign requirement. The fake predictions are made with the fake factor procedure using: (a) the "Pid-And-Iso"-denominator definition. (b) the "Pid"-denominator definition (c) the "Isolation"-denominator definition. Results are from the 5.8 fb^{-1} 7 TeV data set. 199
9.28 Feynman diagram for W+charm production where the charm quark decays semi-leptonically. The charge of the W is opposite that of the lepton from the charm quark decay. 200

9.29 Test of W+jet modeling in the "Tight-Inter-Iso" validation region defined in Table 9.9. Sub-leading p_{T} distribution is shown for events in the μe-channel. The W+jet predictions are made with the fake factor procedure using: (a) the "Pid-And-Iso"-denominator definition, (b) the "Pid"-denominator definition, and (c) the "Isolation"-denominator definition. Results are from the 5.8 fb^{-1} 7 TeV data set. 201

9.30 Test of W+jet modeling in the "Medium-Not-Tight" validation region defined in Table 9.9. Sub-leading p_{T} distribution is shown for events in the μe-channel. The fake predictions are made with the fake factor procedure using: (a) the "Pid-And-Iso"-denominator definition. (b) the "Pid"-denominator definition (c) the "Isolation"-denominator definition. Results are from the 5.8 fb^{-1} 7 TeVdata set. 202

9.31 Conceptual description of the extended fake factor method using the "Pid"-denominator for $\mathrm{D}_{\mathrm{l.f.}}$ and the "Isolation"-denominator for $\mathrm{D}_{\mathrm{h.f.}}$. Each control region is extrapolated into the signal region along a different dimension of "PID"-space. 213

9.32 Corrected light-flavor fake factors, $f^{\mathrm{l.f.}}$, using the numerator selection defined in Table 9.1, and the "Pid"-denominator (b), and the "Pid-And-Iso"-denominator (a). 215

9.33 Corrected heavy-flavor fake factors, $f^{\mathrm{h.f.}}$, using the numerator selection defined in Table 9.1, and the "Iso"-denominator (a), the "Isolation–BTag"-denominator (a), the "BTag"-denominator (c). 215

9.34 Test of the W+jet modeling in same sign events using separate light-flavor and heavy-flavor predictions. Sub-leading p_{T} distribution is shown for events in the μe-channel with a same sign requirement. The fake predictions are made with the fake factor procedure using: (a) the "Pid" light-flavor denominator definition and the "Isolation" heavy-flavor denominator definition. (b) the "Pid" light-flavor denominator definition and the "Isolation" heavy-flavor denominator definition. (c) the "Pid-And-Iso" light-flavor denominator definition and the "BTag" heavy-flavor denominator definition. Results are from the 5.8 fb^{-1} 7 TeV data set. 216

9.35 Test of the W+jet modeling in the "Tight-Inter-Iso" validation region using separate light-flavor and heavy-flavor predictions. Sub-leading p_{T} distribution is shown for events in the μe-channel. The W+jet predictions are made using: (a) the "Pid" light-flavor denominator definition and the "Isolation" heavy-flavor denominator definition. (b) the "Pid" light-flavor denominator definition and the "Isolation" heavy-flavor denominator definition. (c) the "Pid-And-Iso" light-flavor denominator definition and the "BTag" heavy-flavor denominator definition. Results are from the 5.8 fb^{-1} 7 TeV data set. . . . 217

9.36 Test of the W+jet modeling in the "Medium-Not-Tight" validation region using separate light-flavor and heavy-flavor predictions. Sub-leading p_{T} distribution is shown for events in the μe-channel. (a) the "Pid" light-flavor denominator definition and the "Isolation" heavy-flavor denominator definition. (b) the "Pid" light-flavor denominator definition and the "Isolation" heavy-flavor denominator definition. (c) the "Pid-And-Iso" light-flavor denominator definition and the "BTag" heavy-flavor denominator definition. Results are from the 5.8 fb^{-1} 7 TeV data set. 218

10.1 Invariant mass in the three channels after the pre-selection requirements. The left-hand plot shows the ee-channel, the middle plot the $\mu\mu$-channel, and the right-hand plot the $e\mu$-channel. The points show the observed data and the stacked histograms represent the signal and background expectation. Scale factors as outlined in Section 10.2 are applied to MC. 223

10.2 $E_{\mathrm{T}}^{\mathrm{miss,Rel}}$distributions for ee(left), $\mu\mu$(middle) and $e\mu$ channels after the Z-veto cut. The points show the observed data and the stacked histograms represent the signal and background expectation. Scale factors as outlined in Section 10.2 are applied to MC. 224

10.3 Jet multiplicity distributions for the ee-channel (left-hand side), the $\mu\mu$-channel (middle) and $e\mu$-channel (right-hand side) before the jet veto. The points show the observed data and the stacked histograms represent the signal and background expectation. Scale factors as described in Section 10.2 are applied to MC. 225

10.4 Kinematic distributions of selected events in the WW signal region. The $E_{\mathrm{T}}^{\mathrm{miss}}$ is shown on the left-hand side, m_{ll} is shown on the right-hand side. The same-flavor and opposite-flavor channels have been combined. The points show the observed data and the stacked histograms represent the signal and background expectation. 225

10.5 Missing energy distributions in the Z mass window for the ee (left) and $\mu\mu$(right) channels. 227

10.6 Comparison between the MC $E_{\mathrm{T}}^{\mathrm{miss,Rel}}$ distributions for Z/γ^{*} events in the ee, $e\mu$, and $\mu\mu$ channels. The distributions are normalized to unity. 228

10.7 Jet multiplicity distributions in the b-tagged control sample. 229

10.8 Muon fake factors measured in the di-jet sub-samples. The purple line shows the weighted average of the fake factors and the hashing indicates the ±30% band. The statistical and the systematic error from electro-weak MC subtraction are included in the error bars. . 230

10.9 Extracted light-flavor $f_{\mathrm{l.f.}}$ (left) and heavy-flavor $f_{\mathrm{h.f.}}$ (right) fake factors. 231

10.10 Kinematics for events in the same-sign control region without applying the jet veto. The observed data is shown with the background modeling including the data-driven W+jet prediction. The sub-leading lepton p_{T} is shown in the upper left, the transverse mass ($m_{\mathrm{T}} = \sqrt{2p_{\mathrm{T}}E_{\mathrm{T}}^{\mathrm{miss}}(1 - cos(\Delta\phi))}$) is shown in the upper right, The $E_{\mathrm{T}}^{\mathrm{miss}}$ is shown in the lower left, and $\Delta\phi_{ll}$ is shown in the lower right 232

11.1 $E_{\mathrm{T}}^{\mathrm{miss,Rel}}$ distributions after the di-lepton pre-selection in the 2011 analysis. The same-flavor (ee) channel is shown on the left. The opposite-flavor channel is shown on the right. The points show the observed data and the stacked histograms represent the signal and background expectation. 244

11.2 $E_{\mathrm{T}}^{\mathrm{miss,Rel}}$ distributions after the di-lepton pre-selection in the 2012 analysis. The points show the observed data and the stacked histograms represent the signal and background expectation. 244

11.3 Jet multiplicity distributions after the $E_{\mathrm{T}}^{\mathrm{miss,Rel}}$ requirement for 2011 analysis (left-hand side) and the 2012 analysis (right-hand side). The points show the observed data and the stacked histograms represent the signal and background expectation. The signal distribution in the left-hand plot has been scale up by a factor of 10 for clarity. 245

11.4 $p_{T_{ll}}$ distribution after the jet veto for 2011 analysis (left-hand side) and the 2012 analysis (right-hand side). The points show the observed data and the stacked histograms represent the signal and background expectation. The signal distribution in the left-hand plot has been scale up by a factor of 10 for clarity. 246

11.5 m_{ll} distribution before the $p_{T_{ll}}$ requirement for the 2011 analysis (left-hand side) and after the $p_{T_{ll}}$ requirement for 2012 analysis (right-hand side). The 2011 analysis is shown before the $p_{T_{ll}}$ because in that analysis the m_{ll} cut is made before the $p_{T_{ll}}$ requirement. The points show the observed data and the stacked histograms represent the signal and background expectation. The signal distribution in the left-hand plot has been scale up by a factor of 10 for clarity. 246

11.6 m_{T} distribution after the full 0-jet selection for the 2011 analysis (left-hand side) and the 2012 analysis (right-hand side). The points show the observed data and the stacked histograms represent the signal and background expectation. The signal distribution in the left-hand plot has not been scale up. 248

11.7 $|\mathbf{p}_{\mathrm{T}}^{\mathrm{tot}}|$ distribution after the b-jet veto in the 2011 analysis (left-hand side) and the 2012 analysis (right-hand side). The points show the observed data and the stacked histograms represent the signal and background expectation. The signal distribution in the left-hand plot has been scale up by a factor of 10 for clarity. 249

11.8 m_{ll} distribution after the $Z \to \tau\tau$ veto for the 2011 analysis (left-hand side) and the 2012 analysis (right-hand side). The points show the observed data and the stacked histograms represent the signal and background expectation. The signal distribution in the left-hand plot has been scale up by a factor of 10 for clarity. 250

11.9 m_{T} distribution after the full 1-jet selection for the 2011 analysis (left-hand side) and the 2012 analysis (right-hand side). The points show the observed data and the stacked histograms represent the signal and background expectation. The signal distribution in the left-hand plot has not been scale up. 251

11.10m_{T} distribution in the WW control region for the 0-jet 2012 analysis (left-hand side) and the 1-jet 2012 analysis (right-hand side). The points show the observed data and the stacked histograms represent the signal and background expectation. 255

11.11m_{T} distribution in the Top control region for the 1-jet 2011 analysis. The distribution for the 2-jet analysis is not shows as the statistics are too poor to make a meaningful shape comparison. The points show the observed data and the stacked histograms represent the signal and background expectation. 256

11.12Measured electron (left) and muon (right) fake factors for the 2011 analysis. The systematic uncertainties are included in the error bands. 258

11.13Measured electron (left) and muon (right) fake factors for the 2011 analysis. The systematic uncertainties are included in the error bands. 258

11.14Modeling of the same sign validation region after the jet-veto in the 2011 0-jet analysis. The sub-leading lepton p_{T} is shown on the left, $\Delta\phi_{ll}$ is shown in the middle, and m_{T} is given on the right. The W+jet prediction is obtained from the fake factor method, the other background contributions are estimated from MC. The error band represents the systematic uncertainty associated to the W+jet prediction. 259

11.15Modeling of the same sign validation region after the jet-veto in the 2012 0-jet analysis. The sub-leading lepton p_{T} is shown on the left, $\Delta\phi_{ll}$ is shown in the middle, and m_{T} is given on the right. The W+jet prediction is obtained from the fake factor method, the other background contributions are estimated from MC. The error band represents the systematic uncertainty associated to the W+jet prediction. 259

11.16Probabilities for the background-only hypothesis, p_0, as a function of m_h, for the 2011 analysis. The left-hand plot shows m_h in the range 110 - 600 GeV, the right-hand plot focuses on m_h between 110 and 180 GeV. The solid line shows the observed probability. The dashed line shows the corresponding expectation for the signal+background hypothesis at the given value of m_h. The red, horizontal dashed lines indicate the corresponding significance. 265

11.17Observed and expected limits on the Higgs production cross section as a function of m_h, for the 2011 analysis. The left-hand plot shows m_h in the range 110 - 600 GeV, the right-hand plot focuses on m_h between 110 and 150 GeV. The curves show the 95% CL upper limits. The green and yellow regions indicate the 1σ and 2σ uncertainty bands on the expected limit. 266

11.18Observed and expected limits on the Higgs production cross section for the 0-jet (left), 1-jet (middle), and 2-jet (right) 2011 analyses. 266

11.19Probabilities for background-only hypothesis, p_0, as a function of m_h, for the 2012 analysis. The solid line shows the observed probability. The dashed line shows the corresponding expectation for the signal+background hypothesis at the given value of m_h. The red, horizontal dashed lines indicate the corresponding significance. 267

11.20The m_{T} distribution in data with the estimated background subtracted, overlaid with the predicted signal for $m_h = 125$GeV. The distributions are summed for the 0-jet and 1-jet analyses and for the 2012 analysis. The statistical errors of both the data and the subtracted background are reflected in the data points. The systematic uncertainty on the background estimate is not included. 268

11.21Fitted signal strength parameter (μ) as a function of m_h for the 2012 analysis. 268

11.22Probabilities for background-only hypothesis, p_0, as a function of m_h, for the combined 2011 and 2012 analysis. The solid lines show the observed probability. The dashed line in the left-hand plot shows the corresponding expectation for the signal+background hypothesis at the given value of m_h. In the right-hand plot, the dashed line shows the corresponding expectation for the $m_h = 126$ GeV hypothesis. The green and yellow regions indicate the 1σ and 2σ uncertainty bands on the expected p_0. The red, horizontal dashed lines indicate the corresponding significance. 269

11.23The m_{T} distribution in data with the estimated background subtracted, overlaid with the predicted signal for $m_h = 125$GeV. The distributions are summed for the 0-jet and 1-jet analyses and for the 2011 and 2012 analyses. The statistical errors of both the data and the subtracted background are reflected in the data points. The systematic uncertainty on the background estimate is not included. 270

11.24Fitted signal strength parameter, indicated in the solid black line with cyan band, as a function of m_h for the combined 2011 and 2012 analysis. The expected result for a signal hypothesis of $m_h = 126$ GeV is shown in the red lines for comparison. 270

12.1 Event display of a selected $H \to ZZ^{(*)} \to llll$ event with four identified electrons. The electrons are shown in red and correspond to localized high energy deposits in the calorimeter matched to tracks in the inner detector, indicated by the red lines. The electrons have a combined invariant mass of 124.6 GeV. The upper-left panel shows the projection of the detector in the plane perpendicular to the beam line. The lower-left panel shows the projection of the detector along the beam line, running left to right in the panel. The upper-right and lower-right panels are zoom-ins of interesting regions. The middle-right panel depicts the energy deposited in the calorimeters as a function of ϕ and η. 273

12.2 The four-lepton invariant mass distribution, m_{4l}, for selected events in the $H \to ZZ^{(*)} \to llll$ analysis using the combined 7 TeV and 8 TeV data sets. The observed data is compared to the background expectation. The signal expectation for a SM Higgs with m_H= 125 GeV is shown. 274

12.3 The observed p_0 as a function of m_h for the $H \to ZZ^{(*)} \to llll$ channel. The dashed line shows the corresponding expectation for the signal+background hypothesis at the given value of m_h. Results are shown separately for the $\sqrt{s}$= 7 TeV data (dark, blue), the $\sqrt{s}$= 8 TeV data (light, red), and their combination (black). 275

12.4 Best fit values for μ and m_h in the combined $H \to ZZ^{(*)} \to llll$ analysis. The contours that correspond to the 68% and 95% confidence levels are shown. The lighter lines indicate the effect of important systematic uncertainties effecting the measurements. . 276

12.5 Event display of a selected $H \to \gamma\gamma$ event. The photons are shown in yellow and correspond to localized high energy deposits in the calorimeter not matched to tracks in the inner detector. The photons have a combined invariant mass of 126.9 GeV. The upper-left panel shows the projection of the detector in the plane perpendicular to the beam line. The lower-left panel shows the projection of the detector along the beam line, running left to right in the panel. The lower-middle and lower-right panels are zoom-ins of interesting regions. The middle-right panel depicts the energy deposited in the calorimeters as a function of ϕ and η. 277

12.6 The distributions of the invariant mass of di-photon candidates after all selections for the combined 7 TeV and 8 TeV data sample. The inclusive sample is shown in upper figure, marked a). The distribution weighted according to the event categories is shown in the lower figure marked c). The result of a fit using a m_h= 126.5 GeV signal component and the background component is superimposed. The excess of data with respect to the background fit are displayed in panels marked b) and d). 278

12.7 The observed p_0 as a function of m_h for the $H \to \gamma\gamma$ channel. The dashed line shows the corresponding expectation for the signal+background hypothesis at the given value of m_h. Results are shown separately for the $\sqrt{s}$= 7 TeV data (dark, blue), the $\sqrt{s}$= 8 TeV data (light, red), and their combination (black). 279

12.8 Best fit values for μ and m_h in the combined $H \to \gamma\gamma$ analysis. The contours that correspond to the 68% and 95% confidence levels are shown. The lighter lines indicate effect of the important systematic uncertainties effecting the measurements. 280

12.9 Event display of a WW event in the $e\nu e\nu$ channel. The electrons are shown in yellow and correspond to localized high energy deposits in the calorimeter matched to tracks in the inner detector, indicated by the red and orange lines. The dashed line, label $E_{\mathrm{T}}^{\mathrm{miss}}$, indicates the direction of the measured momentum imbalance. The left panel shows the projection of the detector in the plane perpendicular to the beam line. The upper-right panel shows the projection of the detector along the beam line, running left to right in the panel. The lower-right panel depicts the energy deposited in the calorimeters and the direction of the $E_{\mathrm{T}}^{\mathrm{miss}}$, as a function of ϕ and η. 281

12.10 Estimated Higgs mass distribution, m_{T}, in data with the estimated background subtracted. The predicted signal for m_h= 125 GeV is overlaid. 282

12.11 The observed p_0 as a function of m_h for the $H \to WW^{(*)}$ channel. The dashed line shows the corresponding expectation for the signal+background hypothesis at the given value of m_h. Results are shown separately for the $\sqrt{s}$= 7 TeV data (dark, blue), the $\sqrt{s}$= 8 TeV data (light, red), and their combination (black). 282

12.12 Best fit values for μ and m_h in the $H \to WW^{(*)} \to l\nu l\nu$ analysis. The results from the $H \to ZZ^{(*)} \to llll$ and $H \to \gamma\gamma$ analyses shown above are repeated for comparison. The contours that correspond to the 68% and 95% confidence levels are shown. 283

12.13 The expected 95% CL cross section upper limits as a function of m_h for the individual search channels and their combination. The expected limits are those for the background-only hypothesis, in the absence of a Higgs boson signal. 285

12.14 The observed and expected p_0 as a function of m_h in the low mass range for the combined Higgs search. The dashed curve shows the corresponding expectation for p_0 for the signal+background hypothesis at the given values of m_h; the blue band gives the ± 1 one sigma region. The horizontal dashed lines indicate the p-values corresponding to significances of 1 to 6 sigma. 286

12.15 Measurements of the signal strength parameter μ for $m_h = 126$GeV for the individual channels and their combination. 287

12.16 The observed and expected p_0 as a function of m_h for the entire search range for the combined analysis. The dashed curve shows the corresponding expectation for p_0 for the signal+background hypothesis at the given values of m_h. The horizontal dashed lines indicate the p-values corresponding to significances of 2 to 6 sigma. 288

12.17 The observed (solid) 95% CL upper limit on the signal strength as a function of m_h. The dashed line gives the expected exclusion under the background-only hypothesis. The green and yellow shaded bands give the one and two sigma uncertainties on the expected exclusion. 288

12.18 The observed (solid) and expected (dashed) 95% CL cross section upper limits for the individual search channels and the combination as a function of m_h. 289

A.1 Description of a straw. The nominal position is at the origin, misalignment is seen in red. 291

A.2 Track parameters x_0 and ϕ_0. 291

A.3 Straw misalignments. 293

A.4 Reconstructed Vs True Alignment. 293

A.5 Residual Misalignment. 294

A.6 Residual Misalignment. 294

A.7 RMS of residual misalignments as a function of number of hits used in alignment . . . 295
A.8 RMS of residual misalignments as a function of the hit resolution used. 295
A.9 RMS of residual misalignments as a function of phi spread of tracks used in alignment. 296

Bibliography

[1] S. L. Glashow, *Partial-symmetries of weak interactions*, Nucl. Phys. **22** (1961) no. 4, 579. 1.1

[2] S. Weinberg, *A Model of Leptons*, Phys. Rev. Lett. **19** (1967) 1264. 1.1

[3] A. Salam, *in Elementary Particle Theory, p. 367.* Almqvist and Wiksell, Stockholm, 1968. 1.1

[4] G. 't Hooft and M. Veltman, *Regularization and Renormalization of Gauge Fields*, Nucl. Phys. **B**44 (1972) 189. 1.1

[5] S. Weinberg, *The Quantum Theory of Fields.* Cambridge Univ. Press, Cambridge, 1995. 1.1

[6] W. Bartel et al., *Observation of planar three-jet events in e^+e^- annihilation and evidence for gluon bremsstrahlung*, Physics Letters B **9**1 (1980) . 1.1

[7] C. Berger et al., *Evidence for gluon bremsstrahlung in e^+e^- annihilations at high energies*, Physics Letters B **8**6 (1979) 418–425. 1.1

[8] F. Englert and R. Brout, *Broken Symmetry and the Mass of Gauge Vector Mesons*, Phys. Rev. Lett. **13** (1964) 321–322. 1.1

[9] P. W. Higgs, *Broken symmetries, massless particles and gauge fields*, Phys. Lett. **12** (1964) 132–133. 1.1

[10] P. W. Higgs, *Broken symmetries and the masses of gauge bosons*, Phys. Rev. Lett. **13** (1964) 508. 1.1

[11] G. S. Guralnik, C. R. Hagen, and T. W. B. Kibble, *Global conservation laws and massless particles*, Phys. Rev. Lett. **13** (1964) 585. 1.1

[12] P. W. Higgs, *Spontaneous symmetry breakdown without massless bosons*, Phys. Rev. **145** (1966) 1156. 1.1

[13] T. W. B. Kibble, *Symmetry breaking in non-Abelian gauge theories*, Phys. Rev. **155** (1967) 1554. 1.1

[14] The ALEPH, CDF, DØ, DELPHI, L3, OPAL, SLD Collaborations, the LEP Electroweak Working Group, the Tevatron Electroweak Working Group, and the SLD electroweak and heavy flavour groups, *Precision Electroweak Measurements and Constraints on the Standard Model*, CERN-PH-EP-2010-095 (2010) , arXiv:1012.2367 [hep-ex]. 1.1, 1.2

[15] ATLAS Collaboration. Online. https://twiki.cern.ch/twiki/bin/view/AtlasPublic/CombinedSummaryPlots. 1.1

[16] J. Gunion, H. Haber, G. Kane, and S. Dawson, *The Higgs Hunter's Guide*. Frontiers in Physics, V. 80. Basic Books, 2000. 1.1

[17] A. Djouadi, *The Anatomy of electro-weak symmetry breaking. I: The Higgs boson in the standard model*, Phys.Rept. **457** (2008) 1–216, arXiv:hep-ph/0503172 [hep-ph]. 1.1

[18] A. Djouadi, *The Anatomy of electro-weak symmetry breaking. II. The Higgs bosons in the minimal supersymmetric model*, Phys.Rept. **459** (2008) 1–241, arXiv:hep-ph/0503173 [hep-ph]. 1.1

[19] F. Hasert et al., *Observation of neutrino-like interactions without muon or electron in the gargamelle neutrino experiment*, Physics Letters B **46** (1973) no. 1, 138 – 140. http://www.sciencedirect.com/science/article/pii/0370269373904991. 1.2

[20] UA1 Collaboration, G. Arnison et al., *Experimental observation of isolated large transverse energy electrons with associated missing energy at s=540 GeV*, Physics Letters B **122** (1983) no. 1, 103 – 116. http://www.sciencedirect.com/science/article/pii/0370269383911772. 1.2

[21] UA2 Collaboration, M. Banner et al., *Observation of Single Isolated Electrons of High Transverse Momentum in Events with Missing Transverse Energy at the CERN anti-p p Collider*, Phys.Lett. **B**122 (1983) 476–485. 1.2

[22] UA1 Collaboration, G. Arnison et al., *Experimental Observation of Lepton Pairs of Invariant Mass Around 95-GeV/c**2 at the CERN SPS Collider*, Phys.Lett. **B**126 (1983) 398–410. 1.2

[23] UA2 Collaboration, P. Bagnaia et al., *Evidence for $Z0 \to e^+e^-$ at the CERN anti-p p Collider*, Phys.Lett. **B**129 (1983) 130–140. 1.2

[24] *LEP design report*. CERN, Geneva, 1984. http://cdsweb.cern.ch/record/102083. 1.2, 2.1

[25] S. Center, *Slac Linear Collider Conceptual Design Report*. General Books, 2012. http://books.google.com/books?id=6wWAMQEACAAJ. 1.2

[26] CDF Collaboration Collaboration, F. Abe et al., *Observation of Top Quark Production in $\overline{p}p$ Collisions with the Collider Detector at Fermilab*, Phys. Rev. Lett. **74** (1995) 2626–2631. http://link.aps.org/doi/10.1103/PhysRevLett.74.2626. 1.2

[27] Tevatron Electroweak Working Group, CDF and D0 Collaboration, *Combination of CDF and D0 results on the mass of the top quark using up to 5.8 fb-1 of data*, arXiv:1107.5255 [hep-ex]. 1.2

[28] Tevatron Electroweak Working Group Collaboration, *Combination of CDF and D0 Results on the Width of the W boson*, arXiv:1003.2826 [hep-ex]. 1.2

[29] The LEP Electroweak Working Group. On line. http://lepewwg.web.cern.ch/LEPEWWG/plots/summer2011/. 1.2

[30] LEP Working Group for Higgs boson searches, ALEPH, DELPHI, L3 and OPAL Collaborations, *Search for the standard model Higgs boson at LEP*, Phys. Lett. **B** 565 (2003) 61. 1.2

[31] CDF Collaboration, T. Aaltonen et al., *Combined search for the standard model Higgs boson decaying to a bb pair using the full CDF data set*, submitted to Phys. Rev. Lett. (2012) , arXiv:1207.1707 [hep-ex]. 1.2

[32] D0 Collaboration, V. M. Abazov et al., *Combined search for the standard model Higgs boson decaying to b bbar using the D0 Run II data set*, arXiv:1207.6631 [hep-ex]. 1.2

[33] CDF Collaboration, D0 Collaboration, *Evidence for a particle produced in association with weak bosons and decaying to a bottom-antibottom quark pair in Higgs boson searches at the Tevatron*, submitted to Phys. Rev. Lett. (2012) , arXiv:1207.6436 [hep-ex]. 1.2

[34] LHC Higgs Cross Section Working Group, S. Dittmaier, C. Mariotti, G. Passarino, and R. Tanaka (Eds.), *Handbook of LHC Higgs Cross Sections: 1. Inclusive Observables*, CERN-2011-002 (CERN, Geneva, 2011) , arXiv:1101.0593 [hep-ph]. 1.3, 8.1, 11.5

[35] LHC Higgs Cross Section Working Group, S. Dittmaier, C. Mariotti, G. Passarino, and R. Tanaka (Eds.), *Handbook of LHC Higgs Cross Sections: 2. Differential Distributions*, CERN-2012-002 (CERN, Geneva, 2012) , arXiv:1201.3084 [hep-ph]. 1.3, 11.5

[36] T. S. Pettersson and P. Lefevre, *The Large Hadron Collider: conceptual design.*, Tech. Rep. CERN-AC-95-05 LHC, CERN, Geneva, Oct, 1995. https://cdsweb.cern.ch/record/291782. 2

[37] L. Evans and P. Bryant, *LHC Machine*, JINST **3** (2008) no. 08, S08001. 2

[38] T. Linnecar et al., *Hardware and Initial Beam Commissioning of the LHC RF Systems. oai:cds.cern.ch:1176380*, Tech. Rep. LHC-PROJECT-Report-1172. CERN-LHC-PROJECT-Report-1172, CERN, Geneva, Oct, 2008. https://cdsweb.cern.ch/record/1176380. 2

[39] The ALICE Collaboration, *The ALICE experiment at the CERN LHC*, Journal of Instrumentation **3** (2008) no. 08, S08002. http://stacks.iop.org/1748-0221/3/i=08/a=S08002. 2.1

[40] ATLAS Collaboration, *The ATLAS Experiment at the CERN Large Hadron Collider*, JINST **3** (2008) S08003. 2.1, 3

[41] The CMS Collaboration, *The CMS experiment at the CERN LHC*, Journal of Instrumentation **3** (2008) no. 08, S08004. 2.1

[42] The LHCb Collaboration, *The LHCb Detector at the LHC*, Journal of Instrumentation **3** (2008) no. 08, S08005. 2.1

[43] M. Bajko et al., *Report of the Task Force on the Incident of 19th September 2008 at the LHC. oai:cds.cern.ch:1168025*, Tech. Rep. LHC-PROJECT-Report-1168. CERN-LHC-PROJECT-Report-1168, CERN, Geneva, Mar, 2009. https://cdsweb.cern.ch/record/1168025. 2.2

[44] ATLAS Collaboration. Online. https://twiki.cern.ch/twiki/bin/view/AtlasPublic/LuminosityPublicResults. 2.2

[45] ATLAS Collaboration, *ATLAS detector and physics performance: Technical Design Report, 1.* Technical Design Report ATLAS. CERN, Geneva, 1999. https://cdsweb.cern.ch/record/391176. 3

[46] ATLAS Collaboration, *Studies of the performance of the ATLAS detector using cosmic-ray muons*, The European Physical Journal C - Particles and Fields **7**1 (2011) 1–36. http://dx.doi.org/10.1140/epjc/s10052-011-1593-6. 10.1140/epjc/s10052-011-1593-6. 3

[47] ATLAS Collaboration, *The ATLAS Inner Detector commissioning and calibration*, The European Physical Journal C - Particles and Fields **7**0 (2010) 787–821. http://dx.doi.org/10.1140/epjc/s10052-010-1366-7. 10.1140/epjc/s10052-010-1366-7. 3, 5.1, 5.4, 5.4, 6.3

[48] ATLAS Collaboration, *Performance of the ATLAS detector using first collision data*, Journal of High Energy Physics **2**010 (2010) 1–66. http://dx.doi.org/10.1007/JHEP09(2010)056. 10.1007/JHEP09(2010)056. 3, 5.4, 6.4

[49] ATLAS Collaboration, *ATLAS inner detector: Technical Design Report 1*. Technical Design Report ATLAS. CERN, Geneva, 1997. https://cdsweb.cern.ch/record/331063. 3.1, 5.1, 5.4

[50] ATLAS Collaboration, *ATLAS inner detector: Technical Design Report, 2*. Technical Design Report ATLAS. CERN, Geneva, 1997. https://cdsweb.cern.ch/record/331064. 3.1

[51] ATLAS Collaboration, *ATLAS pixel detector: Technical Design Report*. Technical Design Report ATLAS. CERN, Geneva, 1998. https://cdsweb.cern.ch/record/381263. 3.1

[52] ATLAS Collaboration, *ATLAS pixel detector electronics and sensors*, JINST **3** (2008) P07007. 3.1

[53] ATLAS Collaboration, *The barrel modules of the ATLAS semiconductor tracker*, Nucl.Instrum.Meth. **A**568 (2006) 642–671. 3.1

[54] ATLAS Collaboration, *The ATLAS semiconductor tracker end-cap module*, Nucl.Instrum.Meth. **A**575 (2007) 353–389. 3.1

[55] ATLAS Collaboration, *The Silicon microstrip sensors of the ATLAS semiconductor tracker*, Nucl.Instrum.Meth. **A**578 (2007) 98–118. 3.1

[56] The ATLAS TRT Collaboration, *The ATLAS TRT barrel detector*, JINST **3** (2008) P02014. 3.1, 6.1, 6.1

[57] The ATLAS TRT Collaboration, *The ATLAS TRT end-cap detectors*, JINST **3** (2008) P10003. 3.1, 6.1, 6.1

[58] The ATLAS TRT Collaboration, *The ATLAS Transition Radiation Tracker (TRT) proportional drift tube: Design and performance*, JINST **3** (2008) P02013. 3.1, 6.1

[59] ATLAS Collaboration, *ATLAS central solenoid: Technical Design Report*. Technical Design Report ATLAS. CERN, Geneva, 1997. https://cdsweb.cern.ch/record/331067. 3.1

[60] ATLAS Collaboration, *ATLAS calorimeter performance: Technical Design Report*. Technical Design Report ATLAS. CERN, Geneva, 1996. https://cdsweb.cern.ch/record/331059. 3.1

[61] ATLAS Collaboration, *ATLAS liquid-argon calorimeter: Technical Design Report*. Technical Design Report ATLAS. CERN, Geneva, 1996. https://cdsweb.cern.ch/record/331061. 3.1, 4.3

[62] ATLAS Collaboration, *ATLAS tile calorimeter: Technical Design Report*. Technical Design Report ATLAS. CERN, Geneva, 1996. https://cdsweb.cern.ch/record/331062. 3.1

[63] ATLAS Collaboration, *ATLAS muon spectrometer: Technical Design Report*. Technical Design Report ATLAS. CERN, Geneva, 1997. https://cdsweb.cern.ch/record/331068. 3.1

[64] ATLAS Collaboration, *ATLAS barrel toroid: Technical Design Report*. Technical Design Report ATLAS. CERN, Geneva, 1997. https://cdsweb.cern.ch/record/331065. 3.1

[65] ATLAS Collaboration, *ATLAS end-cap toroids: Technical Design Report*. Technical Design Report ATLAS. CERN, Geneva, 1997. https://cdsweb.cern.ch/record/331066. 3.1

[66] F. Bauer, U. Bratzler, H. Dietl, H. Kroha, T. Lagouri, et al., *Construction and test of MDT chambers for the ATLAS muon spectrometer*, Nucl.Instrum.Meth. **A**461 (2001) 17–20. 3.4

[67] T. Argyropoulos, K. A. Assamagan, B. H. Benedict, V. Chernyatin, E. Cheu, et al., *Cathode strip chambers in ATLAS: Installation, commissioning and in situ performance*, IEEE Trans.Nucl.Sci. **5**6 (2009) 1568–1574. 3.4

[68] G. Aielli, A. Aloisio, M. Alviggi, V. Aprodu, V. Bocci, et al., *The RPC first level muon trigger in the barrel of the ATLAS experiment*, Nucl.Phys.Proc.Suppl. **1**58 (2006) 11–15. 3.4

[69] S. Majewski, G. Charpak, A. Breskin, and G. Mikenberg, *A Thin Multiwire Chamber Operating in the High Multiplication Mode*, Nucl.Instrum.Meth. **2**17 (1983) 265–271. 3.4

[70] T. Cornelissen, M. Elsing, S. Fleischmann, W. Liebig, E. Moyse, et al., *Concepts, Design and Implementation of the ATLAS New Tracking (NEWT)*, tech. rep., 2007. https://cdsweb.cern.ch/record/1020106. 4.1

[71] W. Lampl, S. Laplace, D. Lelas, P. Loch, H. Ma, et al., *Calorimeter clustering algorithms: Description and performance*, tech. rep., 2008. https://cdsweb.cern.ch/record/1099735. 4.1, 7.1

[72] ATLAS Collaboration, *Commissioning of the ATLAS Muon Spectrometer with Cosmic Rays*, Eur.Phys.J. **C**70 (2010) 875–916, arXiv:1006.4384 [physics.ins-det]. 4.1

[73] M. Hance, *Measurement of Inclusive Isolated Prompt Photon Production in Proton-Proton Collisions at $\sqrt{s} = 7$ TeV with the ATLAS Detector*, Thesis. http://cds.cern.ch/record/1367057. 4.1, 7.2

[74] ATLAS Collaboration, *Properties of Jets and Inputs to Jet Reconstruction and Calibration with the ATLAS Detector Using Proton-Proton Collisions at $\sqrt{s} = 7$ TeV*, Tech. Rep. ATLAS-CONF-2010-053, CERN, Geneva, Jul, 2010. https://cdsweb.cern.ch/record/1281310. 4.1

[75] ATLAS Collaboration, *Measurement of inclusive jet and dijet cross sections in proton-proton collisions at 7 TeV centre-of-mass energy with the ATLAS detector*, Eur.Phys.J. **C**71 (2011) 1512, arXiv:1009.5908 [hep-ex]. 4.1

[76] ATLAS Collaboration, *Jet energy measurement with the ATLAS detector in proton-proton collisions at $\sqrt{s} = 7$ TeV*, arXiv:1112.6426 [hep-ex]. 4.1

[77] ATLAS Collaboration, *Commissioning of the ATLAS high-performance b-tagging algorithms in the 7 TeV collision data*, Tech. Rep. ATLAS-CONF-2011-102, CERN, Geneva, Jul, 2011. https://cdsweb.cern.ch/record/1369219. 4.1, 10.3

[78] ATLAS Collaboration, *ATLAS level-1 trigger: Technical Design Report*. Technical Design Report ATLAS. CERN, Geneva, 1998. https://cdsweb.cern.ch/record/381429. 4.2, 7.1

[79] P. Jenni, M. Nessi, M. Nordberg, and K. Smith, *ATLAS high-level trigger, data-acquisition and controls: Technical Design Report*. Technical Design Report ATLAS. CERN, Geneva, 2003. https://cdsweb.cern.ch/record/616089. 4.2, 7.1

[80] ATLAS Collaboration, *ATLAS detector and physics performance: Technical Design Report, 1*. Technical Design Report ATLAS. CERN, Geneva, 1999. https://cdsweb.cern.ch/record/391176. 5.1

[81] ATLAS Collaboration, *Expected Performance of the ATLAS Experiment - Detector, Trigger and Physics*, arXiv:0901.0512 [hep-ex]. 5.1, 9.1

[82] T. Golling, *Alignment of the silicon tracking detector using survey constraints*, Tech. Rep. ATL-INDET-2006-001, 2006. https://cdsweb.cern.ch/record/941076. 5.1

[83] J. Boudreau and V. Tsulaia, *The GeoModel Toolkit for Detector Description*, Tech. Rep. Proceedings from Computing in High Energy Physics and Nuclear Physics, 2004. https://cdsweb.cern.ch/record/865601. 5.1

[84] W. Bocci, A; Hulsbergen, *TRT Alignment for the SR1 Cosmics and Beyond*, Tech. Rep. ATL-INDET-PUB-2007-009, 2007. http://cdsweb.cern.ch/record/1039585. 5.2, 5.2.1, 3, 6.3

[85] P. Brckman, A. Hicheur, and S. Haywood, *Global chi2 approach to the Alignment of the ATLAS Silicon Tracking Detectors*, Tech. Rep. ATL-INDET-PUB-2005-002, 2005. http://cds.cern.ch/record/835270. 5.2, 5.2.1

[86] ATLAS Collaboration, *Alignment of the ATLAS Inner Detector Tracking System with 2010 LHC proton-proton collisions at sqrts = 7 TeV*, Tech. Rep. ATLAS-CONF-2011-012, CERN, Geneva, Mar, 2011. https://cdsweb.cern.ch/record/1334582. 5.2, 5.2.1, 5.4, 5.4

[87] ATLAS Collaboration, *The ATLAS Simulation Infrastructure*, The European Physical Journal C - Particles and Fields **70** (2010) 823–874. http://dx.doi.org/10.1140/epjc/s10052-010-1429-9. 10.1140/epjc/s10052-010-1429-9. 5.2.1

[88] W. Press, S. Teukolsky, W. Vetterling, and B. Flannery, *Numerical Recipes 3rd Edition: The Art of Scientific Computing*. Numerical Recipes: The Art of Scientific Computing. Cambridge University Press, 2007. http://books.google.com/books?id=DyykEZo4fwUC. 5.2.2

[89] ATLAS Collaboration, *Study of alignment-related systematic effects on the ATLAS Inner Detector tracking*, Tech. Rep. ATLAS-CONF-2012-141, CERN, Geneva, Oct, 2012. https://cdsweb.cern.ch/record/1483518. 5.2.3, 5.4, 5.4

[90] ATLAS Collaboration, *Alignment Performance of the ATLAS Inner Detector Tracking System in 7 TeV proton-proton collisions at the LHC*, Tech. Rep. ATLAS-CONF-2010-067, CERN, Geneva, Jul, 2010. https://cdsweb.cern.ch/record/1281342. 5.4, 5.4

[91] J. Stahlman. Plots from internal atlas presentation. jonathan.mark.stahlman@cern.ch. 6.46, 6.47, 6.52, D

[92] M. Hurwitz. Plots from internal atlas presentation. Martina.Hurwitz@cern.ch. 6.48, 6.53, D

[93] K. Brendlinger. Plots from internal atlas presentation. Kurt.Brendlinger@cern.ch. 6.49, D

[94] ATLAS Collaboration, *Improved electron reconstruction in ATLAS using the Gaussian Sum Filter-based model for bremsstrahlung*, Tech. Rep. ATLAS-CONF-2012-047, CERN, Geneva, May, 2012. http://cdsweb.cern.ch/record/1449796. 7.1

[95] ATLAS Collaboration, *Electron performance measurements with the ATLAS detector using the 2010 LHC proton-proton collision data*, Eur.Phys.J. **C**72 (2012) 1909, arXiv:1110.3174 [hep-ex]. 7.1, 7.1, 7.3.2

[96] ATLAS Collaboration, *Expected electron performance in the ATLAS experiment*, Tech. Rep. ATL-PHYS-PUB-2011-006, CERN, Geneva, Apr, 2011. http://cdsweb.cern.ch/record/1345327. 7.1, 7.2, 9.1, 9.1

[97] ATLAS Collaboration, *Measurements of the electron and muon inclusive cross-sections in proton-proton collisions at* $\sqrt{s} = 7$ *TeV with the ATLAS detector*, Phys.Lett. **B**707 (2012) 438–458, arXiv:1109.0525 [hep-ex]. 7.1, 9.1, 9.2, D

[98] J. Saxon. Private communication. james.saxon@cern.ch. 7.5, D

[99] ATLAS Collaboration, *Particle Identification Performance of the ATLAS Transition Radiation Tracker*, Tech. Rep. ATLAS-CONF-2011-128, CERN, Geneva, Sep, 2011. http://cdsweb.cern.ch/record/1383793. 7.2

[100] A. Hoecker, P. Speckmayer, J. Stelzer, J. Therhaag, E. von Toerne, and H. Voss, *TMVA: Toolkit for Multivariate Data Analysis*, PoS **A**CAT , arXiv:physics/0703039. 7.3.1

[101] S. Frixione and B. R. Webber, *Matching NLO QCD computations and parton shower simulations*, Journal of High Energy Physics **2**002 (2002) no. 06, 029. http://stacks.iop.org/1126-6708/2002/i=06/a=029. 8.1, 10

[102] T. Binoth, M. Ciccolini, N. Kauer, and M. Kramer, *Gluon-induced W-boson pair production at the LHC*, JHEP **0**612 (2006) 046, arXiv:hep-ph/0611170 [hep-ph]. 8.1, 10, 10.5

[103] ATLAS Collaboration, *Observation of a new particle in the search for the Standard Model Higgs boson with the ATLAS detector at the LHC*, Phys.Lett. **B**716 (2012) 1–29, arXiv:1207.7214 [hep-ex]. 8.1, 11.8, 12

[104] ATLAS Collaboration, *Measurement of the WW cross section in* $\sqrt{s} = 7$ *TeV pp collisions with the ATLAS detector and limits on anomalous gauge couplings*, Phys.Lett. **B**712 (2012) 289–308, arXiv:1203.6232 [hep-ex]. 8.2

[105] ATLAS Collaboration, *Measurement of the WW cross section in sqrt(s) = 7 TeV pp collisions with ATLAS*, Phys.Rev.Lett. **1**07 (2011) 041802, arXiv:1104.5225 [hep-ex]. 8.3.1, 8.3.3, 9.1

[106] ATLAS Collaboration, *Measurement of the WW cross section in sqrt(s) = 7 TeV pp collisions with the ATLAS detector and limits on anomalous gauge couplings*, Phys.Lett. **B**712 (2012) 289–308, arXiv:1203.6232 [hep-ex]. 8.3.1, 8.3.2, 8.3.3, 9.1, 10

[107] ATLAS Collaboration, *Search for the Higgs boson in the* $H \to WW^{(*)} \to l\nu l\nu$ *decay channel in pp collisions at* $\sqrt{s} = 7$ *TeV with the ATLAS detector*, Phys.Rev.Lett. **1**08 (2012) 111802, arXiv:1112.2577 [hep-ex]. 8.3.1, 8.3.3, 8.4

[108] ATLAS Collaboration, *Search for the Standard Model Higgs boson in the* $H \to WW(*) \to \ell\nu\ell\nu$ *decay mode with 4.7 /fb of ATLAS data at* $\sqrt{s} = 7$ *TeV*, Phys.Lett. **B**716 (2012) 62–81, arXiv:1206.0756 [hep-ex]. 8.3.1, 8.3.3, 8.4

[109] ATLAS Collaboration, *Search for the Standard Model Higgs boson in the H→WW→llnunu decay mode using 1.7 fb-1 of data collected with the ATLAS detector at sqrt(s)=7 TeV*, Tech. Rep. ATLAS-CONF-2011-134, CERN, Geneva, Sep, 2011. https://cdsweb.cern.ch/record/1383837. 8.4

[110] ATLAS Collaboration, *Search for the Higgs boson in the $H \to WW^{(*)} \to l\nu l\nu$ decay channel in pp collisions at sqrts = 7 TeV with the ATLAS detector*, Phys.Rev.Lett. **1**08 (2012) 111802, arXiv:1112.2577 [hep-ex]. 8.4

[111] ATLAS Collaboration, *Extraction of the prompt muon component in inclusive muons produced at $\sqrt{s} = 7$ TeV*, Tech. Rep. ATLAS-CONF-2010-075, CERN, Geneva, Jul, 2010. http://cdsweb.cern.ch/record/1281366. 9.1

[112] ATLAS Collaboration Collaboration, G. Aad et al., *Measurement of the cross section for the production of a W boson in association with b^- jets in pp collisions at $\sqrt{s} = 7$ TeV with the ATLAS detector*, Phys.Lett. **B**707 (2012) 418–437, arXiv:1109.1470 [hep-ex]. 9.3.3.1, 9.15, D

[113] ATLAS Collaboration, *Measurement of the inclusive and dijet cross section of b-jets in pp collisions at $\sqrt{s} = 7$ TeV with the ATLAS detector*, Tech. Rep. ATLAS-CONF-2011-056, CERN, Geneva, Apr, 2011. http://cdsweb.cern.ch/record/1342571. 9.3.3.1

[114] B. Jager, C. Oleari, and D. Zeppenfeld, *Next-to-leading order QCD corrections to W+W-production via vector-boson fusion*, hep-ph/0603177. 10.1

[115] K. Arnold, J. Bellm, G. Bozzi, M. Brieg, F. Campanario, et al., *VBFNLO: A parton level Monte Carlo for processes with electroweak bosons – Manual for Version 2.5.0*, arXiv:1107.4038 [hep-ph]. 10.1, 11.2

[116] K. Arnold, M. Bahr, G. Bozzi, F. Campanario, C. Englert, et al., *VBFNLO: A Parton level Monte Carlo for processes with electroweak bosons*, Comput.Phys.Commun. **1**80 (2009) 1661–1670, arXiv:0811.4559 [hep-ph]. 10.1

[117] ATLAS Collaboration, *Measurement of the inclusive $W^{\pm}$ and Z/gamma cross sections in the electron and muon decay channels in pp collisions at $\sqrt{s} = 7$ TeV with the ATLAS detector*, Phys.Rev. **D**85 (2012) 072004, arXiv:1109.5141 [hep-ex]. 10.1, 10.1

[118] ATLAS Collaboration, *Luminosity Determination in pp Collisions at sqrt(s) = 7 TeV using the ATLAS Detector in 2011*, Tech. Rep. ATLAS-CONF-2011-116, CERN, Geneva, Aug, 2011. https://cdsweb.cern.ch/record/1376384. 10.2

[119] GEANT4 Collaboration, S. Agostinelli et al., *GEANT4 - a simulation toolkit*, Nucl. Instrum. Methods A **5**06 (2003) 250. 10.2

[120] M. L. Mangano et al., *ALPGEN, a generator for hard multiparton processes in hadronic collisions*, JHEP **0**7 (2003) 001. 10.2

[121] T. Sjöstrand et al., *High-Energy-Physics Event Generation with PYTHIA 6.1*, Computer Phys. Commun. **1**35 (2001) 238. 10.2

[122] S. Frixione and B. R. Webber, *Matching NLO QCD computations and parton shower simulations*, JHEP **0**6 (2002) 029. 10.2

[123] B. P. Kersevan and E. Richter-Was, *The Monte Carlo event generator AcerMC version 2.0 with interfaces to PYTHIA 6.2 and HERWIG 6.5*, arXiv:hep-ph/0405247. 10.2

[124] G. Corcella et al., *Herwig 6.5*, JHEP **0**1 (2001) 010. 10.2

[125] J. M. Butterworth, J. R. Forshaw, and M. H. Seymour, *Multiparton Interactions in Photoproduction at HERA*, Z. Phys. C **72** (1996) 637. 10.2

[126] J. M. Campbell, R. K. Ellis, and C. Williams, *Vector boson pair production at the LHC*, JHEP **07** (2011) 018, arXiv:1105.0020 [hep-ph]. 10.2

[127] M. Cacciari, G. P. Salam, and G. Soyez, *The Anti-k(t) jet clustering algorithm*, JHEP **0804** (2008) 063, arXiv:0802.1189 [hep-ph]. 10.3

[128] ATLAS Collaboration, *Search for the Standard Model Higgs boson in the $H \to WW(*) \to \ell\nu\ell\nu$ decay mode with 4.7 /fb of ATLAS data at $\sqrt{s} = 7$ TeV*, Phys.Lett. **B716** (2012) 62–81, arXiv:1206.0756 [hep-ex]. 11

[129] ATLAS Collaboration, *Observation of an Excess of Events in the Search for the Standard Model Higgs Boson in the $H \to WW^{(*)} \to \ell\nu\ell\nu$ Channel with the ATLAS Detector*, Tech. Rep. ATLAS-CONF-2012-098, CERN, Geneva, Jul, 2012. https://cdsweb.cern.ch/record/1462530. 11

[130] ATLAS Collaboration, *Combined search for the Standard Model Higgs boson in pp collisions at $\sqrt{s} = 7$ TeV with the ATLAS detector*, Phys.Rev. **D86** (2012) 032003, arXiv:1207.0319 [hep-ex]. 11.1, 11.7.1, 12

[131] R. V. Harlander and W. B. Kilgore, *Next-to-Next-to-Leading Order Higgs Production at Hadron Colliders*, Phys. Rev. Lett. **88** (2002) 201801. http://prl.aps.org/abstract/PRL/v88/i20/e201801. 11.2

[132] C. Anastasiou and K. Melnikov, *Higgs boson production at hadron colliders in NNLO QCD*, Nucl. Phys. **B646** (2002) 220. 11.2

[133] V. Ravindran, J. Smith, and W. L. van Neerven, *NNLO corrections to the total cross section for Higgs boson production in hadron-hadron collisions*, Nucl. Phys. **B665** (2003) 325. 11.2

[134] S. Actis, G. Passarino, C. Sturm, and S. Uccirati, *NLO electroweak corrections to Higgs boson production at hadron colliders*, Phys. Lett. B **670** (2008) 12. 11.2

[135] U. Aglietti, R. Bonciani, G. Degrassi, and A. Vicini, *Two-loop light fermion contribution to Higgs production and decays*, Phys. Lett. **B** 595 (2004) 432. 11.2

[136] C. Anastasiou, R. Boughezal, and F. Petriello, *Mixed QCD-electroweak corrections to Higgs boson production in gluon fusion*, JHEP **0904** (2009) 003, arXiv:0811.3458 [hep-ph]. 11.2

[137] D. de Florian and M. Grazzini, *Higgs production through gluon fusion: Updated cross sections at the Tevatron and the LHC*, PLB **674** (2009) 291, arXiv:0901.2427 [hep-ph]. 11.2

[138] J. Baglio and A. Djouadi, *Higgs production at the LHC*, JHEP **03** (2011) 055. 11.2

[139] G. Bozzi, S. Catani, D. de Florian, and M. Grazzini, *Transverse-momentum resummation and the spectrum of the Higgs boson at the LHC*, Nucl. Phys. **B** 737 (2006) 73. 11.2

[140] M. Ciccolini, A. Denner, and S. Dittmaier, *Strong and electroweak corrections to the production of Higgs + 2 jets via weak interactions at the Large Hadron Collider*, Phys. Rev. Lett. **99** (2007) 161803. 11.2

[141] M. Ciccolini, A. Denner, and S. Dittmaier, *Electroweak and QCD corrections to Higgs production via vector-boson fusion at the Large Hadron Collider*, Phys. Rev. **D77** (2008) 013002. 11.2

[142] P. Bolzoni, F. Maltoni, S.-O. Moch, and M. Zaro, *Higgs boson production via vector-boson fusion at next-to-next-to-leading order in QCD*, Phys. Rev. Lett. **105** (2010) 011801. 11.2

[143] A. Djouadi, J. Kalinowski, and M. Spira, *HDECAY: A program for Higgs boson decays in the standard model and its supersymmetric extension*, Comput. Phys. Commun. **108** (1998) 56. 11.2

[144] R.K. Ellis et al., *Higgs decay to $\tau^+\tau^-$: A possible signature of intermediate mass Higgs bosons at the SSC*, Nucl. Phys. **B**297 (1988) 221. 11.3.2

[145] I. Stewart and F. Tackmann, *Theory uncertainties for Higgs mass and other searches using jet bins*, Phys. Rev. **D**85 (2012) 034011. 11.4.5, 11.5

[146] ATLAS and CMS Collaborations, *Procedure for the LHC Higgs boson search combination in Summer 2011*, ATL-PHYS-PUB-2011-011, CERN-CMS-NOTE-2011-005 (2011) . http://cdsweb.cern.ch/record/1375842. 11.5

[147] H.-L. Lai et al., *New parton distributions for collider physics*, Phys. Rev. **D**82 (2010) 074024. 11.5

[148] S. Alekhin, S. Alioli, R. D. Ball, V. Bertone, J. Blumlein, et al., *The PDF4LHC Working Group Interim Report*, arXiv:1101.0536 [hep-ph]. 11.5

[149] A. Martin, W. Stirling, R. Thorne, and G. Watt, *Parton distributions for the LHC*, Eur.Phys.J. **C**63 (2009) 189. 11.5

[150] R. D. Ball, V. Bertone, F. Cerutti, L. D. Debbio, S. Forte, et al., *Impact of heavy quark masses on parton distributions and LHC phenomenology*, Nucl. Phys. **B**849 (2011) 296, arXiv:1101.1300 [hep-ph]. 11.5

[151] ATLAS Collaboration, *Jet energy measurement with the ATLAS detector in proton-proton collisions at $\sqrt{s} = 7$ TeV*, submitted to Eur. Phys. J. **C** (2011) , arXiv:1112.6426 [hep-ex]. 11.5

[152] G. Cowan, K. Cranmer, E. Gross, and O. Vitells, *Asymptotic formulae for likelihood-based tests of new physics*, Eur. Phys. J. **C**71 (2011) 1554. 11.6, 11.6

[153] A. L. Read, *Presentation of search results: The CL_s technique*, J. Phys. **G**28 (2002) 2693. 11.6

[154] ATLAS Collaboration, *Observation of an excess of events in the search for the Standard Model Higgs boson in the $H \to ZZ^{(*)} \to 4\ell$ channel with the ATLAS detector*, ATLAS-CONF-2012-092 (2012) . http://cdsweb.cern.ch/record/1460411. 12

[155] ATLAS Collaboration, *Observation of an excess of events in the search for the Standard Model Higgs boson in the gamma-gamma channel with the ATLAS detector*, ATLAS-CONF-2012-091 (2012) . http://cdsweb.cern.ch/record/1460410. 12

[156] ATLAS Collaboration, *Search for the Standard Model Higgs boson in the $H \to \tau^+\tau^-$ decay mode in $\sqrt{s} = 7$ TeV pp collisions with ATLAS*, submitted to JHEP (2012) , arXiv:1206.5971 [hep-ex]. 12.2

[157] ATLAS Collaboration, *Search for the Standard Model Higgs boson produced in association with a vector boson and decaying to a b-quark pair with the ATLAS detector*, submitted to Phys. Lett. **B** (2012) , arXiv:1207.0210 [hep-ex]. 12.2

[158] ATLAS Collaboration, *Search for a Standard Model Higgs boson in the $H \to ZZ \to ll\nu\nu$ decay channel using 4.7 fb^{-1} of $\sqrt{s} = 7$ TeV data with the ATLAS detector*, submitted to Phys. Lett. **B** (2012) , arXiv:1205.6744 [hep-ex]. 12.2

[159] ATLAS Collaboration, *Search for a Standard Model Higgs boson in the mass range 200-600 GeV in the $H \to ZZ \to llqq$ decay channel*, submitted to Phys. Lett. **B** (2012) , arXiv:1206.2443 [hep-ex]. 12.2

[160] ATLAS Collaboration, *Search for the Higgs boson in the $H \to WW \to l\nu jj$ decay channel at $\sqrt{s} = 7$ TeV with the ATLAS detector*, submitted to Phys. Lett. **B** (2012) , arXiv:1206.6074 [hep-ex]. 12.2

[161] L. D. Landau, *The moment of a 2-photon system*, Dokl. Akad. Nawk. **U**SSR 60 (1948) 207. 12.3

[162] C. N. Yang, *Selection Rules for the Dematerialization of a Particle Into Two Photons*, Phys. Rev. **77** (1950) 242. 12.3